



# REE MARINE GEOCHEMISTRY IN THE 21ST CENTURY: A TRIBUTE TO THE PIONEERING RESEARCH OF HENRY ELDERFIELD (1943–2016)

EDITED BY: Johan Schijf, Catherine Jeandel, Karen Johannesson and  
Anne H. Osborne

PUBLISHED IN: Frontiers in Marine Science



# frontiers

## Frontiers eBook Copyright Statement

The copyright in the text of individual articles in this eBook is the property of their respective authors or their respective institutions or funders. The copyright in graphics and images within each article may be subject to copyright of other parties. In both cases this is subject to a license granted to Frontiers.

The compilation of articles constituting this eBook is the property of Frontiers.

Each article within this eBook, and the eBook itself, are published under the most recent version of the Creative Commons CC-BY licence.

The version current at the date of publication of this eBook is CC-BY 4.0. If the CC-BY licence is updated, the licence granted by Frontiers is automatically updated to the new version.

When exercising any right under the CC-BY licence, Frontiers must be attributed as the original publisher of the article or eBook, as applicable.

Authors have the responsibility of ensuring that any graphics or other materials which are the property of others may be included in the CC-BY licence, but this should be checked before relying on the CC-BY licence to reproduce those materials. Any copyright notices relating to those materials must be complied with.

Copyright and source acknowledgement notices may not be removed and must be displayed in any copy, derivative work or partial copy which includes the elements in question.

All copyright, and all rights therein, are protected by national and international copyright laws. The above represents a summary only. For further information please read Frontiers' Conditions for Website Use and Copyright Statement, and the applicable CC-BY licence.

ISSN 1664-8714

ISBN 978-2-88963-655-6

DOI 10.3389/978-2-88963-655-6

## About Frontiers

Frontiers is more than just an open-access publisher of scholarly articles: it is a pioneering approach to the world of academia, radically improving the way scholarly research is managed. The grand vision of Frontiers is a world where all people have an equal opportunity to seek, share and generate knowledge. Frontiers provides immediate and permanent online open access to all its publications, but this alone is not enough to realize our grand goals.

## Frontiers Journal Series

The Frontiers Journal Series is a multi-tier and interdisciplinary set of open-access, online journals, promising a paradigm shift from the current review, selection and dissemination processes in academic publishing. All Frontiers journals are driven by researchers for researchers; therefore, they constitute a service to the scholarly community. At the same time, the Frontiers Journal Series operates on a revolutionary invention, the tiered publishing system, initially addressing specific communities of scholars, and gradually climbing up to broader public understanding, thus serving the interests of the lay society, too.

## Dedication to Quality

Each Frontiers article is a landmark of the highest quality, thanks to genuinely collaborative interactions between authors and review editors, who include some of the world's best academicians. Research must be certified by peers before entering a stream of knowledge that may eventually reach the public - and shape society; therefore, Frontiers only applies the most rigorous and unbiased reviews.

Frontiers revolutionizes research publishing by freely delivering the most outstanding research, evaluated with no bias from both the academic and social point of view. By applying the most advanced information technologies, Frontiers is catapulting scholarly publishing into a new generation.

## What are Frontiers Research Topics?

Frontiers Research Topics are very popular trademarks of the Frontiers Journals Series: they are collections of at least ten articles, all centered on a particular subject. With their unique mix of varied contributions from Original Research to Review Articles, Frontiers Research Topics unify the most influential researchers, the latest key findings and historical advances in a hot research area! Find out more on how to host your own Frontiers Research Topic or contribute to one as an author by contacting the Frontiers Editorial Office: [researchtopics@frontiersin.org](mailto:researchtopics@frontiersin.org)

# REE MARINE GEOCHEMISTRY IN THE 21ST CENTURY: A TRIBUTE TO THE PIONEERING RESEARCH OF HENRY ELDERFIELD (1943–2016)

Topic Editors:

**Johan Schijf**, University of Maryland Center for Environmental Science (UMCES), United States

**Catherine Jeandel**, UMR5566 Laboratoire d'études en géophysique et océanographie spatiales (LEGOS), France

**Karen Johannesson**, University of Massachusetts Boston, United States

**Anne H. Osborne**, GEOMAR Helmholtz Center for Ocean Research Kiel, Germany

**Citation:** Schijf, J., Jeandel, C., Johannesson, K. H., Osborne, A. H., eds. (2020). REE Marine Geochemistry in the 21st Century: A Tribute to the Pioneering Research of Henry Elderfield (1943–2016). Lausanne: Frontiers Media SA. doi: 10.3389/978-2-88963-655-6

# Table of Contents

- 04 Editorial: REE Marine Geochemistry in the 21st Century: A Tribute to the Pioneering Research of Henry Elderfield (1943–2016)**  
Johan Schijf, Catherine Jeandel, Karen H. Johannesson and Anne H. Osborne
- 06 Rare Earth Elements Geochemistry and Nd Isotopes in the Mississippi River and Gulf of Mexico Mixing Zone**  
Segun B. Adebayo, Minming Cui, Travis Hong, Christopher D. White, Ellen E. Martin and Karen H. Johannesson
- 24 Rare Earth Elements in Andaman Island Surface Seawater: Geochemical Tracers for the Monsoon?**  
Ed C. Hathorne, Martin Frank and P. M. Mohan
- 43 Effect of Mg and Ca on the Stability of the MRI Contrast Agent Gd–DTPA in Seawater**  
Johan Schijf and Isabel J. Christy
- 60 TAG Plume: Revisiting the Hydrothermal Neodymium Contribution to Seawater**  
Torben Stichel, Katharina Pahnke, Brian Duggan, Steven L. Goldstein, Alison E. Hartman, Ronja Paffrath and Howie D. Scher
- 71 The Impact of Benthic Processes on Rare Earth Element and Neodymium Isotope Distributions in the Oceans**  
Brian A. Haley, Jianghui Du, April N. Abbott and James McManus
- 83 Are Clay Minerals the Primary Control on the Oceanic Rare Earth Element Budget?**  
April N. Abbott, Stefan Löhr and Megan Trethewy
- 102 Shelf Inputs and Lateral Transport of Mn, Co, and Ce in the Western North Pacific Ocean**  
Peter L. Morton, William M. Landing, Alan M. Shiller, Amy Moody, Thomas D. Kelly, Michael Bizimis, John R. Donat, Eric H. De Carlo and Joseph Shacat
- 127 The Influence of Basaltic Islands on the Oceanic REE Distribution: A Case Study From the Tropical South Pacific**  
Mario Molina-Kescher, Ed C. Hathorne, Anne H. Osborne, Melanie K. Behrens, Martin Kölling, Katharina Pahnke and Martin Frank
- 146 Rare Earth Element Distribution in the NE Atlantic: Evidence for Benthic Sources, Longevity of the Seawater Signal, and Biogeochemical Cycling**  
Kirsty C. Crocket, Emily Hill, Richard E. Abell, Clare Johnson, Stefan F. Gary, Tim Brand and Ed C. Hathorne
- 168 Differentiating Lithogenic Supplies, Water Mass Transport, and Biological Processes On and Off the Kerguelen Plateau Using Rare Earth Element Concentrations and Neodymium Isotopic Compositions**  
Melanie Grenier, Ester Garcia-Solsona, Nolwenn Lemaitre, Thomas W. Trull, Vincent Bouvier, Philippe Nonnotte, Pieter van Beek, Marc Souhaut, Francois Lacan and Catherine Jeandel





# Editorial: REE Marine Geochemistry in the 21st Century: A Tribute to the Pioneering Research of Henry Elderfield (1943–2016)

Johan Schijf<sup>1\*</sup>, Catherine Jeandel<sup>2</sup>, Karen H. Johannesson<sup>3</sup> and Anne H. Osborne<sup>4</sup>

<sup>1</sup> Chesapeake Biological Laboratory, University of Maryland Center for Environmental Science, Solomons, MD, United States, <sup>2</sup> LEGOS, Université Toulouse III—Paul Sabatier (CNRS, UPS, IRD, CNES), Toulouse, France, <sup>3</sup> School for the Environment, University of Massachusetts Boston, Boston, MA, United States, <sup>4</sup> GEOMAR, Helmholtz Centre for Ocean Research, Kiel, Germany

**Keywords:** Henry Elderfield, rare earth elements (REE), Nd isotopes, seawater, mass balance, trace metal cycling, scavenging, boundary exchange

## Editorial on the Research Topic

### REE Marine Geochemistry in the 21st Century: A Tribute to the Pioneering Research of Henry Elderfield (1943–2016)

This Research Topic (RT), inspired by an identically titled special session at the 2017 ASLO Aquatic Sciences Meeting in Honolulu, was established in honor and recognition of the pioneering research of Henry (Harry) Elderfield, who passed away in April 2016 after a long career in marine geochemistry. Although Harry's scientific interests and impacts were manifold, he will probably be most remembered for his seminal work on the chemical analysis and interpretation of rare earth element (REE) distributions in the ocean. In his early landmark monograph (Elderfield, 1988), which was based on very limited data yet, as several of our authors note, remains relevant to this day, Harry keenly recognized the main REE sources in seawater: rivers, aerosols, hydrothermal vents, and marine sediments. Their relative importance is a major focus of this RT.

Adebayo et al. analyzed water and suspended particles from the Mississippi River estuary, one of the largest in the world. They show HREE-enriched dissolved patterns and a degree of REE removal well below the global average, attributing this to the elevated pH and extensive complexation with organic ligands. Labile fractions of particles and sediments were found to have more radiogenic  $\epsilon_{Nd}$  values than the river water. These observations illustrate that the scavenging processes that curtail the riverine REE flux are still not fully understood. Hathorne et al. investigated the temporal and spatial dynamics of REE patterns and  $\epsilon_{Nd}$  in a 3-year time series of surface water samples from the Bay of Bengal and Andaman Sea. They discuss putative signals of seasonal discharge from major rivers to the north (including the Ganges and Irrawaddy) within the context of regional geology and the influence of the Andaman Islands, aerosols, and exchange between colloidal and particulate REE pools. Their ultimate goal is to examine whether such signals, potentially recorded in coral skeletons, might be used as a geochemical tracer of the Asian summer monsoon. Schijf and Christy measured the stability of the MRI contrast agent Gd–DTPA in the presence of Mg and Ca at seawater ionic strength. While this organic complex appears impervious to estuarine scavenging and its global release since the late 1980s has caused Gd anomalies in rivers and coastal seawater to increase by orders of magnitude, their results suggest that competition from Mg and Ca may release up to 15% of the bound Gd. This would have significant implications for the bioavailability of this toxic element in sensitive nearshore ecosystems. Stichel et al. demonstrate substantial Nd

## OPEN ACCESS

### Edited and reviewed by:

Sunil Kumar Singh,  
Physical Research Laboratory, India

### \*Correspondence:

Johan Schijf  
schijf@umces.edu

### Specialty section:

This article was submitted to  
Marine Biogeochemistry,  
a section of the journal  
Frontiers in Marine Science

**Received:** 19 December 2019

**Accepted:** 12 February 2020

**Published:** 04 March 2020

### Citation:

Schijf J, Jeandel C, Johannesson KH  
and Osborne AH (2020) Editorial: REE  
Marine Geochemistry in the 21st  
Century: A Tribute to the Pioneering  
Research of Henry Elderfield  
(1943–2016). *Front. Mar. Sci.* 7:114.  
doi: 10.3389/fmars.2020.00114

depletion within the Trans-Atlantic Geotraverse (TAG) hydrothermal plume, accompanied by a shift to more radiogenic  $\epsilon_{\text{Nd}}$  values. Extrapolation to a global estimate, using on-axis heat fluxes, an empirical correlation with excess  $^3\text{He}$ , and comparison with vertical profiles at the nearby unaffected Bermuda Atlantic Time-Series (BATS) station, yields a Nd sink equal to about 70% of the combined river and dust inputs (6–8% of the global REE flux). The  $\epsilon_{\text{Nd}}$  shift confirms that REE scavenging within hydrothermal plumes involves a process similar to marine boundary exchange, but at only 0.1% of the scale.

Although Harry was already aware of the importance of sediments and porewaters as an oceanic REE source (Elderfield, 1988), he may not then have realized the extent to which this flux was underestimated and likely accounts for the puzzling “Nd paradox”. Using a review of existing data, Haley et al. argue that the Nd paradox is more likely to be reconciled by a “bottom-up” model based on predominantly benthic inputs than by current “top-down” models that emphasize surface inputs and reversible scavenging. They discuss the ramifications of such a model for the interpretation of modern and paleoceanic Nd distributions. Abbott et al. aim to formalize this idea by presenting micro-spectroscopic analyses of various sediments and pore waters from the Pacific Ocean that promote authigenic clays as the mineral phase primarily responsible for the benthic REE inputs. They propose that REE–Fe correlations, generally interpreted in terms of REE sorption by ferromanganese oxides, may actually be due to control by Fe-rich clay minerals like glauconite.

Two papers study boundary exchange in more detail, but in very different settings. Morton et al. show that the northwest Pacific shelf is the source of an extensive dissolved Mn plume that is oxidized to particulate Mn, possibly by biological activity, and rapidly transported offshore by the Kuroshio Current, while scavenging other redox-sensitive elements like Ce and Co. However, whereas Mn and Ce are removed by settling within the coastal zone, the Co signal endures (probably by organic complexation of the higher oxidation state) and can be tracked across most of the Pacific basin. Molina-Kescher et al. measured REE concentrations and  $\epsilon_{\text{Nd}}$  in coastal, river, and sub-marine

groundwater discharge (SGD) samples throughout Tahiti and in seawater within the predominant circulation downstream of the islands. They find that all terrestrial and coastal seawater samples have a clear signature of the local basaltic rock with elevated MREE concentrations and Eu anomalies and radiogenic  $\epsilon_{\text{Nd}}$  values. The REE pattern characteristics are lost in mid-depth AAIW as it mixes with other water masses, but the isotopic signal persists, indicating that basaltic islands may have a significant capacity for influencing  $\epsilon_{\text{Nd}}$  on basin-wide scales.

The last two papers view oceanic REE cycling from a broader perspective, including benthic and advective processes in the deep ocean, as well as authigenic and/or biologically driven reversible scavenging near the surface. Crockett et al. highlight the role of complex hydrography across the major channels between Iceland and Scotland. Grenier et al. highlight terrestrial inputs across the Kerguelen Plateau in the Indian sector of the Southern Ocean. Both studies were conducted against the backdrop of an incipient spring plankton bloom, conveying clear REE fractionation signals in the upper water column.

If all these excellent papers are any indication, the next decades of REE marine geochemistry promise to be equally exciting. We hope they will be enjoyed by many readers of *Frontiers*.

## AUTHOR CONTRIBUTIONS

JS wrote the editorial with contributions and final approval from the other three authors, who are listed in alphabetical order. All editors were equal participants in this Research Topic.

## ACKNOWLEDGMENTS

We all owe a debt of gratitude to Harry Elderfield, to whom this RT is dedicated, either for his professional guidance and personal kindness, or as one of the founding fathers of our common research field. We thank all authors of this RT for their contributions and their patience, as well as the reviewers for their time and dedication. This is UMCES contribution #5754.

## REFERENCES

- Elderfield, H. (1988). The oceanic chemistry of the rare-earth elements. *Phil. Trans. Royal Soc. London A* 325, 105–126.

**Conflict of Interest:** The authors declare that the research was conducted in the absence of any commercial or financial relationships that could be construed as a potential conflict of interest.

Copyright © 2020 Schijf, Jeandel, Johannesson and Osborne. This is an open-access article distributed under the terms of the Creative Commons Attribution License (CC BY). The use, distribution or reproduction in other forums is permitted, provided the original author(s) and the copyright owner(s) are credited and that the original publication in this journal is cited, in accordance with accepted academic practice. No use, distribution or reproduction is permitted which does not comply with these terms.



# Rare Earth Elements Geochemistry and Nd Isotopes in the Mississippi River and Gulf of Mexico Mixing Zone

Segun B. Adebayo<sup>1\*</sup>, Minming Cui<sup>1</sup>, Travis Hong<sup>1</sup>, Christopher D. White<sup>1</sup>, Ellen E. Martin<sup>2</sup> and Karen H. Johannesson<sup>1</sup>

<sup>1</sup> Department of Earth and Environmental Sciences, Tulane University, New Orleans, LA, United States, <sup>2</sup> Department of Geological Sciences, University of Florida, Gainesville, FL, United States

## OPEN ACCESS

### Edited by:

Selvaraj Kandasamy,  
Xiamen University, China

### Reviewed by:

Waliur Rahaman,  
National Centre for Antarctic and  
Ocean Research, India  
Nagender Nath Bejugam,  
National Institute of Oceanography  
(CSIR), India  
Armstrong-Altrin John S.,  
Universidad Nacional Autónoma de  
México, Mexico

### \*Correspondence:

Segun B. Adebayo  
sadebay@tulane.edu

### Specialty section:

This article was submitted to  
Marine Biogeochemistry,  
a section of the journal  
Frontiers in Marine Science

Received: 05 December 2017

Accepted: 25 April 2018

Published: 16 May 2018

### Citation:

Adebayo SB, Cui M, Hong T,  
White CD, Martin EE and  
Johannesson KH (2018) Rare Earth  
Elements Geochemistry and Nd  
Isotopes in the Mississippi River and  
Gulf of Mexico Mixing Zone.  
Front. Mar. Sci. 5:166.  
doi: 10.3389/fmars.2018.00166

Rare earth elements (REE) concentrations were measured in surface waters collected across the salinity gradient in the Mississippi River estuary (i. e., Mississippi River plume, MRP), which includes the near-shore portion of the Louisiana Shelf. In addition, the neodymium (Nd) isotope compositions of two river water samples, and the acid leachable fractions of the associated suspended particulate matter (SPM), were quantified to compare Mississippi River water, and SPM with Gulf of Mexico waters. Despite the spatial limitations associated with sampling due to the size of the Mississippi River system, this study provides some important insights into the REE geochemistry of the MRP. The Mississippi River and its estuarine waters are enriched in the heavy REE (HREE) compared to the light REE (LREE) when normalized to shale composites. All water samples from the estuary also exhibit substantial negative Ce anomalies. In contrast to the majority of other estuaries investigated, removal of REE in the low salinity reaches of the Mississippi River estuary is less substantial. For example, approximately 50% of the river borne Nd is removed in the low salinity region ( $S < 10$ ) of the Mississippi River estuary, compared to the estimated global average of ca. 70% removal of Nd for estuaries worldwide. We propose that the relatively low REE removal in the Mississippi estuary reflects the high pH ( $\sim 8$ ) of the Mississippi River, where REE complexation with carbonate ions and natural organic ligands act to stabilize REE in solution. The Nd isotope composition of Mississippi River water near its outflow to the Gulf of Mexico is  $\epsilon_{Nd(0)} = -10.5$ . The acid leachable fraction of the associated SPM is more radiogenic ( $-9.95 \leq \epsilon_{Nd(0)} \leq -9.77$ ), and closer to the generally more radiogenic Gulf of Mexico [ $\epsilon_{Nd(0)} = -9.0$ ]. Sequential extraction of the Mississippi River bank sediment reveals substantially different Sm/Nd ratios for the operationally defined fractions of the sediment, which suggests variations in Nd isotope compositions between the labile fractions and the bulk sediment.

**Keywords:** Mississippi River, rare earth elements, Nd isotopes, estuary, Gulf of Mexico

## INTRODUCTION

Rivers, followed by atmospheric deposition, are considered the chief sources of rare earth elements (REE), and hence neodymium (Nd), to the ocean (Goldstein et al., 1984; Tachikawa et al., 2003). The REE and Nd isotopes are applied in tracing biogeochemical processes, and past/modern ocean circulation, hence, the need to better understand REE speciation and mass transfer between

major rivers and the ocean. Estuaries are the interface between rivers and the ocean, wherein REE compositions of rivers undergo substantial transformation. This non-conservative behavior of REE in estuaries is commonly attributed to sea salt induced coagulation of colloids (Edzwald et al., 1974; Elderfield et al., 1990; Sholkovitz and Szymczak, 2000; Rousseau et al., 2015). However, other complex processes are increasingly reported to exert important controls over mass transfer to the oceans. These processes include: (1) “boundary exchange”, shallow pore water fluxes, and submarine groundwater discharge (SGD) acting along ocean–continent margins; (2) pore water fluxes in the deep ocean; and (3) reversible scavenging with sinking particles, in the water column (Lacan and Jeandel, 2001; Johannesson and Burdige, 2007; Abbott et al., 2015; Du et al., 2016; Jeandel, 2016). Sorting out the relative importance of these processes to mass fluxes in the ocean remains a daunting challenge.

The application of Nd isotopes in tracing oceanic water mass circulation is limited by the relatively poor constraints on Nd sources and sinks in the ocean (Lacan and Jeandel, 2001; Goldstein and Hemming, 2003; Jeandel et al., 2007; Jeandel and Oelkers, 2015). Related to this is the so-called “Nd paradox,” which is the apparent decoupling of dissolved Nd concentrations and Nd isotopes (Lacan and Jeandel, 2001; Goldstein and Hemming, 2003; Tachikawa et al., 2003; Siddall et al., 2008; Arsouze et al., 2009). Specifically, Nd concentrations have nutrient-like water column profiles suggestive of vertical cycling and relatively long, ca.  $10^4$  years, oceanic residence times, whereas Nd isotope ratios exhibit inter- and intra-ocean differences, which supports an oceanic Nd residence time similar to <500–1,500 years. Hence, more quantitative spatial and temporal understanding of the sources and sinks of the REE in the ocean is required to resolve the Nd paradox, which includes better understanding of the dynamics of REE in estuaries.

The lower Mississippi River and its associated estuary is an ideal location to investigate the importance of riverine REE fluxes from a major world river that debouches over a broad, shallow continent-ocean margin, where “boundary exchange” may be important. This is because the Mississippi River is the chief source of freshwater and sediment to the Gulf of Mexico (Trefry and Shokes, 1981), which is a partially closed ocean basin that is characterized by an extensive continent-ocean margin (ca. 33% of area). Prior studies of the Mississippi River system have looked at the REE geochemistry at locations distant from its mixing zone with the Gulf of Mexico. These previous studies provide important insights, such as compositions of the REE in the river water, suspended particulate matter, and Nd isotopic compositions of the phases (e.g., Goldstein and Jacobsen, 1988a,b; Sholkovitz, 1995; Shiller, 2002; Bayon et al., 2015), coupled with temporal variations in the REE compositions of the river water (Shiller, 2002). Although it seems likely that the Mississippi River is a substantial source of REE to the Gulf of Mexico, and especially the northern and eastern Gulf, there have been no systematic investigations of the REE or Nd isotopes in its associated estuary. Consequently, there is a need to ascertain the importance of the Mississippi River water and/or sediment as source(s) of REE to the Gulf of Mexico.

Here, we present new REE and Nd isotope data for waters, suspended particulate matter (SPM), and riverbank sediment from the lower Mississippi River and its associated estuary (i.e., Mississippi River plume; MRP) on the Louisiana Shelf. These data are employed to probe the geochemical processes that influence the transfer of REE from the Mississippi River to the Gulf of Mexico, in an effort to begin to assess the importance of the river on the REE and Nd isotope systematics of the Gulf.

## STUDY SITE

The study site along the lower Mississippi River and its associated estuary on the Louisiana Shelf is shown in **Figure 1**. The Mississippi River is the seventh largest river in the world in terms of both water and sediment discharge to the ocean, and is the largest river draining North America, with sediment and water discharges of  $210 \times 10^6$  tons year<sup>-1</sup> and  $530 \times 10^9$  m<sup>3</sup> year<sup>-1</sup>, respectively (McKee et al., 2004). During high flow periods, which commonly occur in spring and early summer, discharge from the Mississippi River mouth is great enough to form a stratified estuary over the Louisiana Shelf (i.e., the MRP), whereas during low discharge, a partially mixed salt wedge estuary forms within the distributary channels of the river, in the birdfoot delta (Shiller and Boyle, 1991). The differences in seasonal discharge typically lead to highly variable spatial salinity distributions in the Mississippi River estuary and Louisiana Shelf. Most of the Mississippi River discharge reaches the Gulf of Mexico through three major distributaries in the birdfoot delta: Pass á l’Ostre, Southwest Pass, and South Pass (Shiller and Boyle, 1991). The samples reported in this study were collected along the Southwest Pass and out into the Louisiana Bight of the Gulf of Mexico. The Southwest Pass was chosen for this study because it empties westward along the Louisiana-Texas shelf, where approximately 50% of the Mississippi River’s discharge flows (Bianchi et al., 2010).

## METHODS

### Sample Collection

Water sampling was done using Teflon<sup>®</sup> tubing via a peristaltic pump and transferred into high-density polyethylene (HDPE) sample bottles, all of which were pre-cleaned following trace metal cleaning procedures (e.g., Johannesson et al., 2004). A total of 15 water samples were collected for analysis of REE concentrations. Thirteen water samples from the Louisiana Bight (labeled 0–10, **Figure 1**; **Table 1**), which include 9 surface water samples (~1 m depths), and 4 deeper water samples (>6 m depths) from two locations (labeled 6 and 10, **Figure 1**; **Table 1**), were collected in June 2014. Two “fresh” (salinity,  $S \approx 0$ ) Mississippi River water and SPM samples were collected in January 2016, for REE concentrations and Nd isotopes analyses. Both river water samples are labeled “MR” in **Figure 1**, with one collected in the river channel, whereas the second water sample was obtained nearby, from a crevasse where the river spills across its natural levee into Breton Sound. The water samples were filtered through 0.45  $\mu$ m Gelman Sciences (polysulfone ether membrane) high capacity filters during sample collection.



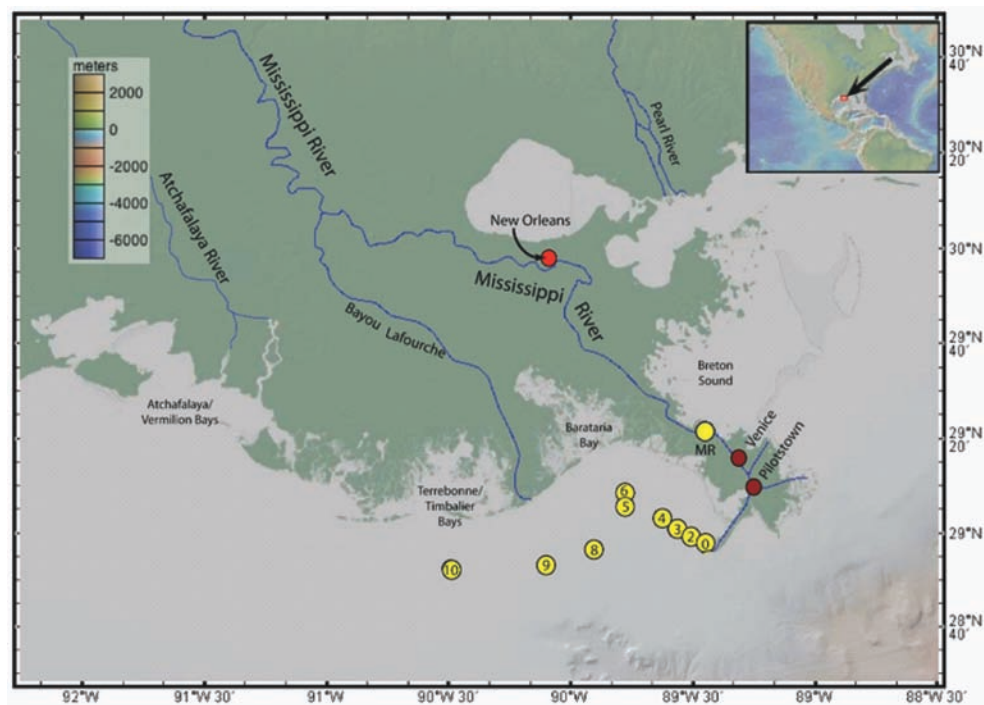


**FIGURE 1** | Lower Mississippi River delta showing the sampling locations of waters (yellow circles), SPM (yellow circle labeled “MR”), and sediment (bright red circle labeled “New Orleans”). The dark red circles labeled “Venice” and “Pilotstown” show the locations of the earlier  $\epsilon_{\text{Nd}(t)}$  measurements by Stordal and Wasserburg (1986). Atchafalaya River and Bayou Lafourche are major and minor, respectively, distributaries of the MR. Base map from GeoMapApp.

The filter capsules were transferred to clean zip-lock<sup>®</sup> style polyethylene bags for analysis of the SPM collected by the filter membrane.

The filtered water samples were returned to the laboratory where they were acidified inside a class 100 (ISO 5 rated) clean room to pH < 2 with ultrapure HNO<sub>3</sub> (Thermo Fisher Optima<sup>™</sup>) within 24 h of collection. Acidification is to prevent iron and manganese oxide/oxyhydroxide precipitation, and adsorption losses of the REE to the sample bottle walls. In addition to the water samples, a sediment sample was collected from the Mississippi River bank at New Orleans (labeled “New Orleans”; **Figure 1**), for analysis of total REE contents and by sequential extraction. The sediment sample was collected by grab sampling into clean zip-lock<sup>®</sup> style polyethylene plastic bags for transport to the laboratory where it was oven dried at ca. 80°C and stored prior to analysis.

## Sample Analysis

Sample preparation procedures for all analyses in this study were performed within a Class 100 (ISO 5 rated) laminar flow clean bench and/or clean laboratory. Major cations (Ca<sup>2+</sup>, Mg<sup>2+</sup>, Na<sup>+</sup>, K<sup>+</sup>) concentrations in Mississippi River water were analyzed on acidified samples by high resolution inductively coupled plasma mass spectrometry (HR-ICP-MS; Thermo Fisher Element II), as described previously (Chevis et al., 2015; Johannesson et al., 2017). Anion concentrations (Cl<sup>-</sup>, SO<sub>4</sub><sup>2-</sup>, NO<sub>3</sub><sup>-</sup>, F<sup>-</sup>) were determined in unacidified river water samples by Dr. Susan Welch via ion chromatography (Dionex DX-3000) at Ohio State

University, following the approach of Welch et al. (1996). The temperature, dissolved oxygen concentrations, turbidity, and salinity of the Mississippi River estuary samples were determined on-site using a Seabird SBE 19+ v2 multi-meter, whereas pH was measured using a waterproof double junction pHTestr<sup>®</sup> 30 pH electrode.

Mississippi River and estuary waters were analyzed for REE using pre-established methods (e.g., Johannesson et al., 2011, 2017; Chevis et al., 2015). Aliquots (30 mL) of the filtered and acidified water samples were loaded onto Bio-Rad<sup>®</sup> Poly-Prep columns packed with ~2 mL of Bio-Rad<sup>®</sup> AG 50W-X8 (200–400 mesh, hydrogen form) cation exchange resin. Prior to loading, the columns were pre-cleaned using alternating 10 mL rinses of 6 M ultra-pure hydrochloric acid (HCl) and Millipore-Q water (18.2 MΩ cm). After loading the samples on the columns, Fe and Ba were sequentially eluted from the columns by rinsing, first with 3 mL of 1.75 M ultra-pure HCl, followed by 3 mL of 2 M ultra-pure HNO<sub>3</sub> (Greaves et al., 1989). The REE were then eluted from the columns using 10 mL of 8 M ultrapure HNO<sub>3</sub>, and collected into pre-cleaned Teflon<sup>®</sup> beakers. The REE eluents were subsequently evaporated to near dryness and then re-dissolved in 10 mL of 1% (v/v) ultrapure HNO<sub>3</sub> solution. Aliquots (30 mL) of the National Research Council Canada (Ottawa, Canada) Standard Reference Material (SRM) for estuarine waters (SLEW-3) were also loaded onto identical columns, as were 30 mL aliquots of Millipore-Q water, which acted as analytical blanks (e.g., Johannesson et al., 2017). The column separation converted the original 30 mL sample aliquot



**TABLE 1** | Field parameters characterizing the Mississippi River and estuary water samples, with individual sampling location and collection depth.

Sampling point no. <sup>‡</sup>	Latitude	Longitude	Sample Depth (m)	Temp (°C)	Salinity	DO (mmol kg <sup>-1</sup> )	Turbidity (NTU)	pH
MR	29°21.463'N	89°26.461'W	~1	–	0	–	–	7.8
0	28°58.156'N	89°25.820'W	1.3	28.0	8.2	0.26	54.5	8.1
2	28°59.104'N	89°30.211'W	1.3	29.8	22.8	0.22	1.1	8.3
3	29°00.668'N	89°33.842'W	1.1	29.6	22.6	0.22	28.7	8.4
4	29°03.164'N	89°37.448'W	1.2	29.6	20.9	0.21	39.9	8.4
5	29°05.951'N	89°46.504'W	1.4	29.3	21.4	0.21	50.0	8.4
6a	29°08.564'N	89°46.462'W	17.5	24.4	36.0	0.05	7.5	7.8
6b	29°08.564'N	89°46.462'W	6.2	28.1	31.4	0.16	40.3	8.1
6c	29°08.564'N	89°46.462'W	0.8	29.2	19.8	0.22	44.6	8.4
8	28°56.470'N	89°54.109'W	1.2	30.1	22.4	0.21	83.5	8.5
9	28°53.162'N	90°05.988'W	1.3	30.2	23.1	0.22	39.8	8.5
10a	28°52.284'N	90°29.326'W	16.8	23.6	35.7	0.04	5.7	7.8
10b	28°52.284'N	90°29.326'W	11.1	24.9	34.4	0.11	18.4	8.0
10c	28°52.284'N	90°29.326'W	1.5	29.5	27.5	0.21	36.3	8.3

<sup>‡</sup>Numbers correspond to those given on **Figure 1**.

to a final volume of 10 mL, producing a 3-fold increase in REE concentrations in the solutions introduced to the HR-ICP-MS, which in effect lowered the detection limit by a factor of ~3 for each REE.

Prior to analysis, each 10 mL concentrated aliquot was spiked with <sup>115</sup>In (at 1 µg kg<sup>-1</sup>), as an internal standard. To minimize various polyatomic, oxide/hydroxide, and other mass interferences, multiple resolution configurations were used on the HR-ICP-MS (Chevis et al., 2015). The REE isotopes monitored at various resolutions are as follows: <sup>139</sup>La, <sup>140</sup>Ce, <sup>141</sup>Pr, <sup>143</sup>Nd, <sup>145</sup>Nd, <sup>146</sup>Nd, <sup>147</sup>Sm, <sup>149</sup>Sm, <sup>151</sup>Eu, <sup>153</sup>Eu, <sup>155</sup>Gd, <sup>157</sup>Gd, <sup>158</sup>Gd, <sup>159</sup>Tb, <sup>161</sup>Dy, <sup>163</sup>Dy, <sup>165</sup>Ho, <sup>166</sup>Er, <sup>167</sup>Er, <sup>169</sup>Tm, <sup>172</sup>Yb, <sup>173</sup>Yb, and <sup>175</sup>Lu, at low and high-resolution modes; <sup>139</sup>La, <sup>140</sup>Ce, <sup>141</sup>Pr, <sup>143</sup>Nd, and <sup>145</sup>Nd, at low and medium-resolution modes. We also monitored <sup>151</sup>Eu, <sup>153</sup>Eu, and the HREE in high-resolution mode to resolve interferences from BaO<sup>+</sup> and LREEO<sup>+</sup> species formed in the plasma stream on the two Eu isotopes, and other REEO<sup>+</sup> species on the HREE. A series of REE calibration standard solutions with concentrations 5, 10, 20, 100, 500, and 1,000 ng kg<sup>-1</sup> were prepared from NIST traceable High Purity Standards (Charleston, SC). As an additional check of accuracy, we compared our measured values of the REE for SLEW-3 with those reported by Lawrence and Kamber (2006). The relative standard deviations (RSD) were better than 5% for the determination of REE in the water samples.

Neodymium isotopic compositions of the Mississippi River water samples (labeled “MR”; **Figure 1**), as well as acid leachates of the SPM collected on the 0.45 µm filters, used for filtering these water samples were determined on a Nu Instruments multi-collector ICP-MS at the University of Florida. The Nd isotopic composition is expressed as epsilon neodymium units, ε<sub>Nd(0)</sub>. Epsilon notation is defined as:

$$\varepsilon_{\text{Nd}(0)} = \left[ \frac{(^{143}\text{Nd}/^{144}\text{Nd})_{\text{measured}}}{(^{143}\text{Nd}/^{144}\text{Nd})_{\text{CHUR}}} - 1 \right] \times 10^4, \quad (1)$$

in which  $(^{143}\text{Nd}/^{144}\text{Nd})_{\text{measured}}$  is the isotopes ratio measured in the sample and  $(^{143}\text{Nd}/^{144}\text{Nd})_{\text{CHUR}}$  is the present day Nd isotopes ratio (0.512638) for CHUR (Chondritic Uniform Reservoir; Jacobsen and Wasserburg, 1980).

Before transfer to the University of Florida, the freshwater samples (3 L each) were evaporated to near dryness and then diluted to 30 mL with 2% HNO<sub>3</sub>. The filters were leached to obtain the REE concentrations and Nd isotopic composition of the combined acid leachable fractions (carbonate and/or Fe/Mn oxide/oxyhydroxide minerals) following the procedure of Landing and Lewis (1991). Briefly, the filters were leached at room temperature for 4 h each, first with 20 mL of 25% acetic acid, followed by 20 mL (1:1; volume) mixture of 2 M HCl/1M HNO<sub>3</sub>. The leachates were then combined, evaporated to near dryness, and diluted to 30 mL with 2% HNO<sub>3</sub>, prior to analysis for REE concentrations and Nd isotopic composition.

At the University of Florida, the 30 mL samples were again evaporated to near dryness, and then diluted with 1 M HNO<sub>3</sub>, before passing through TruSpec resins to isolate REE, followed by LnSpec resin to isolate Nd, as modified from Pin and Zalduegui (1997). Procedural blanks of 14 pg Nd, or minimum three orders of magnitude lower than sample abundances were monitored. Samples of isolated Nd were diluted with 2% HNO<sub>3</sub> to achieve <sup>143</sup>Nd monitor peak values of 2–5 V. All samples were analyzed using a desolvating nebulizer (DSN-100), and a time-resolved analysis (TRA) method adopted from Kamenov et al. (2008). All ratios were corrected for mass fractionation using  $^{146}\text{NdO}/^{144}\text{NdO} = 0.7219$ . JNd-1 was run between every 4–5 samples and unknown samples were corrected using the difference between the average of the standard runs and the JNd-1 value of 0.512115 (Tanaka et al., 2000). Long-term external reproducibility of replicate runs of JNd-1 is ±0.000014 (2 sigma), which is equivalent to ±0.3 ε<sub>Nd</sub> units. This external uncertainty is typically larger than internal uncertainties, and the larger of the two errors is assigned to all samples.

The REE concentrations in different operationally defined fractions of Mississippi riverbank sediment were investigated using the sequential extraction procedure of Tessier et al. (1979) and detailed in Willis and Johannesson (2011). Briefly, this procedure consisted of five duplicate sequential leaches of the sediment, with each duplicate step targeting the REE composition of an operationally defined fraction of the sediment. The sediment residue following each step served as input for leaching of the subsequent fraction. The sediment residue was separated from the leachate by centrifugation, and rinsed with Millipore-Q water, before the next leaching step. Fraction 1 represents the easily exchangeable fraction, referring to REE sorbed onto the surface of the sediment. Fraction 2 represents the acid labile fraction, referring to the REE content of the carbonate minerals in the sediment. Fraction 3 represents the reducible fraction, referring to the REE content of the Fe/Mn oxides/oxyhydroxides within the sediment. Fraction 4 represents the oxidizable fraction, referring to the REE content of the organic matter and/or sulfide minerals in the sediment. Lastly, fraction 5 represents the residual fraction, referring to the REE content of silicates and framework minerals in the sediment.

## Solution Complexation Model

Solution complexation modeling of the REE concentrations in Mississippi River water was performed using the Windermere Humic Aqueous Model VII (WHAM VII), which includes the latest version of the Humic Ion Binding Model VII (Tipping, 1994; Tipping et al., 2011). WHAM VII was chosen for the REE speciation modeling because: (1) it is able to model REE complexation with both organic and inorganic ligands; (2) the model predictions agree well with the results of ultrafiltration experiments; and (3) sensitivity analysis indicates that the model correctly predicts the impact of changing ionic strength and competing cations (i.e.,  $\text{Fe}^{3+}$ ,  $\text{Al}^{3+}$ ) on REE complexation with natural organic ligands (Tang and Johannesson, 2003; Pourret et al., 2007; Marsac et al., 2017).

For REE complexation with inorganic ligands, the infinite dilution stability constants for the bicarbonate, carbonate, and dicarbonate lanthanide complexes in the WHAM VII default database were replaced with those from Luo and Byrne (2004). In addition, we replaced the following default database stability constants: hydroxyl complexes with those from Klungness and Byrne (2000); sulfate complexes with those from Schijf and Byrne (2004); chloride complexes with those from Luo and Byrne (2001); and fluoride complexes with those from Luo and Byrne (2000). Furthermore, for REE complexation with humic matter (i.e., humic and fulvic acids), we modified the default database of WHAM VII by replacing the average intrinsic equilibrium constants ( $K_{MA}$ ), with the corresponding values determined by Pourret et al. (2007).

We evaluated REE complexation with dissolved organic and inorganic ligands in the Mississippi River, and for comparison, the Amazon River, the world's largest river, which has been the focus of extensive studies of the REE (e.g., Rousseau et al., 2015 and references therein). The major ions concentrations used for REE complexation modeling (Table 2) in the Mississippi River water are those measured in this study, whereas both major ions,

**TABLE 2 |** Summary of input parameters used for the WHAM VII geochemical modeling.

Major ions*	Miss. River mmol kg <sup>-1</sup>	Amazon River mmol kg <sup>-1</sup>	REE*	Miss. River pmol kg <sup>-1</sup>	Amazon River pmol kg <sup>-1</sup>
HCO <sub>3</sub>	0.94	0.28	La	150	763
Na	0.44	0.07	Ce	239	1,556
Mg	0.51	0.03	Pr	41	220
Ca	0.40	0.09	Nd	184	943
K	0.10	0.02	Sm	42	232
F	0.01	–	Eu	11	68
Cl	0.65	0.03	Gd	52	226
NO <sub>3</sub>	0.03	–	Tb	7	27
SO <sub>4</sub>	0.41	0.02	Dy	41	205
			Ho	9	39
DOC <sup>P</sup>	0.29	0.42	Er	27	108
pH*	7.80	6.89	Tm	4	20
			Yb	24	92
			Lu	4	13

\*Mississippi River data are from river water sample in this study, whereas Amazon River data are from Gaillardet et al. (1997).

<sup>P</sup> Dissolved organic carbon (DOC) in mmol kg<sup>-1</sup>, data from Thurman (1985).

and REE concentrations used for the Amazon River are from the “Amazon 20 after Santarem” location from Gaillardet et al. (1997). Dissolved organic carbon (DOC) concentrations used for modeling of the Mississippi and Amazon Rivers are 290  $\mu\text{mol kg}^{-1}$  and 417  $\mu\text{mol kg}^{-1}$  respectively, obtained from Thurman (1985). Following the approach of Tang and Johannesson (2010), we assumed that fulvic acid is the sole organic phase in the organic matter and that it constitutes 80% of the reported DOC concentrations.

## RESULTS

### General Geochemistry and Major Ions in the Mississippi River Water

Field parameters that characterize the Mississippi River and estuary water samples are presented in Table 1, along with information detailing the specific sample locations (i.e., latitude and longitude), and collection depth. The pH of the waters range from 7.8 in the Mississippi River to 8.5 in the Louisiana Bight. Also, the salinities range from 0 in the Mississippi River to 36 in the Louisiana Bight. Major ions concentrations, including bicarbonate alkalinity of 0.94 mmol kg<sup>-1</sup> measured in the Mississippi river water, as input for geochemical modeling are presented in Table 2, along with data for the Amazon River from Gaillardet et al. (1997).

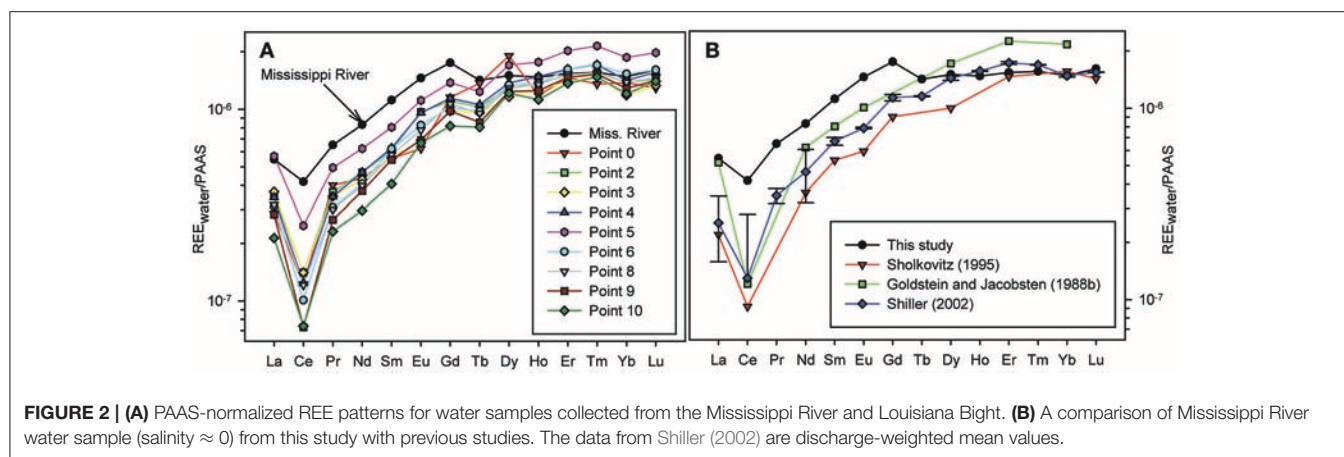
### REE Concentrations of Mississippi River Estuary Waters

The REE concentrations in the water samples are presented in Table 3, and the Post Archean Australian Shale (PAAS; McLennan, 1989) normalized REE fractionation patterns are shown in Figure 2. Shale-normalized REE patterns of Mississippi

**TABLE 3 |** The REE concentrations, relative standard deviation (i.e., instrumental precision), and computed Ce and Gd anomalies of samples from the Mississippi River and Louisiana Shelf.

Sampling Point No.	Concentrations (pmol kg <sup>-1</sup> ) ± RSD.															Gd/Gd*
	La	Ce	Pr	Nd	Sm	Eu	Gd	Tb	Dy	Ho	Er	Tm	Yb	Lu	Ce/Ce*	
MR-channel	150	239	41	184	42	11	52	6.9	41	9.0	27	3.7	24	4.0	0.70	1.34
	1.6	0.6	0.9	2.7	0.5	0.9	3.8	0.2	0.3	0.1	0.1	0.2	0.5	0.1		
MR-crevasse	133	210	37	168	38	10	46	6.4	39	8.5	25	3.5	23	3.8	0.69	1.28
	1.5	0.9	0.4	1.7	0.9	1.6	4.2	0.1	0.5	0.0	0.2	0.1	0.1	0.1		
0	78	70	25	97	21	5	35	6.6	52	7.2	25	3.2	22	3.2	0.36	1.07
	2.4	0.7	1.1	6.6	0.3	0.7	3.5	0.7	2.1	0.7	1.2	0.1	0.8	0.1		
2	98	80	23	104	23	7	33	5.0	35	8.3	26	3.7	22	3.5	0.39	1.24
	2.4	0.1	0.2	2.9	0.7	2.5	1.1	0.2	2.1	0.1	0.8	0.1	1.3	0.1		
3	102	80	22	95	21	5	29	4.6	32	7.7	24	3.5	19	3.3	0.39	1.20
	0.9	2.3	0.7	1.2	0.9	1.8	0.9	0.2	0.6	0.2	0.3	0.1	0.1	0.2		
4	95	71	22	104	23	7	34	5.1	37	9.0	28	4.1	23	3.9	0.36	1.26
	1.1	0.4	0.1	4.5	0.7	0.8	1.1	0.1	0.5	0.1	0.9	0.1	0.3	0.2		
5	155	141	31	138	30	8	41	6.0	46	10.7	35	5.1	30	4.9	0.47	1.27
	2.8	0.5	0.4	1.5	1.2	3.0	0.4	0.1	1.9	0.4	1.4	0.1	0.4	0.1		
6a	94	32	15	71	15	5	23	4.2	34	7.6	25	3.4	21	3.3	0.19	1.10
	0.9	0.4	0.2	1.3	0.3	1.9	0.7	0.1	1.5	0.1	0.6	0.1	0.9	0.1		
6b	75	52	15	68	15	6	21	3.2	26	5.7	19	2.8	16	2.5	0.35	1.21
	1.1	0.8	0.2	2.7	0.7	0.8	0.7	0.1	0.6	0.2	0.8	0.1	0.7	0.2		
6c	85	58	19	90	23	6	31	4.7	36	8.3	28	4.0	25	4.0	0.33	1.20
	1.1	0.1	0.3	1.2	1.3	2.7	1.0	0.1	0.6	0.2	1.1	0.1	0.4	0.1		
8	77	42	17	83	20	5	29	4.1	34	7.6	25	3.6	21	3.5	0.27	1.32
	0.6	0.6	0.3	1.8	0.3	0.9	0.9	0.1	1.7	0.1	0.3	0.1	0.9	0.1		
9	87	69	19	88	22	6	32	4.6	35	8.2	26	3.6	22	3.6	0.39	1.29
	1.0	0.8	0.5	1.8	0.6	2.6	1.6	0.1	1.4	0.2	0.9	0.2	0.8	0.1		
10a	65	28	11	51	12	4	18	3.0	26	5.9	20	2.8	18	2.8	0.24	1.15
	1.0	0.1	0.2	2.4	0.8	1.1	1.0	0.1	0.6	0.1	0.4	0.1	0.6	0.1		
10b	62	37	14	59	12	4	20	3.0	28	5.7	20	2.9	16	2.5	0.30	1.26
	0.2	0.5	0.2	2.3	0.8	1.6	0.4	0.1	0.3	0.2	0.4	0.1	0.3	0.1		
10c	58	42	15	66	15	5	24	3.9	33	6.8	24	3.5	20	3.4	0.33	1.23
	1.0	1.0	0.3	1.9	1.6	1.8	0.6	0.2	0.6	0.3	0.9	0.1	0.8	0.1		

Anomalies:  $Ce/Ce^* = 2[Ce]n/([La]n + [Pr]n)$ ;  $Gd/Gd^* = [Gd]n/(0.33[Sm]n + 0.67[Tb]n)$ , where  $n$  refers to shale-normalized values.

**FIGURE 2 |** (A) PAAS-normalized REE patterns for water samples collected from the Mississippi River and Louisiana Bight. (B) A comparison of Mississippi River water sample (salinity ≈ 0) from this study with previous studies. The data from Shiller (2002) are discharge-weighted mean values.

River and estuarine waters are heavy REE (HREE) enriched (**Figure 2A**), which is consistent with results from previous studies (Goldstein and Jacobsen, 1988a,b; Sholkovitz, 1995; Shiller, 2002; **Figure 2B**). Light REE (LREE) concentrations reported here for the Mississippi River are higher than many of the previous analyses, whereas the HREE concentrations fall within the same range. For example, we measured a Nd concentration of  $184 \text{ pmol kg}^{-1}$  (sample MR in **Table 3**), which is 2.3 times higher than the Nd concentration ( $80 \text{ pmol kg}^{-1}$ ) reported by Sholkovitz (1995), 1.8-fold higher than the discharge-weighted mean ( $103 \text{ pmol kg}^{-1}$ ) of Shiller (2002), and a factor of 1.4 higher than the value of  $138 \text{ pmol kg}^{-1}$  reported by Goldstein and Jacobsen (1988b). However, our La value ( $150 \text{ pmol kg}^{-1}$ ) compares well with the value ( $142 \text{ pmol kg}^{-1}$ ) reported by Goldstein and Jacobsen (1988b). In contrast, our measured Yb concentration of  $24 \text{ pmol kg}^{-1}$  is identical to those determined by Sholkovitz (1995) and Shiller (2002), who reported  $25.3 \text{ pmol kg}^{-1}$  and  $24 \text{ pmol kg}^{-1}$  respectively, and lower than the Yb concentration of  $35 \text{ pmol kg}^{-1}$  reported by Goldstein and Jacobsen (1988b).

All the Mississippi River estuary samples show negative Ce anomalies, with the more saline waters of the Louisiana Bight commonly exhibiting more pronounced negative Ce anomalies compared to the fresh river water (**Table 3; Figure 2**). Specifically, the river water has a Ce anomaly of 0.7, whereas the mean  $\pm 1\sigma$  of waters from the Louisiana Bight is  $0.34 \pm 0.07$ . The estuarine samples also have small, positive Gd anomalies, which initially decrease from  $\sim 1.32$  in the fresh river water to  $\sim 1.05$  in the low salinity sample ( $S = 8$ ), before increasing to values between  $\sim 1.2$  and  $1.3$  within the Louisiana Bight. The mean  $\pm 1\sigma$  of Gd anomalies for waters from the Louisiana Bight is  $1.22 \pm 0.07$ .

Concentrations of selected LREE, middle REE (MREE), and HREE are shown in **Figures 3A–C** as a function of salinity within the Mississippi River estuary. The LREE show a pronounced decrease in concentration with increasing salinity in the Mississippi River estuary, which is not obvious for MREE or HREE. For example, the Nd concentration of the surface waters decrease from  $184 \text{ pmol kg}^{-1}$  in the fresh river water (sample MR) to  $65.8 \text{ pmol kg}^{-1}$  in the most saline water sample collected from the Louisiana Bight (sample 10c,  $S = 27.5$ ; **Figure 3A**). In

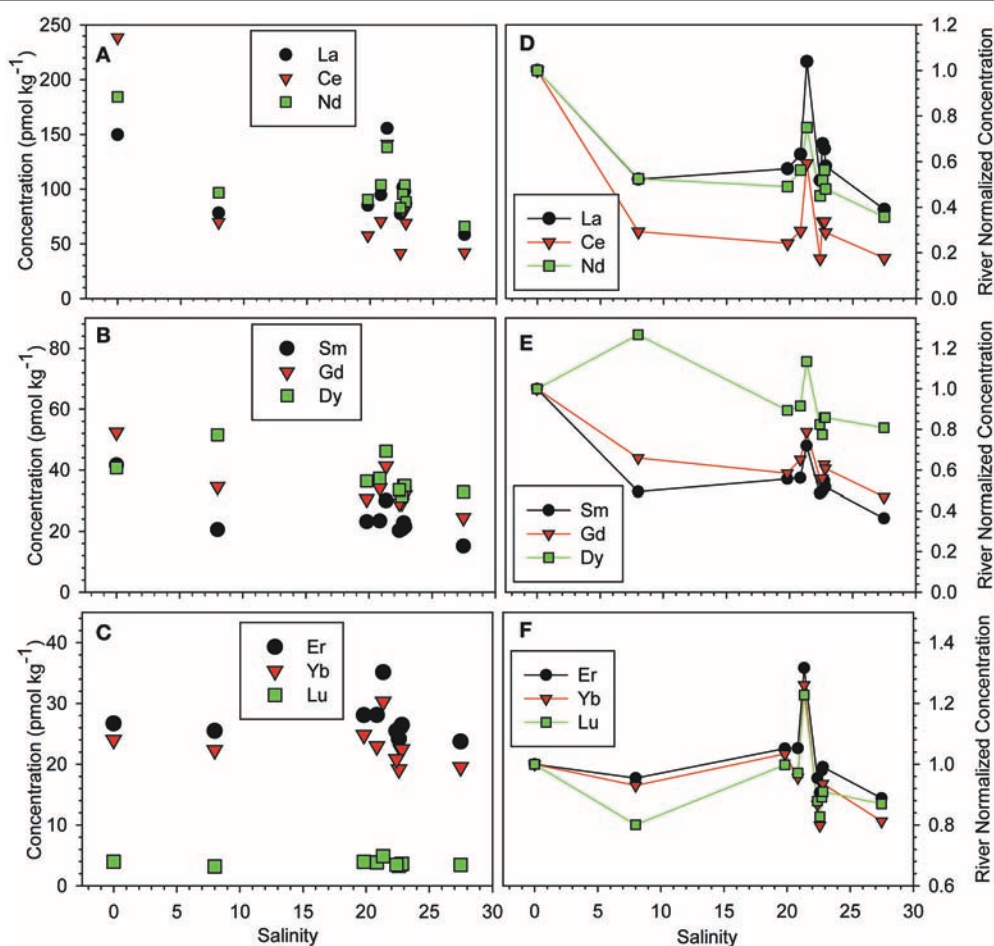


**FIGURE 3 |** Concentrations of selected **(A)** LREE (La, Ce, Nd), **(B)** MREE (Sm, Gd, Dy), and **(C)** HREE (Er, Yb, Lu) as a function of salinity in the Mississippi River estuary. **(D–F)** River normalized concentrations of the same selected LREE, MREE, and HREE as a function of salinity in the Mississippi River estuary.



contrast, the Lu concentration decreases from  $3.96 \text{ pmol kg}^{-1}$  to  $3.45 \text{ pmol kg}^{-1}$  for these same samples (Figure 3C). A notable feature of the Mississippi River estuary is the “spike” in REE concentrations in the mid to high salinity region (i.e.,  $20 \leq S \leq 25$ ), which affects all the REE (Figure 3). For example, Nd increases from 90.4 to  $138.2 \text{ pmol kg}^{-1}$  between salinities 19.8 and 21.3, before decreasing to  $103.8 \text{ pmol kg}^{-1}$  at salinity 22.7. The data indicate that Tm concentrations in this region of the estuary are as much as 40% greater than in the Mississippi River, and Dy values are roughly 27% higher (Figure 3E).

Rare earth elements concentrations of the estuary waters are normalized to the fresh river water sample, and plotted as a function of salinity in Figures 3D–F. These plots reveal that within the low salinity region of the estuary (i.e.,  $S \leq 8$ ), the river water-normalized REE concentrations decrease by as much as 71% for Ce and 48% for Nd (Figure 3D), and as little as 5 and 7% for Er and Yb, respectively (Figure 3F). River water-normalized Nd concentrations for the Mississippi River estuary are compared in Figure 4, to data for the majority of other estuaries studied to date. The outstanding feature of these data is that Nd removal in the Mississippi River estuary is substantially less than observed in these other estuaries. For example, Nd only decreases by ca. 50% in the Mississippi River estuary, compared to ca. 90% in the Amazon River estuary over the same salinity range. The most saline surface water sample from the Mississippi River estuary has a Nd concentration that is ca. 38% of the river water endmember, which translates to an overall removal of 62% for river sourced Nd across the estuary.

## Complexation Model Results

Results of the solution complexation modeling are presented in Figure 5 for the Mississippi River and Amazon River for comparison. In the Mississippi River water, the model predicts that >95% of each REE occurs complexed with humic matter (Figure 5A). For the inorganic complexes, the model predicts e.g., Carbonato complexes,  $\text{LnCO}_3^+$ , to account for at most ~1% of Ce in solution, with the dicarbonato complexes,  $\text{Ln}(\text{CO}_3)_2^-$ , accounting for at most 0.1% of Ce (Figure 5A). Speciation modeling predictions for the Amazon River are similar to those for the Mississippi River, with >90% of each REE predicted as organic matter complexes (Figure 5B). However, the model predicts that greater amounts of the LREE will occur in Amazon River waters as carbonato complexes (e.g., 6–7% for Ce) and as free metal ions (e.g., ~1% for La; compare Figures 5A,B). The predicted dominance of organic REE complexes in both the Mississippi and Amazon Rivers is consistent with previous studies, that REE are carried in most major world rivers as organic matter complexes (e.g., Tang and Johannesson, 2003; Pourret et al., 2007).

## REE Content of Mississippi River Sediment

The REE content of the operationally defined fractions of the Mississippi River bank sediment are presented in Table 4. Percentage distribution of the REE in each fraction, and the shale-normalized REE patterns are shown in Figure 6. The REE concentrations increase with successive leaching as follows: exchangeable < acid leachable < reducible < oxidizable <

residual. The total bulk sediment, sum of all five sequential extractions, and the residual fraction of the sediment have flat shale-normalized patterns. The oxidizable, reducible and acid leachable fractions have MREE enriched shale-normalized patterns, whereas the readily exchangeable fraction is depleted in the LREE. The differences in shale-normalized REE patterns of the various leached fractions are also reflected in their Sm/Nd ratios. For example, the highest Sm/Nd ratio (0.58) is observed for the exchangeable fraction, which is strongly depleted in the LREE, whereas the residual fraction has the lowest Sm/Nd ratio (0.18). The computed MREE enrichments (i.e.,  $\text{MREE}/\text{MREE}^*$ ; Haley et al., 2004) range from a low of 1.06 for the residual silicates, to a high of 2.05 for the acid leachable.

## Mississippi River Water and SPM $\epsilon_{\text{Nd}(0)}$

Neodymium isotope values [i.e.,  $\epsilon_{\text{Nd}(0)}$ ] for Mississippi River water samples, and the labile fraction of the associated SPM analyzed in this study are presented in Table 5. In addition, all known Nd isotope data for the Mississippi River system from the literature are reproduced in Table 5. These data include variously filtered river waters and associated SPM from different locations along the river, as well as sediment samples. The Nd isotope composition of the two Mississippi River waters sampled are identical, within analytical error (i.e.,  $2\sigma$ ), exhibiting  $\epsilon_{\text{Nd}(0)}$  values of  $-10.5$  (Table 5). In contrast,  $\epsilon_{\text{Nd}(0)}$  values for the acid leachable fraction of SPM from the MR site in the lower Mississippi River are more radiogenic than the river water from the same location [i.e., mean  $\epsilon_{\text{Nd}(0)}$  ca.  $-9.9$ ; Table 5].

## DISCUSSION

### Controls on REE in the Mississippi River Estuary

The REE concentrations measured in the Mississippi River water in this study are in general agreement with previous studies, and the difference in LREE concentrations shown in Figure 2B likely reflects seasonal variations. For example, Shiller (2002) reported a Nd concentration of  $163 \text{ pmol kg}^{-1}$  in January 1992, which is higher than his discharge-weighted mean Nd concentration, and closer to the Nd concentration ( $184 \text{ pmol kg}^{-1}$ ) we measured in this study, which was also sampled in January. Shiller (2002) noted that seasonal variability is more pronounced for the LREE relative to the HREE in Mississippi River water, with the LREE exhibiting a 5-fold variation between winter and summer. Another possible factor that could explain our higher LREE concentrations may be related to sampling locations. All previous samplings of the Mississippi River were upstream of Baton Rouge, Louisiana, whereas we sampled the river near its mouth (Figure 1).

Shale-normalized REE patterns in this study show both Ce and Gd anomalies in all the water samples (Table 3; Figure 2A). The observed negative Ce anomaly becomes greater as the “fresh” water from the Mississippi River (Ce anomaly = 0.7) mixes with the more saline water in the Louisiana Bight (mean  $\pm 1\sigma$ ;  $0.34 \pm 0.07$ ). These negative Ce anomalies are attributable to the higher particle reactivity of Ce owing to its redox sensitivity, relative to its neighboring REE. This higher particle reactivity of



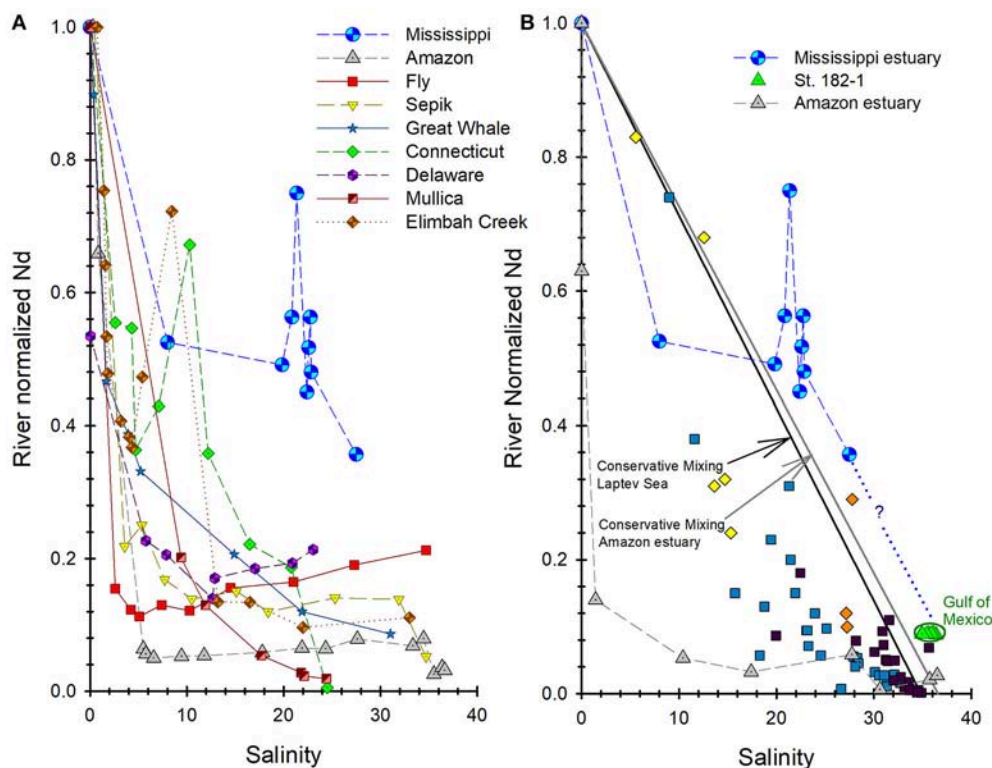


**FIGURE 4 |** River water-normalized Nd concentrations through the Mississippi River (MR) estuary (locations from **Figure 1**; this study) compared to other river/estuarine systems. **(A)** Compares the MR estuary to estuarine systems reviewed in Rousseau et al. (2015). **(B)** Compares the MR estuary's "conservative mixing" with station 182-1 in Osborne et al. (2015) to river/estuarine systems of the Laptev Sea (Figure 8a in Laukert et al., 2017), and the Amazon River estuary (Rousseau et al., 2015).

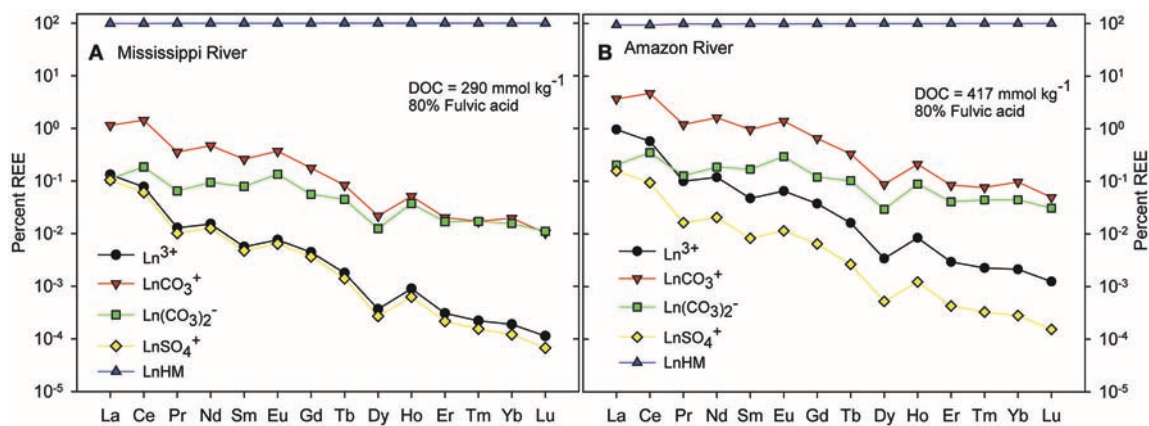


**FIGURE 5 |** Solution complexation modeling (WHAM VII) results for **(A)** the Mississippi River water, and **(B)** the Amazon River water, where Ln represents individual REE, and HM represents humic material. Note that the ordinate scales are logarithmic.

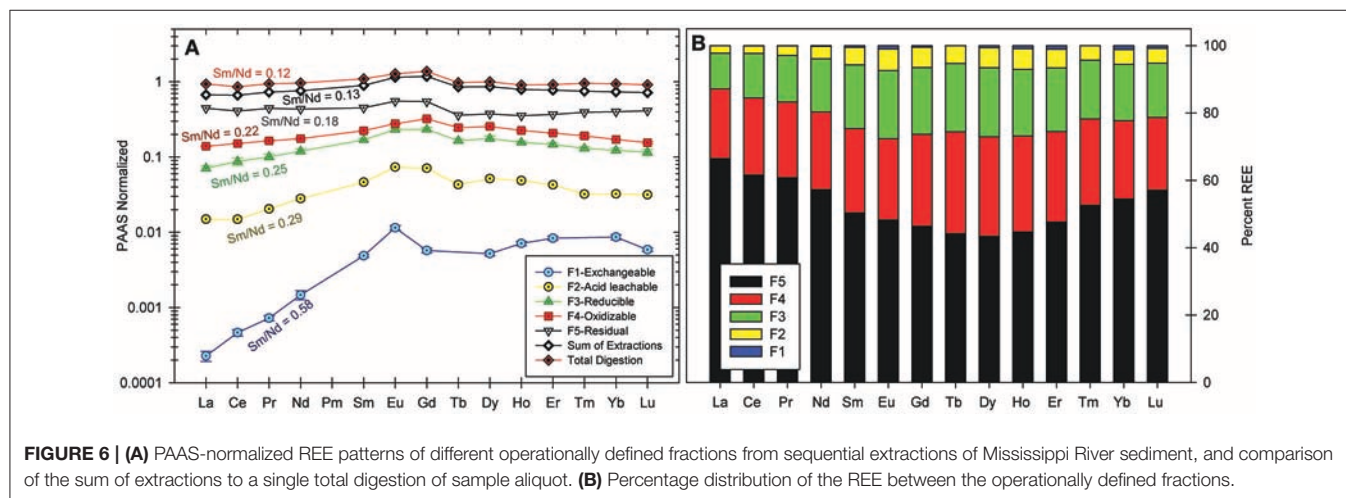
Ce becomes amplified during salt induced coagulation of colloids in the estuary, which is responsible for the increase in the negative Ce anomaly with increasing salinity (Elderfield et al., 1990; Sholkovitz, 1995; Shiller, 2002). For Gd anomalies, we recognize that anthropogenic Gd from the use of gadopentetic acid in magnetic resonance imaging may contribute to the positive Gd

anomalies observed in Mississippi River water (1.34) and waters from the Louisiana Bight (mean  $\pm 1\sigma$ ;  $1.22 \pm 0.07$ ). In which case we assume that dilution effect due to the size of the Mississippi River results in the small magnitude of these values. On the other hand, the positive Gd anomalies found in all the water samples in this study are within the range typical of unpolluted

**TABLE 4 |** The REE concentrations of the sequentially extracted operationally defined fractions of Mississippi River sediment, and computed Sm/Nd ratios and MREE enrichment.

	– Fractions –											
	Exchangeable - F1		Acid leachable - F2		Reducible - F3		Oxidizable - F4		Residual - F5		Sum of extractions	Total digestion
	µg kg <sup>-1</sup>	±	µg kg <sup>-1</sup>	±	µg kg <sup>-1</sup>	±	µg kg <sup>-1</sup>	±	µg kg <sup>-1</sup>	µg kg <sup>-1</sup>	µg kg <sup>-1</sup>	
La	9	1	567	45	2,697	211	5,285	124	16,928	25,486	35,503	
Ce	37	4	1,192	121	6,997	804	12,120	193	32,660	53,007	68,785	
Pr	6	1	182	13	895	78	1,462	53	3,945	6,491	8,358	
Nd	47	6	898	62	3,824	279	5,612	181	13,895	24,276	30,810	
Sm	27	1	259	20	949	40	1,256	51	2,525	5,017	6,133	
Eu	13	1	81	3	255	11	305	5	608	1,262	1,403	
Gd	27	2	333	26	1,097	71	1,512	39	2,567	5,536	6,472	
Tb	nd	–	33	3	127	8	189	13	277	626	750	
Dy	23	2	227	17	778	61	1,123	48	1,647	3,797	4,400	
Ho	7	0	49	4	157	7	226	8	354	792	907	
Er	24	2	124	6	425	26	603	13	1,070	2,247	2,664	
Tm	nd	–	13	0	52	3	77	4	157	299	382	
Yb	24	2	90	6	344	23	479	3	1,121	2,058	2,637	
Lu	3	0	14	0	50	5	67	2	176	309	393	
Sm/Nd	0.58		0.29		0.25		0.22		0.18	0.21	0.20	
147Sm/144Nd	0.35		0.18		0.15		0.13		0.11	0.13	0.12	
MREE/MREE*	1.56		2.05		1.69		1.52		1.06		1.19	

nd, below detection limit. \*MREE enrichments (Haley et al., 2004).



natural waters, including seawater, and much less than the values ( $\geq 4$ ) reported for most waters affected by anthropogenic Gd input (e.g., Kim et al., 1991; Bau and Dulski, 1996). Hence, the positive Gd anomalies observed here may be analogous to naturally occurring positive Gd anomalies, which are attributed to ionic radius independent fractionation due to Gd's half-filled 4-f electron shell, which affects both the solution and surface complexation behavior of Gd compared to Eu and Tb (Kim et al., 1991; Bau and Dulski, 2003).

Two observations have been extensively reported regarding REE concentrations in estuaries: removal in the low salinity

region and release in the mid to high salinity region. For example, such behavior has been described for the estuary of the world's largest river, the Amazon River (e.g., Rousseau et al., 2015 and references therein). Rare earth elements concentrations also decrease as Mississippi River water first mixes with Gulf of Mexico water on the Louisiana Shelf (Figure 3). These observations are consistent with change in water chemistry (e.g., ionic strength) with increase in salinity, which nullifies the repulsive energy barrier between colloidal particles, bringing about flocculation and settling out of colloids (Edzwald et al., 1974). In this study, the removal by this mechanism follows the

**TABLE 5 |** Neodymium concentrations and isotopic compositions,  $\epsilon_{\text{Nd}(0)}$  values, of Mississippi River water, suspended particulate matter (SPM), and sediment.

Sample type	Filter ( $\mu\text{m}$ )	Nd	$\epsilon_{\text{Nd}(0)}$	Location
Water <sup>a</sup>	0.1	32.6 pmol kg <sup>-1</sup>	-12.1 $\pm$ 0.5	Pilotstown, LA
Water <sup>b</sup>	0.2	318 pmol kg <sup>-1</sup>	-19.5	Jackson, MN
Water <sup>b</sup>	0.2	165 pmol kg <sup>-1</sup>	-8.6	Chester, IL
Water <sup>a</sup>	0.4	81.1 pmol kg <sup>-1</sup>	-10.5 $\pm$ 0.5	Pilotstown, LA
Water <sup>a</sup>	0.4	76.3 pmol kg <sup>-1</sup>	-12.1 $\pm$ 0.5	Venice, LA
Water <sup>c</sup> (River channel)	0.45	184 pmol kg <sup>-1</sup>	-10.55 $\pm$ 0.29	Near Venice, LA
Water-2 <sup>c</sup> (Breton Sound)	0.45	168 pmol kg <sup>-1</sup>	-10.53 $\pm$ 0.33	Near Venice, LA
SPM <sup>d</sup>	>0.2	30.4 ppm	-19.4	Jackson, MN
SPM <sup>d</sup>	>0.2	40.8 ppm	-10.1	Chester, IL
SPM <sup>c</sup> (Acid leachable)	0.45	0.12 ppm	-9.95 $\pm$ 0.20	Near Venice, LA
SPM-2 <sup>c</sup> (Acid leachable)	0.45	0.15 ppm	-9.77 $\pm$ 0.23	Near Venice, LA
Sediment <sup>e</sup>		32.6 ppm	-10.9	Near Venice, LA
Sediment <sup>f</sup> (clays)		39.8 ppm	-10.8	Delta front
Sediment <sup>f</sup> (silts)		30.3 ppm	-12.3	Delta front

<sup>a</sup>Stordal and Wasserburg (1986); <sup>b</sup>Goldstein and Jacobsen (1987); <sup>c</sup>This study (location MR in **Figure 1**); <sup>d</sup>Goldstein and Jacobsen (1988a); <sup>e</sup>Goldstein et al. (1984); <sup>f</sup>Bayon et al. (2015).

general order LREE > MREE > HREE (**Figure 3**), likely because of the higher particle reactivity of the LREE. Also because the HREE, and to a lesser extent, the MREE, form stronger solution complexes than the LREE (Sholkovitz, 1995; Nozaki et al., 2000; Sholkovitz and Szymczak, 2000).

The global average removal of Nd in estuaries has been estimated to be roughly 70% of the river borne Nd concentration (Goldstein and Jacobsen, 1987), although many estuaries exhibit greater amounts of Nd removal (e.g., > 90% for the Amazon; **Figure 4A**). Many, but not all estuaries also exhibit release of REE back to the water column at mid to high salinities (**Figure 4A**). Others, including the Connecticut River estuary, the Chao Phraya River estuary (Thailand), and Elimbah Creek (Australia) exhibit concentration “spikes” over relatively narrow salinity ranges at various salinities (**Figure 4A**). These concentration “spikes,” such as observed on the Louisiana Shelf are commonly attributed to sediment resuspension, remineralization of estuary sediments, and/or desorption of REE from SPM (Nozaki et al., 2000; Lawrence and Kamber, 2006).

An outstanding feature of the Mississippi River estuary is what appears to be lower amounts of REE removal in the low salinity region of the estuary when compared to the majority of other estuaries investigated (**Figures 3, 4**). For example, 97% of the Nd in the Amazon River is estimated to be removed in the low salinity region of its estuary, compared to only ca. 50% in the Mississippi River estuary (**Figure 4**). More specifically, our data suggest that slightly more than 62% of the river borne Nd in the Mississippi River is removed from solution by salinity ca. 30 compared to between 94 and 99% removal of river borne Nd in the Amazon River estuary at the same salinity (**Figure 4**). This

relative stability of REE in the Mississippi River estuary compared to most other estuaries is intriguing and requires explanation.

There are a number of possibilities that could explain this apparent stability of the REE in the Mississippi River estuary. First, the high pH of the Mississippi River water ( $\sim 8.0$ ) may in part be responsible for the relatively lower REE removal during estuarine mixing compared to other estuaries, such as the Amazon estuary, which has a lower pH of 6.9 (Rousseau et al., 2015). The higher pH of the Mississippi River water translates to lower REE concentrations compared to the Amazon River. For example, we measured a Nd concentration of 184 pmol kg<sup>-1</sup> in the Mississippi River, whereas a Nd concentration of 942 pmol kg<sup>-1</sup> was reported for the Amazon River (Amazon 20) by Gaillardet et al. (1997), and Rousseau et al. (2015) reported a Nd concentration of 852 pmol kg<sup>-1</sup>. Lower amounts of REE available for removal during flocculation follows similar argument advanced to explain the relatively low Fe removal in the Mississippi River estuary (Shiller and Boyle, 1991). In addition, the high pH of Mississippi River water suggests that greater proportions of each REE will occur in solution as stable aqueous complexes with organic ligands and carbonate ions (**Figure 5**). A previous study of the Mississippi River estuary also attributed low Fe removal, in part, to formation of strong aqueous complexes with dissolved natural organic ligands (Powell and Wilson-Finelli, 2003).

Although broadly similar, the aqueous complexation model predicts that REE complexes with natural organic matter account for more of each REE in Mississippi River water compared to the Amazon River (**Figure 5**), despite the latter having higher DOC concentration (i.e., 417  $\mu\text{mol kg}^{-1}$  compared to 290  $\mu\text{mol kg}^{-1}$  in the Mississippi River; Thurman, 1985). Specifically, the model predicts that 99.4% of Nd in the Mississippi River, compared to 97.9% of Nd in the Amazon River is complexed with natural organic matter. Conversely, 0.02% free Nd ions [Nd<sup>3+</sup>] is in solution in the Mississippi River, compared to approximately an order of magnitude greater, 0.12% as Nd<sup>3+</sup> in the Amazon River. Because the free metal ion species, Ln<sup>3+</sup>, is the most chemically reactive form of the REE in solution, the higher proportion of Ln<sup>3+</sup> in the Amazon River indicates that it has relatively more REE available for binding onto the surface of colloids than the Mississippi River. These arguments are consistent with recent field and experimental studies of estuaries, where it was shown that river waters dominated by organic nanoparticles and colloids (NPCs) exhibited markedly less removal of REE from solution when mixed with seawater compared to rivers with predominantly inorganic NPCs (Tepe and Bau, 2016; Merschel et al., 2017). These studies employed various filtration techniques including ultrafiltration to investigate colloidal and “truly” dissolved fractions of the REE, and the organic matter phase in WHAM VII is defined as colloidal (Tipping et al., 2011).

Another possible explanation for the apparent stability of the REE across the salinity gradient in the Mississippi River estuary is that REE contributions from sediment sources on the Louisiana Shelf mask the true amount of estuarine removal. Shallow estuaries associated with large rivers discharging along coasts with extensive continental shelf regions exhibit pronounced release of REE from the shelf sediments, owing to intense

sediment-water interactions (Sholkovitz and Szymczak, 2000). Processes such as disaggregation, desorption, mineralization, and bioturbation may influence the REE content of both particulate and dissolved phases in shallow estuaries (McKee et al., 2004; Abbott et al., 2015). The Louisiana Bight is such a setting, with an average depth of  $\sim 20$  m, possibly explaining the “spike” in REE concentrations in the MRP for salinities between 20 and 25 (Figure 3). Also, a conservative mixing line appears to be generated (Figure 4B), by plotting the river water-normalized REE concentrations of the Mississippi River estuary waters from this study with seawater samples from station 182-1 (Osborne et al., 2015) located approximately 130 km due east of the birdfoot delta, see Figure 8. This observation parallels conservative mixing lines for the Amazon River estuary and estuaries from the Laptev Sea (Figure 4B). This parallel relationship further suggests that dissolution of labile mineral phases from sediment resuspension impacts the distribution of the REE in the estuary. Nonetheless, it is not known whether the observed REE concentrations “spikes” are a common feature of the Mississippi River estuary or are spatially and/or temporally limited.

Dissolution of the labile mineral phases of river sourced sediments in coastal regions is recognized as an important flux of trace elements to the ocean (e.g., Pearce et al., 2013; Jeandel and Oelkers, 2015). Because of the substantial sediment load of the Mississippi River, which covers large regions of the Gulf of Mexico, the river sediments likely exert important controls on REE concentrations and Nd isotope composition of the Gulf (Trefry and Shokes, 1981; Figure 8). A previous study demonstrated that Mississippi River sediments play an important role in the Sr isotope systematics of the Gulf of Mexico (Xu and Marcantonio, 2004). More specifically, Xu and Marcantonio (2004) showed, using the sequential extraction procedure of Tessier et al. (1979) that the sediment's residual fraction is the chief reservoir (70–87%) of Sr, and further, that Sr isotope ratios become more radiogenic with successive leaching from the exchangeable to the residual fraction. Nevertheless, it is well known that sequential extraction techniques are subject to artifacts that result from incomplete dissolution, re-adsorption, and non-selectivity of the extractant solutions, prompting caution when interpreting the results (Sholkovitz, 1989).

Although only one sediment sample was analyzed in this study, the results from Xu and Marcantonio (2004) showed consistency in the distribution of Sr and Fe between the different operationally defined fractions for all three samples they analyzed, which suggests consistency in REE distribution. Similar to Sr, majority of the REE (43–66%) are contained within the non-labile, residual silicate mineral phases of the Mississippi River sediment. These likely include secondary clay minerals (e.g., kaolinite) and resistant accessory minerals like zircon (Armstrong-Altrin et al., 2015; Armstrong-Altrin and Machain-Castillo, 2016), as well as primary minerals like muscovite and feldspars. In contrast to Sr, Sm/Nd ratios decrease with successive leaching from the exchangeable to the residual fraction (Table 4; Figure 6), which suggests that  $^{143}\text{Nd}/^{144}\text{Nd}$  ratios become less radiogenic with successive leaching. The sediment's labile REE

fractions (34–57%) may become mobilized by changes in solution ionic strength, pH, and redox conditions, all of which are characteristic of estuaries. For example, although the readily exchangeable fraction accounts for much less than 1% by weight of the total REE content of each REE (e.g., 326 nmol kg<sup>-1</sup> for Nd) in the Mississippi riverbank sediment (Table 4), this fraction has Nd concentration nearly 1800 times higher than that of the Mississippi River water (184 pmol kg<sup>-1</sup> for Nd). Hence, REE release from labile fractions of the river sediments and/or SPM at the estuary will likely substantially influence the REE geochemistry of the Gulf of Mexico.

Water column profiles at two sampling locations on the Louisiana Shelf (i.e., locations 6 and 10 in Figure 1) show that REE concentrations generally decrease from surface waters to mid depths ( $\sim 6$ –10 m), before increasing near the sea bottom (Figure 7). The HREE exhibit greater decreases to these mid depths, as well as greater relative increases from mid depths to the sea bottom, compared to the LREE. For example, at sampling location 6, Lu shows a ca. 35% decrease in concentration (4.0–2.5 pmol kg<sup>-1</sup>) at mid depth, before a ca. 29% increase in concentration near the bottom (2.5–3.3 pmol kg<sup>-1</sup>), whereas Nd shows a ca. 25% decrease (90–68 pmol kg<sup>-1</sup>) at mid depth, and only a ca. 5% increase (68–71 pmol kg<sup>-1</sup>) near the bottom. The generally higher dissolved REE concentrations in the deep samples may be attributed to dissolution of the labile mineral phases within the resuspended sediments, or possibly a benthic REE flux into the water column (Nozaki et al., 2000; Haley et al., 2004; Lawrence and Kamber, 2006; Abbott et al., 2015).

To summarize, a combination of factors (i.e., higher pH, lower REE concentrations, and solution complexation; Figure 5) may be responsible for the apparent lower REE removal in the low salinity region of the Mississippi River estuary, as compared to other major estuaries (Figure 4A). However, without additional data we cannot unequivocally rule out the possibility that this apparent stability of REE across the salinity gradient is a complex response to secondary REE source(s) within the shallow Louisiana Shelf (Figure 4B). Although we acknowledge the spatial and temporal limitations of the sampling in our study, which introduce some uncertainties in our interpretations, our data present an important finding about REE stability in the Mississippi River estuary. This study begins the process to better understand the influence of the Mississippi River estuary on the REE systematics of the Gulf of Mexico. Hence, we suggest that detailed investigations of REE in the Mississippi River estuary and estuaries of other high pH major rivers (e.g., Changjiang, pH 7.8; Huanghe, pH 8.3; Ganges, pH 7.7; Indus, pH 7.8; Mackenzie, pH 8.1; St. Lawrence, pH 8; Gaillardet et al., 2003) should be undertaken, to investigate whether REE stability in the estuaries of alkaline rivers is a feature common to these systems or an anomaly characteristic of the Mississippi River.

## Impact of Mississippi River on Nd Isotopes in the Gulf of Mexico

A remarkable feature of the new  $\epsilon_{\text{Nd}(0)}$  data for the Mississippi River in this study (Table 5) is that they are identical to the Nd isotope composition of similarly filtered river water (0.4 vs.



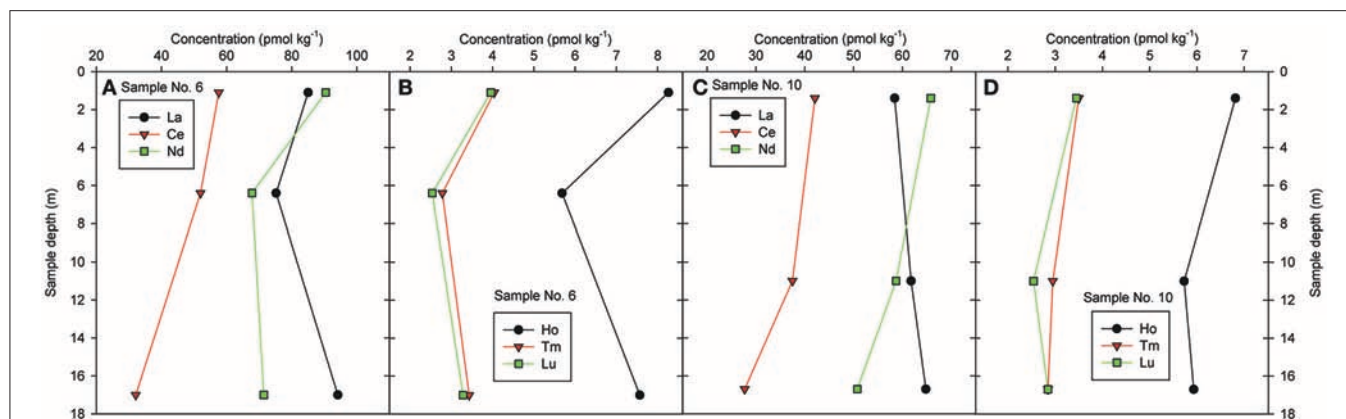


**FIGURE 7 |** Depth profiles of REE concentrations for samples No. 6 and 10 in the Louisiana Bight (details in **Table 1**) for selected REE, **(A,C)** LREE: La, Ce, Nd, and **(B,D)** HREE: Ho, Tm, Lu.

0.45  $\mu\text{m}$  filters in this study) collected and analyzed more than 30 years ago from the same location (Stordal and Wasserburg, 1986). An identically filtered river water sample from Venice, Louisiana exhibited a less radiogenic  $\epsilon_{\text{Nd}(0)}$  value (i.e.,  $-12.1 \pm 0.5$ ), and a river water sample that was filtered through a smaller pore size filter (0.1  $\mu\text{m}$ ) also had an  $\epsilon_{\text{Nd}(0)}$  value of  $-12.1 \pm 0.5$  (Stordal and Wasserburg, 1986). The  $\epsilon_{\text{Nd}(0)}$  of the acid leachable fraction of SPM from the lower Mississippi River (i.e., mean ca.  $-9.9$ ) is also more radiogenic than  $\epsilon_{\text{Nd}(0)}$  of bulk river sediment collected nearby ( $-10.9$ ; Goldstein et al., 1984), as well as the silt and clay fraction of sediment collected at the river mouth ( $-12.8$  and  $-10.8$ , respectively; Bayon et al., 2015). The other published  $\epsilon_{\text{Nd}(0)}$  analyses of SPM from the Mississippi River are from near the river's headwaters in Minnesota [ $\epsilon_{\text{Nd}(0)} = -19.4$ ], and from the river in Illinois [ $\epsilon_{\text{Nd}(0)} = -10.1$ ]. The  $\epsilon_{\text{Nd}(0)}$  values of SPM from the river in Minnesota and Illinois clearly reflect the age and Nd isotope composition of the underlying rocks in each region (Goldstein and Jacobsen, 1988a,b).

**Figure 8** shows the locations of water column profiles within the Gulf of Mexico where Osborne et al. (2014, 2015) measured Nd isotope compositions and REE concentrations (REE only for St. 182-1). To the best of our knowledge, water column  $\epsilon_{\text{Nd}(0)}$  and REE concentrations data for other locations in the Gulf are not available in peer-reviewed literature. From the mean and standard error of the  $\epsilon_{\text{Nd}(0)}$  measured in the water column (Osborne et al., 2014), the seawater appears to become slightly more radiogenic between the Yucatan Straits ( $-9.37 \pm 0.69$ ;  $n = 4$ ; St. 166-1), the eastern Gulf ( $-8.92 \pm 0.38$ ;  $n = 6$ ; St. 194-13), and the Florida Straits ( $-9.08 \pm 0.27$ ;  $n = 10$ ; St. 200-2) as it moves through the Gulf of Mexico (**Figure 9**). Both the mean and standard error were weighted by the inverse of measurement standard deviations. Gulf of Mexico waters, and in particular, shallow waters from the eastern Gulf (Stations 194-13 and 200-2), are more radiogenic than Mississippi River water ( $-10.5$ , up to 3  $\epsilon_{\text{Nd}}$  units), as well as SPM and sediments from the river (**Table 5**; **Figure 9**). Hence, the relatively radiogenic surface waters of the eastern Gulf cannot be chiefly composed of Mississippi River water.

Furthermore, despite substantial portions of the Gulf being covered with clastic sediments sourced from the Mississippi River (**Figure 8**; Trefry and Shokes, 1981), the limited  $\epsilon_{\text{Nd}(0)}$  data for Mississippi River sediments (e.g., Goldstein et al., 1984; Bayon et al., 2015) indicate that these materials are likely to be substantially less radiogenic (as much as 5  $\epsilon_{\text{Nd}}$  units) than eastern Gulf, as well as Mississippi River waters (**Table 5**; Osborne et al., 2014). Although, the  $\epsilon_{\text{Nd}(0)}$  ( $\pm 2\sigma$ ) values for some of the deep waters overlap with the  $\epsilon_{\text{Nd}(0)}$  value reported for Mississippi River clay (**Table 5**; **Figure 9**; Bayon et al., 2015). Hence, the Nd isotopic composition of waters in the Gulf are likely impacted by contributions from radiogenic source(s) associated with the Florida peninsula (Figure A1 in Osborne et al., 2014). Other potential radiogenic sources include materials from young mafic and intermediate volcanic rocks in the vicinity of Veracruz, Mexico, which make up substantial portions of the continental shelf and deep sea sediments in the southwestern Gulf of Mexico (Armstrong-Altrin et al., 2015; Armstrong-Altrin and Machain-Castillo, 2016).

The labile fraction of SPM collected in this study exhibits the most radiogenic  $\epsilon_{\text{Nd}(0)}$  values (i.e.,  $-9.95 \pm 0.1$ ,  $-9.77 \pm 0.23$ ) reported for the lower Mississippi River, and these values are distinct ( $\pm 2\sigma$ ) from Mississippi River waters (**Table 5**; **Figure 9**). Furthermore, we note that the Sm/Nd ratios of Mississippi riverbank sediment are highly variable, ranging from 0.18 for the residual fraction to a high of 0.5 for the readily exchangeable fraction (**Table 4**). Recasting these Sm/Nd ratios as approximate  $^{147}\text{Sm}/^{144}\text{Nd}$  ratios using the conversion  $^{147}\text{Sm}/^{144}\text{Nd} = 0.6049 \times \text{weight ratio of Sm/Nd}$  (Goldstein et al., 1984; DePaolo, 1988), leads to estimates of  $^{147}\text{Sm}/^{144}\text{Nd}$  that range from 0.11 for the residual fraction to 0.35 for the exchangeable fraction (**Table 4**). The estimated  $^{147}\text{Sm}/^{144}\text{Nd}$  values of the different fractions of Mississippi riverbank sediment are consistent with the notion that the labile portions of the riverbank sediment are more radiogenic than the bulk sediment. These observations are also consistent with the measured  $\epsilon_{\text{Nd}(0)}$  values of the labile fraction of the SPM.



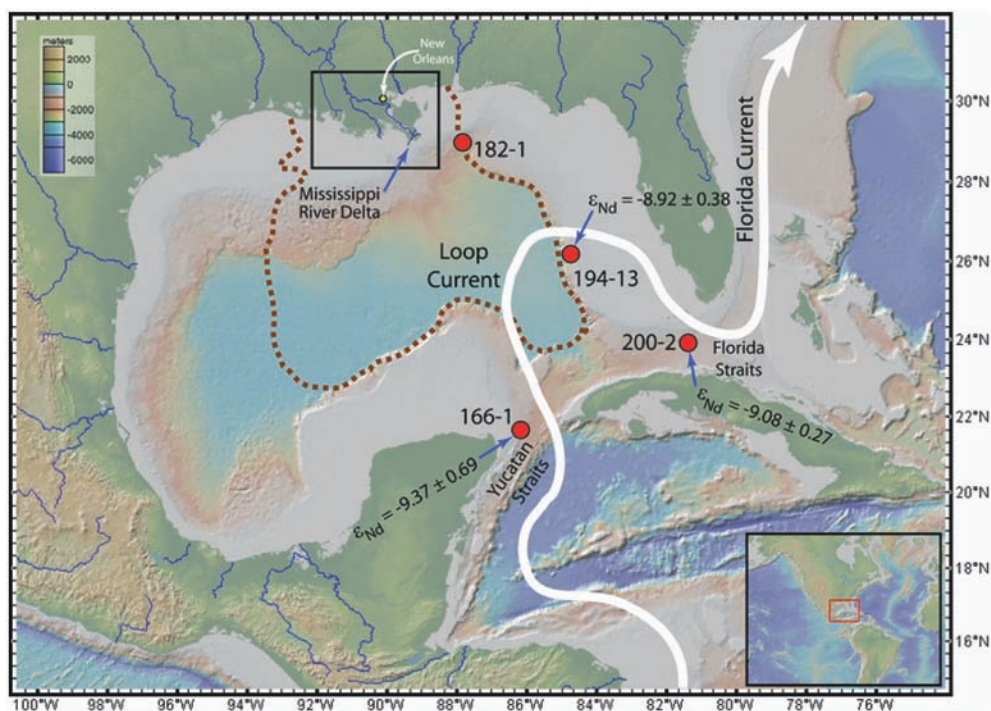


**FIGURE 8 |** Map of the Gulf of Mexico showing the locations of water column profiles (red circles) for REE and  $\epsilon_{\text{Nd}(t)}$  from Osborne et al. (2014, 2015), the Gulf region subject to deposition of Mississippi River sediment (brown dashed line; Trefry and Shokes, 1981), and generalized track of the Loop Current (thick white arrow). The study area (black rectangle around the MR delta) is shown in more details in **Figure 1**. The mean and standard error (see text for details) of the  $\epsilon_{\text{Nd}(t)}$  measured in the water column in the Yucatan Straits, the eastern Gulf, and the Florida Straits (Osborne et al., 2014).

It was recently argued, that rapid exchange of Nd between river waters and SPM leads to isotope equilibration, between the dissolved and sorbed fractions in the Amazon River estuary (Rousseau et al., 2015). A comparison of the Mississippi River waters and bulk sediments to the more radiogenic labile fraction of its SPM (**Table 5**), indicates that isotope equilibration between dissolved and sorbed fractions does not describe Nd behavior in the lower Mississippi River. Rousseau et al. (2015) argued that dissolution of relatively non-radiogenic Amazon River SPM, and/or sediments, occurred within the estuary, which was responsible for lowering the  $\epsilon_{\text{Nd}(t)}$  values of the dissolved phase by about 2  $\epsilon_{\text{Nd}}$  units to Nd isotope values more similar to the river sediments. Although our dataset is currently insufficient to unequivocally evaluate whether similar processes might also occur within the Mississippi River estuary, the existing data suggest that the labile Nd fraction of SPM in the Mississippi River is more radiogenic than the dissolved fraction (**Table 5**). Hence, exchange of Nd between Mississippi River water and SPM should lead to higher  $\epsilon_{\text{Nd}(t)}$  values in the estuary waters, and not a decrease in  $\epsilon_{\text{Nd}(t)}$  values as reported for the Amazon River estuary. Such exchange of more radiogenic Nd from SPM to the dissolved phase may help to explain the generally more radiogenic values of the Gulf of Mexico waters.

Ideally, it would be beneficial to develop a mass balance model for Nd in the Gulf of Mexico to quantitatively assess the importance of the Mississippi River on the  $\epsilon_{\text{Nd}(t)}$  composition of the Gulf. However, considering the paucity of Nd isotope

data that currently exists for the Gulf of Mexico, it seems unlikely that forward or inverse modeling (e.g., Singh et al., 2012) could provide meaningful information to help identify sources or sinks of Nd in the Gulf. Besides the Mississippi River system, the Nd budget of the Gulf of Mexico is also likely impacted by other rivers that discharge to the Gulf (e.g., >40 major estuarine systems occur within the Gulf; Wen et al., 1999), benthic porewater fluxes, submarine groundwater discharge (SGD), and/or atmospheric deposition. Although Johannesson et al. (2011) and Chevis et al. (2015) demonstrated that SGD is an important source of REE to Florida's Atlantic coastal waters, to the best of our knowledge no studies have examined REE or Nd isotopes in SGD entering the Gulf. Hence, the possibility of ascertaining the potential importance of SGD fluxes of REE and Nd isotope to the Gulf of Mexico awaits future study. Similar arguments can be made for the research gap on REE fluxes from the other rivers discharging to the Gulf, as well as benthic porewater fluxes. Hence, more sampling of the Gulf of Mexico is necessary to address the possible contributions of these and other sources.

## CONCLUSIONS

Two outstanding features of the Mississippi River estuary are apparent lower REE removal at low salinity, compared to other major estuaries studied to date, and the "spike" in REE concentrations at mid to high salinity on the Louisiana Shelf.

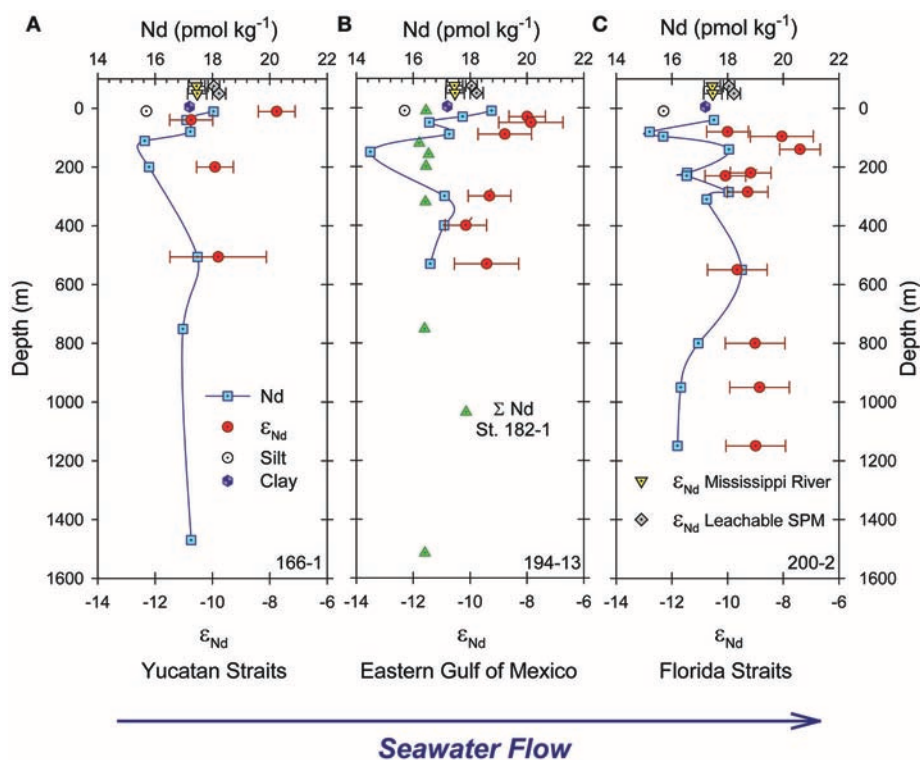


**FIGURE 9 |** Neodymium concentrations (blue squares) and  $\epsilon_{Nd(0)}$  (red circles) for water column samples from stations 166-1, 194-13, and 200-2 shown in **Figure 8** (data from Osborne et al., 2014, 2015). Green triangles in **(B)** are Nd concentrations for station 182-1 (**Figure 8**; Osborne et al., 2015). Yellow inverted triangles and gray diamonds plotted above 0 m depth in each panel are  $\epsilon_{Nd(0)} \pm 2\sigma$  for Mississippi River (MR) water and the labile fraction of the associated SPM, respectively, measured in this study (**Table 5**). The open circle and purple hexagon show  $\epsilon_{Nd(0)}$  values for the silt and clay fractions of sediments at the mouth of the MR (Bayon et al., 2015).

Only ca. 50% of river borne Nd is removed from solution in the Mississippi River estuary compared to ca. 97% in the Amazon estuary, and 70% for many other estuaries. Rare earth elements removal is attributed to flocculation, followed by settling out of colloids as the fresh river water and the more saline Gulf of Mexico water mix. Strong aqueous complexation of REE with natural organic ligands and carbonate ions in the alkaline (pH  $\sim 8$ ) Mississippi River water may explain the diminished removal of the REE. Alternatively, low REE concentrations, which is a consequence of the river's alkaline pH, may also play a role. The mechanism(s) responsible for REE "spike" at mid to high salinity in the estuary remains unclear at this point, but may be related to sediment resuspension on the shallow Louisiana Shelf.

Mississippi River water from near the river's mouth is less radiogenic than Gulf of Mexico water [ $\epsilon_{Nd(0)} = -10.5$  compared to  $-9.0$ , respectively]. The river water exhibits Nd isotope compositions that are similar to or more radiogenic than bulk Mississippi River sediments. The Nd isotope composition values of the labile fraction of SPM collected from the river waters are the most radiogenic values reported for the lower Mississippi River [i.e.,  $\epsilon_{Nd(0)} = -9.9$ ]. Sequential leaching of Mississippi River sediment reveals that Sm/Nd ratios decrease with successive leaching from the highly labile, exchangeable fraction, to the residual, chiefly silicate mineral fraction. These

observations suggest that labile fractions of Mississippi River sediment are likely more radiogenic than the bulk sediment. This assertion is supported by the  $\epsilon_{Nd(0)}$  values of the labile fraction of river borne SPM. Consequently, if the Mississippi River system impacts the Nd isotope composition of the Gulf of Mexico, it must do so by geochemical reactions between Gulf water and the more labile fractions of the Mississippi River sediments (or SPM). Additional studies focused on the evolution of the Nd isotope signatures as the waters mix will help to better understand how Mississippi River water and its sediments/SPM influence the REE and Nd isotope compositions of the Gulf of Mexico.

## AUTHOR CONTRIBUTIONS

SA participated in sample collection, preparations, analyses, modeling, and wrote most of the manuscript. MC collected samples in the Mississippi River and Louisiana Bight, and was involved in sample analyses and preparation of manuscript figures. TH performed sample pre-concentrations and was involved in ICP-MS analysis. CW performed statistical analysis of data and wrote discussion on this analysis. EM performed Nd isotopes analysis and wrote the method section on this analysis.

KJ was responsible for the research design and wrote some parts of manuscript.

## ACKNOWLEDGMENTS

SA wishes to thank the Department of Earth and Environmental Sciences at Tulane University for support via graduate assistantships and the Volkes Fellowship. KJ thanks Michael

and Mathilda Cochran for endowing the Cochran Family Professorship at Tulane University, which helped support the sampling and geochemical analyses. In addition, KJ thanks the NSF awards OCE-0825920 and EAR-1141692, both of which also supported the sampling and geochemical analyses. We are grateful to Tanya Goehring for assistance with the XRD analysis, and Dr. Deborah Grimm for assistance with the ICP-MS analysis.

## REFERENCES

- Abbott, A. N., Haley, B. A., and McManus, J. (2015). Bottoms up: sedimentary control of the deep North Pacific Ocean's  $\epsilon$ Nd signature. *Geology* 43, 1035–1035. doi: 10.1130/G37114.1
- Armstrong-Altrin, J. S., and Machain-Castillo, M. L. (2016). Mineralogy, geochemistry, and radiocarbon ages of deep sea sediments from the Gulf of Mexico, Mexico. *J. South Am. Earth Sci.* 71, 182–200. doi: 10.1016/j.jsames.2016.07.010
- Armstrong-Altrin, J. S., Machain-Castillo, M. L., Rosales-Hoz, L., Carranza-Edwards, A., Sanchez-Cabeza, J. A., and Ruiz-Fernández, A. C. (2015). Provenance and depositional history of continental slope sediments in the Southwestern Gulf of Mexico unraveled by geochemical analysis. *Cont. Shelf Res.* 95, 15–26. doi: 10.1016/j.csr.2015.01.003
- Arsouze, T., Dutay, J. C., Lacan, F., and Jeandel, C. (2009). Reconstructing the Nd oceanic cycle using a coupled dynamical-biogeochemical model. *Biogeosciences* 6, 2829–2846. doi: 10.5194/bg-6-2829-2009
- Bau, M., and Dulski, P. (1996). Anthropogenic origin of positive gadolinium anomalies in river waters. *Earth Planet. Sci. Lett.* 143, 245–255. doi: 10.1016/0012-821X(96)00127-6
- Bau, M., and Dulski, P. (2003). Three types of fractionation of REY: Application in geology, astrobiology, and oceanography. *XIII Goldschmidt Conf. Abs.* A35.
- Bayon, G., Toucanne, S., Skonieczny, C., André, L., Bermell, S., Cheron, S., et al. (2015). Rare earth elements and neodymium isotopes in world river sediments revisited. *Geochim. Cosmochim. Acta* 170, 17–38. doi: 10.1016/j.gca.2015.08.001
- Bianchi, T. S., DiMarco, S. F., Cowan, J. H. Jr., Hetland, R. D., Chapman, P., Day, J. W., et al. (2010). The science of hypoxia in the Northern Gulf of Mexico: a review. *Sci. Total Environ.* 408, 1471–1484. doi: 10.1016/j.scitotenv.2009.11.047
- Chevis, D. A., Johannesson, K. H., Burdige, D. J., Cable, J. E., Martin, J. B., and Roy, M. (2015). Rare earth element cycling in a sandy subterranean estuary in Florida, USA. *Mar. Chem.* 176, 34–50. doi: 10.1016/j.marchem.2015.07.003
- DePaolo, D. J. (1988). *Neodymium Isotope Geochemistry: An Introduction*. Berlin: Springer-Verlag.
- Du, J., Haley, B. A., and Mix, A. C. (2016). Neodymium isotopes in authigenic phases, bottom waters and detrital sediments in the Gulf of Alaska and their implications for paleo-circulation reconstruction. *Geochim. Cosmochim. Acta* 193, 14–35. doi: 10.1016/j.gca.2016.08.005
- Edzwald, J. K., Upchurch, J. B., and O'Melia, C. R. (1974). Coagulation in estuaries. *Environ. Sci. Technol.* 8, 58–63. doi: 10.1021/es60086a003
- Elderfield, H., Upstill-Goddard, R., and Sholkovitz, E. R. (1990). The rare earth elements in rivers, estuaries, and coastal seas and their significance to the composition of ocean waters. *Geochim. Cosmochim. Acta* 54, 971–991. doi: 10.1016/0016-7037(90)90432-K
- Gaillardet, J., Dupre, B., Allegre, C. J., and Négrel, P. (1997). Chemical and physical denudation in the Amazon River Basin. *Chem. Geol.* 142, 141–173. doi: 10.1016/S0009-2541(97)00074-0
- Gaillardet, J., Viers, J., and Dupre, B. (2003). Trace elements in river waters. *Treat. Geochem.* 5:605. doi: 10.1016/B0-08-043751-6/05165-3
- Goldstein, S. J., and Jacobsen, S. B. (1987). The Nd and Sr isotopic systematics of river-water dissolved material: implications for the sources of Nd and Sr in seawater. *Chem. Geol.* 66, 245–272. doi: 10.1016/0168-9622(87)90045-5
- Goldstein, S. J., and Jacobsen, S. B. (1988a). Nd and Sr isotopic systematics of river water suspended material: implications for crustal evolution. *Earth Planet. Sci. Lett.* 87, 249–265. doi: 10.1016/0012-821X(88)90013-1
- Goldstein, S. J., and Jacobsen, S. B. (1988b). Rare earth elements in river waters. *Earth Planet. Sci. Lett.* 89, 35–47. doi: 10.1016/0012-821X(88)90031-3
- Goldstein, S. L., and Hemming, S. R. (2003). Long-lived isotopic tracers in oceanography, paleoceanography, and ice-sheet dynamics. *Treat. Geochem.* 6:625. doi: 10.1016/B0-08-043751-6/06179-X
- Goldstein, S. L., O'Nions, R. K., and Hamilton, P. J. (1984). A Sm-Nd isotopic study of atmospheric dusts and particulates from major river systems. *Earth Planet. Sci. Lett.* 70, 221–236. doi: 10.1016/0012-821X(84)90007-4
- Greaves, M. J., Elderfield, H., and Klinkhammer, G. P. (1989). Determination of the rare earth elements in natural waters by isotope-dilution mass spectrometry. *Anal. Chim. Acta* 218, 265–280. doi: 10.1016/S0003-2670(00)80303-7
- Haley, B. A., Klinkhammer, G. P., and McManus, J. (2004). Rare earth elements in pore waters of marine sediments. *Geochim. Cosmochim. Acta* 68, 1265–1279. doi: 10.1016/j.gca.2003.09.012
- Jacobsen, S. B., and Wasserburg, G. J. (1980). Sm-Nd isotopic evolution of chondrites. *Earth Planet. Sci. Lett.*, 50, 139–155. doi: 10.1016/0012-821X(80)90125-9
- Jeandel, C. (2016). Overview of the mechanisms that could explain the 'Boundary Exchange' at the land-ocean contact. *Phil. Trans. R. Soc. A* 374:20150287. doi: 10.1098/rsta.2015.0287
- Jeandel, C., Arsouze, T., Lacan, F., Techine, P., and Dutay, J. C. (2007). Isotopic Nd compositions and concentrations of the lithogenic inputs into the ocean: a compilation, with an emphasis on the margins. *Chem. Geol.* 239, 156–164. doi: 10.1016/j.chemgeo.2006.11.013
- Jeandel, C., and Oelkers, E. H. (2015). The influence of terrigenous particulate material dissolution on ocean chemistry and global element cycles. *Chem. Geol.* 395, 50–66. doi: 10.1016/j.chemgeo.2014.12.001
- Johannesson, K. H., and Burdige, D. J. (2007). Balancing the global oceanic neodymium budget: evaluating the role of groundwater. *Earth Planet. Sci. Lett.* 253, 129–142. doi: 10.1016/j.epsl.2006.10.021
- Johannesson, K. H., Chevis, D. A., Burdige, D. J., Cable, J. E., Martin, J. B., and Roy, M. (2011). Submarine groundwater discharge is an important net source of light and middle REEs to coastal waters of the Indian River Lagoon, Florida, USA. *Geochim. Cosmochim. Acta* 75, 825–843. doi: 10.1016/j.gca.2010.11.005
- Johannesson, K. H., Palmore, C. D., Fackrell, J., Prouty, N. G., Swarzenski, P. W., Chevis, D. A., et al. (2017). Rare earth element behavior during groundwater-seawater mixing along the Kona Coast of Hawaii. *Geochim. Cosmochim. Acta* 198, 229–258. doi: 10.1016/j.gca.2016.11.009
- Johannesson, K. H., Tang, J., Daniels, J. M., Bounds, W. J., and Burdige, D. J. (2004). Rare earth element concentrations and speciation in organic-rich blackwaters of the Great Dismal Swamp, Virginia, USA. *Chem. Geol.* 209, 271–294. doi: 10.1016/j.chemgeo.2004.06.012
- Kamenov, G. D., Perfit, M. R., Mueller, P. A., and Jonasson, I. R. (2008). Controls on magmatism in an island arc environment: study of lavas and sub-arc xenoliths from the Tabar-Lihir-Tanga-Feni island chain, Papua New Guinea. *Contr. Mineral. Petrol.* 155, 635–656. doi: 10.1007/s00410-007-0262-0
- Kim, K. H., Byrne, R. H., and Lee, J. H. (1991). Gadolinium behavior in seawater: a molecular basis for gadolinium anomalies. *Mar. Chem.* 36, 107–120. doi: 10.1016/S0304-4203(09)90057-3
- Klungness, G. D., and Byrne, R. H. (2000). Comparative hydrolysis behavior of the rare earths and yttrium: the influence of temperature and ionic strength. *Polyhedron* 19, 99–107. doi: 10.1016/S0277-5387(99)00332-0
- Lacan, F., and Jeandel, C. (2001). Tracing Papua New Guinea imprint on the central Equatorial Pacific Ocean using neodymium isotopic compositions



- and Rare Earth Element patterns. *Earth Planet. Sci. Lett.* 186, 497–512. doi: 10.1016/S0012-821X(01)00263-1
- Landing, W. M., and Lewis, B. L. (1991). Collection, processing, and analysis of marine particulate and colloidal material for transition metals. *Marine Particles* 63, 263–272. doi: 10.1029/GM063p0263
- Laukert, G., Frank, M., Bauch, D., Hathorne, E. C., Gutjahr, M., Janout, M., et al. (2017). Transport and transformation of riverine neodymium isotope and rare earth element signatures in high latitude estuaries: a case study from the Laptev Sea. *Earth Planet. Sci. Lett.* 477, 205–217. doi: 10.1016/j.epsl.2017.08.010
- Lawrence, M. G., and Kamber, B. S. (2006). The behaviour of the rare earth elements during estuarine mixing—revisited. *Mar. Chem.* 100, 147–161. doi: 10.1016/j.marchem.2005.11.007
- Luo, Y. R., and Byrne, R. H. (2000). The ionic strength dependence of rare earth and yttrium fluoride complexation at 25°C. *J. Solution Chem.* 29, 1089–1099. doi: 10.1023/A:1005186932126
- Luo, Y. R., and Byrne, R. H. (2001). Yttrium and rare earth element complexation by chloride ions at 25°C. *J. Solution Chem.* 30, 837–845. doi: 10.1023/A:1012292417793
- Luo, Y. R., and Byrne, R. H. (2004). Carbonate complexation of yttrium and the rare earth elements in natural waters I. *Geochim. Cosmochim. Acta* 68, 691–699. doi: 10.1016/S0016-7037(03)00495-2
- Marsac, R., Banik, N. L., Lützenkirchen, J., Catrouillet, C., Marquardt, C. M., and Johannesson, K. H. (2017). Modeling metal ion-humic substances complexation in highly saline conditions. *Appl. Geochem.* 79, 52–64. doi: 10.1016/j.apgeochem.2017.02.004
- McKee, B. A., Aller, R. C., Allison, M. A., Bianchi, T. S., and Kineke, G. C. (2004). Transport and transformation of dissolved and particulate materials on continental margins influenced by major rivers: benthic boundary layer and seabed processes. *Cont. Shelf Res.* 24, 899–926. doi: 10.1016/j.csr.2004.02.009
- McLennan, S. M. (1989). Rare earth elements in sedimentary rocks; influence of provenance and sedimentary processes. *Rev. Mineral. Geochem.* 21, 169–200.
- Merschel, G., Bau, M., and Dantas, E. L. (2017). Contrasting impact of organic and inorganic nanoparticles and colloids on the behavior of particle-reactive elements in tropical estuaries: an experimental study. *Geochim. Cosmochim. Acta* 197, 1–13. doi: 10.1016/j.gca.2016.09.041
- Nozaki, Y., Lerche, D., Alibo, D. S., and Snidvongs, A. (2000). The estuarine geochemistry of rare earth elements and indium in the Chao Phraya River, Thailand. *Geochim. Cosmochim. Acta* 64, 3983–3994. doi: 10.1016/S0016-7037(00)00473-7
- Osborne, A. H., Haley, B. A., Hathorne, E. C., Flögel, S., and Frank, M. (2014). Neodymium isotopes and concentrations in Caribbean seawater: tracing water mass mixing and continental input in a semi-enclosed ocean basin. *Earth Planet. Sci. Lett.* 406, 174–186. doi: 10.1016/j.epsl.2014.09.011
- Osborne, A. H., Haley, B. A., Hathorne, E. C., Plancherel, Y., and Frank, M. (2015). Rare earth element distribution in Caribbean seawater: continental inputs versus lateral transport of distinct REE compositions in subsurface water masses. *Mar. Chem.* 177, 172–183. doi: 10.1016/j.marchem.2015.03.013
- Pearce, C. R., Jones, M. T., Oelkers, E. H., Pradoux, C., and Jeandel, C. (2013). The effect of particulate dissolution on the neodymium (Nd) isotope and Rare Earth Element (REE) composition of seawater. *Earth Planet. Sci. Lett.* 369, 138–147. doi: 10.1016/j.epsl.2013.03.023
- Pin, C., and Zalduendi, J. S. (1997). Sequential separation of light rare-earth elements, thorium and uranium by miniaturized extraction chromatography: application to isotopic analyses of silicate rocks. *Anal. Chim. Acta* 339, 79–89. doi: 10.1016/S0003-2670(96)00499-0
- Pourret, O., Davranche, M., Gruau, G., and Dia, A. (2007). Organic complexation of rare earth elements in natural waters: evaluating model calculations from ultrafiltration data. *Geochim. Cosmochim. Acta* 71, 2718–2735. doi: 10.1016/j.gca.2007.04.001
- Powell, R. T., and Wilson-Finelli, A. (2003). Importance of organic Fe complexing ligands in the Mississippi River plume. *Estuar. Coast. Shelf Sci.* 58, 757–763. doi: 10.1016/S0272-7714(03)00182-3
- Rousseau, T. C., Sonke, J. E., Chmieleff, J., Van Beek, P., Souhaut, M., Boaventura, G., et al. (2015). Rapid neodymium release to marine waters from lithogenic sediments in the Amazon estuary. *Nat. Commun.* 6:7592. doi: 10.1038/ncomms8592
- Schiff, J., and Byrne, R. H. (2004). Determination of SO<sub>4</sub>δ<sup>1</sup> for yttrium and the rare earth elements at I = 0.66 m and t = 25° C—implications for YREE solution speciation in sulfate-rich waters I. *Geochim. Cosmochim. Acta* 68, 2825–2837. doi: 10.1016/j.gca.2003.12.003
- Shiller, A. M. (2002). Seasonality of dissolved rare earth elements in the lower Mississippi River. *Geochem. Geophys. Geosys.* 3, 1–14. doi: 10.1029/2002GC000372
- Shiller, A. M., and Boyle, E. A. (1991). Trace elements in the Mississippi River Delta outflow region: behavior at high discharge. *Geochim. Cosmochim. Acta* 55, 3241–3251. doi: 10.1016/0016-7037(91)90486-O
- Sholkovitz, E. R. (1989). Artifacts associated with the chemical leaching of sediments for rare-earth elements. *Chem. Geol.* 77, 47–51. doi: 10.1016/0009-2541(89)90014-4
- Sholkovitz, E. R. (1995). The aquatic chemistry of rare earth elements in rivers and estuaries. *Aquat. Geochem.* 1, 1–34. doi: 10.1007/BF01025229
- Sholkovitz, E., and Szymczak, R. (2000). The estuarine chemistry of rare earth elements: comparison of the Amazon, Fly, Sepik and the Gulf of Papua systems. *Earth Planet. Sci. Lett.* 179, 299–309. doi: 10.1016/S0012-821X(00)00112-6
- Siddall, M., Khatala, S., van de Flierdt, T., Jones, K., Goldstein, S. L., Hemming, S., et al. (2008). Towards explaining the Nd paradox using reversible scavenging in an ocean general circulation model. *Earth Planet. Sci. Lett.* 274, 448–461. doi: 10.1016/j.epsl.2008.07.044
- Singh, S. P., Singh, S. K., Goswami, V., Bhushan, R., and Rai, V. K. (2012). Spatial distribution of dissolved neodymium and εNd in the Bay of Bengal: role of particulate matter and mixing of water masses. *Geochim. Cosmochim. Acta* 94, 38–56. doi: 10.1016/j.gca.2012.07.017
- Stordal, M. C., and Wasserburg, G. J. (1986). Neodymium isotopic study of Baffin Bay water: sources of REE from very old terranes. *Earth Planet. Sci. Lett.* 77, 259–272. doi: 10.1016/0012-821X(86)90138-X
- Tachikawa, K., Athias, V., and Jeandel, C. (2003). Neodymium budget in the modern ocean and paleo-oceanographic implications. *J. Geophys. Res.* 108:3254. doi: 10.1029/1999JC000285
- Tanaka, T., Togashi, S., Kamioka, H., Amakawa, H., Kagami, H., Hamamoto, T., et al. (2000). JNd-1: a neodymium isotopic reference in consistency with LaJolla neodymium. *Chem. Geol.* 168, 279–281. doi: 10.1016/S0009-2541(00)00198-4
- Tang, J., and Johannesson, K. H. (2003). Speciation of rare earth elements in natural terrestrial waters: assessing the role of dissolved organic matter from the modeling approach. *Geochim. Cosmochim. Acta* 67, 2321–2339. doi: 10.1016/S0016-7037(02)01413-8
- Tang, J., and Johannesson, K. H. (2010). Ligand extraction of rare earth elements from aquifer sediments: implications for rare earth element complexation with organic matter in natural waters. *Geochim. Cosmochim. Acta* 74, 6690–6705. doi: 10.1016/j.gca.2010.08.028
- Tepe, N., and Bau, M. (2016). Behavior of rare earth elements and yttrium during simulation of arctic estuarine mixing between glacial-fed river waters and seawater and the impact of inorganic (nano-) particles. *Chem. Geol.* 438, 134–145. doi: 10.1016/j.chemgeo.2016.06.001
- Tessier, A., Campbell, P. G., and Bisson, M. (1979). Sequential extraction procedure for the speciation of particulate trace metals. *Anal. Chem.* 51, 844–851. doi: 10.1021/ac50043a017
- Thurman, E. M. (1985). *Organic Geochemistry of Natural Waters*. Dordrecht: Martinus Nijhoff/Dr. Junk Publishers.
- Tipping, E. (1994). WHAMC—a chemical equilibrium model and computer code for waters, sediments, and soils incorporating a discrete site/electrostatic model of ion-binding by humic substances. *Comput. Geosci.* 20, 973–1023. doi: 10.1016/0098-3004(94)90038-8
- Tipping, E., Lofts, S., and Sonke, J. E. (2011). Humic Ion-Binding Model VII: a revised parameterisation of cation-binding by humic substances. *Environ. Chem.* 8, 225–235. doi: 10.1071/EN11016
- Trefry, J. H., and Shokes, R. F. (1981). “History of heavy-metal inputs to Mississippi Delta sediments,” in *Elsevier Oceanography Series*, Vol. 27, ed R. A. Geyer (Texas, TX: Elsevier), 193–208.
- Welch, K. A., Lyons, W. B., Graham, E., Neumann, K., Thomas, J. M., and Mikesell, D. (1996). Determination of major element chemistry in terrestrial waters from Antarctica by ion chromatography. *J. Chromatogr. A* 739, 257–263. doi: 10.1016/0021-9673(96)00044-1

- Wen, L. S., Shiller, A., Santschi, P. H., and Gill, G. (1999). "Trace element behavior in Gulf of Mexico estuaries," in *Biogeochemistry of Gulf of Mexico Estuaries* eds T. S. Bianchi, J. R. Pennock, and R. R. Twilley (New York, NY: John Wiley and Sons), 303–346.
- Willis, S. S., and Johannesson, K. H. (2011). Controls on the geochemistry of rare earth elements in sediments and groundwaters of the Aquia aquifer, Maryland, USA. *Chem. Geol.* 285, 32–49. doi: 10.1016/j.chemgeo.2011.02.020
- Xu, Y., and Marcantonio, F. (2004). Speciation of strontium in particulates and sediments from the Mississippi River mixing zone1. *Geochim. Cosmochim. Acta* 68, 2649–2657. doi: 10.1016/j.gca.2003.12.016

**Conflict of Interest Statement:** The authors declare that the research was conducted in the absence of any commercial or financial relationships that could be construed as a potential conflict of interest.

Copyright © 2018 Adebayo, Cui, Hong, White, Martin and Johannesson. This is an open-access article distributed under the terms of the Creative Commons Attribution License (CC BY). The use, distribution or reproduction in other forums is permitted, provided the original author(s) and the copyright owner are credited and that the original publication in this journal is cited, in accordance with accepted academic practice. No use, distribution or reproduction is permitted which does not comply with these terms.





# Rare Earth Elements in Andaman Island Surface Seawater: Geochemical Tracers for the Monsoon?

Ed C. Hathorne<sup>1\*</sup>, Martin Frank<sup>1</sup> and P. M. Mohan<sup>2</sup>

<sup>1</sup> GEOMAR Helmholtz Centre for Ocean Research Kiel, Kiel, Germany, <sup>2</sup> Department of Ocean Studies and Marine Biology, Pondicherry University, Port Blair, India

## OPEN ACCESS

### Edited by:

Catherine Jeandel,  
UMR 5566 Laboratoire d'Études en  
Géophysique et Océanographie  
Spatiales (LEGOS), France

### Reviewed by:

Johan Schijf,  
University of Maryland Center  
for Environmental Science (UMCES),  
United States  
Germain Bayon,  
Institut Français de Recherche pour  
l'Exploitation de la Mer (IFREMER),  
France  
Ester Garcia-Solsona,  
University of Barcelona, Spain

### \*Correspondence:

Ed C. Hathorne  
ehathorne@geomar.de

### Specialty section:

This article was submitted to  
Marine Biogeochemistry,  
a section of the journal  
Frontiers in Marine Science

**Received:** 01 December 2018

**Accepted:** 27 November 2019

**Published:** 09 January 2020

### Citation:

Hathorne EC, Frank M and  
Mohan PM (2020) Rare Earth  
Elements in Andaman Island Surface  
Seawater: Geochemical Tracers  
for the Monsoon?  
Front. Mar. Sci. 6:767.  
doi: 10.3389/fmars.2019.00767

The Asian summer monsoon affects the lives of billions of people. With the aim of identifying geochemical tracers for the monsoon-related freshwater input from the major rivers draining into the Bay of Bengal (BoB) and the Andaman Sea (AnS), we have analyzed the yttrium and rare earth element (YREE) concentration of surface seawater samples from various locations spanning the Andaman Islands in 2011 to 2013. In some locations, samples have been taken in March, July, and November 2011, thus spanning the seasonal cycle and including different monsoon phases. Generally, the YREE patterns are similar to those reported for offshore samples from the BoB and AnS in January 1997, with seawater-normalized patterns of most samples characterized by middle REE enrichments. An enhancement of these middle REE bulges accompanies large increases in dissolved REE concentrations from streams and sediment-rich areas such as mangrove environments. Conversely, some samples, in particular those taken 1–2 days after heavy rainfall in March 2011, show pronounced REE scavenging accompanied by the preferential removal of dissolved light REEs (LREEs) and by higher Y/Ho ratios. The Nd isotope signature of the remaining dissolved REE phase of these low YREE samples is more radiogenic than local rocks and sediments. The time series at a location away from local input sources show remarkably similar REE patterns and concentrations in March and July. Then in October–November, following the peak in monsoon-induced river discharge, the dissolved REE concentrations increase by almost a factor of two, whereas Nd isotopes become less radiogenic by 1.5  $\epsilon$ Nd units. These unradiogenic values are found at the same site in the winter dry season of the following year, demonstrating the decoupling of sea surface salinity (SSS) and Nd. The large sub-annual variability of YREE concentrations and Nd isotopes encountered was likely caused by the conversion of YREE from the dissolved (probably colloidal) pool to the labile particulate fraction. The comparison of unfiltered and filtered sample concentrations reveals the existence of a large labile particulate pool in the BoB and AnS that most likely originates from the massive river sediment fluxes and is instrumental in the seasonal changes observed.

**Keywords:** yttrium and lanthanides, Bay of Bengal, Andaman Island, Nd isotope composition, river seasonality

## INTRODUCTION

The rare earth elements (REEs) have been recognized as a means to detect trace metal input from rivers to coastal waters since the pioneering work of Elderfield and colleagues in the 1980s (Hoyle et al., 1984; Goldstein and Jacobsen, 1988b; Sholkovitz and Elderfield, 1988; Elderfield et al., 1990). Examining the relative concentrations of some or all of the 14 naturally occurring REEs and yttrium provides a wealth of information, as fractionation among this chemically coherent group of elements reflects solution speciation, particle exchange processes, source oxidation state, and the preferential incorporation into and subsequent release from different minerals (e.g., Cantrell and Byrne, 1987; Byrne et al., 1991; Moffett, 1994; Bau, 1999; Hannigan and Sholkovitz, 2001; Quinn et al., 2006; see Elderfield, 1988 for a review that still remains insightful and relevant after 30 years). Even more information can be gleaned from the radiogenic isotope composition of the light REE (LREE) neodymium as  $^{143}\text{Nd}$  is the alpha decay product of  $^{147}\text{Sm}$  and hence the  $^{143}\text{Nd}/^{144}\text{Nd}$  ratio (expressed relative to the initial bulk Earth composition called CHUR in epsilon units) reflects the type and age of rocks, which impart their signature to rivers and seawater through weathering (e.g., Goldstein and Jacobsen, 1987, 1988a; Bertram and Elderfield, 1993; Frank, 2002; Lacan et al., 2012; van de Flierdt et al., 2016). Elderfield et al. (1990) suggested the relative REE concentrations or “REE pattern” of filtered river water is controlled by two pools: (1) the colloidal pool consisting of REE bound to small particles like Fe oxy-hydroxides or organic matter and (2) the truly dissolved pool in which the REEs are bound to simple inorganic ligands like carbonate. The relative proportion of these pools is a function of river chemistry including organic and inorganic ligand concentrations and pH (Tang and Johannesson, 2010). The importance of the colloidal pool is most obvious when river water first meets salty water in the estuary and salt-induced coagulation removes most, if not all, of the REEs contained in the colloidal pool (e.g., Sholkovitz and Szymczak, 2000). This results in a range of estuarine Nd removal from 97 to 40% (Rousseau et al., 2015 and the references therein; Adebayo et al., 2018) and exerts a fundamental control on the REE signal of river input and the REE budget of the oceans. Experiments with filtered river and seawater suggest that much of the variability in estuarine removal is related to the character of the colloid fraction REE. Organic matter-bound REE behaves nearly conservatively, whereas waters rich in inorganic colloids quickly lose their REE load as salinity increases (Merschel et al., 2017a).

The South Asian monsoon (SAM) affects the livelihoods of more than a billion people, providing vital water resources on the one hand and devastating floods and landslides on the other (Krishna Kumar et al., 2004; Gadgil and Gadgil, 2006; Turner and Annamalai, 2012; Duncombe, 2018). Four of Earth's great rivers—the Ganges (Ganga) and Brahmaputra (G-B), Irrawaddy (or Ayeyarwady), and Salween (I-S)—discharge more than 1000 km<sup>3</sup>/year of freshwater (Dai et al., 2009) into the Bay of Bengal (BoB) and the Andaman Sea (AnS) (**Figure 1**). These monsoon-fed rivers also deliver some of the highest

sediment loads globally (Milliman and Syvitski, 1992), which has built the Bengal and Nicobar fan, the largest submarine fan system on Earth (Curry et al., 2002). The discharge of these monsoonal rivers is highly seasonal following spring snow melt and most importantly summer monsoon precipitation (Shaman et al., 2005; Jian et al., 2009). Large sub-seasonal and inter-annual variability of G-B discharge is tightly linked to monsoon precipitation peaking from June to October (Jian et al., 2009), and these variations impact BoB sea surface salinity (SSS). As such, the BoB and AnS are characterized by a thin (<20 m) low-salinity mixed layer persisting all year round, which is maintained by a roughly equal mixture of river discharge and direct monsoon precipitation over the ocean and often displays two steps of increasing salinity with depth (Sengupta et al., 2006). The halocline below this fresh layer is normally shallower than the thermocline, and the layer between them is referred to as the barrier layer (e.g., Girishkumar et al., 2011). This barrier layer has been implicated in cyclone intensification (Sengupta et al., 2006), and the thickness of the fresh mixed layer and barrier layer is driven by seasonally reversing winds and ocean currents with mesoscale eddies facilitating vertical mixing (Durand et al., 2011; Girishkumar et al., 2011, 2013; Akhil et al., 2014, 2016). Recent observations of SSS variability suggest that this feature is dominated by the freshwater flux and not surface circulation (Chaitanya et al., 2015), although weakened currents resulting from Indian Ocean dipole modes may play a role in trapping freshwater in the BoB (Pant et al., 2015). Recent mooring observations in the northern BoB between the G-B and I river mouths demonstrate that SSS can drop by 4 psu units in 5 days as river discharge fronts pass (Sengupta et al., 2016). Despite recent advances in observational coverage of the region (e.g., Girishkumar et al., 2011), the hydrographic variability in areas like the AnS remains poorly understood (Chatterjee et al., 2012) and undersampled.

Amakawa et al. (2000) first reported elevated REE concentrations of BoB and AnS surface waters compared with the rest of the Indian Ocean, with a distinctive REE pattern and unradiogenic Nd isotopes most likely reflecting the weathering input from South Asia. These elevated REE concentrations with a globally distinctive broad middle REE enrichment and similar normalized La and Lu values were found to extend to deeper BoB and AnS waters (Nozaki and Alibo, 2003). This most likely originates from the inputs of the great rivers, but the dissolved river flux (estimated as very few dissolved river REE data exist for the region) is a factor of 10 too low, leading Nozaki and Alibo (2003) to suggest that the supply of excess BoB REEs could be accounted for by the dissolution of no more than 0.3% of the sediments brought by the rivers. More recent studies focusing on Nd isotopes and concentrations have revealed a substantial excess Nd concentration throughout the BoB, which has a calculated Nd isotope composition similar to that of modern G-B river sediments and suggests release from Bengal Fan sediments (Singh et al., 2012). The resampling of similar locations a few years later found significantly lower Nd concentrations and more radiogenic Nd isotope signatures leading to the suggestion that the Nd isotope composition of BoB seawater varies seasonally and inter-annually with river

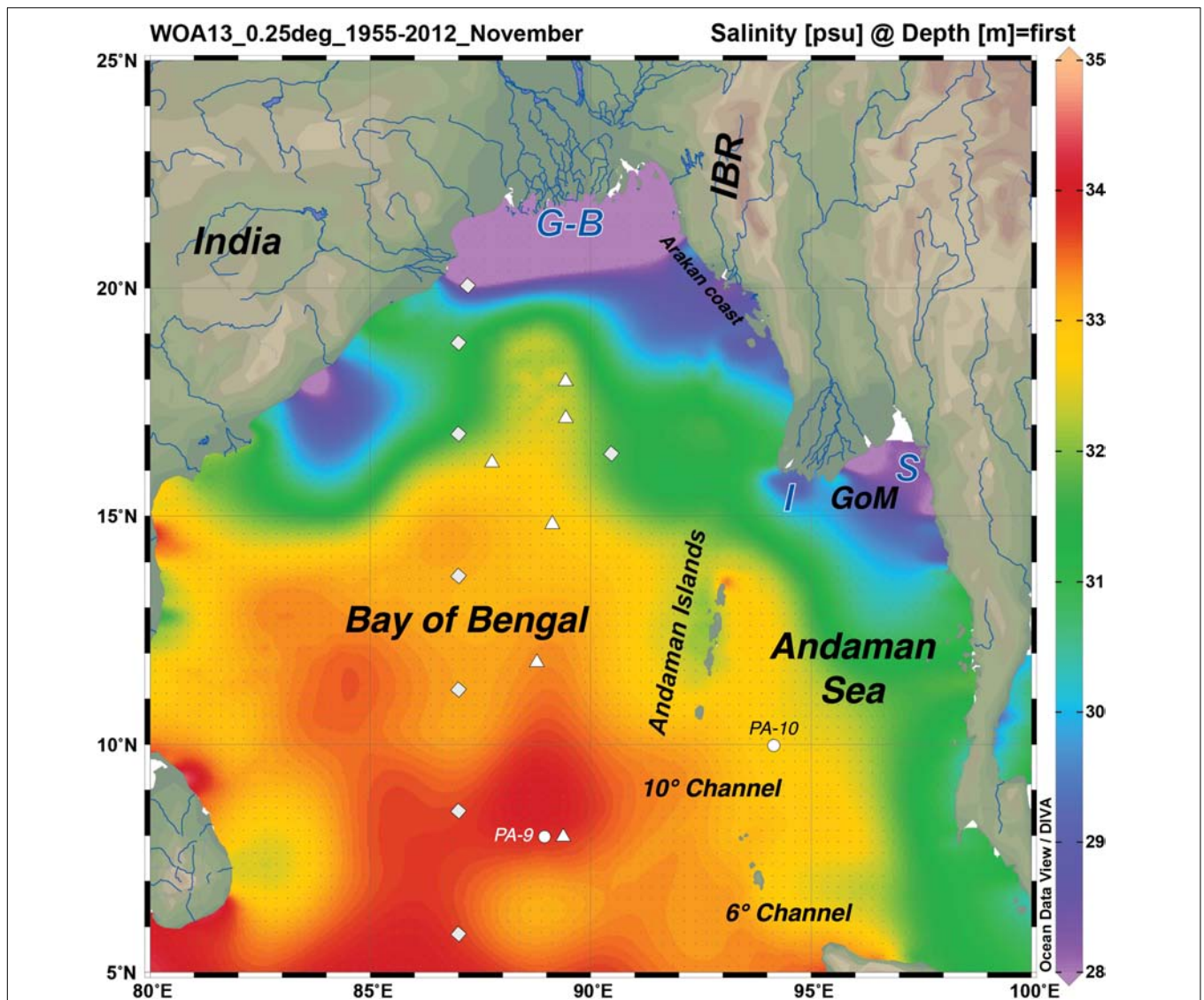


**FIGURE 1 |** Regional map of the Bay of Bengal (BoB) and Andaman Sea (AnS) showing the mouths of the big four rivers: Ganga and Brahmaputra (G-B), Irrawaddy or Ayeyarwady (I) and Salween (S), the Andaman Islands, and the WOA2013 sea surface salinity climatology for November (1955–2012). This figure was made using Ocean Data View (Schlitzer, R., Ocean Data View, <http://odv.awi.de>, 2016). Other features of interest are marked: Indo-Burmese Ranges (IBR), Gulf of Martaban (GoM), and the two deep channels connecting the BoB and the AnS. The sampling stations from the other studies of seawater Nd isotopes and rare earth elements (REEs) in the region are shown; labeled circles for Amakawa et al. (2000) and Nozaki and Alibo (2003), square rhombuses for Singh et al. (2012), and triangles for Yu et al. (2017a; 2017b).

sediment discharge (Yu et al., 2017a). Furthermore, these authors presented Y and REE data for their BoB samples, which suggested that the freshwater input into the BoB can be traced with YREE ratios (Yu et al., 2017b). Such variability is hard to reconcile with the Nd oceanic residence time in the order of centuries (e.g., Tachikawa et al., 1999) and the calculated YREE residence times for BoB surface water (Yu et al., 2017b). Despite these clear signals, it was not possible to conclude if the variability observed between these studies was truly seasonal/inter-annual or resulted from spatial heterogeneity (Yu et al., 2017a). If these potential proxies for river discharge into the BoB and AnS are to be used for filling the large data gaps in this region, the seasonal

fluctuation of the REE concentrations and signatures needs to be verified with a stationary time series, and suitable archives for past REE variations need to be identified.

Despite a compelling consensus that the vast majority of REE associated with planktonic foraminifera shells is acquired at the sea floor from bottom waters or porewaters during early diagenesis (Roberts et al., 2010, 2012; Kraft et al., 2013; Tachikawa et al., 2013; Osborne et al., 2017; Skinner et al., 2019), some workers have used the Nd/Ca of planktonic foraminifera shells to infer past changes in monsoon-induced runoff (Liu et al., 2015; Nilsson-Kerr et al., 2019). In contrast, the annual density bands of massive coral skeletons are a promising recorder of



mixed-layer seawater REE concentrations (e.g., Wyndham et al., 2004; Saha et al., 2016), but the processes controlling the YREE concentrations and Nd isotope signatures of seawater within and around the coral reef system need to be understood before such proxies can be reliably applied in the past. With this goal in mind, we have systematically sampled surface seawater from around coral reefs of the Andaman Islands, which form the geographic boundary between the BoB and AnS. These data demonstrate that seawater REE concentrations in the BoB do vary seasonally with the monsoon-induced river water discharge. However, we also identify many local processes that can modify the YREE and Nd isotope signal on short time and length scales, meaning coral REE signatures from such settings must be interpreted with caution.

## MATERIALS AND METHODS

### Study Area

The Andaman Islands are situated some 600 km west of Thailand and 1300 km east of mainland India and extend from around 10°N to 14°N (**Figure 1**). Formed by the uplift of the accretionary prism of the Sunda Trench, the Andaman Islands are composed of sedimentary rocks of late Cretaceous to Miocene age sitting on top of ophiolitic volcanics and basalts (Allen et al., 2008a; Garzanti et al., 2013). Barren Island to the east of the other islands is the only active volcano representing the active arc. Arc materials are present throughout much of the turbiditic mudrocks and sandstones of the Andaman Flysch and Mithakhari Group (Allen et al., 2008a), and it is these Paleogene rocks that are most exposed on the main three islands of South, Middle, and North Andaman (Garzanti et al., 2013) (**Figure 2**). These sedimentary rocks represent the erosional product of the Himalayan orogeny delivered mostly by the Irrawaddy river (Garzanti et al., 2013), and sediments with similar composition and zircon ages extend from the Indo-Burman Ranges (IBR) in the north (Allen et al., 2008b) to the Nicobar fan in the south (McNeill et al., 2017). On the smaller surrounding islands, where coral reefs are abundant, are exposures of the Neogene Archipelago group, which contain sandstones, chalk, and limestones (Allen et al., 2008a) deposited on the slope (Pal et al., 2005). The summer monsoon rains usually begin in May on the Andaman Islands, earlier than in mainland India (Fasullo and Webster, 2003), and the high-precipitation season is normally at full strength by early July (**Figure 3**). Being sparsely populated, with most development centered around the capital Port Blair, the Andaman Islands are mostly undisturbed and covered by dense rain forest that extends to the beach and the coral reefs. In low-lying areas, mangrove forests and glades are found next to the reefs. As such, they present an increasingly rare opportunity to study the geochemistry of virtually undisturbed reef ecosystems. Unfortunately, these islands are not immune from global change and substantial coral bleaching (Sarkar and Ghosh, 2013).

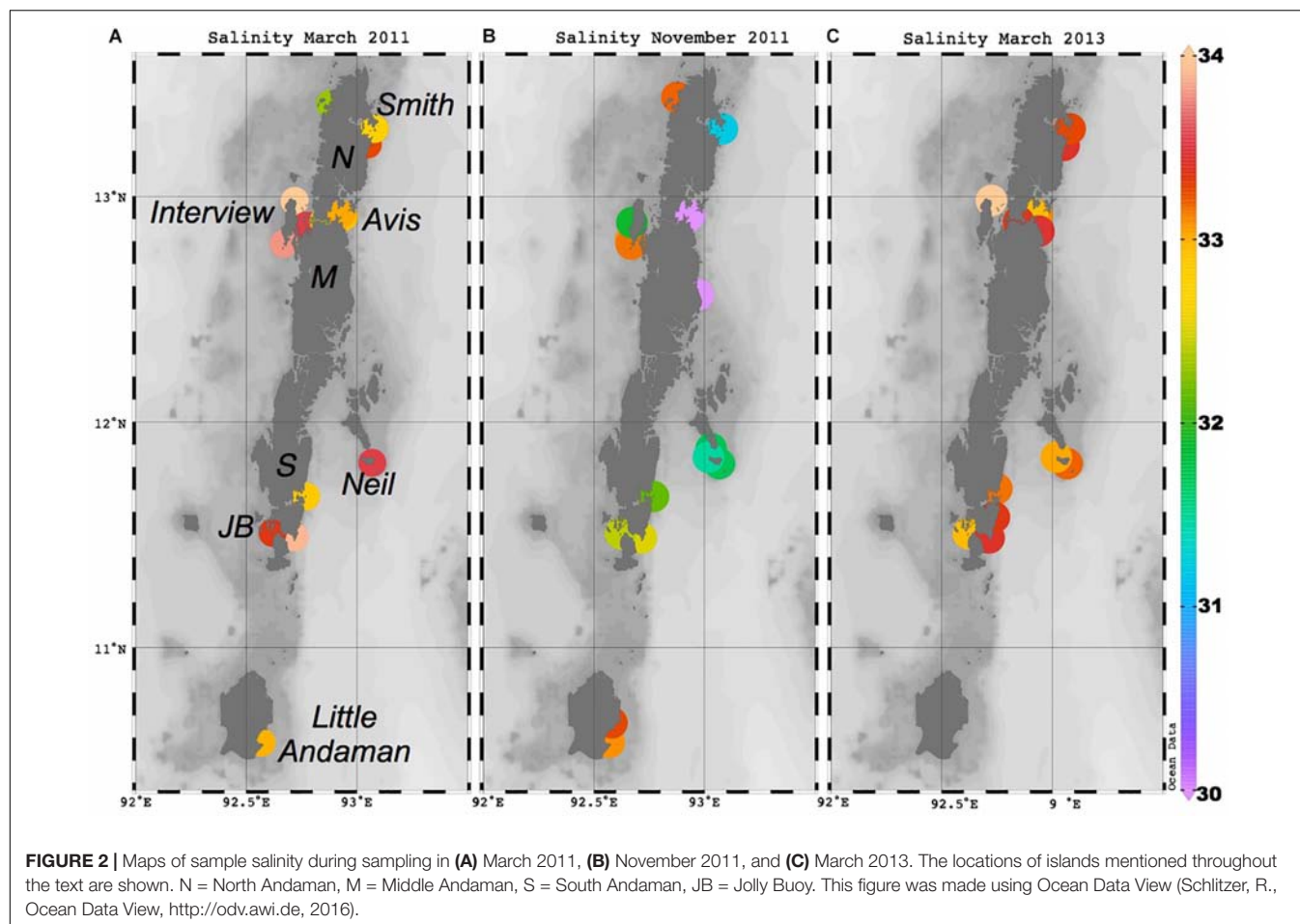
Regrettably, the oceanography of the AnS is very poorly studied, and even today, relatively few Argo floats make it there to improve this dearth of knowledge (e.g., Thadathil et al., 2007). Even less is known about the oceanography around the Andaman

Islands. The water chemistry around the islands is likely driven by the monsoon rains, river discharge, and seasonally reversing ocean currents (Chatterjee et al., 2017). The AnS is open to surface water exchange with the BoB at the Prepairs Channel between North Andaman Island and the Ayeyarwady (Irrawaddy) delta in Myanmar, whereas the 10 Degree Channel between Little Andaman and Great Nicobar Islands and the Great (or 6 Degree) Channel between the Nicobar Islands and Sumatra provide deeper connections. Generally, it is thought that the surface circulation in the AnS is cyclonic during the SW monsoon and the reverse during the northeast (NE) monsoon (Varkey et al., 1996), but more modern analyses suggest that the situation is more complex with a mean flow toward the southeast (SE) in summer and toward the southwest (SW) in winter (Rizal et al., 2012). Forced by both remote equatorial Wyrski jets and local winds, strong surface currents probably form along the Islands during the monsoon transitions in spring and autumn (Chatterjee et al., 2017). Much of the large monsoonal sediment flux from the nearby Ayeyarwady (Irrawaddy) and Salween rivers is trapped in the Gulf of Martaban (Ramaswamy et al., 2004), but the surface waters of the reefs become noticeably turbid during the summer monsoon season. The study of recent sediments from the NE BoB and AnS indicates that the small Arakan coast rivers supply a disproportionately large fraction of terrigenous sediments with radiogenic Nd isotope signatures to the region (Colin et al., 1999; Damodararao et al., 2016).

### Sample Collection and Processing

Surface samples were collected in PE bottles while swimming or from the side of small wooden boats (no deeper than an arm's length) from open ocean locations with extensive coral reefs and more inshore locations (see **Supplementary Figure S1** for an example). In a few instances, a small Niskin bottle on a rope was employed. Freshwater samples were collected by holding the PE bottle in the stream or waterfall. All samples were filtered within a few hours at 0.22 or 0.45  $\mu\text{m}$  (cellulose acetate membranes) using the vacuum produced by a water jet and a Nalgene PC 42-mm-diameter filter holding device. This was rinsed with  $> 18.2\text{ M}\Omega$  water between samples, and the first 500 ml of filtered sample was discarded. During the first sampling campaign, an unfiltered sample aliquot was also kept for some selected samples. In all subsequent sampling, an unfiltered sample aliquot was kept for all samples, with the exception of the large volume samples, which were limited in number by logistical reasons. The large volume samples for Nd isotope analyses were obtained by filling two 20-l collapsible cubic containers as much as possible while snorkeling or from the side of a wooden boat. These were then filtered directly after collection using a hand-operated peristaltic pump and a 142-mm-diameter filter holder with 0.45- $\mu\text{m}$  cellulose nitrate filter membranes into an acid-cleaned 20-l collapsible cubic container. The cubic containers used for sample collection were rinsed with 10% HCl (analytical grade) and  $> 18.2\text{ M}\Omega$  water (Milli-Q) before the next use. During collection, the cubic containers were first rinsed with sample before the sample was taken. Particularly, sediment-rich samples required the use of multiple membranes. Filtered and unfiltered samples (125 ml) were acidified to pH 2 in the field using distilled HCl prepared in





the clean labs at GEOMAR, Germany. A small aliquot of filtered sample was filled into a 1.4-ml glass vial with no head space and sealed with a septum lid and Parafilm<sup>TM</sup> for stable isotope and chloride analyses.

Salinity was measured in the field to 0.1 psu during sample collection and after filtering using a handheld conductivity sensor made for domestic aquarium purposes. This was cross-calibrated with a WTW conductivity sensor and gravimetrically prepared NaCl solutions before going into the field.

Jolly Buoy Island was sampled in 2011, in February and March 2012, and again in March 2013. A few key locations distributed along the islands have been resampled in March 2013.

Rainwater samples were obtained in January 2015 from the deck of the JOIDES Resolution drill ship while operating near Little Andaman Island. Rain was collected in an acid-cleaned PE beaker and filtered through a 0.2- $\mu$ m polysulfone disk filter with an acid-cleaned syringe directly after collection. The filtered rain samples were acidified to 1% by volume with Seastar grade HNO<sub>3</sub>.

In the laboratory at Pondicherry University in Port Blair, FeCl solution (purified in the GEOMAR laboratory) was added to the 20-l volume samples for Nd isotope analysis and allowed to equilibrate for 24–48 h. After equilibration, the pH was raised to 7.5 to 8 by the stepwise addition of Merck Suprapur grade

(imported by Sigma–Aldrich, India) ammonia solution. The resulting FeOH precipitate was allowed to settle for 24–48 h before the excess seawater was siphoned off, and only the FeOH precipitate was taken to Germany. Back in the laboratory at GEOMAR, the FeOH precipitate was further concentrated and dissolved, and excess Fe was removed by an ether back-extraction before Nd was purified using routine techniques in our laboratory (Stichel et al., 2012), producing yields of approximately 70%.

## Analytical Methods

### Salinity and $\delta^{18}\text{O}$ – $\delta^2\text{H}$

Samples were analyzed for  $\delta^{18}\text{O}$  and  $\delta^2\text{H}$  by isotope ratio infrared spectroscopy (L 1102-i WS-CRDS, Picarro Inc., Santa Clara, CA, United States) at the Friedrich-Alexander University Erlangen-Nürnberg, Germany. All values are reported in the standard  $\delta$ -notation (‰) vs. Vienna Standard Mean Ocean Water (VSMOW), and external reproducibility based on repeated analyses of a control sample was better than 0.1 and 0.5‰ ( $\pm 1$  sigma) for  $\delta^{18}\text{O}$  and  $\delta^2\text{H}$ , respectively. A detailed description of the analytical procedure used is given in van Geldern and Barth (2012). Following stable isotope analyses, the chloride concentration of the samples was determined by titration with silver nitrate using a METROHM auto-titrator. IAPSO standard seawater (Cl = 19.376 g/kg or as specified on the bottle; the

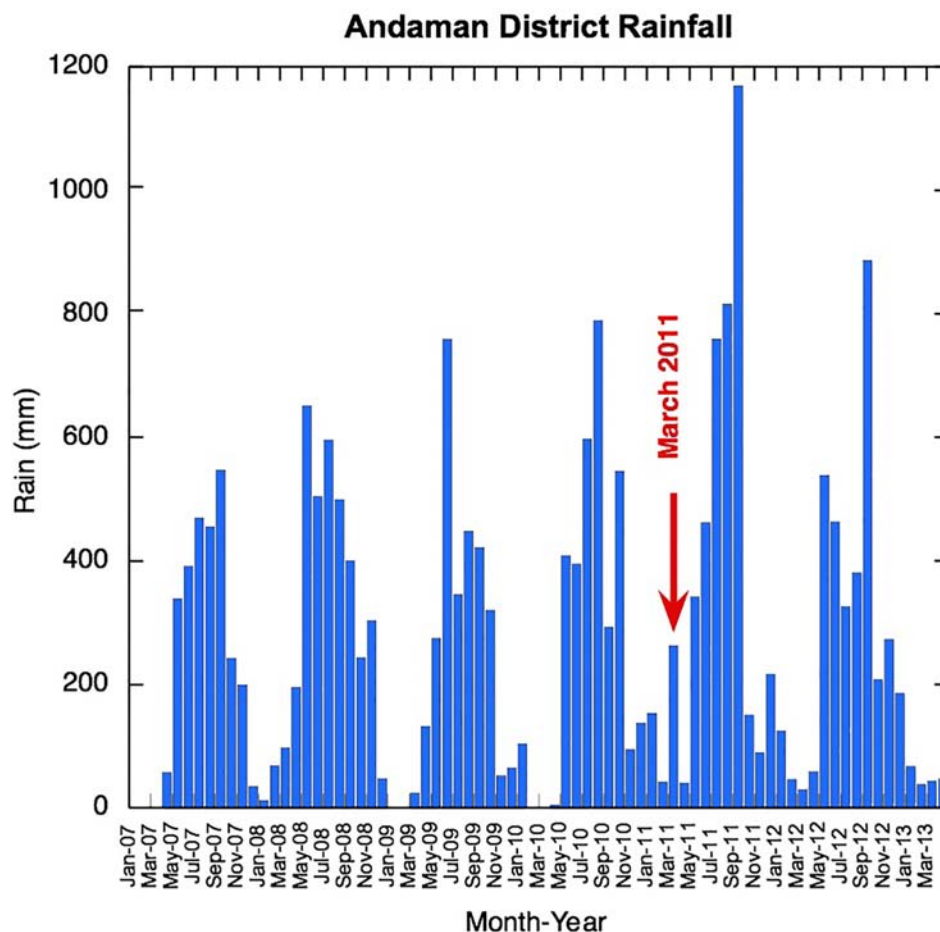


**FIGURE 3 |** Andaman Island district monthly rainfall before and during sampling (data from India Meteorological Department Hydromet division reports).

sum of chloride and bromide is 559 mM) was used to calibrate the results, and the precision is estimated to be 0.3% based on repeated measurements of IAPSO.

### Yttrium and REE

Analysis of the YREE concentration of most of the samples was performed using a seaFAST online preconcentration (OP) system coupled to an Agilent 7500ce inductively coupled plasma mass spectrometer (ICP-MS) as described in Hathorne et al. (2012). This method was part of the GEOTRACES intercalibration exercise (van de Flierdt et al., 2012) and has been demonstrated to produce accurate Nd concentrations, compared with isotope dilution measurements of the same samples on numerous occasions (Hathorne et al., 2012; Grasse et al., 2017; Laukert et al., 2017). The long-term average value obtained for the Bermuda Atlantic Time-Series (BATS) 15-m sample during the course of this study is presented in **Supplementary Table S1**.

YREE data obtained for the March 2013 samples utilized a newer syringe pump type seaFAST instrument (SV400) coupled with a Thermo Fisher Element XR sector field (SF)-ICP-MS. These measurements employed a 4-ml loop, and the instrument

was run in low resolution and scan speed optimization mode to obtain time-resolved data. Such time-resolved analysis has been found to improve precision for such low-volume analyses (Osborne et al., 2015). Calibration curves for these measurements were obtained by standard additions of a mixed YREE solution with a seawater-like pattern to a large volume surface seawater sample from the South Atlantic. The average values obtained for the 15-m BATS reference seawater during these analyses, is presented in **Supplementary Table S1**.

Unfiltered samples were first centrifuged at 3500 r/min (Eppendorf 5810 max 2900 × g) for 30 min before the supernatant was transferred to a fresh tube for analysis. The filtered sample concentrations are operationally defined as “dissolved,” while the unfiltered samples represent both the dissolved and weak HCl soluble pool referred to here as “easily exchangeable” or labile.

Procedural blanks taken in the field ( $n = 5$ ) by filtering > 18.2 MΩ water acidifying and storing with the samples were also analyzed by OP-ICP-MS with the samples. Repeated analyses of these blanks in the most recent analytical session reveal that they are < 0.5 pmol/kg for the LREE to below detection limits (e.g., <0.03 pmol/kg of Lu) for the heavy

REE (HREE). For the LREE, this is 20% for the anomalously low-concentration samples, but only in the order of 1% for LREE in the vast majority of samples and is also negligible for the mid-REE (MREE) and HREE (including Y).

Neodymium isotope measurements were performed with either a Nu instrument MC-ICP-MS at GEOMAR or a Thermo Fisher Neptune Plus MC-ICP-MS at the Institute for Chemistry and Biology of the Marine Environment (ICBM), University of Oldenburg, Germany. Solutions with concentrations from 5 ppb and higher were measured, and values were normalized to the accepted  $^{143}\text{Nd}/^{144}\text{Nd}$  of the JNdi-1 isotope standard of 0.512115 (Tanaka et al., 2000). Based on repeated measurements of the JNdi-1 and an in-house Nd standard “Merck” from the ICBM, the 2-s external precision of the measurements expressed as  $\epsilon\text{Nd}$  is 0.4 units. Repeated measurements of one sample with a high Nd concentration (AN12) on both instruments gave a comparable precision of 0.4 epsilon units.

## RESULTS

The field measured salinities and those determined later by silver nitrate titration generally agree very well (slope of 0.98 with a zero intercept  $R^2 = 0.94$ ).

Freshwater samples (apart from the rain) plot on the global  $\delta^{18}\text{O}$  vs.  $\delta^2\text{H}$  meteoric water line, and the other samples generally form a mixing line between the seawater and freshwater (Supplementary Figure S2). One sample deviated from this relationship, suggesting that evaporation may have occurred since collection. The  $\delta^{18}\text{O}$ ,  $\delta^2\text{H}$ , and salinity data for this sample were excluded and are not reported or discussed.

### Geographical Variability

Salinity varies widely, and this patchiness is also clear in the high resolution World Ocean Atlas climatology shown here for November (Figure 1) and in recently acquired field data (Kiran Kumar et al., 2018). Away from river or stream mouths, the salinity ranged from 34 to 31 over our sampling period, with the freshest values found on the AnS side of the Islands during November 2011 (Figure 2). Some of the variability of salinity observed across the islands is also likely to be temporal, as these locations were sampled over a few weeks during each sampling campaign. March 2011 was particularly wet with anomalously high rainfall on the Andaman Islands (Figure 3). NE Interview Island showed the saltiest waters in both March 2011 and 2013 (Figure 2). This suggests that either surface circulation brought more saline waters to this northerly exposed location or there was supply from a local source of saltier water, perhaps a very shallow lagoon nearby formed by uplifted coral reefs.

The concentration of REEs in the filtered seawater samples varied greatly with Nd ranging from 1.6 to 120 pmol/kg, whereas Yb concentrations varied from 2.15 to 20.5 pmol/kg (shown as shale-normalized values in Figure 4 and Supplementary Table S1). The lowest concentrations were encountered after a rain event in March 2011 (Figure 3) and consistently at one beach location on Neil (Shaheed Dweep) Island in both

2011 and 2013 (Figure 4, samples AN48, AN54, and AN124). The highest concentrations are from locations inland up tidal creeks (Figure 4, samples AN13 and AN140) or next to small river mouths where the sediment loading was high (Figure 4, samples AN88 and AN146). Shale-normalized patterns (Figure 4) broadly resemble seawater from other locations including an HREE enrichment and relatively depleted Ce concentrations (negative Ce anomaly), but in some samples, a MREE enrichment is clearly evident. There is no simple relationship between salinity and YREE concentrations except for the few filtered samples with salinities less than 31.5, which display a clear negative relationship, especially for the HREE. However, the vast majority of samples with salinities  $> 31.5$  have higher YREE concentrations.

Filtered freshwater concentrations range from 26 to 277 pmol/kg of Nd and 3.3 to 25 pmol/kg of Yb. Concentrations in the filtered rainwaters are low but substantial, with Nd ranging from 1.4 to 4.5 pmol/kg, whereas Yb concentrations range from 0.2 to 0.7 pmol/kg. Shale-normalized patterns for the freshwaters display either strong MREE enrichments or more seawater-like patterns with enhanced HREE concentrations (Figure 5).

The concentrations encountered in the unfiltered samples represent the particulate YREE that is leachable in 0.1% HCl over months to years, as well as the dissolved YREE. This ranges from values similar to filtered samples to extremes of 780 pmol/kg of Nd and 141 pmol/kg of Yb. For example, samples from Jolly Buoy Island exhibit very little difference (unfiltered/filtered near 1), whereas some of the stream and river mouth samples have the highest easily exchangeable YREE concentrations (unfiltered/filtered  $> 10$ ).

### Temporal Variability

At three readily accessible locations, Smith Island, Avis Island, and Jolly Buoy Island, we were able to obtain multi-season and in some cases multi-year time series. Both Smith and Avis island time series reveal anomalously low YREE concentrations 1–2 days after a sustained 2-day rain event in March 2011 (Figure 6), whereas the salinity was only significantly lower at Avis island in July and both Avis and Smith islands in November. The Avis Island time series exhibits a large range of concentrations similar those encountered in all other samples, but at one single location, where very high concentrations (83 pmol/kg of Nd) occurred during the monsoon in July 2011 (Figure 6). At Jolly Buoy Island, the range in concentrations is smaller, and the maximum concentrations occurred later in the year in November (Figure 7). Between March and November, the salinity at Jolly Buoy Island decreased by 1 psu, and the Nd (YREE) concentration peaks but decreased again whereas salinity remained low (Figure 8). A similar relationship between Nd concentrations and salinity in the inter-annual samples is not observed.

### Neodymium Isotopes

A wide range of Nd isotope values are encountered in the filtered samples, from -9.6 to -2.6, with an apparent relationship with Nd concentrations (Figure 9). The Nd isotope composition

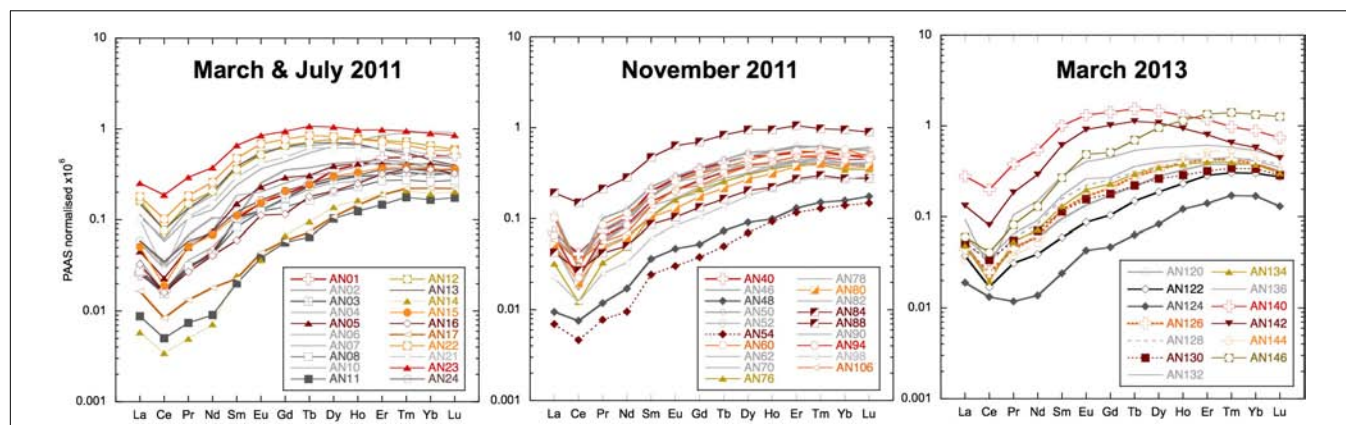


**FIGURE 4 |** Filtered seawater samples shale-normalized to Post-Archean Average Australian Sedimentary rocks (PAAS) (Nance and Taylor, 1976). Samples from the main locations use the same symbols: squares for Smith Island, vertical triangles for Avis Island, square rhombuses for Niel (Shaheed Dweep) Island, and horizontal triangles for Little Andaman Island.

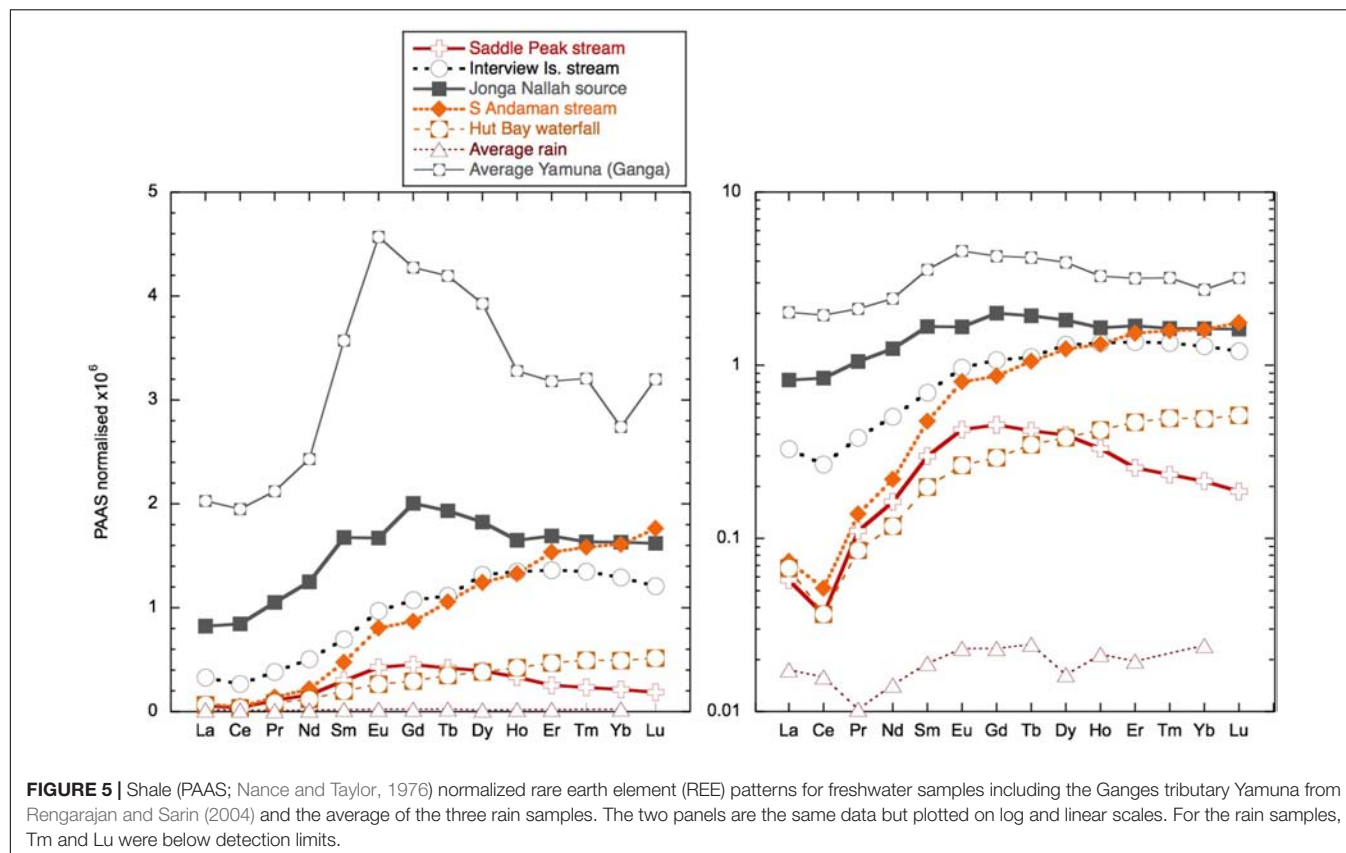


**FIGURE 5 |** Shale (PAAS; Nance and Taylor, 1976) normalized rare earth element (REE) patterns for freshwater samples including the Ganges tributary Yamuna from Rengarajan and Sarin (2004) and the average of the three rain samples. The two panels are the same data but plotted on log and linear scales. For the rain samples, Tm and Lu were below detection limits.

at the Jolly Buoy site was -7.6 in March 2011 and then an invariable signature of -9 in November 2011 and February and March 2012 (Figure 8). This consistency is in strong contrast to the variations in salinity and Nd concentration between these sampling periods. The other sample from the western BoB side of the Islands (Interview Island) also has a similar Nd isotope composition, whereas samples from the eastern side of the Islands in the AnS have more radiogenic values ranging from -7 to -2.6. The most radiogenic values

were measured for the samples with the lowest Nd and YREE concentrations (Figure 9).

## DISCUSSION

### Local Sources of YREE to Seawater

The dissolved Nd isotope composition measured is overall consistent with the local and regional geology (Figure 9),



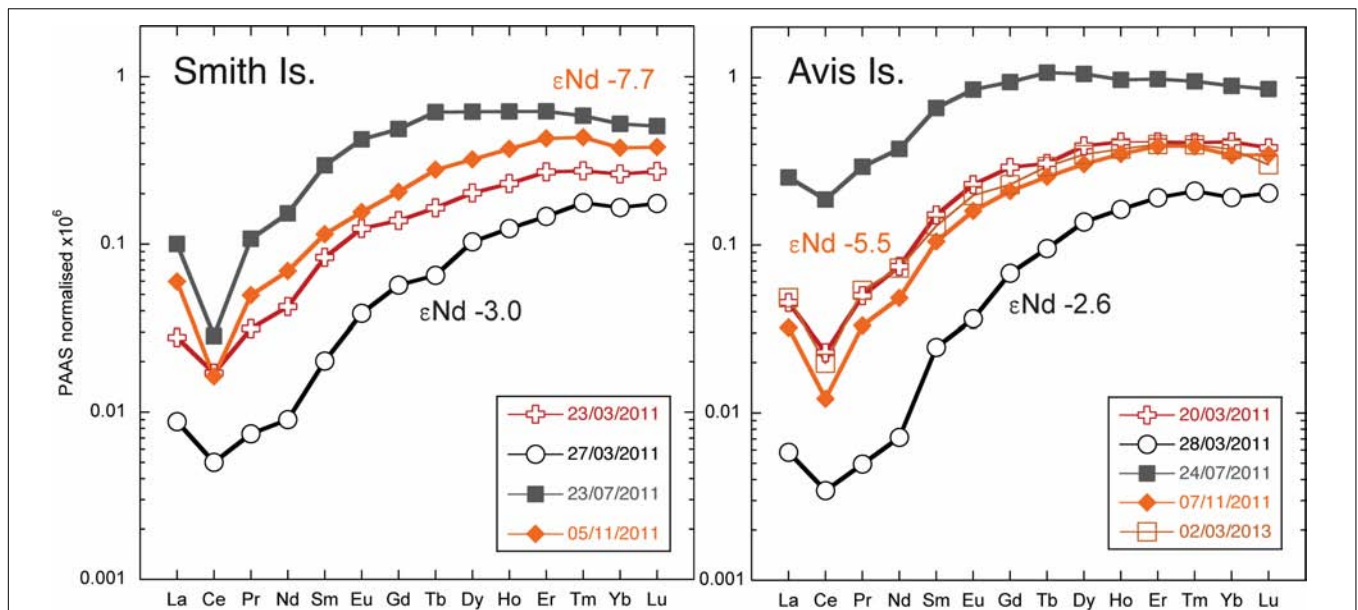


**FIGURE 6** | Shale (PAAS; Nance and Taylor, 1976) normalized rare earth element (REE) patterns for Smith and Avis Island time series. The Nd isotope composition measured for samples from March and November are marked with the same color as the associated REE pattern.

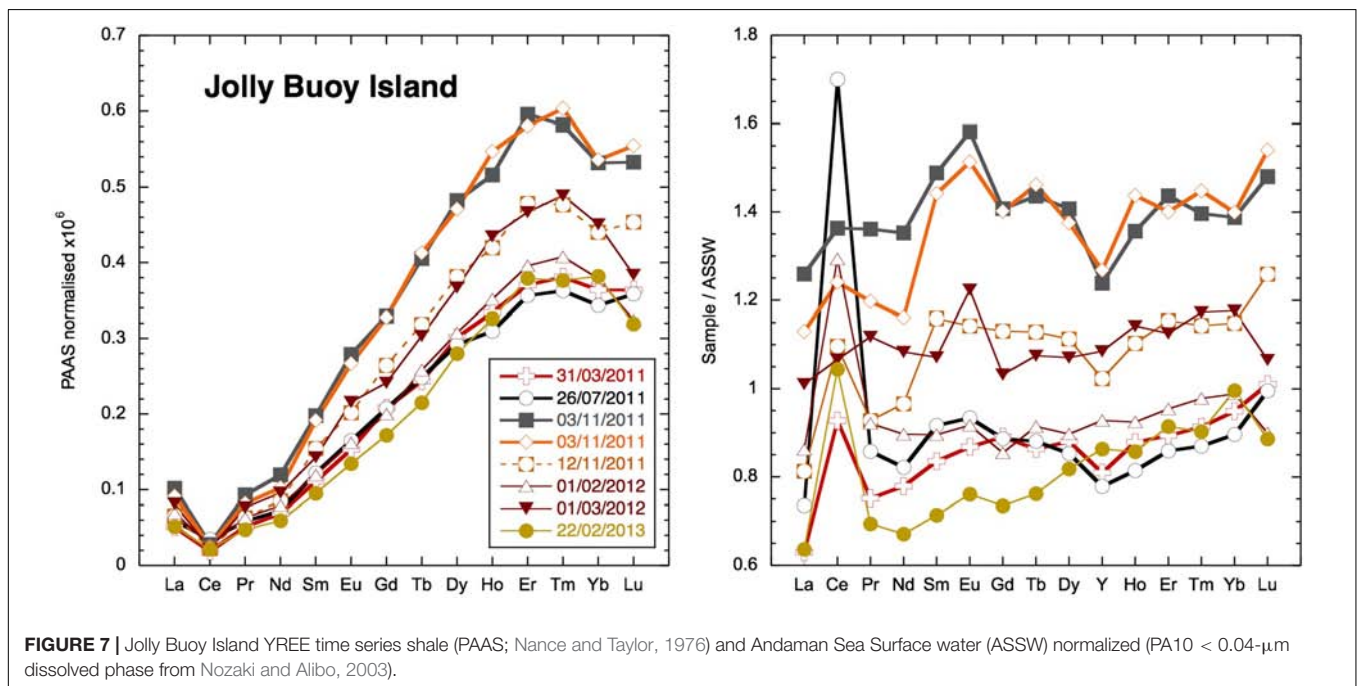


**FIGURE 7** | Jolly Buoy Island YREE time series shale (PAAS; Nance and Taylor, 1976) and Andaman Sea Surface water (ASSW) normalized (PA10 < 0.04-μm dissolved phase from Nozaki and Alibo, 2003).

although the more radiogenic values were measured in clay size separates from the Archipelago group and from Karmatang Beach (Ali et al., 2015), which may represent a mixture of source rock contributions from the ophiolite and Mithakhari Melange (Garzanti et al., 2013). However, these rocks will only be of local importance, and the widespread enrichment of surface waters in Nd, evident also far away from the islands (Amakawa et al., 2000; Nozaki and Alibo, 2003), suggests that most of the radiogenic Nd likely originates from the Irrawaddy or IBR rivers

(Allen et al., 2008b), especially in November. Like all samples from the BoB measured so far, the surface waters of the Andaman Islands exhibit a pronounced enrichment of the MREE relative to other ocean regions (Figure 10). An MREE enrichment has been found in many rivers (e.g., Elderfield et al., 1990; Sholkovitz, 1995) and has been attributed to phosphate mineral weathering (Hannigan and Sholkovitz, 2001), release from iron oxides/hydroxides (Tang and Johannesson, 2010), or possibly from sedimentary organic matter (Freslon et al., 2014). The

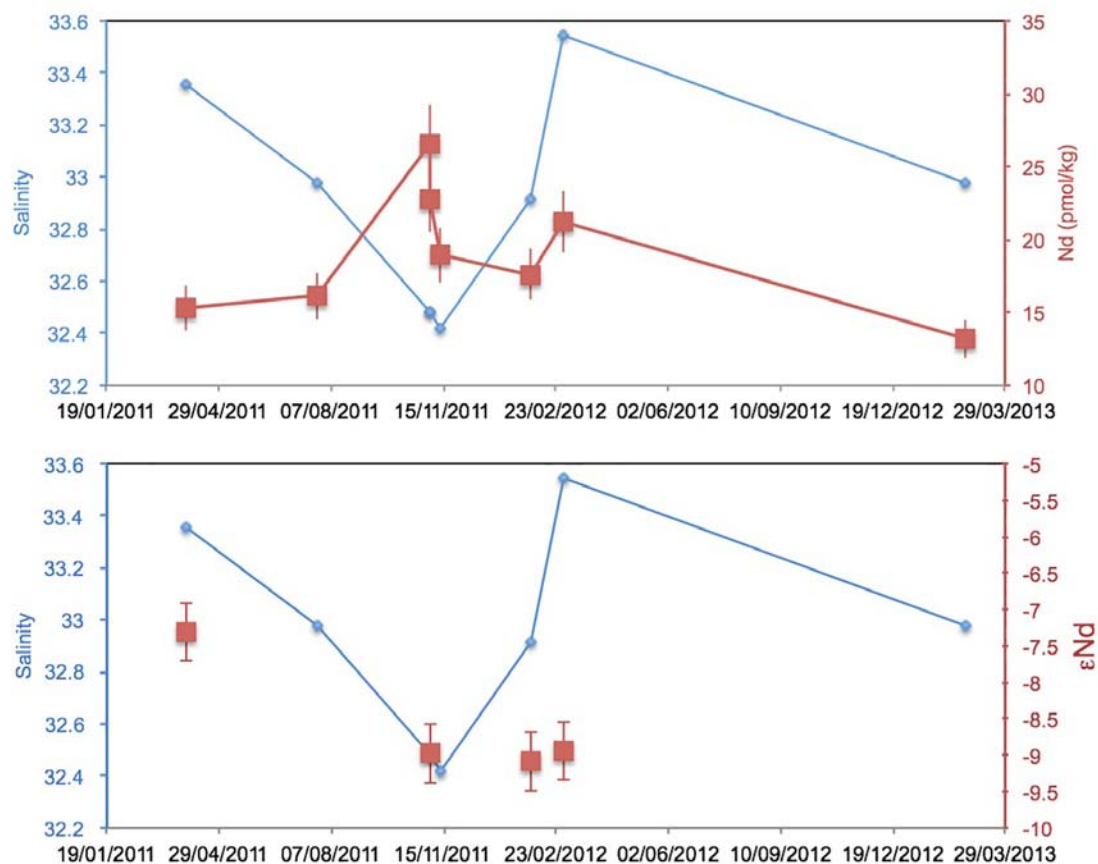
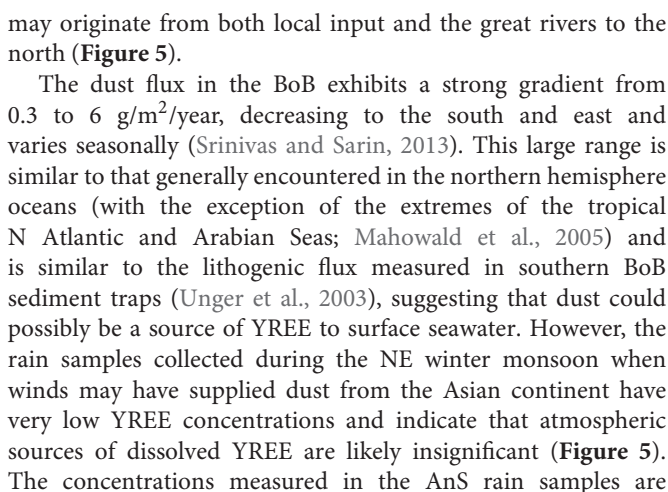


**FIGURE 8** | Jolly Buoy Island time series of Nd isotope composition and Nd concentration with measured salinity.

carrier of the MREE enrichment is likely present in the colloidal phase, as it is not observed in the truly dissolved measurements of the Amazon tributary Solimões, which drains the Andes and is rich in inorganic colloids (Merschel et al., 2017b). A MREE bulge is also observed in the Yamuna tributary of the Ganga and local Andaman Island streams Jonga Nallah and Saddle Peak (Figure 5). The Saddle Peak stream samples ophiolite rocks, while the Jonga Nallah source (AN92) is located in the Mithakhari Melange (Garzanti et al., 2013). The other streams sampled exhibit seawater-like REE patterns like those observed for rivers with higher pH values such as the Mississippi (e.g., Shiller, 2002; Adebayo et al., 2018), although with strong variations in concentrations. The stream on Interview Island flows through the carbonate-rich Archipelago group and has relatively high YREE concentrations. The waterfall sampled on Little Andaman Island most likely flows across the Archipelago group with Miocene limestones (Sarkar and Ghosh, 2015) and has the lowest stream REE concentrations. Interestingly, the south (S) Andaman Island stream near the east coast flows over the ophiolite rocks (Allen et al., 2008a) but has REE concentrations intermediate between Interview Island and Little Andaman Island streams with LREEs similar to those of Little Andaman and HREEs similar to those of Interview Island. Overall it appears that the local geology is not the only factor controlling the REE concentrations in the streams.

The potential of local streams to influence the surface seawater YREE pattern will depend on the removal of YREE during mixing with seawater and salt-induced coagulation and the transfer of colloidal bound YREE to particles and their subsequent re-release from sediments (e.g., Elderfield et al., 1990; Sholkovitz and Szymczak, 2000; Rousseau et al., 2015; Adebayo et al., 2018). The few brackish water samples taken at the stream mixing zones suggest < 50% removal (the difference between the freshwater and brackish sample pair) of LREEs and virtually no removal for the HREE (Supplementary Table S1). Such limited removal is less than the global river average of 70% (see Rousseau et al., 2015 and the references therein), but similar results have been found for the Mississippi river and may be attributable to the relatively low YREE concentrations in the river water (Adebayo et al., 2018). Besides the Jonga Nallah and Interview Island samples, the stream water concentrations are of a similar magnitude to the highest seawater samples (Figures 4, 5). The highest concentrations are from locations inland up tidal creeks surrounded by mangroves (Figure 4, samples AN13 and AN140) or at small river mouths where the sediment loading is high (Figure 4, samples AN88 and AN146). Most importantly, these samples have MREE bulges like observed in many of the samples (Figure 10). However, this MREE bulge pattern is found throughout the AnS and BoB and



In summary, local inputs are clearly important to more inland samples and immediately at the mouths of streams, whereas the vast majority of the samples from around the reefs and outer islands reflect a more regional source of REE.

The highly radiogenic values encountered following the removal of much of the Nd from the dissolved phase during the March 2011 rain event suggest that the remaining Nd was sourced from more mantle-derived radiogenic rock formations. The REEs remaining in solution have a similar concentration and shale-normalized pattern (**Figure 11**) to the ultrafiltered measurements of the truly dissolved fraction in the Amazon tributary Solimões (Merschel et al., 2017b). It also is interesting to note that the truly dissolved Solimões sample is some 2  $\epsilon$ Nd units more radiogenic than the  $> 1$ -kDa fraction (Merschel et al., 2017b), consistent with the radiogenic nature of the low REE samples observed here. Although a very general comparison made necessary by the scarcity of ultrafiltered water data, this suggests that the remaining REEs may represent the truly dissolved fraction characterized by a radiogenic Nd isotope composition. The rain sample (from a different place and time) has a Nd concentration similarly low to seawater after the rain event. However, the YREE patterns of the rain and the YREE-depleted surface water are distinctive and suggest that the rain was not a likely source for the highly radiogenic waters. Considering the likely dust sources to the region, Indian deserts with Himalayan-derived sediments or even Asian loess (e.g., Srinivas and Sarin, 2013) have much less radiogenic Nd isotope signatures, the rain itself cannot be responsible for the low Nd concentrations with radiogenic signatures. The change in salinity observed after the rain event in March 2011 is also too small for any significant volume of rainwater to have mixed with the surface waters causing these radiogenic values. The comparison of concentrations in the unfiltered and filtered samples reveals that there is much more Nd in the leachable particulate phase than needed to offset the loss from the dissolved pool after the rain event. The highest unfiltered/filtered values of 100 (see section “Discussion”) were found for these samples with active removal of YREE from the dissolved phase (e.g., AN11, AN14, AN17, and AN124), which have more extreme LREE-enriched unfiltered/filtered patterns than have those samples whose unfiltered/filtered ratio is high because they were taken at stream or river mouths or inshore locations (e.g., AN44, AN104, and AN146). Importantly, these unfiltered samples have relatively high concentrations, suggesting the active conversion from the colloidal fraction to the labile particulate pool (**Figure 12**). Additionally, the concentrations in these unfiltered samples are many times higher than the amount of REE removed following the rain event (e.g., 84 vs. 7 pmol/kg at Smith Island) and also much higher than



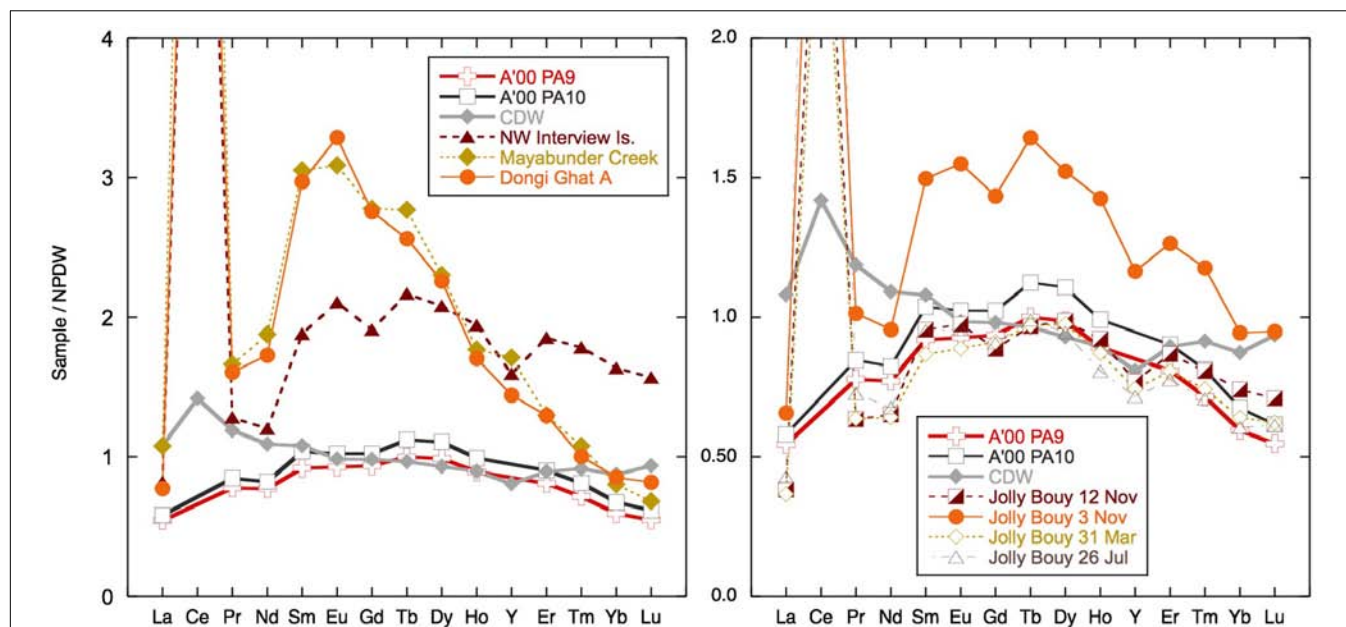


**FIGURE 10 |** Selected samples normalized to North Pacific Deep water (NPDW) after Alibo and Nozaki (1999). The two surface samples measured by Amakawa et al. (2000) in the Bay of Bengal (BoB) and Andaman Sea (AnS) and Circumpolar Deep Water (CDW) from the Southern Ocean taken from Hathorne et al. (2015) are plotted for comparison.

observed in unfiltered samples at the same location during later visits (**Figure 12**). The shale-normalized pattern of these unfiltered samples does not suggest the presence of fresh volcanic material (**Figure 12**) that would help to explain the radiogenic Nd isotope values encountered in the filtered seawater but not the low dissolved YREE concentrations. Instead, the unfiltered YREE patterns suggest the input of locally derived suspended particulates (compared with inland sample AN12 unfiltered in **Figure 12**) as a result of the rain event, which then removed the colloidal component of the seawater. This could potentially occur in two ways: (1) the fresh local particles, not being equilibrated with seawater, could attract nearby colloids and/or simply collect colloids that they collide with, or (2) transported in a thin layer of freshwater runoff, the fresh particles and freshwater are mixed with the underlying seawater and colloidal flocculation mimicking estuarine mixing occurs on small length scales. It could also be the case that addition of dissolved Fe in the runoff would promote Fe hydroxide precipitation once mixed with seawater. It is informative to note that similarly low dissolved YREE concentrations associated with a high labile particulate fraction were also found for samples from the western (sun set) beach on Niel (Shaheed Dweep) Island (**Figure 12**). Variable salinity at the beach during sampling may be indicative of some groundwater discharge component, which may have introduced some particles that enhanced the removal of YREE from the dissolved pool or seawater recirculating through the aquifer encountering freshwater, and colloidal flocculation occurs. This feature was persistent at this location over all sampling visits and should be the focus of future work. More ultrafiltration work on river, seawater, and groundwater samples is required to confirm these suggestions, but the fortuitous sampling achieved

here demonstrates that migration of YREEs from the dissolved pool to the labile particulate pool occurs on the timescale of days (**Figure 6**).

### Labile Particulate YREE

The leachable (0.1% HCl by volume making the pH around 2) particulate concentrations of Al, Fe, and Mn obtained in a similar manner to here from unfiltered samples from the shelf off South Georgia Island have been shown to correspond to particulate concentrations obtained from filters (Schlosser et al., 2018). Those samples from the Southern Ocean displayed high unfiltered/filtered concentration ratios for Fe and Al, but not for Mn, and direct comparison with particulate data indicates a fraction of the particulate Al and Fe was not leached from the particles in the unfiltered seawater (Schlosser et al., 2018). This suggests that the YREE concentrations measured in the unfiltered acidified seawater represent the labile particulate pool. The comparison of filtered and unfiltered samples reveals a very large readily exchangeable (in weak HCl) pool of suspended particulate YREE around the islands. Unfiltered/filtered values of up to 100 for Nd and many samples with values > 10 are in stark contrast to studies of open ocean waters where labile particulate YREE is around 5% of the dissolved pool (unfiltered/filtered values around 1.05; Sholkovitz et al., 1994; Alibo and Nozaki, 1999). The highest unfiltered/filtered values observed here are in the order of 100 and are from the samples with anomalously low REE concentrations resulting from active removal of YREE from the dissolved phase (**Figure 12**; AN11, AN14, AN17, and AN124). These have more extreme LREE-enriched unfiltered/filtered patterns than have those samples whose unfiltered/filtered ratio is high because of being close to



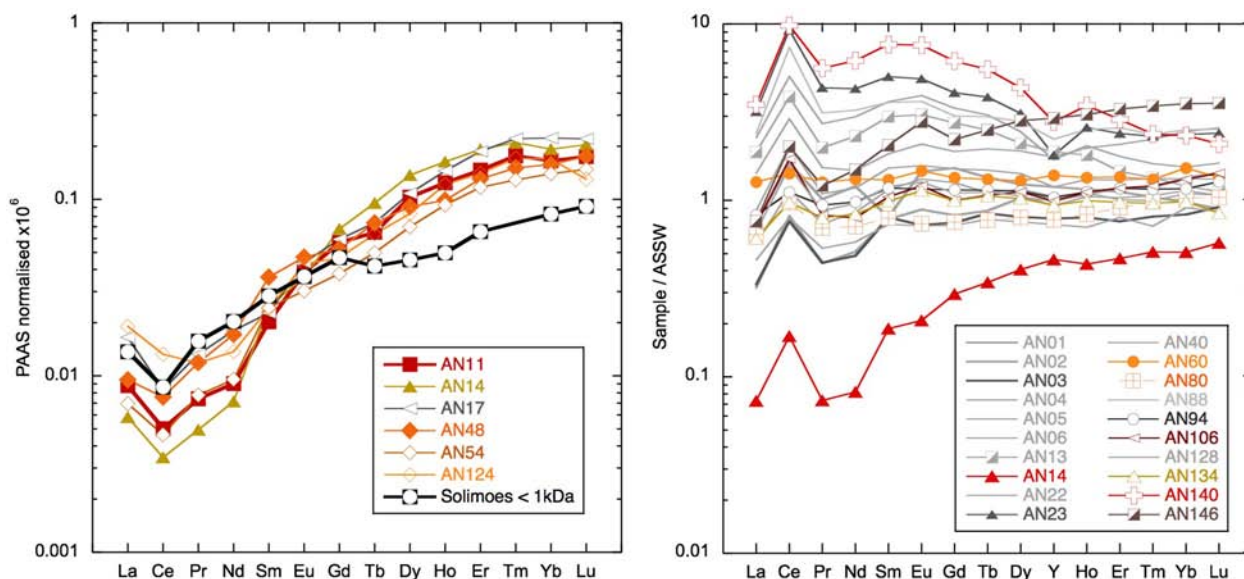


**FIGURE 11 | Left:** low rare earth element (REE) concentration samples compared with < 1 kDa truly dissolved fraction from the Amazon tributary Solimões (Merschel et al., 2017b). **Right:** selected samples normalized to Andaman Sea Surface Water (ASSW) (PA10 < 0.04  $\mu\text{m}$  of dissolved phase from Nozaki and Alibo, 2003).

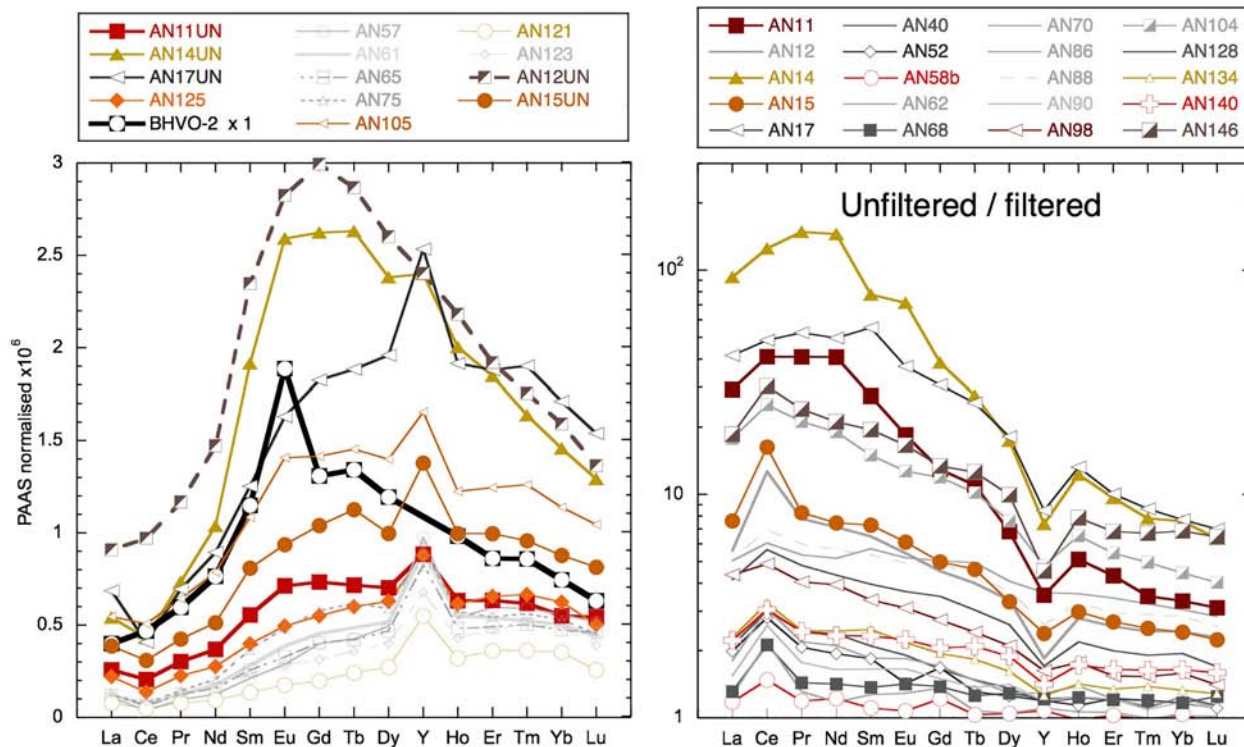


**FIGURE 12 | Left:** unfiltered seawater samples and BHVO-2 basalt values (taken from GeoReM database Jochum et al., 2005) normalized to PAAS (Nance and Taylor, 1976). **Right:** unfiltered YREE/filtered YREE for various examples. Samples from the main locations use the same symbols: squares for Smith Island, vertical triangles for Avis Island, square rhombuses for Niel (Shaheed Dweep) Island, and horizontal triangles for Little Andaman Island.

local river or sediment input (**Figure 12**; AN104 and AN146). The samples with high-to-intermediate YREE concentrations exhibit unfiltered/filtered values generally between 2 and 20 demonstrating the persistence of a large labile particulate fraction in the region. Many of the unfiltered/filtered patterns display a clear Y/Ho fractionation, with Y being less enriched in the labile particulate fraction than Ho (**Figure 12**). This is to be expected as Y is less particle reactive than Ho despite having very similar ionic radii and charge (e.g., Bau, 1996; Nozaki et al., 1997). Both filtered and unfiltered samples from some stream waters and inland creeks with active input exhibit near crustal Y/Ho [Post-Archean Average Australian Sedimentary rocks (PAAS) has a molar Y/Ho of 50] with molar ratios around 60. However, for many sample pairs, the Y/Ho ratio of the filtered sample is higher, around 80, the most extreme examples being the samples with anomalously low filtered YREE concentrations having molar Y/Ho ratios around 100. In the same samples the labile particulate fraction has shale-like ratios of around 50 (**Supplementary Table S1**), which have also been observed for Ayeyarwady (Irrawaddy) shelf sediments (Kurian et al., 2008). These observations illustrate the control that the large labile particulate fraction has on the dissolved YREE patterns while indicating the dominance of crustal YREE in this fraction.

## YREE Concentrations as Tracers of River Discharge

The elevated surface water YREE concentrations in the BoB have been taken as evidence for discharge of YREE from the great rivers draining into the Bay (Amakawa et al., 2000; Singh et al., 2012; Yu et al., 2017b). Based on N-S gradients in YREE concentrations in the BoB, Yu et al. (2017b) suggested high MREE\* (MREE anomaly or bulge index) and low crustal Y/Ho ratios as good tracers for G-B river input, but we have found similar patterns from local input from Andaman sediments. However, the high MREE\* values  $> 2$  observed in some Andaman stream samples are significantly eroded during stream mixing, and there is no clear relationship between MREE\* and salinity. The dissolved YREE concentrations from the Yamuna tributary of the Ganga, some 500 pmol/kg of Nd, are high compared with those of Andaman streams (**Figure 5**); but the removal in the G-B, Irrawaddy, and Salween estuaries is unknown, and the removal upon mixing of Andaman streams appears relatively low (only 50%). Therefore, it is not surprising that in many locations, it seems that the local input of YREE, from runoff directly or released from particles and sediments, produces the dominant signal in surface water concentrations. This is evident in both Smith and Avis island time series where there are distinctive peaks in YREE concentrations (with high MREE\* and low Y/Ho) in the July samples exhibiting low salinities with the local monsoon rains (compare July and November samples in **Figure 6**). Additionally, strong monsoon winds may lead to enhance sediment resuspension and YREE release. This contrasts with the Jolly Buoy time series where the YREE pattern remains similar throughout the year, whereas YREE concentrations peak not in July following local monsoon rains but in November when the monsoon-induced river discharge

would most likely pass the islands (Jian et al., 2009). It seems that the relatively remote location of Jolly Buoy Island, on the BoB side away from the larger islands and sediment sources (**Figure 2**), is the likely reason for the different timing of the YREE concentration peak. The Jolly Buoy samples also exhibit some of the smallest labile particulate YREE fractions measured here (**Figure 12**: plain circles), with the notable exception being the March 2011 sample (AN15), suggesting the labile particulate pool here is not sourced from discharge from the great rivers. Additionally, the samples from November with the highest YREE concentrations have very similar Y/Ho ratios to samples from the other seasons, and the labile particulate pool has a slightly higher Y/Ho, strongly arguing against a fresh crustal source. At the same time, the Jolly Buoy Island samples have relatively flat AnS Surface Water (ASSW PA-10 from Nozaki and Alibo, 2003) normalized patterns (**Figure 11**), suggesting that these samples are representative of the wider region. The positive Indian Ocean dipole event of 2011 and 2012 led to strong freshening events in the BoB from rainfall (Pant et al., 2015) but importantly not river discharge. It may be, therefore, that our sampling missed a large river discharge event and the associated YREE signal. Instead, exceptional rainfall in March 2011 appears to have generated the most distinctive YREE and Nd isotope signal in our dataset through the rapid migration of YREE from the dissolved to the labile particulate pool.

Although the YREE distributions are clearly sensitive to interaction with particles, the Nd isotope signatures of seawater are considered a more conservative tracer of input sources. As such, we compare the  $\epsilon_{\text{Nd}}$  with YREE indices of BoB surface waters from this study and the literature (Amakawa et al., 2000; Yu et al., 2017a,b). The YREE indices suggested as being good potential proxies for G-B sediment input, namely, Y/Ho and MREE\* (Yu et al., 2017a), exhibit relatively little variability and no consistent relationship with  $\epsilon_{\text{Nd}}$ , whereas the La/Yb molar ratio and the PAAS-normalized Yb/Nd (referred to as HREE/LREE in Yu et al., 2017a) show a clear relationship with  $\epsilon_{\text{Nd}}$  (**Figure 13**). The one inshore sample influenced by local sediments (AN12 and marked in **Figure 9**) does not fit with the other data, again demonstrating that the  $\epsilon_{\text{Nd}}$  of the other Andaman surface seawater samples likely reflects a regional signal. The close relationship between La/Yb and  $\epsilon_{\text{Nd}}$  suggests that this can also be used to trace this regional signal.

## Seasonal Changes of Neodymium Isotopes

Recent studies of Nd isotopes and concentrations in the BoB have revealed a substantial excess of Nd throughout the BoB when compared with those of the rest of the Indian Ocean, and this excess has a calculated Nd isotope composition similar to that of modern G-B river sediments (Singh et al., 2012). The resampling of similar locations (**Figure 1**) a couple of years later found significantly lower Nd concentrations and more radiogenic Nd isotope signatures (Yu et al., 2017a). These authors thought this difference is most likely explained by the Nd isotope composition of BoB seawater varying seasonally and inter-annually with sediment discharge from the G-B river system

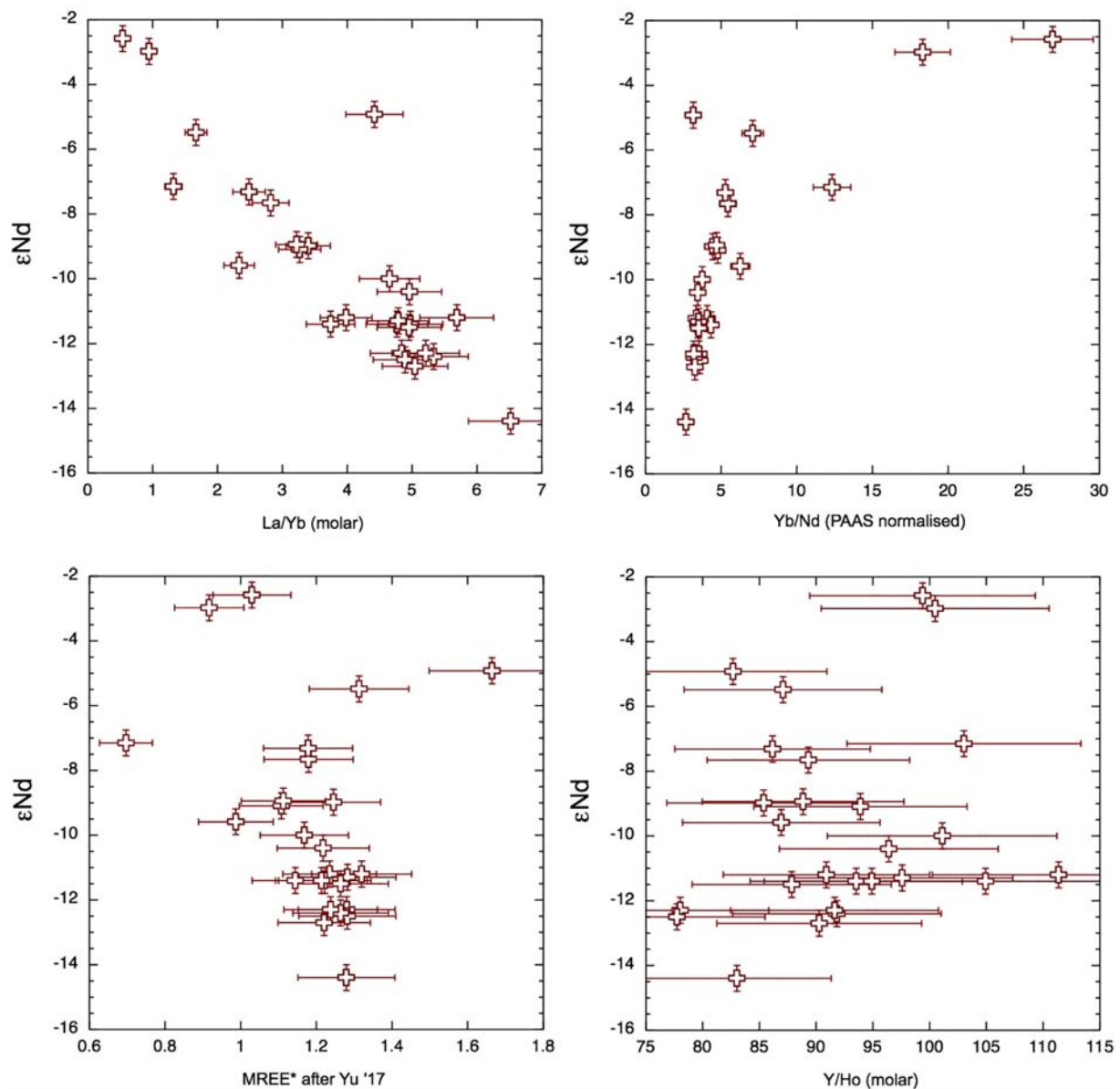


**FIGURE 13** | Radiogenic Nd isotope composition vs. YREE indices for samples of this study together with values from the literature (Amakawa et al., 2000; Yu et al., 2017a,b) for samples from the upper 50-m water depth of the Bay of Bengal (BoB) and Andaman Sea (AnS) (**Figure 1**).

(Yu et al., 2017a). However, as the samples were not taken at exactly the same location, it was not possible to conclusively distinguish if the variability observed between these studies was truly seasonal/inter-annual or resulted from spatial heterogeneity (Yu et al., 2017a). Here, we have shown with samples collected at three fixed locations over a year that indeed the Nd isotope composition of filtered seawater can change on sub-annual timescales (**Figures 6, 9**). We have compared the Nd isotope data from around the Andaman Islands with those from the surface (for this purpose, we assume a mixed layer depth of 50 m) BoB from Amakawa et al. (2000), Singh et al. (2012), and Yu et al. (2017a), and a clear correlation between the Nd isotope

composition and concentration appears (**Figure 9**). It must be noted that Amakawa et al. (2000) measured the Nd isotopes from winter (non-monsoon) collected samples from the BoB and AnS that were not filtered, whereas they measured Nd (and YREE) concentrations on filtered waters. It seems that the isotope composition of filtered seawater in the BoB is a function of mixing between a very low concentration radiogenic endmember that we encountered after the rain event in March 2011 and a high concentration unradiogenic endmember from the G-B river (Singh et al., 2012). Samples move away from this line with reduced Nd concentrations, and a third endmember could be BoB subsurface water (**Figure 9**). Singh et al. (2012) considered the



surface water from the south to be 100% Indonesian throughflow water with a Nd concentration of only 7 pmol/kg and a radiogenic isotope composition of  $-4$ . This endmember (but again from Amakawa et al., 2000, so unfiltered for isotopes) plots near the low-concentration samples from the AnS (Figure 9) following the rain event in March 2011 when it appears that the colloidal fraction rapidly migrated to the labile particulate pool. The remaining Nd, hypothesized to be truly dissolved, may have been sourced from Indonesian throughflow water, but as it is even more radiogenic, it is more likely that more local radiogenic sources like the Indo-Burmese Ranges (Damodararao et al., 2016) also contributed. It follows that the apparent mixing between Indonesian throughflow water and G-B outflow water masses used to explain the BoB surface water composition (Singh et al., 2012) could potentially be a function of the proportion of the filtered BoB seawater in the truly dissolved and colloidal phases (Figure 9). It seems that this proportion can be rapidly changed by interaction with the large labile particulate fraction observed here, and this may also be responsible for the observed inter-annual changes in the Nd isotope composition of BoB surface water (Yu et al., 2017a). This is an extension to the idea of Elderfield et al. (1990) that the river water REE composition is controlled by the balance between truly dissolved and colloidal pools with the addition of a third pool, which is the labile particulate fraction. Future sampling campaigns should include both filtered and unfiltered samples for Nd isotope analyses as well as YREE concentrations, and ultrafiltration should be performed whenever logistically possible. Eventually, we would hope to be able to carry out residence time calculations, such as performed by Amakawa et al. (2000) and revisited by Yu et al. (2017b), for the YREE in each pool individually. The labile particulate pool may also help to explain variations in seawater Nd isotopes in the entire oceanic water column on the timescale of years observed in other regions (Grasse et al., 2017).

## CONCLUSION

The dissolved YREE composition of filtered seawater around the Andaman Islands reveals both local input to and removal of YREE from the dissolved phase. Rapid removal following an exceptional rainfall event in March 2011 left the remaining Nd with a markedly radiogenic isotope composition, and as a result of this, the dissolved Nd isotope composition varies by some 7  $\epsilon$ Nd units across the islands. Changes in the YREE and Nd isotope composition within 1 year are observed at three fixed locations, confirming recent suggestions that short-term

temporal variations occur in the BoB. The similarity of YREE patterns across the BoB and AnS suggests a common source for their enrichment in Indian Ocean surface waters. Taken together, the data for surface waters from this study and the literature appear to form a mixing relationship, but we hypothesize that this reflects the proportions of radiogenic Nd in the truly dissolved phase and of unradiogenic Nd in the colloidal pool. Based on comparison of filtered and unfiltered samples a third phase, a labile particulate pool is identified, which controls the proportion of dissolved YREE phases by removing the colloidal fraction. This control by particulate YREE phases is likely also important in other sediment and particle rich regions.

## DATA AVAILABILITY STATEMENT

All datasets generated for this study are included in the article/Supplementary Material.

## AUTHOR CONTRIBUTIONS

EH and PM collected the samples. EH performed the analyses and wrote the manuscript with contributions from MF and PM.

## ACKNOWLEDGMENTS

We thank the National Geographic Committee for Exploration for funding the fieldwork on the Andaman Islands, and Sachin, Das, and numerous fishermen for their assistance in the field. We are grateful to the Andaman and Nicobar Administration Wildlife Division for allowing water sampling and in particular the officers in Mayabunder for their assistance. Katharina Pahnke-May and Philip Böning from the ICBM at the University of Oldenburg helped with the low-concentration Nd isotope measurements using their Neptune MC-ICPMS, and Eric Achterberg at GEOMAR and Christian Schlosser are thanked for use of their seaFAST and Element XR instrument, as well as for scientific discussion.

## SUPPLEMENTARY MATERIAL

The Supplementary Material for this article can be found online at: <https://www.frontiersin.org/articles/10.3389/fmars.2019.00767/full#supplementary-material>

## REFERENCES

- Adebayo, S. B., Cui, M., Hong, T., White, C. D., Martin, E. E., and Johannesson, K. H. (2018). Rare earth elements geochemistry and nd isotopes in the mississippi river and gulf of mexico mixing zone. *Front. Mar. Sci.* 5:166. doi: 10.3389/fmars.2018.00166
- Akhil, V. P., Durand, F., Lengaigne, M., Vialard, J., Keerthi, M. G., Gopalakrishna, V. V., et al. (2014). A modeling study of the processes of surface salinity seasonal cycle in the Bay of Bengal. *J. Geophys. Res.* 119, 3926–3947. doi: 10.1002/2013JC009632
- Akhil, V. P., Lengaigne, M., Vialard, J., Durand, F., Keerthi, M. G., Chaitanya, A. V. S., et al. (2016). A modeling study of processes controlling the Bay of Bengal sea surface salinity interannual variability. *J. Geophys. Res.* 121, 8471–8495. doi: 10.1002/2016JC011662
- Ali, S., Hathorne, E. C., Frank, M., Gebregiorgis, D., Stattegger, K., Stumpf, R., et al. (2015). South Asian monsoon history over the past 60 kyr recorded by radiogenic isotopes and clay mineral assemblages in the Andaman Sea. *Geochem. Geophys. Geosyst.* 16, 505–521. doi: 10.1002/2014GC005586
- Alibo, D. S., and Nozaki, Y. (1999). Rare earth elements in seawater: particle association, shale-normalization, and Ce oxidation.



- Geochim. Cosmochim. Acta* 63, 363–372. doi: 10.1016/S0016-7037(98)00279-8
- Allen, R., Carter, A., Najman, Y., Bandopadhyay, P. C., Chapman, H. J., Bickle, M. J., et al. (2008a). “New constraints on the sedimentation and uplift history of the Andaman-Nicobar accretionary prism, South Andaman Island,” *Special Paper 436: Formation and Applications of the Sedimentary Record in Arc Collision Zones*. Geological Society of America, Boulder, CL, 223–255. doi: 10.1130/2008.2436(11)
- Allen, R., Najman, Y., Carter, A., Barfod, D., Bickle, M. J., Chapman, H. J., et al. (2008b). Provenance of the Tertiary sedimentary rocks of the Indo-Burman Ranges, Burma (Myanmar): Burman arc or Himalayan-derived? *J. Geol. Soc.* 165, 1045–1057. doi: 10.1144/0016-76492007-143
- Amakawa, H., Alibo, D. S., and Nozaki, Y. (2000). Nd isotopic composition and REE pattern in the surface waters of the eastern Indian Ocean and its adjacent seas. *Geochim. Cosmochim. Acta* 64, 1715–1727. doi: 10.1016/S0016-7037(00)00333-1
- Bau, M. (1996). Controls on the fractionation of isoivalent trace elements in magmatic and aqueous systems: evidence from Y/Ho, Zr/Hf, and lanthanide tetrad effect. *Contrib. Mineral. Petrol.* 123, 323–333. doi: 10.1007/s004100050159
- Bau, M. (1999). Scavenging of dissolved yttrium and rare earths by precipitating iron oxyhydroxide: experimental evidence for Ce oxidation. Y-Ho fractionation, and lanthanide tetrad effect. *Geochim. Cosmochim. Acta* 63, 67–77. doi: 10.1016/S0016-7037(99)00014-9
- Bertram, C. J., and Elderfield, H. (1993). The geochemical balance of the rare earth elements and neodymium isotopes in the oceans. *Geochim. Cosmochim. Acta* 57, 1957–1986. doi: 10.1016/0016-7037(93)90087-D
- Byrne, R. H., Lee, J. H., and Bingler, L. S. (1991). Rare earth element complexation by PO43- ions in aqueous solution. *Geochim. Cosmochim. Acta* 55, 2729–2735. doi: 10.1016/0016-7037(91)90439-C
- Cantrell, K. J., and Byrne, R. H. (1987). Rare earth element complexation by carbonate and oxalate ions. *Geochim. Cosmochim. Acta* 51, 597–605. doi: 10.1016/0016-7037(87)90072-X
- Chaitanya, A. V. S., Durand, F., Mathew, S., Gopalakrishna, V. V., Papa, F., Lengaigne, M., et al. (2015). Observed year-to-year sea surface salinity variability in the Bay of Bengal during the 2009–2014 period. *Ocean Dyn.* 65, 173–186. doi: 10.1007/s10236-014-0802-x
- Chatterjee, A., Shankar, D., McCreary, J. P., Vinayachandran, P. N., and Mukherjee, A. (2017). Dynamics of Andaman Sea circulation and its role in connecting the equatorial Indian Ocean to the Bay of Bengal. *J. Geophys. Res.* 122, 3200–3218. doi: 10.1002/2016JC012300
- Chatterjee, A., Shankar, D., Sheno, S. S. C., Reddy, G. V., Michael, G. S., Ravichandran, M., et al. (2012). A new atlas of temperature and salinity for the North Indian Ocean. *J. Earth Syst. Sci.* 121, 559–593. doi: 10.1007/s12040-012-0191-9
- Colin, C., Turpin, L., Bertaux, J., Desprairies, A., and Kissel, C. (1999). Erosional history of the Himalayan and Burman ranges during the last two glacial-interglacial cycles. *Earth Planet. Sci. Lett.* 171, 647–660. doi: 10.1016/S0012-821X(99)00184-3
- Curry, J. R., Emmel, F. J., and Moore, D. G. (2002). The Bengal Fan: morphology, geometry, stratigraphy, history and processes. *Mar. Petrol. Geol.* 19, 1191–1223. doi: 10.1016/S0264-8172(03)00035-7
- Dai, A., Qian, T., Trenberth, K. E., and Milliman, J. D. (2009). Changes in continental freshwater discharge from 1948 to 2004. *J. Clim.* 22, 2773–2792. doi: 10.1175/2008JCLI2592.1
- Damodararao, K., Singh, S. K., Rai, V. K., Ramaswamy, V., and Rao, P. S. (2016). Lithology, monsoon and sea-surface current control on provenance, dispersal and deposition of sediments over the andaman continental shelf. *Front. Mar. Sci.* 3:118. doi: 10.3389/fmars.2016.00118
- Duncombe, J. (2018). Making sense of landslide danger after kerala's floods - eos. *Eos* 99:7.
- Durand, F., Papa, F., Rahman, A., and Bala, S. K. (2011). Impact of Ganges-Brahmaputra interannual discharge variations on Bay of Bengal salinity and temperature during 1992–1999 period. *J. Earth Syst. Sci.* 120, 859–872. doi: 10.1007/s12040-011-0118-x
- Elderfield, H. (1988). The oceanic chemistry of the rare-earth elements. *Philos. Trans. R. Soc. Lond. A* 325:105. doi: 10.1098/rsta.1988.0046
- Elderfield, H., Upstill-Goddard, R., and Sholkovitz, E. R. (1990). The rare earth elements in rivers, estuaries, and coastal seas and their significance to the composition of ocean waters. *Geochim. Cosmochim. Acta* 54, 971–991. doi: 10.1016/0016-7037(90)90432-K
- Fasullo, J., and Webster, P. J. (2003). A hydrological definition of indian monsoon onset and withdrawal. *J. Climate* 16, 3200–3211. doi: 10.1175/1520-04422003016
- Frank, M. (2002). Radiogenic isotopes: tracers of past ocean circulation and erosional input. *Rev. Geophys.* 40:1-1-1-38
- Freslon, N., Bayon, G., Toucanne, S., Bermell, S., Bollinger, C., Chéron, S., et al. (2014). Rare earth elements and neodymium isotopes in sedimentary organic matter. *Geochim. Cosmochim. Acta* 140, 177–198. doi: 10.1016/j.gca.2014.05.016
- Gadgil, S., and Gadgil, S. (2006). The Indian monsoon, GDP and agriculture. *Econom. Polit. Weekly* 4887, 4889–4895.
- Garzanti, E., Limonta, M., Resentini, A., Bandopadhyay, P. C., Najman, Y., Andò, S., et al. (2013). Sediment recycling at convergent plate margins (Indo-Burman ranges and Andaman–Nicobar ridge). *Earth Sci. Rev.* 123, 113–132. doi: 10.1016/j.earscirev.2013.04.008
- Giosan, L., Naing, T., Min Tun, M., Clift, P. D., Filip, F., Constantinescu, S., et al. (2018). On the Holocene evolution of the Ayeyawady megadelta. *Earth Surf. Dyn.* 6, 451–466. doi: 10.5194/esurf-6-451-2018
- Girishkumar, M. S., Ravichandran, M., and McPhaden, M. J. (2013). Temperature inversions and their influence on the mixed layer heat budget during the winters of 2006–2007 and 2007–2008 in the Bay of Bengal. *J. Geophys. Res. Oceans* 118, 3336–3349. doi: 10.1002/jgrc.20192
- Girishkumar, M. S., Ravichandran, M., McPhaden, M. J., and Rao, R. R. (2011). Intraseasonal variability in barrier layer thickness in the south central Bay of Bengal. *J. Geophys. Res.* 116:3009. doi: 10.1029/2010JC006657
- Goldstein, S. J., and Jacobsen, S. B. (1987). The Nd and Sr isotopic systematics of river-water dissolved material: implications for the sources of Nd and Sr in seawater. *Chem. Geol.* 66, 245–272. doi: 10.1016/0168-9622(87)90045-5
- Goldstein, S. J., and Jacobsen, S. B. (1988a). Nd and Sr isotopic systematics of river water suspended material: implications for crustal evolution. *Earth Planet. Sci. Lett.* 87, 249–265. doi: 10.1016/0012-821X(88)90013-1
- Goldstein, S. J., and Jacobsen, S. B. (1988b). Rare earth elements in river waters. *Earth Planet. Sci. Lett.* 89, 35–47. doi: 10.1016/0012-821X(88)90031-3
- Grasse, P., Bosse, L., Hathorne, E. C., Böning, P., Pahnke, K., and Frank, M. (2017). Short-term variability of dissolved rare earth elements and neodymium isotopes in the entire water column of the Panama Basin. *Earth Planet. Sci. Lett.* 475, 242–253. doi: 10.1016/j.epsl.2017.07.022
- Hannigan, R. E., and Sholkovitz, E. R. (2001). The development of middle rare earth element enrichments in freshwaters: weathering of phosphate minerals. *Chem. Geol.* 175, 495–508. doi: 10.1016/S0009-2541(00)00355-7
- Hathorne, E. C., Haley, B., Stichel, T., Grasse, P., Zieringer, M., and Frank, M. (2012). Online preconcentration ICP-MS analysis of rare earth elements in seawater. *Geochim. Geophys. Geosyst.* 13:Q01020. doi: 10.1029/2011GC003907
- Hathorne, E. C., Stichel, T., Brück, B., and Frank, M. (2015). Rare earth element distribution in the Atlantic sector of the Southern Ocean: the balance between particle scavenging and vertical supply. *Mar. Chem.* 177, 157–171. doi: 10.1016/j.marchem.2015.03.011
- Hoyle, J., Elderfield, H., Gledhill, A., and Greaves, M. (1984). The behaviour of the rare earth elements during mixing of river and sea waters. *Geochim. Cosmochim. Acta* 48, 143–149. doi: 10.1016/0016-7037(84)90356-9
- Jian, J., Webster, P. J., and Hoyos, C. D. (2009). Large-scale controls on Ganges and Brahmaputra river discharge on intraseasonal and seasonal time-scales. *Q. J. R. Meteorol. Soc.* 135, 353–370. doi: 10.1002/qj.384
- Jochum, K. P., Nohl, U., Herwig, K., Lammel, E., Stoll, B., and Hofmann, A. W. (2005). GeoReM: a new geochemical database for reference materials and isotopic standards. *Geostand. Geoanal. Res.* 29, 333–338. doi: 10.1111/j.1751-908X.2005.tb00904.x
- Kiran Kumar, P., Singh, A., and Ramesh, R. (2018). Controls on  $\delta^{18}\text{O}$ ,  $\delta\text{D}$  and  $\delta^{18}\text{O}$ -salinity relationship in the northern Indian Ocean. *Mar. Chem.* 207, 55–62. doi: 10.1016/j.marchem.2018.10.010
- Kraft, S., Frank, M., Hathorne, E. C., and Weldeab, S. (2013). Assessment of seawater Nd isotope signatures extracted from foraminiferal shells and authigenic phases of Gulf of Guinea sediments. *Geochim. Cosmochim. Acta* 121, 414–435. doi: 10.1016/j.gca.2013.07.029

- Krishna Kumar, K., Rupa Kumar, K., Ashrit, R. G., Deshpande, N. R., and Hansen, J. W. (2004). Climate impacts on Indian agriculture. *Int. J. Climatol.* 24, 1375–1393. doi: 10.1002/joc.1081
- Kurian, S., Nath, B. N., Ramaswamy, V., Naman, D., Gnaneshwar Rao, T., Kamesh Raju, K. A., et al. (2008). Possible detrital, diagenetic and hydrothermal sources for Holocene sediments of the Andaman backarc basin. *Mar. Geol.* 247, 178–193. doi: 10.1016/j.margeo.2007.09.006
- Lacan, F., Tachikawa, K., and Jeandel, C. (2012). Neodymium isotopic composition of the oceans: a compilation of seawater data. *Chem. Geol.* 30, 177–184. doi: 10.1016/j.chemgeo.2012.01.019
- Laukert, G., Frank, M., Bauch, D., Hathorne, E. C., Rabe, B., von Appen, W.-J., et al. (2017). Ocean circulation and freshwater pathways in the Arctic Mediterranean based on a combined Nd isotope. REE and oxygen isotope section across Fram Strait. *Geochim. Cosmochim. Acta* 202, 285–309. doi: 10.1016/j.gca.2016.12.028
- Liu, Y., Lo, L., Shi, Z., Wei, K.-Y., Chou, C.-J., Chen, Y.-C., et al. (2015). Obliquity pacing of the western Pacific Intertropical Convergence Zone over the past 282,000 years. *Nat. Commun.* 6:10018. doi: 10.1038/ncomms10018
- Mahowald, N. M., Baker, A. R., Bergametti, G., Brooks, N., Duce, R. A., Jickells, T. D., et al. (2005). Atmospheric global dust cycle and iron inputs to the ocean. *Glob. Biogeochem. Cycles* 19:GB4025. doi: 10.1029/2004GB002402
- McNeill, L. C., Dugan, B., Backman, J., Pickering, K. T., Pouderoux, H. F. A., Henstock, T. J., et al. (2017). Understanding Himalayan erosion and the significance of the Nicobar Fan. *Earth Planet. Sci. Lett.* 475, 134–142. doi: 10.1016/j.epsl.2017.07.019
- Merschel, G., Bau, M., and Dantas, E. L. (2017a). Contrasting impact of organic and inorganic nanoparticles and colloids on the behavior of particle-reactive elements in tropical estuaries: an experimental study. *Geochim. Cosmochim. Acta* 197, 1–13. doi: 10.1016/j.gca.2016.09.041
- Merschel, G., Bau, M., Schmidt, K., Munker, C., and Dantas, E. L. (2017b). Hafnium and neodymium isotopes and REY distribution in the truly dissolved, nanoparticulate/colloidal and suspended loads of rivers in the Amazon Basin, Brazil. *Geochim. Cosmochim. Acta* 213, 383–399. doi: 10.1016/j.gca.2017.07.006
- Milliman, J. D., and Syvitski, J. P. M. (1992). Geomorphic/tectonic control of sediment discharge to the ocean: the importance of small mountainous rivers. *J. Geol.* 100, 525–544. doi: 10.1086/629606
- Moffett, J. W. (1994). The relationship between cerium and manganese oxidation in the marine environment. *Limnol. Oceanogr.* 39, 1309–1318. doi: 10.4319/lo.1994.39.6.1309
- Nance, W., and Taylor, S. (1976). Rare earth element patterns and crustal evolution—I. Australian post-Archean sedimentary rocks. *Geochim. Cosmochim. Acta* 40, 1539–1551. doi: 10.1016/0016-7037(76)90093-4
- Nilsson-Kerr, K., Anand, P., Sexton, P. F., Leng, M. J., Misra, S., Clemens, S. C., et al. (2019). Role of Asian summer monsoon subsystems in the inter-hemispheric progression of deglaciation. *Nat. Geosci.* 12, 290–295. doi: 10.1038/s41561-019-0319-5
- Nozaki, Y., and Alibo, D. S. (2003). Importance of vertical geochemical processes in controlling the oceanic profiles of dissolved rare earth elements in the northeastern Indian Ocean. *Earth Planet. Sci. Lett.* 205, 155–172. doi: 10.1016/S0012-821X(02)01027-0
- Nozaki, Y., Zhang, J., and Amakawa, H. (1997). The fractionation between Y and Ho in the marine environment. *Earth Planet. Sci. Lett.* 148, 329–340. doi: 10.1016/S0012-821X(97)00034-4
- Osborne, A. H., Haley, B. A., Hathorne, E. C., Plancherel, Y., and Frank, M. (2015). Rare earth element distribution in Caribbean seawater: continental inputs versus lateral transport of distinct REE compositions in subsurface water masses. *Mar. Chem.* 177, 172–183. doi: 10.1016/j.marchem.2015.03.013
- Osborne, A. H., Hathorne, E. C., Schijf, J., Plancherel, Y., Böning, P., and Frank, M. (2017). The potential of sedimentary foraminiferal rare earth element patterns to trace water masses in the past. *Geochem. Geophys. Geosyst.* 18, 1550–1568. doi: 10.1002/2016GC006782
- Pal, T., Gupta, T. D., Chakraborty, P. P., and Gupta, S. C. D. (2005). Pyroclastic deposits of Mio-Pliocene age in the Arakan Yoma-Andaman-Java subduction complex, Andaman Islands, Bay of Bengal, India. *Geochem. J.* 39, 69–82. doi: 10.2343/geochemj.39.69
- Pant, V., Girishkumar, M. S., Udaya Bhaskar, T. V. S., Ravichandran, M., Papa, F., and Thangaprakash, V. P. (2015). Observed interannual variability of near-surface salinity in the Bay of Bengal: salinity variability in the BoB. *J. Geophys. Res.* 120, 3315–3329. doi: 10.1002/2014JC010340
- Quinn, K. A., Byrne, R. H., and Schijf, J. (2006). Sorption of yttrium and rare earth elements by amorphous ferric hydroxide: Influence of solution complexation with carbonate. *Geochim. Cosmochim. Acta* 70, 4151–4165. doi: 10.1016/j.gca.2006.06.014
- Ramaswamy, V., Rao, P., Rao, K., Thwin, S., Rao, N. S., and Raiker, V. (2004). Tidal influence on suspended sediment distribution and dispersal in the northern Andaman Sea and Gulf of Martaban. *Mar. Geol.* 208, 33–42. doi: 10.1016/j.margeo.2004.04.019
- Rengarajan, R., and Sarin, M. M. (2004). Distribution of rare earth elements in the Yamuna and the Chambal rivers, India. *Geochem. J.* 38, 551–569. doi: 10.2343/geochemj.38.551
- Rizal, S., Damm, P., Wahid, M. A., Sundermann, J., Ilhamsyah, Y., Iskandar, T., et al. (2012). General circulation in the Malacca Strait and Andaman Sea: a numerical model study. *Am. J. Environ. Sci.* 8, 479–488. doi: 10.3844/ajessp.2012.479.488
- Roberts, N. L., Piotrowski, A. M., Elderfield, H., Eglinton, T. I., and Lomas, M. W. (2012). Rare earth element association with foraminifera. *Geochim. Cosmochim. Acta* 94, 57–71. doi: 10.1016/j.gca.2012.07.009
- Roberts, N. L., Piotrowski, A. M., McManus, J. F., and Keigwin, L. D. (2010). Synchronous deglacial overturning and water mass source changes. *Science* 327, 75–78. doi: 10.1126/science.1178068
- Rousseau, T. C. C., Sonke, J. E., Chmieleff, J., van Beek, P., Souhaut, M., Boaventura, G., et al. (2015). Rapid neodymium release to marine waters from lithogenic sediments in the Amazon estuary. *Nat. Commun.* 6:8592. doi: 10.1038/ncomms8592
- Saha, N., Webb, G. E., and Zhao, J.-X. (2016). Coral skeletal geochemistry as a monitor of inshore water quality. *Sci. Total Environ.* 56, 652–684. doi: 10.1016/j.scitotenv.2016.05.066
- Sarkar, S., and Ghosh, A. K. (2013). Coral bleaching a nemesis for the Andaman reefs: building an improved conservation paradigm. *Ocean Coast. Manag.* 71, 153–162. doi: 10.1016/j.ocecoaman.2012.09.010
- Sarkar, S., and Ghosh, A. K. (2015). Evaluation of coralline algal diversity from the Serravallian carbonate sediments of Little Andaman Island (Hut Bay), India. *Carbonates Evaporites* 30, 13–24. doi: 10.1007/s13146-014-0190-9
- Schlösser, C., Schmidt, K., Aquilina, A., Homoky, W. B., Castrillejo, M., Mills, R. A., et al. (2018). Mechanisms of dissolved and labile particulate iron supply to shelf waters and phytoplankton blooms off South Georgia, Southern Ocean. *Biogeosciences* 15, 4973–4993. doi: 10.5194/bg-15-4973-2018
- Sengupta, D., Bharath Raj, G. N., Ravichandran, M., Sree Lekha, J., and Papa, F. (2016). Near-surface salinity and stratification in the north Bay of Bengal from moored observations: salinity in the North Bay of Bengal. *Geophys. Res. Lett.* 43, 4448–4456. doi: 10.1002/2016GL068339
- Sengupta, D., Bharath Raj, G. N., and Shenoi, S. S. C. (2006). Surface freshwater from Bay of Bengal runoff and Indonesian throughflow in the tropical Indian Ocean. *Geophys. Res. Lett.* 33, 1–7. doi: 10.1029/2006GL027573
- Shaman, J., Cane, M., and Kaplan, A. (2005). The relationship between Tibetan snow depth, ENSO, river discharge and the monsoons of Bangladesh. *Int. J. Remote Sens.* 26, 3735–3748. doi: 10.1080/01431160500185599
- Shiller, A. M. (2002). Seasonality of dissolved rare earth elements in the lower Mississippi River. *Geochem. Geophys. Geosyst.* 3, 1–14. doi: 10.1029/2002GC000372
- Sholkovitz, E., and Szymczak, R. (2000). The estuarine chemistry of rare earth elements: comparison of the Amazon, Fly, Sepik and the Gulf of Papua systems. *Earth Planet. Sci. Lett.* 179, 299–309. doi: 10.1016/S0012-821X(00)00112-6
- Sholkovitz, E. R. (1995). The aquatic chemistry of rare earth elements in rivers and estuaries. *Aquatic Geochem.* 1, 1–34. doi: 10.1007/BF01025229
- Sholkovitz, E. R., Church, T. M., and Arimoto, R. (1993). Rare Earth element composition of precipitation, precipitation particles, and aerosols. *J. Geophys. Res.* 98:20587. doi: 10.1029/93JD01926
- Sholkovitz, E. R., and Elderfield, H. (1988). Cycling of dissolved rare earth elements in Chesapeake Bay. *Glob. Biogeochem. Cycles* 2, 157–176. doi: 10.1029/GB002i002p00157
- Sholkovitz, E. R., Landing, W. M., and Lewis, B. L. (1994). Ocean particle chemistry: the fractionation of rare earth elements between suspended particles and seawater. *Geochim. Cosmochim. Acta* 58, 1567–1579. doi: 10.1016/0016-7037(94)90559-2

- Singh, S. K., and France-Lanord, C. (2002). Tracing the distribution of erosion in the Brahmaputra watershed from isotopic compositions of stream sediments. *Earth Planet. Sci. Lett.* 202, 645–662. doi: 10.1016/S0012-821X(02)00822-1
- Singh, S. P., Singh, S. K., Goswami, V., Bhushan, R., and Rai, V. K. (2012). Spatial distribution of dissolved neodymium and  $\epsilon\text{Nd}$  in the Bay of Bengal: role of particulate matter and mixing of water masses. *Geochim. Cosmochim. Acta* 94, 38–56. doi: 10.1016/j.gca.2012.07.017
- Skinner, L. C., Sadekov, A., Brandon, M., Greaves, M., Plancherel, Y., de la Fuente, M., et al. (2019). Rare Earth Elements in early-diagenetic foraminifer ‘coatings’: pore-water controls and potential palaeoceanographic applications. *Geochim. Cosmochim. Acta* 245, 118–132. doi: 10.1016/j.gca.2018.10.027
- Srinivas, B., and Sarin, M. M. (2013). Atmospheric dry-deposition of mineral dust and anthropogenic trace metals to the Bay of Bengal. *J. Mar. Syst.* 126, 56–68. doi: 10.1016/j.jmarsys.2012.11.004
- Stichel, T., Frank, M., Rickli, J., and Haley, B. A. (2012). The hafnium and neodymium isotope composition of seawater in the Atlantic sector of the Southern Ocean. *Earth Planet. Sci. Lett.* 31, 282–294. doi: 10.1016/j.epsl.2011.11.025
- Tachikawa, K., Jeandel, C., and Roy-Barman, M. (1999). A new approach to the Nd residence time in the ocean: the role of atmospheric inputs. *Earth Planet. Sci. Lett.* 170, 433–446. doi: 10.1016/S0012-821X(99)00127-2
- Tachikawa, K., Toyofuku, T., Basile-Doelsch, I., and Delhaye, T. (2013). Microscale neodymium distribution in sedimentary planktonic foraminiferal tests and associated mineral phases. *Geochim. Cosmochim. Acta* 100, 11–23. doi: 10.1016/j.gca.2012.10.010
- Tanaka, T., Togashi, S., Kamioka, H., Amakawa, H., Kagami, H., Hamamoto, T., et al. (2000). JNdI-1: a neodymium isotopic reference in consistency with LaJolla neodymium. *Chem. Geol.* 168, 279–281. doi: 10.1016/S0009-2541(00)00198-4
- Tang, J., and Johannesson, K. H. (2010). Ligand extraction of rare earth elements from aquifer sediments: implications for rare earth element complexation with organic matter in natural waters. *Geochim. Cosmochim. Acta* 74, 6690–6705. doi: 10.1016/j.gca.2010.08.028
- Thadathil, P., Muralidharan, P. M., Rao, R. R., Somayajulu, Y. K., Reddy, G. V., and Revichandran, C. (2007). Observed seasonal variability of barrier layer in the Bay of Bengal. *J. Geophys. Res.* 112:C02009
- Turner, A. G., and Annamalai, H. (2012). Climate change and the South Asian summer monsoon. *Nat. Climate Change* 2, 587–595. doi: 10.1038/nclimate1495
- Unger, D., Ittekkot, V., Schäfer, P., Tiemann, J., and Reschke, S. (2003). Seasonality and interannual variability of particle fluxes to the deep Bay of Bengal: influence of riverine input and oceanographic processes. *Deep Sea Res. Part II* 50, 897–923. doi: 10.1016/S0967-0645(02)00612-4
- van de Flierdt, T., Griffiths, A. M., Lambelet, M., Little, S. H., Stichel, T., and Wilson, D. J. (2016). Neodymium in the oceans: a global database, a regional comparison and implications for palaeoceanographic research. *Philos. Trans. R. Soc. A* 374, 20150293. doi: 10.1098/rsta.2015.0293
- van de Flierdt, T., Pahnke, K., Amakawa, H., Andersson, P., Basak, C., Coles, B., et al. (2012). GEOTRACES intercalibration of neodymium isotopes and rare earth element concentrations in seawater and suspended particles. Part 1: reproducibility of results for the international intercomparison: intercalibration of Seawater Nd Isotopes. *Limnol. Oceanogr.* 10, 234–251. doi: 10.4319/lom.2012.10.234
- van Geldern, R., and Barth, J. A. C. (2012). Optimization of instrument setup and post-run corrections for oxygen and hydrogen stable isotope measurements of water by isotope ratio infrared spectroscopy (IRIS): water stable isotope analysis with IRIS. *Limnol. Oceanogr.* 10, 1024–1036. doi: 10.4319/lom.2012.10.1024
- Varkey, M. J., Murty, V. S. N., and Suryanarayana, A. (1996). Physical oceanography of the Bay of Bengal and Andaman Sea. *Oceanogr. Mar. Biol.* 34, 1–70.
- Wyndham, T., McCulloch, M., Fallon, S., and Alibert, C. (2004). High-resolution coral records of rare earth elements in coastal seawater: biogeochemical cycling and a new environmental proxy. *Geochim. Cosmochim. Acta* 68, 2067–2080. doi: 10.1016/j.gca.2003.11.004
- Yu, Z., Colin, C., Douville, E., Meynadier, L., Duchamp-Alphonse, S., Sepulcre, S., et al. (2017a). Yttrium and rare earth element partitioning in seawaters from the Bay of Bengal. *Geochim. Geophys. Geosyst.* 18, 1388–1403. doi: 10.1002/2016GC006749
- Yu, Z., Colin, C., Meynadier, L., Douville, E., Dapoigny, A., Reverdin, G., et al. (2017b). Seasonal variations in dissolved neodymium isotope composition in the Bay of Bengal. *Earth Planet. Sci. Lett.* 479, 310–321. doi: 10.1016/j.epsl.2017.09.022

**Conflict of Interest:** The authors declare that the research was conducted in the absence of any commercial or financial relationships that could be construed as a potential conflict of interest.

The reviewer JS declared a past co-authorship with several of the authors EH, MF to the handling Editor.

Copyright © 2020 Hathorne, Frank and Mohan. This is an open-access article distributed under the terms of the Creative Commons Attribution License (CC BY). The use, distribution or reproduction in other forums is permitted, provided the original author(s) and the copyright owner(s) are credited and that the original publication in this journal is cited, in accordance with accepted academic practice. No use, distribution or reproduction is permitted which does not comply with these terms.



# Effect of Mg and Ca on the Stability of the MRI Contrast Agent Gd-DTPA in Seawater

Johan Schijf<sup>1\*</sup> and Isabel J. Christy<sup>2</sup>

<sup>1</sup> Chesapeake Biological Laboratory, University of Maryland Center for Environmental Science, Solomons, MD, United States,

<sup>2</sup> Department of Chemistry, Whitman College, Walla Walla, WA, United States

## OPEN ACCESS

### Edited by:

Antonio Tovar-Sanchez,  
Consejo Superior de Investigaciones  
Científicas (CSIC), Spain

### Reviewed by:

Miguel Caetano,  
Portuguese Sea and Atmosphere  
Institute, Portugal  
Vanessa Hatje,  
Universidade Federal da Bahia, Brazil

### \*Correspondence:

Johan Schijf  
schijf@umces.edu

### Specialty section:

This article was submitted to  
Marine Biogeochemistry,  
a section of the journal  
Frontiers in Marine Science

**Received:** 07 December 2017

**Accepted:** 15 March 2018

**Published:** 10 April 2018

### Citation:

Schijf J and Christy IJ (2018) Effect of  
Mg and Ca on the Stability of the MRI  
Contrast Agent Gd-DTPA in Seawater.  
Front. Mar. Sci. 5:111.  
doi: 10.3389/fmars.2018.00111

Gadolinium diethylenetriaminepentaacetic acid (Gd-DTPA) is widely applied as a contrast enhancer in medical MRI. As Gd-DTPA is only minimally captured in wastewater treatment plants (WTPs) or degraded by UV light and other oxidative processes, concentrations in rivers have increased globally by orders of magnitude following its introduction in 1987. The complex also seems impervious to estuarine scavenging and is beginning to emerge in coastal waters, yet it is unknown how its stability is changed by competition for the DTPA ligand from major seawater cations. We performed potentiometric titrations at seawater ionic strength (0.7 M NaClO<sub>4</sub>) to determine dissociation constants of the five DTPA carboxylic acid groups, as well as stability constants of Mg, Ca, and Gd complexes with the fully deprotonated and single-protonated ligand. These are in general agreement with literature values at low ionic strength and confirm that complexes with Ca are more stable than with Mg. A new finding, that the DTPA complexes of Mg and Ca appear to be hydrolyzed at elevated pH, implies that their coordination in these chelates is less than hexadentate, enabling additional competition with Gd from dinuclear Mg and Ca species. Side-reaction coefficients for trace-metal-free seawater, calculated from our results, suggest that the higher abundance of Mg and Ca may significantly destabilize Gd-DTPA in coastal waters, causing dissociation and release of as much as 15% of the organically complexed Gd from the ligand. This effect could magnify the particle-reactivity and bioavailability of anthropogenic Gd in sensitive estuarine habitats, indicating an urgent need to further study the fate of this contaminant in marine environments.

**Keywords:** gadolinium, DTPA, MRI contrast agent, stability constant, side-reaction coefficient, seawater, magnesium, calcium

## INTRODUCTION

The rare earth elements (REE) are Sc, Y, and La in group IIIA of the Periodic Table and the 14 elements following La, up to Lu. The term “earth” refers to an old word for oxide minerals, while the term “rare” refers not so much to their abundance, but to the fact that they are rarely found in ore deposits sufficiently enriched to be of economic interest. Actually, their crustal abundance is much higher than that of more familiar elements, like Hg and Pt; it is comparable to that of metals like Cu and Pb for the more abundant light REE, and to that of Cd for the less abundant heavy REE (e.g., Lide and Haynes, 2009; Table 14-18).



Until a few decades ago, the REE were mainly a scientific curiosity, valued by geologists and geochemists for their remarkable chemical coherence as tracers of waters, rocks, and their myriad interactions in a broad range of marine and terrestrial environments (Henderson, 1984). However, in our increasingly technological society, even the REE are finding their way into a multitude of consumer products and industrial processes (Du and Graedel, 2011). These new applications bring with them a number of specific concerns. The unusual ore deposits that contain the most REE-rich minerals, such as bastnäsite, occur in only a few places around the world. This and certain complex market forces have caused the balance of REE supply and demand to be unequally divided among countries with very different economic and political views (Kanazawa and Kamitani, 2006; Showstack, 2012). In addition, the exploding worldwide use of electronic devices like cellular phones and flat-screen displays has led to REE demand rapidly outpacing global production (Du and Graedel, 2011; Izatt et al., 2014). Combined with the high financial and environmental cost of mining, this has prompted a search for ways to minimize losses during manufacturing and to enable recovery through recycling, as well as more efficient extraction from the primary ores and from process waste and landfills (Binnemans et al., 2015; Nanchaiah et al., 2016). Finally, like many industrial chemicals, the REE have started to enter the environment as pollutants, yet we know little about their toxicity and fate. Some organisms are known to incorporate REE in certain enzymes (Chistoserdova, 2016) and they are readily taken up and stored by plants (Chua, 1998; Brioschi et al., 2013). In Asia, REE are routinely applied as fertilizers since they appear to stimulate crop growth (Zhang and Shan, 2001; Xu et al., 2002). On the other hand, there are strong indications that REE ions are toxic to microorganisms (Fuma et al., 2001; d'Aquino et al., 2009) and animals (Shimada et al., 1995; Zhang et al., 2010) on individual to ecosystem scales (González et al., 2014, 2015; Lingott et al., 2016). Release of Gd from MRI contrast agents can lead to accumulation in bone, brain, and kidneys (Rogosnitzky and Branch, 2016) and is the suspected cause of a disabling pathology termed nephrogenic systemic fibrosis in patients with impaired renal function (Port et al., 2008).

A salient feature of the industrial use of REE is that, unlike their natural occurrence as a group, chemical and manufacturing processes often require just a single element. Upon entering the environment, the contrasting geochemical behavior or sheer abundance of these pollutants leads to anomalies against a natural background of otherwise smooth normalized REE patterns, allowing them to be identified as anthropogenic (Kulaksız and Bau, 2007). Anomalies of La, Ce, and Sm have been found in various rivers (Kulaksız and Bau, 2011a, 2013; de Campos and Enzweiler, 2016) and while a distinct source could not always be determined, these elements are critical ingredients of catalysts, car catalytic converters, and rechargeable batteries (Du and Graedel, 2011). Even when used collectively, as in zeolite catalysts for oil cracking, the contaminants often have a unique REE pattern that makes them stand out (Olmez et al., 1991).

One novel application of an REE that has greatly enhanced its release into the environment is the use of gadolinium (Gd)

as a contrast enhancer in medical magnetic resonance imaging (MRI) diagnostics. Contrast enhancers are employed for high-resolution tomography of organs where signal gradients are small, such as the brain or other soft tissues. The chemistry of the REE is characterized by the gradual filling of the 4f shell, which can hold a total of 14 electrons. The f shell consists of 7 sub-shells that can each hold a pair of electrons with opposite spin. Starting from La, each sub-shell is initially filled with one electron. At Gd, which is halfway along the REE series, every sub-shell contains a single electron, all with parallel spin. This gives Gd and several other REE unusually high magnetic moments, making it especially suited as an MRI contrast enhancer. Due to its severe toxicity and strong tendency to bind to organic molecules, it is not possible to administer Gd to patients directly. Instead, a number of open-chain and macrocyclic polyaminopolycarboxylic acid ligands have been designed that form highly stable anionic and non-ionic complexes with Gd (Behra-Miellet et al., 1998; Port et al., 2008). In pharmaceutical preparations these are often combined with the aminosugar meglumine for improved uptake and tolerance. The agent is orally or intravenously administered to the patient shortly before the MRI treatment and then excreted again via urination within several hours. A typical dose is 0.1 mmol per kg of bodyweight, amounting to ~1–2 g of Gd for an average patient, whereby it should be noted that background concentrations of Gd in nature range from nanomolar in rivers to picomolar in the ocean (Elderfield et al., 1990).

The same engineered stability that keeps these MRI contrast agents from dissociating inside the human body also prevents their environmental degradation. They appear to be impervious to bacterial attack and removal in wastewater treatment plants (WTPs) (Verplanck et al., 2005, 2010; Lawrence et al., 2009) and to behave conservatively in natural waters, even in estuaries where geogenic REE are extensively scavenged (Elderfield et al., 1990; Kulaksız and Bau, 2007). Consequently, since the introduction of MRI contrast agents in the late 1980s, anthropogenic Gd concentrations have increased by 2–3 orders of magnitude above the natural background in rivers and drinking water throughout Europe (Bau and Dulski, 1996; Möller et al., 2002, 2003; Rabiet et al., 2009; Kulaksız and Bau, 2011b), and more recently in North America (Bau et al., 2006), South America (de Campos and Enzweiler, 2016), Asia (Nozaki et al., 2000; Ogata and Terakado, 2006), and Australia (Lawrence, 2010). Anthropogenic Gd anomalies often completely overwhelm natural Gd anomalies that were previously used as tracers of subtle geochemical fractionation processes (e.g., Garcia-Solsona et al., 2014). At the same time, they are increasingly utilized as a conservative tracer of wastewater effluents, groundwater inputs, and hydrological processes (Fuganti et al., 1996; Möller et al., 2000).

The reputed environmental persistence of Gd-based MRI contrast agents is mostly inferred from geochemical observations, but accurate regional mass balances can be difficult to obtain (Kümmerer and Helmers, 2000) and their ultimate environmental fate is uncertain. Eventually, however, they must dissociate and release Gd into the natural REE cycle. This does not only raise the concern of toxicological effects but

also complicates their detection, which is typically based on its distinctive behavior relative to geogenic Gd and the other REE. There are a number of processes that may degrade Gd-polyaminopolycarboxylate complexes, including bacterial attack, UV photo-oxidation, and competition for the ligand from other strongly binding metals (transmetallation). These have been investigated primarily in clinical and pharmacological studies aimed at patient well-being (Idée et al., 2006; Künnemeyer et al., 2009b), yet some studies have taken a broader perspective (Holzbecher et al., 2005; Birka et al., 2016). One process that has received little attention is the effect of increased ionic strength and high concentrations of competing metal ions where rivers meet the salty ocean, notwithstanding the fact that anthropogenic Gd is increasingly being detected in coastal seawater (Zhu et al., 2004; Kulaksız and Bau, 2007; Hatje et al., 2016).

In this study, we focus on potential instability of the anionic Gd-DTPA complex, used as an MRI contrast agent under the brandname Magnevist<sup>®</sup>, upon mixing of river water with seawater in estuaries. Specifically, we conducted laboratory experiments to investigate displacement of Gd from the complex by high levels of Mg and Ca. The most suitable technique, potentiometric titration, cannot distinguish DTPA complexes with different metals in the same solution and therefore cannot be applied directly to natural or even synthetic seawater samples. Instead, following the approach of our earlier work (Christenson and Schijf, 2011; Schijf and Burns, 2016) on the stability of REE complexes with the siderophore desferrioxamine B (DFOB), we sequentially measured stability constants of DTPA complexes with Mg, Ca, and Gd in an inert medium at seawater ionic strength (0.7 M NaClO<sub>4</sub>). Using these values in a speciation model, we then calculated the side-reaction coefficient of DTPA in seawater, which in turn permits us to calculate a conditional stability constant for the Gd-DTPA complex. Our results suggest that the effective stability of Gd-DTPA is diminished by almost 6 orders of magnitude, which may cause the release of toxic Gd into the marine food chain and compromises our ability to distinguish anthropogenic from geogenic Gd.

The experiments with DTPA, although conceptually similar to those with DFOB, are considerably more analytically challenging. Unlike DFOB, which can exchange four protons over a limited range of moderately alkaline pH (~8–11), DTPA can exchange as many as eight protons over a pH range from alkaline (~10) to strongly acidic (<1). Due to the structural symmetry of the DTPA molecule, several of these exchanges occur in closely spaced pairs, making their individual dissociation constants difficult to determine. Moreover, while DFOB is always fully protonated and thus positively charged at pH < 7, DTPA fully protonates only in acidic medium, leading to a solubility minimum around pH 2 (Kragten and Decnop-Weever, 1983), where our titrations normally start. Thirdly, DTPA can potentially form a wider array of mononuclear and polynuclear complexes. And lastly, the stability constants of REE-DTPA complexes are orders of magnitude larger than those of the REE-DFOB complexes (Martell et al., 2004) and at the very edge of the analytical window for our titration method. Conversely, since the stability constants of Mg and Ca complexes are also much larger than for DFOB,

these are actually easier to measure and problems with hydrolysis at elevated pH are alleviated.

## MATERIALS AND METHODS

### Reagents and Standards

All standards and experimental solutions were prepared with Milli-Q water (18.2 MΩ·cm) inside a class-100 laminar-flow bench and stored in acid-cleaned Teflon containers. Only the titration vessel is fabricated from acid-rinsed high-quality glass. Certified titrants (HCl and carbonate-free NaOH) were supplied by Brinkmann. High-purity magnesium oxide (MgO, 99.995%), calcium oxide (CaO, 99.995%), and gadolinium chloride hexahydrate (GdCl<sub>3</sub>·6H<sub>2</sub>O, 99.999%) were purchased from Sigma-Aldrich, as well as diethylenetriaminepentaacetic acid [DTPA; (CH<sub>2</sub>COOH)<sub>2</sub>NC<sub>2</sub>H<sub>4</sub>N(CH<sub>2</sub>COOH)<sub>2</sub>C<sub>2</sub>H<sub>4</sub>N(CH<sub>2</sub>COOH)<sub>2</sub>, ≥99%] and gadolinium DTPA dihydrogen salt hydrate (GdH<sub>2</sub>DTPA·xH<sub>2</sub>O, 97%), desferrioxamine B mesylate (DFOB, ≥92.5%), sodium perchlorate hydrate (NaClO<sub>4</sub>·xH<sub>2</sub>O, 99.99%), and sodium chloride (NaCl, 99.999%). Concentrated TraceMetal Grade perchloric acid (HClO<sub>4</sub>) was acquired from Thermo Fisher. All chemicals were used as received.

A pH standard (0.7 M) was prepared by dissolving NaCl in water and setting the pH to 3.000 ± 0.004 with certified HCl. The background electrolyte was prepared by dissolving NaClO<sub>4</sub> in water and adjusting the density to obtain a solution of 0.700 ± 0.001 M (Janz et al., 1970). Its pH was then set to 2.0 ± 0.1 with calibrated HClO<sub>4</sub> (11.40 ± 0.02 M). An unacidified electrolyte solution was also made for titrations starting at pH > 10. Solutions of about 100 mM Mg or Ca were obtained by dissolving the oxides in the acidified electrolyte and adding excess HClO<sub>4</sub>. The final pH of these solutions was 1–2. Their exact concentrations were measured via ICP-MS as described by Schijf and Burns (2016). Due to hydration of the oxide, the concentration of the Ca standard and the corresponding metal-to-ligand (M:L) molar ratios of the experimental solutions were somewhat lower than intended, which was accounted for in the calculations.

A solution of about 40 mM DTPA was initially produced by dissolving the solid acid in the acidified electrolyte. At this pH, DTPA remains mostly protonated and is thus rather non-polar and poorly soluble in aqueous solutions. The solubility was improved by adding NaOH solution adjusted to the same ionic strength. In later experiments, DTPA was dissolved in the unacidified electrolyte and titrations were started at a high pH, although this approach could not be used for Mg (see section Stability Constants of Mg-DTPA and Ca-DTPA Complexes). A solution of about 40 mM Gd was made by dissolving GdCl<sub>3</sub> in the acidified electrolyte. Some titrations were also conducted with a solution of about 40 mM GdH<sub>2</sub>DTPA, which is quite soluble at pH 2. The exact concentrations of both Gd standards were determined via ICP-MS as described by Christenson and Schijf (2011). Comparison of the exact Gd concentration with the gravimetric value indicates that the GdH<sub>2</sub>DTPA·xH<sub>2</sub>O salt is a nonahydrate (x = 9). A full ICP-MS mass spectral scan of the diluted GdH<sub>2</sub>DTPA standard detected no other REE or

metals that are known to bind strongly to DTPA, such as Al and Fe. Some Gd titrations were done in the presence of DFOB. A solution of about 40 mM DFOB was prepared on the day of the experiment by dissolving ~265 mg of the mesylate salt in 10 mL of the acidified electrolyte.

## Potentiometric Titrations

Potentiometric titration largely followed the protocols outlined in detail by Christenson and Schijf (2011), Schijf et al. (2015b), and Schijf and Burns (2016). Briefly, experimental solutions of 50 mL were dynamically titrated with certified NaOH or HCl using a Brinkmann Metrohm 809 Titrando autotitrator, generally in the pH window 2–11, but occasionally up to pH ~ 12 or down to pH < 1. The titrations were conducted in a closed glass vessel, maintained at a constant temperature of  $25.0 \pm 0.1^\circ\text{C}$ , while the solutions were magnetically stirred and continuously sparged with humidified ultrahigh-purity  $\text{N}_2$  gas to exclude atmospheric  $\text{CO}_2$ . The solution pH was monitored with a glass combination electrode that was calibrated against the pH standard on the free proton concentration scale before each run. Blank titrations were conducted with 50 mL of the acidified background electrolyte. Regressions of the blank titrations with FITEQL4.0 (Herbelin and Westall, 1999) confirm the absence of acid/base contaminants such as bicarbonate, although a slight excess of hydrolysis at high pH indicates the presence, at trace levels (~10  $\mu\text{M}$ ), of a metal with a first hydrolysis constant ( $\log \beta_1^*$ ) of  $-4.5 \pm 0.1$ , possibly Al (Baes and Mesmer, 1981). This is less than 1% of the metal and ligand concentrations in the experiments and Al binds to DTPA nearly as strongly as Gd and much more strongly than Mg or Ca (Taqui Khan and Hussain, 1980), hence it is unlikely to have interfered with the titrations.

A total of 27 titrations was conducted with DTPA solutions of 1, 2, and 4 mM to determine acid dissociation constants, 14 with 1 M NaOH starting at low pH and 13 with 1 M HCl starting at high pH. Nine titrations were conducted for each of the metals, over a range of M:L ratios, in the presence of 2 mM DTPA for Mg and Ca, and 2 or 4 mM DTPA for Gd. Some early Mg and Ca titrations were done with 0.1 M NaOH as before (Schijf and Burns, 2016) but, due to the lower starting pH and larger number of protons exchanged within the analytical pH window, this was found to cause too much dilution and depression of the ionic strength. All subsequent titrations were therefore conducted with 1 M NaOH for Mg and Gd, or 1 M HCl for Ca. Four Gd titrations were done with 2 mM  $\text{GdH}_2\text{DTPA}$ , two of which in the presence of 2 and 4 mM DFOB, respectively. The other five were done using separate metal and ligand standards.

## Non-linear Regressions

Non-linear regressions of the data were conducted with FITEQL4.0 as described by Schijf et al. (2015b), selecting the optimal speciation model for each series of titrations. A single FITEQL model was always used for all titrations within a series, although certain adjustable parameters were sometimes fixed in sequential or iterative regressions. Additional details are provided below. Quality-of-fit was assessed from the Weighted Sum-Of-Squares per Degree-of-Freedom (WSOS/DF) parameter (Herbelin and Westall, 1999), where values between

0.1 and 20 are considered acceptable; values lower than 0.1 generally indicate an under-constrained fit. Metal and ligand concentrations were usually fixed at the ICP-MS and gravimetric value, respectively, but the ligand concentration was sometimes used as an adjustable parameter. The initial proton excess,  $[\text{H}^+]_T^0$ , was always used as an adjustable parameter and negative values were allowed, to accommodate proton deficiencies. The ability of DTPA to exchange protons at very low pH often made its initial degree of protonation difficult to determine. Values of  $[\text{H}^+]_T^0$  are thus much higher than for DFOB (Christenson and Schijf, 2011), typically several hundred  $\mu\text{M}$ . They seem randomly divided between positive and negative values, albeit negative values appear more likely for the metal titrations. The initial proton excess is reported for all titrations, but not further discussed.

The nomenclature for stability constants with protonated organic ligands varies widely in the literature and they will be indexed here in the order L-M-H, following Duffield et al. (1984):

$$\beta_{\text{pqr}} = \frac{[\text{M}_q\text{H}_r\text{L}_p]}{[\text{M}]^q[\text{H}]^r[\text{L}]^p} \quad (1)$$

Acid dissociation of the ligand ( $q = 0$ ) will be described by means of stepwise constants,  $K_{\text{ai}}$ , as defined in section Deprotonation of DTPA, where  $\beta_{101} = (K_{\text{a5}})^{-1}$ ,  $\beta_{102} = (K_{\text{a5}} \times K_{\text{a4}})^{-1}$ ,  $\beta_{103} = (K_{\text{a5}} \times K_{\text{a4}} \times K_{\text{a3}})^{-1}$  etc. To simplify speciation modeling, it is convenient to express stability constants in terms of dissociation of the metal from the protonated ligand, which shall be indicated with a superscript M, where only complexation with a single ligand molecule ( $p = 1$ ) will be considered:

$$^{\text{M}}\beta_{1\text{qr}} = \frac{[\text{M}_q\text{H}_r\text{L}]}{[\text{M}]^q[\text{H}_r\text{L}]} \quad (2)$$

A more specific list of the equilibrium constants used here is given in Table 1.

## PRESENTATION AND DISCUSSION OF THE EXPERIMENTAL RESULTS

### Deprotonation of DTPA

The backbone of the DTPA molecule consists of three amine groups separated by two ethylene groups ( $\text{N}-\text{C}_2\text{H}_4-\text{N}-\text{C}_2\text{H}_4-\text{N}$ ). The terminal amines each contain two acetate groups ( $-\text{CH}_2(\text{C}=\text{O})\text{OH}$ ), while the central amine contains a fifth (Figure 1). The molecule is essentially an enlargement of the common ligand ethylenediaminetetraacetic acid (EDTA), with one additional amine and one additional acetate group. The longer backbone gives DTPA greater steric freedom and the extra amine and acetate group increase its denticity, improving its binding to larger ions with higher coordination numbers, like the REE.

The protonation of DTPA is complicated. In the neutral molecule, each of the five acetate groups is associated with one exchangeable proton. The acid dissociation constants of these protons are usually numbered  $K_{\text{a1}}$  through  $K_{\text{a5}}$ . However, it appears that each of the three amine groups can also accept

**TABLE 1** | Definitions of equilibrium constants used throughout the text.

Constant	Equilibrium reaction
$K_W$	$H_2O(l) \rightleftharpoons H^+ + OH^-$
$K_{a-2}$	$H_8L^{3+} \rightleftharpoons H^+ + H_7L^{2+}$
$K_{a-1}$	$H_7L^{2+} \rightleftharpoons H^+ + H_6L^+$
$K_{a0}$	$H_6L^+ \rightleftharpoons H^+ + H_5L$
$K_{a1}$	$H_5L \rightleftharpoons H^+ + H_4L^-$
$K_{a2}$	$H_4L^- \rightleftharpoons H^+ + H_3L^{2-}$
$K_{a3}$	$H_3L^{2-} \rightleftharpoons H^+ + H_2L^{3-}$
$K_{a4}$	$H_2L^{3-} \rightleftharpoons H^+ + HL^{4-}$
$K_{a5}$	$HL^{4-} \rightleftharpoons H^+ + L^{5-}$
$\beta_1^*$	$M^{2+} + H_2O(l) \rightleftharpoons MOH^+ + H^+$ $Gd^{3+} + H_2O(l) \rightleftharpoons GdOH^{2+} + H^+$
$M_{\beta 112}$	$M^{2+} + H_2L^{3-} \rightleftharpoons MH_2L^-$
$M_{\beta 111}$	$M^{2+} + HL^{4-} \rightleftharpoons MHL^{2-}$ $Gd^{3+} + HL^{4-} \rightleftharpoons GdHL^-$
$M_{\beta 110}$	$M^{2+} + L^{5-} \rightleftharpoons ML^{3-}$ $Gd^{3+} + L^{5-} \rightleftharpoons GdL^{2-}$
$H_{\beta 110}$	$ML^{3-} + H_2O(l) \rightleftharpoons M(OH)L^{4-} + H^+$
$M_{\beta 120}$	$2M^{2+} + L^{5-} \rightleftharpoons M_2L^-$
$R_4$	$M^{2+} + H_3L^{2-} \rightleftharpoons MHL^{2-} + 2H^+$ $Gd^{3+} + H_3L^{2-} \rightleftharpoons GdHL^- + 2H^+$
$R_5$	$M^{2+} + H_3L^{2-} \rightleftharpoons ML^{3-} + 3H^+$ $Gd^{3+} + H_3L^{2-} \rightleftharpoons GdL^{2-} + 3H^+$
$R_5^*$	$M^{2+} + H_3L^{2-} + H_2O(l) \rightleftharpoons M(OH)L^{4-} + 4H^+$

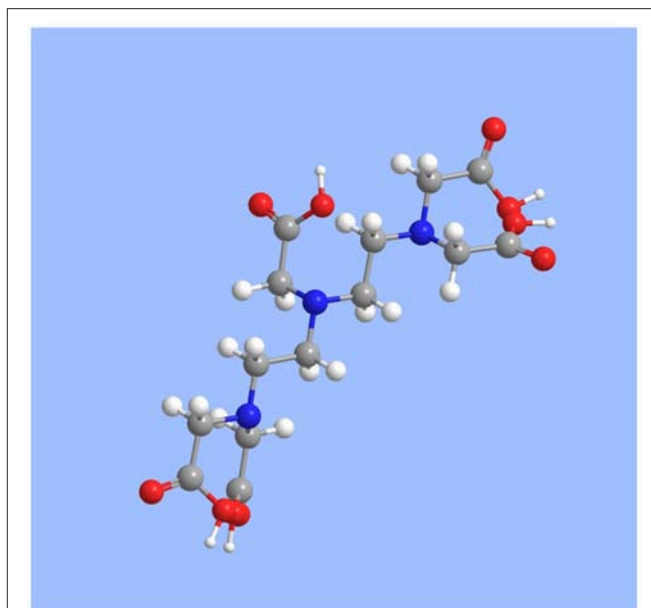
Each constant is shown with its corresponding equilibrium reaction(s). All reagents and products are aqueous species, unless indicated otherwise.  $M^{2+}$  is  $Mg^{2+}$  or  $Ca^{2+}$ ,  $L^{5-}$  the fully deprotonated DTPA ligand.

a proton to form a positively charged molecule at low pH, increasing the number of exchangeable protons to eight, with acid dissociation constants defined as follows (Table 1):

$$K_{ai} = \frac{[H^+][H_{5-i}L^{(-i)+}]}{[H_{6-i}L^{(1-i)+}]} \quad (i = -2, -1, 0, 1, \dots, 5). \quad (3)$$

It is possible that, at low pH, one or more of the acetate protons are translocated to the adjacent amines, forming complex zwitterions with multiple positively and negatively charged groups. Harder and Chaberek (1959) show the neutral DTPA molecule with the central and two opposing terminal acetate groups deprotonated and one proton translocated to each of the three amines, making the former negatively and the latter positively charged.

The values of  $pK_{a1}$  and  $pK_{a2}$  are around pH 2–3,  $pK_{a3}$  is just above pH 4, and  $pK_{a4}$  and  $pK_{a5}$  are around pH 8–10 (Martell et al., 2004). There is a good deal of uncertainty about the other three acid dissociation constants. At 25°C, reported values of  $pK_{a0}$  are 1.75 in 0.1 M  $KNO_3$  (Letkeman and Martell, 1979) and 1.67 in KCl at  $I = 1$  (Merciny et al., 1978; Mioduski, 1980), while somewhat lower values are found at lower temperature: 1.45 in NaCl ( $I = 0.11$ ) at 20°C (Matorina et al., 1969) and 1.22 in  $NaClO_4$  ( $I = 1$ ) at 21°C (Kragten and Decnop-Weever, 1983).

**FIGURE 1** | Rendering of the molecular structure of DTPA, produced with ChemDraw v.12.0. Gray = C; white = H; red = O; blue = N.

The same authors report congruent values for  $pK_{a-1}$  under the given conditions: 0.75 (Kragten and Decnop-Weever, 1983), 0.88 (Merciny et al., 1978; Mioduski, 1980), and 0.89 (Matorina et al., 1969), except for Letkeman and Martell (1979), who found a value of 1.45. Only Mioduski (1980) reports a value for  $pK_{a-2}$  ( $0.81 \pm 0.05$ ), but Martell et al. (2004) estimate that it is probably less than zero. It seems that the eight acid dissociation constants form three rather closely spaced pairs separated by two more distinct values ( $pK_{a0}$  and  $pK_{a3}$ ). In view of the symmetry of the DTPA molecule, it is likely that the three pairs are associated with protonation of the terminal amines and their acetate groups, whereas the two single values are associated with protonation of the central amine and acetate group.

We performed non-linear regressions of 27 titrations of 1, 2, and 4 mM DTPA solutions with 1 M NaOH or HCl. Although acid titrations were conducted to circumvent the poor solubility of DTPA at low pH, they often yielded marginal fits, most commonly caused by a reversal of  $pK_{a1}$  and  $pK_{a2}$ , and many were ultimately rejected. Similar to our study of DFOB (Christenson and Schijf, 2011), FITEQL models were initially constructed with all six (de)protonated forms of DTPA ( $H_{5-i}L^{(-i)+}$  with  $i = 0-5$ ) as the component and, as before, it was found that the model with  $H_3L^{2-}$  yields  $pK_{ai}$  values with the highest precision that are least dependent on the ligand concentration. All regressions were subsequently performed with this model. It was also found that titrations of 1 mM DTPA solutions gave persistently bad results and these were rejected. In the end, 10 titrations with NaOH and 3 titrations with HCl were selected to determine the final  $pK_{ai}$  values (Table 2). Analogous to our titrations of DFOB (Christenson and Schijf, 2011), the regressions were performed with the initial proton excess,  $[H^+]_T^0$ , and the  $pK_{ai}$  values as free parameters. All regressions converged after a small number of



**TABLE 2** | Thirteen titrations of diethylenetriaminepentaacetic acid (DTPA) in 50 mL of 0.7 M NaClO<sub>4</sub> solution.

[DTPA] <sub>T</sub> (mM) <sup>a</sup>	titrant (M)	pH window	[H <sup>+</sup> ] <sub>T</sub> <sup>0</sup> (μM) <sup>b</sup>	pK <sub>a1</sub>	pK <sub>a2</sub>	pK <sub>a3</sub>	pK <sub>a4</sub>	pK <sub>a5</sub>	n <sup>c</sup>	WSOS/DF <sup>d</sup>
4.01	1.0005	2.7–11.0	+449	2.283	2.695	4.171	8.198	9.483	65	0.474
4.01	1.0005	2.7–11.1	+922	2.459	2.582	4.150	8.206	9.496	68	0.872
4.01	1.0005	2.7–11.0	+239	2.256	2.655	4.149	8.209	9.502	67	0.271
4.00	0.9986	2.2–10.1	−692	2.329	2.581	4.135	8.189	9.507	82	0.161
4.00	0.9986	2.2–10.0	−590	2.327	2.565	4.118	8.177	9.490	83	0.165
4.00	0.9986	2.2–11.0	−614	2.333	2.557	4.114	8.187	9.503	88	0.379
2.01	1.0005	2.2–11.0	+455	2.390	2.678	4.202	8.176	9.457	67	1.31
2.01	1.0005	2.2–11.1	+339	2.338	2.679	4.192	8.184	9.454	69	1.80
2.00	0.9986	2.1–11.0	−514	2.432	2.547	4.135	8.173	9.473	88	1.27
2.00	0.9986	2.1–10.1	−592	2.455	2.577	4.146	8.182	9.493	79	0.395
2.01	1.0027 <sup>†</sup>	10.1–3.0	+36.9	2.398	2.512	4.163	8.159	9.552	39	1.04
2.01	1.0027 <sup>†</sup>	10.1–2.9	−46.4	2.422	2.600	4.179	8.129	9.494	41	0.993
2.01	1.0027 <sup>†</sup>	10.1–2.9	−22.8	2.421	2.617	4.188	8.134	9.495	40	0.978

The final ionic strength was raised by ≤1% due to addition of the titrants. Non-linear regressions were performed with FITEQL4.0, keeping the ionization constant of water fixed at pK<sub>w</sub> = 13.740 (Christenson and Schijf, 2011). The five acid dissociation constants, pK<sub>ai</sub>, and the initial proton excess, [H<sup>+</sup>]<sub>T</sub><sup>0</sup>, were used as adjustable parameters. All regressions converged in ≤6 iterations.

<sup>a</sup> Gravimetric concentration.

<sup>b</sup> Negative values signify an initial proton deficiency.

<sup>c</sup> Number of titration points.

<sup>d</sup> Quality-of-fit parameter (Weighted Sum-Of-Squares per Degree-of-Freedom); values of 0.1–20 indicate a good fit (Herbelin and Westall, 1999).

<sup>†</sup> HCl titrant.

iterations and the quality-of-fit parameter, WSOS/DF, was of the order 0.1–1, indicating good fits (Herbelin and Westall, 1999).

The average pK<sub>ai</sub> values are given in **Table 3**, where they are compared with values from the literature. Relative standard deviations are 2–3% for pK<sub>a1</sub> and pK<sub>a2</sub> and <1% for the other three constants, confirming that results are independent of the DTPA concentration and the titrant. The literature contains dozens of studies of DTPA protonation in many different media, using many different techniques. Unlike DFOB (Christenson and Schijf, 2011), it seems that pK<sub>ai</sub> values for DTPA do depend on medium composition and data in NaClO<sub>4</sub> were therefore selected for the comparison in **Table 3**. In studies where different definitions of the acid dissociation constants were used, values were recalculated to match the form of Equation (3). Not all data in **Table 3** are internally or mutually consistent. The pK<sub>a1</sub> and pK<sub>a3</sub> values of Grimes and Nash (2014) (I = 2.0 M) are higher than other literature data for this ionic strength range, although the remaining constants are concordant. The first three pK<sub>ai</sub> values of Nozaki and Koshiba (1967) (I = 0.5) are anomalous as well. Their value for pK<sub>a2</sub> is more similar to published values for pK<sub>a1</sub>. In addition, their values for pK<sub>a3</sub> (3.39) and pK<sub>a1</sub> (1.13) are remarkably close to, respectively, the average of our values for pK<sub>a2</sub> and pK<sub>a4</sub> (3.38) at I = 0.7 M and the average of the values for pK<sub>a−1</sub> and pK<sub>a0</sub> (1.12) at I = 1 (KCl) reported by Merciny et al. (1978) and Mioduski (1980). It seems that pK<sub>a3</sub> was not resolved in the regression, causing an upward shift of the lower pK<sub>ai</sub>.

The most comprehensive study is that of Thakur et al. (2007), who determined acid dissociation constants over a wide range of ionic strength (I = 0.3–6.6). They found that, again unlike DFOB, the pK<sub>ai</sub> values of DTPA display a definite dependence on ionic strength. In **Figure 2**, the data in **Table 3** are shown for

pK<sub>a2</sub>, pK<sub>a3</sub>, and pK<sub>a5</sub>, with extended Debye-Hückel fits through the data of Thakur et al. (2007). For pK<sub>a2</sub>, the values reported by Thakur et al. (2007) are the highest at each ionic strength for which literature data exist, hence a fit through all data is also shown. Our values are satisfactorily close to these curves.

Protonation of the DTPA amine groups occurs outside the pH window of our titrations. Nevertheless, including these reactions in our FITEQL models, with the corresponding pK<sub>ai</sub> fixed at values appropriate for our experimental conditions, might improve the quality of regressions for the metal-ligand titrations. However, our attempts to determine these values were unsuccessful. Four slightly alkaline DTPA solutions of 1 or 2 mM were titrated down to pH ~ 0.9 by adding 1 M HCl in small increments (400–500 shots). Reactions for the protonation of one, two, or all amine groups were added to the FITEQL model, yet despite choosing a range of starting values, or limiting the degrees of freedom by fixing some higher pK<sub>ai</sub> at the average values given in **Table 3**, the regressions would not converge to reproducible results (data not shown). This may be due in part to poor solubility of the ligand at low pH (Kragten and Decnop-Weever, 1983) or non-linear behavior of the glass electrode, and to a very small degree of proton exchange in a highly acidic matrix, producing inadequate signal-to-noise ratios. Gritmon et al. (1977) emphasized that the response of even high-quality glass electrodes deteriorates at pH < 2. To assess the effect of omitting these protonation reactions from FITEQL models, additional regressions of some Mg and Ca titrations were conducted with pK<sub>a−1</sub> and pK<sub>a0</sub> fixed at literature values for NaClO<sub>4</sub> (I = 1) at 21°C (Kragten and Decnop-Weever, 1983), but excluding pK<sub>a−2</sub>. The resulting stability constants for Mg-DTPA and Ca-DTPA complexes were not substantially different

**TABLE 3** | Literature values for the five highest DTPA acid dissociation constants in NaClO<sub>4</sub> solutions.

I (m)	T (°C)	pK <sub>a1</sub>	pK <sub>a2</sub>	pK <sub>a3</sub>	pK <sub>a4</sub>	pK <sub>a5</sub>	References
0.304	25.0	2.18 ± 0.11	2.90 ± 0.09	4.20 ± 0.03	8.64 ± 0.04	9.87 ± 0.06	Thakur et al., 2007
0.40	25	1.75	2.43	4.20	8.45	10.02	Kodama et al., 1968
0.50	20	(1.13)	2.35	(3.39)	8.18	9.49	Nozaki and Koshiba, 1967
0.5 M	25.0	2.20 <sup>†</sup>	2.56 <sup>†</sup>	4.08 <sup>†</sup>	8.09 <sup>†</sup>	9.42	Napoli, 1975
0.50 M	25.0	1.95 ± 0.05	2.85 ± 0.06	4.12 ± 0.07	8.32 ± 0.08	9.86 ± 0.14	Gritmon et al., 1977
0.511	25.0	2.16 ± 0.09	2.79 ± 0.10	4.18 ± 0.02	8.53 ± 0.03	9.72 ± 0.02	Thakur et al., 2007
0.70 M	25.0	<b>2.37 ± 0.07</b>	<b>2.60 ± 0.06</b>	<b>4.16 ± 0.03</b>	<b>8.18 ± 0.02</b>	<b>9.49 ± 0.02</b>	This work
1 M	20	2.5	2.5	4.19	8.26	9.48	Anderegg, 1967
1.03	25.0	2.14 ± 0.12	2.68 ± 0.09	4.15 ± 0.03	8.32 ± 0.04	9.52 ± 0.03	Thakur et al., 2007
1.05	25	2.35 ± 0.06 <sup>†</sup>	2.54 ± 0.05 <sup>†</sup>	4.21 ± 0.04 <sup>†</sup>	8.24 ± 0.03 <sup>†</sup>	9.41 ± 0.02	Tian and Rao, 2010
2.0 M	25.0	2.41 ± 0.01	2.53 ± 0.03	4.38 ± 0.01	8.31 ± 0.01	9.50 ± 0.01	Grimes and Nash, 2014
2.18	25.0	2.12 ± 0.11	2.64 ± 0.09	4.13 ± 0.09	8.28 ± 0.04	9.46 ± 0.05	Thakur et al., 2007
3.44	25.0	2.21 ± 0.11	2.87 ± 0.07	4.22 ± 0.04	8.42 ± 0.06	9.58 ± 0.04	Thakur et al., 2007
4.92	25.0	2.28 ± 0.08	2.92 ± 0.08	4.38 ± 0.06	8.58 ± 0.05	9.83 ± 0.07	Thakur et al., 2007
6.60	25.0	2.32 ± 0.09	2.94 ± 0.07	4.41 ± 0.02	8.62 ± 0.04	9.98 ± 0.08	Thakur et al., 2007

Results from the present work are shown in bold type. Data in parentheses are questionable. Gritmon et al. (1977) reported constants in 0.50 M KNO<sub>3</sub>, but the authors noted no difference with results in 0.50 M NaClO<sub>4</sub>. <sup>†</sup>Calculated from cumulative constants.

from those presented in the next section and protonation of the DTPA amine groups was therefore not further considered.

## Stability Constants of Mg-DTPA and Ca-DTPA Complexes

We performed 9 titrations each of Mg+DTPA and Ca+DTPA solutions in 0.7 M NaClO<sub>4</sub>, over a range of M:L ratios. The results are presented in **Tables 4, 5**. Although Mg and Ca bind more strongly to DTPA than to DFOB (Schijf and Burns, 2016), precipitation of Mg(OH)<sub>2</sub> was still observed at M:L ratios around 3 (for 2 mM DTPA). The highest M:L ratio used for Mg was 2.6. Calcium is much less prone to hydroxide precipitation and M:L ratios of up to 3.3 were used. Despite these lower ratios, the titration curves were easily distinguishable from the titration curve for DTPA alone (**Figure 3**), unlike DFOB (Schijf and Burns, 2016). For Ca, which does not precipitate, titrations could be started at high pH, where DTPA is more soluble, and titrated down with HCl. The results were in good agreement with those obtained from titrations with NaOH (**Table 5**). Titrations of Mg were all conducted with NaOH (**Table 4**). The first hydrolysis constants of Mg and Ca were included and their values fixed in the FITEQL model for all regressions (Schijf and Burns, 2016).

Complexes of Mg and Ca with DTPA that have been reported in the literature include those with zero, one, two, and three protons (ML<sup>3+</sup>, MHL<sup>2+</sup>, MH<sub>2</sub>L<sup>+</sup>, MH<sub>3</sub>L<sup>0</sup>), and the dinuclear complex, M<sub>2</sub>L<sup>+</sup> (Duffield et al., 1984). The M:L ratios of our titrations (as well as the DTPA concentrations) were too high to detect the double- and triple-protonated forms and too low to detect the dinuclear complex. Nonetheless, it was found that models with only the ML<sup>3+</sup> and MHL<sup>2+</sup> complexes did not yield optimal fits, especially in the highest pH region. This was amended by assuming that Mg and Ca can be hydrolyzed inside the fully deprotonated DTPA complex at elevated pH to form the ternary complex, M(OH)L<sup>4+</sup>. This complex has not been

previously reported for Mg or Ca, but it has been observed for more strongly hydrolyzing elements, such as Al, Ga, In (Harris and Martell, 1976; Taqui Khan and Hussain, 1980), and Fe (Vandegaer et al., 1959; Ahrlund et al., 1990). The following stability constant was added to the FITEQL model (**Table 1**):

$$H\beta_{110} = \frac{[M(OH)L^{4-}][H^+]}{[ML^{3+}]} \quad (4)$$

This constant could not be resolved in titrations with 0.1 M NaOH for either Mg or Ca. In order to have a single FITEQL model for all regressions, values of all three stability constants were first determined from titrations with 1 M NaOH (Mg) or HCl (Ca). Regressions of titrations with 0.1 M NaOH were then performed with  $H\beta_{110}$  fixed at the average of the values so obtained. The values of  $M\beta_{110}$  and  $M\beta_{111}$  were in good agreement for both sets of regressions (**Tables 4, 5**).

Only a limited number of studies exists on the stability of DTPA complexes with Ca and even fewer for Mg. **Table 7** shows only those where more than one constant was measured, most of which also include a value for  $M\beta_{120}$ . One was conducted at physiological conditions (0.150 M NaCl, T = 37°C), while all others were conducted at I = 0.1 and none in NaClO<sub>4</sub>. Nevertheless, our results for  $M\beta_{110}$  and  $M\beta_{111}$  are generally consistent with literature values, considering the higher ionic strength of our experiments. Our values are lower than those of the careful study by Duffield et al. (1984), which in turn are lower than results at I = 0.1 (except  $M\beta_{111}$  for Mg). This suggests a definite ionic strength dependence for these constants, which is broadly consistent with what is observed for DFOB (Schijf and Burns, 2016), although that finding was essentially based on a single published study. It should be noted that the relative values of our stability constants are also in marked agreement with Duffield et al. (1984). Our values of  $M\beta_{110}$  and  $M\beta_{111}$  are lower by 0.76 and 0.73 log units, respectively, for Ca and by 0.86 and 0.82

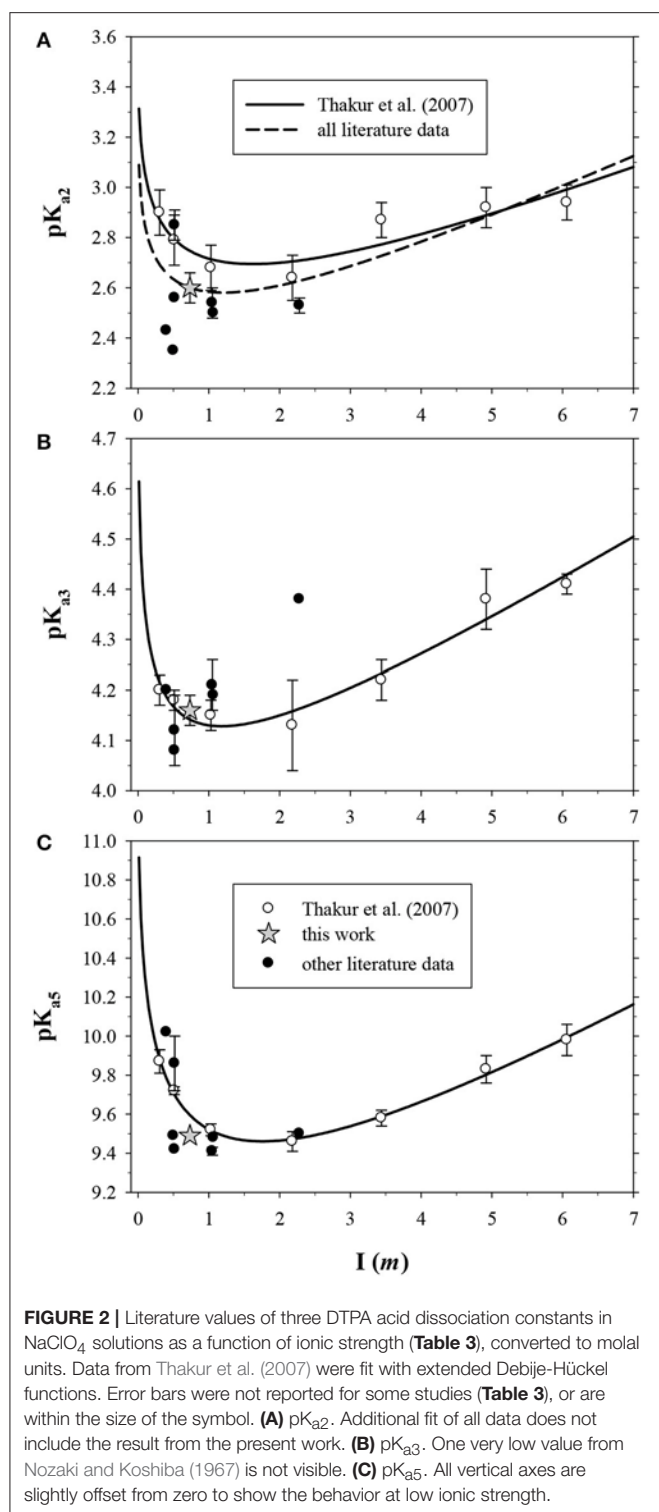


**FIGURE 2 |** Literature values of three DTPA acid dissociation constants in  $\text{NaClO}_4$  solutions as a function of ionic strength (Table 3), converted to molal units. Data from Thakur et al. (2007) were fit with extended Debye-Hückel functions. Error bars were not reported for some studies (Table 3), or are within the size of the symbol. (A)  $\text{pK}_{a2}$ . Additional fit of all data does not include the result from the present work. (B)  $\text{pK}_{a3}$ . One very low value from Nozaki and Koshihara (1967) is not visible. (C)  $\text{pK}_{a5}$ . All vertical axes are slightly offset from zero to show the behavior at low ionic strength.

log units for Mg. We will use this observation to estimate values of  $M\beta_{120}$  and  $M\beta_{112}$  for our speciation calculations in seawater (sections Calculation of the DTPA Side-Reaction Coefficient and Implications for the Stability of Gd-DTPA Complexes in Seawater). In contrast with DFOB (Schijf and Burns, 2016),

DTPA complexes with Ca are more stable than those with Mg. This is clearly illustrated by the titration curves (Figure 3) and by the buffer intensities of the corresponding solutions (Figure 4).

No literature data are available for comparison with our values of  $H\beta_{110}$ . However, they can be compared with first hydrolysis constants of the free metal,  $\log \beta_1^*$  (Table 1), which are  $-12.04$  and  $-13.00$ , respectively, for Mg and Ca in  $0.7 \text{ M NaClO}_4$  (Schijf and Burns, 2016). These constants, while similar in value to  $H\beta_{110}$ , indicate that hydrolysis of the metal inside the complex is thermodynamically distinct from hydrolysis of the free metal and that especially Ca is more readily hydrolyzed inside the complex. It also suggests that Mg and Ca retain at least one water of hydration and are consequently not fully coordinated by DTPA, even when the latter is completely deprotonated. This may explain the unusually high stability of the dinuclear complexes (Table 7 and see section Calculation of the DTPA Side-Reaction Coefficient). The fact that the dinuclear Mg complex was only observed by Duffield et al. (1984) may be due to the low solubility of Mg at elevated pH, which complicates the necessary titrations at high M:L ratios.

### Stability Constants of Gd-DTPA Complexes

Nine titrations of Gd+DTPA were performed in  $0.7 \text{ M NaClO}_4$  and the results are shown in Table 6. Initial runs were conducted with  $\text{GdH}_2\text{DTPA}$ . In the regressions, the M:L ratio of this compound was assumed to be 1 and the ligand concentration was fixed and set equal to the Gd concentration measured by ICP-MS. The stability of the Gd-DTPA complex is extremely high and at the very edge of the analytical window for our method (Figures 3, 4). In an attempt to enhance the exchange of protons, two runs were performed in the presence of DFOB as a competing ligand, where the stability constant ( $\log \beta_3 = \log M\beta_{110}$ ) of the hexadentate Gd-DFOB complex is  $13.67$  in  $0.7 \text{ M NaClO}_4$  (Christenson and Schijf, 2011). However, this is 7 orders of magnitude less stable than the DTPA complex and the speciation of Gd throughout the titrations was little affected by additions of up to  $4 \text{ mM}$  DFOB. To allow variation of the M:L ratio, additional titrations were conducted wherein Gd and DTPA were added separately. In the regressions of these data, the DTPA concentration was used as an adjustable parameter. In a few cases this led to under-constrained fits ( $\text{WSOS/DF} < 0.1$ ) and the optimized DTPA concentration was always 4–6% lower than the gravimetric value (Table 6).

Previous studies of Gd have reported the formation of a deprotonated and a single-protonated DTPA complex (Table 7) and both were included in the FITEQL model. The corresponding stability constants could be determined simultaneously for all nine titrations, but the values of  $M\beta_{111}$  were poorly constrained and significantly different for the titrations with  $\text{GdH}_2\text{DTPA}$ . For one titration with the lowest M:L ratio (0.46), the values of both stability constants were anomalous. Results were significantly improved by adding two iterative steps to the initial regressions. In the second step, the value of  $M\beta_{110}$ , which was fairly well constrained, was fixed at the average obtained in the first step, excluding the one anomalous run, yielding a more

**TABLE 4** | Nine titrations of magnesium in 0.7 M NaClO<sub>4</sub> solutions containing 2.01 mM DTPA (gravimetric concentration).

[Mg] <sub>T</sub> /[DTPA] <sub>T</sub>	Titratant (M)	pH window	[H <sup>+</sup> ] <sub>T</sub> <sup>0</sup> (μM) <sup>a</sup>	log <sup>M</sup> β <sub>111</sub>	log <sup>M</sup> β <sub>110</sub>	log <sup>H</sup> β <sub>110</sub>	[DTPA] <sub>T</sub> (mM) <sup>b</sup>	n <sup>c</sup>	WSOS/DF <sup>d</sup>
1.06	0.9986	2.4–10.6	−403	5.039	7.708	−11.85	1.97	73	0.184
1.06	0.9986	1.9–10.6	−327	5.043	7.706	−11.90	2.03	101	1.89
1.59	0.9986	1.9–10.7	−444	5.040	7.695	−11.79	2.02	101	1.73
2.12	0.9986	1.9–10.6	−498	5.040	7.726	−11.88	1.98	101	1.63
2.12	0.9986	1.9–10.6	−423	5.033	7.688	−11.71	2.04	100	1.73
2.65	0.9986	1.9–10.6	−435	5.023	7.706	−11.40	2.04	101	1.35
1.06	0.1001	2.2–10.0	+43.1	5.026	7.661	<b>−11.75</b>	1.97	161	0.139
1.59	0.1001	2.2–10.1	+112	5.005	7.685	<b>−11.75</b>	1.90	162	0.264
2.12	0.1001	2.2–10.1	−113	5.024	7.681	<b>−11.75</b>	1.89	161	0.169

The final ionic strength was raised by ≤1% and lowered by ≤11% for titrations with 1 M and 0.1 M NaOH, respectively. Non-linear regressions were performed with FITEQL4.0, keeping the ionization constant of water fixed at  $pK_W = 13.740$  (Christenson and Schijf, 2011) and the acid dissociation constants,  $pK_{a1}$ , of DTPA at the values listed in **Table 3**. Total metal concentrations were fixed at values determined by ICP-MS. Three stability constants ( $\log \sup{M}\beta_{111}$ ,  $\log \sup{M}\beta_{110}$ , and  $\log \sup{H}\beta_{110}$ ), the total DTPA concentration, and the initial proton excess,  $[H^+]_T^0$ , were used as adjustable parameters. Values in bold type were fixed at the average of the preceding six titrations. All regressions converged in ≤7 iterations.

<sup>a</sup>Negative values signify an initial proton deficiency.

<sup>b</sup>Determined by non-linear regression.

<sup>c</sup>Number of titration points.

<sup>d</sup>Quality-of-fit parameter (Weighted Sum-Of-Squares per Degree-of-Freedom); values of 0.1–20 indicate a good fit (Herbelin and Westall, 1999).

**TABLE 5** | Nine titrations of calcium in 0.7 M NaClO<sub>4</sub> solutions containing 2.01 mM DTPA (gravimetric concentration).

[Ca] <sub>T</sub> /[DTPA] <sub>T</sub>	Titratant (M)	pH window	[H <sup>+</sup> ] <sub>T</sub> <sup>0</sup> (μM) <sup>a</sup>	log <sup>M</sup> β <sub>111</sub>	log <sup>M</sup> β <sub>110</sub>	log <sup>H</sup> β <sub>110</sub>	[DTPA] <sub>T</sub> (mM) <sup>b</sup>	n <sup>c</sup>	WSOS/DF <sup>d</sup>
1.65	1.0027 <sup>†</sup>	11.4–2.0	−90.8	5.368	9.057	−11.27	1.99	86	1.40
1.65	1.0027 <sup>†</sup>	11.4–2.0	−145	5.369	9.054	−11.28	2.01	86	1.36
2.48	1.0027 <sup>†</sup>	11.4–2.0	−161	5.390	9.045	−11.36	2.01	84	1.09
2.48	1.0027 <sup>†</sup>	11.4–2.0	−230	5.398	9.061	−11.37	1.99	84	1.14
3.31	1.0027 <sup>†</sup>	11.3–2.0	−212	5.381	9.032	−11.44	2.00	82	0.560
3.31	1.0027 <sup>†</sup>	11.3–2.0	−262	5.387	9.033	−11.40	2.01	83	0.798
0.83	0.1001	2.2–10.0	−36.5	5.407	9.063	<b>−11.35</b>	1.99	165	0.313
1.24	0.1001	2.2–10.0	−13.4	5.464	9.104	<b>−11.35</b>	1.97	176	0.248
1.65	0.1001	2.2–10.0	−74.4	5.458	9.099	<b>−11.35</b>	1.98	179	0.277

The final ionic strength was raised by ≤1% and lowered by <12% for titrations with 1 M HCl and 0.1 M NaOH, respectively. All regressions converged in ≤8 iterations. See **Table 4** for additional details.

<sup>a</sup>Negative values signify an initial proton deficiency.

<sup>b</sup>Determined by non-linear regression.

<sup>c</sup>Number of titration points.

<sup>d</sup>Quality-of-fit parameter (Weighted Sum-Of-Squares per Degree-of-Freedom); values of 0.1–20 indicate a good fit (Herbelin and Westall, 1999).

<sup>†</sup>HCl titrant.

consistent value of  $\log \sup{M}\beta_{111}$  for all nine titrations. In the third and final step, the value of  $\log \sup{M}\beta_{111}$  was fixed at the average obtained in the second step to yield a final, optimized value of  $\log \sup{M}\beta_{110}$ .

Studies of DTPA complexation with the REE and actinides are more plentiful in the literature, because of its importance in chemical purification (Baybarz, 1965; Grimes and Nash, 2014), medical diagnostics (Sherry et al., 1988), and the potential treatment of actinide toxicity in humans (Duffield et al., 1984), but most have been conducted at low ionic strength. In **Table 7** our results are compared with only three studies conducted in NaClO<sub>4</sub>, as well as with the widely cited study of Moeller and Thompson (1962), in KNO<sub>3</sub>. The results of Moeller and Thompson (1962) and Yin et al. (1987) at  $I = 0.1$  are identical, although the latter authors do not report a value for  $\log \sup{M}\beta_{111}$ . Our

value for  $\log \sup{M}\beta_{110}$  at  $I = 0.7$  M is in excellent agreement with the result of Gritmon et al. (1977) at  $I = 0.5$  M. Similar to the behavior of Mg and Ca (**Table 7**), but unlike REE complexes with DFOB (Christenson and Schijf, 2011), the value of  $\log \sup{M}\beta_{110}$  for Gd appears to decrease going from low to intermediate ionic strength. Moreover, its value appears to increase again going on to  $I = 2.0$  M. While this is generally consistent with a Debye-Hückel-type behavior (*cf.* **Figure 2**), it should be regarded as a preliminary finding in view of the scarcity of data. A slightly different trend is seen for  $\log \sup{M}\beta_{111}$ , which appears to decrease continuously from  $I = 0.1$  to 2.0 M, yet this observation is currently based on just two previously reported values (**Table 7**). Still, our value falls comfortably between these earlier results and, like  $\log \sup{M}\beta_{110}$ , somewhat closer to the value at  $I = 2.0$  M.



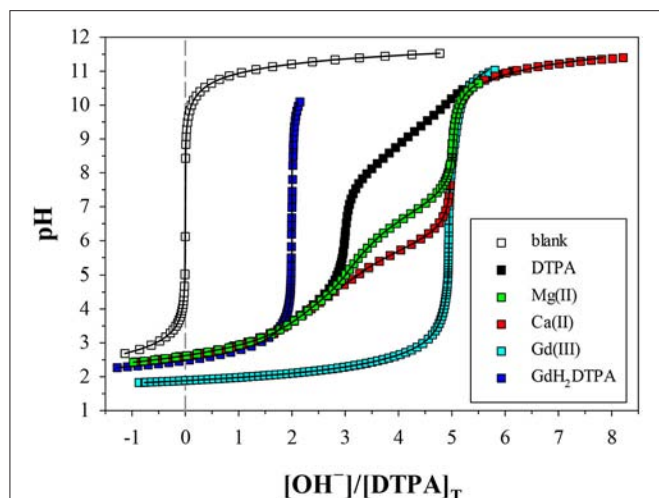


**FIGURE 3 |** Potentiometric titrations of DTPA and metal-DTPA solutions in 0.7 M NaClO<sub>4</sub>, where pH is plotted against moles of base (OH<sup>-</sup>) added per mole of DTPA. The more a metal titration deviates from that of DTPA alone, the higher the stability of the DTPA complexes formed. Symbols are measurements. Solid lines are non-linear regressions performed with FITEQL4.0. The blank consists of the acidified background electrolyte (0.7 M NaClO<sub>4</sub>/HClO<sub>4</sub>). All other solutions contain 2 mM DTPA, except the Gd titration (4 mM). The M:L ratios are 1.06 for Mg, 1 for GdH<sub>2</sub>DTPA, and 1.65 for Ca. The curve for the Gd titration, with an M:L ratio of 0.85, was scaled to overlap the Mg and Ca curves.

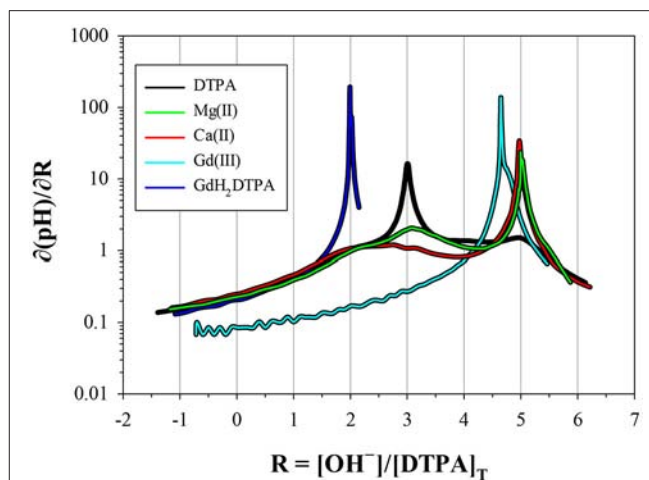


**FIGURE 4 |** Derivatives of the titration curves in **Figure 3**, taken with respect to the x-coordinate. Peaks indicate low buffer intensity. The DTPA curve has a prominent peak at  $R = 3$ , corresponding to the release of three protons at low pH, and fainter peaks at  $R = 2, 4$ , and  $5$ . The metal curves have a prominent peak at  $R = 5$ , indicating strong interaction with the fully deprotonated ligand. The fainter peak at  $R = 3$  for Mg is from a higher fraction of free ligand, resulting from the lower stability of its DTPA complexes. The Gd curve (not scaled) has an M:L ratio of 0.85; 15% is present as free DTPA and 85% as virtually inert Gd-DTPA complexes, yielding a peak at  $0.15 \times 3 + 0.85 \times 5 = 4.71$ . The GdH<sub>2</sub>DTPA compound has only two protons, producing a single peak at  $R = 2$ .

## SPECIATION MODELING OF THE MG-CA-GD-DTPA-H<sub>2</sub>O-CO<sub>2</sub> SYSTEM IN SEAWATER

### Calculation of the DTPA Side-Reaction Coefficient

Strong complexation of DTPA with Mg and Ca can have a significant effect on the stability of the Gd-DTPA complex in seawater, by effectively lowering the amount of available ligand. This is quantified by the side-reaction coefficient, as defined by Ringbom and Still (1972). The calculation of the side-reaction coefficient for polyprotic organic ligands is complicated by the fact that the free ligand may exist in multiple protonated forms. A side-reaction coefficient calculated relative to a particular protonated form is less meaningful if the metal does not form a strong complex with that form of the ligand, or if that form is a minor species in the system of interest. Schijf and Burns (2016) outlined the calculation of a more generic side-reaction coefficient,  $\alpha_f$ , that converts any thermodynamic stability constant to a conditional constant for a specific system, independent of what protonated forms of the ligand the metal binds to or relative to what form the stability constants are expressed. The coefficient is pH-dependent but does not affect the distribution of the ligand among its various protonated forms. Here, the side-reaction coefficient of DTPA in seawater is calculated using the same approach, as shown in **Table 8**.

The coefficient  $\alpha_f$  was calculated for seawater at  $S = 35.0$  and  $\text{pH} = 8.2$  (8.33 on the free proton scale). The concentrations of

Mg and Ca are 54.0 and 10.5 mM, respectively, of which about 89% is present as the free cation in each case (Schijf and Burns, 2016). A simple speciation model, using the acid dissociation constants in **Table 3**, reveals that, ignoring any complexation, only three forms of DTPA are relevant at this pH; about 56.5% is present as the single-protonated species, 39.6% as the double-protonated species, and 3.9% as the deprotonated species, while the other forms are negligible (**Figure 5A**). To demonstrate some of its behavior, the traditional side-reaction coefficient was calculated for each of these forms, although the coefficient  $\alpha_f$  is the same for all three (**Table 8**). To accurately account for the contribution of Mg and Ca to the DTPA speciation, all complexes were included, except for  $\text{MH}_3\text{L}^0$ , since its stability constant is quite small (Duffield et al., 1984) and  $\text{H}_3\text{L}^{2-}$  has very low abundance in seawater. In **Table 7**, values of the stability constants  $M\beta_{111}$ ,  $M\beta_{110}$ , and  $H\beta_{110}$  are presented that are appropriate for seawater. Values of  $M\beta_{112}$  and  $M\beta_{120}$  were reported by Duffield et al. (1984) in NaCl, but at lower ionic strength (**Table 7**). It was observed in section Stability Constants of Mg-DTPA and Ca-DTPA Complexes that our constants are offset from those of Duffield et al. (1984) by an average of 0.84 log units for Mg and 0.75 log units for Ca. Assuming this to be true for the other constants, we can estimate the values of  $M\beta_{112}$  and  $M\beta_{120}$  in seawater to be 1.55 and 11.21 for Ca, and 1.42 and 9.79 for Mg, respectively.

The results in **Table 8** show that the speciation of DTPA in seawater is entirely dominated by the  $\text{ML}^{3-}$  and  $\text{M}_2\text{L}^-$  complexes for both Mg and Ca, whereas the contribution of the

**TABLE 6** | Nine titrations of gadolinium in 0.7 M NaClO<sub>4</sub> solutions containing DTPA.

#	[DTPA] <sub>T</sub> (mM) <sup>a</sup>	[Gd] <sub>T</sub> /[DTPA] <sub>T</sub>	[H <sup>+</sup> ] <sub>T</sub> <sup>0</sup> (μM) <sup>b</sup>	log <sup>M</sup> β <sub>111</sub>	log <sup>M</sup> β <sub>110</sub>	[DTPA] <sub>T</sub> (mM) <sup>c</sup>	n <sup>d</sup>	WSOS/DF <sup>e</sup>
1	4.00	0.85	–192	13.17	<b>20.71</b>	3.81	106	0.0193
			–158	<b>13.24</b>	20.72	3.79		0.0549
2	4.00	0.85	–225	13.14	<b>20.71</b>	3.77	104	0.0352
			–217	<b>13.24</b>	20.77	3.77		0.0301
3	4.00	0.85	–546	13.09	<b>20.71</b>	3.83	114	0.225
			–526	<b>13.24</b>	20.79	3.81		0.260
4	4.00	0.46	–479	13.24	<b>20.71</b>	3.86	94	0.879
			–437	<b>13.24</b>	20.59	3.82		0.796
5	2.00	0.85	–359	13.27	<b>20.71</b>	1.89	86	0.115
			–343	<b>13.24</b>	20.63	1.87		0.0512
6	4.13	1 <sup>†</sup>	+185	13.24	<b>20.71</b>	–	94	0.150
			+188	<b>13.24</b>	20.71	–		0.151
7	2.06	1 <sup>†</sup>	–166	13.31	<b>20.71</b>	–	83	0.240
			–164	<b>13.24</b>	20.64	–		0.194
8	2.06 <sup>†</sup>	1 <sup>†</sup>	–172	13.41	<b>20.71</b>	–	103	1.48
			–174	<b>13.24</b>	20.58	–		1.56
9	2.06 <sup>†</sup>	1 <sup>†</sup>	–240	13.31	<b>20.71</b>	–	93	0.185
			–240	<b>13.24</b>	20.65	–		0.177

The pH window was 2–10, except for titration #3 (2–11). Titration with 0.9986 M NaOH caused the final ionic strength to be lowered by ≤1%. For each titration, the two lines represent the final two steps of a 3-step iterative regression, in which the values of <sup>M</sup>β<sub>110</sub> and <sup>M</sup>β<sub>111</sub>, respectively, were fixed at the average value determined in the preceding step (bold type). Neither parameter was fixed in the first step (not shown); see text for details. All regression steps converged in ≤5 iterations, except for titration #4 (≤16).

<sup>a</sup>Gravimetric concentration (except titration #6–9).

<sup>b</sup>Negative values signify an initial proton deficiency.

<sup>c</sup>Determined by non-linear regression.

<sup>d</sup>Number of titration points.

<sup>e</sup>Quality-of-fit parameter (Weighted Sum-of-Squares per Degree-of-Freedom); values of 0.1–20 indicate a good fit (Herbelin and Westall, 1999).

<sup>†</sup> DFOB was added as competing ligand (4.03 mM in #8 and 2.01 mM in #9).

<sup>\*</sup>Titration of GdH<sub>2</sub>DTPA; M:L ratio was assumed to be 1 and the DTPA concentration was fixed at the Gd concentration determined by ICP-MS.

MHL<sup>2–</sup> complex is comparatively small and that of the MH<sub>2</sub>L<sup>–</sup> and M(OH)L<sup>4–</sup> complexes negligible. The greater uncertainty in the values of <sup>M</sup>β<sub>112</sub> and <sup>H</sup>β<sub>110</sub> is therefore of minor importance. On the other hand, the high stability and abundance of the dinuclear complexes was not observed for DFOB (Schijf and Burns, 2016) and is somewhat surprising. The importance of the dinuclear complexes can be further stressed by pointing out that the value of the coefficient α<sub>f</sub> is lowered by 0.5 log units if they are omitted from the calculation (Table 8). This indicates that additional studies are warranted to determine a more accurate value for the stability constant <sup>M</sup>β<sub>120</sub> in seawater. Nonetheless, in either case, the value of α<sub>f</sub> (5.71 or 6.21) implies that the stability of DTPA complexes in seawater, including those with Gd, is about 6 orders of magnitude lower than in freshwater, due to substantial competition from abundant Mg and Ca. In the next section we will illustrate this effect by modeling the Gd speciation in seawater in the presence of DTPA, with and without Mg and Ca complexation, and also with and without the M<sub>2</sub>L<sup>–</sup> complexes.

Side-reaction coefficients for DFOB in seawater, calculated relative to different forms of the ligand, increase strongly with decreasing protonation (Schijf and Burns, 2016). This is because the abundance of free ligand species increase with their degree of protonation, whereas the stability of their complexes with Mg

and Ca is similar. For DTPA, the deprotonated form of the ligand is a minor species in seawater yet forms very stable complexes with Mg and Ca. The two protonated forms are much more abundant, but their complexes are less stable. The balance of these two effects causes their three side-reaction coefficients to be nearly equal in size, yet the coefficient α<sub>HL</sub>, corresponding to the single-protonated form of DTPA, is the smallest (Table 8).

## Implications for the Stability of Gd–DTPA Complexes in Seawater

Using the side-reaction coefficient α<sub>f</sub>, calculated in the previous section, we can now model the speciation of Gd and DTPA in a typical seawater sample. A recent survey of archived water samples from San Francisco Bay by Hatje et al. (2016) found that the sample from 2013, the most recent one analyzed, contained about 170 pM dissolved Gd, 110 pM of which was very strongly complexed and probably of anthropogenic origin. We will assume here that this fraction consists of Gd–DTPA. Some of the remaining 60 pM may also be from industrial sources but this fraction is present as reactive species, predominantly complexes with dissolved inorganic and less stable organic complexes (Schijf et al., 2015a). Speciation was calculated with MINEQL2.0 (Westall et al., 1986) for the same standard seawater referred to in the previous section. The sample of Hatje et al. (2016) had a

**TABLE 7** | Selected literature values of stability constants for DTPA complexes with Mg, Ca, and Gd in NaClO<sub>4</sub> solutions, unless otherwise specified.

	I (m)	T (°C)	log <sup>M</sup> β <sub>112</sub>	log <sup>M</sup> β <sub>111</sub>	log <sup>M</sup> β <sub>110</sub>	log <sup>H</sup> β <sub>110</sub>	log <sup>M</sup> β <sub>120</sub>	References
Mg	0.10 <sup>a</sup>	20.0	—	5.59	9.03	—	—	Durham and Ryskiewicz, 1958
	0.1 M <sup>b</sup>	25.0	—	5.72 <sup>¶</sup>	9.3	—	—	Wänninen, 1960
	0.150 M <sup>c</sup>	37	2.26 <sup>¶</sup>	5.85 <sup>¶</sup>	8.56 ± 0.016	—	10.63 ± 0.060	Duffield et al., 1984
	0.70 M	25.0	—	<b>5.03 ± 0.01</b>	<b>7.70 ± 0.02</b>	<b>−11.8 ± 0.2</b>	—	This work
Ca	0.10 <sup>a</sup>	20.0	—	6.17	10.63	—	—	Durham and Ryskiewicz, 1958
	0.1 <sup>d</sup>	20	—	6.42 ± 0.1	10.89 ± 0.1	—	12.87 <sup>¶</sup>	Anderegg et al., 1959
	0.1 <sup>b</sup>	25	—	6.43	10.74	—	12.34 <sup>¶</sup>	Chaberek et al., 1959
	0.1 M <sup>b</sup>	25.0	—	6.52 <sup>¶</sup>	10.6	—	12.6 <sup>¶</sup>	Wänninen, 1960
	0.1 <sup>e</sup>	—	—	5.91	10.58	—	12.22	Zakrzewski and Geisler, 1984
	0.150 M <sup>c</sup>	37	2.29 <sup>¶</sup>	6.13 <sup>¶</sup>	9.82 ± 0.008	—	11.95 ± 0.037	Duffield et al., 1984
	0.70 M	25.0	—	<b>5.40 ± 0.04</b>	<b>9.06 ± 0.03</b>	<b>−11.35 ± 0.07</b>	—	This work
Gd	0.1 <sup>b</sup>	25	—	14.42 <sup>¶</sup>	22.46 ± 0.07	—	—	Moeller and Thompson, 1962
	0.10 M	25.0	—	—	22.46	—	—	Yin et al., 1987
	0.50 M	25.0	—	—	20.73 ± 0.06	—	—	Gritmon et al., 1977
	0.70 M	25.0	—	<b>13.24 ± 0.10</b>	<b>20.68 ± 0.07</b>	—	—	This work
	2.0 M	25.0	—	12.88 <sup>¶</sup>	21.15 ± 0.02	—	—	Grimes and Nash, 2014

Results from the present work are shown in bold type. <sup>¶</sup>Calculated from stepwise stability constants or from acid dissociation constants of the metal complex.

<sup>a</sup>KCl.

<sup>b</sup>KNO<sub>3</sub>.

<sup>c</sup>NaCl.

<sup>d</sup>KCl or NaNO<sub>3</sub> (not specified).

<sup>e</sup>Medium and temperature not reported.

salinity of 28.2, which would lower the side-reaction coefficient as a result of diminished contributions from DTPA complexes with Mg and Ca. However, San Francisco Bay water will eventually enter the open ocean and it is furthermore preferable to keep this exercise consistent with our prior work (Schijf et al., 2015a,b; Schijf and Burns, 2016).

First, the speciation of Gd and DTPA was modeled without any competition from Mg and Ca. All (de)protonated forms of DTPA were included, as well as both Gd-DTPA complexes, using the acid dissociation constants from Table 3 and the stability constants from Table 7. The result is shown in Figure 5B. Since Gd is present in excess, 100% of DTPA is complexed with Gd in the fully deprotonated complex, despite the fact that its stability constant is nearly 2 orders of magnitude lower at the ionic strength of seawater. The contribution of the single-protonated complex is negligible. The reactive Gd fraction displays the usual speciation in standard seawater (Schijf et al., 2015a), dominated by carbonate complexes, where the Gd(CO<sub>3</sub>)<sub>2</sub><sup>−</sup> species makes up nearly 70% and the GdCO<sub>3</sub><sup>+</sup> species nearly 30% of the total. The remaining few percent consist of other Gd species, mainly free and hydrolyzed cations and the sulfate complex. The fraction of Gd-DTPA is essentially unchanged from what Hatje et al. (2016) found based on an interpolation of the shale-normalized pattern to estimate the Gd background concentration, Gd\*.

Next, competition from mononuclear complexes with Mg and Ca was included. As explained by Schijf and Burns (2016), these do not have to be explicitly added to the speciation model. Instead, log α<sub>f</sub> = 5.71 (Table 8) is subtracted from the stability

constants of the two Gd-DTPA complexes, resulting in values of 14.97 and 7.53 for log <sup>M</sup>β<sub>110</sub> and log <sup>M</sup>β<sub>111</sub>, respectively (Table 7). The values of the pK<sub>ai</sub> stay the same. As shown in Figure 5C, only 93.4% of DTPA is now complexed with Gd, meaning that nearly 7% has dissociated due to competition from Mg and Ca. The rest consists almost entirely of fully deprotonated Mg-DTPA and Ca-DTPA complexes.

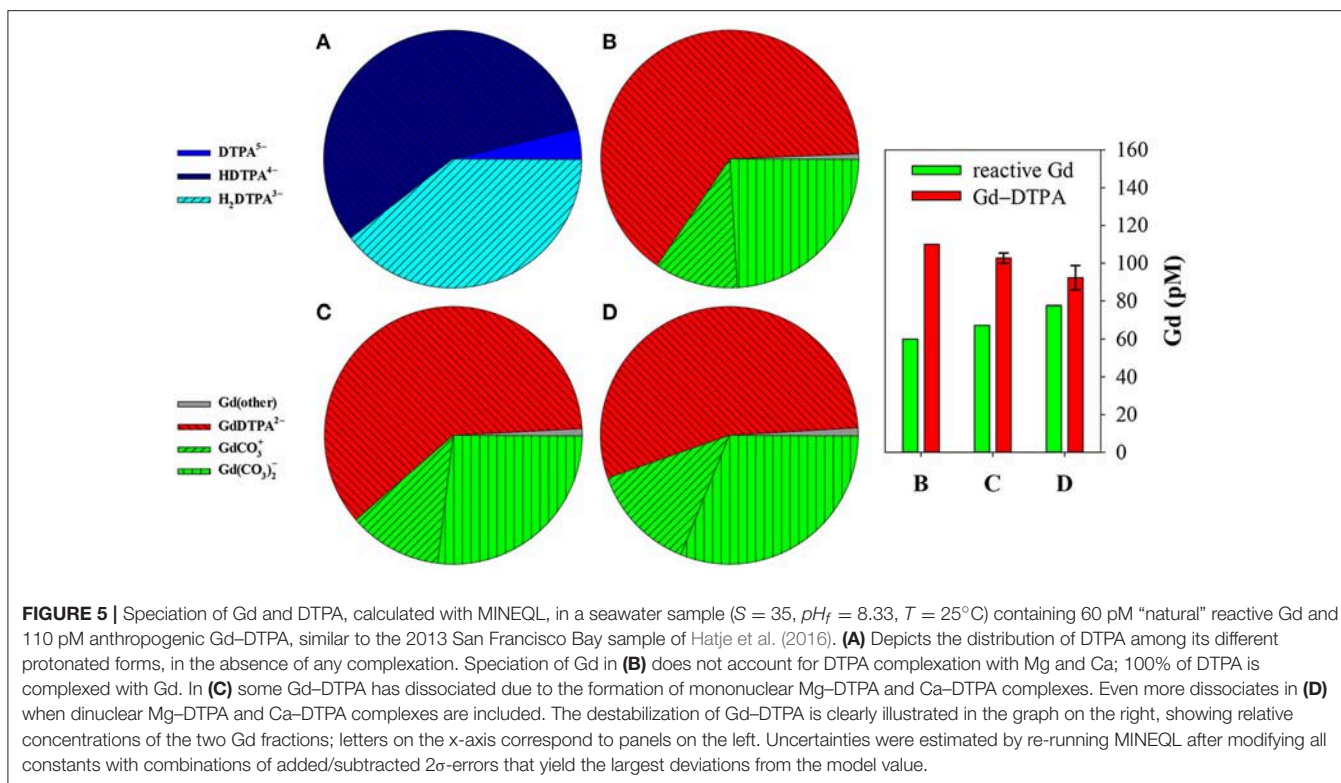
Finally, the last calculation was repeated with the inclusion of dinuclear Mg-DTPA and Ca-DTPA complexes. This was done by subtracting log α<sub>f</sub> = 6.21 (Table 8) from the stability constants of the two Gd-DTPA complexes, resulting in values of 14.47 and 7.03 for log <sup>M</sup>β<sub>110</sub> and log <sup>M</sup>β<sub>111</sub>, respectively (Table 7). The contribution of Mg and Ca complexes to the DTPA speciation increases to about 16% (Figure 5D), causing an additional 9% of the Gd-DTPA complex to dissociate. The graph on the right in Figure 5 shows the effect on the anthropogenic and reactive Gd fractions in terms of their relative concentrations. Specifically, the concentration of the reactive fraction increases from 60 to 78 pM, a gain of 30%.

Estuarine scavenging of reactive Gd resulting from salt-induced coagulation of organic colloids is strongest at salinities < 5 (Elderfield et al., 1990). Although Gd-DTPA is expected to progressively destabilize with increasing Mg and Ca concentration i.e., with increasing salinity, each DTPA complex has a unique, non-linear dependence on ionic strength that is as yet poorly constrained (Figure 2) and affects Gd speciation in a non-obvious manner (Table 8 and Figure 5), making it hard to predict where along the salinity gradient most

**TABLE 8** | Calculation of the side-reaction coefficient in seawater for the three most abundant (de)protonated forms of DTPA, using data from **Tables 3, 7**.

Species [X]	Equation for $\alpha_L$	$\alpha_L = \frac{[X]}{[L^{5-}]}$	$\alpha_{HL} = \frac{[X]}{[HL^{4-}]^a}$	$\alpha_{H2L} = \frac{[X]}{[H_2L^{3-}]^b}$
[H <sub>5</sub> L]	$[H^+]^5 / (K_{a1} \times K_{a2} \times K_{a3} \times K_{a4} \times K_{a5})$	$1.41 \times 10^{-15}$	$9.77 \times 10^{-17}$	$1.38 \times 10^{-16}$
[H <sub>4</sub> L <sup>-</sup> ]	$[H^+]^4 / (K_{a2} \times K_{a3} \times K_{a4} \times K_{a5})$	$1.29 \times 10^{-9}$	$8.91 \times 10^{-11}$	$1.26 \times 10^{-10}$
[H <sub>3</sub> L <sup>2-</sup> ]	$[H^+]^3 / (K_{a3} \times K_{a4} \times K_{a5})$	0.000692	0.0000479	0.0000676
[H <sub>2</sub> L <sup>3-</sup> ]	$[H^+]^2 / (K_{a4} \times K_{a5})$	10.2	0.708	1
[HL <sup>4-</sup> ]	$[H^+] / K_{a5}$	14.5	1	1.41
[L <sup>5-</sup> ]	Per definition	1	0.0692	0.0977
[CaH <sub>2</sub> L <sup>-</sup> ]	$(\beta_{112} \times [Ca^{2+}] \times [H^+]^2) / (K_{a4} \times K_{a5})$	3.34	0.231	0.326
[CaHL <sup>2-</sup> ]	$(\beta_{111} \times [Ca^{2+}] \times [H^+]) / K_{a5}$	33,739	2,334	3,297
[CaL <sup>3-</sup> ]	$\beta_{110} \times [Ca^{2+}]$	$1.07 \times 10^7$	738,130	1,042,636
[Ca(OH)L <sup>4-</sup> ]	$(\beta_{110} \times \beta_{110} \times [Ca^{2+}] \times [H^+]) / [H^+]$	10,189	705	996
[Ca <sub>2</sub> L <sup>-</sup> ]	$\beta_{120} \times [Ca^{2+}]^2$	$1.38 \times 10^7$	957,779	1,352,898
[MgH <sub>2</sub> L <sup>-</sup> ]	$(\beta_{112} \times [Mg^{2+}] \times [H^+]^2) / (K_{a4} \times K_{a5})$	13.0	0.896	1.27
[MgHL <sup>2-</sup> ]	$(\beta_{111} \times [Mg^{2+}] \times [H^+]) / K_{a5}$	74,520	5,156	7,282
[MgL <sup>3-</sup> ]	$\beta_{110} \times [Mg^{2+}]$	2,411,412	166,829	235,652
[Mg(OH)L <sup>4-</sup> ]	$(\beta_{110} \times \beta_{110} \times [Mg^{2+}] \times [H^+]) / [H^+]$	817	56.5	79.8
[Mg <sub>2</sub> L <sup>-</sup> ]	$\beta_{120} \times [Mg^{2+}]^2$	$1.43 \times 10^7$	987,513	1,394,900
	$\Sigma \alpha_{(H)} iL$	$4.13 \times 10^7$	2,858,504	4,037,745
	$\log \Sigma \alpha_{(H)} iL$	<b>7.62</b>	<b>6.46</b>	<b>6.61</b>
With M <sub>2</sub> L <sup>-</sup>	$\alpha_f = L_T / \Sigma [H_i L^{i-5}]$	1,608,452	1,608,452	1,608,452
	$\log \alpha_f$	<b>6.21</b>	<b>6.21</b>	<b>6.21</b>
Without M <sub>2</sub> L <sup>-</sup>	$\alpha_f = L_T / \Sigma [H_i L^{i-5}]$	513,856	513,856	513,856
	$\log \alpha_f$	<b>5.71</b>	<b>5.71</b>	<b>5.71</b>

See text for details.

<sup>a</sup>  $\alpha_{HL} = \alpha_L \times K_{a5} / [H^+]$ .<sup>b</sup>  $\alpha_{H2L} = \alpha_{HL} \times K_{a4} / [H^+]$ .



of the decomposition takes place. It is possible that a significant amount of reactive and potentially biotoxic Gd is released well beyond the low-salinity zone of most effective removal and thus reaches the ocean, where it will continue to be scavenged on settling particles (Schijf et al., 2015a). In coastal seas, which are characterized by high productivity, shallow waters, and high settling rates, a sizable fraction of these particles may be transferred to the sediment, thereby making anthropogenic Gd available to the benthic ecosystem.

It should be clear from our investigation that the Gd–DTPA complex, which is generally deemed chemically inert and conservative, can be substantially destabilized upon mixing of river water with seawater in estuaries. We found that, while the increase of ionic strength has a minor effect, as much as 15% of the complex can dissociate due to competition from Mg and Ca. This number should be considered a lower-bound estimate, because several processes that may further destabilize the complex were not considered here and should be the focus of future research: (1) transmetallation with other REE and strongly binding metals like Fe(III) and U, or competition from other strong organic ligands (Bundy et al., 2015) may displace Gd from the DTPA complex; (2) although DTPA complexes with  $\text{Na}^+$  were inherently accounted for in our experiments, significant differences in protonation constants measured in media containing potassium vs. tetramethylammonium ( $(\text{CH}_3)_4\text{N}^+$ ) salts imply that DTPA also forms fairly stable complexes with  $\text{K}^+$  (Anderegg, 1967); (3) as the released Gd is gradually removed by scavenging, the organically complexed fraction maintains thermodynamic equilibrium by continued dissociation; (4) competition for the DTPA ligand is due in large part to the formation of dinuclear Mg and Ca complexes. The stability constants of these complexes are not well known, but their values are difficult to measure under seawater conditions; and (5) Gd–DTPA is just one of nearly a dozen MRI contrast agents that may well possess a variety of properties and effective stabilities.

Dissociation of complexes like Gd–DTPA will also complicate the interpretation of normalized REE patterns in the coastal environment and the tracking of these anthropogenic and potentially toxic contaminants. Large anthropogenic Gd

anomalies may endure, but they will be partly comprised of released Gd that will merge with and behave like the geogenic background. It can then no longer be assumed that anthropogenic Gd anomalies solely represent the chemically inert complex, leaving its concentration uncertain. Although the released Gd is highly particle-reactive and should be quickly transferred to the particulate phase, it may eventually be remobilized by diagenetic processes and rejoin any remnant undissociated Gd complexes that are transported away from the estuary. In this regard, the ongoing development of advanced analytical techniques that can identify and quantify individual organic Gd species directly will be particularly beneficial (Künemeyer et al., 2009a).

## AUTHOR CONTRIBUTIONS

IC: performed some of the potentiometric titrations; JS: performed the majority of the potentiometric titrations, calculated acid dissociation constants, stability constants, and the side-reaction coefficient, conducted the speciation modeling, and wrote the manuscript.

## FUNDING

The REU project of IC was funded by NSF (OCE-1262374) and administered by the Maryland Sea Grant Program.

## ACKNOWLEDGMENTS

Our manuscript was significantly improved by constructive comments of the two reviewers. JS dedicates this work to the late Harry Elderfield, who was a kind and patient member of the examination committee for his Ph.D. defense at the University of Utrecht (The Netherlands) in 1992 and a most gracious host during an earlier visit to Harry's Cambridge laboratory and home. These experiments were partly inspired by the excellent past and present research of Michael Bau and Vanessa Hatje. We are grateful to all the editors of this Research Topic of Frontiers in Marine Science for allowing us to present our results. This is UMCES contribution #5481.

## REFERENCES

- Ahrland, S., Dahlgren, Å., and Persson, I. (1990). Stabilities and hydrolysis of some iron(III) and manganese(III) complexes with chelating ligands. *Acta Agric. Scand.* 40, 101–111.
- Anderegg, G. (1967). Komplexe XL. Die Protonierungskonstanten einiger Komplexe in verschiedenen wässrigen Salzmedien ( $\text{NaClO}_4$ ,  $(\text{CH}_3)_4\text{NCl}$ ,  $\text{KNO}_3$ ). *Helv. Chim. Acta* 50, 2333–2340.
- Anderegg, G., Nägeli, P., Müller, F., and Schwarzenbach, G. (1959). Komplexe XXX. Diäthylentriamin-pentaessigsäure (DTPA). *Helv. Chim. Acta* 42, 827–836.
- Baes, C. F. Jr., and Mesmer, R. E. (1981). The thermodynamics of cation hydrolysis. *Am. J. Sci.* 281, 935–962.
- Bau, M., and Dulski, P. (1996). Anthropogenic origin of positive gadolinium anomalies in river waters. *Earth Planet. Sci. Lett.* 143, 245–255.
- Bau, M., Knappe, A., and Dulski, P. (2006). Anthropogenic gadolinium as a micropollutant in river waters in Pennsylvania and in Lake Erie, northeastern United States. *Chem. Erde* 66, 143–152. doi: 10.1016/j.chemer.2006.01.002
- Baybarz, R. D. (1965). Dissociation constants of the transplutonium element chelates of diethylenetriaminepentaacetic acid (DTPA) and the application of DTPA chelates to solvent extraction separations of transplutonium elements from the lanthanide elements. *J. Inorg. Nucl. Chem.* 27, 1831–1839.
- Behra-Miellet, J., Briand, G., Kouach, M., Gressier, B., Cazin, M., and Cazin, J. C. (1998). On-line HPLC-electrospray ionization mass spectrometry: a pharmacological tool for identifying and studying the stability of  $\text{Gd}^{3+}$  complexes used as magnetic resonance imaging contrast agents. *Biomed. Chromatogr.* 12, 21–26.
- Binnemans, K., Jones, P. T., Blanpain, B., van Gerven, T., and Pontikes, Y. (2015). Towards zero-waste valorisation of rare-earth-containing

- industrial process residues: a critical review. *J. Cleaner Prod.* 99, 17–38. doi: 10.1016/j.jclepro.2015.02.089
- Birka, M., Roscher, J., Holtkamp, M., Sperling, M., and Karst, U. (2016). Investigating the stability of gadolinium based contrast agents towards UV radiation. *Water Res.* 91, 244–250. doi: 10.1016/j.watres.2016.01.012
- Brioschi, L., Steinmann, M., Lucot, E., Pierret, M. C., Stille, P., Prunier, J., et al. (2013). Transfer of rare earth elements (REE) from natural soil to plant systems: implications for the environmental availability of anthropogenic REE. *Plant Soil* 366, 143–163. doi: 10.1007/s11104-012-1407-0
- Bundy, R. M., Abdulla, H. A. N., Hatcher, P. G., Biller, D. V., Buck, K. N., and Barbeau, K. A. (2015). Iron-binding ligand and humic substances in the San Francisco Bay estuary and estuarine-influenced shelf regions of coastal California. *Mar. Chem.* 173, 183–194. doi: 10.1016/j.marchem.2014.11.005
- Chaberek, S., Frost, A. E., Doran, M. A., and Bicknell, N. J. (1959). Interaction of some divalent metal ions with diethylenetriaminepentaacetic acid. *J. Inorg. Nucl. Chem.* 11, 184–196.
- Chistoserdova, L. (2016). Lanthanides: new life metals? *World J. Microbiol. Biotechnol.* 32:138. doi: 10.1007/s11274-016-2088-2
- Christenson, E. A., and Schijf, J. (2011). Stability of YREE complexes with the trihydroxamate siderophore desferrioxamine B at seawater ionic strength. *Geochim. Cosmochim. Acta* 75, 7047–7062. doi: 10.1016/j.gca.2011.09.022
- Chua, H. (1998). Bio-accumulation of environmental residues of rare earth elements in aquatic flora *Eichhornia crassipes* (Mart.) Solms in Guangdong Province of China. *Sci. Total Environ.* 214, 79–85. doi: 10.1016/S0048-9697(98)00055-2
- d'Aquino, L., Morgana, M., Carboni, M. A., Staiano, M., Antisari, M. V., Re, M., et al. (2009). Effect of some rare earth elements on the growth and lanthanide accumulation in different *Trichoderma* strains. *Soil Biol. Biochem.* 41, 2406–2413. doi: 10.1016/j.soilbio.2009.08.012
- de Campos, F. F., and Enzweiler, J. (2016). Anthropogenic gadolinium anomalies and rare earth elements in the water of Atibaia River and Anhumas Creek, Southeast Brazil. *Environ. Monit. Assess.* 188, 1–18. doi: 10.1007/s10661-016-5282-7
- Du, X., and Graedel, T. E. (2011). Global in-use stocks of the rare earth elements: a first estimate. *Environ. Sci. Technol.* 45, 4096–4101. doi: 10.1021/es102836s
- Duffield, J. R., May, P. M., and Williams, D. R. (1984). Computer simulation of metal ion equilibria in biofluids. IV. Plutonium speciation in human blood plasma and chelation therapy using polyaminopolycarboxylic acids. *J. Inorg. Biochem.* 20, 199–214. doi: 10.1016/0162-0134(84)85019-9
- Durham, E. J., and Ryskiewicz, D. P. (1958). The acid dissociation constants of diethylenetriaminepentaacetic acid and the stability constants of some of its metal chelates. *J. Amer. Chem. Soc.* 80, 4812–4817.
- Elderfield, H., Upstill-Goddard, R., and Sholkovitz, E. R. (1990). The rare earth elements in rivers, estuaries, and coastal seas and their significance to the composition of ocean waters. *Geochim. Cosmochim. Acta* 54, 971–991.
- Fuganti, A., Möller, P., Morteani, G., and Dulski, P. (1996). Gadolinio ed altre terre rare usabili come traccianti per stabilire l'età, il movimento ed i rischi delle acque sotterranee: esempio dell'area di Trento. *Geol. Tecn. Ambient.* 4, 13–18.
- Fuma, S., Takeda, H., Miyamoto, K., Yanagisawa, K., Inoue, Y., Ishii, N., et al. (2001). Ecological evaluation of gadolinium toxicity compared with other heavy metals using an aquatic microcosm. *Bull. Environ. Contam. Toxicol.* 66, 231–238. doi: 10.1007/s001280000229
- Garcia-Solsona, E., Jeandel, C., Labatut, M., Lacan, F., Vance, D., Chavagnac, V., et al. (2014). Rare earth elements and Nd isotopes tracing water mass mixing and particle-seawater interactions in the SE Atlantic. *Geochim. Cosmochim. Acta* 125, 351–372. doi: 10.1016/j.gca.2013.10.009
- González, V., Vignati, D. A. L., Leyval, C., and Giamberini, L. (2014). Environmental fate and ecotoxicity of lanthanides: are they a uniform group beyond chemistry? *Environ. Intern.* 71, 148–157. doi: 10.1016/j.envint.2014.06.019
- González, V., Vignati, D. A. L., Pons, M.-N., Montarges-Pelletier, E., Bojic, C., and Giamberini, L. (2015). Lanthanide ecotoxicity: first attempt to measure environmental risk for aquatic organisms. *Environ. Pollut.* 199, 139–147. doi: 10.1016/j.envpol.2015.01.020
- Grimes, T. S., and Nash, K. L. (2014). Acid dissociation constants and rare earth stability constants for DTPA. *J. Solut. Chem.* 43, 298–313. doi: 10.1007/s10953-014-0139-6
- Gritmon, T. F., Goedken, M. P., and Choppin, G. R. (1977). The complexation of lanthanides by aminocarboxylate ligands—I. Stability constants. *J. Inorg. Nucl. Chem.* 39, 2021–2023.
- Harder, R., and Chaberek, S. (1959). The interaction of rare earth ions with diethylenetriaminepentaacetic acid. *J. Inorg. Nucl. Chem.* 11, 197–209.
- Harris, W. R., and Martell, A. E. (1976). Aqueous complexes of gallium(III). *Inorg. Chem.* 15, 713–720.
- Hatje, V., Bruland, K. W., and Flegel, A. R. (2016). Increases in anthropogenic gadolinium anomalies and rare earth element concentrations in San Francisco Bay over a 20 year record. *Environ. Sci. Technol.* 50, 4159–4168. doi: 10.1021/acs.est.5b04322
- Henderson, P. (1984). *Rare Earth Element Geochemistry*. Amsterdam: Elsevier.
- Herbelin, A. L., and Westall, J. C. (1999). *FITEQL. A Computer Program for Determination of Chemical Equilibrium Constants from Experimental Data*. Version 4.0. Corvallis, OR: Department of Chemistry, Oregon State University.
- Holzbecher, E., Knappe, A., and Pekdeger, A. (2005). Identification of degradation characteristics – exemplified by Gd-DTPA in a large experimental column. *Environ. Model. Assessm.* 10, 1–8. doi: 10.1007/s10666-004-4269-x
- Idée, J. M., Port, M., Raynal, I., Schaefer, M., Le Greneur, S., and Corot, C. (2006). Clinical and biological consequences of transmetallation induced by contrast agents for magnetic resonance imaging: a review. *Fund. Clin. Pharmacol.* 20, 563–576. doi: 10.1111/j.1472-8206.2006.00447.x
- Izatt, R. M., Izatt, S. R., Bruening, R. L., Izatt, N. E., and Moyer, B. A. (2014). Challenges to achievement of metal sustainability in our high-tech society. *Chem. Soc. Rev.* 43, 2451–2475. doi: 10.1039/C3CS60440C
- Janz, G. J., Oliver, B. G., Lakshminarayanan, G. R., and Mayer, G. E. (1970). Electrical conductance, diffusion, viscosity, and density of sodium nitrate, sodium perchlorate, and sodium thiocyanate in concentrated aqueous solutions. *J. Phys. Chem.* 74, 1285–1289.
- Kanazawa, Y., and Kamitani, M. (2006). Rare earth minerals and resources in the world. *J. Alloys Compd.* 408–412, 1339–1343. doi: 10.1016/j.jallcom.2005.04.033
- Kodama, M., Noda, T., and Murata, M. (1968). D.C. and A.C. polarographic behavior of thallium(I) ions in diethylenetriaminepentaacetate solutions. *Bull. Chem. Soc. Japan* 41, 354–358.
- Kragten, J., and Decnop-Weever, L. G. (1983). Solubility and protonation of EDTA, DCTA and DTPA in acidic perchlorate medium. *Talanta* 30, 623–625. doi: 10.1016/0039-9140(83)80145-3
- Kulaksız, S., and Bau, M. (2007). Contrasting behaviour of anthropogenic gadolinium and natural rare earth elements in estuaries and the gadolinium input into the North Sea. *Earth Planet. Sci. Lett.* 260, 361–371. doi: 10.1016/j.epsl.2007.06.016
- Kulaksız, S., and Bau, M. (2011a). Rare earth elements in the Rhine River, Germany: first case of anthropogenic lanthanum as a dissolved microcontaminant in the hydrosphere. *Environ. Intern.* 37, 973–979. doi: 10.1016/j.envint.2011.02.018
- Kulaksız, S., and Bau, M. (2011b). Anthropogenic gadolinium as a microcontaminant in tap water used as drinking water in urban areas and megacities. *Appl. Geochem.* 26, 1877–1885. doi: 10.1016/j.apgeochem.2011.06.011
- Kulaksız, S., and Bau, M. (2013). Anthropogenic dissolved and colloidal/nanoparticle-bound samarium, lanthanum and gadolinium in the Rhine River and the impending destruction of the natural rare earth element distribution in rivers. *Earth Planet. Sci. Lett.* 362, 43–50. doi: 10.1016/j.epsl.2012.11.033
- Kümmerer, K., and Helmers, E. (2000). Hospital effluents as a source of gadolinium in the aquatic environment. *Environ. Sci. Technol.* 34, 573–577. doi: 10.1021/es990633h
- Künemeyer, J., Terborg, L., Meermann, B., Brauckmann, C., Möller, I., Scheffer, A., et al. (2009a). Speciation analysis of gadolinium chelates in hospital effluents and wastewater treatment plant sewage by a novel HILIC/ICP-MS method. *Environ. Sci. Technol.* 43, 2884–2890. doi: 10.1021/es803278n
- Künemeyer, J., Terborg, L., Nowak, S., Telgmann, L., Tokmak, F., Krämer, B. K., et al. (2009b). Analysis of the contrast agent Magnevist and its transmetalation products in blood plasma by capillary electrophoresis/electrospray ionization time-of-flight mass spectrometry. *Anal. Chem.* 81, 3600–3607. doi: 10.1021/ac8027118

- Lawrence, M. G. (2010). Detection of anthropogenic gadolinium in the Brisbane River plume in Moreton Bay, Queensland, Australia. *Mar. Pollut. Bull.* 60, 1113–1116. doi: 10.1016/j.marpolbul.2010.03.027
- Lawrence, M. G., Ort, C., and Keller, J. (2009). Detection of anthropogenic gadolinium in treated wastewater in South East Queensland, Australia. *Water Res.* 43, 3534–3540. doi: 10.1016/j.watres.2009.04.033
- Letskman, P., and Martell, A. E. (1979). Nuclear magnetic resonance and potentiometric protonation study of polyaminopolyacetic acids containing from two to six nitrogen atoms. *Inorg. Chem.* 18, 1284–1289.
- Lide, D. R., and Haynes, W. M. (2009). *CRC Handbook of Chemistry and Physics*, 90th Edn. Boca Raton, FL: CRC Press.
- Lingott, J., Lindner, U., Telgmann, L., Esteban-Fernández, D., Jakubowski, N., and Panne, U. (2016). Gadolinium-uptake by aquatic and terrestrial organisms: distribution determined by laser ablation inductively coupled plasma mass spectrometry. *Environ. Sci. Proc. Imp.* 18, 200–207. doi: 10.1039/c5em00533g
- Martell, A. E., Smith, R. M., and Motekaitis, R. J. (2004). *NIST Critically Selected Stability Constants of Metal Complexes*. NIST Standard Reference Database 46 Version 8.0, Gaithersburg, MD.
- Matorina, N. N., Shepetyuk, L. V., and Chmutov, K. V. (1969). Thermodynamic functions of the sorption of ethylenediaminetetraacetate and diethylenetriaminepentaacetate by KU-2 cation-exchange resin. *Russ. J. Phys. Chem.* 43, 1175–1178.
- Merciny, E., Gatez, J. M., and Duyckaerts, G. (1978). Constantes de formation des complexes de stoechiométrie 1:1 et 1:2 ainsi que des complexes mixtes formes entre le plutonium(III) et divers acides aminopolyacétiques. *Anal. Chim. Acta* 100, 329–342.
- Mioduski, T. (1980). Protonation constants of 1-hydroxyethylidene-1,1-diphosphonic acid, diethylenetriamino-N,N,N',N''-penta-acetic acid, and trans-1,2-diaminocyclohexane-N,N,N',N'-tetra-acetic acid. *Talanta* 27, 299–303. doi: 10.1016/0039-9140(80)80062-2
- Moeller, T., and Thompson, L. C. (1962). Observations on the rare earths—LXXV. The stabilities of diethylenetriaminepentaacetic acid chelates. *J. Inorg. Nucl. Chem.* 24, 499–510.
- Möller, P., Dulski, P., Bau, M., Knappe, A., Pekdeger, A., and Sommer-von Jarmersted, C. (2000). Anthropogenic gadolinium as a conservative tracer in hydrology. *J. Geochem. Explor.* 69–70, 409–414. doi: 10.1016/S0375-6742(00)00083-2
- Möller, P., Morteani, G., and Dulski, P. (2003). Anomalous gadolinium, cerium, and yttrium contents in the Adige and Isarco river waters and in the water of their tributaries (provinces Trento and Bolzano/Bozen, NE Italy). *Acta Hydrochim. Hydrobiol.* 31, 225–239. doi: 10.1002/ahch.200300492
- Möller, P., Paces, T., Dulski, P., and Morteani, G. (2002). Anthropogenic Gd in surface water, drainage system, and the water supply of the city of Prague, Czech Republic. *Environ. Sci. Technol.* 36, 2387–2394. doi: 10.1021/es010235q
- Nanchaiah, Y. V., Mohan, S. V., and Lens, P. N. L. (2016). Biological and bioelectrochemical recovery of critical and scarce metals. *Trends Biotechnol.* 34, 137–154. doi: 10.1016/j.tibtech.2015.11.003
- Napoli, A. (1975). Studies on vanadyl complexes with aminopolycarboxylic acids. I. Vanadyl complexes with EGTA and DTPA. *Gazz. Chim. Ital.* 105, 1073–1081.
- Nozaki, T., and Koshiba, K. (1967). Ultraviolet spectrophotometric determination of the compositions and the stabilities of some aminopolycarboxylate complexes of bismuth(III). *Nippon Kagaku Zasshi* 88, 1287–1291.
- Nozaki, Y., Lerche, D., Alibo, D. S., and Tsutsumi, M. (2000). Dissolved indium and rare earth elements in three Japanese rivers and Tokyo Bay: evidence for anthropogenic Gd and In. *Geochim. Cosmochim. Acta* 64, 3975–3982. doi: 10.1016/S0016-7037(00)00472-5
- Ogata, T., and Terakado, Y. (2006). Rare earth element abundances in some seawaters and related river waters from the Osaka Bay area, Japan: significance of anthropogenic Gd. *Geochem. J.* 40, 463–474. doi: 10.2343/geochemj.40.463
- Olmez, I., Sholkovitz, E. R., Hermann, D., and Eganhouse, R. P. (1991). Rare earth elements in sediments off southern California: a new anthropogenic indicator. *Environ. Sci. Technol.* 25, 310–316. doi: 10.1021/es00014a015
- Port, M., Idée, J. M., Medina, C., Robic, C., Sabatou, M., and Corot, C. (2008). Efficiency, thermodynamic and kinetic stability of marketed gadolinium chelates and their possible clinical consequences: a critical review. *Biomaterials* 21, 469–490. doi: 10.1007/s10534-008-9135-x
- Rabiet, M., Brissaud, F., Seidel, J. L., Pistre, S., and Elbaz-Poulichet, F. (2009). Positive gadolinium anomalies in wastewater treatment plant effluents and aquatic environment in the Hérault watershed (South France). *Chemosphere* 75, 1057–1064. doi: 10.1016/j.chemosphere.2009.01.036
- Ringbom, A., and Still, E. (1972). The calculation and use of  $\alpha$  coefficients. *Anal. Chim. Acta* 59, 143–146.
- Rogosnitzky, M., and Branch, S. (2016). Gadolinium-based contrast agent toxicity: a review of known and proposed mechanisms. *Biomaterials* 29, 365–376. doi: 10.1007/s10534-016-9931-7
- Schijf, J., and Burns, S. M. (2016). Determination of the side-reaction coefficient of desferrioxamine B in trace-metal-free seawater. *Front. Mar. Sci.* 3:117. doi: 10.3389/fmars.2016.00117
- Schijf, J., Christenson, E. A., and Byrne, R. H. (2015a). YREE scavenging in seawater: a new look at an old model. *Mar. Chem.* 177, 460–471. doi: 10.1016/j.marchem.2015.06.010
- Schijf, J., Christenson, E. A., and Potter, K. J. (2015b). Different binding modes of Cu and Pb vs. Cd, Ni, and Zn with the trihydroxamate siderophore desferrioxamine B at seawater ionic strength. *Mar. Chem.* 173, 40–51. doi: 10.1016/j.marchem.2015.02.014
- Sherry, A. D., Cachier, W. P., and Kuan, K. T. (1988). Stability constants for  $Gd^{3+}$  binding to model DTPA-conjugates and DTPA-proteins: implications for their use as magnetic resonance contrast agents. *Magn. Reson. Medic.* 8, 180–190. doi: 10.1002/mrm.1910080208
- Shimada, H., Kubota, R., Funakoshi, T., and Kojima, S. (1995). Effects of lanthanum, terbium and ytterbium on the absorption of saccharides in the small intestine of mice. *Jpn. J. Toxicol. Environ. Health* 41, 35–41.
- Showstack, R. (2012). U.S. trade dispute with China over rare earth elements. *EOS Trans. AGU* 93, 134–135. doi: 10.1029/2012EO130002
- Taqi Khan, M. M., and Hussain, A. (1980). Aminopolycarboxylic acid complexes of Al(III), Ga(III), and In(III). *Indian J. Chem.* 19A, 50–57.
- Thakur, P., Mathur, J. N., Moore, R. C., and Choppin, G. R. (2007). Thermodynamics and dissociation constants of carboxylic acids at high ionic strength and temperature. *Inorg. Chim. Acta* 360, 3671–3680. doi: 10.1016/j.ica.2007.06.002
- Tian, G., and Rao, L. (2010). Effect of temperature on the protonation of the TALSPEAK ligands: lactic and diethylenetriaminopentaacetic acids. *Separ. Sci. Technol.* 45, 1718–1724. doi: 10.1080/01496395.2010.494712
- Vandegaer, J., Chaberek, S., and Frost, A. E. (1959). Iron chelates of diethylenetriaminepentaacetic acid. *J. Inorg. Nucl. Chem.* 11, 210–221.
- Verplanck, P. L., Furlong, E. T., Gray, J. L., Phillips, P. J., Wolf, R. E., and Esposito, K. (2010). Evaluating the behavior of gadolinium and other rare earth elements through large metropolitan sewage treatment plants. *Environ. Sci. Technol.* 44, 3876–3882. doi: 10.1021/es903888t
- Verplanck, P. L., Taylor, H. E., Nordstrom, D. K., and Barber, L. B. (2005). Aqueous stability of gadolinium in surface waters receiving sewage treatment plant effluent, Boulder Creek, Colorado. *Environ. Sci. Technol.* 39, 6924–6929. doi: 10.1021/es048456u
- Wänninen, E. (1960). Complexometric titrations with diethylenetriaminepentaacetic acid. *Acta Acad. Aboensis* 21, 1–110.
- Westall, J. C., Zachary, J. L., and Morel, F. M. M. (1986). *MINEQL. A Computer Program for the Calculation of the Chemical Equilibrium Composition of Aqueous Systems*. Version 1. Corvallis, OR: Department of Chemistry, Oregon State University.
- Xu, X., Zhu, W., Wang, Z., and Witkamp, G.-J. (2002). Distributions of rare earths and heavy metals in field-grown maize after application of rare earth-containing fertilizer. *Sci. Total Environ.* 293, 97–105. doi: 10.1016/S0048-9697(01)01150-0
- Yin, J., Jiang, B., Sun, T., and Sun, H. (1987). Determination of heats of coordination for rare-earth ions with aminopolycarboxylate ligands. *Wuji Huaxue Xuebao* 3, 69–77.

- Zakrzewski, A., and Geisler, J. (1984). Stałe trwałości kompleksów Ca i Sm z niektórymi fosfonowymi pochodnymi DTPA. *Chemia Analityczna* 29, 631–634.
- Zhang, H., He, X., Bai, W., Guo, X., Zhang, Z., Chai, Z., et al. (2010). Ecotoxicological assessment of lanthanum with *Caenorhabditis elegans* in liquid medium. *Metallomics* 2, 806–810. doi: 10.1039/c0mt00059k
- Zhang, S., and Shan, X. (2001). Speciation of rare earth elements in soil and accumulation by wheat with rare earth fertilizer application. *Environ. Pollut.* 112, 395–405. doi: 10.1016/S0269-7491(00)00143-3
- Zhu, Y., Hoshino, M., Yamada, H., Itoh, A., and Haraguchi, H. (2004). Gadolinium anomaly in the distributions of rare earth elements observed for coastal seawater and river waters around Nagoya City. *Bull. Chem. Soc. Japan* 77, 1835–1842. doi: 10.1246/bcsj.77.1835
- Conflict of Interest Statement:** The authors declare that the research was conducted in the absence of any commercial or financial relationships that could be construed as a potential conflict of interest.
- Copyright © 2018 Schijf and Christy. This is an open-access article distributed under the terms of the Creative Commons Attribution License (CC BY). The use, distribution or reproduction in other forums is permitted, provided the original author(s) and the copyright owner are credited and that the original publication in this journal is cited, in accordance with accepted academic practice. No use, distribution or reproduction is permitted which does not comply with these terms.





# TAG Plume: Revisiting the Hydrothermal Neodymium Contribution to Seawater

Torben Stichel<sup>1\*</sup>, Katharina Pahnke<sup>2</sup>, Brian Duggan<sup>3</sup>, Steven L. Goldstein<sup>4</sup>,  
Alison E. Hartman<sup>4</sup>, Ronja Paffrath<sup>2</sup> and Howie D. Scher<sup>3</sup>

<sup>1</sup> School of Ocean and Earth Sciences, University of Hawaii at Manoa, Honolulu, HI, United States, <sup>2</sup> Max Planck Research Group for Marine Isotope Geochemistry, Institute for Chemistry and Biology of the Marine Environment, University of Oldenburg, Oldenburg, Germany, <sup>3</sup> Department of Earth and Ocean Sciences, University of South Carolina, Columbia, SC, United States, <sup>4</sup> Lamont-Doherty Earth Observatory and Department of Earth and Environmental Sciences, Columbia University, Palisades, NY, United States

## OPEN ACCESS

### Edited by:

Johan Schijf,  
Chesapeake Biological Laboratory,  
United States

### Reviewed by:

Hiroshi Amakawa,  
Japan Agency for Marine-Earth  
Science and Technology, Japan  
Kazuyo Tachikawa,  
UMR7330 Centre Européen de  
Recherche et D'enseignement de  
Géosciences de L'environnement  
(CEREGE), France

### \*Correspondence:

Torben Stichel  
torben.stichel@awi.de

### † Present Address:

Torben Stichel,  
Alfred Wegener Institute, Helmholtz  
Centre for Polar and Marine Research,  
Bremerhaven, Germany

### Specialty section:

This article was submitted to  
Marine Biogeochemistry,  
a section of the journal  
Frontiers in Marine Science

**Received:** 15 December 2017

**Accepted:** 07 March 2018

**Published:** 23 March 2018

### Citation:

Stichel T, Pahnke K, Duggan B,  
Goldstein SL, Hartman AE, Paffrath R  
and Scher HD (2018) TAG Plume:  
Revisiting the Hydrothermal  
Neodymium Contribution to Seawater.  
Front. Mar. Sci. 5:96.  
doi: 10.3389/fmars.2018.00096

We present results on the distribution of  $\epsilon_{\text{Nd}}$  and  $[\text{Nd}]$  from the TAG hydrothermal vent field and adjacent locations collected during the GEOTRACES GA03 cruise in October 2011. Our results show that Nd isotopes directly below and above the plume do not significantly deviate from average NADW ( $\epsilon_{\text{Nd}} = -12.3 \pm 0.2$ ). Within the plume, however, isotope values are shifted slightly toward more radiogenic values up to  $\epsilon_{\text{Nd}} = -11.4$ . Interestingly at the same time a significant decrease in  $[\text{Nd}]$  along with rare earth element (REE) fractionation is observed, indicating enhanced scavenging within the plume despite the change in Nd isotopes. Elemental concentrations of Nd are reduced by 19.6–18.5 pmol/kg, coinciding with the maximum increase of mantle derived helium ( $x\text{s}^3\text{He}$ ) from 0.203 to 0.675 fmol/kg, resulting in an average 1.8 pmol/kg decrease in  $[\text{Nd}]$  relative to an expected linear increase with depth. The inventory loss of Nd within the plume sums up to 614 nmoles/m<sup>2</sup>, or 6%, if a continuous increase of  $[\text{Nd}]$  with depth is assumed. Compared to BATS and the western adjacent station USGT11-14, the local inventory loss is even higher at 10%. The tight relationship of  $x\text{s}^3\text{He}$  increase and  $[\text{Nd}]$  decrease allows us to estimate scavenging rates at TAG suggesting 40 mol/year are removed within the TAG plume. A global estimate using power output along ocean ridges yields an annual Nd removal of  $3.44 \times 10^6$  mol/year, which is about 71% of riverine and dust flux combined or 6–8% of the estimated global flux of Nd into the ocean. The change in Nd isotopic composition of up to 0.7 more radiogenic  $\epsilon_{\text{Nd}}$  values suggests an exchange process between hydrothermally derived particles and seawater in which during the removal process an estimated 1.1 mol/year of hydrothermal Nd is contributed to the seawater at the TAG site. This estimate is only 0.1% of the global Nd signal added to the ocean by boundary exchange processes at ocean margins, limiting the ability of changing the Nd isotopic composition on a global scale in contrast to the more significant estimated sink of elemental Nd in hydrothermal plumes from this study.

**Keywords:** neodymium isotopic compositions, GEOTRACES, hydrothermal plume, rare earth elements, seawater, TAG

## INTRODUCTION

The isotopic composition of the rare earth elements (REE) neodymium (Nd), expressed in  $\epsilon_{\text{Nd}} = \{(^{143}\text{Nd}/^{144}\text{Nd})_{\text{sample}} / (^{143}\text{Nd}/^{144}\text{Nd})_{\text{CHUR}} - 1\} \times 10^4$ , with CHUR = 0.512638 (Jacobsen and Wasserburg, 1980), has been widely used as water mass tracer for modern and paleo ocean circulation patterns (Piepgras and Wasserburg, 1982; Goldstein and Hemming, 2003; Piotrowski et al., 2004; Pena and Goldstein, 2014). Despite continued investigation, the sources and sinks in the Nd cycle are complicated to quantify: Rivers and dust input only contribute a relatively small amount of Nd into the ocean and influence mostly the upper mixed layer with  $\sim 4.3 \times 10^6$  moles/year (Goldstein and Jacobsen, 1987; Tachikawa et al., 1999, 2003; Arsouze et al., 2009; Rempfer et al., 2011), an additional “missing flux” of  $3.8$  to  $5.5 \times 10^7$  mol/year (Tachikawa et al., 2003; Rempfer et al., 2011) is needed to yield an oceanic residence time short enough to explain the heterogeneous distribution of  $\epsilon_{\text{Nd}}$  in seawater (Goldstein and Hemming, 2003; Tachikawa et al., 2003; Arsouze et al., 2009). The missing flux has been identified as an exchange process, which enables decoupling of Nd isotope composition from Nd concentration (Lacan and Jeandel, 2005; Arsouze et al., 2007, 2009). Recently, the role of ocean margins has received particular attention, as they are a principle player in the global marine cycle of trace elements and their isotopes (TEI) (Lacan and Jeandel, 2001; Jeandel and Oelkers, 2015; Rousseau et al., 2015). From these and other studies, it arose that shelf sediments are a key source and sink of TEI. A more complex source-sink interplay has been invoked for hydrothermal activity and their associated plume dispersion in the deep ocean. While for iron (Fe) (Klunder et al., 2011; Conway and John, 2014; Resing et al., 2015) or manganese (Mn) (Middag et al., 2010; Hattal et al., 2015), hydrothermal activities are an important source, REE are scavenged when hydrothermal fluid mixes with seawater (Klinkhammer et al., 1983; German et al., 1991; Elderfield and Schultz, 1996). In addition, a potential influence of hydrothermal activity on the marine Nd isotopic composition has not been documented yet. One of the most recent studies in the Southeast Pacific Ocean has already suggested that the deep water Nd isotopic composition is influenced by hydrothermal activity (Jeandel et al., 2013). These authors observed an  $\epsilon_{\text{Nd}}$  increase from  $-6$  in the Southeastern Pacific, typical for water masses of Southern Ocean origin (Carter et al., 2012; Grasse et al., 2012; Stichel et al., 2012; Basak et al., 2015), to  $-3.7$ , which was interpreted as potential influence from the East Pacific Rise. However, REE patterns did not show any difference from the other samples in that profile. The scarcity of available combined REE and  $\epsilon_{\text{Nd}}$  data from hydrothermal plumes has so far limited the study of the impact of hydrothermal activity in geochemical models to the Nd cycle, whereas such systems were not included in previous modeling studies of the global seawater  $\epsilon_{\text{Nd}}$  distribution (Jones et al., 2008; Siddall et al., 2008; Arsouze et al., 2009; Rempfer et al., 2011).

Here we present for the first time a coupled profile of REE concentrations and Nd isotopic composition within the Trans-Atlantic Geotraverse (TAG) hydrothermal plume, one of the most intensely studied hydrothermal sites. We will

compare the TAG profile with stations in the West Atlantic, such as the Bermuda Atlantic Time Series (BATS: USGT11-10 and Pahnke et al., 2012) and an adjacent station west of the vent field (USGT11-14) to determine changes in the Nd budget caused by hydrothermal plumes (Figure 1). The three profiles were sampled along the US-GEOTRACES North Atlantic Zonal Transect (NAZT). The TAG station and USGT11-14 are located within the North Atlantic Gyre between the Gulf Stream and North Atlantic Drift (NAD) in the north and the North Equatorial Current (NEC) in the south. Station BATS is located at the western edge of the North Atlantic Gyre, where the Deep Western Boundary Current (DWBC) transports North Atlantic Deep Water (NADW) to the south (Figure 1). The presence of the hydrothermal plume at TAG is indicated by a significant increase in primordial He ( $\delta^3\text{He}$ , Jenkins et al., 2015a). In this study, we will use this enrichment in  $\delta^3\text{He}$ , expressed in excess He ( $\text{xs}^3\text{He}$ ), to identify the extent of the plume, referring to all samples with this enrichment as “within the plume.”

## METHODS

Samples were collected during the second leg of the US-GEOTRACES GA03 North Atlantic Zonal Transect (NAZT) on the R/V Knorr (KN204-1). The TAG station was sampled Nov. 28 2011 with 11 consecutive CTD casts. Neodymium and other REE concentrations, Nd isotopes and He isotopes were measured from the same cast and bottles. Sample preparation for Nd and Nd isotopes is described in Stichel et al. (2015). Samples were collected in 10 L Niskin bottles mounted on a stainless steel CTD rosette (Conductivity, Temperature, Depth) with additional sensors for beam attenuation and fluorescence. Sub-samples of about 5 L were filtered through AcroPak500 (0.8/0.45  $\mu\text{m}$ ) filter cartridges into acid-cleaned pre-weighed LDPE collapsible containers and acidified to pH < 2 with 2 mL 6 M HCl (quartz distilled, for all mineral acids) per L seawater. In the home laboratory sub-samples were weighed and an enriched  $^{146}\text{Nd}$  spike was added gravimetrically to yield an optimum  $^{146}\text{Nd}/^{142}\text{Nd}$  close to 1. Sub-samples were pre-concentrated by adjusting the pH to  $\sim 3.5$  and successively pumping through C18 cartridges (waters, WAT051910) loaded with 350  $\mu\text{L}$  Bis(2-ethylhexyl) hydrogen phosphate (HDEHP, CAS:298-07-7) at 20 mL/min. Barium and remaining sea salts were eluted with 5 mL 0.01 M HCl and REEs were collected with 30 mL 6 M HCl. Prior to pre-concentration the loaded cartridges were cleaned with 2 mL 6 M HCl followed by a rinse with MilliQ water (18.2 M $\Omega\text{cm}$ ) until pH settled to 5. The eluted REE solution was dried down and 600  $\mu\text{L}$  aqua regia was added to oxidize organic compounds followed by an evaporation step. The residual was dried down again twice using 1 mL 1 M  $\text{HNO}_3$ . The final sample was taken up in 0.5 mL 1 M  $\text{HNO}_3$  and loaded onto a 100  $\mu\text{L}$  TRU-resin bed (Eichrom, 100–150  $\mu\text{m}$  bead size). Further elution of 5 resin volumes 1 M  $\text{HNO}_3$  removed Ca, Sr and remaining Ba. Light REE were collected with 4 resin volumes of 1 M HCl. Purification of Nd was achieved using Teflon distilled 0.2 M  $\alpha$ -hydroxyisobutyric acid ( $\alpha$ -HIBA) adjusted to a pH of 4.5 on  $\sim 700$   $\mu\text{L}$  of AG50W-X8 (200–400 mesh) resin. Procedural blanks (onboard

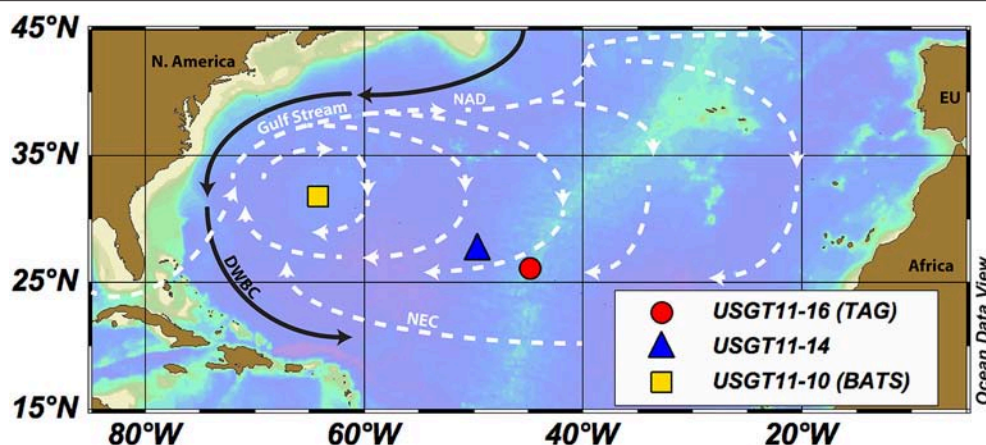


**FIGURE 1** | Study area with sampled locations USGT11-10 (BATS, yellow square), USGT11-14 (blue triangle), and USGT11-16 (TAG, red circle). Major currents of the North Atlantic Gyre are illustrated as surface currents in dashed white lines (Gulf Stream, North Atlantic Drift, NAD and North Equatorial Current, NEC) and the Deep Western Boundary Current (DWBC, black line). The figure is designed with ODV<sup>®</sup> software (Schlitzer, 2016a).

acidified MilliQ water) showed a negligible amount of Nd of <1.5% of the smallest sample size.

Isotopic composition of TAG was measured on a Thermal Ionization Mass Spectrometer (TIMS, VG-Sector) as  $\text{NdO}^+$  using 1  $\mu\text{L}$  silica gel as activator (see Stichel et al. (2015) for details) at University of Hawaii yielding an external error of  $\pm 0.2 \epsilon_{\text{Nd}}$ , 2SD with  $n = 29$ . Isotopic composition of USGT11-10 and USGT11-14 was measured using a Thermo Neptune-Plus Multi-Collector ICP-MS at Lamont-Doherty Earth Observatory (LDEO) and University of South Carolina (USC), respectively. At LDEO, a JNdi-1 Nd standard was measured before and after every sample and for three analysis periods yielded an average external error of  $\pm 0.3 \epsilon_{\text{Nd}}$ , 2SD, with  $n = 83$ . At USC, a JNdi-1 standard was measured every four samples with an aimed intensity of 2.5 V on  $^{145}\text{Nd}$ . The resulting average external error of  $^{143}\text{Nd}/^{144}\text{Nd}$  was  $\pm 0.4 \epsilon_{\text{Nd}}$ , 2SD,  $n = 53$ .

All three labs corrected for internal mass fractionation using  $^{146}\text{Nd}/^{144}\text{Nd} = 0.7219$  in an exponential mass fractionation law and their respective biases from the accepted value of  $^{143}\text{Nd}/^{144}\text{Nd} = 0.512115$  (Tanaka et al., 2000) for the JNdi-1 Nd standard.

Rare earth elements concentrations were measured at the University of Oldenburg using an offline seaFAST isotope dilution ICP-MS method described in Behrens et al. (2016). The method is intercalibrated with three other laboratories and agrees within analytical uncertainty with the intercalibration results from BATS (Pahnke et al., 2012; Behrens et al., 2016). The external reproducibility of the data presented here is <4% (RSD) except for La (5%) and Ce (8%).

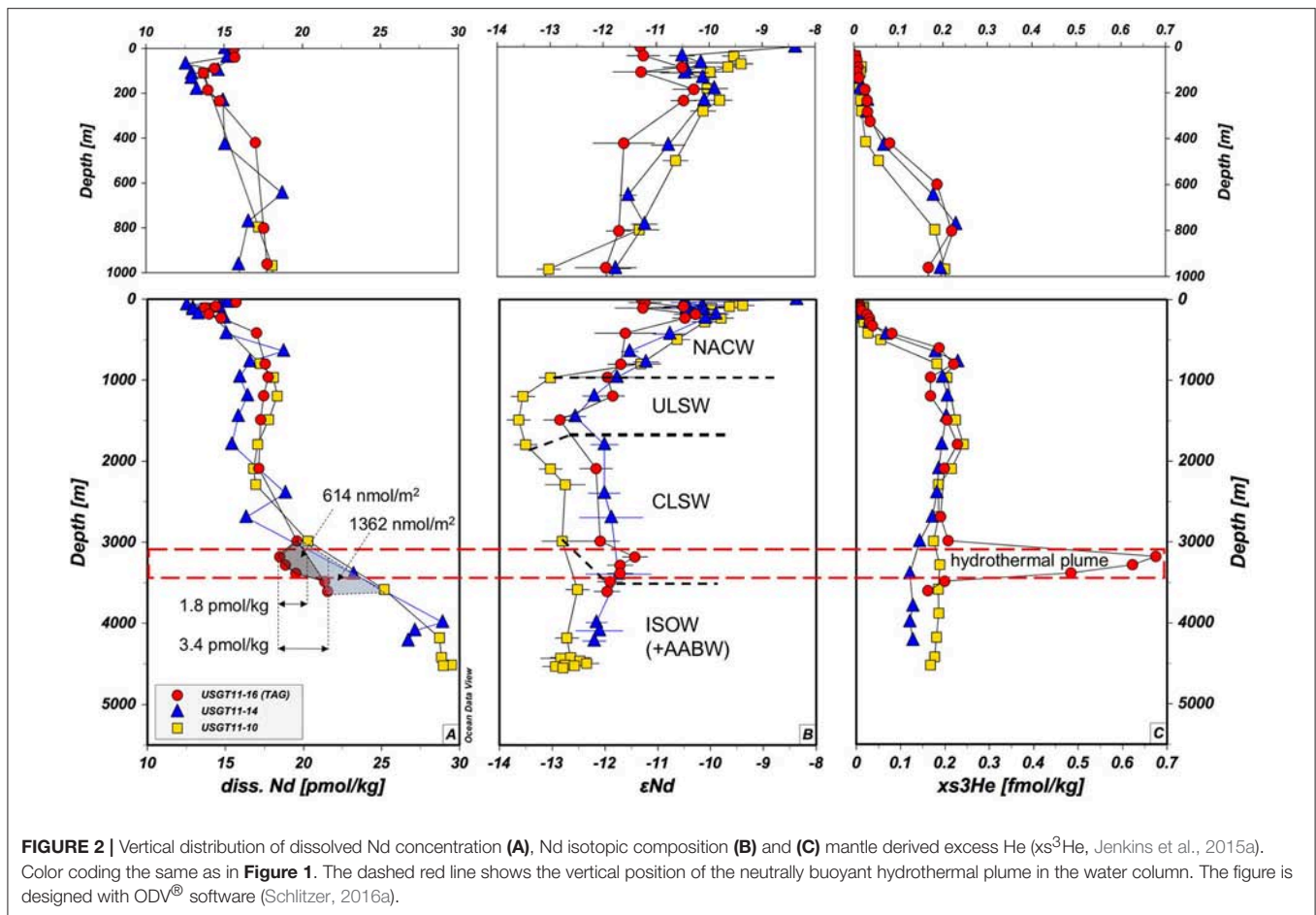
## RESULTS AND DISCUSSION

### Vertical and Lateral Distribution of Water Masses at TAG

With a few exceptions, the vertical distribution in **Figure 2** and **Table 1** of Nd concentrations [Nd] and isotopic compositions

( $\epsilon_{\text{Nd}}$ ) in the water column at TAG follows similar patterns as profiles in the West Atlantic (BATS and USGT11-14) and the East Atlantic (e.g., USGT10-05, Stichel et al., 2015 not shown). Surface [Nd] of 15.6 pmol/kg at TAG is slightly elevated and with an isotopic composition of  $\epsilon_{\text{Nd}} = -11.3 \pm 0.2$  less radiogenic compared to USGT11-14 (15.1 pmol/kg,  $\epsilon_{\text{Nd}} = -8.4 \pm 1.6$ ), BATS (14 pmol/kg,  $\epsilon_{\text{Nd}} = -9.5$  to  $-9.2$ , this study and Pahnke et al., 2012) and USGT10-05 (12.5 pmol/kg,  $\epsilon_{\text{Nd}} = -9.9$ , Stichel et al., 2015), which can be attributed to dust deposits from the extension of the Sahara dust plume (Mahowald et al., 2005). Within the surface layer at TAG, [Nd] decrease to a minimum at 111 m coinciding with the fluorometer potential maximum, suggesting scavenging within the mixed layer by biological productivity (**Figure 2**, **Table 1**). From this minimum in [Nd], an increase from 13.7 to 17.8 pmol/kg at 960 m is attributed to remineralization (Stichel et al., 2015; Lambelet et al., 2016). The sharpest increase in [Nd] is between 111 and 420 m (+3.3 pmol/kg). Within this depth range,  $\epsilon_{\text{Nd}}$  stays fairly constant with some fluctuations  $-10.9 \pm 1.3$  (2SD) and gradually decreases to less radiogenic values of  $\epsilon_{\text{Nd}} = -11.9$  at around 1,000 m marking the transition of North Atlantic Central Water (NACW) to NADW. At about 1,500 m, the presence of ~80% Upper Labrador Sea Water (ULSW, Jenkins et al., 2015b) corresponds to the least radiogenic isotope composition of  $\epsilon_{\text{Nd}} = -12.8$ . Within the Classical Labrador Seawater (CLSW), at 2,100 and 2,990 m, the isotopic composition is more radiogenic and constant at around  $-12.1 \pm 0.1$ . From 420 m, [Nd] is constant to 2,100 m and increases from  $17.5 \pm 0.5$  to 19.6 pmol/kg at 2,990 m. The typical increase below 2,000 m was documented in other studies in the Atlantic Ocean and most recently, based on high resolution profiles, has been attributed to a combination of increase from particle release and lateral advection of preformed REE along with reversible scavenging (Siddall et al., 2008; Stichel et al., 2015; Lambelet et al., 2016; Zheng et al., 2016). This increasing slope in [Nd] is interrupted by a sudden decrease at 3,184 m, coinciding with the upper





extent of the TAG hydrothermal plume (Jenkins et al., 2015a). [Nd] reaches a minimum of 18.48 pmol/kg within the plume, at the depth of maximum mantle derived excess helium ( $x\text{s}^3\text{He}$ , Jenkins et al., 2015a). Neodymium isotopes increase by +0.7 at this maximum of  $x\text{s}^3\text{He}$ . Below the plume, [Nd] and  $\epsilon_{\text{Nd}}$  settle back to values that would follow their respective trends above the plume. Using the average [Nd] of two sample depths and multiplying by the vertical distance between these samples, we can calculate the inventory of Nd in the water column by adding up the inventories of each depth interval. If the [Nd] profile followed a simplified but expected linear increase with depth from 2,000 m to the seafloor, the inventory at the plume depth should be 10,493 nmol/m<sup>2</sup>. The actual Nd inventory, however, is 9,879 nmol/m<sup>2</sup> due to the lower [Nd] at the TAG plume. The calculated deficit in the Nd inventory between 2,987 m and 3,487 m at TAG station therefore adds up to 614 nmol/m<sup>2</sup> or about 6% (Figure 2A). However, compared to stations USGT11-14 at 27.58°N 49.63°W and BATS (USGT11-10), the overall [Nd] at TAG is much lower. Using the [Nd] increase slope of these 2 stations as a reference, the Nd inventory is reduced by roughly 10% (1,362 nmol/m<sup>2</sup>) between 2,987 and 3,605 m from the BATS inventory of about 13,837 to 12,474 nmol/m<sup>2</sup> at this depth (Figure 2).

## TAG Hydrothermal Plume and Its Influence on REE Distribution

At the TAG site, other dissolved REE overall show a similar trend as [Nd] (Table 2). However, we observe some fractionation of light and heavy REE (LREE, HREE) within the water column. At about 110 m water depth, where [Nd] is at its lowest value (13.7 pmol/kg, Figure 2) the enrichment of PAAS (Taylor and McLennan, 1985) normalized HREE ( $\text{Tm} + \text{Yb} + \text{Lu}$ )<sub>N</sub> over LREE ( $\text{La} + \text{Pr} + \text{Nd}$ )<sub>N</sub> is at a maximum value of 5.29 (Figure 3), with N for normalization to Post Archaean Australian Shale (PAAS, Taylor and McLennan, 1985). It has been documented in earlier studies that LREE are preferentially scavenged onto particles in the upper water column over HREE (Elderfield and Greaves, 1982) and corroborates that scavenging on particles formed at the chl-max is the main driver of [Nd] decrease. Toward 960 m  $\text{HREE}_N/\text{LREE}_N$  continue their decreasing trend, suggesting release from particles as [Nd] increases in the water column. At the core of upper NADW (1,200 m), these ratios peak at 4.19 and only slightly change up to 4.62 in lower NADW (1,500–2,000 m). Within the TAG plume a preferential scavenging of LREE is observed again. This feature coincides with a strong increase in  $\text{Eu}/\text{Eu}^* = (2 \times \text{Eu}_N / \{\text{Sm}_N + \text{Gd}_N\})$  from 0.965 to 1.22, suggesting the presence of mantle derived Eu



**TABLE 1** | Vertical distribution of Nd isotopic composition and concentration, along with  $xs^3He$ ,  $\delta^3He$  and He concentrations of Jenkins et al. (2015a).

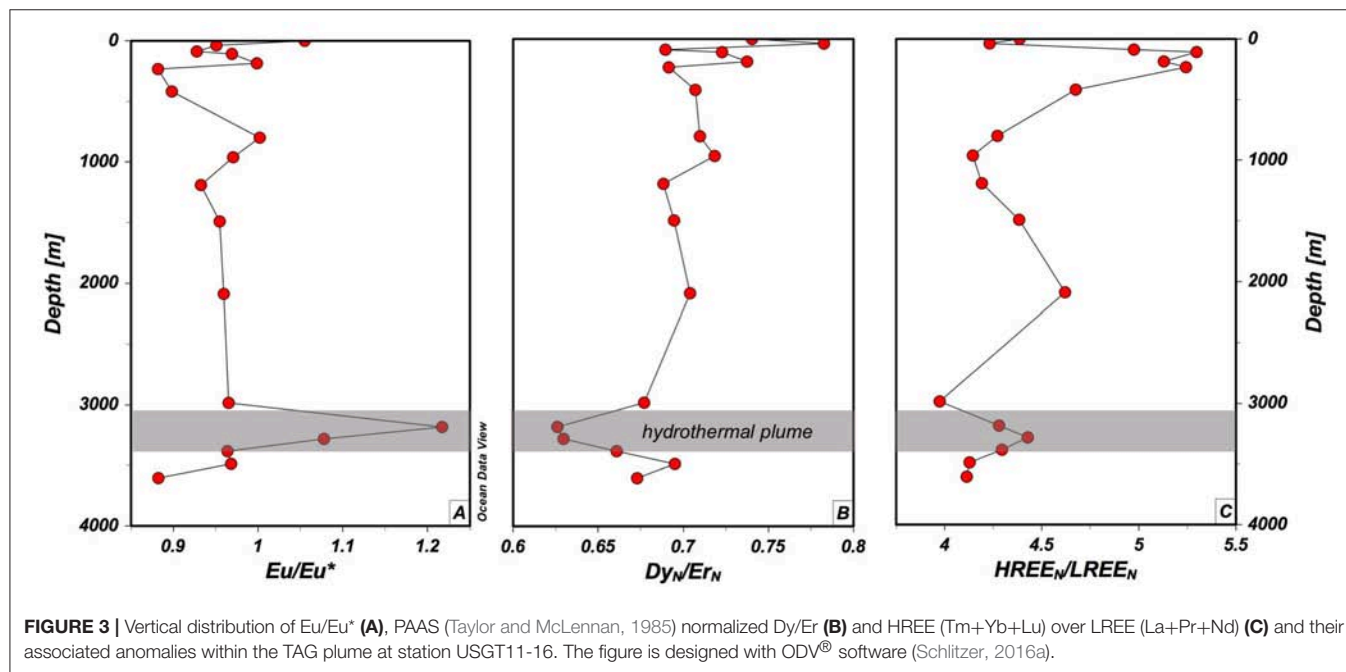
	Depth (m)	$^{143}Nd/^{144}Nd$	int. error (SEM)	$\epsilon_{Nd}^a$	ext. error (2SD)	[Nd] (pmol/kg)	$xs^3He^b$ (fmol/kg)	$\delta^3He^b$ (%)	[He] <sup>b</sup> (pmol/kg)
USGT11-16	3	0.512058	0.000006	-11.30	0.22	15.6			
26.136°N/44.826°W	40	0.512062	0.000008	-11.24	0.31	15.7	0.005	-1.43	1.68
Depth: 3,810 m	90	0.512099	0.000009	-10.51	0.36	14.4	0.010	-1.21	1.68
	111	0.512060	0.000014	-11.28	0.53	13.7	0.008	-1.31	1.69
	186	0.512111	0.000010	-10.28	0.40	14.0	0.025	-0.62	1.70
	235	0.512101	0.000005	-10.48	0.24	14.7	0.030	-0.43	1.70
	420	0.512043	0.000015	-11.61	0.58	17.0	0.081	1.62	1.74
	801	0.512038	0.000005	-11.70	0.24	17.5	0.220	7.26	1.76
	962	0.512026	0.000015	-11.95	0.58	17.7	0.168	5.02	1.78
	1,194	0.512030	0.000006	-11.85	0.22	17.4	0.168	5.01	1.78
	1,493	0.511979	0.000008	-12.85	0.31	17.3	0.205	6.54	1.77
	2,092	0.512014	0.000008	-12.17	0.31	17.1	0.199	6.23	1.79
	2,987	0.512018	0.000009	-12.09	0.36	19.6	0.207	6.35	1.83
	3,184	0.512052	0.000005	-11.43	0.24	18.5	0.675	24.4	1.86
	3,284	0.512038	0.000005	-11.71	0.24	18.8	0.623	22.5	1.85
	3,384	0.512038	0.000005	-11.71	0.24	19.5	0.484	16.8	1.88
	3,487	0.512028	0.000005	-11.90	0.24	21.4	0.200	6.09	1.83
	3,605	0.512025	0.000005	-11.96	0.24	21.6	0.162	4.66	1.80
USGT11-10	42	0.512149	0.000005	-9.53	0.22		0.004	-1.49	1.68
31.737°N/64.19°W	76	0.512157	0.000004	-9.39	0.22		0.001	-1.59	1.68
Depth: 4,527 m	89	0.512144	0.000005	-9.64	0.22		0.017	-0.94	1.72
	110	0.512126	0.000006	-9.98	0.38	13.7	0.015	-1.06	1.70
	182	0.512124	0.000005	-10.03	0.38		0.012	-1.20	1.70
	233	0.512136	0.000005	-9.80	0.24		0.016	-1.04	1.71
	281	0.512120	0.000004	-10.11	0.24		0.017	-0.98	1.72
	497	0.512093	0.000005	-10.63	0.24		0.055	0.60	1.71
	797	0.512058	0.000003	-11.32	0.38	17.2	0.182	5.71	1.76
	969	0.511970	0.000004	-13.03	0.22	18.1	0.205	6.56	1.77
	1,197	0.511943	0.000006	-13.55	0.22	18.3			
	1,493	0.511939	0.000003	-13.63	0.22	17.8	0.224	7.28	1.78
	1,794	0.511946	0.000005	-13.50	0.22	17.1	0.242	7.97	1.79
	2,094	0.511970	0.000004	-13.03	0.22	16.8	0.215	6.80	1.80
	2,289	0.511984	0.000005	-12.75	0.38	16.9	0.185	5.42	1.84
	2,990	0.511981	0.000004	-12.81	0.38	20.3	0.174	5.10	1.82
	3,584	0.511996	0.000004	-12.52	0.22	25.2	0.185	5.46	1.83
	4,179	0.511986	0.000003	-12.72	0.22	28.7	0.181	4.90	1.94
	4,419	0.511990	0.000003	-12.65	0.38	28.9	0.177	4.87	1.91
	4,431	0.511980	0.000003	-12.84	0.38				
	4,462	0.511998	0.000006	-12.48	0.24				
	4,493	0.512005	0.000005	-12.35	0.24				
	4,511	0.511984	0.000003	-12.76	0.24	29.5			
	4,523	0.511993	0.000004	-12.58	0.22	29.0	0.168	4.88	1.81
	4,531	0.511975	0.000004	-12.94	0.24				
	4,550	0.511982	0.000007	-12.79	0.24				
USGT11-14	1	0.512209	0.000041	-8.37	1.58	15.1			
27.583°N/49.633°W	40	0.512099	0.000006	-10.51	0.24	15.2	0.000	-1.62	1.68
Depth: 4,501 m	69	0.512118	0.000011	-10.15	0.42	12.5	0.002	-1.56	1.69
	99	0.512104	0.000004	-10.42	0.14	14.6	0.010	-1.26	1.70

(Continued)

TABLE 1 | Continued

Depth (m)	$^{143}\text{Nd}/^{144}\text{Nd}$	int. error (SEM)	$\epsilon_{\text{Nd}}^a$	ext. error (2SD)	[Nd] (pmol/kg)	$\text{xs}^3\text{He}^b$ (fmol/kg)	$\delta^3\text{He}^b$ (‰)	[He] <sup>b</sup> (pmol/kg)
114	0.512102	0.000012	-10.46	0.45	12.9	0.009	-1.28	1.70
134	0.512119	0.000007	-10.12	0.26	12.9	0.014	-1.09	1.71
184	0.512130	0.000006	-9.90	0.24	13.2	0.031	-0.38	1.71
234	0.512121	0.000005	-10.09	0.19	14.9	0.067	1.11	1.71
429	0.512086	0.000008	-10.77	0.32	15.1	0.179	5.67	1.74
647	0.512047	0.000004	-11.53	0.16	18.7	0.229	7.63	1.76
773	0.512063	0.000006	-11.22	0.24	16.6	0.195	6.19	1.76
965	0.512035	0.000007	-11.77	0.29	15.9	0.206	6.55	1.78
1,196	0.512013	0.000006	-12.20	0.22	16.4			
1,448	0.511994	0.000005	-12.56	0.2	15.8	0.203	6.50	1.77
1,794	0.512022	0.000007	-12.01	0.26	15.4	0.193	5.97	1.79
2,394	0.512022	0.000008	-12.01	0.3	18.8	0.182	5.46	1.81
2,696	0.512029	0.000016	-11.88	0.6	16.3	0.172	5.03	1.81
3,395	0.512036	0.000016	-11.74	0.62	23.2	0.121	2.99	1.81
3,990	0.512015	0.000005	-12.16	0.2	28.9	0.121	2.98	1.82
4,094	0.512018	0.000011	-12.10	0.44	27.2			
4,218	0.512013	0.000006	-12.20	0.22	26.7	0.128	3.28	1.81

<sup>a</sup> $\epsilon_{\text{Nd}} = \{R/\text{CHUR} - 1\} \times 10,000$ , with  $R = ^{143}\text{Nd}/^{144}\text{Nd}$  and  $\text{CHUR} = 0.512638$  (Jacobsen and Wasserburg, 1980). <sup>b</sup>Data from Jenkins et al. (2015a).



leached out of basaltic plagioclases, and a moderate decrease from 0.704 to 0.626 in the overall homogenous  $\text{Dy}_\text{N}/\text{Er}_\text{N}$  at the highest  $\text{xs}^3\text{He}$ , indicating the influence of hydrothermal activity on REE (Figure 3).

### Implications on the Global Nd Cycle

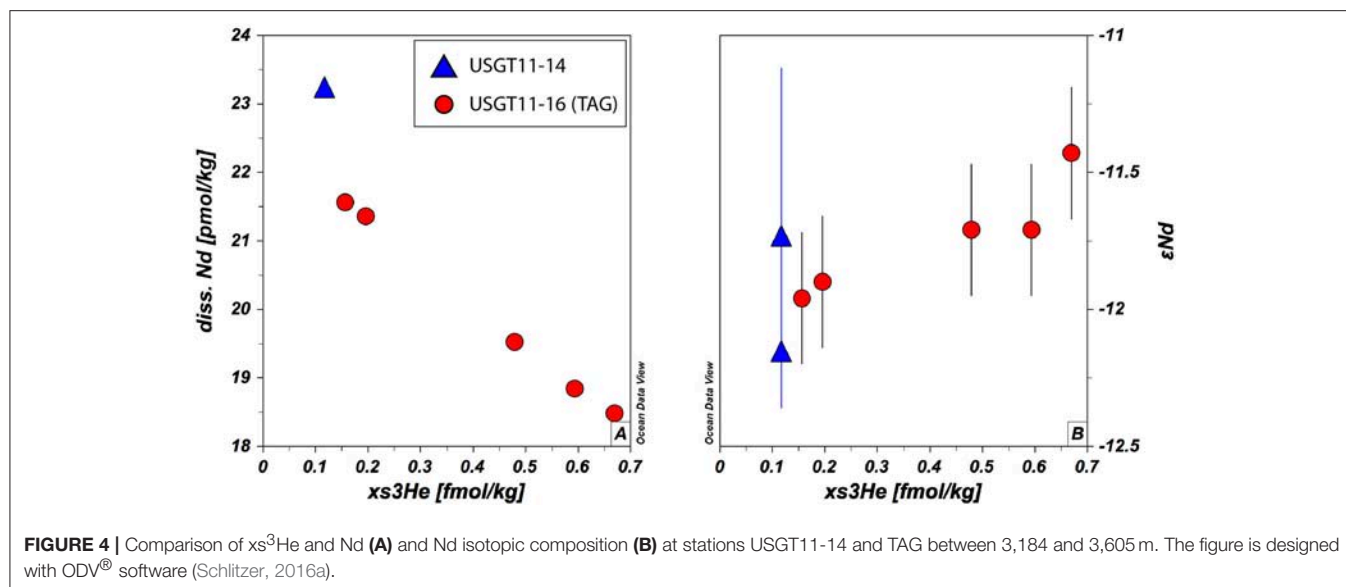
The significant depletion of [Nd] within the hydrothermal plume correlates well with  $\text{xs}^3\text{He}$  (Jenkins et al., 2015a), in that high excess He corresponds to low [Nd] and vice versa (Figure 4A).

The depletion of [Nd] within the TAG plume thus corroborates that hydrothermal activity is a net sink for Nd and other REE (German et al., 1990) and is attributed to the formation of ferrihydrite (Ohnemus and Lam, 2015) co-precipitating REE. With paired He and Nd data available from one hydrothermal plume for the first time, we revisit this scavenging by estimating the annual removal of Nd using an approach suggested in Jenkins et al. (2015a). If we assume a linear increase of Nd with depth below ~2,000 m such as observed at stations USGT11-10

**TABLE 2 |** REE concentrations and ratios at USGT11-16 (TAG).

Depth (m)	La	Ce	Pr	Nd	Sm	Eu	Gd (pmol/kg)	Tb	Dy	Ho	Er	Tm	Yb	Lu	$\frac{\text{Eu}}{\text{Eu}^*}$ $(2 \times \text{Eu}_N / (\text{Sm}_N + \text{Gd}_N))$	$\frac{\text{HREE}_N / \text{REE}_N}{(\text{Tm} + \text{Yb} + \text{Lu})_N / (\text{La} + \text{Pr} + \text{Nd})_N}$	$\text{Dy}_N / \text{Er}_N$
1	12.9	19.7	3.55	15.7	3.32	0.852	4.05	0.733	6.02	1.27	4.81	0.603	3.95	0.631	1.06	4.39	0.740
40	15.0	17.1	3.53	15.4	3.29	0.859	4.90	0.776	5.53	1.37	4.18	0.631	3.68	0.643	0.951	4.24	0.783
90	13.5	11.9	3.12	13.4	2.94	0.772	4.56	0.722	5.07	1.37	4.35	0.662	3.89	0.649	0.928	4.98	0.690
111	12.5	12.2	2.94	13.4	2.82	0.770	4.36	0.726	5.73	1.27	4.69	0.632	4.24	0.666	0.969	5.29	0.723
186	13.7	19.7	3.01	13.9	2.94	0.798	4.32	0.747	5.96	1.37	4.78	0.657	4.25	0.670	1.00	5.12	0.738
235	14.5	7.60	3.58	14.1	3.34	0.837	5.26	0.842	5.81	1.58	4.97	0.780	4.38	0.745	0.882	5.25	0.692
420	17.2	7.16	3.90	16.3	3.70	0.887	5.29	0.886	6.42	1.56	5.37	0.755	4.76	0.754	0.898	4.70	0.707
801	18.4	2.92	4.06	16.5	3.53	0.885	4.57	0.743	5.28	1.37	4.40	0.682	4.25	0.790	1.00	4.27	0.710
962	21.4	3.18	3.85	17.5	3.37	0.889	4.94	0.722	5.55	1.38	4.57	0.696	4.30	0.817	0.971	4.13	0.719
1,194	22.7	3.67	3.99	18.2	3.39	0.840	4.79	0.767	5.48	1.46	4.71	0.742	4.53	0.867	0.933	4.19	0.688
1,493	22.1	3.49	4.10	16.9	3.28	0.891	5.14	0.756	5.60	1.46	4.77	0.736	4.70	0.892	0.955	4.38	0.695
2,093	22.7	3.31	3.40	16.9	3.03	0.830	4.78	0.666	5.45	1.36	4.58	0.711	4.91	0.907	0.960	4.62	0.704
2,987	26.0	3.75	4.53	19.9	3.43	0.900	5.02	0.742	5.94	1.41	5.19	0.727	5.29	0.920	0.965	3.97	0.677
3,184	25.5	4.38	4.50	18.9	3.32	1.03	4.39	0.739	5.79	1.40	5.47	0.758	5.48	0.977	1.22	4.27	0.626
3,284	25.2	3.53	4.83	17.9	3.65	1.02	4.96	0.810	5.77	1.58	5.42	0.804	5.56	1.02	1.08	4.44	0.630
3,384	26.9	4.40	5.17	18.7	3.77	0.981	5.45	0.819	6.01	1.53	5.38	0.804	5.73	1.07	0.964	4.30	0.661
3,487	25.7	4.96	5.20	19.9	4.30	1.05	5.59	0.866	6.92	1.54	5.89	0.783	5.52	1.03	0.968	4.14	0.695
3,605	28.5	4.26	5.55	20.4	4.29	1.01	6.10	0.955	6.53	1.73	5.74	0.885	5.64	1.07	0.882	4.10	0.673

*N = normalized to PAAS (Taylor and McLennan, 1985).*



and -14, the minimum average deficit of Nd within the plume is about 1.8 pmol/kg by the shape of the profile of TAG station. Since [Nd] in the plume negatively correlate with  $xs^3\text{He}$ , we can make use of this relationship to estimate Nd scavenging rates based on He fluxes (Jenkins et al., 2015a). The net heat injection into the plume is  $\sim 100$  J/kg at the plume maximum, which is accompanied by an  $xs^3\text{He}$  anomaly of 0.73 fmol/kg yielding a He:heat ratio of  $\sim 7.3 \times 10^{-18}$  mol/J (Jenkins et al., 2015a). Applying this to Nd, we get a Nd:heat ratio  $-1.8 \times 10^{-14}$  mol/J. Jenkins et al. (2015a) have used the estimated power output at TAG of  $70 \times 10^6$  W (Goto et al., 2003) to compute  $^3\text{He}$  output (15 mmol/year), and based on the tight correlation of He and Nd, we derive a scavenging rate of  $\sim 40$  mol/year. This local removal of Nd is around 6 orders of magnitude smaller than the annual estimated Nd flux of  $3.8\text{--}5.5 \times 10^7$  mol/year (Tachikawa et al., 2003; Rempfer et al., 2011) into the ocean. We are aware that it is difficult and prone to high uncertainty to extrapolate from a single site to a global estimate. However, if we assume similar particle loads in other hydrothermal vent fields, and we extrapolate this He-Nd-heat relationship to a global estimate using a global heat flux of  $\sim 3.2 \times 10^{12}$  W along ocean ridges (Stein et al., 2013), the removal rate by hydrothermal activity sums up to  $\sim 1.8 \times 10^6$  mol/year. This is about the same as the estimated dust input of  $1.8 \times 10^6$  mol/year (Rempfer et al., 2011). Again, this is an estimate based on the data this study here provides and it does not take into account factors that could influence hydrothermal plume dispersion such as changing deep ocean currents or differences in ridge geometry. Nevertheless, we argue that the heat flux-He relationship is a valid approach, because the global  $^3\text{He}$  flux is only slightly higher than recently modeled global  $^3\text{He}$  fluxes of  $450 \pm 50$  mol/year (Schlitzer, 2016b) compared to 686 mol/year using the values reported in Jenkins et al. (2015a). Our estimate suggests that global hydrothermal activity removes as much Nd from the water column as Nd is released from dust. As mentioned earlier, this number is based on Nd deficit within the profile of the TAG

station. If we use the inventory deficit based on the increase of [Nd] with depth at USGT11-10 and -14, which show stronger [Nd] increase with depth, the Nd loss would be about 1.9 times higher, yielding  $\sim 3.4 \times 10^6$  mol/year, which is about 71% of riverine and dust flux combined (Goldstein and Jacobsen, 1987; Tachikawa et al., 1999, 2003; Arsouze et al., 2009; Rempfer et al., 2011) or 6–8% of the estimated total global flux (Tachikawa et al., 2003; Rempfer et al., 2011) of Nd into the ocean.

## Isotopic Exchange Processes

The [Nd] depletion is accompanied by a slight increase in  $\epsilon_{\text{Nd}}$  from  $-12.1 \pm 0.4$  above to  $-11.4 \pm 0.2$  (2SD) at the maximum of the plume (Figures 2, 4B and Table 1), suggesting an exchange of Nd isotopes between seawater and a hydrothermal source. While scavenging of REE within a hydrothermal plume by Fe-Mn oxide particles that form as hydrothermal fluids get in contact with oxic seawater has been suggested earlier (German et al., 1990), an isotopic influence on the water column by hydrothermal activity has, to our knowledge, not been documented before. Even though Nd is removed from the water column, the shift in isotopic composition toward more radiogenic values suggests an exchange process that releases radiogenic Nd into the water column to alter its isotopic composition locally. The peak excursion of  $\sim 0.7$   $\epsilon_{\text{Nd}}$  units coincides with the local minimum of [Nd] within the plume. We therefore use the above derived removal flux for Nd (40 mol/year) for a mass balance to calculate the extra Nd needed to explain the shift in the seawater isotopic composition using an end-member  $\epsilon_{\text{Nd}}$  composition close to that of vent fluids ( $\epsilon_{\text{Ndvent}} = +11.9$ , Mills et al., 2001). We assume here that this end-member composition is found in an unknown hydrothermal flux added to the system ( $F_{\text{vent}}$ ) that is then scavenged within the plume in exchange with ambient seawater. In steady state, the removal of Nd within the plume ( $F_{\text{plume}}$ , i.e., 40 mol/year) must be further balanced by the addition of seawater ( $F_{\text{sw}}$ ), hence the sum of 'fresh' Nd supplied by seawater and  $F_{\text{vent}}$  is equal to  $F_{\text{plume}}$ . The mass balance would



then follow this relationship:  $\epsilon_{\text{Ndplume}}(F_{\text{plume}}) = \epsilon_{\text{Ndsw}}(F_{\text{plume}} - F_{\text{vent}}) + \epsilon_{\text{Ndvent}}(F_{\text{vent}})$ . With  $\epsilon_{\text{Ndplume}}$  and  $\epsilon_{\text{Ndsw}}$  representing the isotopic composition within the plume (−11.4) and outside the plume (−12.1), respectively. Solving for  $F_{\text{vent}}$ , the observed shift in the Nd isotopic composition along with the scavenging of 40 mol/year needs to be balanced by a release of ~1.1 mol/year Nd to yield the observed isotopic composition within the plume. So the TAG hydrothermal plume is a net sink for Nd and REE in general, however, by isotopic exchange processes the Nd isotopic composition of seawater is altered toward more radiogenic values relative to surrounding water masses. If we assume similar exchange processes in other hydrothermal systems, we can estimate a global flux released from hydrothermal systems. This yields  $5.2 \times 10^4$  mol/year, accounting for only 0.1% of the estimated release (Tachikawa et al., 2003; Rempfer et al., 2011) from boundary exchange. This suggests that the removal of Nd from seawater by hydrothermal vents is about 35–66 times higher than the Nd added to seawater by these systems. This estimate suggests that on a basin wide scale, the influence of a hydrothermally derived Nd isotopic signal is low and limits the ability to change Nd isotopic seawater composition. However, the influence on [Nd] as a sink is noticeable as mentioned in the previous section and should be taken into account in forthcoming modeling estimates of the Nd cycle.

## SUMMARY

For the first time a neutrally buoyant hydrothermal plume was sampled for seawater Nd isotopic composition and REE concentrations and compared with  $\text{xs}^3\text{He}$  on a GEOTRACES section cruise (GA03). The data show a clear influence of the hydrothermal plume on the REE concentrations and Nd isotopes. Shale (PAAS, Taylor and McLennan, 1985) normalized  $\text{Eu}/\text{Eu}^*$ ,  $\text{Dy}/\text{Er}$  and HREE ( $\text{Tm} + \text{Yb} + \text{Lu}$ ) over LREE ( $\text{La} + \text{Pr} + \text{Nd}$ ) show clear influence within the hydrothermal plume. The presence of mantle derived Eu is indicated by a significant positive  $\text{Eu}/\text{Eu}^*$  at the maximum of  $\text{xs}^3\text{He}$ . Fractionation of REE is evident by the relative enrichment of HREE over LREE within the plume. This is further corroborated by decreasing  $\text{Dy}_\text{N}/\text{Er}_\text{N}$ . Elemental concentrations of Nd are reduced by 19.6–18.5 pmol/kg, coinciding with the maximum increase of  $\text{xs}^3\text{He}$  from 0.205 to 0.675 fmol/kg, resulting in an average 1.8 pmol/kg decrease in [Nd] relative to an expected linear increase with depth. The inventory loss of Nd within the plume sums up to ~614 nmol/m<sup>2</sup>, or 6%. Compared to BATS and the western

adjacent station USGT11-14, the local inventory loss is even higher at 10%. The tight relationship of  $\text{xsHe}^3$  increase and [Nd] decrease allows us to estimate scavenging rates at TAG suggesting ~40 mol/year are removed within the TAG plume. A global estimate using power output of  $\sim 3.2 \times 10^{12}$  W along ocean ridges (Stein et al., 2013) yields an annual Nd removal of  $\sim 3.4 \times 10^6$  mol/year, which is about 71% of riverine and dust flux combined (Goldstein and Jacobsen, 1987; Tachikawa et al., 1999, 2003; Arsouze et al., 2009; Rempfer et al., 2011) or 6–8% of the estimated total global flux (Tachikawa et al., 2003; Rempfer et al., 2011) of Nd into the ocean. The change in Nd isotopic composition of up to 0.7 more radiogenic  $\epsilon_{\text{Nd}}$  values suggests an exchange process between hydrothermally derived particles and seawater in which during the removal process an estimated 1.1 mol/year of hydrothermal Nd is contributed to the seawater at the TAG site. This estimate is ~0.1% of the global Nd signal added to the ocean by boundary exchange processes at ocean margins (Tachikawa et al., 2003; Rempfer et al., 2011), limiting the ability of changing the Nd isotopic composition on a global scale in contrast to the more significant estimated sink of elemental Nd in hydrothermal plumes from this study.

## AUTHOR CONTRIBUTIONS

TS wrote the manuscript. KP, SG, and HS wrote the funding proposal. TS, AH, and BD measured Nd isotopic composition and Nd concentration, RP measured REE concentrations.

## ACKNOWLEDGMENTS

The authors would like to thank the scientific party and crew of KN204, especially M. Fleisher and C. Hayes for help with cruise preparations, sampling onboard, and sample storage at LDEO. Thanks to the ODF team for help onboard, and the chief-scientists G. Cutter, W. Jenkins, and E. Boyle. W. Jenkins also provided the He data, which was essential for the scope of this paper. Thanks to D. Vonderhaar, D. Pyle (both UH), L. Pena, L. Bolge (both LDEO), W. Buckley (USC) for their help in the lab and R.A. Mills for valuable discussions. The very constructive suggestions of the two reviewers Dr. Kazuyo Tachikawa and Dr. Hiroshi Amakawa and editor Dr. Johan Schijf improved this paper substantially. The research was funded by a collaborative NSF grant OCE09-27241 (UH), –28409 (LDEO), and –26981 (USC). This is LDEO contribution number 8186.

## REFERENCES

- Arsouze, T., Dutay, J.-C., Lacan, F., and Jeandel, C. (2009). Reconstructing the Nd oceanic cycle using a coupled dynamical–biogeochemical model. *Biogeosciences* 6, 2829–2846. doi: 10.5194/bg-6-2829-2009
- Arsouze, T., Dutay, J., Lacan, F., and Jeandel, C. (2007). Modeling the neodymium isotopic composition with a global ocean circulation model. *Chem. Geol.* 239, 165–177. doi: 10.1016/j.chemgeo.2006.12.006
- Basak, C., Pahnke, K., Frank, M., Lamy, F., and Gersonde, R. (2015). Neodymium isotopic characterization of Ross Sea Bottom Water and its advection through the southern South Pacific. *Earth Planet. Sci. Lett.* 1, 211–221. doi: 10.1016/j.epsl.2015.03.011
- Behrens, M. K., Muratli, J., Pradoux, C., Wu, Y., Böning, P., Brumsack, H. J., et al. (2016). Rapid and precise analysis of rare earth elements in small volumes of seawater-Method and intercomparison. *Mar. Chem.* 186, 110–120. doi: 10.1016/j.marchem.2016.08.006
- Carter, P., Vance, D., Hillenbrand, C. D., Smith, J. A., and Shoosmith, D. R. (2012). The neodymium isotopic composition of waters masses in the eastern Pacific sector of the Southern Ocean. *Geochim. Cosmochim. Acta* 79, 41–59. doi: 10.1016/j.gca.2011.11.034

- Conway, T. M., and John, S. G. (2014). Quantification of dissolved iron sources to the North Atlantic Ocean. *Nature* 511, 212–215. doi: 10.1038/nature13482
- Elderfield, H., and Greaves, M. J. (1982). The rare earth elements in seawater. *Nature* 296, 214–219. doi: 10.1038/296214a0
- Elderfield, H., and Schultz, A. (1996). Mid-ocean ridge hydrothermal fluxes and the chemical composition of the ocean. *Annu. Rev. Earth Planet. Sci.* 24, 191–224. doi: 10.1146/annurev.earth.24.1.191
- German, C. R., Campbell, A. C., and Edmond, J. M. (1991). Hydrothermal scavenging at the Mid-Atlantic Ridge: modification of trace element dissolved fluxes. *Earth Planet. Sci. Lett.* 107, 101–114. doi: 10.1016/0012-821X(91)90047-L
- German, C. R., Klinkhammer, G. P., Edmond, J. M., Mura, A., and Elderfield, H. (1990). Hydrothermal scavenging of rare-earth elements in the ocean. *Nature* 345, 516–518. doi: 10.1038/345516a0
- Goldstein, S. J., and Jacobsen, S. B. (1987). The Nd and Sr isotopic systematics of river-water dissolved material: implications for the sources of Nd and Sr in seawater. *Chem. Geol. Isot. Geosci. Sect.* 66, 245–272. doi: 10.1016/0168-9622(87)90045-5
- Goldstein, S. L., and Hemming, S. R. (2003). “Long-lived isotopic tracers in oceanography, paleoceanography, and ice-sheet dynamics,” in *Treatise on Geochemistry: The Oceans and Marine Geochemistry*, eds H. D. Holland, K. Turekian, and H. Elderfield (Pergamon: Oxford), 453–489.
- Goto, S., Kinoshita, M., Schultz, A., and Von Herzen, R. P. (2003). Estimate of heat flux and its temporal variation at the TAG hydrothermal mound, Mid-Atlantic Ridge 26°N. *J. Geophys. Res. Solid Earth* 108, 1–14. doi: 10.1029/2001JB000703
- Grasse, P., Stichel, T., Stumpf, R., Stramma, L., and Frank, M. (2012). The distribution of neodymium isotopes and concentrations in the Eastern Equatorial Pacific: water mass advection versus particle exchange. *Earth Planet. Sci. Lett.* 353–354, 198–207. doi: 10.1016/j.epsl.2012.07.044
- Hatta, M., Measures, C. I., Wu, J., Roshan, S., Fitzsimmons, J. N., Sedwick, P., et al. (2015). An overview of dissolved Fe and Mn distributions during the 2010–2011 U.S. GEOTRACES north Atlantic cruises: GEOTRACES GA03. *Deep Sea Res. II Top. Stud. Oceanogr.* 116, 117–129. doi: 10.1016/j.dsr2.2014.07.005
- Jacobsen, S. B., and Wasserburg, G. J. (1980). Sm-Nd isotopic evolution of chondrites. *Earth Planet. Sci. Lett.* 50, 139–155. doi: 10.1016/0012-821X(80)90125-9
- Jeandel, C., Delattre, H., Grenier, M., Pradoux, C., and Lacan, F. (2013). Rare earth element concentrations and Nd isotopes in the Southeast Pacific Ocean. *Geochem. Geophys. Geosyst.* 14, 328–341. doi: 10.1029/2012GC004309
- Jeandel, C., and Oelkers, E. H. (2015). The influence of terrigenous particulate material dissolution on ocean chemistry and global element cycles. *Chem. Geol.* 395, 50–66. doi: 10.1016/j.chemgeo.2014.12.001
- Jenkins, W. J., Lott, D. E., Longworth, B. E., Curtice, J. M., and Cahill, K. L. (2015a). The distributions of helium isotopes and tritium along the U.S. GEOTRACES North Atlantic sections (GEOTRACES GAO3). *Deep Sea Res. II Top. Stud. Oceanogr.* 116, 21–28. doi: 10.1016/j.dsr2.2014.11.017
- Jenkins, W. J., Smethie, W. M., Boyle, E. A., and Cutter, G. A. (2015b). Water mass analysis for the U.S. GEOTRACES (GA03) North Atlantic sections. *Deep Sea Res. II Top. Stud. Oceanogr.* 116, 6–20. doi: 10.1016/j.dsr2.2014.11.018
- Jones, K. M., Khatiwala, S. P., Goldstein, S. L., Hemming, S. R., and van de Flierdt, T. (2008). Modeling the distribution of Nd isotopes in the oceans using an ocean general circulation model. *Earth Planet. Sci. Lett.* 272, 610–619. doi: 10.1016/j.epsl.2008.05.027
- Klinkhammer, G., Elderfield, H., and Hudson, A. (1983). Rare earth elements in seawater near hydrothermal vents. *Nature* 305, 185–188. doi: 10.1038/305185a0
- Klunder, M. B., Laan, P., Middag, R., De Baar, H. J. W., and van Ooijen, J. C. (2011). Dissolved iron in the Southern Ocean (Atlantic sector). *Deep Sea Res. II Top. Stud. Oceanogr.* 58, 2678–2694. doi: 10.1016/j.dsr2.2010.10.042
- Lacan, F., and Jeandel, C. (2001). Tracing Papua New Guinea imprint on the central Equatorial Pacific Ocean using neodymium isotopic compositions and Rare Earth Element patterns. *Earth Planet. Sci. Lett.* 186, 497–512. doi: 10.1016/S0012-821X(01)00263-1
- Lacan, F., and Jeandel, C. (2005). Neodymium isotopes as a new tool for quantifying exchange fluxes at the continent–ocean interface. *Earth Planet. Sci. Lett.* 232, 245–257. doi: 10.1016/j.epsl.2005.01.004
- Lambelet, M., van de Flierdt, T., Crockett, K., Rehkämper, M., Kreissig, K., Coles, B., et al. (2016). Neodymium isotopic composition and concentration in the western North Atlantic Ocean: results from the GEOTRACES GA02 section. *Geochim. Cosmochim. Acta* 177, 1–29. doi: 10.1016/j.gca.2015.12.019
- Mahowald, N. M., Baker, A. R., Bergametti, G., Brooks, N., Duce, R. A., Jickells, T. D., et al. (2005). Atmospheric global dust cycle and iron inputs to the ocean. *Global Biogeochem. Cycles* 19:GB4025. doi: 10.1029/2004GB002402
- Middag, R., de Baar, H. J. W., Laan, P., Cai, P. H., and van Ooijen, J. C. (2010). Dissolved manganese in the Atlantic sector of the Southern Ocean. *Deep Sea Res. II Top. Stud. Oceanogr.* 58, 2661–2677. doi: 10.1016/j.dsr2.2010.10.043
- Mills, R. A., Wells, D. M., and Roberts, S. (2001). Genesis of ferromanganese crusts from the TAG hydrothermal field. *Chem. Geol.* 176, 283–293. doi: 10.1016/S0009-2541(00)00404-6
- Ohnemus, D. C., and Lam, P. J. (2015). Cycling of lithogenic marine particles in the US GEOTRACES North Atlantic transect. *Deep Sea Res. II Top. Stud. Oceanogr.* 116, 283–302. doi: 10.1016/j.dsr2.2014.11.019
- Pahnke, K., van de Flierdt, T., Jones, K. M., Lambelet, M., Hemming, S. R., and Goldstein, S. L. (2012). GEOTRACES intercalibration of neodymium isotopes and rare earth element concentrations in seawater and suspended particles. Part 2: systematic tests and baseline profiles. *Limnol. Oceanogr. Methods* 10, 252–269. doi: 10.4319/lom.2012.10.252
- Pena, L. D., and Goldstein, S. L. (2014). Thermohaline circulation crisis and impacts during the mid-Pleistocene transition. *Science* 345, 318–322. doi: 10.1126/science.1249770
- Piegras, D. J., and Wasserburg, G. J. (1982). Isotopic composition of neodymium in waters from the drake passage. *Science* 217, 207–214. doi: 10.1126/science.217.4556.207
- Piotrowski, A. M., Goldstein, S. L., Hemming, S. R., and Fairbanks, R. G. (2004). Intensification and variability of ocean thermohaline circulation through the last deglaciation. *Earth Planet. Sci. Lett.* 225, 205–220. doi: 10.1016/j.epsl.2004.06.002
- Rempfer, J., Stocker, T. F., Joos, F., Dutay, J.-C., and Siddall, M. (2011). Modelling Nd-isotopes with a coarse resolution ocean circulation model: sensitivities to model parameters and source/sink distributions. *Geochim. Cosmochim. Acta* 75, 5927–5950. doi: 10.1016/j.gca.2011.07.044
- Resing, J. A., Sedwick, P. N., German, C. R., Jenkins, W. J., Moffett, J. W., Sohst, B. M., et al. (2015). Basin-scale transport of hydrothermal dissolved metals across the South Pacific Ocean. *Nature* 523, 200–203. doi: 10.1038/nature14577
- Rousseau, T. C., Sonke, J. E., Chmieleff, J., van Beek, P., Souhaut, M., Boaventura, G., et al. (2015). Rapid neodymium release to marine waters from lithogenic sediments in the Amazon estuary. *Nat. Commun.* 6, 7592. doi: 10.1038/ncomms8592
- Schlitzer, R. (2016a). *Ocean Data View*. Available online at: <http://odv.awi.de>.
- Schlitzer, R. (2016b). Quantifying He fluxes from the mantle using multi-tracer data assimilation. *Philos. Trans. R. Soc. A Math. Phys. Eng. Sci.* 374, 20150288. doi: 10.1098/rsta.2015.0288
- Siddall, M., Khatiwala, S., van de Flierdt, T., Jones, K., Goldstein, S. L., Hemming, S., et al. (2008). Towards explaining the Nd paradox using reversible scavenging in an ocean general circulation model. *Earth Planet. Sci. Lett.* 274, 448–461. doi: 10.1016/j.epsl.2008.07.044
- Stein, C. A., Stein, S., and Pelayo, A. M. (2013). “Heat Flow and Hydrothermal Circulation,” in *Seafloor Hydrothermal Systems: Physical, Chemical, Biological, and Geological Interactions*, eds S. E. Humphris, R. A. Zierenberg, L. S. Mullineaux, and R. E. Thomson (Washington, DC: American Geophysical Union), 425–445.
- Stichel, T., Frank, M., Rickli, J., and Haley, B. A. (2012). The hafnium and neodymium isotope composition of seawater in the Atlantic sector of the Southern Ocean. *Earth Planet. Sci. Lett.* 317–318, 282–294. doi: 10.1016/j.epsl.2011.11.025
- Stichel, T., Hartman, A. E., Duggan, B., Goldstein, S. L., Scher, H., and Pahnke, K. (2015). Separating biogeochemical cycling of neodymium from water mass mixing in the Eastern North Atlantic. *Earth Planet. Sci. Lett.* 412, 245–260. doi: 10.1016/j.epsl.2014.12.008
- Tachikawa, K., Athias, V., and Jeandel, C. (2003). Neodymium budget in the modern ocean and paleo-oceanographic implications. *J. Geophys. Res.* 108, 3254. doi: 10.1029/1999JC000285
- Tachikawa, K., Jeandel, C., and Roy-Barman, M. (1999). A new approach to the Nd residence time in the ocean: the role of atmospheric inputs. *Earth Planet. Sci. Lett.* 170, 433–446. doi: 10.1016/S0012-821X(99)00127-2

- Tanaka, T., Togashi, S., Kamioka, H., Amakawa, H., Kagami, H., Hamamoto, T., et al. (2000). JNdi-1: a neodymium isotopic reference in consistency with LaJolla neodymium. *Chem. Geol.* 168, 279–281. doi: 10.1016/S0009-2541(00)00198-4
- Taylor, S. R., and McLennan, S. M. (1985). *The Continental Crust: Its Composition and Evolution*. Malden, MA: Blackwell.
- Zheng, X. Y., Plancherel, Y., Saito, M. A., Scott, P. M., and Henderson, G. M. (2016). Rare earth elements (REEs) in the tropical South Atlantic and quantitative deconvolution of their non-conservative behavior. *Geochim. Cosmochim. Acta* 177, 217–237. doi: 10.1016/j.gca.2016.01.018

**Conflict of Interest Statement:** The authors declare that the research was conducted in the absence of any commercial or financial relationships that could be construed as a potential conflict of interest.

Copyright © 2018 Stichel, Pahnke, Duggan, Goldstein, Hartman, Paffrath and Scher. This is an open-access article distributed under the terms of the Creative Commons Attribution License (CC BY). The use, distribution or reproduction in other forums is permitted, provided the original author(s) and the copyright owner are credited and that the original publication in this journal is cited, in accordance with accepted academic practice. No use, distribution or reproduction is permitted which does not comply with these terms.



# The Impact of Benthic Processes on Rare Earth Element and Neodymium Isotope Distributions in the Oceans

Brian A. Haley<sup>1\*</sup>, Jianghui Du<sup>1</sup>, April N. Abbott<sup>2</sup> and James McManus<sup>3</sup>

<sup>1</sup> College of Earth, Ocean, and Atmospheric Sciences (CEOAS), Oregon State University, Corvallis, OR, United States,

<sup>2</sup> Department of Earth and Planetary Sciences, Macquarie University, Sydney, NSW, Australia, <sup>3</sup> Bigelow Laboratory for Ocean Sciences, East Boothbay, ME, United States

## OPEN ACCESS

### Edited by:

Catherine Jeandel,  
UMR5566 Laboratoire d'études en  
Géophysique et Océanographie  
Spatiales (LEGOS), France

### Reviewed by:

Tina Van De Flierdt,  
Imperial College London,  
United Kingdom  
Vineet Goswami,  
Colorado State University,  
United States

### \*Correspondence:

Brian A. Haley  
bhaley@coas.oregonstate.edu

### Specialty section:

This article was submitted to  
Marine Biogeochemistry,  
a section of the journal  
Frontiers in Marine Science

**Received:** 02 October 2017

**Accepted:** 12 December 2017

**Published:** 21 December 2017

### Citation:

Haley BA, Du J, Abbott AN and  
McManus J (2017) The Impact of  
Benthic Processes on Rare Earth  
Element and Neodymium Isotope  
Distributions in the Oceans.  
Front. Mar. Sci. 4:426.  
doi: 10.3389/fmars.2017.00426

Neodymium (Nd) isotopes are considered a valuable tracer of modern and past ocean circulation. However, the promise of Nd isotope as a water mass tracer is hindered because there is not an entirely self-consistent model of the marine geochemical cycle of rare earth elements (REEs, of which Nd is one). That is, the prevailing mechanisms to describe the distributions of elemental and isotopic Nd are not completely reconciled. Here, we use published [Nd] and Nd isotope data to examine the prevailing model assumptions, and further compare these data to emergent alternative models that emphasize benthic processes in controlling the cycle of marine REEs and Nd isotopes. Our conclusion is that changing from a “top-down” driven model for REE cycling to one of a “bottom-up” benthic source model can provide consistent interpretations of these data for both elemental and isotopic Nd distributions. We discuss the implications such a benthic flux model carries for interpretation of Nd isotope data as a tracer for understanding modern and past changes in ocean circulation.

**Keywords:** rare earth elements, neodymium isotopes, marine geochemistry, benthic flux

## INTRODUCTION

Neodymium (Nd) isotopes (denoted  $\epsilon_{Nd}$ , which reflects the  $^{143}Nd/^{144}Nd$  ratio normalized to a Chondritic Uniform Reservoir; Jacobsen and Wasserburg, 1980) are widely recognized as a valuable tracer for ocean circulation (e.g., Piegras and Wasserburg, 1980, 1987; Elderfield, 1988; von Blanckenburg, 1999; Frank, 2002; Goldstein and Hemming, 2003; Piotrowski et al., 2004; van de Flierdt and Frank, 2010). The potential for Nd isotopes to serve as a circulation tracer lies with the observation that  $\epsilon_{Nd}$  distributions appear to mirror the pattern of global deep-water thermohaline circulation. These observations support the assumption that  $\epsilon_{Nd}$  is conservative or “quasi-conservative” in the oceans and will trace water masses in a manner similar to temperature and salinity (Frank, 2002; Goldstein and Hemming, 2003). Furthermore, elemental Nd is assumed to have negligible bioactivity, although recent work suggests that there are important caveats to this assumption (Shiller et al., 2017). However, because of the concerted efforts invested into measuring neodymium in the oceans as well as within sedimentary archives, inconsistencies between the observed distributions and the assumptions inherent in the use of the Nd as a tracer are becoming increasingly apparent. The best known of these inconsistencies is the “Nd paradox” (Jeandel et al., 1995, 1998; Tachikawa et al., 1999a; Lacan and Jeandel, 2001). Described in many ways, this paradox fundamentally describes the contradictory observations that while  $\epsilon_{Nd}$  appears to behave conservatively, the water column profile of dissolved elemental Nd ([Nd]) appears to reflect the behavior of a reactive element, showing a nutrient-like distribution (see discussion in Goldstein and Hemming, 2003). In short,



$\epsilon_{\text{Nd}}$  distributions imply a residence time of  $\leq 10^3$  years, while [Nd] distributions imply a residence time of  $\geq 10^4$  years (Bertram and Elderfield, 1993; Jones et al., 1994). This discrepancy appears in paired geochemical mixing models (Goldstein and Hemming, 2003) and models that attempt to reproduce the global distribution of  $\epsilon_{\text{Nd}}$  (Tachikawa et al., 2003; Jones et al., 2008; Arsouze et al., 2009; Rempfer et al., 2011). In addition to the “Nd paradox,” inconsistencies have arisen regarding past records of authigenic  $\epsilon_{\text{Nd}}$ , which sometimes prove to be difficult to explain when assuming water mass mixing of fixed end-members (Osborne et al., 2014; Stewart et al., 2016), or show exceptional disparities between adjacent sites (Stumpf et al., 2010; Roberts and Piotrowski, 2015; Howe et al., 2016; Hu et al., 2016).

The problem with  $\epsilon_{\text{Nd}}$  as a circulation proxy is fundamentally that while  $\epsilon_{\text{Nd}}$  appears to trace water masses effectively, it is not particularly potent at discerning geochemical processes that might impact its distribution. For example, it is difficult to use  $\epsilon_{\text{Nd}}$  to determine *how* a water mass acquires its isotope signature. Although the pattern of global  $\epsilon_{\text{Nd}}$  mirrors that of thermohaline circulation the cause of that apparent coincidence is not straightforward. For example, that the deep North Pacific is a Nd isotope end-member for mixing is difficult to justify given that no deep water forms within this basin. If isotopic end members can develop unassociated with preformed properties of the water mass, then there is clearly a need to explain and constrain the effects of these processes on  $\epsilon_{\text{Nd}}$ , especially for interpretation of  $\epsilon_{\text{Nd}}$  as ancient records of circulation.

Relatively recently, several possible mechanisms for non-conservative behavior of  $\epsilon_{\text{Nd}}$  have been forwarded: boundary exchange, Submarine Groundwater Discharge (SGD) and a benthic Nd flux (Lacan and Jeandel, 2005b; Johannesson and Burdige, 2007; Abbott et al., 2015a). These three hypotheses are all similar in that bottom water can be altered along the sediment-water boundary. Although these hypotheses may have been articulated as distinctly different, the differences among these hypotheses may be simply semantic or reflect our incomplete understanding of the processes involved. Boundary exchange, as described by Lacan and Jeandel (2005b) is typically thought to reflect an isotope exchange of Nd with net zero concentration change that occurs between the sediments and bottom water predominantly at ocean margins (Jeandel, 2016). While this model is highly cited, the specific mechanism or processes are not well defined. In contrast, both the SGD and benthic flux models propose more distinct mechanisms but lack the robust global data sets needed for verification. All three of these hypotheses invoke a potential source of dissolved [Nd] to the oceans from sedimentary fluids; SGD waters are considered here to be originally fresh waters, while the benthic flux model considers seawater as the source fluid origin. These latter hypotheses will differ in the quantity and location of the Nd fluxes they predict and the  $\epsilon_{\text{Nd}}$  that they carry. Clearly, the distinctions among all three models is nuanced, and again, probably simply reflects the need for further investigation or even simple definition. However, all three models challenge the underlying assumptions around the conservative nature of  $\epsilon_{\text{Nd}}$  in the water column.

A more comprehensive understanding of the marine geochemical cycle of REEs in conjunction with  $\epsilon_{\text{Nd}}$  is needed to

build more accurate geochemical models and interpret down core records with respect to ocean circulation. The problems arising from the notion of  $\epsilon_{\text{Nd}}$  as a paleoproxy perhaps reflect the superficial, and perhaps data limited synthesis between analyses of  $\epsilon_{\text{Nd}}$  and the rare earth elements (REEs) throughout the ocean basins. Fortunately, the comprehensive nature of the GEOTRACES water column sampling will go far to improve our understanding of water column processes that affect the REEs and  $\epsilon_{\text{Nd}}$ . Here, we discuss published  $\epsilon_{\text{Nd}}$  and Nd data from the Atlantic Ocean, with the intent to clarify our understanding of these tracers where they appear to be most robust. While we do not present any new data, we attempt to illustrate that a holistic view of published REE and  $\epsilon_{\text{Nd}}$  distributions in the oceans is consistent with predominant control from a benthic sedimentary source. Our conclusion is that processes occurring within the water column (e.g., reversible scavenging) are likely a secondary control on  $\epsilon_{\text{Nd}}$  or [REE] in the oceans, save where particle fluxes are exceptionally high, and that benthic fluxes exert primary control over the distribution of these elements and their isotopes.

## MODERN OCEAN REES AND Nd ISOTOPES

It was originally held that the REEs are input to the oceans predominantly via rivers, with potential additions via dust where such inputs are relatively high (Byrne and Sholkovitz, 1996; Greaves et al., 1999; Tachikawa et al., 1999b; Goswami et al., 2014; Dunlea et al., 2015; Stichel et al., 2015; also see Bayon et al., 2004 for the alternative view that dust is a sink term). More recently, the emphasis of REE input to the oceans has shifted to greater consideration of a benthic continental margin source for REEs, as we will discuss further later (Spivack and Wasserburg, 1988; Jeandel et al., 1998; Goldstein and Hemming, 2003; Tachikawa et al., 2003; Arsouze et al., 2009; Rickli et al., 2009, 2010, 2014; Carter et al., 2012; Grasse et al., 2012; Singh et al., 2012; Grenier et al., 2013; Wilson et al., 2013; Garcia-Solsona et al., 2014).

In the open ocean, REEs are thought to be transferred from shallow to deep ocean via reversible scavenging on particles sinking through the water column (Elderfield, 1988; Byrne and Kim, 1990; Sholkovitz et al., 1994; Byrne and Sholkovitz, 1996). However, the heavier atomic mass REEs (HREEs, such as Yb, Lu) tend to have vertical profiles that are more “Si-like,” which is thought to reflect the tendency for greater complexation across the REE series (Cantrell and Byrne, 1987; Elderfield, 1988; Byrne and Sholkovitz, 1996). Finally, removal of REEs from the ocean is thought to be predominantly via metal-oxides, although the role of organic matter, phosphates, or even carbonates, is likely to be important (Byrne and Kim, 1990; Byrne and Sholkovitz, 1996; Schijf et al., 2015). This model is considered the standard of marine REEs. Nd isotopes should also behave in a manner that is consistent with this model, although as pointed out previously this does not appear to be the case (Goldstein and Hemming, 2003; Jones et al., 2008; Arsouze et al., 2009). Successful efforts to reconcile the inconsistent behavior between elemental Nd and its isotopes, i.e., the Nd paradox, will likely

begin with an examination of these first principles of marine REE cycling.

The shift from considering riverine point sources to broad marginal inputs improves model results (Tachikawa et al., 2003; Arsouze et al., 2009) and offers an explanation for some of the irregularities observed when comparing Nd and its isotopes such as the constancy of surface ocean water  $\epsilon_{\text{Nd}}$  ( $-7.8$  upstream vs.  $-7.9/-8.0$  downstream; Osborne et al., 2014) around the mouth of the Mississippi river that carries a far less radiogenic signal (at  $\epsilon_{\text{Nd}} < -11$ ; Goldstein and Jacobsen, 1987, 1988; Bayon et al., 2015). Budgetary estimates from diffuse benthic REE fluxes, such as SGD or from sedimentary pore water (Sholkovitz et al., 1989; Greaves et al., 1999; Haley and Klinkhammer, 2003; Tachikawa et al., 2003; Johannesson and Burdige, 2007; Schacht et al., 2010; Johannesson et al., 2011, 2017; Abbott et al., 2015a; Fröllje et al., 2016), suggest that they may dominate the flux of REEs to the oceans. Importantly, such diffuse, or at least hard to quantify, sources are consistent with deep-water isopycnal mixing of  $\epsilon_{\text{Nd}}$  signals off margins that cannot be explained through surface water sources (Grasse et al., 2012; Grenier et al., 2013). However, while a diffuse benthic source of Nd appears to better describe the dominant flux of REEs to the ocean, outstanding questions remain. Arguably the most important of these is: what drives this flux? Any mechanism must be reconciled with the remarkably consistent REE pattern of seawater in light of diverse sediment compositions and sedimentary/diagenetic environments. As such, it seems unlikely that simple, unidirectional particulate dissolution can be the mechanism, because the dissolved REE pattern and  $\epsilon_{\text{Nd}}$  would to some extent reflect such an input, following arguments posed by Sholkovitz (1993) and reiterated by Bau et al. (2013).

Another supposition in the current understanding of marine REE cycling is that reversible scavenging controls the vertical distribution of these elements in the water column. In his deeply insightful paper, Elderfield (1988) suggested cause for concern over this conjecture: not for shallow REE adsorption, but in light of a mechanism for desorption at depth. For many trivalent cations the pH-edge/Langmuir-front for adsorption onto particle surfaces lies well under a pH of 7 (Morel and Hering, 1993; Ngwenya et al., 2010); thus, over a typical oceanic pH range of 7.6 and 8.2 desorption is unlikely. The thermodynamics of desorption become even less favorable as the increasing dissolved concentration at depth would tend to push the equilibrium toward further adsorption (reiterating arguments posed by Elderfield, 1988). Moreover, given free Nd is  $<16\%$  of the total dissolved Nd (Millero, 1992; Schijf et al., 2015), and surface adsorption coefficients are typically not exceptionally high (in the range of 3 to 5 onto carboxyl and monocarboxylic groups; Smith and Martell, 1989; Byrne and Kim, 1990; Ngwenya et al., 2010), the potential for REE transfer from the shallow to deep ocean via particle surface scavenging should be limited (Elderfield and Greaves, 1982; Stichel et al., 2015).

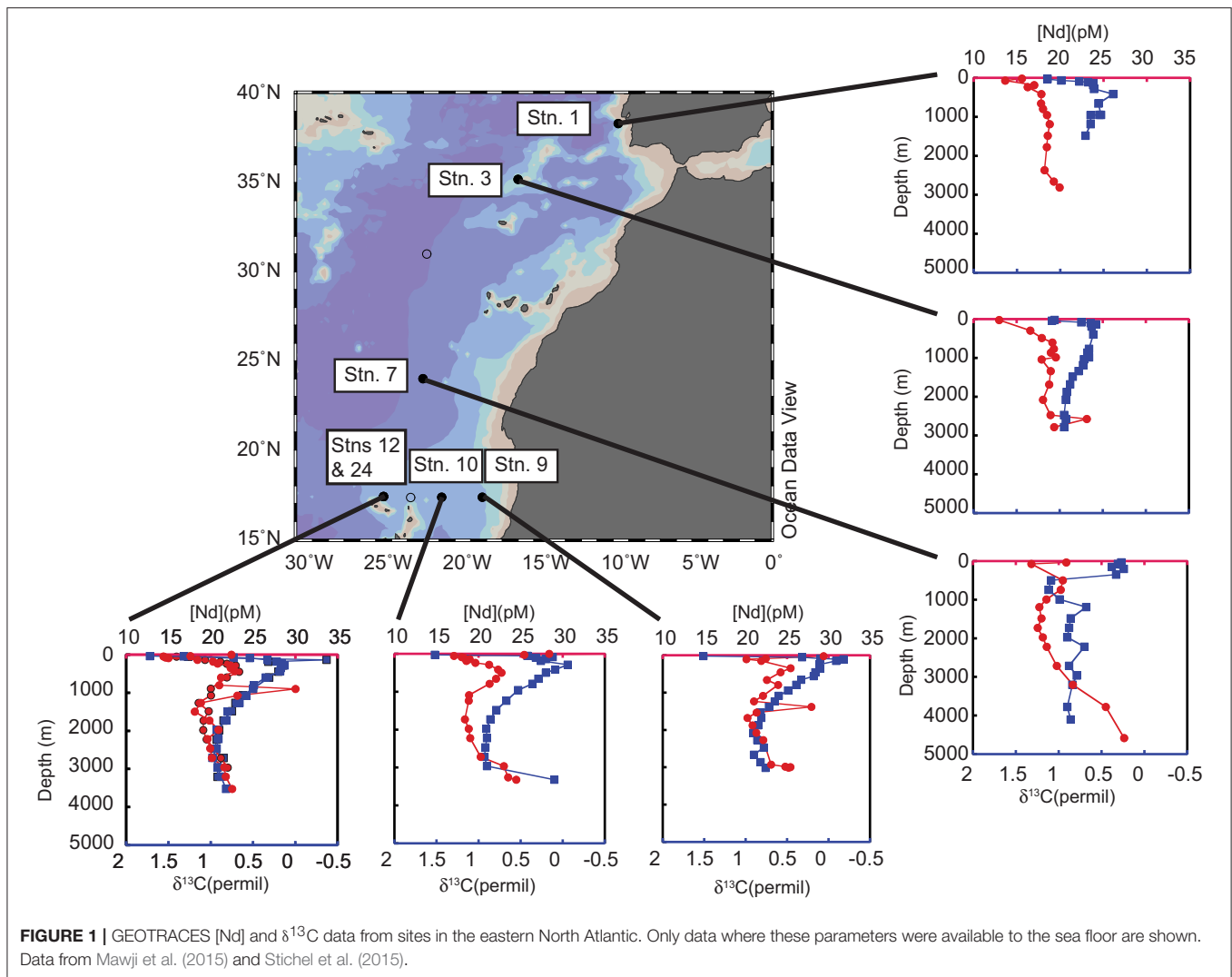
In spite of such arguments, lab and field observations attest that the REEs are indeed highly susceptible to adsorption (Sholkovitz, 1989), and that adsorption onto particles in the ocean certainly does happen (e.g., Sholkovitz et al., 1994; Tachikawa et al., 1999a). One positive test for REE adsorption

in the oceans may be seen in conservative Arctic Ocean REE profiles where particles are near absent (Yang and Haley, 2016). We do note, however, that a counter-argument can be made in that there does not appear to be an appreciable difference in the [Nd] profiles relating to marginal sites vs. distal sites, where particle loading may be very different (German and Elderfield, 1990; Grasse et al., 2012; Goswami et al., 2014; Haley et al., 2014; Abbott et al., 2015b; Stichel et al., 2015).

Considering all the arguments and data, a preferred model is that REEs are most likely transferred from the ocean surface to depth through incorporation onto complex organics, such as humic acids, polysaccharides, or other complex organic molecules that have binding coefficients higher than simple carboxyl groups ( $\log K > 9$ ; Byrne and Kim, 1990; Stanley and Byrne, 1990; Davranche et al., 2005; Pourret et al., 2007; Schijf et al., 2015). In this way, scavenging is actually achieved via an organic coating carrier phase that is remineralized, thus offering a mechanism for transfer of REEs from the particulate to dissolved phase without subsequent re-adsorption (i.e., not a desorptive process, but a remineralization; Sholkovitz et al., 1994). This model implies that [Nd] should behave much like  $\delta^{13}\text{C}$  in the water column, wherein their distributions reflect a preformed signal modified by top-down uni-directional input additions related to POC remineralization. Available GEOTRACES data allow us to make an initial comparison of water column [Nd] and  $\delta^{13}\text{C}$  (Mawji et al., 2015; Stichel et al., 2015; **Figure 1**). We consider the comparison inconclusive; these data appear to share many similarities (e.g., at Stations 12, 24, 10, especially in the upper 1,000 m) but not everywhere (e.g., at Stations 1, 3, and 7). Comparison of these [Nd] and  $\delta^{13}\text{C}$  data yields no correlation ( $r^2 < 0.05$ ; Figure S1), although the fit of all the data from the upper 50 to 500 m, ostensibly under highest remineralization, is better ( $r^2 \sim 0.4$ ; Figure S2), which would support scavenging of Nd on isotopically light-C POM. The form of the [Nd] profiles in **Figure 1**, especially in the upper 1,000 m, does appear to share many of the characteristics of POM remineralization in the oceans (e.g., Suess, 1980; Martin et al., 1987) and of AOU (discussed by Stichel et al., 2015). Unfortunately, global compilations, such as presented by Tachikawa et al. (2017), produce poor correlations between  $\delta^{13}\text{C}$  and [Nd] ( $r^2 < 0.001$ ; not shown), and the similarity between deep ( $>1,000$  m) [Nd] and  $\text{P}^*$  (van de Flierdt et al., 2016) becomes difficult to justify under the hypothesis of POM scavenging of Nd.

A similar uni-directional release of REEs at depth can also potentially come from deterioration of the lithogenic minerals themselves (Rousseau et al., 2015; Abadie et al., 2017). This mechanism would differ markedly in its effect on water column [REE] and  $\epsilon_{\text{Nd}}$  in comparison to a model based on an organic surface coating. Unfortunately, the evaluation of [Nd] and  $\epsilon_{\text{Nd}}$  in light of a lithogenic source of Nd at depth has been ambiguous in the eastern North Atlantic (Stichel et al., 2015; van de Flierdt et al., 2016).

Evaluation of modes of scavenging may be complicated through multiple substrates for scavenging, each of which can deliver REEs to depth (e.g., complex organic molecules as well as lithogenic and biogenic silicates; Akagi et al., 2011; Akagi,



2014). Adding additional ambiguity to the assessment of reverse scavenging is the issue of preformed REEs at depth that are likely conservative in nature (Haley et al., 2014; Zheng et al., 2016). Such preformed REEs must be an important component of deep water REEs (at least on basinal scales), such that REE profiles cannot be taken at face value: de-convolution of the conservative and non-conservative REEs is needed for accurate interpretation (Bertram and Elderfield, 1993; Haley et al., 2014; Zheng et al., 2016). Such efforts, either using a water mass approach (e.g., Bertram and Elderfield, 1993; Grasse et al., 2012; Stichel et al., 2012, 2015 or a more statistical approach (Singh et al., 2012; Haley et al., 2014; Zheng et al., 2016), are critical in evaluating the importance of scavenging on water column REEs. It goes beyond the scope of this paper to explore solutions for resolving preformed vs. “reactive” REEs. Our goal here is simply to suggest that much of the difficulty in resolving the “Nd paradox” is caused by undue emphasis placed on the function of reverse scavenging, which likely plays only a minor role in controlling the distribution of REEs and  $\epsilon_{\text{Nd}}$  in the water column.

Our exemplar here is the outstanding work of Bertram and Elderfield (1993). These authors carefully evaluated the possible influence of scavenging and reverse scavenging, largely under an assumption of “top down” forcing, because of the similarities to Si and a lack of sedimentary data (Bertram and Elderfield, 1993). Their conclusion is that particle-water exchange is necessary to explain deep ocean  $\epsilon_{\text{Nd}}$ , and give two possible mechanisms: a “top down” possibility wherein scavenged Nd exchanges over time in the deep ocean and a “...second option [that] simply places the site of exchange close to or within the sediment-porewater system with exchange within the nepheloid zone or transport via diffusion into overlying seawater” (Bertram and Elderfield, 1993). [Interestingly, the authors also note that “the simple (water density) & Si-REE correlations seen in bottom and near-bottom waters may also imply involvement of a benthic source. Unfortunately, no satisfactory data are available on REEs in oxic porewaters.”].

Finally, regardless of the impact on the water column, we emphasize that all of the potential “top down” mechanisms for remobilizing surface REEs at depth would be greatly enhanced

within seafloor sediments (Freslon et al., 2014); i.e., manifest as a pore water flux. In summary, while scavenging certainly happens on particles, we argue that the REE mass transfer is likely relatively small and subsequent desorption at depth in the water column is unlikely. On the other hand, any such desorption or remineralization mechanism is likely to be significant in the sediments, where the chemical environment can change significantly.

## BENTHIC CONTROL

Regardless of the discussions presented above, mechanisms driven via a “top-down” flux of REEs return to the disparity between  $\epsilon_{Nd}$  and [Nd] as discussed by Goldstein and Hemming (2003). The question is fundamentally how can such processes occur that account for [Nd] distributions, yet does not obviate the conservative qualities of  $\epsilon_{Nd}$ ? That a water mass such as North Atlantic Deep Water (NADW) can maintain its signature on ocean-basin scales is arguably less justifiable in a “top-down” explanation of marine REEs than it is in the “bottom-up” explanation that will be discussed below.

If we consider our prior argument that reversible scavenging does not significantly impact Nd's water column distribution, what then can explain the distribution of [Nd]/ $\epsilon_{Nd}$  at depth? A “bottom up” hypothesis argues that Nd and  $\epsilon_{Nd}$  are truly conservative below the permanent thermocline, except when exposed to a benthic flux. This benthic flux will certainly impact overlying bottom water, but its influence may also be carried laterally along isopycnals, for example off the continental slope (as indicated by Grasse et al., 2012; Singh et al., 2012; Stichel et al., 2015). The interaction with the sediments is then what makes  $\epsilon_{Nd}$  “quasi-conservative,” vs. being truly conservative, as has been suggested previously (Lacan and Jeandel, 2004b; Abbott et al., 2015a). The two important aspects of this suggestion are that (1) in the absence of a positive benthic flux, Nd and  $\epsilon_{Nd}$  will behave conservatively and (2) the ocean biogeochemistry of Nd and  $\epsilon_{Nd}$  is thus defined by benthic diagenetic processes. That is, this benthic control model suggests that the REEs and  $\epsilon_{Nd}$  are controlled by the nature of the benthic flux, which can be a positive, negative, or neutral term.

The idea of a benthic source for REEs, as described previously (Abbott et al., 2015a), would certainly help resolve model and observational inconsistencies of REE in the Pacific Ocean (Jones et al., 2008; Arsouze et al., 2009), but is such a source necessary anywhere else-in the Atlantic, Indian, Arctic or Southern Oceans? The North Atlantic, for example, has been well described in “top-down” models (Jones et al., 2008), or even through simple conservative mixing (van de Flierdt et al., 2016). Although we note here that the Denmark Straits is the ‘birthplace’ of the very non-conservative boundary exchange hypothesis (Lacan and Jeandel, 2004a,b, 2005a) and that other models have required benthic source fluxes in the North Atlantic (Tachikawa et al., 2003).

Why then invoke a benthic model? First, if correct, the benthic model would provide a mechanism to reconcile the apparent conflicts in our interpretation of Nd and  $\epsilon_{Nd}$ ; and second, the

benthic model makes different predictions about how changes in  $\epsilon_{Nd}$  and REEs records can be interpreted, when compared to a reversible scavenging model, as will be discussed later.

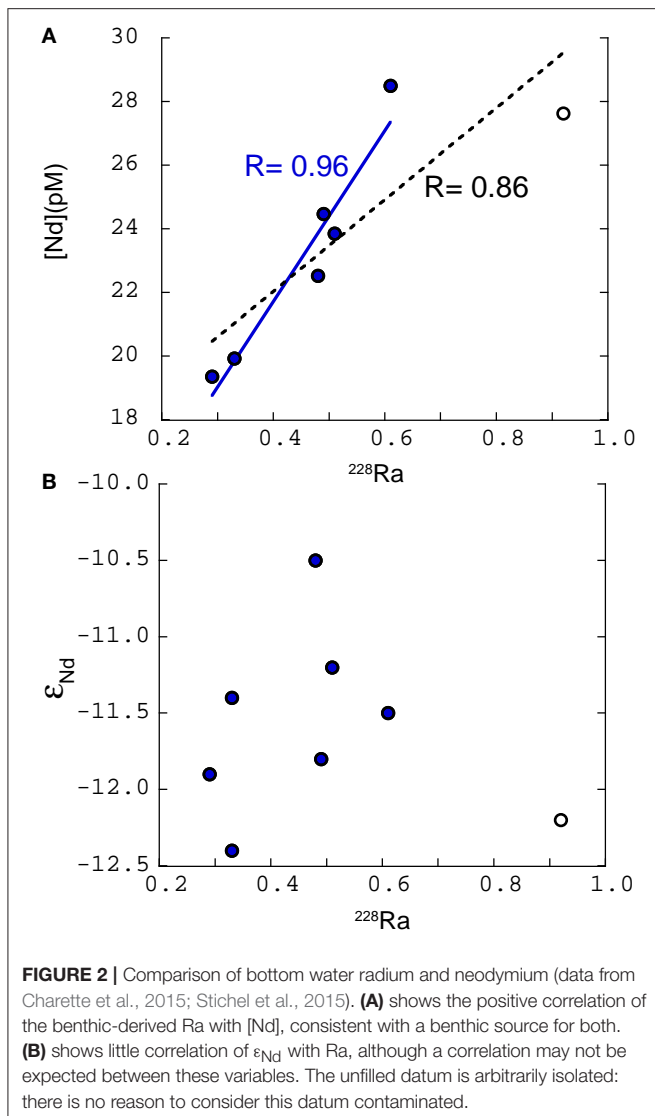
The concept of benthic control of [REE]/ $\epsilon_{Nd}$  on Pacific waters is still a nascent idea (Abbott et al., 2015a, 2016; Du et al., 2016). Here, we expand on this idea in a general sense. First, benthic control of [REE]/ $\epsilon_{Nd}$  will directly influence only the bottom water, such that a water mass detached from the bottom will maintain its  $\epsilon_{Nd}$  so long as it maintains its temperature and salinity (i.e., *all* its conservative properties). Second, benthic control represents a diffuse boundary flux, which implies that deep water [REE]/ $\epsilon_{Nd}$  distributions may be more disposed to being controlled by eddy diffusivity. Because eddy diffusion coefficients in the vertical are  $10^{-5}$ – $10^{-4}$  m<sup>2</sup>/s (or greater; Ku and Luo, 1994), over hundreds to thousands of meters per year (horizontal coefficients are even greater), the impact of a benthic flux may potentially integrate over significant depths within the deep ocean. Furthermore, eddy diffusivity is also an order of magnitude higher on the seafloor relative to the water column because of the turbulence created by topography (Waterhouse et al., 2014); therefore, a benthic flux will be dissipated with great efficiency into the water column. This dissipation is the rationale for the observation that there is an apparent jump in REE concentrations between pore water and overlying water (Abbott et al., 2015b, 2016).

## IMPLICATIONS OF A BENTHIC FLUX IN THE ATLANTIC

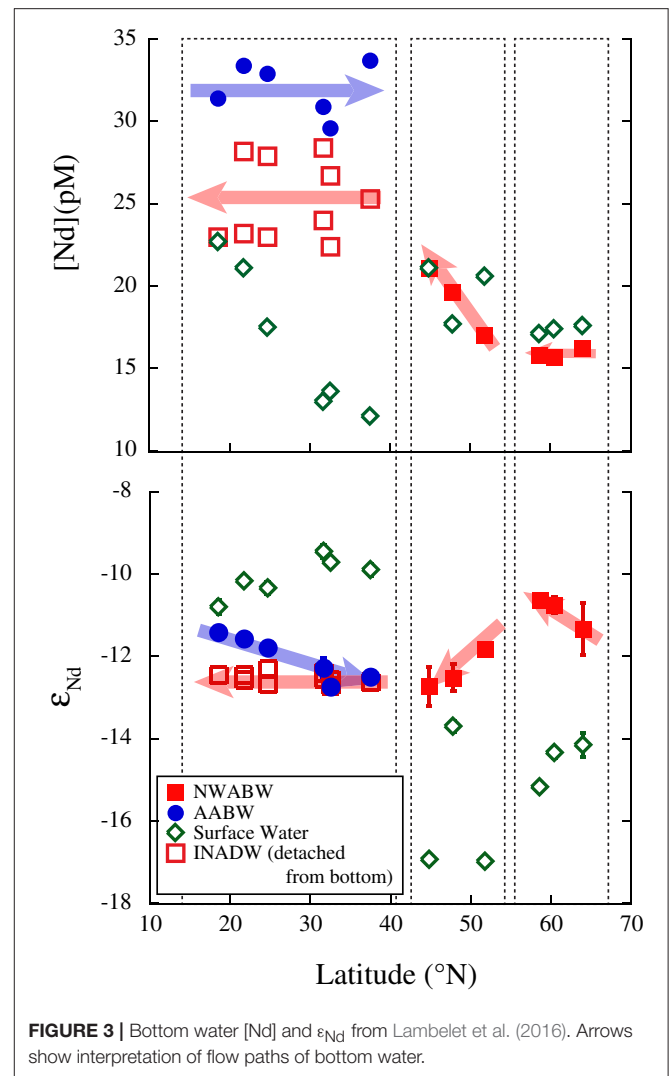
There is little direct observational data regarding the benthic REE flux to the oceans (Sholkovitz et al., 1989; Haley et al., 2004; Abbott et al., 2015b), and even less that tracks the  $\epsilon_{Nd}$  of this flux. However, comparison with radium offers some support for the hypothesis. Again, the holistic nature of GEOTRACES sampling has provided rare, directly comparable Ra-REE- $\epsilon_{Nd}$  data (Charette et al., 2015; Stichel et al., 2015; USGT10/GA03 section from the Gulf of Cadiz to the Mauritanian coast). All isotopes of Ra positively correlate with [Nd] in the bottom water, although we plot only <sup>228</sup>Ra, as this isotope is most directly associated with a benthic source influence (Figure 2A). The correlation of <sup>228</sup>Ra with [Nd] in bottom water is strong ( $r^2 = 0.7$  including all the data, and by omitting Site 7,  $r^2 = 0.9$ ). Such a positive correlation is consistent with both <sup>228</sup>Ra and [Nd] sharing a common benthic source. In contrast, benthic <sup>228</sup>Th does not covary with [Nd], which might otherwise be expected if the source of deep Nd was delivered via top-down particle-based mechanisms.

Bottom water  $\epsilon_{Nd}$  does not covary with Ra isotopes (Figure 2B). While such a correlation is not obligatory under the benthic control model, work with Pacific sediments suggests that certain components of the sediments may be more reactive during diagenesis, and such reactivity is also likely element specific (Abbott et al., 2016; Du et al., 2016). Thus, we might expect that reaction of these sedimentary elements imposes a co-variation between the magnitude and isotopic composition of the flux.

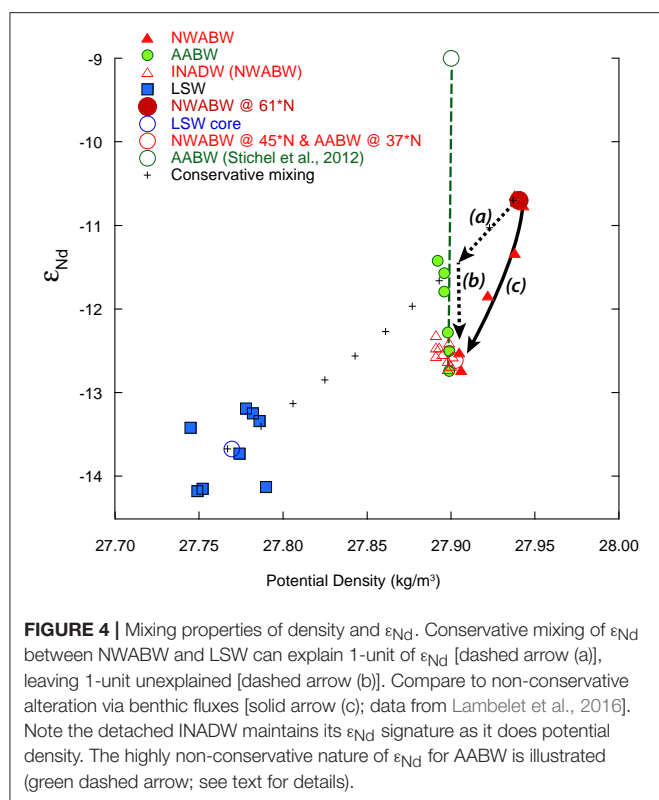




We reiterate that there is undeniable evidence in support of the idea that seawater  $\epsilon_{Nd}$  traces basin scale modern water mass circulation, and the benthic control hypothesis suggested here does not detract or contradict these observations. On the contrary, we suggest that records of  $\epsilon_{Nd}$  may potentially be used to actually quantify current velocities, given that the “exposure time” of a water mass to the bottom (Abbott et al., 2015a) implies a temporal sensitivity necessary to establish velocity. As an example, the bottom water data of Lambelet et al. (2016) for the North Atlantic, can be plotted vs. latitude (Figure 3). A benthic control based interpretation of these data may be that there are three diagenetic regimes in the North Atlantic: north of 55°N, between 45 and 55°N and south of 40°N. We will first focus on the increasing [Nd] and decreasing  $\epsilon_{Nd}$  of the middle regime (~43°–55°N). In this region, there is a total change in  $\epsilon_{Nd}$  of ~2 units, of which conservative mixing with LSW can account for ~1 unit (Figure 4; using water properties defined in van de Flierdt et al. (2016)). Applying the simple exposure time model of



Abbott et al., 2015a; assuming flux of 20 pmol/cm<sup>2</sup>/yr with  $\epsilon_{Nd}$  of –15, which is reasonable but arbitrarily chosen, and a deep water [Nd] of 15 pM, which is measured), we might estimate that the residual 1-unit corresponds to ~35 years of benthic flux exposure on a 1 km thick bottom water layer, occurring over ~12° latitude. This combination results in a bottom water current velocity of 0.2 cm/s. This estimate of effective transport rate, despite its obvious simplifications and assumptions, is not incomparable to the 1.8–2 cm/s estimates derived from CFC and tritium/He<sup>3</sup> (Smethie et al., 2000; Steinfeldt and Rhein, 2004). This simple model scenario also predicts [Nd] of the water mass increases to 23 pM, similar to that observed (Figure 3). Other scenarios are obviously possible; for example, a 5 pmol/cm<sup>2</sup>/yr flux with  $\epsilon_{Nd}$  of –20 offers a similar 40 year exposure estimate, but predicts a final [Nd] of only 17 pM. The only existing pore waters from the Atlantic (Buzzard’s Bay; Sholkovitz et al., 1989) show pore water [Nd] of >700 pM at ~13 cm depth in the sediment, which compares to fluxes as large as any seen in the Pacific (up to 30 pmol/cm<sup>2</sup>/yr; Haley and Klinkhammer, 2003; Abbott et al., 2015b). Such a flux of



30 pmol/cm<sup>2</sup>/yr with an  $\epsilon_{Nd}$  of  $-25$ , as implied might be the case in this region (Lambelet et al., 2016), predicts only 4 years of exposure for  $\sim 1$   $\epsilon_{Nd}$  unit change, which equates to 1.1 cm/s velocity, but an increase of [Nd] to just 16 pM. Again, these calculations are obviously crude, and poorly constrained; we use them simply to illustrate sensitivity of deep water to benthic fluxes, and the feasibility of using the concept for quantitative reconstruction of circulation.

The Lambelet et al. (2016) data show constancy of  $\epsilon_{Nd}$  in the Northwest Atlantic Bottom Water (NWABW) after it detaches (or is displaced) from contact with the bottom south of  $\sim 40^\circ\text{N}$ . At these lower latitudes, Antarctic Bottom Water (AABW) is in contact with the sediments, and it is this southern-sourced water mass that appears to be modified during its transit northwards. While such a pattern can be explained with a benthic control model for [REE]/ $\epsilon_{Nd}$ , a “top-down” process that clearly alters bottom water but not the deep water overlying bottom water seems difficult to reconcile. Moreover, the potential density of AABW is remarkably stable along its flow path:  $\sigma = 27.9 \text{ kg/m}^3$  at  $\sim 60^\circ\text{S}$  (Stichel et al., 2012) vs.  $\sigma = 27.903 \text{ kg/m}^3$  at  $\sim 37^\circ\text{N}$  (from Lambelet et al., 2016 data; **Figure 4**). This constancy indicates that little water mass mixing occurs during this bottom water transit, yet  $\epsilon_{Nd}$  changes significantly: at least one unit in just the northern hemisphere data of Lambelet et al. (2016). Again, if we argue that conservation of NADW  $\epsilon_{Nd}$  precludes a top down driver for AABW  $\epsilon_{Nd}$  change, the logical conclusion is that benthic alteration impacts bottom water (i.e., AABW)  $\epsilon_{Nd}$ . Through the same approximations done above (assuming an arbitrarily chosen 5 pmol/cm<sup>2</sup>/yr flux with  $\epsilon_{Nd}$  of  $-15$  and

measured 30 pM [Nd] of bottom water), we might estimate that the 1-unit  $\Delta\epsilon_{Nd}$  of AABW observed corresponds to  $\sim 150$  years of exposure. Over  $25^\circ$  of latitude, this corresponds to a current velocity of 0.06 cm/s, implying that AABW has about one third the velocity as NWABW. (Note that because this calculation is based on a concentration gradient, the exact positions of where the slope is calculated can differ, making such estimations amenable to paleo-reconstructions where end-members may not be well constrained.) This effective transport rate estimate is, as was the case for our NADW estimate, lower than the CFC estimate of  $\sim 1.2 \text{ cm/s}$  for AABW (Haine et al., 1998). We can predict that the benthic fluxes affecting AABW must be more complex, because linear extrapolation of the rate of change in  $\epsilon_{Nd}$  over latitude as shown in **Figures 3, 4** would imply that AABW has an  $\epsilon_{Nd}$  of  $-6$  at  $60^\circ\text{S}$ , which it does not (Stichel et al., 2012). The likely rationale for this difference is that the diagenetic fluxes along the greater AABW flow path are more nuanced in both their magnitude and composition than can be expressed by our simplified approximations.

There are three further points relevant to this discussion. First, the benthic control hypothesis does not invoke water mass mixing to explain patterns in  $\epsilon_{Nd}$  such as those shown in **Figures 3, 4**. That is, there is no obligate change in conservative properties, such as temperature or salinity, as the bottom water  $\epsilon_{Nd}$  is modified. Again, mid-depth water masses detached from the sediment will likely maintain their  $\epsilon_{Nd}$  signatures, or mix them as they would other conservative tracer properties along isopycnals, for example.

Second, the North Atlantic appears to have a propensity to mask the impacts of a benthic flux because ventilation rates are high, and thus exposure times are low. Instances where benthic influences may be directly observed in the North Atlantic (e.g., Lacan and Jeandel, 2004c) would thus reflect rather extreme cases of high flux or divergent isotopic composition. In contrast, AABW in the South Atlantic (and PDW in the Pacific) circulate rather more slowly and thus would be prone to longer benthic exposure, resulting in more obvious impacts of a benthic source flux.

Third, the benthic flux mechanism seems to be intimately connected to authigenic metal oxides in the sediments (Abbott et al., 2016), which appear to modulate the REE flux and its  $\epsilon_{Nd}$  signature. Authigenic metal oxides appear to act as a “capacitor” of REE: i.e., both a source and sink of pore water and bottom water REE. Analogous to electrical capacitance, more abundant sedimentary metal oxides will produce greater Nd fluxes with less temporally variable  $\epsilon_{Nd}$  signatures (Abbott et al., 2016). While this mechanism is clearly far from resolved, it offers an explanation for the apparent lack of influence from the non-radiogenic lithogenic sediments of the central North Pacific (Jones et al., 1994). Specifically, we predict that there is no positive benthic flux from these sediments, or that reactive diagenetic materials are not present in these sediments (Abbott et al., 2016; Du et al., 2016), or both. We also note that the non-radiogenic Nd data presented by Jones et al. (1994) reflect the post-leach lithogenic fraction of the sediments, which may not play a role at all in defining the benthic flux as defined by our proposed mechanism.

## PALEOPROXY Nd

Arguably the most important implication of benthic control on marine  $[REE]/\epsilon_{Nd}$  is how we interpret paleoceanographic records of water mass change. For these studies, the difference between a “top-down” or “bottom-up” control on bottom water and on the marine budget of REEs becomes paramount for two reasons:

Firstly, most interpretations of paleo-data treat  $\epsilon_{Nd}$  as fundamentally conservative, discounting the possibility of changes in REE supply that is not the result of water mass mixing or circulation. In a reversible scavenging model, this may be a valid assumption if deep-water sensitivity to surface ocean change is small. However, this supposition then begs the question of why reversible scavenging controls the modern deep  $[REE]/\epsilon_{Nd}$ ? On the other hand, in a benthic control scenario the  $\epsilon_{Nd}$  of bottom water may evolve through non-mixing processes: such as a change in the benthic flux or a change in the “exposure time” of the bottom water to this flux (Abbott et al., 2015b). As such, an  $\epsilon_{Nd}$  record interpreted through a benthic control model may reflect a change in benthic flux or exposure time, the latter of which may well be the result of changing circulation patterns or velocities. Despite the ostensible complications, we argue that interpreting  $\epsilon_{Nd}$  records purely as a conservative tracer discounts the “pseudo-conservative” nature of the tracer. Our benthic control model offers an internal cycling constraint on  $[Nd]$  and  $\epsilon_{Nd}$  compared to a reverse scavenging model. Both models require the ability to reconstruct fluxes through time to accurately use  $\epsilon_{Nd}$  as a tracer: the reversible scavenging model requires estimation of vertical particle fluxes and particulate type over time, whereas the benthic control model requires estimation of the benthic flux over time. Determining either of these fluxes will be non-trivial tasks, but may be resolvable.

Secondly, similarity between surface sediment archival phases (dispersed oxides, coatings, fish teeth, forams) and bottom water is often cited as evidence for record fidelity under the top down model for  $\epsilon_{Nd}$ . In the benthic control model, such correspondence will result from bottom water that is either dominated by a strong positive benthic flux, wherein the preformed bottom water  $\epsilon_{Nd}$  signature is overwhelmed by a pore water signature supported by the authigenic phases, or from a negative or net-zero pore water flux, such that pore water and authigenic phases passively record bottom water signatures. There is also a range of intermediate conditions where  $\epsilon_{Nd}$  of the archival phase may differ from bottom water, and where we would predict there is a significant, but not overwhelming, positive benthic flux into bottom water (e.g., Du et al., 2016 in the Pacific, or Gutjahr et al., 2008; Huck et al., 2016 in the Atlantic). The relationship between authigenic phases (used as archival records) and contemporaneous bottom water is far more complex in the benthic control model, because the authigenic phases associated with diagenesis are intimately associated with the nature of the benthic flux that impact the bottom water signal (Abbott et al., 2016). Moreover, the concentrations of sedimentary reactive particulate phases, pore water, and bottom water differ by orders of magnitude, so we stress the importance of looking at both  $\epsilon_{Nd}$  and the  $[REEs]$ .

Our benthic model may give an initially grim outlook for paleoproxy work, but the situation is probably not at all intractable: in fact, these challenges are likely to be fully resolvable with further observations and models. Most pressing is the need to better determine the mechanisms and sources that define the Nd sink terms within the sediment column: these processes are ultimately what will define the proxy records. For example, Abbott et al. (2015b) did not discuss the deep (~10 cm) sink term seen in pore water  $[Nd]$  profiles; if this sink records contemporaneous pore water  $\epsilon_{Nd}$ , an apparent temporal offset could be generated in records of  $\epsilon_{Nd}$  from diagenetic Fe-Mn oxides and other isotope and trace element proxies archived in the calcite lattice of foraminifera (Piotrowski et al., 2005).

Theory and observations all indicate that some aspect of bottom water  $\epsilon_{Nd}$  is maintained in authigenic phases, and is likely identifiable in all sediment (Gutjahr et al., 2007; Wilson et al., 2013; Blaser et al., 2016; Du et al., 2016). Furthermore, the additional Nd generated through diagenesis should be far less variable and readily constrained as “baseline” variations in sedimentary records, vs. higher-order changes that are derived from seawater; analogous to Sr isotope records. A compilation of global surface sediment authigenic-phase  $\epsilon_{Nd}$  vs. bottom water  $\epsilon_{Nd}$  (Figure 5) illustrates that authigenic (archival) phases do trend with bottom water globally, but there is a remarkably uniform 1-  $\epsilon_{Nd}$  unit offset toward authigenic phases being more radiogenic: an offset equivalent in the Atlantic and the Pacific. Furthermore, we note that the Pacific data actually have a more robust correlation compared to the Atlantic data, consistent with the preceding discussion that benthic fluxes in the Atlantic are more difficult to identify from bottom water data. Bearing in mind that the concentration of Nd in the authigenic phases (at ppm Nd) is nominally six orders of magnitude greater than the bottom water (at pM Nd), it is difficult to explain these data without invoking a Nd source from within the sediments that is globally persistent. Of course, there are many outstanding questions to answer before better understanding the benthic flux of REEs and  $\epsilon_{Nd}$ : for example, can a flux be more non-radiogenic than the sediment host? How do these fluxes change over time?

In summary, while complex, diagenesis does follow predictable rules that make it amenable to modeling, which, in turn, can provide a robust estimation of past changes in the benthic control on bottom water Nd. In turn, these modeled boundary conditions can be used to calculate current direction and velocities as suggested in the modern examples above. Moreover, such studies may provide further evidence for changes in pore waters that can relate to changes in ocean redox or acid-base chemistry. The benthic model adds complexity, but also potential for the application of  $[REE]/\epsilon_{Nd}$ .

## BEYOND THE REES AND $\epsilon_{Nd}$

The REEs and  $\epsilon_{Nd}$  are often touted as being excellent tracers of processes that impact marine geochemical cycles in a much broader sense. As such, the hypothesis of benthic control on deep ocean REE cycling may support suggestions for the importance

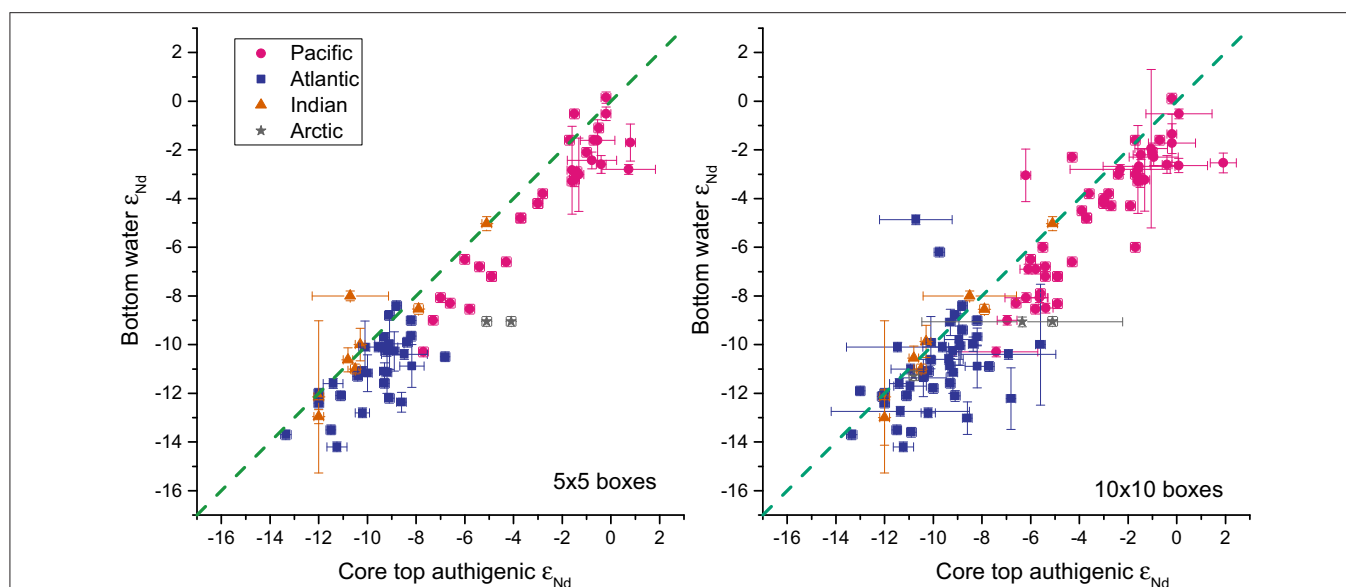


**FIGURE 5 |** Compiled  $\epsilon_{\text{Nd}}$  from core top authigenic phases and Bottom water. These data are compiled as averages from all published data within 5° and 10° boxes (ranges within these boxes are shown as error bars). This data compilation is available upon request, or find a similar compilation from Tachikawa et al. (2017).

of these diagenetic processes in marine geochemical cycles in general. For example, the same authigenic Fe/Mn oxides apparently involved in the marine cycling of  $[\text{REE}]/\epsilon_{\text{Nd}}$  are also rich in other trace metals (e.g., Cu, Zn, Ni, Co). These authigenic metal oxides may be acting in an expansive way as a capacitor for geochemical fluxes; i.e., as both a source and sink of these trace metals.

## AUTHOR CONTRIBUTIONS

All authors listed have made a substantial, direct and intellectual contribution to the work, and approved it for publication.

## REFERENCES

- Abadie, C., Lacan, F., Radic, A., Pradoux, C., and Poitrasson, F. (2017). Iron isotopes reveal distinct dissolved iron sources and pathways in the intermediate versus deep Southern Ocean. *Proc. Natl. Acad. Sci. U.S.A.* 114, 858–863. doi: 10.1073/pnas.1603107114
- Abbott, A. N., Haley, B. A., and McManus, J. (2015a). Bottoms up: sedimentary control of the deep North Pacific Ocean's  $\epsilon_{\text{Nd}}$  signature. *Geology* 43, 1035–1035. doi: 10.1130/G37114.1
- Abbott, A. N., Haley, B. A., and McManus, J. (2016). The impact of sedimentary coatings on the diagenetic Nd flux. *Earth Planet. Sci. Lett.* 449, 217–227. doi: 10.1016/j.epsl.2016.06.001
- Abbott, A. N., Haley, B. A., McManus, J., and Reimers, C. E. (2015b). The sedimentary flux of dissolved rare earth elements to the ocean. *Geochim. Cosmochim. Acta* 154, 186–200. doi: 10.1016/j.gca.2015.01.010
- Akagi, T. (2014). Diatoms spread a high  $\epsilon_{\text{Nd}}$ -signature in the North Pacific Ocean. *Geochim. J.* 48, 121–131. doi: 10.2343/geochimj.2.0292
- Akagi, T., Fu, F., Hongo, Y., and Takahashi, K. (2011). Composition of rare earth elements in settling particles collected in the highly productive North Pacific Ocean and Bering Sea: implications for siliceous-matter dissolution kinetics and formation of two REE-enriched phases. *Geochim. Cosmochim. Acta* 75, 4857–4876. doi: 10.1016/j.gca.2011.06.001

## ACKNOWLEDGMENTS

This work was supported by NSF grants OCE-1147407 to JM and BH, OCE-1357529 to BH, and OCE-1715106 to JM. We thank Drs. V. Goswami and T. van de Flierdt for their comments, and Catherine Jeandel for editorial handling of this manuscript.

## SUPPLEMENTARY MATERIAL

The Supplementary Material for this article can be found online at: <https://www.frontiersin.org/articles/10.3389/fmars.2017.00426/full#supplementary-material>

- Arsouze, T., Dutay, J.-C., Lacan, F., and Jeandel, C. (2009). Reconstructing the Nd oceanic cycle using a coupled dynamical – biogeochemical model. *Biogeosciences* 6, 2829–2846. doi: 10.5194/bg-6-2829-2009
- Bau, M., Tepe, N., and Mohwinkel, D. (2013). Siderophore-promoted transfer of rare earth elements and iron from volcanic ash into glacial meltwater, river and ocean water. *Earth Planet. Sci. Lett.* 364, 30–36. doi: 10.1016/j.epsl.2013.01.002
- Bayon, G., German, C. R., Burton, K. W., Nesbitt, R. W., and Rogers, N. (2004). Sedimentary Fe–Mn oxyhydroxides as paleoceanographic archives and the role of aeolian flux in regulating oceanic dissolved REE. *Earth Planet. Sci. Lett.* 224, 477–492. doi: 10.1016/j.epsl.2004.05.033
- Bayon, G., Toucanne, S., Skonieczny, C., André, L., Bermell, S., Cheron, S., et al. (2015). Rare earth elements and neodymium isotopes in world river sediments revisited. *Geochim. Cosmochim. Acta* 170, 17–38. doi: 10.1016/j.gca.2015.08.001
- Bertram, C., and Elderfield, H. (1993). The geochemical balance of the rare earth elements and neodymium isotopes in the oceans. *Geochim. Cosmochim. Acta* 57, 1957–1986.
- von Blanckenburg, F. (1999). Tracing past ocean circulation? *Science* 286, 1862–1863. doi: 10.1126/science.286.5446.1862b
- Blaser, P., Lippold, J., Gutjahr, M., Frank, N., Link, J. M., and Frank, M. (2016). Extracting foraminiferal seawater Nd isotope signatures from bulk deep sea sediment by chemical leaching. *Chem. Geol.* 439, 189–204. doi: 10.1016/j.chemgeo.2016.06.024



- Byrne, R. H., and Kim, K.-H. (1990). Rare earth element scavenging in seawater. *Geochim. Cosmochim. Acta* 54, 2645–2656. doi: 10.1016/0016-7037(90)90002-3
- Byrne, R. H., and Sholkovitz, E. R. (1996). Chapter 158 Marine chemistry and geochemistry of the lanthanides. *Handb. Phys. Chem. Rare Earths* 22, 497–593. doi: 10.1016/S0168-1273(96)23009-0
- Cantrell, K. J., and Byrne, R. H. (1987). Rare earth element complexation by carbonate and oxalate ions. *Geochim. Cosmochim. Acta* 51, 597–605. doi: 10.1016/0016-7037(87)90072-X
- Carter, P., Vance, D., Hillenbrand, C. D., Smith, J. A., and Shoosmith, D. R. (2012). The neodymium isotopic composition of waters masses in the eastern Pacific sector of the Southern Ocean. *Geochim. Cosmochim. Acta* 79, 41–59. doi: 10.1016/j.gca.2011.11.034
- Charette, M. A., Morris, P. J., Henderson, P. B., and Moore, W. S. (2015). Radium isotope distributions during the US GEOTRACES North Atlantic cruises. *Mar. Chem.* 177, 184–195. doi: 10.1016/j.marchem.2015.01.001
- Davranche, M., Pourret, O., Gruau, G., Dia, A., and Le Coz-Bouhnik, M. (2005). Adsorption of REE(III)-humate complexes onto MnO<sub>2</sub>: experimental evidence for cerium anomaly and lanthanide tetrad effect suppression. *Geochim. Cosmochim. Acta* 69, 4825–4835. doi: 10.1016/j.gca.2005.06.005
- Du, J., Haley, B., and Mix, A. (2016). Neodymium Isotopes in authigenic phases, bottom waters, and detrital sediments in the Gulf of Alaska and their implications for paleo-circulation reconstruction. *Geochim. Cosmochim. Acta* 193, 14–35. doi: 10.1016/j.gca.2016.08.005
- Dunlea, A. G., Murray, R. W., Sauvage, J., Spivack, A. J., Harris, R. N., and D'Hondt, S. (2015). Dust, volcanic ash, and the evolution of the South Pacific Gyre through the Cenozoic. *Paleoceanography* 30, 1078–1099. doi: 10.1002/2015PA002829
- Elderfield, H. (1988). The oceanic chemistry of the rare-earth elements [and discussion]. *Philos. Trans. R. Soc. Lond. Math. Phys. Eng. Sci.* 325, 105–126. doi: 10.1098/rsta.1988.0046
- Elderfield, H., and Greaves, M. J. (1982). The rare earth elements in seawater. *Nature* 296, 214–219. doi: 10.1038/296214a0
- Frank, M. (2002). Radiogenic isotopes: tracers of past ocean circulation and erosional input. *Rev. Geophys.* 40, 1–1–1–38. doi: 10.1029/2000RG000094
- Freslon, N., Bayon, G., Toucanne, S., Bermell, S., Bollinger, C., Chéron, S., et al. (2014). Rare earth elements and neodymium isotopes in sedimentary organic matter. *Geochim. Cosmochim. Acta* 140, 177–198. doi: 10.1016/j.gca.2014.05.016
- Fröllig, H., Pahnke, K., Schnetger, B., Brumsack, H.-J., Dulai, H., and Fitzsimmons, J. N. (2016). Hawaiian imprint on dissolved Nd and Ra isotopes and rare earth elements in the central North Pacific: local survey and seasonal variability. *Geochim. Cosmochim. Acta* 189, 110–131. doi: 10.1016/j.gca.2016.06.001
- García-Solsona, E., Jeandel, C., Labatut, M., Lacan, F., Vance, D., Chavagnac, V., et al. (2014). Rare earth elements and Nd isotopes tracing water mass mixing and particle-seawater interactions in the SE Atlantic. *Geochim. Cosmochim. Acta* 125, 351–372. doi: 10.1016/j.gca.2013.10.009
- German, C. R., and Elderfield, H. (1990). Rare earth elements in the NW Indian Ocean. *Geochim. Cosmochim. Acta* 54, 1929–1940.
- Goldstein, S. J., and Jacobsen, S. B. (1987). The Nd and Sr isotopic systematics of river-water dissolved material: Implications for the sources of Nd and Sr in seawater. *Chem. Geol. Isot. Geosci. Sect.* 66, 245–272. doi: 10.1016/0168-9622(87)90045-5
- Goldstein, S. J., and Jacobsen, S. B. (1988). Nd and Sr isotopic systematics of river water suspended material: implications for crustal evolution. *Earth Planet. Sci. Lett.* 87, 249–265. doi: 10.1016/0012-821X(88)90013-1
- Goldstein, S. L., and Hemming, S. R. (2003). “Long-lived isotopic tracers in oceanography, paleoceanography, and ice-sheet dynamics,” in *Treatise on Geochemistry*, eds H. D. Holland, and K. K. Turekian (Pergamon; Oxford), 453–489.
- Goswami, V., Singh, S. K., and Bhushan, R. (2014). Impact of water mass mixing and dust deposition on Nd concentration and eNd of the Arabian Sea water column. *Geochim. Cosmochim. Acta* 145, 30–49. doi: 10.1016/j.gca.2014.09.006
- Grasse, P., Stichel, T., Stumpf, R., Stramma, L., and Frank, M. (2012). The distribution of neodymium isotopes and concentrations in the Eastern Equatorial Pacific: water mass advection versus particle exchange. *Earth Planet. Sci. Lett.* 353–354, 198–207. doi: 10.1016/j.epsl.2012.07.044
- Greaves, M. J., Elderfield, H., and Sholkovitz, E. R. (1999). Aeolian sources of rare earth elements to the Western Pacific Ocean. *Mar. Chem.* 68, 31–38.
- Grenier, M., Jeandel, C., Lacan, F., Vance, D., Venchiarutti, C., Cros, A., et al. (2013). From the subtropics to the central equatorial Pacific Ocean: neodymium isotopic composition and rare earth element concentration variations. *J. Geophys. Res. Oceans* 118, 592–618. doi: 10.1029/2012JC008239
- Gutjahr, M., Frank, M., Stirling, C. H., Keigwin, L. D., and Halliday, A. N. (2008). Tracing the Nd isotope evolution of North Atlantic Deep and Intermediate Waters in the western North Atlantic since the Last Glacial Maximum from Blake Ridge sediments. *Earth Planet. Sci. Lett.* 266, 61–77. doi: 10.1016/j.epsl.2007.10.037
- Gutjahr, M., Frank, M., Stirling, C. H., Klemm, V., van de Flierdt, T., and Halliday, A. N. (2007). Reliable extraction of a deepwater trace metal isotope signal from Fe–Mn oxyhydroxide coatings of marine sediments. *Chem. Geol.* 242, 351–370. doi: 10.1016/j.chemgeo.2007.03.021
- Haine, T. W. N., Watson, A. J., Liddicoat, M. I., and Dickson, R. R. (1998). The flow of Antarctic bottom water to the southwest Indian Ocean estimated using CFCs. *J. Geophys. Res. Oceans* 103, 27637–27653. doi: 10.1029/98JC02476
- Haley, B. A., Frank, M., Hathorne, E., and Pisias, N. (2014). Biogeochemical implications from dissolved rare earth element and Nd isotope distributions in the Gulf of Alaska. *Geochim. Cosmochim. Acta* 126, 455–474. doi: 10.1016/j.gca.2013.11.012
- Haley, B. A., and Klinkhammer, G. P. (2003). Complete separation of rare earth elements from small volume seawater samples by automated ion chromatography: method development and application to benthic flux. *Mar. Chem.* 82, 197–220. doi: 10.1016/S0304-4203(03)00070-7
- Haley, B. A., Klinkhammer, G. P., and McManus, J. (2004). Rare earth elements in pore waters of marine sediments. *Geochim. Cosmochim. Acta* 68, 1265–1279. doi: 10.1016/j.gca.2003.09.012
- Howe, J. N. W., Piotrowski, A. M., Oppo, D. W., Huang, K.-F., Mulitza, S., Chiessi, C. M., et al. (2016). Antarctic intermediate water circulation in the South Atlantic over the past 25,000 years. *Paleoc* 31, 1302–1314. doi: 10.1002/2016PA002975
- Hu, R., Piotrowski, A. M., Bostock, H. C., Crowhurst, S., and Rennie, V. (2016). Variability of neodymium isotopes associated with planktonic foraminifera in the Pacific Ocean during the Holocene and last glacial maximum. *Earth Planet. Sci. Lett.* 447, 130–138. doi: 10.1016/j.epsl.2016.05.011
- Huck, C. E., van de Flierdt, T., Jiménez-Espejo, F. J., Bohaty, S. M., Röhl, U., and Hammond, S. J. (2016). Robustness of fossil fish teeth for seawater neodymium isotope reconstructions under variable redox conditions in an ancient shallow marine setting: robustness of fossil fish tooth Nd. *Geochem. Geophys. Geosyst.* 17, 679–698. doi: 10.1002/2015GC006218
- Jacobsen, S. B., and Wasserburg, G. J. (1980). Sm–Nd isotopic evolution of chondrites. *Earth Planet. Sci. Lett.* 50, 139–155. doi: 10.1016/0012-821X(80)90125-9
- Jeandel, C. (2016). Overview of the mechanisms that could explain the ‘Boundary Exchange’ at the land–ocean contact. *Philos. Trans. R. Soc. Math. Phys. Eng. Sci.* 374:20150287. doi: 10.1098/rsta.2015.0287
- Jeandel, C., Bishop, J. K., and Zindler, A. (1995). Exchange of neodymium and its isotopes between seawater and small and large particles in the Sargasso Sea. *Geochim. Cosmochim. Acta* 59, 535–547. doi: 10.1016/0016-7037(94)00367-U
- Jeandel, C., Thouron, D., and Fieux, M. (1998). Concentrations and isotopic compositions of neodymium in the eastern Indian Ocean and Indonesian straits. *Geochim. Cosmochim. Acta* 62, 2597–2607. doi: 10.1016/S0016-7037(98)00169-0
- Johannesson, K. H., and Burdige, D. J. (2007). Balancing the global oceanic neodymium budget: Evaluating the role of groundwater. *Earth Planet. Sci. Lett.* 253, 129–142. doi: 10.1016/j.epsl.2006.10.021
- Johannesson, K. H., Chevis, D. A., Burdige, D. J., Cable, J. E., Martin, J. B., and Roy, M. (2011). Submarine groundwater discharge is an important net source of light and middle REEs to coastal waters of the Indian River Lagoon, Florida, USA. *Geochim. Cosmochim. Acta* 75, 825–843. doi: 10.1016/j.gca.2010.11.005

- Johannesson, K. H., Palmore, C. D., Fackrell, J., Prouty, N. G., Swarzenski, P. W., Chevis, D. A., et al. (2017). Rare earth element behavior during groundwater-seawater mixing along the Kona Coast of Hawaii. *Geochim. Cosmochim. Acta* 198, 229–258. doi: 10.1016/j.gca.2016.11.009
- Jones, C. E., Halliday, A. N., Rea, D. K., and Owen, R. M. (1994). Neodymium isotopic variations in North Pacific modern silicate sediment and the insignificance of detrital REE contributions to seawater. *Earth Planet. Sci. Lett.* 127, 55–66. doi: 10.1016/0012-821X(94)90197-X
- Jones, K. M., Khatriwala, S. P., Goldstein, S. L., Hemming, S. R., and van de Flierdt, T. (2008). Modeling the distribution of Nd isotopes in the oceans using an ocean general circulation model. *Earth Planet. Sci. Lett.* 272, 610–619. doi: 10.1016/j.epsl.2008.05.027
- Ku, T.-L., and Luo, S. (1994). New appraisal of radium 226 as a large-scale oceanic mixing tracer. *J. Geophys. Res. Oceans* 99, 10255–10273. doi: 10.1029/94JC00089
- Lacan, F., and Jeandel, C. (2001). Tracing Papua New Guinea imprint on the central equatorial Pacific Ocean using neodymium isotopic compositions and rare earth element patterns. *Earth Planet. Sci. Lett.* 186, 497–512. doi: 10.1016/S0012-821X(01)00263-1
- Lacan, F., and Jeandel, C. (2004a). Subpolar Mode Water formation traced by neodymium isotopic composition. *Geophys. Res. Lett.* 31:L14306. doi: 10.1029/2004GL019747
- Lacan, F., and Jeandel, C. (2004b). Neodymium isotopic composition and rare earth element concentrations in the deep and intermediate Nordic Seas: constraints on the Iceland Scotland overflow water signature. *Geochim. Geophys. Geosystems* 5:Q11006. doi: 10.1029/2004GC000742
- Lacan, F., and Jeandel, C. (2004c). Denmark Strait water circulation traced by heterogeneity in neodymium isotopic compositions. *Deep Sea Res. I Oceanogr. Res. Pap.* 51, 71–82. doi: 10.1016/j.dsr.2003.09.006
- Lacan, F., and Jeandel, C. (2005a). Acquisition of the neodymium isotopic composition of the North Atlantic Deep Water. *Geochim. Geophys. Geosyst.* 6:Q12008. doi: 10.1029/2005GC000956
- Lacan, F., and Jeandel, C. (2005b). Neodymium isotopes as a new tool for quantifying exchange fluxes at the continent-ocean interface. *Earth Planet. Sci. Lett.* 232, 245–257. doi: 10.1016/j.epsl.2005.01.004
- Lambelet, M., van de Flierdt, T., Crocket, K., Rehkämper, M., Kreissig, K., Coles, B., et al. (2016). Neodymium isotopic composition and concentration in the western North Atlantic Ocean: results from the GEOTRACES GA02 section. *Geochim. Cosmochim. Acta* 177, 1–29. doi: 10.1016/j.gca.2015.12.019
- Martin, J. H., Knauer, G. A., Karl, D. M., and Broenkow, W. W. (1987). VERTEX: carbon cycling in the northeast Pacific. *Deep Sea Res. Oceanogr. Res. Pap.* 34, 267–285.
- Mawji, E., Schlitzer, R., Dodas, E. M., Abadie, C., Abouchami, W., Anderson, R. F., et al. (2015). The GEOTRACES Intermediate Data Product 2014. *Mar. Chem.* 177, 1–8. doi: 10.1016/j.marchem.2015.04.005
- Millero, F. J. (1992). Stability constants for the formation of rare earth-inorganic complexes as a function of ionic strength. *Geochim. Cosmochim. Acta* 56, 3123–3132. doi: 10.1016/0016-7037(92)90293-R
- Morel, F. M. M., and Hering, J. G. (1993). *Principles and Applications of Aquatic Chemistry*, 1st Edn. New York, NY: Wiley-Interscience.
- Ngwenya, B. T., Magennis, M., Olive, V., Mosselmans, J. F. W., and Ellam, R. M. (2010). Discrete Site surface complexation constants for lanthanide adsorption to bacteria as determined by experiments and linear free energy relationships. *Environ. Sci. Technol.* 44, 650–656. doi: 10.1021/es9014234
- Osborne, A. H., Haley, B. A., Hathorne, E. C., Flögel, S., and Frank, M. (2014). Neodymium isotopes and concentrations in Caribbean seawater: Tracing water mass mixing and continental input in a semi-enclosed ocean basin. *Earth Planet. Sci. Lett.* 406, 174–186. doi: 10.1016/j.epsl.2014.09.011
- Piepgas, D. J., and Wasserburg, G. J. (1980). Neodymium isotopic variations in seawater. *Earth Planet. Sci. Lett.* 50, 128–138. doi: 10.1016/0012-821X(80)90124-7
- Piepgas, D. J., and Wasserburg, G. J. (1987). Rare earth element transport in the western North Atlantic inferred from Nd isotopic observations. *Geochim. Cosmochim. Acta* 51, 1257–1271. doi: 10.1016/0016-7037(87)90217-1
- Piotrowski, A. M., Goldstein, S. L., Hemming, S. R., and Fairbanks, R. G. (2004). Intensification and variability of ocean thermohaline circulation through the last deglaciation. *Earth Planet. Sci. Lett.* 225, 205–220. doi: 10.1016/j.epsl.2004.06.002
- Piotrowski, A. M., Goldstein, S. L., Hemming, S. R., and Fairbanks, R. G. (2005). Temporal relationships of carbon cycling and ocean circulation at glacial boundaries. *Science* 307, 1933–1938. doi: 10.1126/science.1104883
- Pourret, O., Davranche, M., Gruau, G., and Dia, A. (2007). Organic complexation of rare earth elements in natural waters: Evaluating model calculations from ultrafiltration data. *Geochim. Cosmochim. Acta* 71, 2718–2735. doi: 10.1016/j.gca.2007.04.001
- Rempfer, J., Stocker, T. F., Joos, F., Dutay, J.-C., and Siddall, M. (2011). Modelling Nd-isotopes with a coarse resolution ocean circulation model: Sensitivities to model parameters and source/sink distributions. *Geochim. Cosmochim. Acta* 75, 5927–5950. doi: 10.1016/j.gca.2011.07.044
- Rickli, J., Frank, M., Baker, A. R., Aciego, S., de Souza, G., Georg, R. B., et al. (2010). Hafnium and neodymium isotopes in surface waters of the eastern Atlantic Ocean: Implications for sources and inputs of trace metals to the ocean. *Geochim. Cosmochim. Acta* 74, 540–557. doi: 10.1016/j.gca.2009.10.006
- Rickli, J., Frank, M., and Halliday, A. N. (2009). The hafnium-neodymium isotopic composition of Atlantic seawater. *Earth Planet. Sci. Lett.* 280, 118–127. doi: 10.1016/j.epsl.2009.01.026
- Rickli, J., Gutjahr, M., Vance, D., Fischer-Gödde, M., Hillenbrand, C.-D., and Kuhn, G. (2014). Neodymium and hafnium boundary contributions to seawater along the West Antarctic continental margin. *Earth Planet. Sci. Lett.* 394, 99–110. doi: 10.1016/j.epsl.2014.03.008
- Roberts, N. L., and Piotrowski, A. M. (2015). Radiogenic Nd isotope labeling of the northern NE Atlantic during MIS 2. *Earth Planet. Sci. Lett.* 423, 125–133. doi: 10.1016/j.epsl.2015.05.011
- Rousseau, T. C. C., Sonke, J. E., Chmieleff, J., van Beek, P., Souhaut, M., Boaventura, G., et al. (2015). Rapid neodymium release to marine waters from lithogenic sediments in the Amazon estuary. *Nat. Commun.* 6:7592. doi: 10.1038/ncomms8592
- Schacht, U., Wallmann, K., and Kutterolf, S. (2010). The influence of volcanic ash alteration on the REE composition of marine pore waters. *J. Geochem. Explor.* 106, 176–187. doi: 10.1016/j.gexplo.2010.02.006
- Schijf, J., Christenson, E. A., and Byrne, R. H. (2015). YREE scavenging in seawater: a new look at an old model. *Mar. Chem.* 177, Part 3, 460–471. doi: 10.1016/j.marchem.2015.06.010
- Shiller, A. M., Chan, E. W., Joung, D. J., Redmond, M. C. and Kessler, J. D. (2017). Light rare earth element depletion during Deepwater Horizon blowout methanotrophy. *Sci. Rep.* 7:10389. doi: 10.1038/s41598-017-11060-z
- Sholkovitz, E. R. (1989). Artifacts associated with the chemical leaching of sediments for rare-earth elements. *Chem. Geol.* 77, 47–51.
- Sholkovitz, E. R. (1993). The geochemistry of rare earth elements in the Amazon River estuary. *Geochim. Cosmochim. Acta* 57, 2181–2190. doi: 10.1016/0016-7037(93)90559-F
- Sholkovitz, E. R., Landing, W. M., and Lewis, B. L. (1994). Ocean particle chemistry: the fractionation of rare earth elements between suspended particles and seawater. *Geochim. Cosmochim. Acta* 58, 1567–1579. doi: 10.1016/0016-7037(94)90559-2
- Sholkovitz, E. R., Piepgas, D. J., and Jacobsen, S. B. (1989). The pore water chemistry of rare earth elements in Buzzards Bay sediments. *Geochim. Cosmochim. Acta* 53, 2847–2856. doi: 10.1016/0016-7037(89)90162-2
- Singh, S. P., Singh, S. K., Goswami, V., Bhushan, R., and Rai, V. K. (2012). Spatial distribution of dissolved neodymium and eNd in the Bay of Bengal: role of particulate matter and mixing of water masses. *Geochim. Cosmochim. Acta*, 94, 38–96. doi: 10.1016/j.gca.2012.07.017
- Smethie, W. M., Fine, R. A., Putzka, A., and Jones, E. P. (2000). Tracing the flow of North Atlantic Deep Water using chlorofluorocarbons. *J. Geophys. Res. Oceans* 105, 14297–14323. doi: 10.1029/1999JC900274
- Smith, R. M., and Martell, A. E. (1989). *Critical Stability Constants*. Boston, MA: Springer.
- Spivack, A. J., and Wasserburg, G. J. (1988). Neodymium isotopic composition of the Mediterranean outflow and the eastern North Atlantic. *Geochim. Cosmochim. Acta* 52, 2767–2773.
- Stanley, J. K., and Byrne, R. H. (1990). The influence of solution chemistry on REE uptake by *Ulva lactuca* L. in seawater. *Geochim. Cosmochim. Acta* 54, 1587–1595. doi: 10.1016/0016-7037(90)90393-Y

- Steinfeldt, R., and Rhein, M. (2004). Spreading velocities and dilution of North Atlantic Deep Water in the tropical Atlantic based on CFC time series. *J. Geophys. Res. Oceans* 109:C03046. doi: 10.1029/2003JC002050
- Stewart, J. A., Gutjahr, M., James, R. H., Anand, P., and Wilson, P. A. (2016). Influence of the Amazon River on the Nd isotope composition of deep water in the western equatorial Atlantic during the Oligocene–Miocene transition. *Earth Planet. Sci. Lett.* 454, 132–141. doi: 10.1016/j.epsl.2016.08.037
- Stichel, T., Frank, M., Rickli, J., and Haley, B. A. (2012). The hafnium and neodymium isotope composition of seawater in the Atlantic sector of the Southern Ocean. *Earth Planet. Sci. Lett.* 317–318, 282–294. doi: 10.1016/j.epsl.2011.11.025
- Stichel, T., Hartman, A. E., Duggan, B., Goldstein, S. L., Scher, H., and Pahnke, K. (2015). Separating biogeochemical cycling of neodymium from water mass mixing in the Eastern North Atlantic. *Earth Planet. Sci. Lett.* 412, 245–260. doi: 10.1016/j.epsl.2014.12.008
- Stumpf, R., Frank, M., Schoenfeld, J., and Haley, B. A. (2010). Late Quaternary variability of Mediterranean Outflow Water from radiogenic Nd and Pb isotopes. *Quat. Sci. Rev.* 29, 2462–2472. doi: 10.1016/j.quascirev.2010.06.021
- Suess, E. (1980). Particulate organic carbon flux in the oceans - surface productivity and oxygen utilization. *Nature* 288, 260–263.
- Tachikawa, K., Arsouze, T., Bayon, G., Bory, A., Colin, C., Dutay, J.-C., et al. (2017). The large-scale evolution of neodymium isotopic composition in the global modern and Holocene ocean revealed from seawater and archive data. *Chem. Geol.* 457, 131–148. doi: 10.1016/j.chemgeo.2017.03.018
- Tachikawa, K., Athias, V., and Jeandel, C. (2003). Neodymium budget in the modern ocean and paleo-oceanographic implications. *J. Geophys. Res. Oceans* 108:3254. doi: 10.1029/1999JC000285
- Tachikawa, K., Jeandel, C., and Roy-Barman, M. (1999b). A new approach to the Nd residence time in the ocean: the role of atmospheric inputs. *Earth Planet. Sci. Lett.* 170, 433–446.
- Tachikawa, K., Jeandel, C., Vangriesheim, A., and Dupré, B. (1999a). Distribution of rare earth elements and neodymium isotopes in suspended particles of the tropical Atlantic Ocean (EUMELI site). *Deep Sea Res. Oceanogr. Res. Pap.* 46, 733–755.
- van de Flierdt, T., and Frank, M. (2010). Neodymium isotopes in paleoceanography. *Quat. Sci. Rev.* 29, 2439–2441. doi: 10.1016/j.quascirev.2010.07.001
- van de Flierdt, T., Griffiths, A. M., Lambelet, M., Little, S. H., Stichel, T., and Wilson, D. J. (2016). Neodymium in the oceans: a global database, a regional comparison and implications for palaeoceanographic research. *Phil. Trans. R. Soc. A* 374:20150293. doi: 10.1098/rsta.2015.0293
- Waterhouse, A. F., MacKinnon, J. A., Nash, J. D., Alford, M. H., Kunze, E., Simmons, H. L., et al. (2014). Global patterns of diapycnal mixing from measurements of the turbulent dissipation rate. *J. Phys. Oceanogr.* 44, 1854–1872. doi: 10.1175/JPO-D-13-0104.1
- Wilson, D. J., Piotrowski, A. M., Galy, A., and Clegg, J. A. (2013). Reactivity of neodymium carriers in deep sea sediments: Implications for boundary exchange and paleoceanography. *Geochim. Cosmochim. Acta* 109, 197–221. doi: 10.1016/j.gca.2013.01.042
- Yang, J., and Haley, B. (2016). The profile of the rare earth elements in the Canada Basin, Arctic Ocean. *Geochim. Geophys. Geosystems* 17, 3241–3253. doi: 10.1002/2016GC006412
- Zheng, X.-Y., Plancherel, Y., Saito, M. A., Scott, P. M., and Henderson, G. M. (2016). Rare earth elements (REEs) in the tropical South Atlantic and quantitative deconvolution of their non-conservative behavior. *Geochim. Cosmochim. Acta* 177, 217–237. doi: 10.1016/j.gca.2016.01.018

**Conflict of Interest Statement:** The authors declare that the research was conducted in the absence of any commercial or financial relationships that could be construed as a potential conflict of interest.

Copyright © 2017 Haley, Du, Abbott and McManus. This is an open-access article distributed under the terms of the Creative Commons Attribution License (CC BY). The use, distribution or reproduction in other forums is permitted, provided the original author(s) or licensor are credited and that the original publication in this journal is cited, in accordance with accepted academic practice. No use, distribution or reproduction is permitted which does not comply with these terms.



# Are Clay Minerals the Primary Control on the Oceanic Rare Earth Element Budget?

April N. Abbott\*, Stefan Löhrr and Megan Trethewy

*Marine Research Centre, Department of Earth and Planetary Sciences, Macquarie University, Sydney, NSW, Australia*

## OPEN ACCESS

### Edited by:

Catherine Jeandel,  
UMR5566 Laboratoire d'Etudes en  
Géophysique et Océanographie  
Spatiales (LEGOS), France

### Reviewed by:

Will Homoky,  
University of Oxford, United Kingdom  
Martine Buatier,  
Université Bourgogne  
Franche-Comté, France

### \*Correspondence:

April N. Abbott  
april.abbott@mq.edu.au

### Specialty section:

This article was submitted to  
Marine Biogeochemistry,  
a section of the journal  
Frontiers in Marine Science

**Received:** 30 November 2018

**Accepted:** 29 July 2019

**Published:** 20 August 2019

### Citation:

Abbott AN, Löhrr S and  
Trethewy M (2019) Are Clay Minerals  
the Primary Control on the Oceanic  
Rare Earth Element Budget?  
*Front. Mar. Sci.* 6:504.  
doi: 10.3389/fmars.2019.00504

The rare earth elements (REEs) are an important tool for understanding biogeochemical cycling and sedimentary processes in the global ocean. However, ambiguities in the marine REE budgets, including questions around the dominant source of REEs to the ocean, hinder the application of this tool. A bottom-up model for REE release into the ocean has recently been proposed, driven by early diagenetic processes such as sediment dissolution, with potentially significant implications for the interpretation of marine REE and Nd isotope paleo-records. Here, our goal is to identify the phase or phases that interact with the pore waters to drive such a benthic flux. We use new pore water REE, microbeam imaging and mineralogical data in combination with published pore water REE data to evaluate potential sedimentary REE host phases. Mineralogical and direct imaging observations suggest that authigenic Fe or Mn oxyhydroxides, which are widely considered a dominant REE host phase, are not sufficiently abundant sediment components to account for the high Nd concentrations recovered in reductive leaches, and are unlikely to be the primary source of pore water REEs. Pore water REE signatures similar to river sourced clays indicate a detrital clay dissolution source, while the spread in heavy to light REE enrichment in pore waters and bottom waters relative to this clay source is best explained by fractionation during authigenic clay uptake of REEs. We therefore conclude that clay mineral dissolution and authigenesis are likely the primary influences on the REE cycling near the seafloor. We propose that the balance between dissolution and authigenesis controls the concentration, ratio of heavy and light REE abundances, and the isotopic composition of the pore waters. We discuss the implications of this hypothesis on an oceanic REE budget controlled by a benthic flux from a sedimentary REE source, and the use of authigenic neodymium isotopes as a paleoproxy for shifts in ocean circulation.

**Keywords:** rare earth elements, diagenesis, clay minerals, neodymium isotopes, isotope geochemistry, benthic source, sediment phases, paleoclimate

## INTRODUCTION

The rare earth elements (REEs) are widely used in paleoceanographic studies. Also known as the lanthanides, the REEs are a series of 14 elements with largely coherent chemical properties (Elderfield and Greaves, 1982) used for applications ranging from reconstructing circulation and oxygen content to examining the influence of diagenesis. These applications rely on examining



fractionation within the REEs or the behavior of individual REEs. The fractionation of REEs is visualized through normalization to a reference such as shale or chondrite and can reveal information on oceanic and sedimentary processes (e.g., Elderfield and Greaves, 1982; Sholkovitz et al., 1994; Nozaki and Alibo, 2003; Alibo and Nozaki, 2004; Haley et al., 2004; Akagi, 2013; Hathorne et al., 2015; Abbott et al., 2015b; Skinner et al., 2019). For example, an increased stability of heavy rare earths (HREEs) in aqueous complexes results in the HREEs complexing more readily and remaining in solution (e.g., Goldberg et al., 1963; Turner et al., 1981; Wood, 1990; Akagi, 2013) whereas the light rare earths (LREEs) will more readily adsorb on particle surfaces (e.g., Byrne and Kim, 1990; Sholkovitz et al., 1994). Neodymium (Nd) is one REE that is commonly used individually as the Nd isotopic composition of seawater is considered a useful tracer of water mass circulation (e.g., von Blanckenburg, 1999). The isotopic signature ( $\epsilon_{\text{Nd}}$ ) of ferromanganese coatings, fossil fish teeth, and foraminifera recovered from the marine sedimentary record is a widely used tool for reconstructing past ocean circulation. Changes in global ocean circulation are inferred from the changes in the  $\epsilon_{\text{Nd}}$  of these authigenic records under the assumption that  $\epsilon_{\text{Nd}}$  is quasi-conservative in the global oceans (e.g., Vance and Burton, 1999; Frank, 2002; Haley et al., 2008; Böhm et al., 2015; Abbott et al., 2016b; Deane et al., 2017).

The usefulness of REEs to our understanding of the ocean is hampered by ambiguities in the modern cycling and oceanic budget of these REEs. Despite extensive progress in field and laboratory research on the utility of REE proxies (e.g., Amakawa et al., 2009; Carter et al., 2012; Grasse et al., 2012; Singh et al., 2012; Grenier et al., 2013; Pearce et al., 2013; Du et al., 2016; Skinner et al., 2019) and REE cycling in the ocean (e.g., Elderfield and Greaves, 1982; de Baar et al., 1985; Byrne and Kim, 1990; Bertram and Elderfield, 1993; Greaves et al., 1994; Zhang and Nozaki, 1996; Douville et al., 1999; Nozaki and Alibo, 2003; Haley et al., 2004, 2017; Lacan and Jeandel, 2005; Zhang et al., 2008; Johannesson et al., 2011; Jeandel et al., 2013; Hathorne et al., 2015; Rousseau et al., 2015; Abbott et al., 2015b; Grenier et al., 2018), the processes governing the modern budget remain surprisingly poorly constrained. The riverine dissolved flux was long considered the primary source of neodymium to the ocean (e.g., Bertram and Elderfield, 1993; Sholkovitz et al., 1999; Frank, 2002) but oceanic budgets that consider dissolved riverine and dust Nd sources still cannot balance the oceanic budget for either Nd concentrations or Nd isotopes (e.g., Bertram and Elderfield, 1993; Tachikawa et al., 2003). Recent estimates suggest that upward of 90% of oceanic neodymium inputs are “missing from the budget” (Tachikawa et al., 2003; Jones et al., 2008; Arsouze et al., 2009) with sediment dissolution, submarine groundwater discharge, dust, hydrothermal input, fluid-particle interaction, and reversible scavenging among the potential sources investigated to date (e.g., Piper, 1974; Bertram and Elderfield, 1993; Douville et al., 1999; Lacan and Jeandel, 2005; Jones et al., 2008; Arsouze et al., 2009; Freslon et al., 2014; Rickli et al., 2014; Rousseau et al., 2015; Stichel et al., 2015; Abbott et al., 2015b; Howe et al., 2016; Stewart et al., 2016; van de Flierdt et al., 2016; Zheng et al., 2016). Similar gaps are predicted for the budgets of the other lanthanides.

Since the particulate flux dominates fluvial REE transport to the ocean, dissolution of less than 3% of the particulate input could represent the largest oceanic REE source term (Jeandel and Oelkers, 2015), consistent with recent estimates that a benthic flux may account for near 90% of oceanic REE budget (Arsouze et al., 2009; Abbott et al., 2015b). Furthermore, the apparent decoupling between the non-conservative behavior of Nd concentrations and the quasi-conservative behavior of Nd isotopes, coined the “neodymium paradox” (e.g., Goldstein and Hemming, 2003; Lacan and Jeandel, 2005; Arsouze et al., 2009) raises questions around the validity of  $\epsilon_{\text{Nd}}$  as a quasi-conservative tracer of ocean circulation.

The uncertainties surrounding oceanic REE cycling are at least in part due to gaps in our understanding of the sedimentary host phase or phases acting as either REE sources or REE sinks. The relevance of these host phases to both the oceanic REE budget and the application of REE paleoproxies centers around (i) whether and under what conditions each potential phase acts as a sink of REE from the fluid phase (e.g., scavenging), a source of REE to the fluid phase (e.g., dissolution, remineralization), or exchanges with the fluid phase and (ii) over what time scale these solid-fluid interactions are occurring. A particulate phase acting as a sink when in contact with seawater will provide the best record of changes in ocean conditions through time. However, a phase that continues to act as a sink during burial will have any original seawater signature diagenetically overprinted as has already been proposed for biogenic phosphates and foraminifera (Palmer and Elderfield, 1985; Toyoda and Tokonami, 1990; Takahashi et al., 2015; Trotter et al., 2016; Zhang et al., 2016; Skinner et al., 2019).

A wide range of sediment components have been identified as potentially important REE host phases. These could either contribute REEs to the dissolved phase and drive a benthic source of REEs to the ocean or act as a sink of REEs from the fluid phase and thus potentially record environmental conditions. However, to date little robust, direct evidence of the role of these phases has been found. Potential host phases include Fe-Mn oxyhydroxides (e.g., Sholkovitz et al., 1994; Bayon et al., 2004; Haley et al., 2004; Ren et al., 2015; Takahashi et al., 2015), cerium oxides (e.g., Haley et al., 2004), phosphates (e.g., Kon et al., 2014; Takahashi et al., 2015; Zhang et al., 2016), biogenic silicates (e.g., Akagi et al., 2014), organic matter (e.g., Duncan and Shaw, 2003; Haley et al., 2004; Schacht et al., 2010; Kim et al., 2012; Freslon et al., 2014), volcanic ash (e.g., Vance et al., 2004; Elmore et al., 2011; Wilson et al., 2013), and clays (e.g., Cullers et al., 1975; Grandjean et al., 1987; Zhang et al., 2016). These sediment components may not contribute equally to REE cycling, and their contributions will vary in space and time as the amount of REEs remobilized from each phase is likely a function of mineralogy, mineral chemistry, reactivity, surface area, and other factors such as local pore water chemistry and redox state (e.g., Elderfield and Sholkovitz, 1987; Wilson et al., 2012). The distinct conditions of formation, alteration or dissolution of each potential host phase makes the identification of this phase important to paleo-interpretations. Currently, Fe-Mn oxyhydroxides are widely considered a sink for seawater REEs found ubiquitously throughout the global ocean and thus an important reactive pool of REEs in the sediments (e.g., Bayon et al., 2004), but clays are likely a larger total reservoir

in the sediments (e.g., Cullers et al., 1975) and the overall impact of silicate dissolution is potentially dominant (e.g., Jeandel and Oelkers, 2015). Uncertainty as to the major REE host phases can be attributed to limitations in the operationally defined techniques used to quantify their abundance and REE signature. The standard protocols used to target the Fe-Mn oxyhydroxide phases, for instance, use prescribed leaching procedures and are often assumed successful based on chemical characterization of the recovered leachate (e.g., Fe/Al and Nd/Fe ratios), while lacking direct observation of the targeted phase. The limitations of this purely geochemical approach is illustrated in recent work which showed that the “oxide coating” in foraminifera consists of Fe, Mn, and REEs absorbed directly from the surrounding pore fluids rather than a discrete oxyhydroxide phase (Skinner et al., 2019).

Here, we combine geochemical, mineralogical, and sedimentological data from sites in the North Pacific and Tasman Sea to identify the sedimentary phase or phases that control benthic cycling of REEs. We use standard mineralogical techniques (i.e., X-ray diffraction) coupled to novel microbeam imaging and mineral mapping for direct, unambiguous identification of potential REE host phases in marine sediments, allowing us to examine the relative abundance of these phases and determine their likely origin. We employ REE fingerprinting to identify the processes influencing the REEs in marine sediments and in the ocean via a pore water controlled benthic flux and examine the implications on the oceanic budget of REEs as well as the use of REEs as proxies in paleoceanographic studies. We argue that a significant role of surface sediments in the REE cycle is consistent with observations that corals, Fe-Mn nodules, and co-located sediment phases have the same  $\epsilon_{\text{Nd}}$  as bottom waters, with sediment diagenesis providing the Nd to bottom waters as well as the nodules and corals (e.g., Elderfield and Greaves, 1982; Abbott et al., 2015a; Roberts and Piotrowski, 2015).

## MATERIALS AND METHODS

### Sites and Sample Collection

We focus on sediment cores collected from three sites in the eastern North Pacific (2012–2013, R/V *Oceanus*) and three sites in the western Tasman Sea (2016, R/V *Investigator*) at water depths of approximately 200, 1500, and 3000 m (**Figure 1** and **Table 1**). For simplicity, we will refer to the 3 North Pacific sites as NP200, NP1500, and NP3000 and the Tasman Sea sites as TS200, TS1500, and TS3000, respectively. Exact water depths, locations, and site names from previous literature are available in **Table 1**. Detailed descriptions of core and pore water collection are available elsewhere (Abbott et al., 2015b; Abbott, 2019). Briefly, a multi-corer was deployed and cores with a visibly intact sediment-water interface were sectioned on board the ship into HCl cleaned centrifuge tubes in a glove bag filled with an inert ( $\text{N}_2$ ) atmosphere. After centrifugation, pore water was pulled off using an HCl cleaned syringe, filtered with a 0.45  $\mu\text{m}$  syringe filter, and acidified to  $\text{pH} \leq 2$  with distilled HCl. Sediments were frozen and later freeze dried prior to analyses.

### REE Analyses

Rare earth element analyses for the North Pacific pore waters have been previously reported (Abbott et al., 2015b, 2016a). Tasman Sea pore waters were analyzed using a SeaFAST II inline with a Thermo X-series II Inductively Coupled Plasma-Mass Spectrometer at the Keck Collaboratory for Plasma Mass Spectrometry (as described by Yang and Haley, 2016; Abbott, 2019). To compare the REE patterns of pore waters to potential host phases, we considered all pore water samples collected from the six sites (three North Pacific and three Tasman Sea) and other published marine pore water values (Haley et al., 2004; Abbott et al., 2015b). We did not include pore waters collected using Rhizons® because of the REE fractionation associated with this technique (Abbott et al., 2015b). We also excluded pore water data with less than ten of the REEs reported because these data did not allow for consistent comparison of REE signatures. The included data were grouped into quartiles using the neodymium concentration in each sample. Neodymium was chosen for its applicability to paleoceanographic reconstructions. All concentration data was normalized to PAAS (Taylor and McLennan, 1985) and then to praseodymium (Pr). The normalization to PAAS facilitates inter-REE comparisons despite large differences in natural abundance and the normalization to Pr facilitates direct inter-sample pattern comparison despite differences in concentration.

### Grain Size

Grain size was measured on the Tasman Sea samples using a MasterSizer 2000 laser granulometer at Macquarie University. Samples were analyzed pre-leach (freeze-dried) and post a buffered acetic acid decarbonization step (leach procedure after Abbott et al., 2016a,b). Two subsamples were loaded into the MasterSizer for each pre- and post-leach steps, which completed 2 measurement cycles 5 s apart per load for a total of four analyses per sample. All samples were analyzed using deionized water with the sample refractive index set to 1.544 and absorption set to 1. Samples were measured for 20 s (20,000 snaps) and the background was measured between each load for 10 s (10,000 snaps). The ultrasonic probe was set at 50% and remained on while the sample was loaded to a laser obscuration between 5 and 20% and then the probe was turned off at the start of each analysis. The stirrer was set at 500 rpm and the pump was set at 1250 rpm and remained on throughout loading and analyses. Grain size data for the North Pacific sites reported for comparison is from Abbott et al. (2016a).

### Mineralogy

Bulk mineralogy of representative samples from each site was determined by X-ray diffractometry (XRD) at Macquarie University. Freeze-dried but otherwise untreated samples were homogenized in an agate mortar and pestle, before back-loading into 25 mm internal diameter stainless steel sample holders. X-ray powder diffraction patterns spanning 5 to 90  $2\theta$  were collected using a PANalytical Aeris benchtop XRD instrument (0.02° step size, Cu-radiation source with 40 kV generator voltage and 15 mA tube current, 1/8 inch divergence slits, and

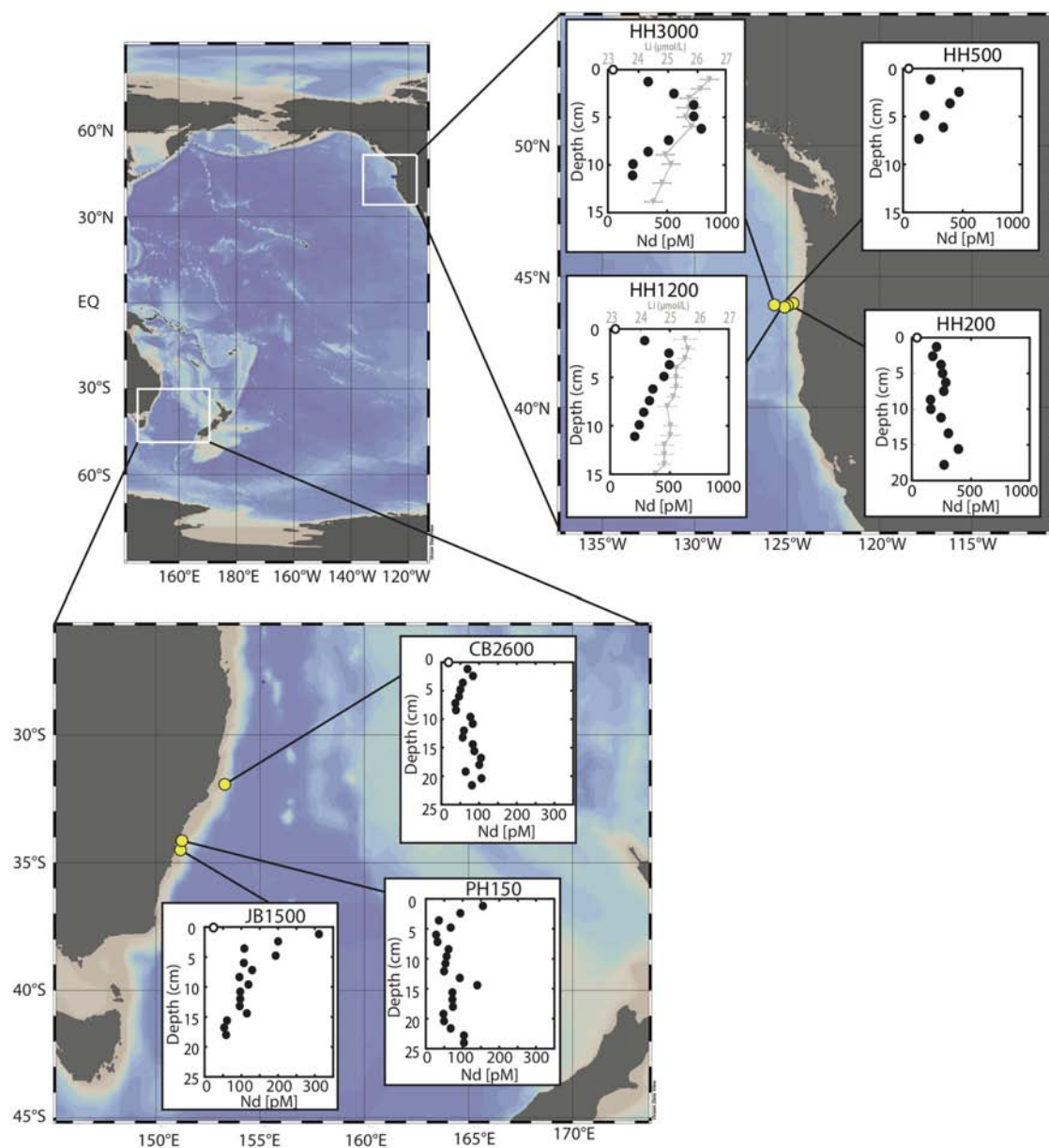


**FIGURE 1** | Site locations in the North Pacific and Tasman Sea. Pore water neodymium profiles shown for each site (neodymium concentrations from Abbott et al., 2015b; Abbott, 2019). Dissolved lithium pore water profiles are provided for NP1500 and NP3000 from Abbott et al., 2016a.

23 mm beam mask). Diffraction patterns were interpreted using Panalytical HighscorePlus software with the ICSD database for phase identification. The detection limit for bulk XRD analyses depends on the density, Z number, and crystal structure of the compounds in the sample, but corresponds to approximately 1% by volume (Cullity and Stock, 2001).

The mineralogy of the clay fraction in representative samples from each site was determined on oriented preparations of  $<2\ \mu\text{m}$  separates. The  $<2\ \mu\text{m}$  fraction was obtained by settling after carbonate removal using sodium acetate buffered acetic acid (for Tasman Sea sites only because North Pacific sites

are low carbonate) and ultrasonic dispersal. An aliquot was pipetted onto low background Si samples holders, air-dried and measured using the same instrument (Tasman Sea samples:  $2-30\ 2\theta$ ,  $0.02^\circ$  step size,  $1/8$  inch slits, 23 mm beam mask, beam knife in low position) or on a PANalytical Xpert-Pro MPD System (Oregon Margin samples:  $2-65\ 2\theta$ ,  $0.0167^\circ$  step size, Cu source with 45 kV generator voltage and 40 mA tube current, automatic slits). Clay diffraction patterns were collected both on air-dried samples and after treatment with ethylene glycol, with interpretation following Moore and Reynolds (1997). We did not attempt to directly geochemically characterize the



**TABLE 1** | Site locations and water depths.

	Site name	Latitude	Longitude	Water depth
Tasman Sea sites	TS200*	−34°07′	151°14′	150 m
	TS1500*	−34°29′	151°12′	1550 m
	TS3000*	−34°57′	153°18′	2660 m
North Pacific sites	NP200**	43° 55′	124° 41′	202 m
	NP1500**	43° 50′	124° 59′	1216 m
	NP3000**	43° 52′	125° 38′	3060 m

Sites denoted with a \* are from Abbott (2019) in which sites were referred to as PH150, JB1500, and CB2600, respectively. Sites denoted with a \*\* are from Abbott et al. (2015b) in which sites were referred to as HH200, HH1200, and HH3000, respectively.

detrital or authigenic clays in the sediments studied here because authigenic clays are typically small, interspersed grains and thus cannot be separated from detrital clays using physical separation techniques. Furthermore, our SEM-based petrographic work shows that even relatively large pellets of authigenic clays contain abundant detrital contaminants including igneous silicates and barite, preventing picked grains from representing a true authigenic signature. Since detrital and authigenic clay phases cannot be confidently separated from <2 μm, non-clay sedimentary fractions, the geochemical characterization of the clay size fraction would represent a mixed detrital clay, non clay, and authigenic clay signature. We therefore use available published characterizations of riverine clay to represent a detrital end member and authigenic phases (fish teeth, Fe-Mn crusts, glauconite) in our phase modeling.

## Electron Microscopy and Mineral Mapping

Polished resin mounts of the freeze-dried but otherwise untreated sediments were prepared using standard methods. The samples were not homogenized prior to resin embedding in order to preserve the spatial associations present within the sediment. Resin mounts were subsequently ion polished using a Hitachi IM4000 Argon Ion Mill (30 min at 10° beam incident angle, 5 kV accelerating voltage and continuous sample rotation) to remove surface damage from mechanical polishing which can otherwise obscure phase relations and the presence of nm-scale coatings. Ion milled samples were carbon-coated prior to scanning electron microscope (SEM) analysis on an FEI Teneo LoVac field emission SEM equipped with dual Bruker XFlash Series 6 energy dispersive X-ray spectroscopy (EDS) detectors. High-resolution back-scatter electron (BSE) images and mineral maps of 1 to 3 regions of interest were collected for each sample (13 mm working distance, 15 kV accelerating voltage). BSE image tilesets (100 nm pixel resolution) and EDS spectra (1 μm step size, 8 ms acquisition time) for mineral mapping were collected sequentially using the FEI Maps Mineralogy software, followed by classification of the individual EDS spectra using the FEI Nanomin software (Haberlah et al., 2015). Mineral identification is achieved by comparing EDS spectra collected in the mapped

area against reference spectra collected on known mineral standards, and is further constrained by independent XRD-based mineral identification. Unlike earlier SEM-based mineral mapping techniques (e.g., QEMSCAN), the Nanomin mineral classification system can de-convolve mixed X-ray spectra and assign up to three minerals per analyzed spot (Haberlah et al., 2015). This is a critical requirement for the correct interpretation of the mixed phase X-ray spectra characteristic of heterogeneous fine-grained sediments, where the X-ray generating electron interaction volume is commonly larger than the grain size. BSE photomicrographs, EDS elemental maps, and classified mineral maps provide direct visual evidence of grain relationships and common associations. While it is possible to convert these mineral maps into quantified percent compositions, the high heterogeneity of the samples coupled with the relatively small mapped areas results in a large uncertainty relative to bulk sample analyses such as XRD. Mineral mapping is employed here solely to test for the presence of, and establish the identity of trace phases that are too low for detection with the XRD.

## Fractionation Feasibility Modeling

We expect the REE pattern of the pore water to be influenced by both the source of REEs to the pore water and any sink of the REEs from the pore water. The fine-grained nature and intermingled distribution of most authigenic clays complicates an assessment of their REE content, and therefore of their potential influence on the pore water REE signature. However, glauconite is a widely occurring authigenic clay mineral which forms easily separated, macroscopic pellets (Baldermann et al., 2013, 2015) for which the REE signature is relatively well constrained (e.g., Huggett et al., 2017). Therefore, to test the feasibility of a clay driven pore water REE signature, we model the impact of glauconite formation on the pore water REE signature. For this calculation, we assume world river average clay (WRAC, Bayon et al., 2015) is the dominant source of pore water REEs (see section “Pore Water REE Patterns Support a Clay Dissolution Source” for a justification). Thus, we set the initial pore water value equivalent to WRAC ( $PW_0 = WRAC$ ) and we average the Shadwell, Abbey Mills, and top and bottom Victoria glauconites of Huggett et al. (2017) for our glauconite REE pattern. We estimate a partition coefficient,  $k$ , by taking the ratio of WRAC to average glauconite concentration of each REE. We model the alteration of the pore water REE pattern with continued uptake into glauconite as:

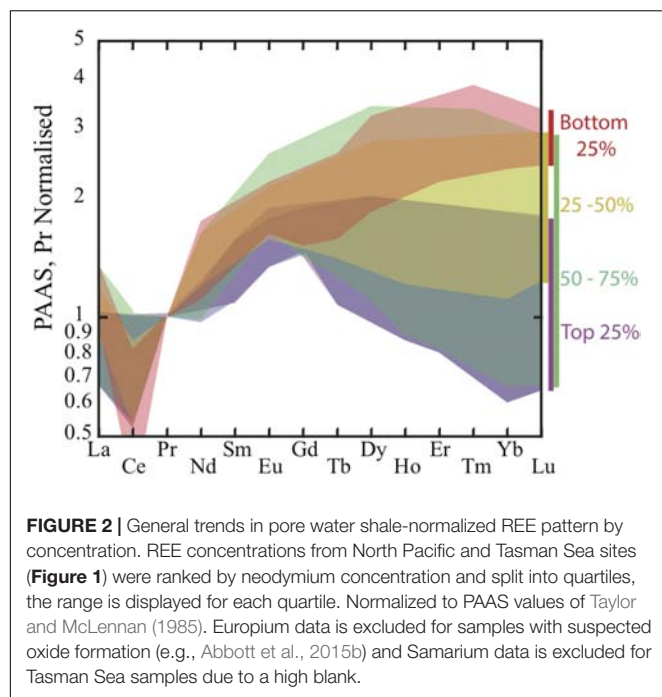
$$PW = P_c \times G + (1 - P_c) \times PW_0$$

where  $P_c$  is the percentage of  $PW_0$  lost to glauconite ( $G$ ) formation.

## RESULTS

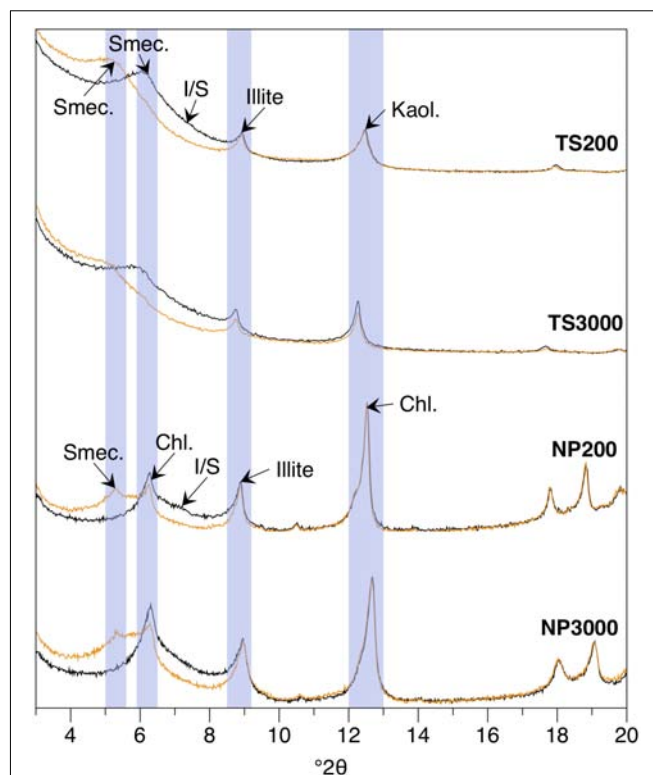
Pore water REE concentrations are up to two orders of magnitude enriched relative to ambient seawater with pore water concentrations ranging from 25 to 790 pmol Nd L<sup>−1</sup> and 1 to 30 pmol Lu L<sup>−1</sup> at these sites. In general, the highest pore water REE concentrations were observed in the North Pacific





(Abbott et al., 2015b) with lower concentrations observed in the Tasman Sea (Abbott, 2019). The enrichment of REE in pore fluid at these six sites is not as high as has been observed at other North Pacific sites (e.g., Haley et al., 2004 – 1280 pmol Nd L<sup>-1</sup> at Station 10; Abbott et al., 2015a – 2250 pmol Nd L<sup>-1</sup> at Station 2; Deng et al., 2017 – 1654 pmol Nd L<sup>-1</sup> at MABC25-1). Pore fluid concentrations show a shallow sub-surface maximum (<10 cm below the sediment water interface) across all sites, occurring in the upper 1–2 cm (Tasman Sea) and in the upper 4–7 cm (North Pacific) of the sediment column (Figure 1), which is consistent with an early diagenetic release of REEs to the pore water and a benthic source of REEs to the ocean (Abbott et al., 2015a,b; Abbott, 2019). The pore water REE maximum does not directly correlate with dissolved iron at the Tasman Sea sites nor the North Pacific sites, with the REE maximum occurring shallower in the sediment column than the appearance of dissolved iron (Abbott et al., 2015a; Abbott, 2019). The pore waters with the highest concentration of REEs have the flattest REE patterns with some middle REE (MREE) enrichment (Figure 2). These patterns typically become increasingly heavy REE (HREE) enriched as the amount of REEs in the pore water decreases (Figure 2). However, even the most HREE enriched pore waters do not match the HREE enrichment of seawater.

Grain size distributions were consistent down-core at each site for both pre- and post-leach measurements. Tasman Sea grain size distributions are largely bimodal pre-leach with only a single peak in post-leach (Supplementary Material). The primary grain size in pre-leached samples was coarse silt to very fine sand at both the 200 and 1500 m Tasman Sea sites, and the two dominant pre-leach grain sizes at the 3000 m site are very fine clay and medium silt. The primary grain size in post-leached samples was very fine clay at the 1500 and 3000 m sites and



medium silt at the 200 m site, reflecting dissolution of coarser biogenic carbonates during the acetic acid leach. The 200 m site in the North Pacific had a similar grain size distribution to the 200 m Tasman Sea site with medium silt the dominant grain size. The 3000 m site in the North Pacific was most similar to both the 1500 m and 3000 m Tasman Sea sites with a dominant grain size of very fine clay in the post-leach samples (Abbott et al., 2016a).

At all three Tasman Sea Sites clay fraction XRD reveals a consistent clay mineral assemblage comprised of kaolinite, illite, smectite and mixed-layer illite-smectite (Figure 3). However, two distinct sediment types can be distinguished on the basis of bulk XRD (Supplementary Material) and SEM-based mineral mapping (Figure 4). The shallow TS200 site features a poorly sorted, clay to fine sand (up to 150 μm) comprised of a mixture of terrestrially derived silt to fine sand grains (quartz, feldspar (albite), kaolinite, ankerite, lithics with quartz and feldspar ± ankerite ± rutile), biogenic calcite, aragonite and high-magnesium calcite (intact and fragmented foraminifera, bivalves, echinoid spines) and opal (sponge spicules) as well as a <5 μm fraction comprised of clay minerals and coccolithophore remains (Figure 4). Samples recovered at the deeper sites TS1500 and TS3000, by contrast, are calcareous oozes containing calcite, quartz, feldspar (albite), along with muscovite/illite, kaolinite,

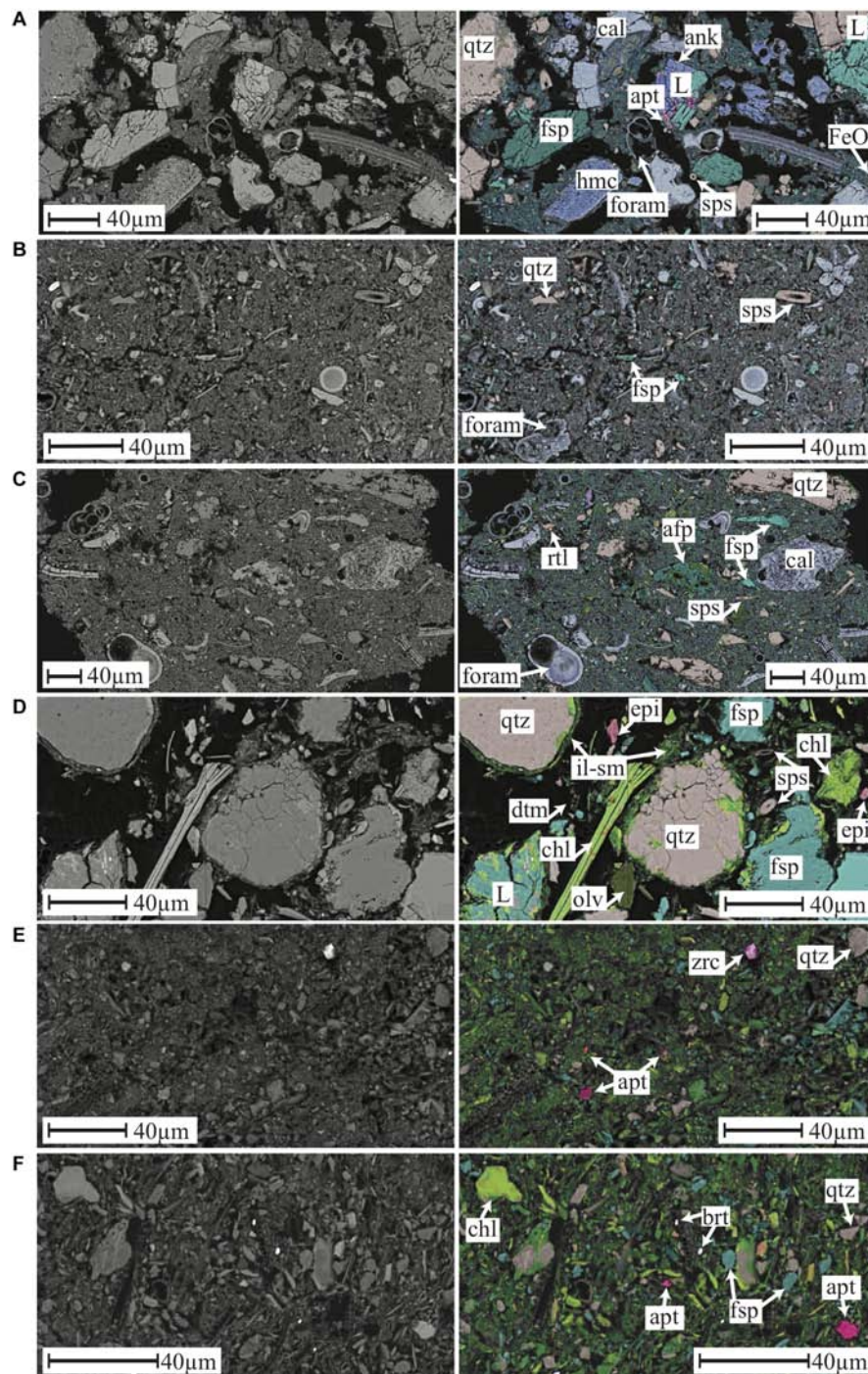


**FIGURE 4 |** SEM images BSE (left) and mineral map (right) for panel **(A)** TS200 1–2 cm, **(B)** TS1500 1–2 cm, **(C)** TS3000 1–2 cm, **(D)** NP200 2–3 cm, **(E)** NP1500 0–1 cm, and **(F)** NP3000 0–1 cm with selected features labeled as: L, lithic grain; cal, calcite; sps, sponge spicule; ank, ankerite; FeO, iron oxide; dol, dolomite; hmc, high Mg calcite; qtz, quartz; rtl, rutile; fsp, feldspar; afp, feldspar partially weathered to kaolinite; dtm, diatom; zrc, zircon; epi, epidote; olv, olivine; il-sm, illite and smectite; apt, apatite; chl, chlorite; brt, barite. Scale bars are 40  $\mu$ m for all panels.

and smectite (**Figures 3, 4**). SEM analysis reveals potentially wind-blown silt size quartz, feldspar and kaolinite at TS1500, with abundant silt and sand size foraminiferal tests, as well as siliceous sponge spicules (**Figure 4** and **Supplementary**

**Figure 2**). The  $<5 \mu$ m fraction is predominantly clay minerals and coccolithophore remains, with trace abundances of Fe-oxide, rutile, barite and silt-size zircon. TS3000 is very similar to TS1500, but has terrestrially derived detrital grains up to 150  $\mu$ m in size.



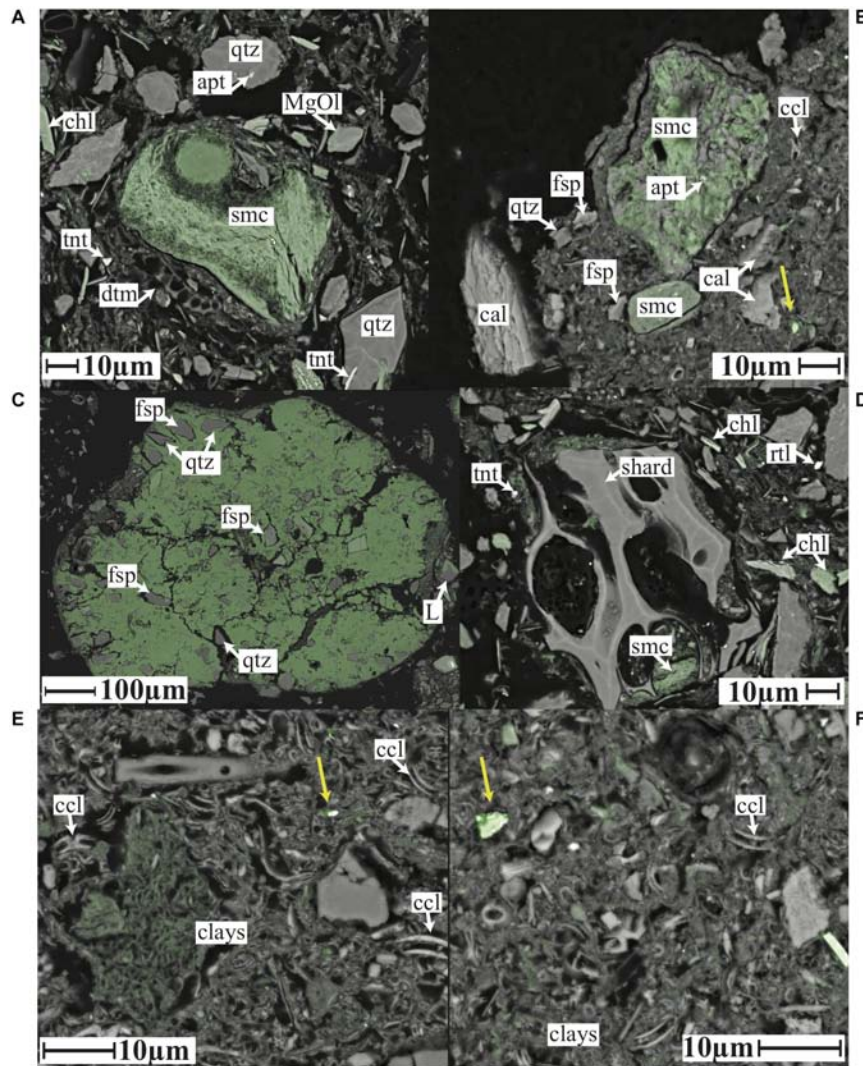


**FIGURE 5 |** Elemental iron (green) maps overlaid on SEM BSE images of (A) an incipient glauconite grain from NP200 2–3 cm, FeSmc, iron rich smectite (B) sediment grains from TS1500 1–2 cm, (C) an immature glauconite grain from the NP1500 0–1 cm that is low in K, high in iron, (D) volcanic glass shards surrounded by clay minerals from NP200 2–3 cm, and (E,F) iron rich clay aggregations from TS3000 1–2 cm. Small detrital iron oxide grains are visible in panels (B,E,F) as indicated by yellow arrows. All scale bars are 10  $\mu\text{m}$  except for panel (C) (100  $\mu\text{m}$ ). Selected features labeled as: MgOl, magnesium olivine; apt, apatite; qtz, quartz; smc, smectite; tnt, titanate; chl, chlorite; dtm, diatom; ccl, coccolithophore; cal, calcite; fsp, feldspar; L, lithic grain; rtl, rutile.

Bulk XRD analysis identifies a mineral assemblage consisting of quartz, feldspar (primarily albite), chlorite, mica (muscovite and/or illite), pyroxenes (augite or clinopyroxene), and amphibole (magnesian hornblende) at all three North Pacific sites (**Supplementary Material**). In addition, the two deeper sites show evidence for a significant X-ray amorphous component, identified as opaline silica (see below). Clay fraction XRD confirms the presence of illite, chlorite and smectite at all three sites (**Figure 3**). Mineral mapping confirms the presence of a similar mineral assemblage across all three North Pacific sites, but with a systematically decreased grain size, increased clay mineral, and increased biogenic component with depth (**Figure 4**). NP200 is a poorly sorted fine sand. The silt to sand size fraction is primarily comprised of quartz, Na-feldspar,

pyroxene (augite), epidote, and a Mg-silicate phase identified as Mg-olivine. Lithic grains (quartz and feldspar  $\pm$  rutile, mica/illite, chlorite, and illmenite) are abundant, while glass shards of likely volcanic origin are also observed (**Figure 5**). Abundant chlorite occurs both as discrete silt to fine sand-sized grains and within larger lithic grains. Siliceous biogenic remains (diatom frustules and sponge spicules) are present in both the silt and clay size fractions. NP1500 has a mineral assemblage similar to NP200, but with detrital mineral grains of silt size or finer ( $<60 \mu\text{m}$  diameter), fewer pyroxene, epidote and olivine, and no volcanic glass. Authigenic Fe smectite and glauconite pellets up to 1500  $\mu\text{m}$  are abundant at this site (**Figure 5**), and there is an increased contribution of clay minerals and siliceous biogenic debris relative to the shallower site. The

EDS elemental maps and subsequent Nanomin mineral maps reveal a wide range of textural maturities of the glauconite and Fe-smectite pellets present, ranging from fully formed mature pellets to fragile incipient pellets. While the mature pellets would be relatively resistant to physical breakdown if transported, the presence of incipient pellets that would not survive such transport makes *in-situ* clay authigenesis most likely. NP3000 is a well sorted siliceous ooze dominated by diatom remains. Detrital grains (feldspar, quartz, chlorite and muscovite, no lithic grains, volcanic glass, or glauconite) are up to 20  $\mu\text{m}$  diameter, with trace abundances of zircon, rutile, and apatite (**Figure 4**). However, the bulk of the detrital sediment component is  $<5 \mu\text{m}$  in size, comprising clays, minor feldspar and quartz, and trace amounts of barite and Fe oxides.

Fe and Mn oxyhydroxides are not evident in bulk X-ray diffraction patterns of any site studied here but can be difficult to detect when present as poorly crystalline or amorphous forms. Mineral mapping does reveal trace quantities of Fe oxides present as discrete,  $\mu\text{m}$  size grains which are likely of detrital origin (**Figure 5**) at all sites. However, EDS elemental maps show that iron is primarily hosted in the clay size fraction (all sites, **Figure 5**), but is also present in silt/sand size chlorite grains, their unaltered igneous precursor minerals (NP sites only – **Figure 4**), as well as Fe-smectite and glauconite pellets (NP1500 only – **Figure 5**). Mineral mapping does not identify Mn oxyhydroxides, but Mn elemental maps show patches of Mn enrichment relative to background at Site NP3000, which may represent local enrichments of nm-scale Mn oxyhydroxide intermingled with the clay mineral fraction. Positive identification of this Mn enriched material is beyond the instrumental resolution. However, while the 1  $\mu\text{m}$  step size and potentially several  $\mu\text{m}^3$  beam interaction volume during the mineral mapping and EDS analyses does not permit the direct identification of nm-scale coatings, the high Z-number of Fe and Mn oxyhydroxides relative to siliciclastic sediment components mean that aggregates of nanoscale Fe-Mn oxyhydroxides and coatings  $>100 \text{ nm}$  should be visible as bright zones in the high resolution backscatter electron images. Higher resolution ( $\sim 30 \text{ nm}$ ) field emission reveals some high Z-number material intermingled with the clay fraction, which may be Fe-Mn oxyhydroxides, but could also be barite, rutile, and apatite minerals as identified in larger grains through mineral maps. While this material is present in all samples, the amount of the material is  $<<1\%$  in all cases. This leads us to conclude that authigenic Fe or Mn grain coatings are a minor component of the sediments studied here, although we cannot rule out the presence of oxyhydroxide nanoparticles (10 s of nm) intermingled with the clay size fraction.

## DISCUSSION

### Fe-Mn Oxyhydroxide Unlikely to Account for Pore Water or Leachable “Authigenic” REE Compositions

Fe-Mn oxyhydroxides in marine sediments are a commonly targeted archive for reconstructing paleocirculation because they

are assumed to precipitate directly from ambient seawater, preserving a record of seawater REE composition (Rutberg et al., 2000; Bayon et al., 2002, 2004; Frank, 2002; Roberts and Piotrowski, 2015). Although macroscale Fe-Mn crusts and nodules are known to be important REE host phases (e.g., Bau et al., 2014; Conrad et al., 2016), they have a limited spatial distribution in the modern ocean. However, it is widely thought that Fe-Mn oxyhydroxides are ubiquitously present as REE enriched, nanoscale authigenic grain coatings similar to the Fe oxyhydroxides coatings known from terrestrially derived detrital silt and sand size grains (Manceau et al., 2007) or the nanoscale particles and aggregates attached to clays in the suspended fraction of tropical rivers (Poulton and Raiswell, 2005). Crucially, the distribution, preservation, and formation of these coatings remains poorly understood (e.g., Bayon et al., 2004) with no direct, imaging-based identification of their systematic presence to date. This is an important gap because the partitioning of REEs into these phases as well as the susceptibility of these coatings to reductive dissolution means that, where present, they are likely important contributors to pore water REE (e.g., Haley et al., 2004).

Attempts to quantify the abundance of these coatings have mostly relied on indirect, operationally defined chemical extractions rather than direct crystallographic, microscopic, or microbeam identification. This is also true more broadly of our knowledge of sedimentary trace element and REE host phases, which is largely informed by operationally defined chemical extractions; procedures known to be hampered by incomplete dissolution of the target phase, redistribution of elemental species through dissolution and subsequent secondary mineral precipitation, and dissolution of non-target phases (e.g., Taylor and McKenzie, 1966; Schwertmann and Pfab, 1994; Koschinsky and Hein, 2003; Wilson et al., 2013; Homoky et al., 2016; Skinner et al., 2019). Although sediment leachate trace metal ratios are reasonably similar to those measured on macroscopic Fe-Mn crusts (e.g., Gutjahr et al., 2007; Du et al., 2016), the well-established presence of phyllosilicate and phosphate phases in many Fe-Mn crusts (e.g., Rao, 1987; Bau et al., 1996; Hein et al., 1997) and the large range in sediment reductive leachate trace element ratios (e.g., Du et al., 2016 and references therein) leaves significant uncertainty as to the identity of the REE host phases dissolved by commonly used operationally defined leaching procedures. Nd/Fe ratios reported for reductive sediment leachates, for example, range from 0.001 to 0.01 compared to a much tighter range of only 0.001 to 0.002 for Fe-Mn crusts and nodules, whereas Al/Nd ratios in reductive sediment leachates are reported to fall between 50 – 400 compared to only 40 – 250 for Fe-Mn nodules and crusts (Du et al., 2016 and references therein) and Nd recovery associated with high Fe high Al phases has been observed (e.g., Wilson et al., 2013).

In addition, the large proportion of REEs recoverable through the same operationally defined sediment leaching procedures discussed above suggest that the phase or phases driving REE cycling in early sediment diagenesis should be sufficiently abundant to be readily identified by XRD or microscopically.



Specifically, mass balance calculations show that 55 to 70% of the bulk sediment REE content is recoverable through combined acetic acid and hydroxylamine hydrochloride sequential leaching, with up to 55% of those REEs recovered during the reductive hydroxylamine hydrochloride leach that is believed to target the oxyhydroxide phase (Abbott et al., 2016b). Based on an average concentration of 58 mg Nd kg<sup>-1</sup> for authigenic Fe-Mn nodules (Bau et al., 2014), 5300 ng Nd cm<sup>-3</sup> recovered through reductive leaching from NP3000 (Abbott et al., 2016a), and assuming a sediment density of 2.6 g cm<sup>-3</sup>, Fe-Mn phases would need to make up 3.5% of the bulk marine sediment to account for the Nd recovered in the reductive leaching procedure using:

$$S_p = \frac{R}{N} \times 100$$

where  $S_p$  is the calculated percent of sediment,  $R$  is the recovered Nd through reductive leaching (in mg Nd kg<sup>-1</sup>) and  $N$  is the measured concentration of Nd in the nodules (in mg Nd kg<sup>-1</sup>). This value ranges from 1.5 to 13% if we consider the entire spread of Fe-Mn nodule Nd concentrations reported by Bau et al. (2014), and the lower proportion of bulk sediment Nd concentrations recovered through reductive leaching at NP200 (Abbott et al., 2016a). Although this assessment of  $S_p$  is likely subject to a substantial margin of error due to the limited data available with which to constrain the proportion of leachable Nd relative to total Nd, in addition to differences in mineralogy between Fe-Mn nodules, crusts and authigenic Fe-Mn oxyhydroxide coatings, it nonetheless allows us to estimate the likely range of Fe-Mn oxyhydroxide abundance required to account for the Nd recovered by chemical leaching. While the lower limit of the  $S_p$  range we calculate is *just* sufficiently small that Fe-Mn oxyhydroxide phases may not be detected by powder X-ray diffraction (detection limit for Fe-Mn oxyhydroxide phases in siliciclastic matrix is approx. 2 wt%), careful microbeam mineralogical characterization of these samples also fails to identify a ubiquitous presence of authigenic Fe-Mn oxyhydroxides (Figures 4, 5) despite 5 to 9 wt% iron in the bulk sediment from each North Pacific site (Abbott et al., 2016a). This microbeam characterization revealed only trace quantities of 2–4 μm, detrital Fe oxyhydroxide grains (Figure 5). Instead, the bulk of the iron present at all sites appears to be hosted in the clay mineral fraction.

This is not to say that nanoscale Fe-Mn oxyhydroxides are not present. Recent work by Blaser et al. (2016), for example, repeatedly applied a modified “weak” reductive leach to sediments from over ten sites in the North Atlantic and consistently identified a rapid decline in Nd and Mn concentrations from the first leach to subsequent leaches. Leachate elemental ratios and Nd isotopic composition indicated only minimal contamination from non-target siliciclastic phases during the first leach step. Overall, this suggests that labile Nd-bearing Mn phases may be widespread but relatively low-abundance phase in marine sediments. Mössbauer spectroscopic analysis of a range of marine sediments further confirms the presence of widespread, low abundance reactive Fe oxyhydroxides in marine sediments, and identifies these to be

dominantly nanoscale (<12 nm diameter) goethite (van der Zee et al., 2003). Interestingly, goethite is considered to be relatively resistant to reductive leaching (Poulton and Canfield, 2005). The imaging approach used here does not have the resolution to identify nanoscale Fe-Mn oxyhydroxide, identifying only aggregates >200 nm in size. It is therefore likely that the Fe-clay association we identify in our samples is *partly* due to nano-scale intermingling and coating of clays by Fe-Mn oxyhydroxides. However, the presence of iron-bearing clays such as chlorite and Fe-smectite (nontronite) and the failure to identify Fe-Mn oxyhydroxides by XRD suggests that the major portion of clay-associated Fe is hosted within the clays, rather than representing discrete nanoscale oxyhydroxide coatings. This interpretation is consistent with the findings of Homoky et al. (2011) that Fe-Mn bearing clays may be a thermodynamically favorable explanation to the presence of nano-scale iron and manganese phases in pore water. We therefore argue that while Fe-Mn oxyhydroxides may be an ubiquitous trace component of marine sediments, they appear to be insufficiently abundant to represent the primary source of Nd in reductive leachates or pore fluids, consistent with recent observations that the REEs recovered by leaching procedures are not necessarily sourced from oxyhydroxide phases (e.g., Vance et al., 2004; Tachikawa et al., 2013; Osborne et al., 2017; Skinner et al., 2019).

The complex, but commonly observed relationship between Fe and Nd in marine pore waters and the range of observed Nd/Fe ratios (e.g., Haley et al., 2004; Gutjahr et al., 2007; Du et al., 2016; Abbott et al., 2016a) leads us to suggest that the REEs are remobilizing from iron containing phases other than Fe oxyhydroxides. This suggestion is consistent with recent research revealing the same sedimentary origin for REEs and iron in the Southern Ocean (Blain et al., 2008; Zhang et al., 2008; Grenier et al., 2018). Our EDS elemental mapping suggests the primary iron host in the sediments studied here to be the clay mineral fraction (Figure 5). Indicators more commonly interpreted as evidence for oxyhydroxide coating recovery during reductive leaches, including trace metal ratios within the leachate (e.g., Gutjahr et al., 2007; Du et al., 2016), REE patterns (e.g., Gutjahr et al., 2007), and the agreement between the recovered neodymium with the overlying seawater (e.g., Elderfield and Greaves, 1982; Palmer and Elderfield, 1985; Rutberg et al., 2000; Roberts and Piotrowski, 2015) are also consistent with a benthic control model of REEs (Haley et al., 2017) that could be driven by clay minerals as we propose here. Further supporting this hypothesis is the correlation between finer average grain sizes, higher pore water REE concentrations (e.g., Abbott et al., 2016a), and higher sediment REE concentrations (e.g., Sa et al., 2018); consistent with higher reactivities of fine-grained, high surface clays than of coarser sediment component. We propose that clay dissolution and authigenesis may provide the universal controls on the sedimentary release (e.g., reverse scavenging; Elderfield and Greaves, 1982; Jeandel et al., 1995) and uptake (e.g., authigenic clay formation; Michalopoulos and Aller, 1995; Rahman et al., 2017) of REEs, and may therefore be the primary driver of REE distribution in seawater, pore water, and marine authigenic phases.

## Mechanisms of REE Release From Clay Minerals

Chemical transfer reactions among terrestrially derived particles and seawater include adsorption/desorption, ion exchange, and dissolution/precipitation reactions (e.g., Elderfield and Sholkovitz, 1987; Jeandel et al., 1995; Rousseau et al., 2015; Homoky et al., 2016). Desorption and ion exchange tend to be relatively rapid processes, driven by salinity increases and changes in fluid major ion composition occurring as soon as river-borne particles come into contact with higher salinity estuarine waters (e.g., Rousseau et al., 2015). The conservative nature of major seawater ions and uniform salinity of bottom water versus pore water therefore suggest that exchange reactions are unlikely to play a significant role in the transfer of REEs from clays to pore water at our study sites. Dissolution and precipitation reactions, on the other hand, are longer-term processes that continue as long as the minerals are out of equilibrium with the adjacent fluid. The rate of dissolution and precipitation will change through time as a function of the saturation of the surrounding pore waters, as seen in batch reactor experiments (Oelkers et al., 2011). While the rates and extent of dissolution are hard to quantify due to simultaneously occurring secondary precipitation reactions (Oelkers et al., 2011; Pearce et al., 2013; Rousseau et al., 2015; Homoky et al., 2016), these experiments and investigations of Nd isotope evolution along estuarine salinity gradients do show that dissolution progresses rapidly (days to weeks) and is of sufficient magnitude to impact on oceanic REE budgets. Closed-system dissolution experiments, for instance, show 0.4% of the Nd contained in natural basaltic particles is released after only one month, sufficient to alter the initial  $\epsilon_{\text{Nd}}$  composition of the seawater to that of the bulk basalt (Pearce et al., 2013). Modeling studies constrained by oceanic  $\epsilon_{\text{Nd}}$  distributions suggest up to 1–3% of the continentally derived sediments may dissolve into seawater (Lacan and Jeandel, 2005; Arsouze et al., 2009). This estimated dissolution is several orders of magnitude greater than the amount of dissolution required (<0.001%) to account for elevated (relative to seawater) pore water Nd concentrations at the North Pacific sites (Abbott et al., 2016a; we do not estimate this for Tasman Sea sites as bulk sediment REE data is currently unavailable).

A disproportional contribution to this 0.001 to 3% total sediment dissolution from clay minerals is likely because mineral dissolution rates are commonly a function of surface area (e.g., Schott et al., 2009, 2012). For comparison, the specific surface areas of common clay minerals [ $\text{N}_2$  sorption Brunauer–Emmett–Teller (BET) surface areas of illite and smectite are 76–91  $\text{m}^2\text{g}^{-1}$  and 32–97  $\text{m}^2\text{g}^{-1}$ , respectively; Van Olphen and Fripiat, 1979] are up to two orders of magnitude greater than that of the ground mineral powders used in typical laboratory dissolution experiments (e.g., Chairat et al., 2007; Oelkers et al., 2008). In addition, ubiquitously distributed  $\text{Fe}^{3+}$  containing clays (including chlorite, illite, smectite, and mixed-layer clays) are susceptible to microbially mediated alteration via reductive dissolution (Kim et al., 2004; Vorhies and Gaines, 2009; Liu et al., 2012; Zhang et al., 2012; Ijiri et al., 2018). Given that

microbially mediated clay mineral dissolution occurs because of the reduction of structural  $\text{Fe}^{3+}$  (Dong et al., 2009), it stands to reason that these same minerals would be targeted by the reductive leachates used to isolate Fe-Mn oxyhydroxide phases. Evidence for dissolution of silicate phases, including clays, by reductive hydroxylamine hydrochloride leaches can be found in a recent sequential leaching study of North Atlantic sediments, which documented substantial Al and Fe mobilization from the silicate fraction after repeated exposure to a “weak” reductive leach (Blaser et al., 2016). This could reconcile the operational defined leachate evidence for a significant Fe-Mn oxyhydroxide REE host phase in the absence of visible authigenic Fe-Mn oxyhydroxide coatings. Furthermore, clay mineral dissolution could at least partly explain the relationship between pore water dissolved iron and REEs in some sedimentary settings and a lack of a clear relationship in others (e.g., Haley et al., 2004; Abbott et al., 2015b), depending on the Fe content of the clays in question.

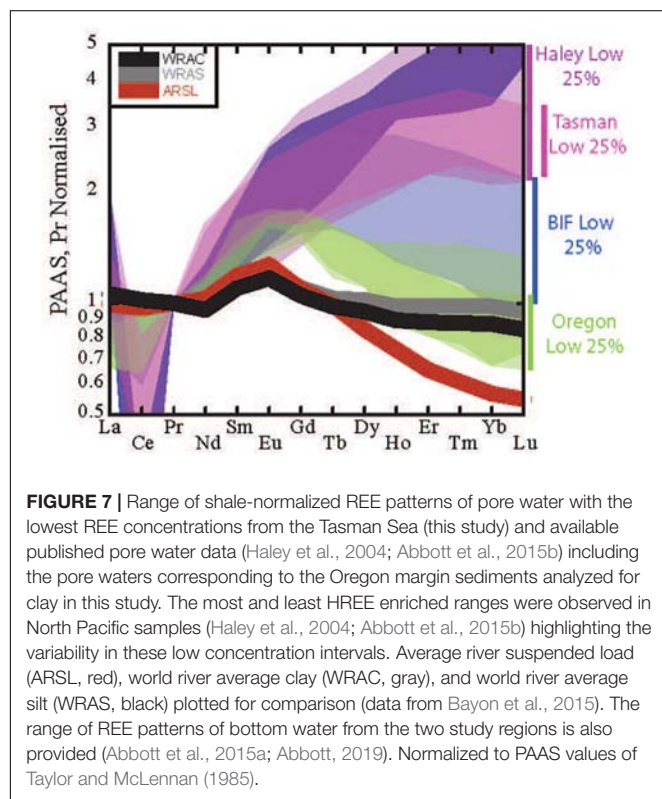
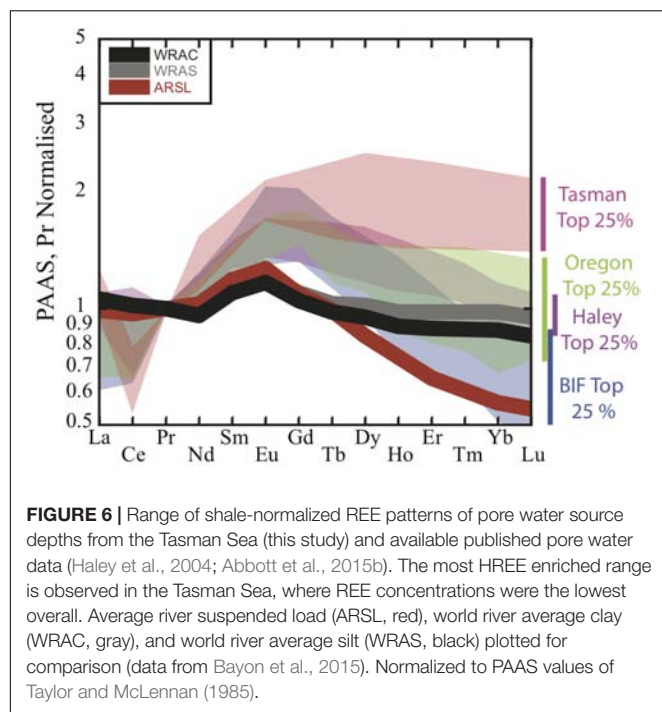
## Pore Water REE Patterns Support a Clay Dissolution Source

If we assume that a single process, or source, dominates the benthic REE cycle then the REE pattern and concentrations of the pore water should be a function of the source of REEs and any simultaneous sink, such that:

$$PW = S - P$$

whereas  $PW$  is the pore water,  $S$  is the host phase of REE in the sediments acting as the source and  $P$  is the loss of REEs through adsorption or authigenic mineral precipitation. In our considerations of  $P$ , we ignore the diffusive flux out of the sediments as this flux is not considered a mechanism for fractionation and thus will not change the REE pattern or isotopic signature of the pore water. Using this basic framework, we can examine the range of REE patterns observed in pore waters and authigenic phases in order to test the hypothesis that clays are the primary drivers of benthic REE cycles.

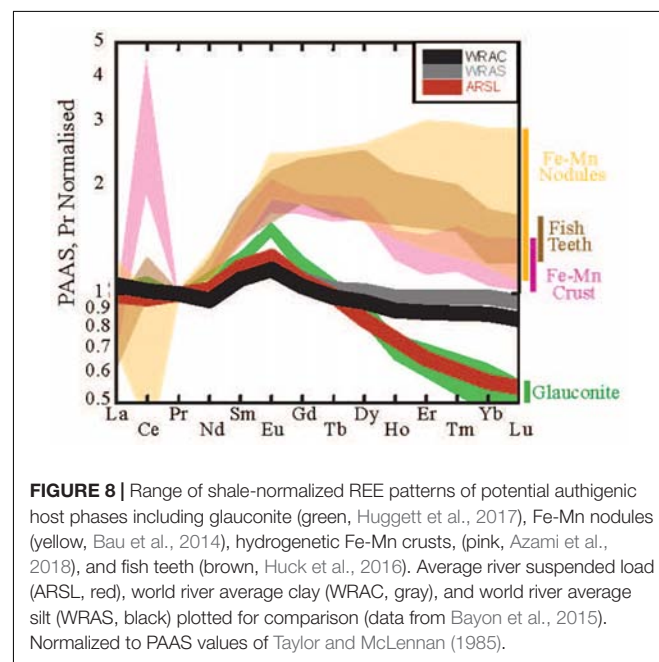
We expect the pore water REE signature to be most similar to the source phase REE signature at depths that have the highest overall pore water REE concentrations, i.e., the depth at which  $P$  is most likely to approach 0 (“source” depth of Abbott et al., 2015b). We find that the most Nd enriched pore waters show REE signatures similar to the pattern of World River Average Clay (WRAC, Figure 6; Bayon et al., 2015), consistent with clay dissolution as the source of REEs. Pore waters with lower REE concentrations, by contrast, have more variable REE patterns that do not closely match the WRAC pattern, and are generally more HREE enriched than the higher concentration pore waters (Figure 7). This could reflect REE sourced from a host phase other than clays (i.e., a different  $S$ -term in framework above), but we argue that this is more likely caused by a modification of the pore water pattern by fractionation from REE sorption or incorporation in authigenic minerals ( $P$  term in framework above).



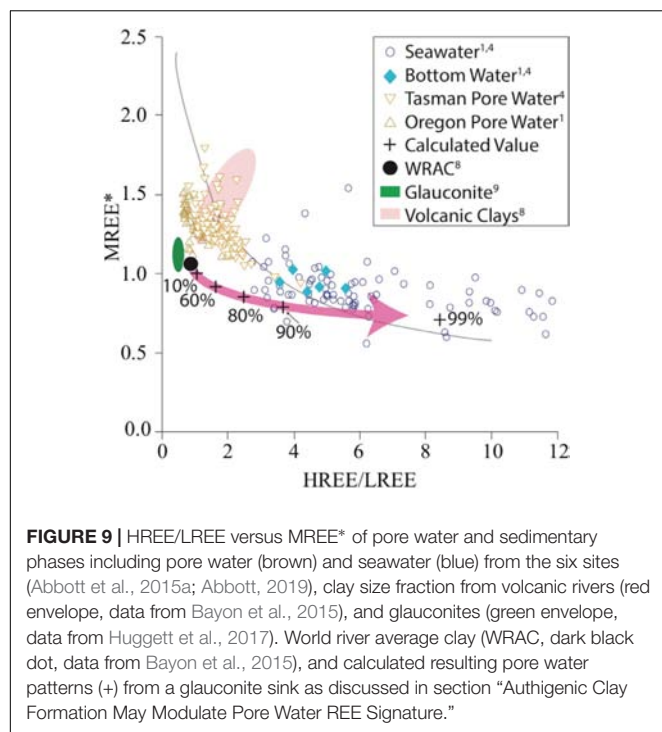
## Authigenic Clay Formation May Modulate Pore Water REE Signature

As noted in section “Mechanisms of REE Release From Clay Minerals,” experimental quantification of the rates and extent

of dissolution of detrital sedimentary material is complicated by simultaneously occurring precipitation reactions producing a range of secondary minerals (e.g., Oelkers et al., 2011), mostly aluminosilicates. A wide range of secondary minerals including phyllosilicates, Fe-Mn oxyhydroxides and phosphates are known to form during early diagenesis, each of which are known to preferential scavenge LREEs, leading to HREE enrichment in the pore water (Cantrell and Byrne, 1987; Byrne and Kim, 1990; Byrne and Kim, 1993; Jeandel and Oelkers, 2015). Of these, authigenic clays are likely the most widespread and quantitatively significant authigenic phase. We explore the impact of secondary mineral precipitation on pore water REE patterns using a simple mass balance calculation, assuming that the starting REE pattern of pore water resembles WRAC (in agreement with section “Pore Water REE Patterns Support a Clay Dissolution Source”), and that the secondary phase responsible for REE uptake is an authigenic glauconite clay (Figure 8, see also section “Fractionation Feasibility Modeling”). We find that increased removal of REEs by glauconite produces an increasingly seawater-like pattern in the residual dissolved phase (Figure 9). Specifically, we observe an increase in HREE/LREE and a decrease in the MREE anomaly. Because experimental and modeling work suggests dissolution of detrital silicates releases up to 0.4 to 3% of the solid phase REEs, but pore water has several orders of magnitude less REEs per volume than the accompanying solid phase (<0.001%, Abbott et al., 2016a), we consider the high authigenic phase REE uptake (~90%) required to produce a seawater-like HREE/LREE and MREE signal from a WRAC dissolution source to be reasonable. However, the resulting MREE anomaly is slightly lower than that observed in pore water, fish teeth, foraminifera, and Fe-Mn nodules. This discrepancy is likely because while WRAC is a useful starting point for our assessment of a clay source,







as an average value WRAC masks the broad range of REE signature of clays sourced from different bedrocks (e.g., Bayon et al., 2015). The dissolution of clay size fraction during early diagenesis is unlikely to be congruous, with some clay phases dissolving more rapidly or more completely than others. For example, clays in suspended load of rivers draining volcanic (basaltic) terrains are known to have greater MREE anomalies than WRAC and this detrital volcanic material may preferentially influence pore water (e.g., Dessert et al., 2003; Vance et al., 2004; Wilson et al., 2013). Rivers draining basaltic terrains contribute heavily to clays throughout the Pacific Ocean, compatible with the MREE enrichment in pore water relative to WRAC even at source depths in the pore water profiles (Figure 9). The deep-sea clay fraction likely contains detrital clays sourced from a range of source areas, and disproportionate dissolution of a particular clay fraction, such as fine-grained, high surface smectite clay that is commonly of volcanic origin, may be what results in MREEs higher than WRAC. Equilibrium modeling identified Fe-bearing smectite clay as the most likely nano-colloidal phase present in pore water (Homoky et al., 2011) supporting the plausibility of this mechanism.

Several other independent lines of evidence support our inference that the HREE enrichment of the lower concentration pore waters is largely due to fractionation from clay authigenesis rather than the formation of authigenic oxyhydroxide or phosphate phases. Firstly, while not conclusive, microbeam characterization of the samples reveals only trace quantities of Fe oxyhydroxide and calcium phosphates, neither of which are of authigenic origin suggesting that these phases are not abundant enough to drive the REE composition of pore water. Secondly, findings that authigenic clays are the primary sink

for Li in the ocean (e.g., Vigier et al., 2008) support the importance of authigenic clay formation in marine elemental cycling. Pore water Li concentrations decrease with depth and with decreasing REE concentration at the same North Pacific sites (Abbott et al., 2015b). Together with the presence of Fe-smectite and glauconite pellets at NP1500, the pore water Li concentrations at sites with and without visible glauconite formation are evidence of authigenic clay formation (e.g., Stoffyn-Egli and Mackenzie, 1984). Furthermore, while we are unable to quantify authigenic clays at our sites, recent studies have proposed a significantly increased magnitude and spatial extent of authigenic clay formation/reverse weathering than previously believed (Michalopoulos and Aller, 1995; Rahman et al., 2017). Baldermann et al. (2015) for example, have shown that authigenic clays (glauconite) are a potentially more significant Fe sink in low-oxygen settings than authigenic Fe sulfides, whereas Rahman et al. (2017) use cosmogenic  $^{32}\text{Si}$  to estimate that authigenic clay formation is responsible for the burial of an estimated  $4.5\text{--}4.9 \times 10^{12}$  mol/yr Si, representing almost 50% of the total dissolved Si inputs to the ocean (Frings et al., 2016). Finally, our simple model demonstrates that clay authigenesis (reverse weathering) has the potential to push the pore water REE pattern away from the REE pattern of the primary host phase toward more seawater-like compositions.

## Implications for the Oceanic REE Budget

Observations of the non-conservative behavior of neodymium isotopes in the ocean have largely been concentrated around the margins (e.g., Lacan and Jeandel, 2005; Arsouze et al., 2009; Grasse et al., 2012; Wilson et al., 2013). In line with these observations, several additional but geographically limited sources of Nd to the ocean have been proposed, including submarine groundwater discharge (e.g., Johannesson et al., 2011), hydrothermal vents (e.g., Douville et al., 1999), and even localized detrital inputs (e.g., Howe et al., 2016). The relatively strict geographic limits of these inputs and the non-conservative behavior of  $\epsilon_{\text{Nd}}$  associated with these has allowed proxy records collected from outside of these regions to be interpreted under the assumption of quasi-conservative behavior of  $\epsilon_{\text{Nd}}$ . However, the ubiquitous distribution of clays throughout the global ocean means that a benthic source driven by clay minerals would not be limited by proximity to land or as a function of water depth. This supports the proposal of Abbott et al. (2015b) that a widespread benthic source of REEs from the pore water could be the major source of REEs to the ocean, thus balancing the oceanic budget. While studies have noted the potential influence of reactive, REE-enriched sedimentary components with distinctive Nd isotopic composition (relative to the bulk sediment) on the oceanic REE budget (e.g., Tachikawa et al., 2004; Wilson et al., 2013; Abbott et al., 2015b; Du et al., 2016), particularly at continental margin sites (e.g., “Boundary Exchange,” Lacan and Jeandel, 2005; Jeandel et al., 2007; Rousseau et al., 2015; Jeandel, 2016), our results suggest the margins are not necessarily the regions with the largest flux. Indeed, the more distal sites with smaller grained sediments likely have larger fluxes (e.g., Holdren and Berner, 1979; Abbott et al., 2016a; Sa et al., 2018). A higher flux from distal sites could explain the isotopic agreement between modern core



top leachates, pore water, and bottom water particularly if such a benthic flux is the dominant source of ocean Nd (e.g., Elderfield and Greaves, 1982; Abbott et al., 2015a; Haley et al., 2017). From this perspective, the absence of an anomalous isotopic signature in deep water regions is not indicative of a modest benthic flux, rather it is a predictable consequence of a long-term benthic flux from a major proportion of the seafloor. In other words, the absence of an anomalous signature in these regions is expected if sediment diagenesis is the dominant source of Nd to bottom waters (Elderfield and Greaves, 1982; Abbott et al., 2015b). On the other hand, regions near the margin are more prone to the additional influence of fresh reactive phases making the  $\epsilon_{\text{Nd}}$  of the flux in these areas more likely to be unique, and therefore noticeable.

Significant variation in  $\epsilon_{\text{Nd}}$  between suspended and dissolved riverine loads, dissolved riverine load and local bedrock, different sized sediment grains, as well as between organic matter and detrital material (VanLaningham et al., 2008; Viers et al., 2008; Freslon et al., 2014; Bayon et al., 2015; Hindshaw et al., 2018) all demonstrate the importance of host phase identification in balancing the oceanic REE budget and for the application of REEs as tools in biogeochemical studies. For instance, in some large river systems there is more than a 1 epsilon unit offset between silt and clay sized fraction, with the smaller clay sized particles being systematically more radiogenic (Bayon et al., 2015). Attributed to preferential weathering (Bayon et al., 2015), this suggests that some of the most labile components of the sediment flux to the ocean are not necessarily representative of the average composition of the corresponding drainage basin. Minor components of the bulk sediment are therefore able to shift pore water  $\epsilon_{\text{Nd}}$  away from the bulk sediment if these components are reactive and enriched in REEs, making for an  $\epsilon_{\text{Nd}}$  of the flux that is noticeably different to the bulk sediment and the expected bottom water value. This discrepancy is most likely to occur proximal to the source (e.g., continental margins), especially in regions with more recently eroded materials, consistent with existing observations of boundary exchange concentrated near the margins (e.g., Lacan and Jeandel, 2005; Arsouze et al., 2009; Jeandel, 2016). Generally, these considerations result in the actual source being more radiogenic than the bulk rock (e.g., Viers et al., 2008; Grenier et al., 2018; Hindshaw et al., 2018). This model could explain North Pacific pore water neodymium isotopes that were more radiogenic than the bulk sediment or leachable phases (Abbott et al., 2016a) and why near shore sites were more radiogenic off the Kerguelen Plateau (Grenier et al., 2018). If the glass shards at NP200 (Figure 5) are relatively easily dissolved after deposition, they may release a more radiogenic signature than that of the bulk sediments at that site.

The array of REE patterns associated with authigenic phases such as those measured in sediment leaches, fish teeth, and pore waters (Figure 9; the “authigenic array” of Du et al., 2016) can largely be explained as a balance between a WRAC REE source and the preferential uptake of LREEs by authigenic clays as demonstrated by the REE pattern of glauconite. While this combination of clay dissolution and clay authigenesis can explain the HREE/LREE variation observed in pore water and

seawater, the low MREE anomaly of these HREE enriched waters may indicate the role of additional processes but the formation of a MREE enriched authigenic phase (Figures 8, 9; e.g., Kang et al., 2014; Bayon et al., 2016; Trotter et al., 2016) would further decrease, rather than increase the MREE anomaly in the fluid phases. However, the MREE anomaly may be a result of local variability in the clay source, preferential dissolution of more labile clay fractions (i.e., volcanic), or fractionation associated with clay authigenesis not captured by the glauconites considered above. WRAC only considered large rivers covering an estimated 30% of the area that drains into the ocean (Bayon et al., 2015) and does not allow for the locally dominant, chemically distinct contribution of smaller river systems as mentioned above. The potential importance of the local to regional variability in the clay supply to the ocean is illustrated by the range of REE patterns associated with clays coming from volcanic landscapes versus large rivers (Figure 8; Bayon et al., 2015). This sensitivity to clay supply also means that the magnitude and signature of the benthic source may vary as a function of continental weathering, ocean circulation, and sediment provenance influences on the overall sediment supply.

## Implications to Paleoreconstructions

The association of iron and REEs with clay phases in the sediments emphasizes the need for caution in interpretations of the marine authigenic record. We suggest the leaching protocols typically employed to recover this authigenic record are not only targeting oxyhydroxide phases, but also attacking clay host phases. Conventional leaching techniques mobilize significant quantities of silicate hosted REEs particularly in carbonate poor sediments and can release up to 16% of sedimentary iron (e.g., Wilson et al., 2013; Blaser et al., 2016). Recent developments in leaching techniques using a gentler approach can minimize the “contamination” from a silicate fraction, but even these refined methods mobilize some of the silicate fraction in the absence of a carbonate buffer (Blaser et al., 2016, 2019). For instance, the recent sequential leaching experiments on a wide range of North Atlantic sediments that used a refined reductive leaching approach demonstrated progressively increased Al/Nd, accompanied by shifts in leachate  $\epsilon_{\text{Nd}}$  away from a foraminiferal/authigenic value toward a volcanoclastic/detrital silicate signature (Blaser et al., 2016). Several clay minerals contain structural  $\text{Fe}^{3+}$ , which is prone to reductive dissolution especially in smectite (Vorhies and Gaines, 2009) and thus could be a source of the iron recovered during reductive leaching protocols. Even our simple model of the effect of glauconite formation on a WRAC-like REE pattern in the pore water demonstrated that uptake by glauconites can plausibly lead to the HREE enrichment commonly observed in pore waters, seawater, and other authigenic phases (Figure 9, e.g., fish teeth, Fe-Mn nodules). We argue that the similarity of the REE pattern of authigenic phases such as Fe-Mn nodules (e.g., Bau et al., 2014) and fish teeth (e.g., Huck et al., 2016) to lower concentration pore waters (Figures 8, 9) is likely due to continuing exchange (and homogenization) between these authigenic phases and the pore waters, and not an original

Fe-Mn or phosphatic source of REEs to the pore water. This argument is consistent with diagenetic transfer of REE from clay minerals to biogenic phosphates in Ce anomaly mass balances (Grandjean et al., 1987) and would mean that the exchange between the sediments and pore water is continuing through early diagenesis. Thus, the authigenic phases in the sediments are going to record the balance of fluid-particle exchange in the pore water rather than a true bottom water signature, consistent with observed pore water-like REE patterns in Fe-Mn oxyhydroxide and biogenic phosphates (Figures 8, 9) with implications for our application of authigenic records to paleocirculation reconstructions.

The magnitude and character of the REE flux is likely to change in response to changing climate and the resulting changes in sediment supply. In this way, the apparent correlation between authigenic  $\epsilon_{Nd}$  records and major climatic events (e.g., Böhm et al., 2015; Howe et al., 2016; Abbott et al., 2016b; Deaney et al., 2017) makes sense. Ocean circulation is going to, at least in part, be responsible for sediment provenance at any given site with the climate and tectonic activity both exerting control over the sources of those sediments (e.g., continental weathering; VanLaningham et al., 2008; Viers et al., 2008); thus, we would still expect a correlation between the timing of  $\epsilon_{Nd}$  value excursions and intervals of climatic or oceanic change. This means that in a clay-driven system, the changes in REE and  $\epsilon_{Nd}$  in authigenic phases may reflect both changes in sediment provenance and changes in continental weathering regime. If widely applicable, clays as a source of pore water REEs may make clay type and distribution potentially useful factors for estimating the diagenetic overprinting of authigenic neodymium isotope records. The resulting authigenic signature in sediments would be a function of the REE content and reactivity of the solid phases present as well as the location, mineral association, and nature of the host phase as observed with strontium (McKinley et al., 2007). Furthermore, if reductive dissolution is an important component of overall sediment dissolution, then we may see a relationship between organic matter production and REE remobilization. If this is the case, a relationship between organic matter supply and the spatial and temporal variability of a benthic flux may exist which could link the benthic source of neodymium to the ocean and changes in continental weathering regimes through time.

## CONCLUSION

This study combined new high-resolution SEM images, mineral maps, pore water REE data, and sedimentological measurements to identify the phases actively involved in REE cycling in the upper sediment column. We conclude that:

- Although the Fe-Mn oxyhydroxide phases commonly invoked as sedimentary REE host phases are likely present as nanoscale grains smaller than the resolution of the imaging techniques used here, our calculations suggest that they are not present at sufficiently high abundances

to account for the REEs recovered using reductive leaching protocols.

- The REEs are likely associated with iron-bearing phases, but we argue that clay minerals are likely more significant REE host phases than Fe-Mn oxyhydroxides. The REE patterns associated with the pore water source depth are consistent with clay dissolution as the primary source of REEs.
- The fractionation associated with REE uptake during clay authigenesis provides a mechanism to explain the HREE/LREE spread of the authigenic array. An additional process or MREE depleted authigenic phase may be needed to completely explain the observed MREE anomalies depending on the variability of clay REE patterns not captured by WRAC and the glauconites included in this model.
- A clay driven benthic REE model also suggests that the sedimentary REE and  $\epsilon_{Nd}$  record will be subject to changes in sediment provenance and continental weathering, but potentially also sensitive to processes such as surface water export production which impact on pore-water pH and redox state and must be interpreted with caution.

A benthic control model of REE cycling that is driven by clay dissolution and clay authigenesis during early diagenesis would be widely applicable throughout the global ocean as a result of the ubiquitous distribution of clay minerals. This suggests sediments from the deep sea play an important role in the oceanic REE budget by supplying a significant benthic flux of REEs that has gone largely undetected due to the similarity between the isotopic value of the flux and the bottom water.

## AUTHOR CONTRIBUTIONS

AA collected the samples on board R/V *Oceanus* and R/V *Investigator* including pore water separations and filtration, and completed the REE analyses on the SeaFAST II. SL and MT prepared the sediment samples and completed the XRD analyses and grain size measurements. SL and AA prepared the samples for SEM imaging, supervised MT during her undergraduate research experience, drafted the manuscript, and prepared the figures. SL performed the mineral classifications. All authors contributed to the data representation and interpretation.

## FUNDING

All analyses were made possible by internal funding from Macquarie University to AA and SL.

## ACKNOWLEDGMENTS

We would like to thank the Captain and Crew of the R/V *Investigator* and the R/V *Oceanus* as well as Mark Lewis, Jason Fazey, and Rebecca D'arcy for making sample collection

possible; Benat Oliveira Bravo for help with data analyses; and Martin Kennedy, Damian Gore, Peter Wieland, Bruce Schaefer, Brian Haley, Chris Russo, and Russell Field for laboratory access and support. We also sincerely thank our reviewers and editor for improvements on previous versions of this manuscript.

## REFERENCES

- Abbott, A. N. (2019). A benthic flux from calcareous sediments results in non-conservative neodymium behavior during lateral transport: a study from the Tasman Sea. *Geology* 47, 363–366. doi: 10.1130/G45904.1
- Abbott, A. N., Haley, B., and McManus, J. (2015a). Bottoms up: sedimentary control of the deep North Pacific Ocean's  $\epsilon$ Nd signature. *Geology* 43, 1035–1038. doi: 10.1130/G37114.1
- Abbott, A. N., Haley, B., McManus, J., and Reimers, C. (2015b). The sedimentary source of dissolved rare earth elements to the ocean. *Geochim. Cosmochim. Acta* 154, 186–200. doi: 10.1016/j.gca.2015.01.010
- Abbott, A. N., Haley, B., and McManus, J. (2016a). The impact of sedimentary coatings on the diagenetic Nd flux. *Earth and Planet. Sci. Lett.* 144, 217–227. doi: 10.1016/j.epsl.2016.06.001
- Abbott, A. N., Haley, B. A., Tripathi, A. K., and Frank, M. (2016b). Constraints on ocean circulation at the paleocene-eocene thermal maximum from neodymium isotopes. *Clim. Past* 12, 837–847. doi: 10.5194/cp-12-837-2016
- Akagi, T. (2013). Rare earth element (REE) silicic acid complexes in seawater to explain the incorporation of REEs in opal and the “leftover” REEs in surface water: new interpretation of dissolved REE distribution profiles. *Geochim. Cosmochim. Acta* 113, 174–192. doi: 10.1016/j.gca.2013.03.014
- Akagi, T., Yasuda, S., Asahara, Y., Emoto, M., and Takahashi, K. (2014). Diatoms spread a high  $\epsilon$ Nd-signature in the North Pacific Ocean. *Geochem. J.* 48, 121–131. doi: 10.2343/geochemj.2.0292
- Alibo, D. S., and Nozaki, Y. (2004). Dissolved rare earth elements in the eastern Indian Ocean: chemical tracers of the water masses. *Deep Sea Res.* 51, 559–576. doi: 10.1016/j.dsr.2003.11.004
- Amakawa, H., Sasaki, K., and Ebihara, M. (2009). Nd isotopic composition in the central North Pacific. *Geochim. Cosmochim. Acta* 73, 4705–4719. doi: 10.1016/j.gca.2009.05.058
- Arsouze, T., Dutay, J.-C., Lacan, F., and Jeandel, C. (2009). Reconstructing the Nd oceanic cycle using a coupled dynamical biogeochemical model. *Biogeosciences* 6, 2829–2846. doi: 10.5194/bg-6-2829-2009
- Azami, K., Hirano, N., Machida, S., Yasukawa, K., and Kato, Y. (2018). Rare earth elements and yttrium (REY) variability with water depth in hydrogenetic ferromanganese crusts. *Chem. Geol.* 493, 224–233. doi: 10.1016/j.chemgeo.2018.05.045
- Baldermann, A., Warr, L. N., Grathoff, G. H., and Dietzel, M. (2013). The Rate and mechanism of deep-sea glauconite formation at the ivory coast – ghana marginal ridge. *Clays Clay Miner.* 61, 258–276. doi: 10.1346/CCMN.2013.0610307
- Baldermann, A., Warr, L. N., Letofsky-Papst, I., and Mavromatis, V. (2015). Substantial iron sequestration during green-clay authigenesis in modern deep-sea sediments. *Nat. Geosci.* 6, 885–889. doi: 10.1038/ngeo2542
- Bau, M., Koschinsky, A., Dulski, P., and Hein, J. R. (1996). Comparison of the partitioning behaviors of yttrium, rare earth elements, and titanium between hydrogenetic marine ferromanganese crusts and seawater. *Geochim. Cosmochim. Acta* 60, 1709–1725. doi: 10.1016/0016-7037(96)00063-4
- Bau, M., Schmidt, K., Koschinsky, A., Hein, J., Kuhn, T., and Usui, A. (2014). Discriminating between different genetic types of marine ferro-manganese crusts and nodules based on rare earth elements and yttrium. *Chem. Geol.* 381, 1–9. doi: 10.1016/j.chemgeo.2014.05.004
- Bayon, G., German, C. R., Boella, R. M., Milton, J. A., Taylor, R. N., and Nesbitt, R. W. (2002). An improved method for extracting marine sediment fractions and its application to Sr and Nd isotopic analysis. *Chem. Geol.* 187, 179–199. doi: 10.1016/S0009-2541(01)00416-8
- Bayon, G., German, C. R., Burton, K. W., Nesbitt, R. W., and Rogers, N. (2004). Sedimentary Fe-Mn oxyhydroxides as paleoceanographic archives and the role of Aeolian flux in regulating oceanic dissolved REE. *Earth Planet. Sci. Lett.* 224, 477–492. doi: 10.1016/j.epsl.2004.05.033
- Bayon, G., Skonieczny, C., Delvigne, C., Toucanne, S., Bermell, S., Ponzevera, E., et al. (2016). Environmental Hf-Nd isotopic decoupling in World river clays. *Earth Planet. Sci. Lett.* 438, 25–36. doi: 10.1016/j.epsl.2016.01.010
- Bayon, G., Toucanne, S., Skonieczny, C., André, L., Bermell, S., Cheron, S., et al. (2015). Rare earth elements and neodymium isotopes in world river sediments revisited. *Geochim. Cosmochim. Acta* 170, 17–38. doi: 10.1016/j.gca.2015.08.001
- Bertram, C. J., and Elderfield, H. (1993). The geochemical balance of the rare earth elements and neodymium isotopes in the ocean. *Geochim. Cosmochim. Acta* 57, 1957–1986. doi: 10.1016/0016-7037(93)90087-d
- Blain, S., Sarthou, G., and Laan, P. (2008). Distribution of dissolved iron during the natural iron-fertilization experiment KEOPS (Kerguelen Plateau, Southern Ocean). *Deep Sea Res. II* 55, 594–605. doi: 10.1016/j.dsr2.2007.12.028
- Blaser, P., Lippold, J., Gutjahr, M., Frank, N., Link, J. M., and Frank, M. (2016). Extracting foraminiferal seawater Nd isotope signatures from bulk deep sea sediment by chemical leaching. *Chem. Geol.* 439, 189–204. doi: 10.1016/j.chemgeo.2016.06.024
- Blaser, P., Pöppelmeier, F., Schulz, H., Gutjahr, M., Frank, M., Lippold, J., et al. (2019). The resilience and sensitivity of Northeast Atlantic deep water  $\epsilon$ Nd to overprinting by detrital fluxes over the past 30,000 years. *Geochim. Cosmochim. Acta* 245, 79–97. doi: 10.1016/j.gca.2018.10.018
- Böhm, E., Lippold, J., Gutjahr, M., Frank, M., Blaser, P., Antz, B., et al. (2015). Strong and deep Atlantic meridional overturning circulation during the last glacial cycle. *Nature* 517, 73–79. doi: 10.10138/nature14059
- Byrne, R. H., and Kim, K.-H. (1990). Rare earth element scavenging in seawater. *Geochim. Cosmochim. Acta* 54, 2645–2656. doi: 10.1016/j.chemosphere.2014.05.049
- Byrne, R. H., and Kim, K. H. (1993). Rare earth precipitation and coprecipitation behavior: the limiting role of PO43- on dissolved rare earth concentrations in seawater. *Geochim. Cosmochim. Acta* 57, 519–526. doi: 10.1016/0016-7037(93)90364-3
- Cantrell, K. J., and Byrne, R. H. (1987). Rare-Earth element complexation by carbonate and oxalate ions. *Geochim. Cosmochim. Acta* 54, 2645–2656.
- Carter, P., Vance, D., Hillenbrand, C. D., Smith, J. A., and Shoosmith, D. R. (2012). The neodymium isotopic composition of water masses in the eastern Pacific sector of the Southern Ocean. *Geochim. Cosmochim. Acta* 79, 41–59. doi: 10.1016/j.gca.2011.11.034
- Châirat, C., Schott, J., Oelkers, E. H., Lartigue, J.-E., and Harouiya, N. (2007). Kinetics and mechanism of natural fluorapatite dissolution at 25°C and pH from 3 to 12. *Geochim. Cosmochim. Acta* 71, 5901–5912. doi: 10.1016/j.gca.2007.08.031
- Conrad, T., Hein, J. R., Paytan, A., and Clague, D. A. (2016). Formation of Fe-Mn crusts within a continental margin environment. *Ore Geol. Rev.* 87, 25–40. doi: 10.1016/j.oregeorev.2016.09.010
- Cullers, R. L., Chaudhuri, S., Arnold, B., Lee, M., and Wolf, C. W. Jr. (1975). Rare earth distributions in clay minerals and in the clay-sized fraction of the Lower Permian Havensville and Eskridge shales of Kansas and Oklahoma. *Geochim. Cosmochim. Acta* 39, 1691–1703. doi: 10.1016/0016-7037(75)90090-3
- Cullity, B. D., and Stock, S. R. (2001). *Elements of X-ray Diffraction*, 3rd Edn. Boston, MA: Addison-Wesley Publishing Co.
- de Baar, H. J. W., Bacon, M. P., Brewer, P. G., and Bruland, K. W. (1985). Rare earth elements in the Pacific and Atlantic Ocean. *Geochim. Cosmochim. Acta* 49, 1943–1959.
- Deaney, E. L., Barker, S., and van de Flierdt, T. (2017). Timing and nature of AMOC recovery across Termination 2 and magnitude of deglacial CO2 change. *Nat. Commun.* 8:14595. doi: 10.1038/ncomms14595

## SUPPLEMENTARY MATERIAL

The Supplementary Material for this article can be found online at: <https://www.frontiersin.org/articles/10.3389/fmars.2019.00504/full#supplementary-material>



- Deng, Y., Ren, J., Guo, Q., Cao, J., Wang, H., and Liu, C. (2017). Rare earth element geochemistry characteristics of seawater and porewater from deep sea in western Pacific. *Sci. Rep.* 7:16539. doi: 10.1038/s41598-017-16379-1
- Dessert, C., Dupre, B., Gaillardet, J., Louis, M., François, L. M., and Allegre, C. J. (2003). Basalt weathering laws and the impact of basalt weathering on the global carbon cycle. *Chem. Geol.* 202, 257–273. doi: 10.1016/j.chemgeo.2002.10.001
- Dong, H., Jaisi, D. P., Kim, J., and Zhang, G. (2009). Microbe-clay mineral interactions. *Am. Mineral.* 94, 1505–1519. doi: 10.2138/am.2009.3246
- Douville, E., Bienvenu, P., Charlou, J. L., Donval, J. P., Fouquet, Y., and Appriou, P. (1999). Yttrium and rare earth elements in fluids from various deep-sea hydrothermal systems. *Geochim. Cosmochim. Acta* 63, 627–643. doi: 10.1016/s0016-7037(99)00024-1
- Du, J., Haley, B. A., and Mix, A. C. (2016). Neodymium isotopes in authigenic phases, bottom waters and detrital sediments in the Gulf of Alaska and their implications for paleo-circulation reconstruction. *Geochim. Cosmochim. Acta* 193, 14–35. doi: 10.1016/j.gca.2016.08.005
- Duncan, T., and Shaw, T. J. (2003). The Mobility of rare earth elements and redox sensitive elements in the groundwater/seawater mixing zone of a shallow coastal aquifer. *Aquat. Geochem.* 9, 233–255. doi: 10.1023/b:aqua.0000022956.20338.26
- Elderfield, H., and Greaves, M. J. (1982). The rare earth elements in seawater. *Nature* 296, 214–219. doi: 10.1038/296214a0
- Elderfield, H., and Sholkovitz, E. R. (1987). Rare earth elements in the pore waters of reducing nearshore sediments. *Earth Planet. Sci. Lett.* 82, 280–288. doi: 10.1016/0012-821x(87)90202-0
- Elmore, A. C., Piotrowski, A. M., Wright, J. D., and Scrivner, A. E. (2011). Testing the extraction of past seawater Nd isotopic composition from North Atlantic deep sea sediments and foraminifera. *Geochem. Geophys. Geosyst.* 12:Q09008. doi: 10.1029/2011gc003741
- Frank, M. (2002). Radiogenic isotopes: tracers of past ocean circulation and erosional inputs. *Rev. Geophys.* 40, 1–1–1–38. doi: 10.1029/2000RG000094
- Freslon, N., Bayon, G., Toucanne, S., Bermell, S., Bollinger, C., Chéron, S., et al. (2014). Rare earth elements and neodymium isotopes in sedimentary organic matter. *Geochim. Cosmochim. Acta* 140, 177–198. doi: 10.1016/j.gca.2014.05.016
- Frings, P. J., Clymans, W., Fontorbe, G., La Rocha, De, C. L., and Conley, D. J. (2016). The continental Si cycle and its impact on the ocean Si isotope budget. *Chem. Geol.* 25, 12–36. doi: 10.1016/j.chemgeo.2016.01.020
- Goldberg, E. D., Koide, M., Schmitt, R. A., and Smith, R. H. (1963). Rare earth distributions in the marine environment. *J. Geophys. Res.* 68, 4209–4217. doi: 10.1029/jz068i014p04209
- Goldstein, S. L., and Hemming, S. R. (2003). “Long lived isotopic tracers in oceanography, paleoceanography, and ice sheet dynamics,” in *Treatise on Geochemistry*, ed. H. Elderfield (Amsterdam: Elsevier Pergamon Press).
- Grandjean, P., Cappetta, H., Michard, A., and Albarede, F. (1987). The assessment of REE patterns and  $^{143}\text{Nd}/^{144}\text{Nd}$  ratios in fish remains. *Earth Planet. Sci. Lett.* 84, 181–196. doi: 10.1016/0012-821x(87)90084-7
- Grasse, P., Stichel, T., Stumpf, R., Stramma, L., and Frank, M. (2012). The distribution of neodymium isotopes and concentrations in the Eastern Equatorial Pacific: water mass advection versus particle exchange. *Earth Planet. Sci. Lett.* 35, 198–207. doi: 10.1016/j.epsl.2012.07.044
- Greaves, M. J., Statham, P. J., and Elderfield, H. (1994). Rare earth element mobilization from marine atmospheric dust into seawater. *Mar. Chem.* 46, 255–260. doi: 10.1016/0304-4203(94)90081-7
- Grenier, M., Garcia-Solsona, E., Lemaitre, N., Trull, T. W., Bouvier, V., Nonnotte, P., et al. (2018). Differentiating lithogenic supplies, water mass transport, and biological processes on and off the Kerguelen Plateau using rare earth element concentrations and neodymium isotopic compositions. *Front. Mar. Sci.* 5:426. doi: 10.3389/fmars.2018.00426
- Grenier, M., Jeandel, C., Lacan, F., Vance, D., Venchiarutti, C., Cros, A., et al. (2013). From the subtropics to the central equatorial Pacific Ocean: neodymium isotopic composition and rare earth element concentration variations. *J. Geophys. Res. Oceans* 118, 592–618. doi: 10.1029/2012JC008239
- Gutjahr, M., Frank, M., Stirling, C. H., Klemm, V., van de Flierdt, T., and Halliday, A. N. (2007). Reliable extraction of a deepwater trace metal isotope signal from Fe-Mn oxyhydroxide coatings of marine sediments. *Chem. Geol.* 242, 351–370. doi: 10.1016/j.chemgeo.2007.03.021
- Haberlah, D., Löhr, S., Kennedy, M. J., Debenham, N., and Lattanzi, D. (2015). “Innovative sub-micron SEM-EDS mineral mapping and analysis applied to Australian shale samples,” in *Proceedings of the AAPG International Conference and Exhibition, Melbourne, Australia 13-16 September 2015: SEG Global Meeting Abstracts*, (Tulsa, OK: Society of Exploration Geophysicists), 419. doi: 10.1190/ice2015-2211146
- Haley, B. A., Du, J., Abbott, A. N., and McManus, J. (2017). The impact of benthic processes on rare earth element and neodymium isotope distributions in the oceans. *Front. Mar. Sci.* 4:426. doi: 10.3389/fmars.2017.00426
- Haley, B. A., Frank, M., Spielhagen, R. F., and Eisenhauer, A. (2008). Influence of brine formation on Arctic Ocean circulation over the past 15 million years. *Nat. Geosci.* 1, 68–72. doi: 10.1038/ngeo.2007.5
- Haley, B. A., Klinkhammer, G. P., and McManus, J. (2004). Rare earth elements in pore waters of marine sediments. *Geochim. Cosmochim. Acta* 68, 1265–1279. doi: 10.1016/j.gca.2003.09.012
- Hathorne, E. C., Stichel, T., Brück, B., and Frank, M. (2015). Rare earth element distribution in the Atlantic sector of the Southern Ocean: the balance between particle scavenging and vertical supply. *Mar. Chem.* 177, 157–171. doi: 10.1016/j.marchem.2015.03.011
- Hein, J. R., Koschinsky, A., Halbach, P., Manheim, F. T., Bau, M., Kanj, J.-K., et al. (1997). Iron and manganese oxide mineralization in the Pacific. *Geol. Soc. Lond.* 119, 123–138. doi: 10.1144/GSL.Sp.1997.119.01.09
- Hindshaw, R. S., Aciego, S. M., Piotrowski, A. M., and Tipper, E. T. (2018). Decoupling of dissolved and bedrock neodymium isotopes during sedimentary cycling. *Geophys. Perspect. Lett.* 8, 43–46. doi: 10.7185/geochemlet.1828
- Holdren, G. R., and Berner, R. A. (1979). Mechanism of feldspar weathering – I. *Experimental studies. Geochim. Cosmochim. Acta* 43, 1161–1171. doi: 10.1016/0016-7037(79)90109-1
- Homoky, W. B., Hepburn, D., Hepburn, L. E., Mills, R. A., Statham, P. J., Fones, G. R., et al. (2011). Iron and manganese diagenesis in deep sea volcanogenic sediments and the origins of pore water colloids. *Geochim. Cosmochim. Acta* 75, 5032–5048. doi: 10.1016/j.gca.2011.06.019
- Homoky, W. B., Weber, T., Berelson, W. M., Conway, T. M., Henderson, G. M., van Hulten, M., et al. (2016). Quantifying trace element and isotope fluxes at the ocean-sediment boundary: a review. *Philos. Trans. A Math. Phys. Eng. Sci.* 374:20160246. doi: 10.1098/rsta.2016.0246
- Howe, J. N. W., Piotrowski, A. M., and Rennie, V. C. F. (2016). Abyssal origin for the early Holocene pulse of unradiogenic neodymium isotopes in Atlantic seawater. *Geology* 44, 831–834. doi: 10.1130/G38155.1
- Huck, C. E., van de Flierdt, T., Jiménez-Espejo, F. J., Bohaty, S. M., Röhl, U., and Hammond, S. J. (2016). Robustness of fossil fish teeth for seawater neodymium isotope reconstructions under variable redox conditions in an ancient shallow marine setting. *Geochem. Geophys. Geosyst.* 17, 679–698. doi: 10.1002/2015GC006218
- Huggett, J., Adetunji, J., Longstaffe, F., and Wray, D. (2017). Mineralogical and geochemical characterisation of warm-water, shallow-marine glaucony from the Tertiary of the London Basin. *Clay Miner.* 52, 25–50. doi: 10.1180/claymin.2017.052.1.02
- Ijiri, A., Tomioka, N., Wakaki, S., Masuda, H., Shozugawa, K., Kim, S., et al. (2018). Low-temperature clay mineral dehydration contributes to porewater dilution in bering sea slope subseafloor. *Front. Earth Sci.* 6:36. doi: 10.3389/feart.2018.00036
- Jeandel, C., Arsouze, T., Lacan, F., Téchiné, P., and Dutay, J.-C. (2007). Isotopic Nd compositions and concentrations of the lithogenic inputs into the ocean: a compilation, with an emphasis on the margins. *Chem. Geol.* 239, 156–164. doi: 10.1016/j.chemgeo.2006.11.013
- Jeandel, C. (2016). Overview of the mechanisms that could explain the ‘Boundary Exchange’ at the land-ocean contact. *Philos. Trans. R. Soc.* 374:20150287. doi: 10.1098/rsta.2015.0287
- Jeandel, C., Bishop, J. K., and Zindler, A. (1995). Exchange of neodymium and its isotopes between seawater and small and large particles in the Sargasso Sea. *Geochim. Cosmochim. Acta* 59, 535–547. doi: 10.1016/0016-7037(94)00367-u
- Jeandel, C., Delattre, H., Grenier, M., Pradoux, C., and Lacan, F. (2013). Rare earth element concentrations and Nd isotopes in the Southeast Pacific Ocean. *Geochem. Geophys. Geosyst.* 14, 328–341. doi: 10.1029/2012GC004309
- Jeandel, C., and Oelkers, E. H. (2015). The influence of terrigenous particulate material dissolution on ocean chemistry and global element cycles. *Chem. Geol.* 395, 50–66. doi: 10.1016/j.chemgeo.2014.12.001



- Johannesson, K. H., Chevis, D. A., Burdige, D. J., Cable, J. E., Martin, J. B., and Roy, M. (2011). Submarine groundwater discharge is an important net source of light and middle REEs to coastal waters of the Indian River Lagoon, Florida, USA. *Geochim. Cosmochim. Acta* 75, 825–843. doi: 10.1016/j.gca.2010.11.005
- Jones, K. M., Khattiwala, S. P., Goldstein, S. L., Hemming, S. R., and van de Flierdt, T. (2008). Modelling the distribution of Nd isotopes in the oceans using an ocean general circulation model. *Earth Planet. Sci. Lett.* 272, 610–619. doi: 10.1016/j.epsl.2008.05.027
- Kang, J., Jeong, K. S., Cho, J. H., Lee, J. H., Jang, S., and Kim, S. R. (2014). Post-depositional redistribution processes and their effects on middle rare earth element precipitation and the cerium anomaly in sediments in the South Korea Plateau, East Sea. *J. Asian Earth Sci.* 82, 66–79. doi: 10.1016/j.jseas.2013.11.019
- Kim, J., Dong, H., Seabaugh, J., Newell, S. W., and Eberl, D. D. (2004). Role of microbes in the smectite-to-illite reaction. *Science* 303, 830–832. doi: 10.1126/science.1093245
- Kim, J., Torres, M. E., Haley, B. A., Kastner, M., Pohlman, J. W., Riedel, M., et al. (2012). The effect of diagenesis and fluid migration on rare earth element distribution in pore fluids of the northern Cascadia accretionary margin. *Chem. Geol.* 291, 152–165. doi: 10.1016/j.chemgeo.2011.10.010
- Kon, Y., Hoshino, M., Sanematsu, K., Morita, S., Tsunematsu, M., Okamoto, N., et al. (2014). Geochemical characteristics of apatite in heavy REE-rich deep-sea mud from the Minami-Torishima area, southeastern Japan. *Resour. Geol.* 64, 47–57. doi: 10.1111/rge.12026
- Koschinsky, A., and Hein, J. R. (2003). Uptake of elements from seawater by ferromanganese crusts: solid-phase associations and seawater speciation. *Mar. Geol.* 198, 331–351. doi: 10.1016/S0025-3227(03)00122-1
- Lacan, F., and Jeandel, C. (2005). Neodymium isotopes as a new tool for quantifying exchange fluxes at the continent-ocean interface. *Earth Planet. Lett.* 232, 245–257. doi: 10.1016/j.epsl.2005.01.004
- Liu, D., Dong, H., Bishop, M. E., Zhang, J., Wang, H., Xie, S., et al. (2012). Microbial reduction of structural iron in interstratified illite-smectite minerals by a sulfate-reducing bacterium. *Geobiology* 10, 150–162. doi: 10.1111/j.1472-4669.2011.00307.x
- Manceau, A., Lanson, M., and Geoffroy, N. (2007). Natural speciation of Ni, Zn, Ba, and Az in ferromanganese coatings on quartz using X-ray fluorescence, absorption, and diffraction. *Geochim. Cosmochim. Acta* 71, 95–128. doi: 10.1016/j.gca.2006.08.036
- McKinley, J. P., Zachara, J. M., Smith, S. C., and Liu, C. (2007). Cation exchange reactions controlling desorption of  $90\text{Sr}^{2+}$  from coarse-grained contaminated sediments at the Hanford site, Washington. *Geochim. Cosmochim. Acta* 71, 305–325. doi: 10.1016/j.gca.2006.09.027
- Michalopoulos, P., and Aller, R. C. (1995). Rapid clay mineral formation in amazon delta sediments: reverse weathering and oceanic elemental cycles. *Science* 270, 614–617. doi: 10.1126/science.270.5236.614
- Moore, D. M., and Reynolds, R. C. (1997). *X-Ray Diffraction and the Identification and Analysis of Clay Minerals*. Oxford: Oxford University Press, 378.
- Nozaki, Y., and Alibo, D. S. (2003). Importance of vertical geochemical processes in controlling the oceanic profiles of dissolved rare earth elements in the northeastern Indian Ocean. *Earth Planet. Sci. Lett.* 205, 155–172. doi: 10.1016/S0012-821X(02)01027-0
- Oelkers, E. H., Gislason, S. R., Eiriksdottir, E. S., Jones, M., Pearce, C. R., and Jeandel, C. (2011). The role of riverine particulate material on the global cycles of the elements. *Appl. Geochem.* 26, S365–S369. doi: 10.1016/j.apgeochem.2011.03.062
- Oelkers, E. H., Schott, J., Gauthier, J.-M., and Herrero-Roncal, T. (2008). An experimental study of the dissolution mechanism and rates of muscovite. *Geochim. Cosmochim. Acta* 72, 4948–4961. doi: 10.1016/j.gca.2008.01.040
- Osborne, A. H., Hathorne, E. C., Schijf, J., Plancherel, Y., Böning, P., and Frank, M. (2017). The potential of sedimentary foraminiferal rare earth element patterns to trace water masses in the past. *Geochem. Geophys. Geosyst.* 18, 1550–1568. doi: 10.1002/2016GC006782
- Palmer, M. R., and Elderfield, H. (1985). Variations in the Nd isotopic composition of foraminifera from Atlantic Ocean sediments. *Earth Planet. Sci. Lett.* 73, 299–305. doi: 10.1016/0012-821X(85)90078-0
- Pearce, C. R., Jones, M. T., Oelkers, E. H., Pradoux, C., and Jeandel, C. (2013). The effect of particulate dissolution on the neodymium (Nd) isotope and rare earth element (REE) composition of seawater. *Earth Planet. Sci. Lett.* 36, 138–147. doi: 10.1016/j.epsl.2013.03.023
- Piper, D. F. (1974). Rare-earth elements in ferromanganese nodules and other marine phases. *Geochim. Cosmochim. Acta* 38, 1007–1022. doi: 10.1016/0016-7037(74)90002-7
- Poulton, S. W., and Canfield, D. E. (2005). Development of a sequential extraction procedure for iron: implications for iron partitioning in continentally derived particulates. *Chem. Geol.* 214, 209–221. doi: 10.1016/j.chemgeo.2004.09.003
- Poulton, S. W., and Raiswell, R. (2005). Chemical and physical characteristics of iron oxides in riverine and glacial meltwater sediments. *Chem. Geol.* 218, 203–221. doi: 10.1016/j.chemgeo.2005.01.007
- Rahman, S., Aller, R. C., and Cochran, J. K. (2017). The Missing silica sink: revisiting the marine sedimentary Si cycle using cosmogenic  $^{32}\text{Si}$ . *Glob. Biogeochem. Cycles* 31, 1559–1578. doi: 10.1002/2017GB005746
- Rao, V. P. (1987). Mineralogy of polymetallic nodules and associated sediments from the Central Indian Ocean Basin. *Mar. Geol.* 74, 151–157. doi: 10.1016/0025-3227(87)90011-9
- Ren, J. B., Yao, H. Q., Zhu, K. C., He, G. W., Deng, X. G., Wang, H. F., et al. (2015). Enrichment mechanism of rare earth elements and yttrium in deep-sea mud of Clarion-Clipperton Region. *Earth Sci. Front.* 22, 200–211. doi: 10.13745/j.esf.2015.04.021
- Rickli, J., Gutjahr, M., Vance, D., Fisher-Gödde, M., Hillenbrand, C.-D., and Kuhn, G. (2014). Neodymium and hafnium boundary contributions to seawater along the West Antarctic continental margin. *Earth Planet. Sci. Lett.* 394, 99–110. doi: 10.1016/j.epsl.2014.03.008
- Roberts, N. L., and Piotrowski, A. M. (2015). Radiogenic Nd isotope labelling of the northern NE Atlantic during MIS 2. *Earth Planet. Sci. Lett.* 423, 125–133. doi: 10.1016/j.epsl.2015.05.011
- Rousseau, T. C. C., Sonke, J. E., Chmieleff, J., van Beek, P., Souhaut, M., Boaventura, G., et al. (2015). Rapid neodymium release to marine waters from lithogenic sediments in the Amazon estuary. *Nat. Commun.* 6:7592. doi: 10.1038/ncomms8592
- Rutberg, R. L., Hemming, S. R., and Goldstein, S. L. (2000). Reduced North Atlantic deep water flux to the glacial Southern Ocean inferred from neodymium isotope ratios. *Nature* 405, 935–938. doi: 10.1038/35016049
- Sa, R., Sun, X., He, G., Xu, L., Pan, Q., Liao, J., et al. (2018). Enrichment of rare earth elements in siliceous sediments under slow deposition: a case study of the central North Pacific. *Ore Geol. Rev.* 94, 12–23. doi: 10.1016/j.oregeorev.2018.01.019
- Schacht, U., Wallman, J., and Kutterolf, S. (2010). The influence of volcanic ash alteration on the REE composition of marine pore waters. *J. Geochem. Explor.* 106, 176–187. doi: 10.1016/j.jgexplo.2010.02.006
- Schott, J., Pokrovsky, O. S., and Oelkers, E. H. (2009). The link between mineral dissolution/precipitation kinetics and solution chemistry. *Rev. Mineral. Geochem.* 70, 207–258. doi: 10.2138/rmg.2009.70.6
- Schott, J., Pokrovsky, O. S., Spalla, O., Devreux, F., Gloter, A., and Mielczarsky, J. A. (2012). Formation, growth and transformation of leached layers during silicate minerals dissolution: the example of wollastonite. *Geochim. Cosmochim. Acta* 98, 259–281. doi: 10.1016/j.gca.2012.09.030
- Schwertmann, U., and Pfab, G. (1994). Structural vanadium in synthetic goethite. *Geochim. Cosmochim. Acta* 58, 4349–4352. doi: 10.1016/0016-7037(94)90338-7
- Sholkovitz, E. R., Elderfield, H., Szymczak, R., and Casey, K. (1999). Island weathering: river sources of rare earth elements to the Western Pacific Ocean. *Mar. Chem.* 68, 39–57. doi: 10.1016/S0304-4203(99)00064-X
- Sholkovitz, E. R., Landing, W. M., and Lewis, B. L. (1994). Ocean particle chemistry: the fractionation of rare earth elements between suspended particles and seawater. *Geochim. Cosmochim. Acta* 58, 1567–1579. doi: 10.1016/0016-7037(94)90559-2
- Singh, S. P., Singh, S. K., Goswami, V., Bhushan, R., and Rai, V. K. (2012). Spatial distribution of dissolved neodymium and  $\epsilon\text{Nd}$  in the Bay of Bengal: role of particulate matter and mixing of water masses. *Geochim. Cosmochim. Acta* 94, 38–56. doi: 10.1016/j.gca.2012.07.017
- Skinner, L. C., Sadekav, A., Brandon, M., Greaves, M., Plancherel, Y., de la Fuente, M., et al. (2019). Rare Earth Elements in early-diagenetic foraminifer 'coatings': Pore-water controls and potential palaeoceanographic applications. *Geochim. Cosmochim. Acta* 245, 118–132. doi: 10.1016/j.gca.2018.10.027

- Stewart, J. A., Gutjahr, M., James, R. H., Anand, P., and Wilson, P. A. (2016). Influence of the Amazon River on Nd isotope composition of deep water in the western equatorial Atlantic during the Oligocene-Miocene transition. *Earth Planet. Sci. Lett.* 454, 132–141. doi: 10.1016/j.epsl.2016.08.037
- Stichel, T., Hartman, A. E., Duggan, B., Goldstein, S. L., Scher, H., and Pahnke, K. (2015). Separating biogeochemical cycling of neodymium from water mass mixing in the Eastern North Atlantic. *Earth Planet. Sci. Lett.* 412, 245–260. doi: 10.1016/j.epsl.2014.12.008
- Stoffyn-Egli, P., and Mackenzie, F. T. (1984). Mass balance of dissolved lithium in the oceans. *Geochim. Cosmochim. Acta* 48, 859–872. doi: 10.1016/0016-7037(84)90107-8
- Tachikawa, K., Athias, V., and Jeandel, C. (2003). Neodymium budget in the modern ocean and paleo-oceanographic implications. *J. Geophys. Res.* 108, 3254–3267. doi: 10.1029/1999JC000285
- Tachikawa, K., Roy-Barman, M., Michard, A., Thouvenot, D., Yeghicheyan, D., and Jeandel, C. (2004). Neodymium isotopes in the Mediterranean Sea: comparison between seawater and sediment signals. *Geochim. Cosmochim. Acta* 68, 3095–3106. doi: 10.1016/j.gca.2004.01.024
- Tachikawa, K., Toyofuku, T., Basile-Doelsch, I., and Delhaye, T. (2013). Microscale neodymium distribution in sedimentary planktonic foraminiferal tests and associated mineral phases. *Geochim. Cosmochim. Acta* 100, 11–23. doi: 10.1016/j.gca.2012.10.010
- Takahashi, Y., Hayasaka, Y., Morita, K., Kashiwabara, T., Nakada, R., Marcus, M. A., et al. (2015). Transfer of rare earth elements (REE) from manganese oxides to phosphates during early diagenesis in pelagic sediments inferred from REE patterns, X-ray absorption spectroscopy, and chemical leaching method. *Geochem. J.* 49, 653–674. doi: 10.2343/geochemj.2.0393
- Taylor, R. M., and McKenzie, R. M. (1966). The association of trace elements with manganese minerals in Australian soils. *Aust. J. Soil Res.* 2, 235–248.
- Taylor, S. R., and McLennan, S. M. (1985). *The Continental Crust: Its Composition and Evolution. An Examination of the Geochemical Record Preserved in Sedimentary Rocks*. Oxford: Blackwell Scientific Publications.
- Toyoda, K., and Tokonami, M. (1990). Diffusion of rare earth elements in fish teeth from deep-sea sediments. *Nature* 345, 607–609. doi: 10.1038/345607a0
- Trotter, J. A., Barnes, C. R., and McCracken, A. D. (2016). Rare earth elements in conodont apatite: seawater or pore-water signatures? *Palaeogeogr. Palaeoclimatol. Palaeoecol.* 462, 92–100. doi: 10.1016/j.palaeo.2016.09.007
- Turner, D. R., Whitfield, M., and Dickson, A. G. (1981). The equilibrium speciation of dissolved components in freshwater and seawater at 25°C and 1 atm pressure. *Geochim. Cosmochim. Acta* 45, 855–881. doi: 10.1016/0016-7037(81)90115-0
- van de Fliedert, T., Griffiths, A. M., Lambelet, M., Little, S. H., Stichel, T., and Wilson, D. J. (2016). Neodymium in the oceans: a global database, a regional comparison and implications for palaeoceanographic research. *Philos. Trans. R. Soc.* 374:20150293. doi: 10.1098/rsta.2015.0293
- van der Zee, C., Roberts, D. R., Rancourt, D. G., and Slomp, C. P. (2003). Nanogothite is the dominant reactive oxyhydroxide phase in lake and marine sediments. *Geology* 31, 993–996. doi: 10.1130/G19924.1
- Van Olphen, H., and Fripiat, J. J. (1979). *Data Handbook for Clay Minerals and other Non Metallic Materials*. Oxford: Pergamon Press, 346.
- Vance, D., and Burton, K. (1999). Neodymium isotopes in planktonic foraminifera: a record of the response of continental weathering and ocean circulation rates to climate change. *Earth Planet. Sci. Lett.* 173, 365–379. doi: 10.1016/S0012-821X(99)00244-7
- Vance, D., Scrivner, A. E., Beney, P., Staubwasser, M., Henderson, G. M., and Slowey, N. C. (2004). The use of foraminifera as a record of past neodymium isotope composition of seawater. *Paleoceanography* 19:A2009. doi: 10.1029/2003PA000957
- VanLaningham, S., Duncan, R. A., Pisias, N. G., and Graham, D. W. (2008). Tracking fluvial response to climate change in the Pacific Northwest: a combined provenance approach using Ar and Nd isotopic systems on fine-grained sediments. *Quat. Sci. Rev.* 27, 497–517. doi: 10.1016/j.quascirev.2007.10.018
- Viers, J., Roddaz, M., Filizola, N., Guyot, J.-L., Sondag, F., Brunet, P., et al. (2008). Seasonal and provenance controls on Nd-Sr isotopic compositions of Amazon rivers suspended sediments and implications for Nd and Sr fluxes exported to the Atlantic Ocean. *Earth Planet. Sci. Lett.* 274, 511–523. doi: 10.1016/j.epsl.2008.08.011
- Vigier, N., Decarreau, A., Millot, R., Carignan, J., Petit, S., and France-Lanord, C. (2008). Quantifying Li isotope fractionation during smectite formation and implications for the Li Cycle. *Geochim. Cosmochim. Acta* 72, 780–792. doi: 10.1016/j.gca.2007.11.011
- von Blanckenburg, F. (1999). Tracing past ocean circulation? *Science* 286, 1862–1863. doi: 10.1126/science.286.5446.1862b
- Vorhies, J. S., and Gaines, R. R. (2009). Microbial dissolution of clay minerals as a source of iron and silica in marine sediments. *Nat. Geosci.* 2, 221–225. doi: 10.1038/ngeo441
- Wilson, D. J., Piotrowski, A. M., Galy, A., and Clegg, J. A. (2013). Reactivity of neodymium carriers in deep sea sediments: implications for boundary exchange and paleoceanography. *Geochim. Cosmochim. Acta* 109, 197–221. doi: 10.1016/j.gca.2013.01.042
- Wilson, D. J., Piotrowski, A. M., Galy, A., and McCave, I. N. (2012). A boundary exchange influence on deglacial neodymium isotope records from the deep western Indian Ocean. *Earth Planet. Sci. Lett.* 34, 35–47. doi: 10.1016/j.epsl.2012.06.009
- Wood, S. A. (1990). The aqueous geochemistry of the rare-earth elements and yttrium: 1. review of available low-temperature data for inorganic complexes and the inorganic REE speciation of natural waters. *Chem. Geol.* 82, 159–186. doi: 10.1016/0009-2541(90)90080-q
- Yang, J., and Haley, B. (2016). The profile of the rare earth elements in the Canada Basin, Arctic Ocean. *Geochem. Geophys. Geosyst.* 17, 3241–3253. doi: 10.1002/2016gc006412
- Zhang, J., Dong, H., Liu, D., Fischer, T. B., Wang, S., and Huang, L. (2012). Microbial reduction of Fe(III) in illite-smectite minerals by methanogen *Methanosarcina mazei*. *Chem. Geol.* 292, 35–44. doi: 10.1016/j.chemgeo.2011.11.003
- Zhang, J., and Nozaki, Y. (1996). Rare earth elements and yttrium in seawater: ICP-MS determinations in the East Caroline, Coral Sea, and South Fiji basins of the western South Pacific Ocean. *Geochim. Cosmochim. Acta* 60, 4631–4644. doi: 10.1016/S0016-7037(96)00276-1
- Zhang, L., Algeo, T. J., Cao, L., Zhao, L., Chen, Z.-C., and Li, Z. (2016). Diagenetic uptake of rare earth elements by conodont apatite. *Palaeogeogr. Palaeoclimatol. Palaeoecol.* 458, 176–197. doi: 10.1016/j.palaeo.2015.10.049
- Zhang, Y., Lacan, F., and Jeandel, C. (2008). Dissolved rare earth elements trace lithogenic inputs over the Kerguelen Plateau (Southern Ocean). *Deep Sea Res. I* 55, 638–652. doi: 10.1016/j.dsr2.2007.12.028
- Zheng, X.-Y., Plancherel, Y., Saito, M. A., Scott, P. M., and Henderson, G. M. (2016). Rare earth elements (REEs) in the tropical South Atlantic and quantitative deconvolution of their non-conservative behavior. *Geochim. Cosmochim. Acta* 177, 217–237. doi: 10.1016/j.gca.2016.01.018

**Conflict of Interest Statement:** The authors declare that the research was conducted in the absence of any commercial or financial relationships that could be construed as a potential conflict of interest.

Copyright © 2019 Abbott, Löhr and Trethewey. This is an open-access article distributed under the terms of the Creative Commons Attribution License (CC BY). The use, distribution or reproduction in other forums is permitted, provided the original author(s) and the copyright owner(s) are credited and that the original publication in this journal is cited, in accordance with accepted academic practice. No use, distribution or reproduction is permitted which does not comply with these terms.



# Shelf Inputs and Lateral Transport of Mn, Co, and Ce in the Western North Pacific Ocean

Peter L. Morton<sup>1\*</sup>, William M. Landing<sup>2</sup>, Alan M. Shiller<sup>3</sup>, Amy Moody<sup>3</sup>, Thomas D. Kelly<sup>2</sup>, Michael Bizimis<sup>4</sup>, John R. Donat<sup>5</sup>, Eric H. De Carlo<sup>6</sup> and Joseph Shacat<sup>7</sup>

<sup>1</sup> National High Magnetic Field Laboratory, Tallahassee, FL, United States, <sup>2</sup> Earth, Ocean, and Atmospheric Science, Florida State University, Tallahassee, FL, United States, <sup>3</sup> Division of Marine Science, University of Southern Mississippi, Hattiesburg, MS, United States, <sup>4</sup> School of the Earth, Ocean and Environment, University of South Carolina, Columbia, SC, United States, <sup>5</sup> Department of Chemistry and Biochemistry, Old Dominion University, Norfolk, VA, United States, <sup>6</sup> Department of Oceanography, University of Hawai'i at Mānoa, Honolulu, HI, United States, <sup>7</sup> National Asphalt Pavement Association, Annapolis, MD, United States

## OPEN ACCESS

### Edited by:

Johan Schijf,  
Chesapeake Biological Laboratory,  
University of Maryland Center for  
Environmental Science (UMCES),  
United States

### Reviewed by:

Hein De Baar,  
Royal Netherlands Institute for Sea  
Research (NIOZ), Netherlands  
Antonio Cobelo-Garcia,  
Spanish National Research Council  
(CSIC), Spain

### \*Correspondence:

Peter L. Morton  
pmorton@fsu.edu

### Specialty section:

This article was submitted to  
Marine Biogeochemistry,  
a section of the journal  
Frontiers in Marine Science

**Received:** 28 February 2019

**Accepted:** 05 September 2019

**Published:** 30 September 2019

### Citation:

Morton PL, Landing WM,  
Shiller AM, Moody A, Kelly TD,  
Bizimis M, Donat JR, De Carlo EH  
and Shacat J (2019) Shelf Inputs  
and Lateral Transport of Mn, Co,  
and Ce in the Western North Pacific  
Ocean. *Front. Mar. Sci.* 6:591.  
doi: 10.3389/fmars.2019.00591

The margin of the western North Pacific Ocean releases redox-active elements like Mn, Co, and Ce into the water column to undergo further transformation through oxide formation, scavenging, and reductive dissolution. Near the margin, the upper ocean waters enriched in these elements are characterized by high dissolved oxygen, low salinity, and low temperature, and are a source of the North Pacific Intermediate Water. High dissolved concentrations are observed across the Western Subarctic Gyre, with a rapid decrease in concentrations away from the margin and across the subarctic-subtropical front. The particulate concentrations of Mn, Co, and Ce are also high in the subarctic surface ocean and enriched relative to Ti and trivalent rare earth elements. Furthermore, the particles enriched in Mn, Co, and Ce coincide at the same depth range, suggesting that these elemental cycles are coupled through microbial oxidation in the subarctic gyre as the waters travel along the margin before being subducted at the subarctic-subtropical front. Away from the margin, the Mn, Co, and Ce cycles decouple, as Mn and Ce settle out as particles while dissolved Co is preserved and transported within the North Pacific Intermediate Water into the central North Pacific Ocean.

**Keywords:** oxygen minimum zone (OMZ), biogeochemistry, North Pacific Intermediate Water (NPIW), western subarctic North Pacific, mixed water region between Kuroshio and Oyashio, manganese, cobalt, cerium anomaly

## INTRODUCTION

The lateral transport of material from continental margins can provide essential trace metals to the ocean (Westerlund et al., 1986; Elrod et al., 2004; Lam et al., 2006; Lam and Bishop, 2008; Aguilar-Islas et al., 2013; Noble et al., 2017; Tagliabue et al., 2017). While surface maxima of manganese (Mn) may result from atmospheric deposition or freshwater inputs (Shiller, 1997; van Hulten et al., 2016), numerous studies have established the importance of Mn as a tracer of redox mobilized sediment inputs from continental margins in the upper ocean. Dissolved Mn (dMn) is released from sediments during reductive dissolution driven by bacterial respiration of organic matter and associated diagenetic processes (Sundby et al., 1986; Burdige, 1993, 2006). Fluxes of dMn can persist across the sediment-water interface even when overlying waters are suboxic or oxic and produce a

characteristic subsurface plume enriched in dissolved Mn (Landing and Bruland, 1980; Bishop and Fleisher, 1987; Stumm and Morgan, 1995; Minakawa et al., 1996; Chase et al., 2005; Vedamati et al., 2015; Oldham et al., 2017).

Manganese-enriched plumes (both dissolved and particulate) have been observed along the coastlines of major ocean basins, including Tokyo Bay (Noriki et al., 1997); the Japan Trench (Otosaka and Noriki, 2000); the North Pacific Ocean (e.g., Martin et al., 1985); the Peru margin (Vedamati et al., 2015); the Arctic Ocean (Aguilar-Islas et al., 2007; Middag et al., 2011b); the Southern Ocean in general (Middag et al., 2011a; Sherrell et al., 2018), especially along the Antarctic Peninsula into the Weddell Sea (Middag et al., 2013) and across the Drake Passage (Middag et al., 2012; Klunder et al., 2014); the Indian Ocean (Saager et al., 1989; Lewis and Luther, 2000; Vu and Sohrin, 2013); the eastern North Atlantic Ocean (Tachikawa et al., 1999); the South Atlantic Ocean at the Benguela/Angola front (Noble et al., 2012); and the Kuril-Kamchatka margin (Lam and Bishop, 2008; Lamborg et al., 2008).

In addition to Mn, other trace elements can be similarly released from margin sediments via redox mobilization, including Co (Noble et al., 2012, 2017; Hawco et al., 2016; Tagliabue et al., 2018) and Ce (Zhang and Nozaki, 1998; Obata et al., 2007; Zheng et al., 2016). While Co also undergoes similar redox cycling in seawater, both reduced and oxidized forms can exist in the soluble phase (Moffett and Ho, 1996), often through stabilization with organic ligands (Saito and Moffett, 2001; Hawco et al., 2016, 2018; Noble et al., 2017; Tagliabue et al., 2018). In contrast, while the reduced forms of Mn and Ce are generally found in the aqueous phase, the oxidized forms are found in the particulate phase (Stumm and Morgan, 1995; Moffett and Ho, 1996; Nozaki, 2001).

Plumes of dMn can be oxidized in the water column to produce particles enriched in Mn over crustal abundance relative to a non-redox active trace element like Al or Ti (Tanoue and Midorikawa, 1995; Lam and Bishop, 2008; Lamborg et al., 2008; Yiğiterhan et al., 2011; Lam et al., 2015; Oldham et al., 2017). These Mn-enriched particles have been reported with similar enrichments in particulate Co and Ce, leading naturally to conclusions that these elements are oxidized via a similar mechanism such as microbial oxidation (Moffett, 1990, 1994b; Moffett and Ho, 1996; Bargar et al., 2000; Tebo et al., 2004; Murray et al., 2007; Spiro et al., 2010). Similar enrichments (or depletions) in Ce can be identified by the Ce anomaly (Elderfield, 1988), where the actual concentration of dissolved or particulate Ce is compared to the concentration of Ce predicted from its lanthanide neighbors (i.e., La and Pr). While all the REEs will passively adsorb and desorb from other marine suspended particles (to varying degrees), Ce(III) can be oxidized to Ce(IV) and form oxides that remain as particles even when the other REEs desorb from particles and return to the dissolved pool, thus producing the observed Ce anomaly (Equation 1):

$$\text{Ce anomaly} = \frac{2(\text{CeSN})}{(\text{LaSN} + \text{PrSN})} \quad (1)$$

where *CeSN*, *LaSN* and *PrSN* represent the shale-normalized REE concentrations using Post-Archean Australian Shale (PAAS) as in Rudnick and Gao (2003).

The redox activities of Mn, Co, and Ce also depend on other chemical and biological factors. Low oxygen conditions in sediments can release dissolved elements into the overlying water column (Sundby et al., 1986). If this bottom water is also low in oxygen, then the reduced forms may enjoy longer residence times. Photochemical reduction (in reactions with dissolved organic carbon and sunlight) may also prolong the residence time of Mn in seawater (Sunda and Huntsman, 1994). Biological Mn oxidation via bacterial or fungal mediated processes can transform dissolved Mn to particles, and numerous studies have shown that Co and Ce are similarly oxidized by the same enzymatic pathway or by secondary oxidation by the reactive particulate Mn-oxides (Tebo et al., 1984; Moffett, 1990, 1994b, 1997; Moffett and Ho, 1996; De Carlo et al., 1997; Murray et al., 2007; Spiro et al., 2010; Schijf et al., 2015; Toyoda and Tebo, 2016). Although Ce has been shown to oxidize abiotically (De Carlo et al., 1997), studies of Ce oxidation kinetics conducted using seawater suggest a microbial role linked to Mn oxidation and rates that are depth-dependent, where oxidation is photo-inhibited in surface waters but increase with depth (Moffett, 1994a,b). Therefore, particles enriched in Mn, Co, and Ce can at least partly (if not primarily) result from biological processes.

Redox mobilized shelf inputs of dissolved trace elements can be preserved and transported offshore when the overlying waters are also low in oxygen, especially in regions like the northern Indian Ocean, the eastern Atlantic Ocean, and the eastern North and South Pacific Oceans (Breitburg et al., 2018; Scholz, 2018). In the northern Indian Ocean, the depths of the minimum oxygen concentrations coincide with plumes of dissolved trace elements like Mn (Saager et al., 1989; Lewis and Luther, 2000), Fe (Saager et al., 1989; Kondo and Moffett, 2013; Vu and Sohrin, 2013; Grand et al., 2015a,b; Chinni et al., 2019), Co (Vu and Sohrin, 2013), and Ce (German and Elderfield, 1990). In the eastern South Atlantic, during the CoFeMUG cruise (Noble et al., 2012; Zheng et al., 2016), Mn, Co, Fe, and Ce were all enriched in subsurface plumes within the depth range of the oxygen minimum zone. Similar inputs of Fe (Buck et al., 2015; Fitzsimmons et al., 2015a; Hatta et al., 2015; Sedwick et al., 2015; Klar et al., 2018), Mn (Wu et al., 2014; Hatta et al., 2015), and Co (Noble et al., 2017) were found in low oxygen waters along the Mauritanian coast. The oxygen minimum zones of the eastern North and/or South Pacific regions contain high concentrations of dissolved Mn (Vedamati et al., 2015; Chen and Wu, 2019), Fe (Noffke et al., 2012; Chever et al., 2015; Glass et al., 2015; Kondo and Moffett, 2015; Heller et al., 2017; Buck et al., 2018; Cutter et al., 2018; Marsay et al., 2018), Co (Saito et al., 2004; Hawco et al., 2016), and other redox active elements like iodide (Cutter et al., 2018). Similar studies conducted in the Cariaco Basin (Jacobs et al., 1987; de Baar et al., 1988) and the Black Sea (e.g., Lewis and Landing, 1991; Yiğiterhan et al., 2011) show the prevalence of concurrent inputs of redox active metals in a variety of basins. In summary, while marine margin sediments can act as a source of redox active trace elements to the overlying waters, the oxygen minimum zones allow for extended residence times



of soluble reduced elements and lateral transport far beyond the immediate coastline.

In the subtropical and subarctic North Pacific Ocean, the oxygen minimum zone extends across the entire basin from east to west (Paulmier and Ruiz-Pino, 2009), and redox-mobilized shelf inputs of dissolved trace elements have been observed along nearly every coast. Margin inputs have been identified by the lateral transport of dissolved Mn (Landing and Bruland, 1980, 1987; Martin et al., 1985; Johnson et al., 1996; Chase et al., 2005; Noble et al., 2008), Fe (Boyle et al., 2005; Chase et al., 2005; Elrod et al., 2004; Noble et al., 2008; Fitzsimmons et al., 2015b), Co (Knauer et al., 1982; Fujishima et al., 2001; Ezoe et al., 2004; Noble et al., 2008), and Ce (de Baar et al., 1985; de Baar et al., 2018). Lateral inputs of particulate Mn and Fe (Lam and Bishop, 2008; Lamborg et al., 2008) were also found in subsurface waters within the oxycline above the low-oxygen waters, but observations in the western North Pacific were limited to a single station (time-series Station K2) so the extent of offshore transport remained undetermined. Nishioka et al. (2007) suggested that material in the western North Pacific could be swept even further into the open ocean by currents circulating in this region. A recent study of three Japanese GEOTRACES cruises established the importance of margin inputs and basin-wide intermediate water masses in the distributions of dissolved Mn and Co (Zheng et al., 2019).

The ocean currents provide boundaries and drive the major features of the North Pacific Ocean. The Western Subarctic Gyre (WSG) is formed by the southward moving East Kamchatka Current along the Kuril-Kamchatka margin, the Alaskan Stream to the north along the Aleutian Islands, and the Kuroshio Current and Extension to the south. This circulation drives upwelling in the WSG, which brings nutrient-rich intermediate waters to the surface and creates a high nutrient-low chlorophyll (HNLC) regime (Brown et al., 2005; Kinugasa et al., 2005; Nishioka et al., 2007; Misumi et al., 2011; Tanaka et al., 2012). The long-distance transport of crustal material from the Kuril-Kamchatka and Aleutian Margins can supply much-needed Fe to the western North Pacific (Brown et al., 2005; Measures et al., 2005; Nishioka et al., 2007; Hsu et al., 2008; Okin et al., 2011; Tanaka et al., 2012; Okubo et al., 2013; Takeda et al., 2014), which remains Fe-limited despite predictions of aerosol fluxes from Asian deserts and industry (Jickells et al., 2005; Mahowald et al., 2005, 2009).

The 2002 Intergovernmental Oceanographic Commission (IOC-2002) expedition was conducted in April-May 2002 and included three vertical profile stations along the western North Pacific margin including Station KNOT (44°N 150°E) as well as six other vertical profile stations and daily surface water collections extending from Japan to Hawaii in the central North Pacific (Figure 1). By analyzing water samples at the three margin stations for dissolved and particulate Mn, Co, and Ce, we demonstrate sedimentary inputs along the entire Kuril-Kamchatka margin. While our research does not directly address biological processes, our evidence suggests that microbial oxidation is partly responsible for converting the dissolved sedimentary inputs to enriched particles which increase in concentration in water masses flowing along the margin. These

currents are identified according to their temperature/salinity signatures, potential densities, and oxygen content, and will be shown to carry some portion of the shelf-derived material into the central North Pacific. Particle settling removes most Mn and Ce, but Co is preserved in the dissolved phase and incorporated into the North Pacific Intermediate Water, observed as far away as Hawaii. Here, using dissolved and particulate concentrations of Mn, Co, Ce and other contextual elements, the spread of redox-mobilized shelf material is shown to be varyingly influenced by microbial oxidation, energetic frontal subduction, and long-range lateral transport.

## MATERIALS AND METHODS

### Surface Sampling

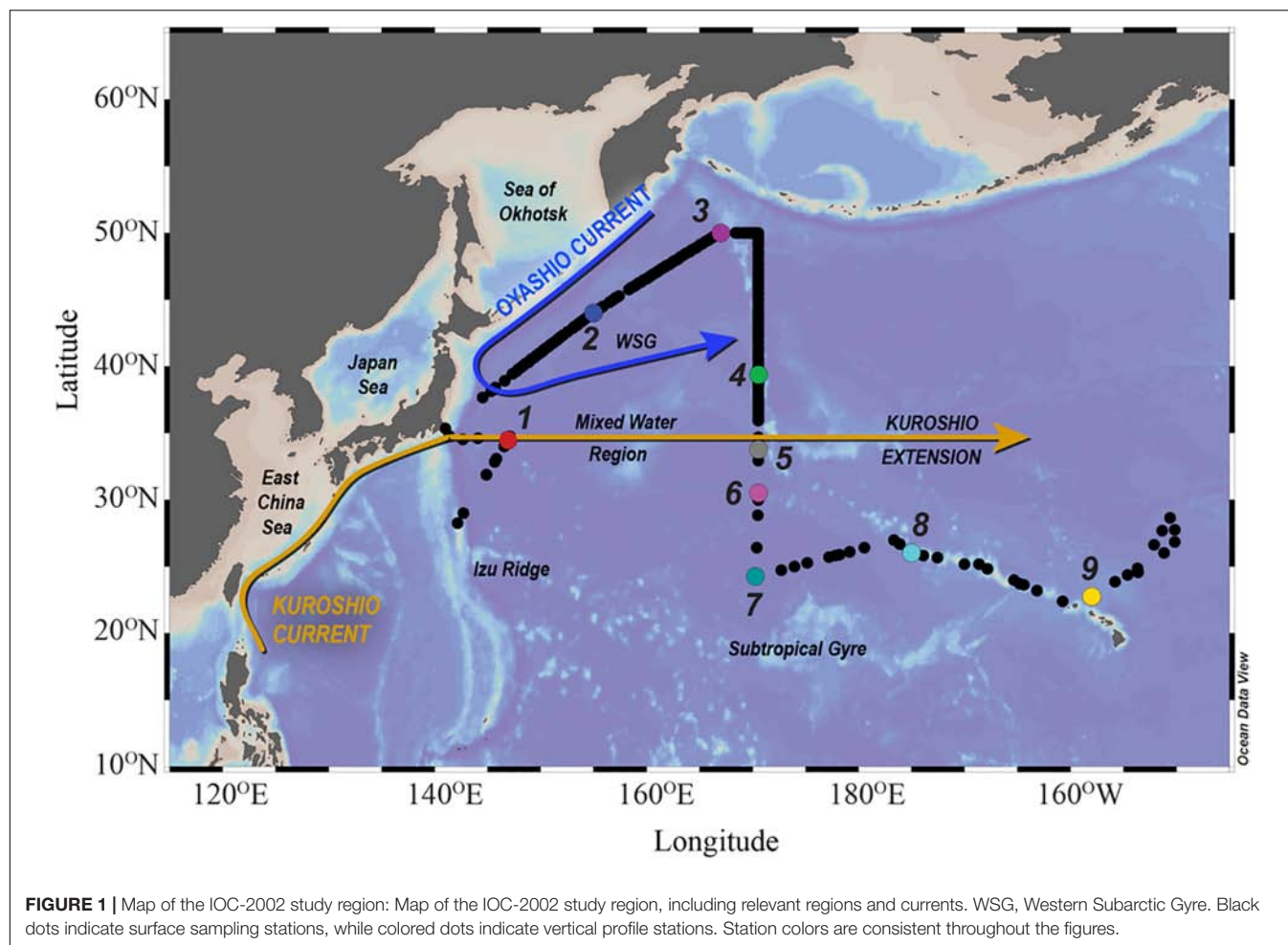
Seawater was pumped through a towed surface-sampler package ("Fish") that was deployed at about 0.5 m depth while the *R/V Melville* was underway (Measures et al., 2006). The seawater was pumped to a HEPA-filtered laminar flow bench through acid-washed Teflon tubing. Dissolved metal samples were collected after the seawater passed through a 0.2- $\mu$ m Gelman Criti-cap polysulfone cartridge filter into acid-washed 1 L HDPE bottles. Samples were acidified ( $\sim$ pH 1.7; 0.024 M), using 2 mL of concentrated ultrapure HCl (Fisher, Optima grade) per 1 L of sample. The samples were stored acidified for at least 6 months before analysis to ensure complete release of metals from any organic complexes.

### Vertical Profile Sampling

Vertical profile samples of dissolved and particulate trace elements were collected using 30-L Teflon-coated Go-Flo bottles (General Oceanics) hung on a Kevlar line and lowered to pre-determined depths at nine stations. After the bottles were tripped and recovered, they were moved inside one of the ship's bays that had been converted into a positive-pressure clean lab supplied with HEPA-filtered air. Subsamples were drawn from the Go-Flo bottles by pressurizing them with filtered compressed air ( $\sim$ 0.5 atm overpressure), forcing the seawater through an acid-washed (1.2 M HCl) 0.4- $\mu$ m pore size, 142-mm diameter polycarbonate track-etched (PCTE) Nuclepore filter. Dissolved samples were collected in acid-washed 1 L HDPE bottles and acidified like the surface samples. The Nuclepore filters were folded into quarters to contain all particulate material on the inside of the filter and placed in plastic zip-lock bags. Particulate samples were immediately frozen and kept frozen until digestion and analysis.

### Dissolved Sample Analysis

Filtered seawater samples were collected for dissolved trace metals and the rare earth element suite. As this paper presents the cycling of Mn, Co, and Ce, only these elements and those supporting their focused interpretation (e.g., La and Pr) are included here. However, additional manuscripts are currently in preparation that will describe the bioactive trace metals (e.g., Fe, Cd) and the extended REE series.



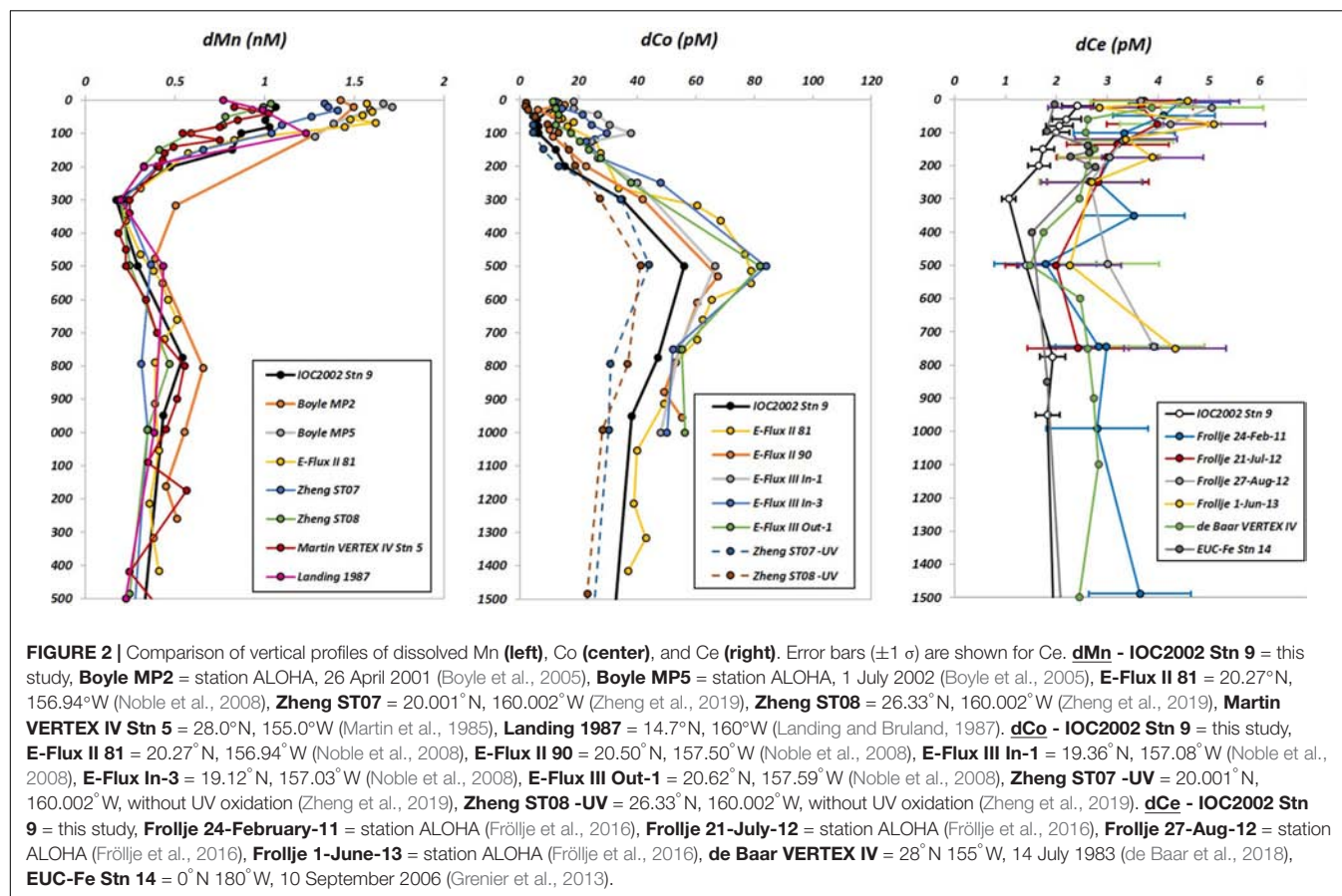
## Dissolved Trace Metals

Dissolved Mn and Co were extracted in 2007–2008 (FSU) from seawater using an 8-hydroxyquinoline (8HQ) resin column according to Milne et al. (2010). In brief, 60 mL aliquots of sample (acidified to pH 1.7) were UV oxidized for 1 h (Hg-vapor lamp, 1200 W). After allowing the UV-treated samples to cool, 12 mL aliquots of each were poured into acid-washed 15-mL polypropylene centrifuge tubes. To quantify the concentrations of dissolved Mn and Co, a series of standard additions ( $n = 4$ ) were made every 6–10 samples, and the samples allowed to equilibrate overnight. Fifteen minutes before extraction onto the 8HQ resin column, each individual aliquot was pH adjusted and buffered using a 2 M ammonium-acetate solution to a final pH of 5.5–6.0 (~0.17 M acetate, or ~1 mL buffer solution per 12 mL acidified seawater sample). Once the trace metals in the samples were loaded onto the column (2 mL/min flow rate), the column was rinsed with ultrapure water and the analyte metals were eluted with 1 mL of 1.5 M quartz distilled  $\text{HNO}_3$  and analyzed using an ELEMENT ICP-MS in medium resolution (National High Magnetic Field Laboratory, Tallahassee, FL, United States). Dissolved concentrations of Mn and Co were measured in the SAFe S and D2 consensus reference materials and were contributed to the original intercalibration

study (Supplementary Table 1). Dissolved Mn concentrations for SAFe S and D2 were determined to be  $0.90 \pm 0.06$  nM (vs. the consensus value of  $0.79 \pm 0.06$  nM) and  $0.46 \pm 0.05$  nM (vs.  $0.35 \pm 0.05$  nM), respectively. Concentrations of dissolved Co in the SAFe D2 samples ( $40.5 \pm 1.7$  pM) were close to the consensus value ( $45.7 \pm 2.9$  pM) while our dCo measurements of the SAFe S sample were lower than the consensus value ( $2.2 \pm 1.5$  pM vs.  $4.8 \pm 1.2$  pM) despite our use of UV oxidation prior to extraction. There is still much uncertainty over the UV intensity and duration required to release dCo from natural organic ligands. Only six labs have reported dCo in the SAFe S samples following UV oxidation, with reported concentrations ranging from 2 to 7 pM (close to the reported detection limits). Because of this uncertainty, we did not make any yield corrections to our dCo data, but this does not affect our interpretation of the dCo distributions and the processes affecting dCo in our study region. Comparisons of dMn and dCo with other studies conducted near the Hawaiian islands are shown in Figure 2.

## Dissolved Rare Earth Elements (REEs)

Another set of concurrently collected samples were analyzed in 2016–2017 (USM) for dissolved La, Ce, and Pr, as part of the entire suite of rare earth elements. A 14-mL aliquot of sample



was spiked with a mixture of isotopically enriched Nd-145, Sm-149, Eu-153, Gd-155, Dy-161, Er-167, and Yb-171 (Oak Ridge National Laboratories). Each spike was >90% enriched in the listed isotopes. The sample/spike ratio was optimized so that the analytical isotope ratios fall at the geometric mean of the natural and enriched spike isotope ratios, thereby minimizing error. Samples were then extracted/pre-concentrated using a SeaFAST system (Elemental Scientific, Inc.) operated in offline mode, similar to the method described by Hathorne et al. (2012). The extracted samples were subsequently analyzed using a ThermoFisher ELEMENT XR ICP-MS operated in low-resolution mode with an Apex-FAST high efficiency sample introduction system with Spiro desolvator (Elemental Scientific, Inc.). The enriched isotope spikes also served to provide counts/second calibration factors for elements that were not spiked with enriched isotopes. This calibration was also examined with a mixed REE standard made in dilute 0.16 M HNO<sub>3</sub>. Precision and recovery were checked by analysis of a large-volume composite North Atlantic surface seawater sample. Spiked (with a natural isotopic abundance elemental spike) and unspiked aliquots of this sample were analyzed twice in each analytical run. Concentrations of La, Ce, and Pr in samples collected at the Bermuda Atlantic Time Series location during the 2011 U.S. GEOTRACES North Atlantic expedition compared favorably with published concentrations (Pahnke et al., 2012; van de Flierdt et al., 2012; Middag et al., 2015) and revealed no significant low REE oxide interferences on

middle and heavy REEs. A detailed report of this intercomparison exercise is included as **Supplementary Document 1**, and the comparison of dCe concentrations with those of other studies conducted near Hawaii is shown in **Figure 2**.

## Particulate Sample Analysis

To determine the lithogenic, biogenic, and authigenic fractions in the particulate samples, a total digestion method was employed (FSU, 2008), modified from the Eggimann and Betzer (1976) procedure and later thoroughly tested in Ohnemus et al. (2014). In brief, 2 mL of an acid mixture containing 4 M each of HNO<sub>3</sub> (quartz distilled), HCl (Fisher Optima), and HF (Teflon distilled) was added to a 15-mL Teflon jar (Saville) to submerge a folded 142 mm PCTE filter. The jars were sealed and placed on an enclosed HEPA-filtered laminar flow hotplate ("flowbox") for 3 h at 100–120°C. The jars were removed from the heat and allowed to cool before removing the lids in a fume hood. Using a Teflon spatula and tweezers, each folded filter was removed from the solution and all possible liquid was squeezed into the digestion jar. The filter was then twice rinsed with ultrahigh purity water (18.2 MOhm-cm), squeezing after each rinse. Once all the filters had been rinsed and removed, the jars were returned to the hotplate where they were heated at 120°C until taken to dryness, usually overnight. To oxidize any remaining organic material, 2 mL of 7M HNO<sub>3</sub> (quartz distilled) was added to the residue and the open jars were returned to the hotplate at 100–120°C until



the samples were once again taken to dryness. Finally, the digest residue was dissolved and transferred to an acid-washed plastic vial using repeated rinses of 0.32 M HNO<sub>3</sub> (~2%, quartz distilled) up to 20 mL final volume. Concentrations were determined using a multi-element standard in 2% HNO<sub>3</sub> (High Purity Standards) with 1 ppb In correction, and validated against similarly digested samples of the USGS CRM RGM-1, using values reported by Eggins et al. (1997) and the Max-Planck Institute database of Geological and Environmental Reference Materials (GeoReM, 2009). Subsequent testing of this method was shown to yield acceptable recoveries for other reference materials such as NRC PACS-2 and BCR-414 (**Supplementary Table 1**; Ohnemus et al., 2014). The procedural sample precision was determined from replicate analyses of the PACS-2 ( $n = 5$ ) and BCR-414 reference materials ( $n = 10$ ) to be 3–5% and 3–4%, respectively, for all elements presented here.

## Hydrographic Parameters and Nutrient Analyses

Temperature, salinity, and dissolved oxygen were determined shipboard on samples collected from the ship's rosette and from *in situ* measurements made by the Seabird 911 + CTD (Measures et al., 2006). Since the original publication of the nitrate, phosphate, and silicate data (Measures et al., 2006), it was determined that the nutrient sample storage and analyses were not performed to contemporary standards, so nutrient concentrations discussed here are for qualitative purposes only.

## RESULTS

The North Pacific Ocean can be divided into three general hydrographic regions (**Figure 1**): the Western Subarctic Gyre (WSG) in the north (stations 2 and 3), the Subtropical Gyre (STG) in the south (stations 7–9), and the Mixed Water Region (MWR) between the two gyres (stations 1 and 4–6). The results presented here begin with an introduction of the general hydrography of each region with additional attention given to specific relevant hydrographic features, followed by a summary of the distributions of the dissolved and particulate elemental concentrations.

### Surface Distributions of Dissolved Trace Elements

The WSG is an upwelling region, characterized by low temperatures (3–4°C), low salinities (32.5–33.1), and high dissolved oxygen concentrations (~320 μM; **Figure 3**). Consistent with the upwelling characterization, the surface waters contain high dissolved trace element concentrations (**Figure 4**). Surface concentrations (0–10 m depth) of dissolved Mn, Co, La, and Ce (as well as Pr, not shown) were highest in the upwelling WSG (**Figure 4**), following the same general distribution of low temperature and salinity values. Concentrations of dMn averaged  $1.25 \pm 0.52$  nM (range: 0.80–3.26 nM), and concentrations of dCo averaged  $23.5 \pm 31.4$  pM (range: 0.4–86.8 pM). The highest dissolved concentrations of both metals in the WSG were found near the outflow of the Sea of Okhotsk near

station 2, and dissolved concentrations were lowest across the STG. Similarly, the average concentrations of the dREEs La ( $8.0 \pm 8.9$  pM), Ce ( $3.7 \pm 2.7$  pM), and Pr ( $1.7 \pm 1.3$  pM) were also highest in the WSG and lowest in the STG and exhibited narrower concentration ranges over the study region than did the other metals.

### Vertical Distributions of Dissolved and Particulate Trace Elements

#### Western Subarctic Gyre (WSG): Stations 2 (KNOT; 44°N, 150°E) and 3 (50°N, 167°E)

The surface properties of the WSG extend through the winter (0–60 m) and spring mixed layers (60–150 m; **Figure 5**) and the vertical profiles of dissolved trace elements follow similar patterns (**Figure 6**). The dMn concentrations were highest (1.7–2.1 nM) in the upper 300 m in the WSG stations 2 and 3, but exhibited dual maxima at both stations: the shallower maximum occurring at 60 m and the deeper maximum occurring at 300 m, with a localized minimum (1.2–1.3 nM) centered at 100–150 m. In contrast, dCo exhibited only a single surface maximum (85–103 pM) at both stations, with the maximum at station 2 more pronounced (centered at 100 m) than the broader maximum (0–300 m) observed at station 3. The vertical profiles of the REEs dLa and dPr steadily increased from the surface (dLa 21–24 pM, dPr 3–3.6 pM) to 1500 m (dLa 44–46 pM, dPr 5–5.6 pM; **Supplementary Table 2**). In contrast, a dCe maximum was observed in the upper 100 m at station 2 (11 pM) and a less pronounced dCe maximum (5 pM) observed in the upper 100 m at station 3. Below 100 m, the dCe concentrations remained between 2 and 4 pM down to 1500 m.

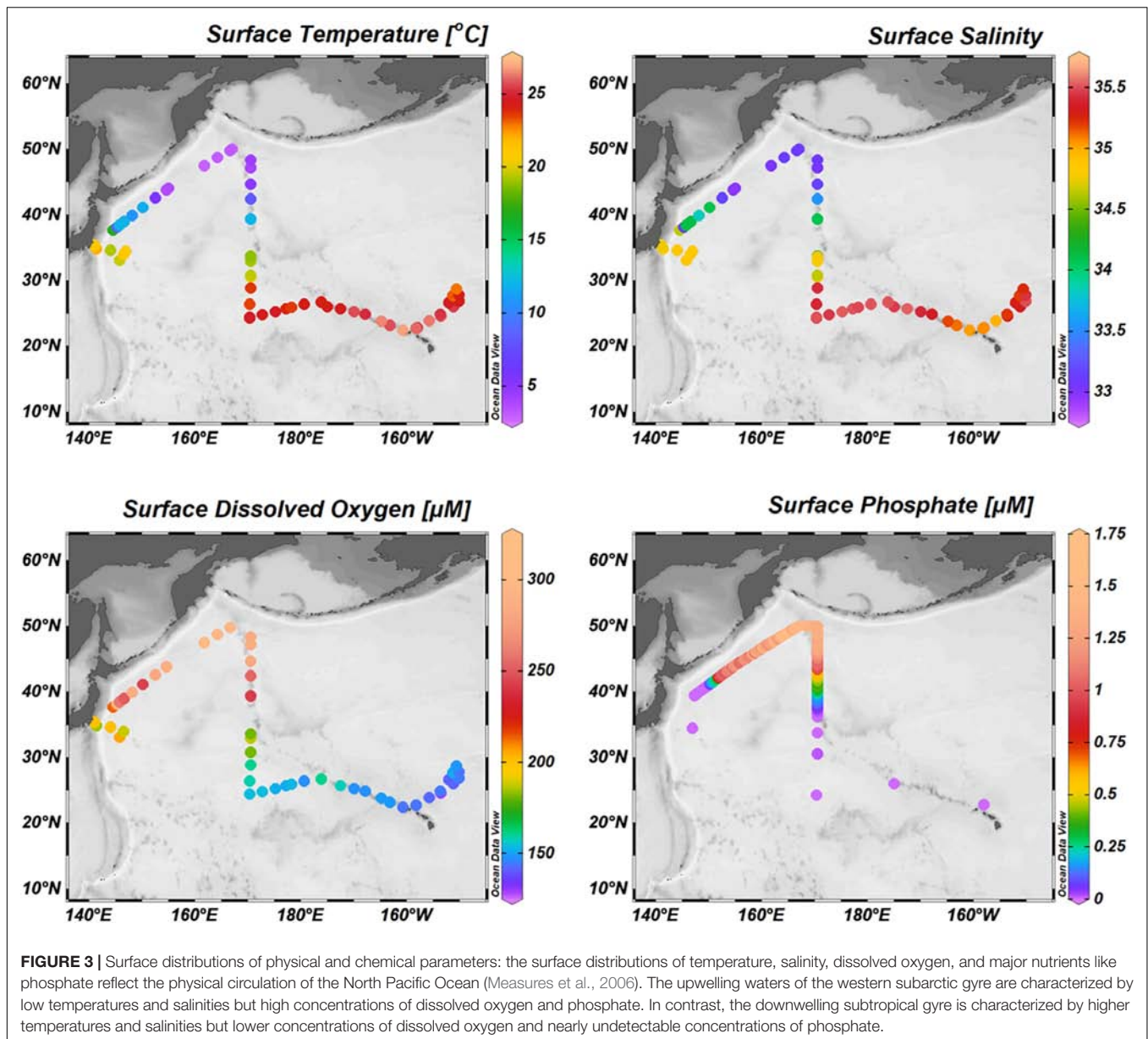
While the vertical distributions of dissolved trace element concentrations were similar between the WSG stations 2 and 3, the particulate concentrations differed greatly (**Figure 7**). At station 2, particulate concentrations of Mn, Co, and Ce were highest in the upper 300 m, with maxima occurring at 100–200 m. The pMn maximum was broader (0.43–0.45 nM at 80–150 m) than that of pCe (2.1 pM at 80 m), and pCo exhibited a dual-maximum feature (3.3 pM at 60 m, 3.5 pM at 150 m). Below these maxima, the concentrations decreased rapidly except for a local maximum at 900 m for pMn, pCo, and pCe (0.17 nM, 2.0 pM, and 1.1 pM, respectively).

At station 3, the pMn concentrations were lower than at station 2, with concentrations increasing from 0.03 nM at 24 m to ~0.10 nM at 153–300 m, and remaining at 0.09–0.13 nM from 500–1500 m. Concentrations of pLa (0.29–0.92 pM) and pPr (0.03–0.09 pM) exhibited maxima at 63–103 m, while pCe (0.32–0.78 pM) increased from the surface to 1500 m and showed a smaller maximum coinciding with those of pLa and pPr at 103 m. In general, pCo concentrations remained steady through the upper 1500 m at values near 1 pM (0.7–1.5 pM) except for a sharp maximum at 83 m.

#### Kuroshio Current/Mixed Water Region: Station 1 (34.5°N, 147°E)

At station 1, located within the MWR just off the coast of Japan (**Figure 1**), multiple water masses converge to form different





layers, distinguishable by their physical and chemical properties (Figure 8). Below the surface waters of the Kuroshio Current (0–300 m,  $24.5\text{--}26.6\ \sigma_\theta$ ), a low temperature-low salinity intrusion can be seen at 455 m (Figure 5) coinciding with  $\sigma_\theta = 26.4$  (Figure 8). A second low temperature/low salinity intrusion is also seen at 647 m ( $26.9\ \sigma_\theta$ ), interwoven with the lower portion of the Kuroshio Current (527 m,  $26.6\ \sigma_\theta$ ; Figure 8).

The water mass observed at 455 m is distinctive, not only because of its low temperature ( $7.3^\circ\text{C}$ ) and salinity (33.8), but also because of its high dissolved oxygen concentration ( $253\ \mu\text{M}$ ) which exceeds even the oxygen concentration in the overlying surface waters. Similar oxygen-rich intrusions have been observed in this region ( $27.5^\circ\text{N}$ ,  $145^\circ\text{E}$ ) and identified as subsurface mesoscale features forming the North Pacific Central Mode Water (CMW; Oka and Suga, 2005; Oka et al., 2007, 2011).

Typically, CMW forms along the subtropical-subarctic frontal zone, eastward along the MWR (Oka et al., 2009). However, the observed CMW-eddy at station 1 was unique with respect to the usual properties of CMW: not only was it oxygen-rich ( $253\ \mu\text{M}$ ), but it was found south of the subtropical front. Because of the similarities in properties between the subsurface CMW eddy described in Oka et al. (2009) and the intrusion observed at station 1 at 455 m, these two features likely result from the same physical mechanism of mesoscale eddy subduction. The second low temperature-low salinity intrusion at 647 m at station 1 ( $26.9\ \sigma_\theta$ ) is interwoven with the lower portion of the Kuroshio Current (527 m;  $26.6\ \sigma_\theta$ ). In contrast to the oxygen-rich water ( $253\ \mu\text{M}$ ) found at 455 m, the dissolved oxygen concentration at 647 m is lower ( $107\ \mu\text{M}$ ). Despite some differences in temperature and salinity, the potential density at

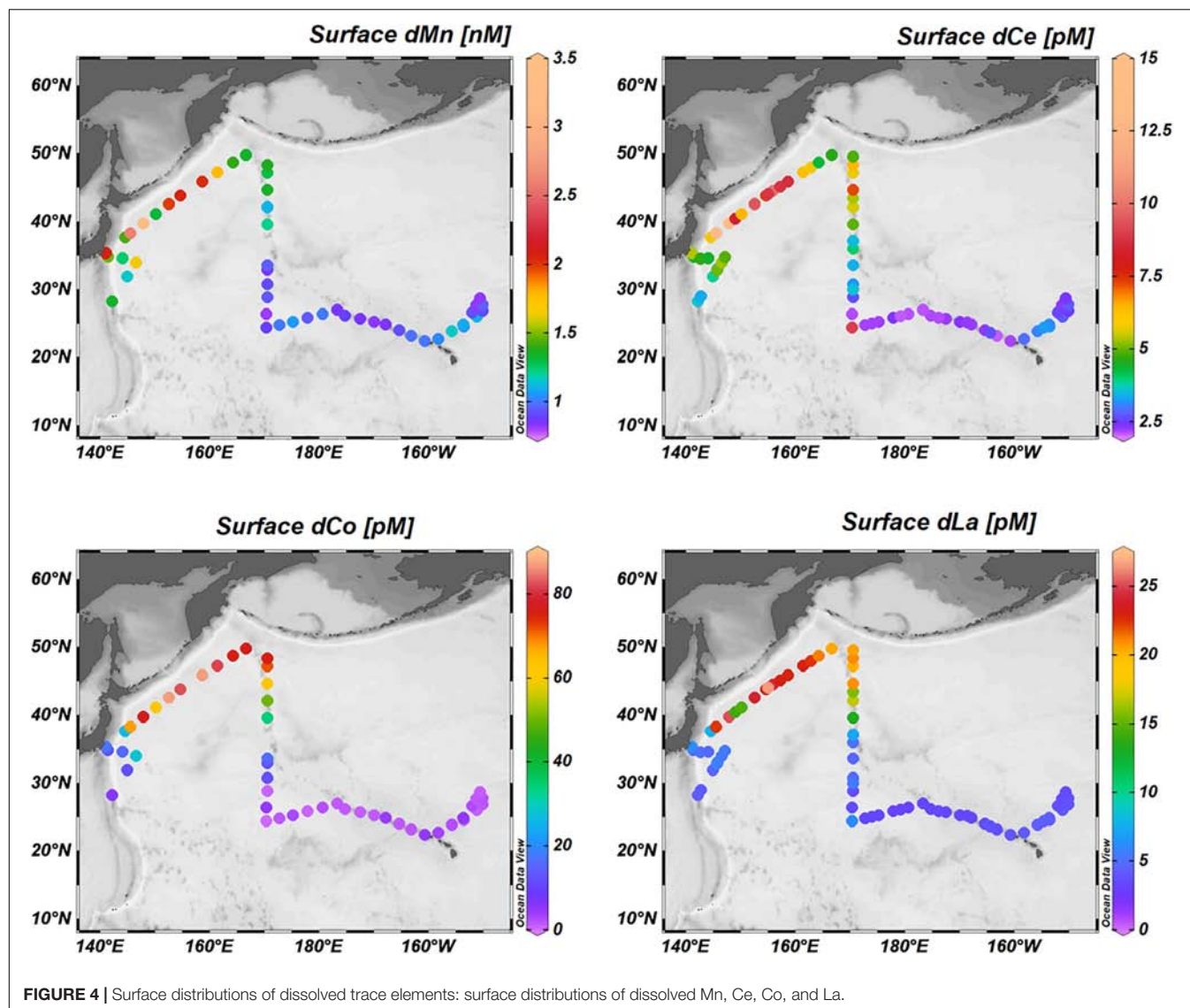


**FIGURE 4 |** Surface distributions of dissolved trace elements: surface distributions of dissolved Mn, Ce, Co, and La.

647 m ( $26.9 \sigma_\theta$ ) is similar to that of intermediate waters from the Sea of Okhotsk: the Dense Shelf Water (DSW:  $\sim 26.8\text{--}27.0 \sigma_\theta$ ) and Okhotsk Sea Intermediate Water (OSIW:  $\sim 26.8\text{--}27.2 \sigma_\theta$ ) (Andreev and Kusakabe, 2001; Shcherbina et al., 2004). Waters from the Sea of Okhotsk enter the North Pacific at depth through the Kuril-Kamchatka Margin, mix with waters from the WSG and are carried south within the Oyashio Current. Intermediate waters from the Sea of Okhotsk compose  $\sim 25\%$  of the Oyashio Current at potential densities of  $26.6\text{--}27.0 \sigma_\theta$  (Yasuda et al., 2002), which is within the potential density range of the intrusion at 647 m at station 1.

The dissolved oxygen concentration at 647 m at station 1 likely reflects the mixing of the oxygen-rich intermediate waters from the Sea of Okhotsk (DSW and OSIW) with the oxygen-poor waters of the WSG near station 2 (Figure 1). The lower Oyashio Current is comprised of  $\sim 25\%$  water from the Sea of Okhotsk and  $\sim 75\%$  water from the WSG (Yasuda et al., 2002). If these two waters mix at the proportions suggested by Yasuda

et al. (2002), and using the DSW dissolved oxygen concentration of  $290\text{--}340 \mu\text{M}$  (Andreev and Kusakabe, 2001) and the oxygen concentrations at the outflow of the Sea of Okhotsk ( $30\text{--}60 \mu\text{M}$ ; station 2), then the predicted oxygen concentrations at 647 m at station 1 would be  $95\text{--}130 \mu\text{M}$ . The measured dissolved oxygen concentration of  $107 \mu\text{M}$  at 647 m at station 1 is within this range, and supports a mix of source waters from both the Sea of Okhotsk and the WSG. The vertical profiles of dissolved Mn and Co concentrations at station 1 (Figure 6) were clearly impacted by the low temperature-low salinity intrusions at 455 and 647 m. The shallower intrusion at 455 m contains  $2.9 \text{ nM dMn}$  and  $109 \text{ pM dCo}$ , while the deeper intrusion at 647 m contains  $6.3 \text{ nM dMn}$  and  $392 \text{ pM dCo}$ . Above, below, and between these intrusions were dMn concentrations of  $0.65\text{--}1.9 \text{ nM}$  and dCo at  $9.6\text{--}87.4 \text{ pM}$ , well below the trace metal-enriched waters of the intrusions.

The dREEs concentrations were also high in the shallower intrusion at 455 m and produce a local maximum, with a

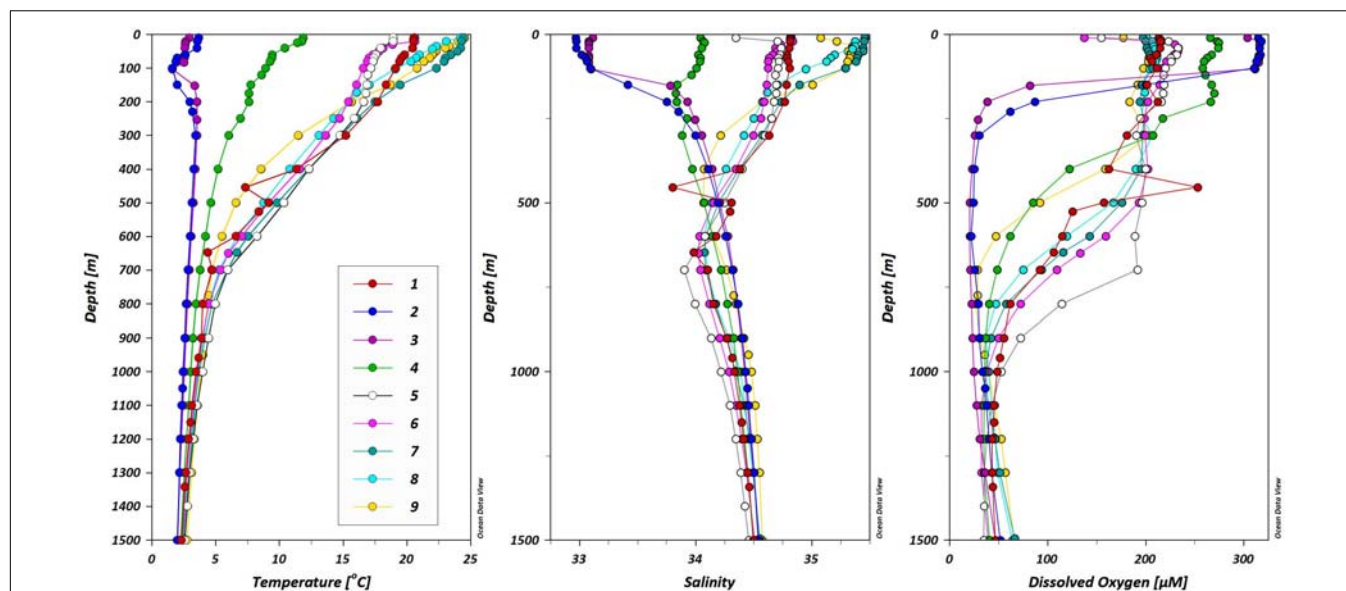


**FIGURE 5 |** Vertical distributions of physical and chemical properties in the North Pacific Ocean: Vertical distributions of physical and chemical properties in the North Pacific Ocean. Station colors match those in the map (Figure 1).

dLa concentration of 23.7 pM, dCe of 102 pM, and dPr of 4.0 pM (Supplementary Table 2). Above the 455 m intrusion, the Kuroshio Current waters have lower concentrations of dLa, dCe, and dPr, below the shallow intrusion, the dREEs steadily increase in concentration with depth, but no second maximum at 647 m is observed for any of the light REEs.

The vertical distributions of particulate Mn, Co, and Ce concentrations were also affected by the intrusions at 455 and 647 m (Figure 7). Particulate Mn and Ce were highest at 455 m (0.97 nM and 3.1 pM, respectively), while the pCo maximum extended across the entire 455–647 m range (3.1–4.6 pM). Smaller maxima were also observed at 40 m for pCo (2.5 pM) and pCe (0.9 pM).

#### Kuroshio Extension/Mixed Water Region: Stations 4 (39.3°N, 170.5°E), 5 (33.5°N, 170.5°E), and 6 (30.5°N, 170.5°E)

Stations 4–6 transect the east-west flow of the Kuroshio Extension (Figure 1), and the hydrographic features at these stations are a mix of the two contrasting gyres that form the MWR. The upper waters of station 4 (0–200 m) have temperature and salinity values that fall between the subarctic and subtropical gyres (Figure 5). Station 4 is midway across the MWR, possessing two small salinity minima at 150 and 300 m. Below these minima (200–1400 m) the temperature and salinity values are similar to those of the WSG stations 2 and 3 in the same depth range. The temperature and salinity at stations 5 and 6 in the upper 400 m are almost identical in structure to station 1 (depths 0–400 m), but also show a broad salinity minimum (300–1400 m) centered at ~600 m. This salinity-minimum feature spreads across much of the North Pacific Ocean (26.3–26.8  $\sigma_\theta$ ; Figure 8) and is known as the North Pacific Intermediate Water (NPIW), which forms

along the western region of the MWR as a combination of waters from the Sea of Okhotsk, the base of the winter mixed layer in the WSG, and the Kuroshio Current (Qiu, 1995; Talley et al., 1995; You, 2003b, 2005).

The dissolved oxygen concentrations at stations 4, 5, and 6 reflected the incomplete mixing of subarctic and subtropical waters. Stations 4 and 5 had similar high oxygen intrusions like the low temperature/low salinity intrusion at station 1 at 455 m (Figure 5), consistent with the continued transport and subduction of WSG waters along the MWR and ongoing formation of the NPIW within the STG. The various intrusions possessed similar physical and chemical properties but were observed at different depths at each station due to the degree of subduction by less-dense Kuroshio waters from the south. Station 4 was located at the northern edge of the MWR, where it was less likely to be influenced by the lower-density Kuroshio waters (from the south) than stations 1 and 5: thus, the CMW was less subducted at station 4 and resided nearer the surface than at the other two stations.

Across the MWR stations, dMn concentrations were highest (1.2–1.6 nM) in the upper 175–250 m (Figure 6). A subsurface dMn maximum (1.4 nM) at station 5 at 300 m (25.7  $\sigma_\theta$ ) is coincident with the local dissolved oxygen minimum, but not observed at stations 4 and 6. Dissolved Ce concentrations are lowest at 500–650 m at all stations (2.5 pM at station 4, 1.7–1.8 pM at stations 5 and 6), and highest in the upper 300 m (5.0 pM at station 4, 3.0–3.6 pM at stations 5 and 6) but increase with depth (3.4–4.0 pM at 1500 m, stations 4–6). Unlike dMn and dCe distributions, dCo concentrations were lowest at the surface (16–42 pM) and reached mid-depth maxima of 47–55 pM at 300–900 m at stations 4–6. Similar to the dMn at station 5, dCo also showed a shallower maximum at 300 m of

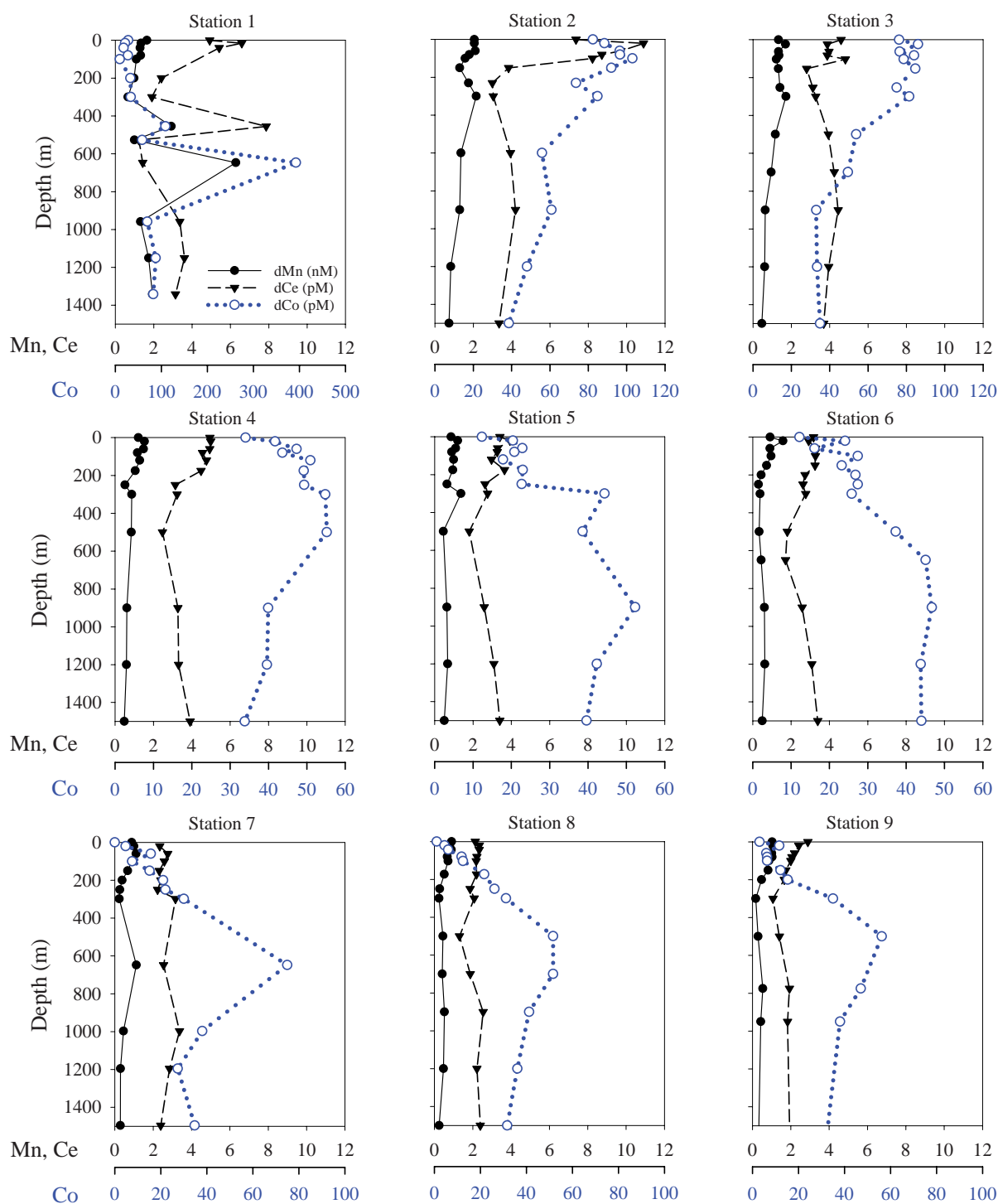


**FIGURE 6** | Vertical properties of dissolved trace elements: Vertical profiles of dissolved Mn (nM), Co (pM), and Ce (pM). Note that Co concentration (in blue) scales change depending on the ranges encountered at each station.

44 pM, coincident with the local dissolved oxygen minimum at this station.

Dissolved REE concentrations increased almost linearly with depth at stations 4–6, with upper ocean

concentrations decreasing southward across the MWR (Supplementary Table 2 and Figure 5). Concentrations were highest in the upper 500 m at station 4 (dLa = 12.9–20.4 pM, dPr = 2.2–3.0 pM) but decreased



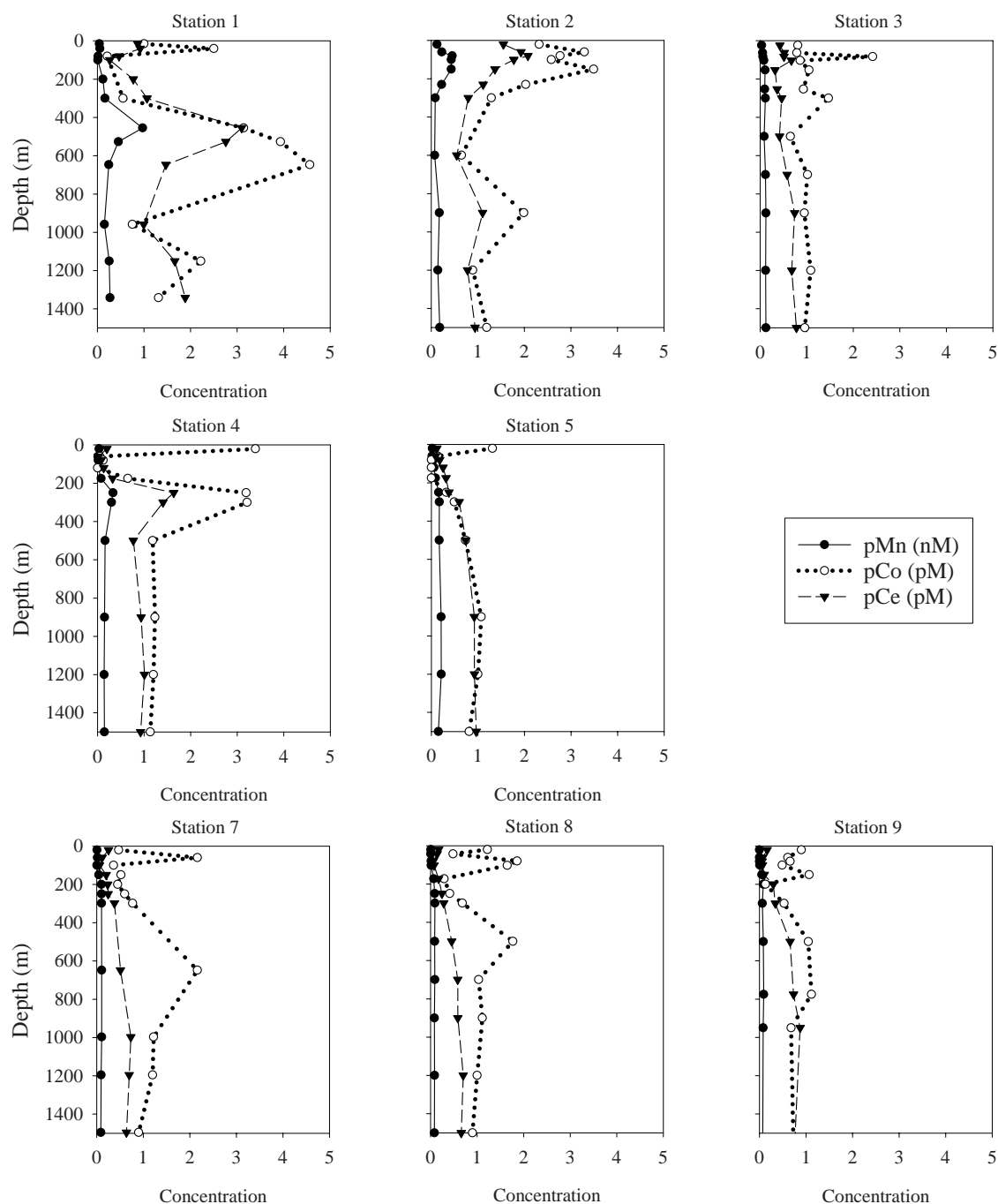


**FIGURE 7 |** Vertical properties of particulate trace elements: Vertical profiles of particulate Mn (nM), Co (pM), and Ce (pM).

at stations 5 and 6 ( $dLa = 4.6\text{--}11.6$  pM,  $dPr = 0.1\text{--}1.8$  pM). Below 500 m, dREE concentrations remained relatively constant at all stations ( $dLa = 30\text{--}40$  pM,  $dPr = 3\text{--}5$  pM).

The vertical distributions of particulate TEs at station 4 were characterized by subsurface maxima at 250–300 m of Mn (0.3 nM), Co (3.2 pM), and Ce (1.6 pM), similar to the dMn and dCo maxima at this same station and depth

(Figure 7). In contrast, particulate concentrations at station 5 showed a slight surface enrichment for pCo (1.3 pM) but not for pMn or pCe and vertical distributions that slightly increased from low surface concentrations with depth. The particulate concentrations at intermediate depths (500–1500 m) were similar at stations 4 and 5 (pMn = 0.1–0.2 nM, pCo = 0.8–1.2 pM, and pCe = 0.8–1.0 pM). Note that particulate concentrations for station 6 are not

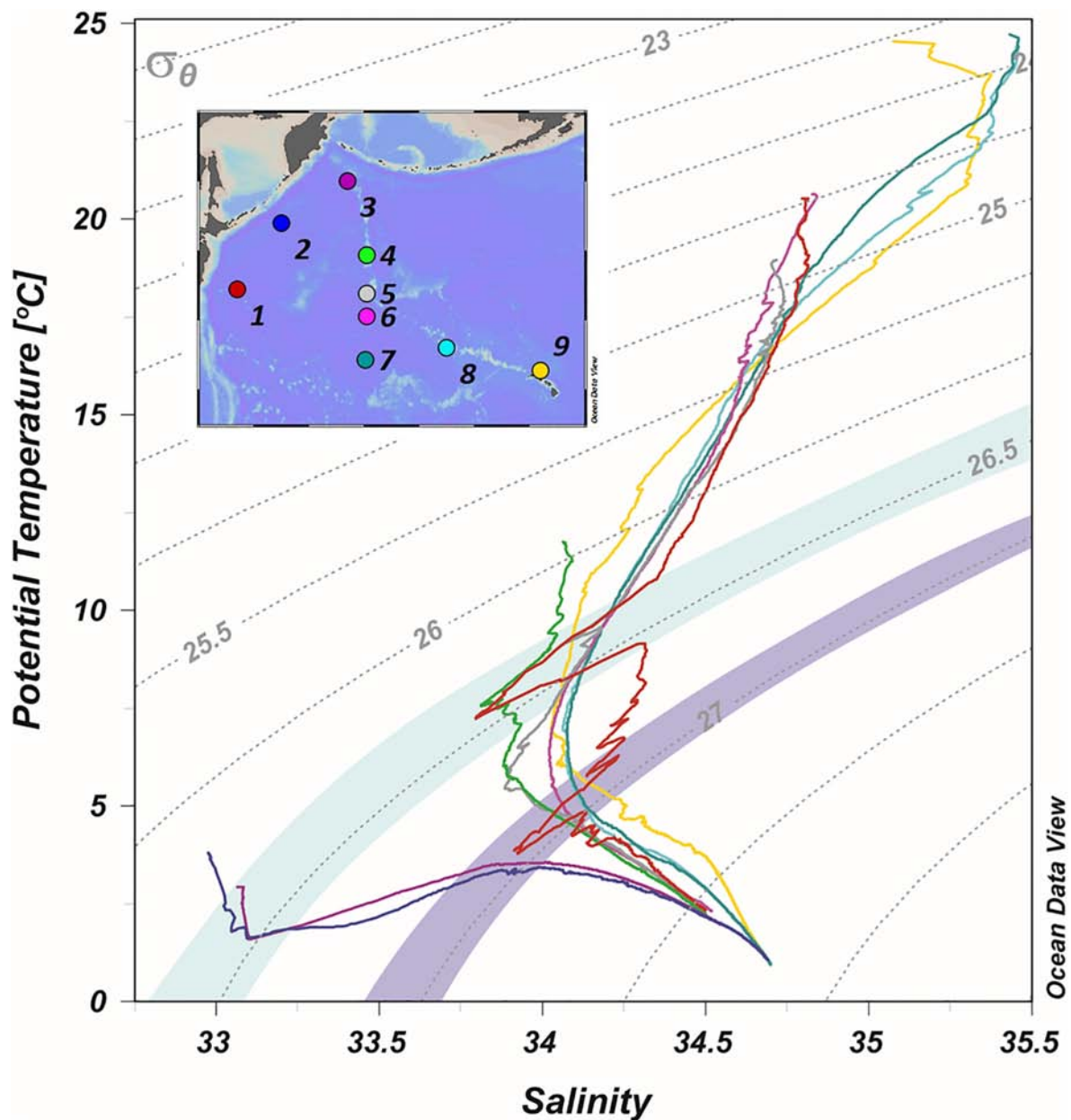


**FIGURE 8 |** Temperature-salinity profiles for all stations, shown with isopycnal layers (dashed lines). Shaded areas show density ranges for the upper (green, 26.3–26.6  $\sigma_\theta$ ) and lower (purple, 26.9–27.1  $\sigma_\theta$ ) low temperature-low salinity intrusions.

reported, as these samples were used initially during method optimization trials.

#### Subtropical Gyre: Stations 7 (24.25°N, 170.3°E), 8 (26°N, 175°W), and 9 (ALOHA; 22.5°N, 158°W)

High temperatures (24–27°C), high salinities (35–35.5), and low densities (23.5–24  $\sigma_\theta$ ) characterize the surface waters of the STG. While the WSG is an upwelling region that can supply trace metal-enriched mid-depth waters to the surface, the STG is a downwelling region that depresses the subsurface waters. In the central STG, the most notable water mass is

the NPIW, identifiable by a salinity minimum that lies at depths of 400–800 m at potential density surfaces of 26.5–27.5  $\sigma_\theta$  (Figure 8).

Dissolved trace element concentrations are influenced by these physical features. Concentrations of dMn were highest (0.7–1.1 nM) in the upper 100 m and decrease to a minimum (~0.2 nM) at 250 m (Figure 6). In general, there was a slight increase in dMn concentrations (0.3–0.5 nM) down to 1500 m, except for a subsurface maximum of 1.1 nM at 648 m at station 7, which was coincident with the salinity minimum at this station. No such feature existed for dMn at stations

8 and 9, but dCo concentrations reached a maximum (52–75 pM) within the salinity minimum at all STG stations. Concentrations of dCo decreased above these maxima to 4–16 pM at the surface and below to 32–35 pM at 1500 m. Dissolved Ce concentrations ranged 1.1–3.4 pM, similar to the concentrations found at depths below 200 m at stations 3–6 (**Figure 6**). However, the vertical profiles lacked any distinguishing features at stations 7 and 8 beyond slightly higher concentrations in the upper 200 m (1.6–2.4 pM) and minimum concentrations (1.1–1.3 pM) at 300–500 m. The vertical profiles of dLa and dPr at all three STG stations were nearly identical: upper ocean (0–300 m) concentrations of dLa were 3.4–7.8 pM which gradually increased to 36–37 pM at 1500 m, and dPr concentrations at 0–300 m were 0.7–1.1 pM increasing to 4.3–4.4 pM at 1500 m (**Supplementary Table 2**).

The STG samples contained some of the lowest particulate concentrations observed in this study (**Figure 7**). Particulate Mn concentrations were less than 0.01 nM in the upper 100 m, increasing to 0.09–0.10 nM at 1500 m. Particulate Ce concentrations were also lowest in the upper 150 m (0.1–0.2 pM) and gradually increase with depth to 0.6–0.9 pM at 1000–1500 m. In contrast to pMn and pCe, vertical distributions of pCo showed some variability throughout the water column, including subsurface maxima (1.1–2.2 pM) at 60–150 m and deeper maxima of 1.1–2.2 pM at all three stations at 500–775 m.

## DISCUSSION

Our results are reasonably explained by the release of redox-mobilized dissolved Mn, which is converted *in situ* to particulate Mn. Our discussion is framed by considering the relative importance of each input, removal, and internal transformation term, even though the individual terms cannot be adequately quantified with our data set. The equation summarizing the rate of change in dissolved or particulate trace elements is given in Equation 2,

$$\frac{dC}{dt} = \nabla C + \nabla^2 C + J \quad (2)$$

where  $dC/dt$  is the net flux of material (e.g., as  $\text{nmol m}^{-3} \text{d}^{-1}$ ),  $\nabla C$  is the advective flux in three dimensions,  $\nabla^2 C$  is the turbulent mixing flux in three dimensions, and  $J$  is the change in concentration from internal processes. The  $J$  term includes scavenging, settling particles, biological uptake, regeneration, and reduction-oxidation processes. The following sections introduce the different processes involved in the shelf inputs and lateral transport, the evidence for biological Mn-oxide production, the effects of Mn-oxides on Ce and Co cycling, and ultimately their lateral transport across the North Pacific Ocean.

## Inputs of Shelf-Derived Redox Active Elements in the WSG

The upper ocean maxima in dissolved and particulate Mn, Co, and Ce in the WSG (station 2, **Figures 6, 7**) suggest a fluvial, atmospheric, and/or shelf input of material. During the IOC-2002 expedition, the strongest evidence of fluvial material to the North Pacific along our transect was near the Hawaiian islands, where high concentrations of dissolved Fe and Al were concurrent with lower salinity (Brown et al., 2005; Measures et al., 2005), far from the Kuril-Kamchatka margin where the upper ocean plume of Mn, Co, and Ce were observed. Aerosol and surface ocean samples were also examined for evidence of atmospheric deposition of trace metals. Aerosol concentrations of Se and Ag (Ranville et al., 2010), Sb (Cutter and Cutter, 2006), and Pb (Gallon et al., 2011; Zurbrick et al., 2017) indicate that coal combustion from Asia produces aerosols enriched in anthropogenic-derived material. After deposition of these aerosols to the surface ocean, nearshore waters enriched in anthropogenic material can be subducted and advected laterally to produce high dissolved concentrations at intermediate depths, as in the case of Ag (Ranville and Flegal, 2005) and Pb (Zurbrick et al., 2017). While anthropogenic aerosols have been shown to be a source for some metals to the western North Pacific in other studies as well (e.g., Lin et al., 2007; Hsu et al., 2010; Kim et al., 2012), the concentrations of lithogenic tracers like Al (Measures et al., 2005; Buck et al., 2006) and Ga (Shiller and Bairamadgi, 2006) in aerosol and surface ocean samples collected during the IOC-2002 expedition fell below model predictions (Measures et al., 2005; Buck et al., 2006), despite the expedition occupying the western North Pacific during the season of maximum Asian dust inputs. During four dust events encountered during this cruise, concentrations of Fe in aerosols were shown to be highest in the western North Pacific and similar in composition to crustal material, but the aerosol Fe concentrations rapidly diminished with distance from the coast (Buck et al., 2006). Overall, dissolved Fe concentrations in surface waters in the western North Pacific were low (0.1–0.3 nM; Brown et al., 2005), consistent with low atmospheric input and rapid biological uptake in an HNLC region. Therefore, while aerosol inputs are important for some elements in the western North Pacific Ocean, especially those elements enriched in anthropogenic sources, relevant research in this region (even during this same expedition) showed that atmospheric deposition is not as likely to be the primary source of redox-active lithogenic elements in a subsurface plume as a shelf source.

When considering the origin of the subsurface Mn, Co, and Ce plume within the western subarctic gyre (Stations 2 and 3), the supply of trace metals like Fe and Mn from the nearby continental margin has been well documented (Nishioka et al., 2007; Lam and Bishop, 2008; Lamborg et al., 2008; Tanaka et al., 2012; Nishioka and Obata, 2017; Zheng et al., 2019). Our own data support that the shelves are an important source of dMn to the WSG, based on the dissolved and particulate Mn distributions at stations 1–3. At station 2, the upper 600-m can be divided

into three layers: a layer of high dMn in the oxygen-rich surface waters (0–80 m), a pMn plume at 80–150 m that coincides with a sharp oxycline and a localized dMn minimum, and a subsurface dMn maximum that decreases with depth, concurrent with low dissolved oxygen concentrations and the disappearance of the pMn plume (below 150 m). High dMn concentrations extend below the immediate surface waters to 300 m and show a double maximum (**Figure 9**), near the surface (0–60 m) and below the oxycline (200–300 m). As dMn is released from the sediments of the Kuril-Kamchatka margin (Lam and Bishop, 2008), it can undergo redox transformations at the sediment-water interface and/or during transport to the WSG. Centered between the two dMn maxima is a maximum in pMn (80–150 m,  $0.44 \pm 0.01$  nM) that overlaps the oxycline (100–230 m) and could result from resuspension of shelf-derived material, scavenging, or biological uptake or oxidation of dMn. Above the pMn maximum, dMn is likely sustained in the surface (0–80 m) by photochemical reactions with dissolved organic carbon that either inhibit the formation of pMn or transform pMn to dMn through reductive photochemical dissolution (Sunda, 2012; Hansel, 2017). Below the pMn maximum (150–300 m), low oxygen concentrations prevent Mn oxidation, and so the dMn plume originating from the margin persists. Furthermore, the pMn plume at 80–150 m is 20–25% of the total Mn (dMn + pMn), and the depth-integrated concentration of pMn over the upper 300 m is  $82.9 \mu\text{mol m}^{-2}$ , which closely matches the “missing” depth-integrated (80–150 m) dMn concentration of  $104.7 \mu\text{mol m}^{-2}$ . Noticeably absent from the upper 600-m is any indication of a concurrent pTi plume (**Supplementary Table 2**), which would indicate offshore transport of atmospheric or marine resuspended lithogenic (i.e., non-redox mobilized) material.

## Enrichments of Mn, Co, and Ce and the Composition of the pMn Plume

The composition of the pMn plume can be better identified by comparing against a crustal tracer like pTi. In the pMn plume at 80–150 m station 2 (**Figure 10**), the pMn/Ti ratio is roughly tenfold higher than crustal abundance (1.7–2.5 mol Mn/mol Ti at 80–150 m, vs. an average crustal abundance value of 0.18 mol Mn/mol Ti, Rudnick and Gao, 2003). This enrichment suggests that the pMn is not simply a result of the resuspension of sedimentary material or atmospheric deposition of crustal material, but more likely is produced during lateral transport of dMn released from the shelf. Microbial processes capable of oxidizing dMn are well-documented (Moffett and Ho, 1996; Bargar et al., 2000; Tebo et al., 2004; Dick et al., 2008; Spiro et al., 2010; Toyoda and Tebo, 2016), and these same microbes or the Mn-oxides they produce can also scavenge and/or oxidize dCo and dCe (Tebo et al., 1984, 2004; Moffett, 1990, 1997; Moffett and Ho, 1996; Learman et al., 2011; Schijf et al., 2015; Hansel, 2017). At station 2, the maxima of particles enriched in Co and Ce (based on the vertical profiles of pCo/Ti and the pCe anomaly) coincide with the pMn/Ti maximum within the oxycline. When all the facts are considered in concert – the concurrence of the localized dMn minimum with the pMn maximum at station 2; the lack of evidence of a plume of resuspended lithogenic particles;

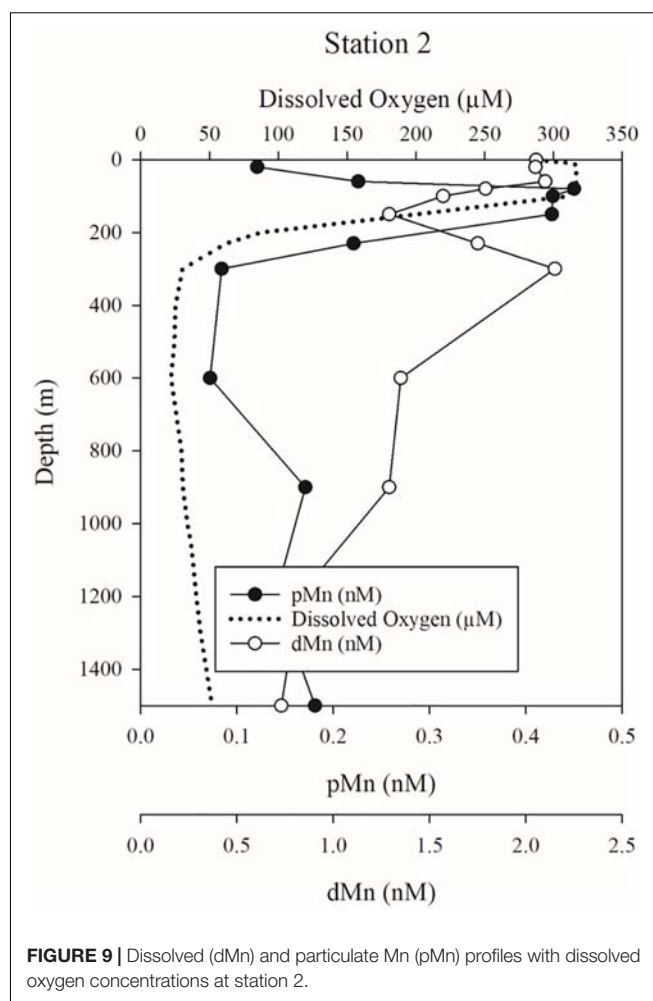


**FIGURE 9** | Dissolved (dMn) and particulate Mn (pMn) profiles with dissolved oxygen concentrations at station 2.

the coincidence of the pMn, pCo, and pCe enrichments; and the extensive documentation of biological Mn oxidation and its influence over other trace element cycles – the natural conclusion is that the pMn plume is composed of Mn-oxides, biologically produced from dMn originating from the nearby shelf.

## Particulate Mn Removal via Settling Particles

The pMn plume could be lost from the upper ocean as settling particles, as was observed by Lamborg et al. (2008). Concentrations of trace elements like Mn and Al were determined in settling material collected in sediment traps at station K2 (47°N 160°E; Lamborg et al., 2008) which is near our station 2 (44°N 155°E). While the analytical and natural variability prevent a more precise estimate of the sediment trap particle composition, the estimated Mn/Al ratios in the sediment traps at K2 suggest that the settling particles are approximately three times enriched over crustal abundance, and our own suspended particles at station 2 are enriched tenfold over crustal abundance (relative to Ti). The differences in enrichment could be due to spatial variations, temporal variations (K2: June–July 2004; station 2: April 2002), filter pore size (K2: 1.0 μm; station



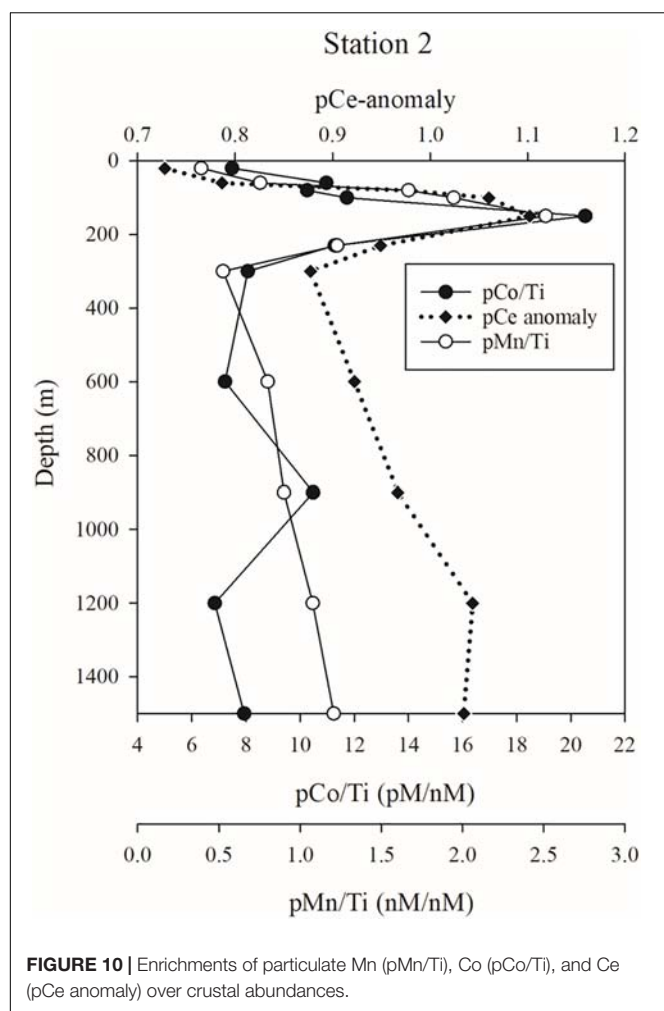


**FIGURE 10 |** Enrichments of particulate Mn (pMn/Ti), Co (pCo/Ti), and Ce (pCe anomaly) over crustal abundances.

2:  $0.4 \mu\text{m}$ ), or even reductive dissolution or desorption of settling particles as they pass through the low oxygen waters below 300 m (Figure 9). Regardless of the differences, both the suspended particles at station 2 and the settling particles from K2 are enriched in Mn and suggest that some fraction of the pMn-oxides are indeed lost by settling.

Therefore, the extent of lateral transport of the Mn plume depends on the contrast between the settling rate of pMn and current velocity that can advect the shelf-derived material offshore. The residence time of the pMn plume can be estimated using the depth-integrated concentration at station 2 and the sediment trap settling fluxes at K2 (Lamborg et al., 2008). The depth-integrated pMn concentration in the upper 150 m at station 2 is  $46 \mu\text{mol m}^{-2}$ , and the range of settling fluxes at nearby station K2 is  $111 \pm 67 \text{ nmol m}^{-2} \text{ day}^{-1}$  from neutrally buoyant sediment traps (NBST) and  $175 \pm 117 \text{ nmol m}^{-2} \text{ day}^{-1}$  from surface tethered “CLAP” traps (Lamborg et al., 2008). The resulting residence time of pMn at station 2 is  $415 \pm 251$  days (NBST) or  $265 \pm 177$  days (CLAP). This pMn residence time exceeds the 54–108 days required for the Oyashio Current to travel from station 3 to station 1 (1860 km), assuming a velocity of 0.2–0.4 m/s (Ohshima et al., 2005), allowing the

concentrations of pMn (and other elements associated with the Mn particles) to accumulate within the Oyashio waters and be transported offshore.

## Dissolved and Particulate Ce-Anomalies

The influence of Mn-oxides over dissolved and particulate REE distributions can be explored by considering both the dissolved and particulate Ce anomalies at station 2. The dCe (Figure 6) and pCe concentrations (Figure 7) are highest in the upper 300 m at station 2, while dissolved concentrations of La and Pr are lowest at the surface and steadily increase with depth (Supplementary Table 2). While an atmospheric source of this surface maximum of Ce (and other REEs) might be plausible, the dissolved and particulate Ce anomalies argue against an atmospheric source of lithogenic material. The dCe anomaly (normalized to PAAS) is overall depleted (0.05–0.25) throughout the upper 500 m (Figure 11). Our dCe anomalies compare favorably with those from VERTEX IV ( $28^\circ\text{N}$ ,  $155^\circ\text{W}$ ; de Baar et al., 2018): the upper waters are similarly depleted, with the highest dCe anomaly of 0.22–0.35 in the upper 150 m, declining quickly to a dCe anomaly of 0.05 by 500 m. This overall depletion indicates that dCe is being preferentially removed relative to dLa and dPr. A likely mechanism for this removal is via oxidation by pMn-oxides or Mn-oxidizing microbes, as evidenced by the pCe anomaly which coincides with the pMn/Ti maximum (Figure 10), which could oxidize dCe to particles that are removed by settling. Furthermore, the dCe anomaly is highest near the surface, coincident with the surface maximum in dMn, but in contrast no such dCe anomaly is observed with the deeper dMn maximum (150–300 m). The contrast between dCe and dMn is consistent with a supply of dMn that is oxidized to pMn during offshore transport. Particulate Mn-oxides are prohibited from forming or are photochemically dissolved near the surface (Sunda et al., 1983; Sunda and Huntsman, 1988, 1994), which in turn would prevent the subsequent oxidation of dCe to pCe oxides in the upper 80 m at station 2. Within the pMn plume (80–150 m), the dCe is oxidized and forms particles enriched in Ce relative to La and Pr, thus producing the pCe anomaly maximum. Below the pMn plume, pMn oxides are transformed to dMn through reductive dissolution in the low oxygen conditions, but pCe appears to be unable to dissolve as quickly as pMn oxides and is therefore likely lost as settling particles from the upper ocean. The production and removal of Ce-enriched particles steadily depletes the dCe relative to the other dREEs. Therefore, the upper 300 m waters are also depleted in pCe (which are produced in dCe-depleted source water) except at the pMn maximum, due to preferential oxidation and scavenging of redox-mobilized dCe from the shelf and exacerbated by low inputs of lithogenic material from atmospheric or resuspended shelf sources.

## Biological Controls Over Particulate Co

Biological demand also influences the distributions of trace metals like Co in the WSG. While Mn is a bioactive trace metal, its concentrations are usually found in excess of biological demand and therefore are not considered limiting (Sunda and Huntsman, 1996, 2000; Morel et al., 2003). Cobalt also plays a critical biological role in marine microbes, as an essential trace

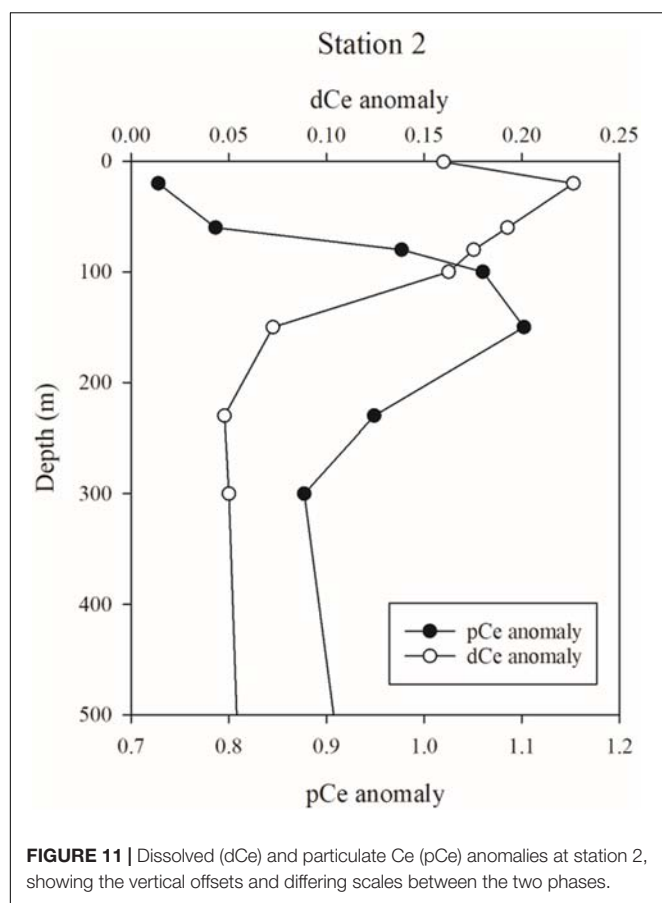


**FIGURE 11** | Dissolved (dCe) and particulate Ce (pCe) anomalies at station 2, showing the vertical offsets and differing scales between the two phases.

nutrient for carbonic anhydrase and cobalamins, for example (Morel et al., 2003; Saito et al., 2005), but its concentrations are much lower than those of dMn. As such, dCo is often observed to be complexed with strong organic ligands in the open ocean, thus preserving its solubility and potential bioavailability (Ellwood and van den Berg, 2001; Saito and Moffett, 2001; Noble et al., 2017; Tagliabue et al., 2018). The dissolved-particulate partitioning of Mn and Co at station 2 is evidence of these differences, where pMn constitutes up to 25% of the total Mn, while the pCo is only a small fraction of the total Co (2–6%), likely due to an oxidized form [i.e., Co(III)] that is soluble (Moffett and Ho, 1996) and complexed by organic ligands (Noble et al., 2012). The vertical profile of pCo concentrations features two maxima in the upper 300 m (Figure 7): the shallower maximum at 60 m coincides with the chlorophyll *a* maximum in the upper 50 m (Measures et al., 2006) while the deeper maximum at 150 m coincides with the pMn/Ti maximum, suggesting co-oxidation with Mn oxides like Ce. Below 150 m, the pCo concentrations rapidly decrease across the oxycline, but dCo concentrations are slightly elevated at 300 m, consistent with the desorption and reductive dissolution of dCo from the pMn-oxides through the oxygen minimum zone. In summary, it is likely that the pCo profile reflects influences by active biological uptake by phytoplankton (50–60 m) and scavenging (and possibly oxidation) by pMn-oxides at 80–150 m. However,

the majority of the dCo originating from the shelf with dMn and dCe is preserved in the dissolved fraction, probably due to the combined effects of an oxidized form that is soluble and the prevention against particulate scavenging and loss by organic ligands.

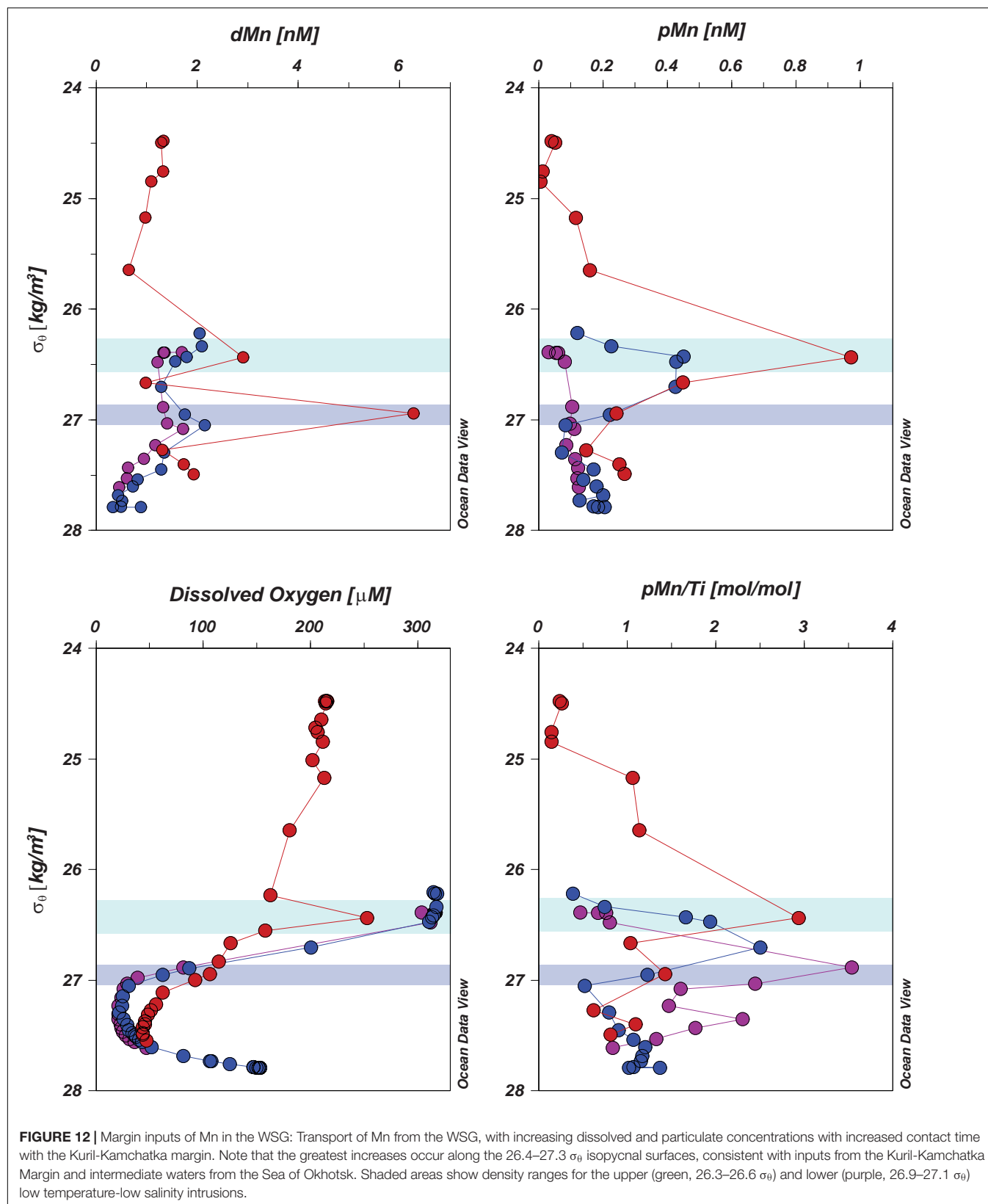
## Lateral Transport of Shelf Material From the WSG

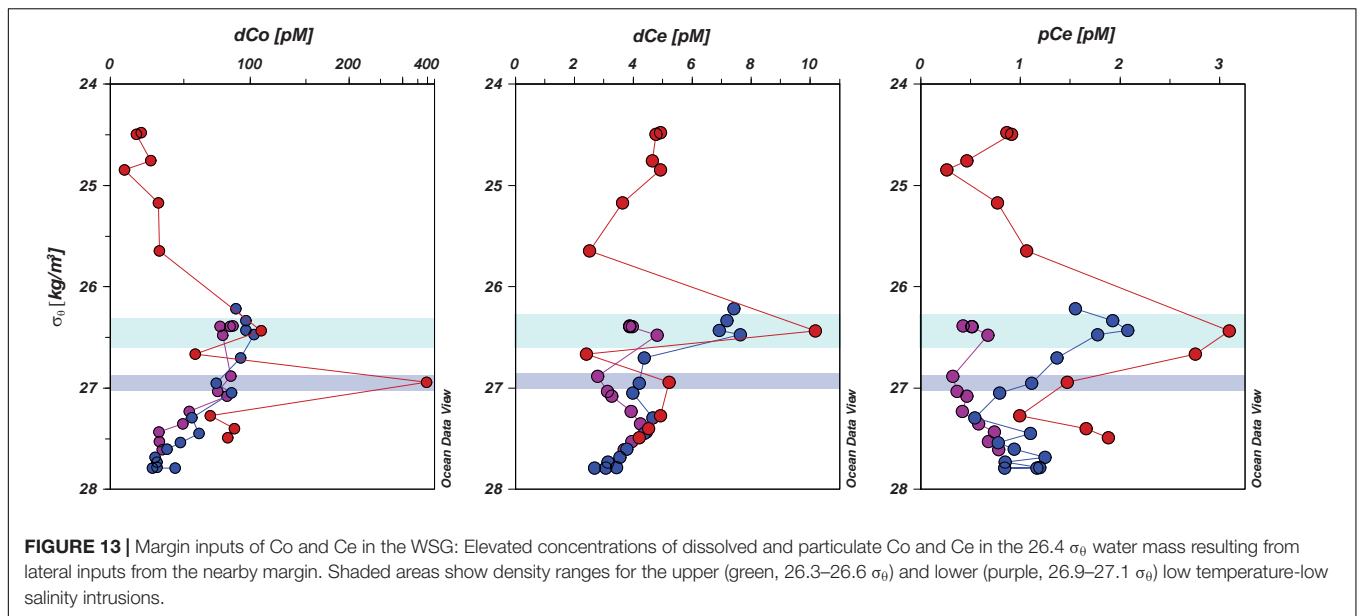
Material supplied to the WSG from the shelf is transported by ocean currents far beyond the source. The Oyashio Current travels along the Kuril-Kamchatka margin from north to south (station 3 to 2) and then collides with the Kuroshio Current coming up from the south (station 1), gradually mixing eastward along the MWR (transected by stations 4–6) and into the central subtropical gyre (stations 7–9; Figure 1). This region between the Oyashio and Kuroshio is known as the MWR for good reason: the confluence of the currents generates numerous surface and subsurface eddies as well as mode and intermediate water masses which can travel throughout the western and central North Pacific Ocean (Talley and Yun, 2001; Mitsudera et al., 2004; You, 2005; Oka et al., 2009; Oka and Qiu, 2012). Depending on the relative rate of transport and removal, waters subducted in the WSG will carry with them any dissolved or particulate material introduced prior to their subduction.

## Enrichment of Trace Element Concentrations in WSG Currents

The oxygen-rich waters transported out of the WSG are also rich in dissolved and particulate Mn (Figure 12). Upon encountering the Kuroshio Current at station 1, the parcel at 26.4  $\sigma_\theta$  is subducted from ~150 m in the WSG to 455 m at station 1, while the parcel at ~27  $\sigma_\theta$  is subducted from 300 m in the WSG to 647 m at station 1. The water parcel at 26.4  $\sigma_\theta$  increases in both dMn and pMn concentrations as well as the pMn/Ti enrichment from north to south (from station 3 to 2 to 1), consistent with ongoing inputs of redox-mobilized shelf material and *in situ* microbial oxidation. The lower parcel at ~27  $\sigma_\theta$  is enriched in dMn but not pMn, as these waters originated below the oxycline and within the oxygen minimum zone. The lower rate of Mn scavenging in the low oxygen waters may have preserved the shelf inputs of Mn in the dissolved state and also dissolved some portion of the settling pMn-oxides. Concentrations of both dMn and pMn continued to accumulate along the shelf until reaching the maximum observed concentrations at station 1.

Cobalt and Ce were also transported along this same pathway (Figure 13). In the 26.4  $\sigma_\theta$  parcel, concentrations of dCo remained almost unchanged, from 103 pM at station 2 to 109 pM at station 1, but dCo concentrations increased greatly in the 27  $\sigma_\theta$  parcel, reaching a concentration of 392 pM at station 1. The lack of a dCo increase between stations 3 and 2 at 27  $\sigma_\theta$  indicates that the source of dCo at these depths is a lateral input located further downstream of station 2, likely generated during the turbulent outflow of intermediate waters from the Sea of Okhotsk (Yasuda et al., 2002; Yasuda, 2004). Similar enrichments of trace metals by this mechanism have been observed for Fe (Nishioka et al., 2007) and possibly even Hg (Laurier et al., 2004). As the 27  $\sigma_\theta$  water mass continues southward beyond the





extent of our sampling locations (You, 2005), the distinctive trace metal properties of this feature have remained largely unexplored except for its influence on the formation of the North Pacific Intermediate Water (NPIW) encountered throughout the central North Pacific Ocean (stations 6–9).

### Shelf Fluxes to the WSG

The shelf fluxes of Mn, Co, and Ce to the WSG can be estimated using the increase in concentrations from station 3 to 1 (1860 km), assuming a current velocity of 0.2–0.4  $\text{m s}^{-1}$  for the Oyashio Current (Ohshima et al., 2005). Within the 26.4  $\sigma_\theta$  water mass, the dMn concentrations increase from 1.34 nM to 2.91 nM, an increase of 1.57 nM over 54–108 days. The resulting flux of dMn from the shelf along the 26.4  $\sigma_\theta$  isopycnal is 5.3–10.6  $\text{nM yr}^{-1}$ . Similarly calculated, the pMn shelf flux is 3.1–6.2  $\text{nM yr}^{-1}$ . Fluxes of dissolved and particulate Co are 96.2–192.3  $\text{pM yr}^{-1}$  and 7.9–15.8  $\text{pM yr}^{-1}$ , respectively, and fluxes of dissolved and particulate Ce are 21.2–42.3  $\text{pM yr}^{-1}$  and 8.7–17.4  $\text{pM yr}^{-1}$ .

### Offshore Transport of Trace Elements

The Oyashio and Kuroshio Currents turn eastward near station 1, away from the supply of trace elements from the shelf. At stations 4 and 5, water masses with low salinities and high dissolved oxygen concentrations are observed within the same isopycnal range as the two intrusions observed at station 1 (Figures 5, 8). While maxima in pMn and pCe are observed at 250–300 m at station 4 (26.6–26.7  $\sigma_\theta$ ), no other particulate maxima are observed within these depths and density ranges at the other STG stations. In contrast, pCo maxima are found at stations 4 and 7–9 at intermediate depths (300–800 m).

The dissolved concentrations of Mn also decrease with distance from the shelf, remaining at concentrations near 1 nM (0.8–1.6 nM) in the upper 300 m (Figures 4, 6). The concentrations of dMn in the upper ocean can be resupplied by episodic atmospheric deposition (Buck et al., 2013) and/or

the photochemical inhibition of oxide production in the surface waters (Sunda and Huntsman, 1988, 1994; Moffett, 1994b, 1997) which would prevent the loss of Mn by particle scavenging. This lack of Mn oxidation could also suppress the conversion of dCe to pCe-oxides through scavenging and co-precipitation with pMn-oxides. While the cycles of Mn, Co, and Ce might be coupled near the shelf, subtle differences in their biogeochemistry should become more apparent once the water masses containing shelf-derived material move further from the shelf source.

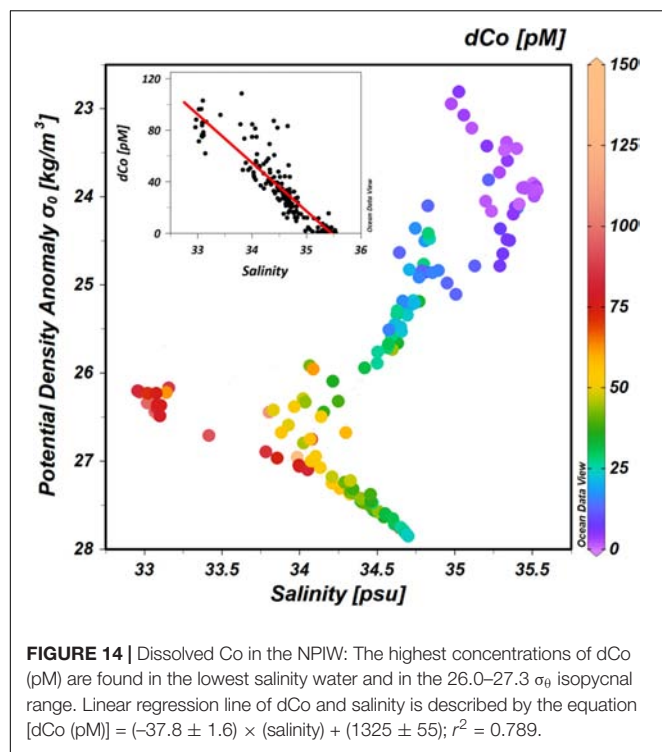
### Rate of Particulate Trace Element Loss With Offshore Transport

Moving offshore along the 26.4  $\sigma_\theta$  isopycnal surface from station 1 to stations 4 (300 m) and 5 (500 m), there is no more shelf supply of dissolved trace elements to the water mass. Without the additional supply of dissolved material, the dissolved Mn, Co, and Ce should decrease due to ongoing scavenging and co-oxidation with pMn. The rates of loss of Mn, Co, and Ce can be estimated by assuming that the conversion of dissolved to particulate phases is the rate-limiting step, is first order using Equation 3

$$A_t = A_0 e^{-kt} \quad (3)$$

where  $A_t$  is the final concentration at station 4 or 5,  $A_0$  is the original concentration at 455 m at station 1, and  $t$  is the travel time from station 1 to stations 4 or 5. While the Kuroshio Current is a fast-moving western boundary current (0.7–1.0  $\text{m s}^{-1}$ ; Mitsudera et al., 2004), we apply a more modest velocity of 0.2–0.4  $\text{m s}^{-1}$  for the offshore extension of the Kuroshio. The dMn decreases from 2.91 nM at station 1 to 0.86 nM and 0.45 nM at stations 4 and 5, respectively, and result in a Mn loss rate of 0.10–0.30%  $\text{d}^{-1}$ . Similarly, the Ce loss rate is 0.09–0.28%  $\text{d}^{-1}$ , closely matching that of Mn and supporting their concurrent removal. These rates are lower than the estimated oxidation rates of Mn (2–3%  $\text{d}^{-1}$ ) and Ce





(0.3–0.8%  $d^{-1}$ ) reported by de Baar et al. (1988) and Moffett (1990), respectively. Moffett (1990) also noted that marine Mn oxidation rates were 3–4 times faster than Ce oxidation rates, in contrast to our similar dissolved Mn and Ce loss rates. Therefore, our dissolved trace element loss rates are likely not accurate estimates of oxidation rates, but include other processes such as scavenging and particle settling that were not incorporated in the direct measurements made by Moffett (1990). The loss rate of dCo (0.05–0.17%  $d^{-1}$ ) is about half of the Mn or Ce loss rate, suggesting that while co-oxidation with Mn-oxides is occurring, other processes such as biological uptake and organic-complexation act to decouple the Co cycle from those of Mn and Ce. In summary, the loss of dMn and dCe are likely to continue through scavenging and microbially mediated oxidation after leaving the shelf. This ongoing conversion of dMn and dCe to settling particles is in contrast to the preservation of Co in the dissolved phase, observable as a subsurface maximum associated with the salinity-minimum core of the NPIW across the North Pacific Ocean (Noble et al., 2008; Zheng et al., 2019).

### Trace Elements in the NPIW

The partially mixed waters at station 1 from 455 to 647 m are the precursor of the NPIW, which forms with a core potential density of  $\sim 26.8 \sigma_\theta$  (26.5–27.5  $\sigma_\theta$ ) from the Kuroshio Current and waters from the WSG, including contributions from both the Oyashio Current and the Sea of Okhotsk (Talley et al., 1995; Yasuda et al., 2002; You, 2005). The changes in temperature and salinity within this potential density range of 26.5–27.5  $\sigma_\theta$ , from the WSG (stations 2 and 3) across the MWR (stations 1, 4–6) and into

the central North Pacific (stations 7–9), show the gradual mixing of multiple water masses to form a single water mass – the NPIW – with a characteristic mid-depth salinity minimum. Evidence of the long-range transport of coastal material, including Fe, Hg, and terrestrial DOC, from the Sea of Okhotsk and the WSG, has been found within the NPIW (Hansell et al., 2002; Hernes and Benner, 2002; Tani et al., 2003; Nakatsuka et al., 2004a,b; Nishioka et al., 2007; Misumi et al., 2011; Hammerschmidt and Bowman, 2012; Tanaka et al., 2012).

The widespread distribution and temporal variability of dissolved trace element distributions in the NPIW can be observed in comparisons with similar studies conducted near our IOC2002 station 9 (ALOHA). Dissolved Mn concentrations at ALOHA and nearby locations in the STG are compared in Figure 2 and show a variable but persistent surface maximum that overlies a subsurface minimum around 300 m (Martin et al., 1985; Landing and Bruland, 1987; Boyle et al., 2005; Noble et al., 2008; Zheng et al., 2019). Dissolved Ce concentrations are consistently low, ranging from 1 to 5 pM (Fröllje et al., 2016), with a slight surface maximum but no other obvious structure throughout the water column, even at sites further from ALOHA (EUC-Fe station 14 at  $0^\circ\text{N}$ ,  $180^\circ\text{W}$ ; Grenier et al., 2013). Unlike dMn and dCe, the concentrations of dCo remain high (maxima near 40–80 pM) in the 300–1000 m range across the MWR and STG (stations 4–9; Figure 6). Similar features in dCo have been reported in waters to the southwest of the Hawaiian islands (Noble et al., 2008) with a subsurface maximum observed at depths of 400–600 m (Figure 2) and a potential density range of 26.5–27.0  $\sigma_\theta$ . A recent high-resolution section along  $160^\circ\text{W}$  further illustrates the extent of this intermediate water dCo maximum, where high dCo concentrations are observed throughout the NPIW at 400–600 m depth, from  $25^\circ$  to  $45^\circ\text{N}$  (Figure 3 of Zheng et al., 2019). When comparing the vertical profiles of dCo concentrations from our IOC2002 expedition with the nearby stations from Noble et al. (2008) and Zheng et al. (2019), the subsurface dCo maximum within the NPIW is observed in all profiles shown in Figure 2 but the magnitude of the maximum itself exhibits some variability. The maximum dCo concentrations observed in the NPIW range from 56.2 pM at station ALOHA (IOC2002 Stn 9) to 84.1 pM at stations to the southwest of the islands (E-Flux III, In 3; Noble et al., 2008). Note that lower dCo concentrations were observed at stations immediately to the north (Zheng ST07) and south (Zheng ST08) of IOC2002 station 9 (ALOHA) by Zheng et al. (2019), due to incomplete Co recoveries resulting from the lack of a UV-oxidation step which liberates organically complexed Co. However, assuming that dCo concentrations without UV-oxidation are  $\sim 60\%$  of those obtained with UV-oxidation (as noted in the 2013 SAFE Co report), the concentrations reported by Zheng et al. (2019) at their stations ST07 and ST08 would be  $\sim 70$  pM and comparable to the concentrations found in the other nearby studies. In addition to variations in the biogeochemical processes along the shelf (sedimentation rates, organic carbon remineralization, etc.) as well as biological uptake and scavenging

rates of dCo offshore, the variations in NPIW dCo concentrations also partially result from annual and seasonal meanders of the Kuroshio Current and Extension and the hydrography of the western subarctic gyre (Bograd et al., 1999; Kinugasa et al., 2005; Oka et al., 2007; e.g., Talley et al., 1995; You, 2003a, 2005; Yasuda, 2004; Qiu and Chen, 2005): each of these circulation patterns directly affect the formation of the NPIW, and subsequently the horizontal distribution of dCo across the central North Pacific Ocean.

The characteristic salinity minimum of the NPIW makes an ideal tracer for testing the hypothesis that dCo is supplied from the margins to the WSG. Other studies have shown strong relationships between dCo and salinity in the northeast Pacific Ocean (Knauer et al., 1982) and the north and south Atlantic Ocean (Saito and Moffett, 2002; Dulaquais et al., 2014). The surface salinities of the WSG are distinctively low (Figure 3), and comparing dCo against salinity across the entire study region reveals that dCo concentrations in the western North Pacific are negatively correlated with salinity (Figure 14), and the relationship can be described by the linear equation  $[dCo] = (-37.8 \pm 1.6) \times (\text{salinity}) + (1325 \pm 55)$  ( $R^2 = 0.789$ ; excluding the highest concentration of 392 pM from the 647 m Okhotsk Sea intrusion at station 1). The strength of the relationship between dCo concentrations and salinity supports our conclusion that the Sea of Okhotsk and the WSG are the primary sources of dCo found in the NPIW, transporting dCo at intermediate depths throughout much of the North Pacific Ocean.

## CONCLUSION

Evidence for margin inputs of Mn, Co, and Ce to the western North Pacific was found along the Kuril-Kamchatka margin. A comparison of the redox active elements Mn, Co, and Ce with the hydrography of the western North Pacific revealed an extensive transport system capable of advecting margin-derived material along surface and intermediate water masses far beyond the immediate continental shelf. Both redox-mobilized and resuspension processes were identified through particulate elemental ratios, which allowed for better identification of the processes responsible for the trace metal distributions. In summary, physical ocean processes can have a tremendous influence on both the input and transport of trace metals.

The significance of margin inputs goes beyond that of dMn supply to the western North Pacific. The biogeochemistry of other bioactive trace metals can be influenced by the transformation of dMn to pMn, and the transport of both phases when entrained into water masses. While Co and Ce can be microbially oxidized

using the same biochemical pathway as that of Mn (Moffett, 1994b; Moffett and Ho, 1996), our results can also be explained by the scavenging and oxidation of Co and Ce by the Mn-oxides themselves (De Carlo et al., 1997; Tebo et al., 2004). Due to the reactivity of the Mn oxide phases, it is possible that the cycling of Mn could affect other trace metals in addition to Co and Ce, through scavenging, oxidation, and/or reductive dissolution.

The physical circulation is also critical to the transport of redox active elements from the shelf to the open ocean. The Sea of Okhotsk is a region of seasonal sea-ice formation and brine rejection, which influence the densities, depths, and intensity of surface and intermediate waters circulating in the WSG. Long-term disruptions of sea ice formation in the Sea of Okhotsk (Paik et al., 2017) will subsequently change the properties of the Okhotsk Sea intermediate waters and the WSG winter mixed layers, both of which play critical roles in determining the properties of the NPIW and the offshore transport of redox-active trace elements to the North Pacific Ocean.

## DATA AVAILABILITY STATEMENT

All datasets generated for this study are included in the manuscript/**Supplementary Files**.

## AUTHOR CONTRIBUTIONS

JD, WL, and AS designed the study. PM and MB optimized the sample analysis for dissolved and particulate Mn and Co, and particulate REEs. JS, ED, AM, and AS analyzed the samples for dissolved REEs. PM, JD, WL, JS, ED, and TK performed the data analysis and led the interpretation. PM and JS wrote the first draft of the manuscript. All authors contributed to manuscript revision.

## FUNDING

This work was supported by United States NSF OCE 0136977 to JD, United States NSF OCE 0117917 to WL, United States NSF OCE 0137359 to AS, and United States NSF DMR-1644779 and the State of Florida.

## SUPPLEMENTARY MATERIAL

The Supplementary Material for this article can be found online at: <https://www.frontiersin.org/articles/10.3389/fmars.2019.00591/full#supplementary-material>

## REFERENCES

- Aguilar-Islas, A. M., Hurst, M. P., Buck, K. N., Sohst, B., Smith, G. J., Lohan, M. C., et al. (2007). Micro- and macronutrients in the southeastern Bering Sea: insight into iron-replete and iron-depleted regimes. *Prog. Oceanogr.* 73, 99–126. doi: 10.1016/j.pcean.2006.12.002
- Aguilar-Islas, A. M., Rember, R., Nishino, S., Kikuchi, T., and Itoh, M. (2013). Partitioning and lateral transport of iron to the Canada Basin. *Polar Sci.* 7, 82–99. doi: 10.1016/j.polar.2012.11.001
- Andreev, A. G. A., and Kusakabe, M. (2001). Interdecadal variability in dissolved oxygen in the intermediate water layer of the Western Subarctic Gyre and

- Kuril Basin (Okhotsk Sea). *Geophys. Res. Lett.* 28, 2453–2456. doi: 10.1029/2000GL012688
- Bargar, J., Tebo, B., and Villinski, J. (2000). In situ characterization of Mn(II) oxidation by spores of the marine *Bacillus* sp. strain SG-1. *Geochim. Cosmochim. Acta* 64, 2775–2778. doi: 10.1016/S0016-7037(00)00368-9
- Bishop, J. K. B., and Fleisher, M. Q. (1987). Particulate manganese dynamics in Gulf Stream warm-core rings and surrounding waters of the N.W. Atlantic. *Geochim. Cosmochim. Acta* 51, 2807–2825. doi: 10.1016/0016-7037(87)90160-8
- Bograd, S. J., Thomson, R. E., Rabinovich, A. B., and LeBlond, P. H. (1999). Near-surface circulation of the Northeast Pacific Ocean derived from WOCE-SVP satellite-tracked drifters. *Deep. Res. Part II* 46, 2371–2403. doi: 10.1016/S0967-0645(99)00068-5
- Boyle, E. A., Bergquist, B. A., Kayser, R. A., and Mahowald, N. (2005). Iron, manganese, and lead at Hawaii Ocean Time-series station ALOHA: temporal variability and an intermediate water hydrothermal plume. *Geochim. Cosmochim. Acta* 69, 933–952. doi: 10.1016/j.gca.2004.07.034
- Breitbart, D., Levin, L. A., Oschlies, A., Grégoire, M., Chavez, F. P., Conley, D. J., et al. (2018). Declining oxygen in the global ocean and coastal waters. *Science* 359:eaam7240. doi: 10.1126/science.aam7240
- Brown, M. T., Landing, W. M., and Measures, C. I. (2005). Dissolved and particulate Fe in the western and central North Pacific: results from the 2002 IOC cruise. *Geochem. Geophys. Geosyst.* 6:Q10001. doi: 10.1029/2004GC000893
- Buck, C. S., Landing, W. M., and Resing, J. (2013). Pacific Ocean aerosols: deposition and solubility of iron, aluminum, and other trace elements. *Mar. Chem.* 157, 117–130. doi: 10.1016/j.marchem.2013.09.005
- Buck, C. S., Landing, W. M., Resing, J. A., and Lebon, G. T. (2006). Aerosol iron and aluminum solubility in the northwest Pacific Ocean: results from the 2002 IOC cruise. *Geochem. Geophys. Geosyst.* 7:Q04M07. doi: 10.1029/2005GC000977
- Buck, K. N., Sedwick, P. N., Sohst, B., and Carlson, C. A. (2018). Organic complexation of iron in the eastern tropical South Pacific: results from US GEOTRACES Eastern Pacific Zonal Transect (GEOTRACES cruise GP16). *Mar. Chem.* 201, 229–241. doi: 10.1016/j.marchem.2017.11.007
- Buck, K. N., Sohst, B., and Sedwick, P. N. (2015). The organic complexation of dissolved iron along the U.S. GEOTRACES (GA03) North Atlantic Section. *Deep Sea Res. Part II Top. Stud. Oceanogr.* 116, 152–165. doi: 10.1016/j.dsr2.2014.11.016
- Burdige, D. J. (1993). The biogeochemistry of manganese and iron reduction in marine sediments. *Earth Sci. Rev.* 35, 249–284. doi: 10.1016/0012-8252(93)90040-e
- Burdige, D. J. (2006). *Geochemistry of Marine Sediments*. Princeton, NJ: Princeton University Press.
- Chase, Z., Johnson, K. S., Elrod, V. A., Plant, J. N., Fitzwater, S. E., Pickell, L., et al. (2005). Manganese and iron distributions off central California influenced by upwelling and shelf width. *Mar. Chem.* 95, 235–254. doi: 10.1016/j.marchem.2004.09.006
- Chen, G., and Wu, J. (2019). Meridional distribution of dissolved manganese in the tropical and Equatorial Pacific. *Geochim. Cosmochim. Acta* 263, 50–67. doi: 10.1016/j.gca.2019.06.048
- Chever, F., Rouxel, O. J., Croot, P. L., Ponzevera, E., Wuttig, K., and Auro, M. (2015). Total dissolvable and dissolved iron isotopes in the water column of the Peru upwelling regime. *Geochim. Cosmochim. Acta* 162, 66–82. doi: 10.1016/j.gca.2015.04.031
- Chinni, V., Singh, S. K., Bhushan, R., Rengarajan, R., and Sarma, V. V. S. S. (2019). Spatial variability in dissolved iron concentrations in the marginal and open waters of the Indian Ocean. *Mar. Chem.* 208, 11–28. doi: 10.1016/j.marchem.2018.11.007
- Cutter, G. A., and Cutter, L. S. (2006). Biogeochemistry of arsenic and antimony in the North Pacific Ocean. *Geochem. Geophys. Geosyst.* 7:12. doi: 10.1029/2005GC001159
- Cutter, G. A., Moffett, J. W., Nielsdóttir, M. C., and Sanial, V. (2018). Multiple oxidation state trace elements in suboxic waters off Peru: *in situ* redox processes and advective/diffusive horizontal transport. *Mar. Chem.* 201, 77–89. doi: 10.1016/j.marchem.2018.01.003
- de Baar, H. J. W., Bruland, K. W., Schijf, J., van Heuven, S. M. A. C., and Behrens, M. K. (2018). Low cerium among the dissolved rare earth elements in the central North Pacific Ocean. *Geochim. Cosmochim. Acta* 236, 5–40. doi: 10.1016/j.gca.2018.03.003
- de Baar, H. J. W., German, C. R., Elderfield, H., and van Gaans, P. (1988). Rare earth element distributions in anoxic waters of the Cariaco Trench. *Geochim. Cosmochim. Acta* 52, 1203–1219. doi: 10.1016/0016-7037(88)90275-X
- de Baar, H. J. W. W., Bacon, M. P., Brewer, P. G., and Bruland, K. W. (1985). Rare earth elements in the Pacific and Atlantic Oceans. *Geochim. Cosmochim. Acta* 49, 1943–1959. doi: 10.1016/0016-7037(85)90089-4
- De Carlo, E. H., Wen, X.-Y., and Irving, M. (1997). The influence of redox reactions on the uptake of dissolved Ce by suspended Fe and Mn oxide particles. *Aquat. Geochem.* 3, 357–389. doi: 10.1023/A:1009664626181
- Dick, G. J., Podell, S., Johnson, H. A., Rivera-Espinoza, Y., Bernier-Latmani, R., McCarthy, J. K., et al. (2008). Genomic insights into Mn(II) oxidation by the marine alphaproteobacterium *Aurantimonas* sp. strain S185-9A1. *Appl. Environ. Microbiol.* 74, 2646–2658. doi: 10.1128/AEM.01656-07
- Dulaquais, G., Boye, M., Middag, R., Owens, S., Puigcorbe, V., Buesseler, K., et al. (2014). Contrasting biogeochemical cycles of cobalt in the surface western Atlantic Ocean. *Glob. Biogeochem. Cycles* 28, 1387–1412. doi: 10.1002/2014GB004903
- Eggemann, D., and Betzer, P. (1976). Decomposition and analysis of refractory oceanic suspended materials. *Anal. Chem.* 48, 886–890. doi: 10.1021/ac60370a005
- Eggins, S. M., Woodhead, J. D., Kinsley, L. P. J., Mortimer, G. E., Sylvester, P., McCulloch, M. T., et al. (1997). A simple method for the precise determination of = 40 trace elements in geological samples by ICPMS using enriched isotope internal standardisation. *Chem. Geol.* 134, 311–326. doi: 10.1016/S0009-2541(96)00100-3
- Elderfield, H. (1988). The oceanic chemistry of the rare-earth elements and discussion. *Philos. Trans. R. Soc. A Math. Phys. Eng. Sci.* 325, 105–126. doi: 10.1098/rsta.1988.0046
- Ellwood, M. J., and van den Berg, C. M. (2001). Determination of organic complexation of cobalt in seawater by cathodic stripping voltammetry. *Mar. Chem.* 75, 33–47. doi: 10.1016/S0304-4203(01)00024-X
- Elrod, V. A., Berelson, W. M., Coale, K. H., and Johnson, K. S. (2004). The flux of iron from continental shelf sediments: a missing source for global budgets. *Geophys. Res. Lett.* 31:L12307. doi: 10.1029/2004GL020216
- Ezoe, M., Ishita, T., Kinugasa, M., Lai, X., Norisuye, K., and Sohrin, Y. (2004). Distributions of dissolved and acid-dissolvable bioactive trace metals in the North Pacific Ocean. *Geochem. J.* 38, 535–550. doi: 10.2343/geochemj.38.535
- Fitzsimmons, J. N., Carrasco, G. G., Wu, J., Roshan, S., Hatta, M., Measures, C. I., et al. (2015a). Partitioning of dissolved iron and iron isotopes into soluble and colloidal phases along the GA03 GEOTRACES North Atlantic Transect. *Deep Sea Res. Part II Top. Stud. Oceanogr.* 116, 130–151. doi: 10.1016/j.dsr2.2014.11.014
- Fitzsimmons, J. N., Hayes, C. T., Al-Subiai, S. N., Zhang, R., Morton, P. L., Weisend, R. E., et al. (2015b). Daily to decadal variability of size-fractionated iron and iron-binding ligands at the Hawaii Ocean time-series station ALOHA. *Geochim. Cosmochim. Acta* 171, 303–324. doi: 10.1016/j.gca.2015.08.012
- Fröllje, H., Pahnke, K., Schnetger, B., Brumsack, H.-J., Dulai, H., and Fitzsimmons, J. N. (2016). Hawaiian imprint on dissolved Nd and Ra isotopes and rare earth elements in the central North Pacific: local survey and seasonal variability. *Geochim. Cosmochim. Acta* 189, 110–131. doi: 10.1016/j.gca.2016.06.001
- Fujishima, Y., Ueda, K., Maruo, M., Nakayama, E., Tokutome, C., Hasegawa, H., et al. (2001). Distribution of trace bioelements in the Subarctic North Pacific Ocean and the Bering Sea (the R/V Hakuho Maru Cruise KH-97-2). *J. Oceanogr.* 57, 261–273. doi: 10.1023/A:1012426411228
- Gallon, C., Ranville, M. A. M. A., Conaway, C. H. C. H., Landing, W. M. W. M., Buck, C. S. C. S., Morton, P. L. P. L., et al. (2011). Asian industrial lead inputs to the North Pacific evidenced by lead concentrations and isotopic compositions in surface waters and aerosols. *Environ. Sci. Technol.* 45, 9874–9882. doi: 10.1021/es2020428
- GeoReM, (2009). *Geological and Environmental Reference Materials*. Available at: [georem.mpch-mainz.gwdg.de/](http://georem.mpch-mainz.gwdg.de/) (accessed August 16, 2019).
- German, C. R., and Elderfield, H. (1990). Rare earth elements in the NW Indian Ocean. *Geochim. Cosmochim. Acta* 54, 1929–1940. doi: 10.1016/0016-7037(90)90262-J
- Glass, J. B. J. B., Kretz, C. B. C. B., Ganesh, S., Ranjan, P., Seston, S. L. S. L., Buck, K. N. K. N., et al. (2015). Meta-omic signatures of microbial metal and nitrogen cycling in marine oxygen minimum zones. *Front. Microbiol.* 6:998. doi: 10.3389/fmicb.2015.00998



- Grand, M. M., Measures, C. I., Hatta, M., Hiscock, W. T., Buck, C. S., and Landing, W. M. (2015a). Dust deposition in the eastern Indian Ocean: the ocean perspective from Antarctica to the Bay of Bengal. *Glob. Biogeochem. Cycles* 29, 357–374. doi: 10.1002/2014GB004898
- Grand, M. M., Measures, C. I., Hatta, M., Morton, P. L., Barrett, P., Milne, A., et al. (2015b). The impact of circulation and dust deposition in controlling the distributions of dissolved Fe and Al in the south Indian subtropical gyre. *Mar. Chem.* 176, 110–125. doi: 10.1016/j.marchem.2015.08.002
- Grenier, M., Jeandel, C., Lacan, F., Vance, D., Venchiarutti, C., Cros, A., et al. (2013). From the subtropics to the central equatorial Pacific Ocean: neodymium isotopic composition and rare earth element concentration variations. *J. Geophys. Res. Ocean* 118, 592–618. doi: 10.1029/2012JC008239
- Hammerschmidt, C. R., and Bowman, K. L. (2012). Vertical methylmercury distribution in the subtropical North Pacific Ocean. *Mar. Chem.* 132–133, 77–82. doi: 10.1016/j.marchem.2012.02.005
- Hansel, C. M. (2017). Manganese in marine microbiology. *Adv. Microb. Physiol.* 70, 37–83. doi: 10.1016/bs.ampbs.2017.01.005
- Hansel, D. A., Carlson, C. A., and Suzuki, Y. (2002). Dissolved organic carbon export with North Pacific intermediate water formation. *Glob. Biogeochem. Cycles* 16, 7–1. doi: 10.1029/2000GB001361
- Hathorne, E. C., Haley, B., Stichel, T., Grasse, P., Zieringer, M., and Frank, M. (2012). Online preconcentration ICP-MS analysis of rare earth elements in seawater. *Geochim. Geophys. Geosyst.* 13, 1–12. doi: 10.1029/2011GC003907
- Hatta, M., Measures, C. I., Wu, J., Roshan, S., Fitzsimmons, J. N., Sedwick, P., et al. (2015). An overview of dissolved Fe and Mn distributions during the 2010–2011 U.S. GEOTRACES north Atlantic cruises: GEOTRACES GA03. *Deep Sea Res. Part II Top. Stud. Oceanogr.* 116, 117–129. doi: 10.1016/j.dsr2.2014.07.005
- Hawco, N. J., Lam, P. J., Lee, J.-M., Ohnemus, D. C., Noble, A. E., Wyatt, N. J., et al. (2018). Cobalt scavenging in the mesopelagic ocean and its influence on global mass balance: synthesizing water column and sedimentary fluxes. *Mar. Chem.* 201, 151–166. doi: 10.1016/j.marchem.2017.09.001
- Hawco, N. J., Ohnemus, D. C., Resing, J. A., Twining, B. S., and Saito, M. A. (2016). A dissolved cobalt plume in the oxygen minimum zone of the eastern tropical South Pacific. *Biogeochemistry* 13, 5697–5717. doi: 10.5194/bg-13-5697-2016
- Heller, M. I., Lam, P. J., Moffett, J. W., Till, C. P., Lee, J.-M., Toner, B. M., et al. (2017). Accumulation of Fe oxyhydroxides in the Peruvian oxygen deficient zone implies non-oxygen dependent Fe oxidation. *Geochim. Cosmochim. Acta* 211, 174–193. doi: 10.1016/j.gca.2017.05.019
- Hernes, P. J., and Benner, R. (2002). Transport and diagenesis of dissolved and particulate terrigenous organic matter in the North Pacific Ocean. *Deep Sea Res. Part I Oceanogr. Res. Pap.* 49, 2119–2132. doi: 10.1016/S0967-0637(02)00128-0
- Hsu, S.-C., Liu, S. C., Huang, Y.-T., Lung, S.-C. C., Tsai, F., Tu, J.-Y., et al. (2008). A criterion for identifying Asian dust events based on Al concentration data collected from northern Taiwan during 2002 and early 2007. *J. Geophys. Res.* 113:D18306. doi: 10.1029/2007JD009574
- Hsu, S.-C., Wong, G. T. F., Gong, G.-C., Shiah, F.-K., Huang, Y.-T., Kao, S.-J., et al. (2010). Sources, solubility, and dry deposition of aerosol trace elements over the East China Sea. *Mar. Chem.* 120, 116–127. doi: 10.1016/j.marchem.2008.10.003
- Jacobs, L., Emerson, S., and Huested, S. S. (1987). Trace metal geochemistry in the Cariaco Trench. *Deep Sea Res. Part A Oceanogr. Res. Pap.* 34, 965–981. doi: 10.1016/0198-0149(87)90048-3
- Jickells, T. D., An, Z. S., Andersen, K. K., Baker, A. R., Bergametti, G., Brooks, N., et al. (2005). Global iron connections between desert dust, ocean biogeochemistry, and climate. *Science* 308, 67–71. doi: 10.1126/science.1105959
- Johnson, K. K. S., Coale, K. H., Berelson, W. W. M., Gordon, R., and Michael Gordon, R. (1996). On the formation of the manganese maximum in the oxygen minimum. *Geochim. Cosmochim. Acta* 60, 1291–1299. doi: 10.1016/0016-7037(96)00005-1
- Kim, W., Doh, S.-J., and Yu, Y. (2012). Asian dust storm as conveyance media of anthropogenic pollutants. *Atmos. Environ.* 49, 41–50. doi: 10.1016/j.atmosenv.2011.12.034
- Kinugasa, M., Ishita, T., Sohrin, Y., Okamura, K., Takeda, S., Nishioka, J., et al. (2005). Dynamics of trace metals during the subarctic Pacific iron experiment for ecosystem dynamics study (SEEDS2001). *Prog. Oceanogr.* 64, 129–147. doi: 10.1016/j.pocean.2005.02.005
- Klar, J. K., Schlosser, C., Milton, J. A., Woodward, E. M. S., Lacan, F., Parkinson, I. J., et al. (2018). Sources of dissolved iron to oxygen minimum zone waters on the Senegalese continental margin in the tropical North Atlantic Ocean: insights from iron isotopes. *Geochim. Cosmochim. Acta* 236, 60–78. doi: 10.1016/j.gca.2018.02.031
- Klunder, M. B., Laan, P., De Baar, H. J. W., Middag, R., Neven, I., and Van Ooijen, J. (2014). Dissolved Fe across the Weddell Sea and Drake passage: impact of DFE on nutrient uptake. *Biogeochemistry* 11, 651–669. doi: 10.5194/bg-11-651-2014
- Knauer, G. A., Martin, J. H., and Gordon, R. M. (1982). Cobalt in north-east Pacific waters. *Nature* 297, 49–51. doi: 10.1038/297049a0
- Kondo, Y., and Moffett, J. W. (2013). Dissolved Fe(II) in the Arabian Sea oxygen minimum zone and western tropical Indian Ocean during the inter-monsoon period. *Deep Sea Res. Part I Oceanogr. Res. Pap.* 73, 73–83. doi: 10.1016/j.dsr.2012.11.014
- Kondo, Y., and Moffett, J. W. (2015). Iron redox cycling and subsurface offshore transport in the eastern tropical South Pacific oxygen minimum zone. *Mar. Chem.* 168, 95–103. doi: 10.1016/j.marchem.2014.11.007
- Lam, P. J., and Bishop, J. K. B. (2008). The continental margin is a key source of iron to the HNLC North Pacific Ocean. *Geophys. Res. Lett.* 35:L07608. doi: 10.1029/2008GL033294
- Lam, P. J., Bishop, J. K. B., Henning, C. C., Marcus, M. A., Waychunas, G. A., and Fung, I. Y. (2006). Wintertime phytoplankton bloom in the subarctic Pacific supported by continental margin iron. *Glob. Biogeochem. Cycles* 20:GB2006. doi: 10.1029/2005GB002557
- Lam, P. J., Ohnemus, D. C., and Auro, M. E. (2015). Size-fractionated major particle composition and concentrations from the US GEOTRACES North Atlantic Zonal Transect. *Deep Sea Res. Part II Top. Stud. Oceanogr.* 116, 303–320. doi: 10.1016/j.dsr2.2014.11.020
- Lamborg, C. H., Buesseler, K. O., and Lam, P. J. (2008). Sinking fluxes of minor and trace elements in the North Pacific Ocean measured during the VERTIGO program. *Deep Sea Res. Part II Top. Stud. Oceanogr.* 55, 1564–1577. doi: 10.1016/j.dsr2.2008.04.012
- Landing, W. M., and Bruland, K. W. (1980). Manganese in the North Pacific. *Earth Planet. Sci. Lett.* 49, 45–56.
- Landing, W. M., and Bruland, K. W. (1987). The contrasting biogeochemistry of iron and manganese in the Pacific Ocean. *Geochim. Cosmochim. Acta* 51, 29–43. doi: 10.1016/0016-7037(87)90004-4
- Laurier, F. J. G., Mason, R. P., Gill, G. A., and Whalin, L. (2004). Mercury distributions in the North Pacific Ocean—20 years of observations. *Mar. Chem.* 90, 3–19. doi: 10.1016/j.marchem.2004.02.025
- Learman, D. R., Wankel, S. D., Webb, S. M., Martinez, N., Madden, A. S., and Hansel, C. M. (2011). Coupled biotic–abiotic Mn(II) oxidation pathway mediates the formation and structural evolution of biogenic Mn oxides. *Geochim. Cosmochim. Acta* 75, 6048–6063. doi: 10.1016/j.gca.2011.07.026
- Lewis, B. L., and Landing, W. M. (1991). The biogeochemistry of manganese and iron in the Black Sea. *Deep Sea Res. Part A Oceanogr. Res. Pap.* 38, S773–S803. doi: 10.1016/S0198-0149(10)80009-3
- Lewis, B. L., and Luther, G. W. (2000). Processes controlling the distribution and cycling of manganese in the oxygen minimum zone of the Arabian Sea. *Deep. Res. Part II Top. Stud. Oceanogr.* 47, 1541–1561. doi: 10.1016/S0967-0645(99)00153-8
- Lin, I. I., Chen, J. P., Wong, G. T. F., Huang, C. W., and Lien, C. C. (2007). Aerosol input to the South China Sea: results from the MODerate resolution imaging spectro-radiometer, the quick scatterometer, and the measurements of pollution in the troposphere sensor. *Deep. Res. Part II* 54, 1589–1601. doi: 10.1016/j.dsr2.2007.05.013
- Mahowald, N. M., Baker, A. R., Bergametti, G., Brooks, N., Duce, R. A., Jickells, T. D., et al. (2005). Atmospheric global dust cycle and iron inputs to the ocean. *Glob. Biogeochem. Cycles* 19:GB4025. doi: 10.1029/2004GB002402
- Mahowald, N. M., Engelstaedter, S., Luo, C., Sealy, A., Artaxo, P., Benitez-Nelson, C., et al. (2009). Atmospheric iron deposition: global distribution, variability, and human perturbations. *Ann. Rev. Mar. Sci.* 1, 245–278. doi: 10.1146/annurev.marine.010908.163727
- Marsay, C. M., Lam, P. J., Heller, M. I., Lee, J.-M., and John, S. G. (2018). Distribution and isotopic signature of ligand-leachable particulate iron along the GEOTRACES GP16 East Pacific Zonal Transect. *Mar. Chem.* 201, 198–211. doi: 10.1016/j.marchem.2017.07.003
- Martin, J. H., Knauer, G. A., and Broenkow, W. W. (1985). VERTEX: the lateral transport of manganese in the northeast Pacific. *Deep Sea Res. Part A Oceanogr. Res. Pap.* 32, 1405–1412, 1414–1427.



- Measures, C. I., Brown, M. T., and Vink, S. (2005). Dust deposition to the surface waters of the Western and Central North Pacific inferred from surface water dissolved aluminum concentrations. *Geochem. Geophys. Geosyst.* 6:Q09M03. doi: 10.1029/2005GC000922
- Measures, C. I., Cutter, G. A., Landing, W. M., and Powell, R. T. (2006). Hydrographic observations during the 2002 IOC contaminant baseline survey in the western Pacific Ocean. *Geochem. Geophys. Geosyst.* 7, 1–14. doi: 10.1029/2004GC000855
- Middag, R., de Baar, H. J. W., Klunder, M. B., and Laan, P. (2013). Fluxes of dissolved aluminum and manganese to the Weddell Sea and indications for manganese co-limitation. *Limnol. Oceanogr.* 58, 287–300. doi: 10.4319/lo.2013.58.1.0287
- Middag, R., de Baar, H. J. W., Laan, P., Cai, P. H., and van Ooijen, J. C. (2011a). Dissolved manganese in the Atlantic sector of the Southern Ocean. *Deep Sea Res. Part II Top. Stud. Oceanogr.* 58, 2661–2677. doi: 10.1016/j.dsr2.2010.10.043
- Middag, R., de Baar, H. J. W., Laan, P., and Klunder, M. B. (2011b). Fluvial and hydrothermal input of manganese into the Arctic Ocean. *Geochim. Cosmochim. Acta* 75, 2393–2408. doi: 10.1016/j.gca.2011.02.011
- Middag, R., de Baar, H. J. W., Laan, P., and Huhn, O. (2012). The effects of continental margins and water mass circulation on the distribution of dissolved aluminum and manganese in Drake Passage. *J. Geophys. Res. Ocean* 117:C01019. doi: 10.1029/2011JC007434
- Middag, R., Séférian, R., Conway, T. M., John, S. G., Bruland, K. W., and de Baar, H. J. W. (2015). Intercomparison of dissolved trace elements at the Bermuda Atlantic Time Series station. *Mar. Chem.* 177, 476–489. doi: 10.1016/J.MARCHEM.2015.06.014
- Milne, A., Landing, W. M., Bizimis, M., and Morton, P. L. (2010). Determination of Mn, Fe, Co, Ni, Cu, Zn, Cd and Pb in seawater using high resolution magnetic sector inductively coupled mass spectrometry (HR-ICP-MS). *Anal. Chim. Acta* 665, 200–207. doi: 10.1016/j.aca.2010.03.027
- Minakawa, M., Noriki, S., and Tsunogai, S. (1996). Manganese in the East China Sea and the Yellow Sea. *Geochem. J.* 30, 41–55. doi: 10.2343/geochemj.30.41
- Misumi, K., Tsumune, D., Yoshida, Y., Uchimoto, K., Nakamura, T., Nishioka, J., et al. (2011). Mechanisms controlling dissolved iron distribution in the North Pacific: a model study. *J. Geophys. Res. Biogeosci.* 116:G03005. doi: 10.1029/2010JG001541
- Mitsudera, H., Taguchi, B., Yoshikawa, Y., Nakamura, H., Waseda, T., and Qu, T. (2004). Numerical study on the Oyashio water pathways in the Kuroshio-Oyashio confluence. *J. Phys. Oceanogr.* 34, 1174–1196. doi: 10.1175/1520-0485(2004)034<1174:nsotow>2.0.co;2
- Moffett, J. W. (1990). Microbially mediated cerium oxidation in sea water. *Nature* 345, 421–423. doi: 10.1038/345421a0
- Moffett, J. W. (1994a). A radiotracer study of cerium and manganese uptake onto suspended particles in Chesapeake Bay. *Geochim. Cosmochim. Acta* 58, 695–703. doi: 10.1016/0016-7037(94)90499-5
- Moffett, J. W. (1994b). The relationship between cerium and manganese oxidation in the marine environment. *Limnol. Oceanogr.* 39, 1309–1318. doi: 10.4319/lo.1994.39.6.1309
- Moffett, J. W. (1997). The importance of microbial Mn oxidation in the upper ocean: a comparison of the Sargasso Sea and equatorial Pacific. *Deep Res. Part I* 44, 1277–1291. doi: 10.1016/s0967-0637(97)00032-0
- Moffett, J. W., and Ho, J. (1996). Oxidation of cobalt and manganese in seawater via a common microbially catalyzed pathway. *Geochim. Cosmochim. Acta* 60, 3415–3424. doi: 10.1016/0016-7037(96)00176-7
- Morel, F. M. M., Milligan, A. J., and Saito, M. A. (2003). “Marine bioinorganic chemistry: the role of trace metals in the oceanic cycles of major nutrients,” in *Treatise on Geochemistry*, eds H. Elderfield, H. D. Holland, and K. K. Turekian, (Cambridge: Elsevier Science Ltd.), 113–143. doi: 10.1016/b0-08-043751-6/06108-9
- Murray, K. J., Webb, S. M., Bargar, J. R., and Tebo, B. M. (2007). Indirect oxidation of Co(II) in the presence of the marine Mn(II)-oxidizing bacterium *Bacillus* sp. strain SG-1. *Appl. Environ. Microbiol.* 73, 6905–6909. doi: 10.1128/aem.00971-07
- Nakatsuka, T., Fujimune, T., Yoshikawa, C., Noriki, S., Kawamura, K., Fukamachi, Y., et al. (2004a). Biogenic and lithogenic particle fluxes in the western region of the Sea of Okhotsk: implications for lateral material transport and biological productivity. *J. Geophys. Res.* 109:C09S13. doi: 10.1029/2003JC001908
- Nakatsuka, T., Toda, M., Kawamura, K., and Wakatsuchi, M. (2004b). Dissolved and particulate organic carbon in the Sea of Okhotsk: transport from continental shelf to ocean interior. *J. Geophys. Res.* 109:C09S14.
- Nishioka, J., and Obata, H. (2017). Dissolved iron distribution in the western and central subarctic Pacific: HNLC water formation and biogeochemical processes. *Limnol. Oceanogr.* 62, 2004–2022. doi: 10.1002/LNO.10548
- Nishioka, J., Ono, T., Saito, H., Nakatsuka, T., Takeda, S., Yoshimura, T., et al. (2007). Iron supply to the Western Subarctic Pacific: importance of iron export from the Sea of Okhotsk. *J. Geophys. Res.* 112:C10012. doi: 10.1029/2006JC004055
- Noble, A. E., Lamborg, C. H., Ohnemos, D. C., Lam, P. J., Goepfert, T. J., Measures, C. I., et al. (2012). Basin-scale inputs of cobalt, iron, and manganese from the Benguela-Angola front to the South Atlantic Ocean. *Limnol. Oceanogr.* 57, 989–1010. doi: 10.4319/lo.2012.57.4.0989
- Noble, A. E., Ohnemos, D. C., Hawco, N. J., Lam, P. J., and Saito, M. A. (2017). Coastal sources, sinks and strong organic complexation of dissolved cobalt within the US North Atlantic GEOTRACES transect GA03. *Biogeosciences* 14, 2715–2739. doi: 10.5194/bg-14-2715-2017
- Noble, A. E., Saito, M. A., Maiti, K., and Benitez-Nelson, C. R. (2008). Cobalt, manganese, and iron near the Hawaiian Islands: a potential concentrating mechanism for cobalt within a cyclonic eddy and implications for the hybrid-type trace metals. *Deep Sea Res. Part II Top. Stud. Oceanogr.* 55, 1473–1490. doi: 10.1016/j.dsr2.2008.02.010
- Noffke, A., Hensen, C., Sommer, S., Scholz, F., Bohlen, L., Mosch, T., et al. (2012). Benthic iron and phosphorus fluxes across the Peruvian oxygen minimum zone. *Limnol. Oceanogr.* 57, 851–867. doi: 10.4319/lo.2012.57.3.0851
- Noriki, S., Shimizu, M., Hamahara, K., Narita, H., Saino, T., and Yanagi, T. (1997). Transportation of particulate material through the mouth of Tokyo Bay to the open ocean. *J. Oceanogr.* 53, 571–578.
- Nozaki, Y. (2001). “Rare earth elements and their isotopes in the ocean,” in *Encyclopedia of Ocean Sciences*, eds J. H. Steele, S. A. Thorpe, and K. K. Turekian (Amsterdam: Elsevier), 653–665. doi: 10.1016/B978-012374473-9.00284-8
- Obata, H., Alibo, D. S., and Nozaki, Y. (2007). Dissolved aluminum, indium, and cerium in the Sea of Japan and the Sea of Okhotsk: comparison to the marginal seas of the western North Pacific. *J. Geophys. Res.* 112:C12003. doi: 10.1029/2006jc003944
- Ohnemos, D. C., Auro, M. E., Sherrell, R. M., Lagerström, M., Morton, P. L., Twining, B. S., et al. (2014). Laboratory intercomparison of marine particulate digestions including Piranha: a novel chemical method for dissolution of polyethersulfone filters. *Limnol. Oceanogr. Methods* 12, 530–547. doi: 10.4319/lom.2014.12.530
- Ohshima, K., Wakatsuchi, M., and Saitoh, S.-I. (2005). Velocity field of the Oyashio region observed with satellite-tracked surface drifters during 1999–2000. *J. Oceanogr.* 61, 845–855. doi: 10.1007/s10872-006-0004-3
- Oka, E., and Qiu, B. (2012). Progress of North Pacific mode water research in the past decade. *J. Oceanogr.* 68, 5–20. doi: 10.1007/s10872-011-0032-5
- Oka, E., and Suga, T. (2005). Differential formation and circulation of North Pacific Central mode water. *J. Phys. Oceanogr.* 35, 1997–2011. doi: 10.1175/jpo2811.1
- Oka, E., Suga, T., Sukigara, C., Toyama, K., Shimada, K., and Yoshida, J. (2011). “Eddy resolving” observation of the North Pacific subtropical mode water. *J. Phys. Oceanogr.* 41, 666–681. doi: 10.1175/2011JPO4501.1
- Oka, E., Talley, L. D., and Suga, T. (2007). Temporal variability of winter mixed layer in the mid-to high-latitude North Pacific. *J. Oceanogr.* 63, 293–307. doi: 10.1007/s10872-007-0029-2
- Oka, E., Toyama, K., and Suga, T. (2009). Subduction of North Pacific central mode water associated with subsurface mesoscale eddy. *Geophys. Res. Lett.* 36:L08607. doi: 10.1029/2009GL037540
- Okin, G. S., Baker, A. R., Tegen, I., Mahowald, N. M., Dentener, F. J., Duce, R. A., et al. (2011). Impacts of atmospheric nutrient deposition on marine productivity: roles of nitrogen, phosphorus, and iron. *Glob. Biogeochem. Cycles* 25:GB2022.
- Okubo, A., Takeda, S., and Obata, H. (2013). Atmospheric deposition of trace metals to the western North Pacific Ocean observed at coastal station in Japan. *Atmos. Res.* 129–130, 20–32. doi: 10.1016/j.atmosres.2013.03.014
- Oldham, V. E., Jones, M. R., Tebo, B. M., and Luther, G. W. (2017). Oxidative and reductive processes contributing to manganese cycling at oxic-anoxic interfaces. *Mar. Chem.* 195, 122–128. doi: 10.1016/J.MARCHEM.2017.06.002

- Otosaka, S., and Noriki, S. (2000). REEs and Mn/Al ratio of settling particles: horizontal transport of particulate material in the northern Japan Trench. *Mar. Chem.* 72, 329–342. doi: 10.1016/S0304-4203(00)00094-3
- Pahnke, K., van de Flierdt, T., Jones, K. M., Lambelet, M., Hemming, S. R., and Goldstein, S. L. (2012). GEOTRACES intercalibration of neodymium isotopes and rare earth element concentrations in seawater and suspended particles. Part 2: systematic tests and baseline profiles. *Limnol. Oceanogr. Methods* 10, 252–269. doi: 10.4319/lom.2012.10.252
- Paik, S., Min, S.-K., Kim, Y.-H., Kim, B.-M., Shioyama, H., and Heo, J. (2017). Attributing causes of 2015 record minimum sea-ice extent in the Sea of Okhotsk. *J. Clim.* 30, 4693–4703. doi: 10.1175/JCLI-D-16-0587.1
- Paulmier, A., and Ruiz-Pino, D. (2009). Oxygen minimum zones (OMZs) in the modern ocean. *Prog. Oceanogr.* 80, 113–128. doi: 10.1016/j.pocean.2008.08.001
- Qiu, B. (1995). Why is the spreading of the north Pacific intermediate water confined on density surfaces around  $\sigma_\theta = 26.8$ ? *J. Phys. Oceanogr.* 25, 168–180. doi: 10.1175/1520-04851995025<0168:witsot>2.0.co;2
- Qiu, B., and Chen, S. (2005). Variability of the Kuroshio extension jet, recirculation gyre, and mesoscale eddies on decadal time scales. *J. Phys. Oceanogr.* 35, 2090–2103. doi: 10.1175/jpo2807.1
- Ranville, M. A., Cutter, G. A., Buck, C. S., Landing, W. M., Cutter, L. S., Resing, J. A., et al. (2010). Aeolian contamination of Se and Ag in the North Pacific from Asian fossil fuel combustion. *Environ. Sci. Technol.* 44, 1587–1593. doi: 10.1021/es902523m
- Ranville, M. A., and Flegal, A. R. (2005). Silver in the North Pacific Ocean. *Geochem. Geophys. Geosyst.* 6:Q03M01.
- Rudnick, R. L., and Gao, S. (2003). Composition of the continental crust. *Treatise Geochem.* 3, 1–64. doi: 10.1016/B0-08-043751-6/03016-4
- Saager, P. M., De Baar, H. J. W., and Burkill, P. H. (1989). Manganese and iron in Indian Ocean waters. *Geochim. Cosmochim. Acta* 53, 2259–2267. doi: 10.1016/0016-7037(89)90348-7
- Saito, M. A., and Moffett, J. W. (2001). Complexation of cobalt by natural organic ligands in the Sargasso Sea as determined by a new high-sensitivity electrochemical cobalt speciation method suitable for open ocean work. *Mar. Chem.* 75, 49–68. doi: 10.1016/S0304-4203(01)00025-1
- Saito, M. A., and Moffett, J. W. (2002). Temporal and spatial variability of cobalt in the Atlantic Ocean. *Geochim. Cosmochim. Acta* 66, 1943–1953. doi: 10.1016/S0016-7037(02)00829-3
- Saito, M. A., Moffett, J. W., and DiTullio, G. R. (2004). Cobalt and nickel in the Peru upwelling region: a major flux of labile cobalt utilized as a micronutrient. *Glob. Biogeochem. Cycles* 18:GB4030. doi: 10.1029/2003GB002216
- Saito, M. A., Rocap, G., and Moffett, J. W. (2005). Production of cobalt binding ligands in a *Synechococcus* feature at the Costa Rica upwelling dome. *Limnol. Oceanogr.* 50, 279–290. doi: 10.4319/lo.2005.50.1.0279
- Schiff, J., Christenson, E. A., and Byrne, R. H. (2015). YREE scavenging in seawater: a new look at an old model. *Mar. Chem.* 177, 460–471. doi: 10.1016/j.marchem.2015.06.010
- Scholz, F. (2018). Identifying oxygen minimum zone-type biogeochemical cycling in Earth history using inorganic geochemical proxies. *Earth Sci. Rev.* 184, 29–45. doi: 10.1016/j.earscirev.2018.08.002
- Sedwick, P., Sohst, B. M., Ussher, S. J., and Bowie, A. R. (2015). A zonal picture of the water column distribution of dissolved iron(II) during the U.S. GEOTRACES North Atlantic transect cruise (GEOTRACES GA03). *Deep Sea Res. Part II Top. Stud. Oceanogr.* 116, 166–175. doi: 10.1016/j.dsr2.2014.11.004
- Shcherbina, A. Y., Talley, L. D., and Rudnick, D. L. (2004). Dense water formation on the northwestern shelf of the Okhotsk Sea: 2. Quantifying the transports. *J. Geophys. Res.* 109:C09S09. doi: 10.1029/2003JC002197
- Sherrell, R. M., Annett, A. L., Fitzsimmons, J. N., Rocanova, V. J., and Meredith, M. P. (2018). A “shallow bathtub ring” of local sedimentary iron input maintains the Palmer Deep biological hotspot on the West Antarctic Peninsula shelf. *Philos. Trans. A. Math. Phys. Eng. Sci.* 376:20170171. doi: 10.1098/rsta.2017.0171
- Shiller, A. M. (1997). Manganese in surface waters of the Atlantic Ocean. *Geophys. Res. Lett.* 24, 1495–1498. doi: 10.1029/97GL01456
- Shiller, A. M., and Bairamadgi, G. R. (2006). Dissolved gallium in the Northwest Pacific and the South and Central Atlantic Oceans: implications for aeolian Fe input and a reconsideration of profiles. *Geochem. Geophys. Geosyst.* 7:Q08M09. doi: 10.1029/2005GC001118
- Spiro, T. G., Bargar, J. R., Sposito, G., and Tebo, B. M. (2010). Bacteriogenic manganese oxides. *Acc. Chem. Res.* 43, 2–9. doi: 10.1021/ar800232a
- Stumm, W., and Morgan, J. J. (1995). *Aquatic Chemistry: Chemical Equilibria and Rates in Natural Waters*, 3rd Edn. New York, NY: Wiley.
- Sunda, W. G. (2012). Feedback interactions between trace metal nutrients and phytoplankton in the ocean. *Front. Microbiol.* 3:204. doi: 10.3389/fmicb.2012.00204
- Sunda, W. G., and Huntsman, S. A. (1988). Effect of sunlight on redox cycles of manganese in the southwestern Sargasso Sea. *Deep Sea Res. Part A Oceanogr. Res. Pap.* 35, 1297–1317. doi: 10.1016/0198-0149(88)90084-2
- Sunda, W. G., and Huntsman, S. A. (1994). Photoreduction of manganese oxides in seawater. *Mar. Chem.* 46, 133–152. doi: 10.1016/0304-4203(94)90051-5
- Sunda, W. G., and Huntsman, S. A. (1996). Antagonisms between cadmium and zinc toxicity and manganese limitation in a coastal diatom. *Limnol. Oceanogr.* 41, 373–387. doi: 10.4319/lo.1996.41.3.0373
- Sunda, W. G., and Huntsman, S. A. (2000). Effect of Zn, Mn, and Fe on Cd accumulation in phytoplankton: implications for oceanic Cd cycling. *Limnol. Oceanogr.* 45, 1501–1516. doi: 10.4319/lo.2000.45.7.1501
- Sunda, W. G., Huntsman, S. A., and Harvey, G. R. (1983). Photoreduction of manganese oxides in seawater and its geochemical and biological implications. *Nature* 301, 234–236. doi: 10.1038/301234a0
- Sundby, B., Anderson, L. G., Hall, P. O. J., Iverfeldt, A., Rutgers van der Loeff, M. M., and Westerlund, S. F. G. (1986). The effect of oxygen on release and uptake of cobalt, manganese, iron and phosphate at the sediment-water interface. *Geochim. Cosmochim. Acta* 50, 1281–1288. doi: 10.1016/0016-7037(86)90411-4
- Tachikawa, K., Jeandel, C., Vangriesheim, A., and Dupré, B. (1999). Distribution of rare earth elements and neodymium isotopes in suspended particles of the tropical Atlantic Ocean (EUMELI site). *Deep. Res. Part I* 46, 733–755. doi: 10.1016/S0967-0637(98)00089-2
- Tagliabue, A., Bowie, A. R., Boyd, P. W., Buck, K. N., Johnson, K. S., and Saito, M. A. (2017). The integral role of iron in ocean biogeochemistry. *Nature* 543, 51–59. doi: 10.1038/nature21058
- Tagliabue, A., Hawco, N. J., Bundy, R. M., Landing, W. M., Milne, A., Morton, P. L., et al. (2018). The role of external inputs and internal cycling in shaping the global ocean cobalt distribution: insights from the first cobalt biogeochemical model. *Global Biogeochem. Cycles* 32, 594–616. doi: 10.1002/2017GB005830
- Takeda, S., Obata, H., Okubo, A., Sato, M., and Kondo, Y. (2014). “Bioavailability and biogeochemical processes of trace metals in the surface ocean,” in *Western Pacific Air-Sea Interaction Study*, eds M. Uematsu, Y. Yokouchi, Y. W. Watanabe, S. Takeda, and Y. Yamanaka, (Tokyo: TERRAPUB), 163–176. doi: 10.5047/w-pass.a03.001
- Talley, L. D., Nagata, Y., Fujimura, M., Iwao, T., Kono, T., Inagake, D., et al. (1995). North Pacific Intermediate Water in the Kuroshio/Oyashio mixed water region. *J. Phys. Oceanogr.* 25, 475–501. doi: 10.1175/1520-04851995025<0475:NPIWIT>2.0.CO;2
- Talley, L. D., and Yun, J.-Y. (2001). The role of cabbeling and double diffusion in setting the density of the North Pacific intermediate water salinity minimum. *J. Phys. Oceanogr.* 31, 1538–1549. doi: 10.1175/1520-0485(2001)031<1538:trocad>2.0.co;2
- Tanaka, T., Yasuda, I., Kuma, K., and Nishioka, J. (2012). Vertical turbulent iron flux sustains the Green Belt along the shelf break in the southeastern Bering Sea. *Geophys. Res. Lett.* 39:L08603. doi: 10.1029/2012GL051164
- Tani, H., Nishioka, J., Kuma, K., Takata, H., Yamashita, Y., Tanoue, E., et al. (2003). Iron (III) hydroxide solubility and humic-type fluorescent organic matter in the deep water column of the Okhotsk Sea and the northwestern North Pacific Ocean. *Deep. Res. Part I* 50, 1063–1078. doi: 10.1016/S0967-0637(03)00098-0
- Tanoue, E., and Midorikawa, T. (1995). “Detection, characterization and dynamics of dissolved organic ligands in oceanic waters,” in *Biogeochemical Processes and Ocean Flux in the Western Pacific*, eds H. Sakai, and Y. Nozaki, (Tokyo: Terra Scientific Publishing Company (TERRAPUB)), 201–224.
- Tebo, B. M., Bargar, J. R., Clement, B. G., Dick, G. J., Murray, K. J., Parker, D., et al. (2004). BIOGENIC MANGANESE OXIDES: properties and mechanisms of formation. *Annu. Rev. Earth Planet. Sci.* 32, 287–328. doi: 10.1146/annurev.earth.32.101802.120213

- Tebo, B. M., Nealson, K. H., Emerson, S., and Jacobs, L. (1984). Microbial mediation of Mn(II) and Co(II) precipitation at the O<sub>2</sub>/H<sub>2</sub>S interfaces in two anoxic fjords. *Limnol. Oceanogr.* 29, 1247–1258. doi: 10.4319/lo.1984.29.6.1247
- Toyoda, K., and Tebo, B. M. (2016). Kinetics of Mn(II) oxidation by spores of the marine *Bacillus* sp. SG-1. *Geochim. Cosmochim. Acta* 189, 58–69. doi: 10.1016/j.gca.2016.05.036
- van de Flierdt, T., Pahnke, K., Amakawa, H., Andersson, P., Basak, C., Coles, B., et al. (2012). GEOTRACES intercalibration of neodymium isotopes and rare earth element concentrations in seawater and suspended particles. Part 1: reproducibility of results for the international intercomparison. *Limnol. Oceanogr. Methods* 10, 234–251. doi: 10.4319/lom.2012.10.234
- van Hulten, M. M. P., Middag, R., Dutay, J.-C., de Baar, H. J. W., Roy-Barman, M., Gehlen, M., et al. (2016). Manganese in the West Atlantic Ocean in context of the first global ocean circulation model of manganese. *Biogeosciences* 14, 1123–1152. doi: 10.5194/bg-14-1123-2017
- Vedamati, J., Chan, C., and Moffett, J. W. (2015). Distribution of dissolved manganese in the Peruvian upwelling and oxygen minimum zone. *Geochim. Cosmochim. Acta* 156, 222–240. doi: 10.1016/J.GCA.2014.10.026
- Vu, H. T. D., and Sohrin, Y. (2013). Diverse stoichiometry of dissolved trace metals in the Indian Ocean. *Sci. Rep.* 3:1745. doi: 10.1038/srep01745
- Westerlund, S. F. G., Anderson, L. G., Hall, P. O. J., Iverfeldt, Å., Van Der Loeff, M. M. R., and Sundby, B. (1986). Benthic fluxes of cadmium, copper, nickel, zinc and lead in the coastal environment. *Geochim. Cosmochim. Acta* 50, 1289–1296. doi: 10.1016/0016-7037(86)90412-6
- Wu, J., Roshan, S., and Chen, G. (2014). The distribution of dissolved manganese in the tropical–subtropical North Atlantic during US GEOTRACES 2010 and 2011 cruises. *Mar. Chem.* 166, 9–24. doi: 10.1016/j.marchem.2014.08.007
- Yasuda, I. (2004). North Pacific intermediate water: progress in SAGE (Subarctic Gyre Experiment) and related projects. *J. Oceanogr.* 60, 385–395. doi: 10.1023/B:JOCE.0000038344.25081.42
- Yasuda, I., Kouketsu, S., Katsumata, K., Ohiwa, M., Kawasaki, Y., and Kusaka, A. (2002). Influence of Okhotsk Sea Intermediate Water on the Oyashio and North Pacific Intermediate Water. *J. Geophys. Res.* 107:3237. doi: 10.1029/2001JC001037
- Yığiterhan, O., Murray, J. W., and Tuğrul, S. (2011). Trace metal composition of suspended particulate matter in the water column of the Black Sea. *Mar. Chem.* 126, 207–228. doi: 10.1016/j.marchem.2011.05.006
- You, Y. (2003a). Implications of cabbeling on the formation and transformation mechanism of North Pacific Intermediate Water. *J. Geophys. Res.* 108:3134.
- You, Y. (2003b). The pathway and circulation of North Pacific intermediate water. *Geophys. Res. Lett.* 30:2291. doi: 10.1038/nature09288
- You, Y. (2005). Unveiling the mystery of North Pacific intermediate water formation. *Eos Trans. Am. Geophys. Union* 86:65. doi: 10.1029/2005EO070002
- Zhang, J., and Nozaki, Y. (1998). Behavior of rare earth elements in seawater at the ocean margin: a study along the slopes of the Sagami and Nankai troughs near Japan. *Geochim. Cosmochim. Acta* 62, 1307–1317. doi: 10.1016/S0016-7037(98)00073-8
- Zheng, L., Minami, T., Konagaya, W., Chan, C.-Y., Tsujisaka, M., Takano, S., et al. (2019). Distinct basin-scale-distributions of aluminum, manganese, cobalt, and lead in the North Pacific Ocean. *Geochim. Cosmochim. Acta* 254, 102–121. doi: 10.1016/j.gca.2019.03.038
- Zheng, X.-Y., Plancherel, Y., Saito, M. A., Scott, P. M., and Henderson, G. M. (2016). Rare earth elements (REEs) in the tropical South Atlantic and quantitative deconvolution of their non-conservative behavior. *Geochim. Cosmochim. Acta* 177, 217–237. doi: 10.1016/j.gca.2016.01.018
- Zurbrick, C. M., Gallon, C., and Flegal, A. R. (2017). Historic and Industrial Lead within the Northwest Pacific Ocean evidenced by lead isotopes in Seawater. *Environ. Sci. Technol.* 51, 1203–1212. doi: 10.1021/acs.est.6b04666

**Conflict of Interest:** The authors declare that the research was conducted in the absence of any commercial or financial relationships that could be construed as a potential conflict of interest.

Copyright © 2019 Morton, Landing, Shiller, Moody, Kelly, Bizimis, Donat, De Carlo and Shacat. This is an open-access article distributed under the terms of the Creative Commons Attribution License (CC BY). The use, distribution or reproduction in other forums is permitted, provided the original author(s) and the copyright owner(s) are credited and that the original publication in this journal is cited, in accordance with accepted academic practice. No use, distribution or reproduction is permitted which does not comply with these terms.



# The Influence of Basaltic Islands on the Oceanic REE Distribution: A Case Study From the Tropical South Pacific

Mario Molina-Kescher<sup>1\*</sup>, Ed C. Hathorne<sup>1</sup>, Anne H. Osborne<sup>1</sup>, Melanie K. Behrens<sup>2</sup>, Martin Kölling<sup>3†</sup>, Katharina Pahnke<sup>2</sup> and Martin Frank<sup>1</sup>

<sup>1</sup> GEOMAR Helmholtz Centre for Ocean Research Kiel, Kiel, Germany, <sup>2</sup> Max Planck Research Group for Marine Isotope Geochemistry, Institute for Chemistry and Biology of the Marine Environment, University of Oldenburg, Oldenburg, Germany, <sup>3</sup> Zentrum für Marine Umweltwissenschaften, Universität Bremen, Bremen, Germany

## OPEN ACCESS

### Edited by:

Sunil Kumar Singh,  
Physical Research Laboratory, India

### Reviewed by:

Hiroshi Amakawa,  
Japan Agency for Marine-Earth  
Science and Technology, Japan  
Vineet Goswami,  
Colorado State University,  
United States

### \*Correspondence:

Mario Molina-Kescher  
mariomolinescher@hotmail.com

<sup>†</sup> Martin Kölling  
orcid.org/0000-0003-2720-2211

### Specialty section:

This article was submitted to  
Marine Biogeochemistry,  
a section of the journal  
Frontiers in Marine Science

**Received:** 17 October 2017

**Accepted:** 02 February 2018

**Published:** 02 March 2018

### Citation:

Molina-Kescher M, Hathorne EC, Osborne AH, Behrens MK, Kölling M, Pahnke K and Frank M (2018) The Influence of Basaltic Islands on the Oceanic REE Distribution: A Case Study From the Tropical South Pacific. *Front. Mar. Sci.* 5:50. doi: 10.3389/fmars.2018.00050

The Rare Earth Elements (REEs) have been widely used to investigate marine biogeochemical processes as well as the sources and mixing of water masses. However, there are still important uncertainties about the global aqueous REE cycle with respect to the contributions of highly reactive basaltic minerals originating from volcanic islands and the role of Submarine Groundwater Discharge (SGD). Here we present dissolved REE concentrations obtained from waters at the island-ocean interface (including SGD, river, lagoon and coastal waters) from the island of Tahiti and from three detailed open ocean profiles on the Manihiki Plateau (including neodymium (Nd) isotope compositions), which are located in ocean currents downstream of Tahiti. Tahitian fresh waters have highly variable REE concentrations that likely result from variable water-rock interaction and removal by secondary minerals. In contrast to studies on other islands, the SGD samples do not exhibit elevated REE concentrations but have distinctive REE distributions and Y/Ho ratios. The basaltic Tahitian rocks impart a REE pattern to the waters characterized by a middle REE enrichment, with a peak at europium similar to groundwaters and coastal waters of other volcanic islands in the Pacific. However, the basaltic island REE characteristics (with the exception of elevated Y/Ho ratios) are lost during transport to the Manihiki Plateau within surface waters that also exhibit highly radiogenic Nd isotope signatures. Our new data demonstrate that REE concentrations are enriched in Tahitian coastal water, but without multidimensional sampling, basaltic island Nd flux estimates range over orders of magnitude from relatively small to globally significant. Antarctic Intermediate Water (AAIW) loses its characteristic Nd isotopic signature (−6 to −9) around the Manihiki Plateau as a consequence of mixing with South Equatorial Pacific Intermediate Water (SEqPIW), which shows more positive values (−1 to −2). However, an additional Nd input/exchange along the pathway of AAIW, eventually originating from the volcanic Society, Tuamotu and Tubuai Islands (including Tahiti), is indicated by an offset from the mixing array of AAIW and SEqPIW to more radiogenic Nd isotope compositions.

**Keywords:** Rare Earth Elements, Nd isotope compositions, Tahiti, tropical South Pacific, Submarine Groundwater Discharge (SGD), Antarctic Intermediate Water (AAIW)



## KEY POINTS

- REE concentrations in Tahitian coastal waters show a clear basaltic island input.
- Tahitian Submarine Groundwater Discharge has relatively low REE concentrations but high Y/Ho.
- Basaltic influence on S Pacific surface waters mostly lost during transit to Manihiki Plateau region.
- Manihiki surface waters have high Y/Ho and radiogenic Nd isotope compositions.

## INTRODUCTION

The distribution of the Rare Earth Elements (REE) in seawater reflects the subtle but systematic differences in their chemical properties (e.g., Elderfield and Greaves, 1982). The relative abundance of the free trivalent REE ions (except Ce) in seawater produces coherent patterns as a function of the decreasing ionic radii across the group (lanthanide contraction). These patterns can be used to track processes such as the biogeochemical behavior (e.g., Elderfield, 1988; Schijf et al., 2015), oceanic water mass advection (e.g., Nozaki, 2001; Osborne et al., 2015), or sourcing of water masses and continental weathering inputs (e.g., Byrne and Sholkovitz, 1996; Molina-Kescher et al., 2014). The REEs are subdivided into light REE (LREE), from La to Sm; middle REE (MREE), from Eu to Dy; and heavy REE (HREE), from Ho to Lu (Nozaki, 2001). As marine waters acquire their REE compositions through weathering of continental rocks, normalization of their seawater REE concentrations to a typical upper continental source, such as the Post-Archean Australian Shale (PAAS) (Taylor and McLennan, 1985) removes the zig-zag pattern in natural abundance that was caused by nucleosynthetic processes, exposing deviations in composition that can reveal the source of the REE or the processes that have changed their relative abundances. For example, rivers are generally enriched in MREE, most likely caused by the weathering of phosphate minerals (Hannigan and Sholkovitz, 2001), although some rivers can have almost seawater-like patterns like the Mississippi (e.g., Sholkovitz, 1995) or the truly dissolved load of the Amazon (Merschel et al., 2017). Typical open ocean PAAS normalized patterns present a continuous increase in abundance from LREE to HREE, caused by the preferential removal of LREE from solution by adsorption processes (Byrne and Kim, 1990; Schijf et al., 2015), and a strong Ce depletion caused by its oxidation to Ce(IV), which is highly insoluble (Moffett, 1990). The “Ce anomaly” ( $Ce/Ce^* = 3*[Ce]/2*[Nd] + [La]$ ) (e.g., Nozaki, 2001) is termed “negative” ( $Ce/Ce^* < 1$ ) when Ce is depleted with respect to its neighbor elements and “strong” when it is closest to 0. Eu also presents anomalies ( $Eu/Eu^* = 3*[Eu]/2*[Sm] + [Tb]$ ) with respect to its neighboring elements Sm and Tb (Gd is omitted from this calculation as it is prone to anthropogenic contamination, Bau and Dulski, 1996), which originate from weathering of basalts and hydrothermal activity (Byrne and Sholkovitz, 1996). However, to allow

interpretation of Eu anomalies, careful separation of Ba from the sample solution or correction for oxide formation during REE analysis is required because of isobaric interferences on Eu (Aries et al., 2000).

Even more information can be obtained with the radiogenic isotope composition of the LREE neodymium (Nd) as this tracks large-scale oceanic circulation in the present day ocean (e.g., Piepgras and Wasserburg, 1982, 1987; Bertram and Elderfield, 1993; Singh et al., 2012; Osborne et al., 2014; Basak et al., 2015; Stichel et al., 2015), and has been applied to reconstruct past circulation (e.g., Wilson et al., 2015; Howe et al., 2016; Hu et al., 2016; Molina-Kescher et al., 2016; Wei et al., 2016). Water masses acquire characteristic Nd isotope compositions ( $^{143}Nd/^{144}Nd$ , expressed in the  $\epsilon_{Nd}$  notation:  $\epsilon_{Nd} = [(^{143}Nd/^{144}Nd_{sample}/^{143}Nd/^{144}Nd_{CHUR}) - 1] * 10,000$ ; CHUR = Chondritic Uniform Reservoir, with  $^{143}Nd/^{144}Nd = 0.512638$ , Jacobsen and Wasserburg, 1980) in their formation regions via continental weathering inputs from rivers, dust, and/or submarine groundwater discharge (e.g., Goldstein and Jacobsen, 1987; Frank, 2002; Goldstein and Hemming, 2003; Johannesson and Burdige, 2007), and also through sediment particulate exchange processes at the continent/ocean interface, broadly defined as “boundary exchange” (e.g., Lacan and Jeandel, 2005; Du et al., 2016). Near the ocean margins, processes such as a benthic flux of REE from pore waters (Elderfield and Sholkovitz, 1987; Abbott et al., 2015), release from river particles (Goldstein and Jacobsen, 1987; Rousseau et al., 2015), and interaction with sinking particles in the water column (Bertram and Elderfield, 1993; Siddall et al., 2008; Grasse et al., 2012, 2017; Chen et al., 2013; Jeandel and Oelkers, 2015) influence the  $\epsilon_{Nd}$  signature of seawater. In the open ocean, the  $\epsilon_{Nd}$  signatures of different intermediate and deep-water masses are quasi-conservative and primarily altered through mixing because the oceanic residence time of Nd (300–2,000 years) is similar to the global oceanic mixing time (e.g., Tachikawa et al., 2003; Arsouze et al., 2009; Rempfer et al., 2011).

Two open questions key to our understanding of global aqueous REE cycling are the significance of inputs from highly reactive basaltic minerals associated with the weathering of volcanic island rocks (Allège et al., 2010; Kim and Kim, 2011; Pearce et al., 2013; Fröllje et al., 2016), and the importance of Submarine Groundwater Discharge (SGD) (e.g., Duncan and Shaw, 2003; Johannesson and Burdige, 2007; Johannesson et al., 2011, 2017). SGD is defined as the total flux of underground water that is introduced from continental margins, of which less than 10% corresponds to waters of terrestrial and meteoric origin. The remaining 90% consists of seawater that is recirculated through the sediments by a variety of processes, such as hydraulic gradients, tidal pumping, or wave set-up, resulting in biogeochemical reactions that significantly modify its geochemistry (including that of REEs; Moore, 1996, 2003; Burnett et al., 2003; Johannesson and Burdige, 2007; Kim and Kim, 2011). Geochemical weathering through SGD is particularly pronounced at the margins of young and highly reactive volcanic islands (Schopka and Derry, 2012; Kwon

et al., 2014). SGD includes fresh, brackish and fully marine waters and has been estimated to be on the same order as the global riverine discharge to the oceans (Johannesson and Burdige, 2007; Moore et al., 2008; Kwon et al., 2014) and is likely an important contributor to the global REE budget (Johannesson and Burdige, 2007) especially in the Pacific Ocean (Kwon et al., 2014). Two recent studies of REEs in groundwater and near costal seawater of the basaltic Hawaiian islands found strongly contrasting concentrations with coastal waters around Oahu showing little or no enrichment compared to open ocean waters (Fröllje et al., 2016) while one sample of surface seawater from near Kona on the Big Island Hawai'i exhibited concentrations >30 times higher for the LREE and >10 times higher for HREE compared to offshore seawater (Johannesson et al., 2017). Although the concentrations indicated little input, the Nd isotopes and REE patterns around Oahu clearly reveal the influence of basaltic REEs on the seawater (Fröllje et al., 2016) suggesting an exchange type process (e.g., Lacan and Jeandel, 2005). Near Kona on the other hand, the high REE concentrations and patterns are similar to those found in groundwaters suggesting a significant input of REEs through SGD with little modification during mixing with seawater (Johannesson et al., 2017). Similarly, another Pacific volcanic island, Jeju (Korea), shows SGD REE fluxes to the ocean comparable to that of major rivers (i.e., Mississippi River) (Kim and Kim, 2011).

In order to assess the importance of exchange with basaltic islands in the oceanic REE cycle, to identify associated REE patterns, and to expand the database for the as yet poorly studied South Pacific, we present REE concentrations obtained from a variety of waters sampled at the land-ocean interface, including river mouths, lagoons, and coastal seawater from a SGD spring in the reef along the margin of the volcanic island of Tahiti (**Figure 1A**). We also present REE concentrations and  $\epsilon_{\text{Nd}}$  signatures obtained from three detailed open ocean profiles above the Manihiki Plateau (between  $\sim 3^\circ\text{S}$ , and  $\sim 13^\circ\text{S}$ ,  $\sim 162^\circ\text{W}$ , and  $\sim 166^\circ\text{W}$ ; **Figure 1B**), located to the NW of Tahiti and thus downstream of the main oceanic circulation pathways that pass the Tuamotu, Tubuai, and Society Islands (to which Tahiti belongs). Oceanographically, this region represents the transition between the formation region of Southern Ocean derived water masses, such as the climatically highly relevant Antarctic Intermediate Water (AAIW) (e.g., Pahnke et al., 2008; Tapia et al., 2015) or Upper Circumpolar Deep Water (UCDW), and the western equatorial Pacific. The latter is a key region for global climate (Hu et al., 2015) (see section "General hydrography"), and the site of important geochemical modifications, including REE and Nd isotopes (Lacan and Jeandel, 2001; Grenier et al., 2013, 2014). Both AAIW and UCDW pass Tahiti and the Manihiki Plateau and are prone to be modified in terms of their REE and Nd isotope compositions as they encounter the first volcanic islands on their NW pathway, even before reaching the western equatorial Pacific. These data allow the evaluation of REE changes in surface, intermediate, and deep waters potentially produced by volcanic islands.

## General Hydrography

The circulation in the tropical South Pacific generally follows a SE to NW direction at all depths (**Figure 1B**) and represents the northern limb of the wind-driven geostrophic anticyclonic gyre that affects the entire water column of the South Pacific (Reid, 1997).

The surface hydrography of the westernmost equatorial Pacific is dominated by the West Pacific Warm Pool (WPWP) (**Figure 1B**), the largest oceanic warm-pool on Earth that plays a key role in the heat transfer between ocean and atmosphere in the tropics and in particular for the dynamics of the El Niño Southern Oscillation (ENSO) (Hu et al., 2015). The WPWP is connected to the central Pacific circulation system via the Equatorial Undercurrent (EUC), which crosses the entire equatorial Pacific from West to East and acts as the counterpart of the equatorial westward surface currents that push warm waters toward the WPWP (Tsuchiya et al., 1989; Tomczak and Godfrey, 2003). Another important feature of the surface waters of the tropical central Pacific is the High Surface Evaporation Area (HSEA) centered at  $\sim 15^\circ\text{S}/130^\circ\text{W}$  (see **Figure 1B** and **Figure S1**), where South Pacific Equatorial Water (SPEW) forms as a consequence of strong evaporation. This water mass is subsequently subducted and carries its high salinity and high oxygen signal to the NW into the WPWP (Tomczak and Hao, 1989; Tsuchiya et al., 1989; Qu and Lindstrom, 2002; Tomczak and Godfrey, 2003). Antarctic Intermediate Water (AAIW) is the major intermediate water mass prevailing between 600 and 1,300 m in the entire South Pacific (Hartin et al., 2011) and is characterized by low salinities (34.3–34.5), low temperatures (3.5–10°C), and high oxygen content (4.5–5.5 ml/l) (Bostock et al., 2010). AAIW forms mainly in the southeastern Pacific as a consequence of cooling of Subantarctic Mode Water (SAMW) (Sloyan and Rintoul, 2001) and flows in a NW direction following the subtropical gyre circulation (Tomczak and Godfrey, 1994) (**Figure 1B**). Equatorial Pacific Intermediate Water (EqPIW) (Bostock et al., 2010) dominates in the tropical region ( $\sim 15^\circ\text{N}$  to  $\sim 15^\circ\text{S}$ ) and is a mixture of AAIW and Pacific Deep Water (PDW). It carries distinct non-conservative tracer signatures such as very low oxygen concentrations (below 2 ml/l) originating from high biological activity and subsequent demineralization of organic material at the equator as a consequence of the upwelling of nutrient rich waters. EqPIW can be further subdivided into South EqPIW (SEqPIW) and North EqPIW (NEqPIW), separated by the equator and characterized by higher biological activity to the north of the equator (NEqPIW) (Bostock et al., 2010) (see **Figure S1**). The main mixing zone between pure AAIW and SEqPIW at the longitude of our seawater profiles ( $\sim 165^\circ\text{W}$ ) is located between  $\sim 13^\circ\text{S}$  and  $\sim 17^\circ\text{S}$ . The locations of the stations of our study at  $13^\circ\text{S}$  (53-4),  $9^\circ\text{S}$  (2-2), and  $3^\circ\text{S}$  (21-1) allow investigation of the consequences of the mixing of these water masses for REE concentrations and Nd isotope compositions (see **Figure S1**). Below the intermediate water layer Upper Circumpolar Deep Water (UCDW) prevails, which detaches from the Antarctic Circumpolar Current (ACC) in the South Pacific near  $120^\circ\text{W}$  and first flows northward and then

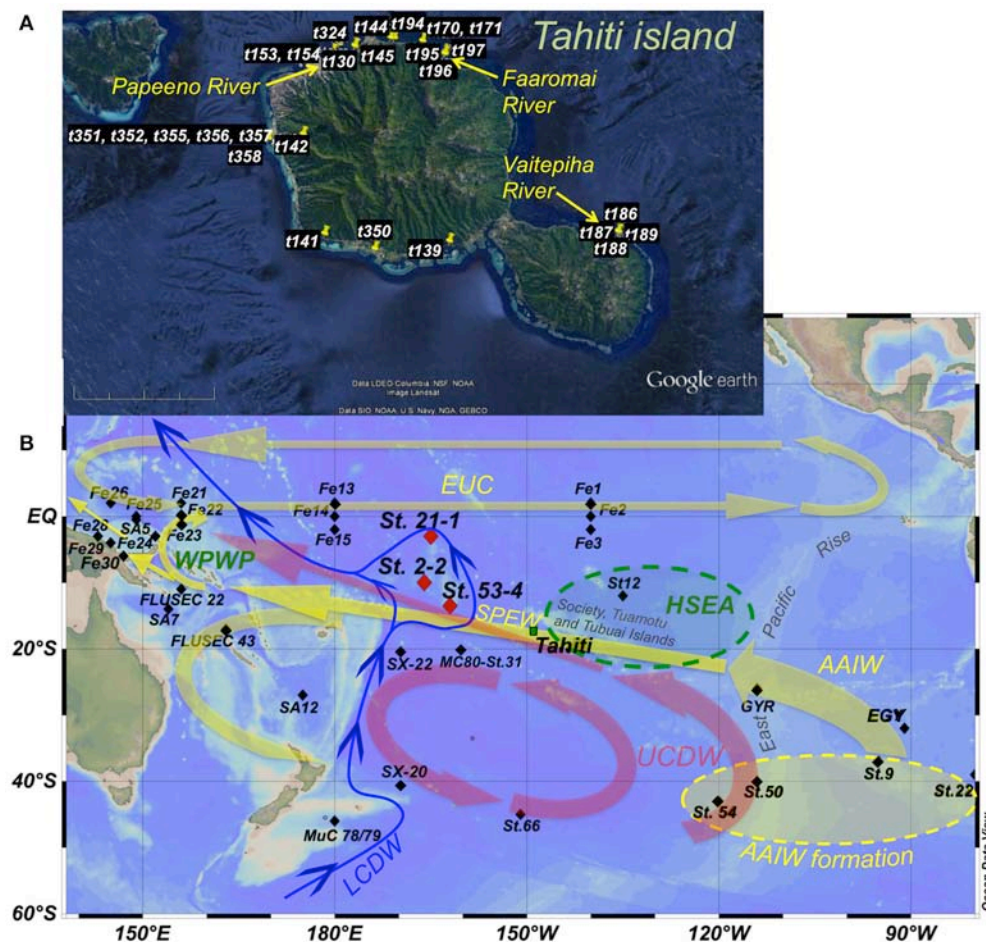


**FIGURE 1 |** Maps of Tahiti ( $17^{\circ} 40'S/149^{\circ} 25'W$ ) (**A**) and the central/ South Pacific (**B**) showing the sampling sites of this and published studies and the main oceanographic features. Red diamonds in (**B**) indicate seawater stations 21-1 ( $3^{\circ} 3.0'S/165^{\circ} 3.5'W$ ), 2-2 ( $9^{\circ} 59.8'S/166^{\circ} 12.0'W$ ), and 53-4 ( $13^{\circ} 30.6'S/162^{\circ} 7.6'W$ ), the last two are located above the Manihiki Plateau. The island of Tahiti is marked by a green square. Black diamonds indicate sites presented in Grenier et al. (2013 and 2014): Fe 1 to Fe 30 plus FLUSEC 22 and 23; Zhang and Nozaki (1996): SA5, SA7, and SA12; Lacan and Jeandel (2001): St12; Jeandel et al. (2013): GYR and EGY; Amakawa et al. (2013): SX-20 and SX-22; Piepgras and Jacobsen (1988): MC80-St.31; and Molina-Kescher et al. (2014): St.22, St.9, St.50, St.54, St.66, and MuC 78/79. Main circulation patterns and directions (according to Kawabe and Fujio, 2010) are indicated with yellow arrows (1,000–1,500 m water depth), red arrows (1,500–3,000 m water depth), and blue arrows (bottom water). Green oval represents the High Surface Evaporation Area (HSEA) and yellow oval indicates AAIW formation region. WPWP stands for West Pacific Warm Pool. Water mass: AAIW, Antarctic Intermediate Water; UCDW, Upper Circumpolar Deep Water; LCDW, Lower Circumpolar Deep Water; SPEW, South Pacific Equatorial Water; EUC, Equatorial Undercurrent. Topographic features mentioned in the text are also presented. A more detailed hydrography of the subsurface (50 m water depth) and intermediate (1,000 m water depth) water column is provided in **Figure S1**.

northwestward (similar to AAIW) toward the equatorial western Pacific (**Figure 1B**; Reid, 1997; Kawabe and Fujio, 2010). Along its pathway through the Pacific Ocean, this initially cold, salty and oxygen rich water mass loses its properties through mixing with PDW that carries a significantly lower oxygen content and dominates the mid-depth water column of the South Pacific (e.g., Molina-Kescher et al., 2014). As a result, the dissolved oxygen maximum of UCDW essentially vanishes north of  $15^{\circ}S$  in the Samoa/New Guinea region (Reid, 1997; Kawabe and Fujio, 2010). Lower Circumpolar Deep Water (LCDW) is the bottom water mass responsible for the ventilation of the entire deep Pacific given that no deep water is formed in the North Pacific. This water mass enters the Pacific basin southeast of New Zealand as a Deep Western Boundary Current and flows

northward embracing the Manihiki Plateau (Kawabe and Fujio, 2010; **Figure 1B**).

## METHODS

### Sampling at Tahiti and Above the Manihiki Plateau

A total of 27 water samples collected at different locations in Tahiti during two sampling campaigns in 2007 and 2009 were measured for REE concentrations. These include coastal and lagoon waters, stream/river waters, and the mixing of these with seawater as well as some samples from an active SGD spring “La source” (**Table 1**). These samples were filtered directly after



**TABLE 1 |** Location, description, hydrological properties, REE concentrations and different REE relationships for Tahitian waters.

Sample	Latitude	Longitude	Description	Category*	Salinity	Dissolved Si (μmol/L)	Alkalinity μM	Y (pmol/kg)	La (pmol/kg)	Ce (pmol/kg)	Pr (pmol/kg)	Nd (pmol/kg)	Sm (pmol/kg)	Eu (pmol/kg)	Gd (pmol/kg)	Tb (pmol/kg)	Dy (pmol/kg)	Ho (pmol/kg)	Er (pmol/kg)	Tm (pmol/kg)	Yb (pmol/kg)	Lu (pmol/kg)
t141	−17.75117	−149.54764	Maraa Papemato well	Fresh water	0	352.86	720	1.9	1.5	2.3	0.35	1.75	0.32	0.07	0.28	0.02	0.13	0.01	0.10	0.01	0.09	-
t142	−17.62811	−149.57503	Punaruu valley waterfall	Fresh water	0	512.50	1850	219.7	73.4	93.6	22.92	114.46	23.33	7.20	23.41	3.14	17.76	3.66	9.58	1.28	7.54	1.22
t1194	−17.50736	−149.45698	Creek mouth pk13/14	Fresh water	0	657.14	1010	12.8	3.4	3.5	0.88	3.95	0.81	0.28	0.77	0.10	0.67	0.13	0.37	0.06	0.23	0.03
t1197	−17.52736	−149.39119	Faaromai river	Fresh water	0	128.57	0	1543.7	634.0	1536.2	191.67	875.27	168.34	51.82	162.54	21.69	116.39	22.19	57.49	7.19	40.32	6.24
t1196	−17.52661	−149.39037	Faaromai river mouth	RMW	18.3	78.57	1360	553.9	222.2	446.2	64.47	300.04	58.19	17.70	56.20	7.69	43.35	8.72	22.70	2.80	16.28	2.56
t1195	−17.52511	−149.39049	Beach near faaromai river	RMW	28.6	32.14	1960	343.1	117.6	192.0	29.89	137.21	25.33	8.28	27.35	3.68	21.25	4.50	12.40	1.59	8.89	1.42
t1189	−17.74805	−149.16387	Vaitepaha river mouth	RMW	1.2	342.86	670	49.8	35.0	35.8	8.43	35.37	6.13	1.65	5.58	0.77	3.66	0.75	2.06	0.23	1.52	0.22
t1188	−17.74794	−149.16398	Vaitepaha river mouth	RMW	6.8	278.57	1130	89.3	49.2	60.0	11.37	45.92	8.23	2.39	8.49	1.04	5.57	1.17	3.14	0.40	2.44	0.38
t1187	−17.74785	−149.16401	Vaitepaha river mouth	RMW	15.5	192.86	1500	131.3	58.3	71.2	12.21	52.61	9.24	2.94	9.81	1.37	7.47	1.67	4.74	0.55	3.35	0.51
t1186	−17.74773	−149.16404	Vaitepaha river mouth	RMW	25.1	103.57	1840	150.6	53.6	54.2	11.31	52.87	9.26	2.79	10.28	1.40	8.19	1.79	4.83	0.60	3.83	0.65
t1171	−17.51144	−149.42014	Papenoo river mouth	RMW	7.5	342.86	1480	100.4	42.0	46.3	9.33	43.29	7.65	2.57	8.79	1.17	6.11	1.37	3.66	0.47	2.73	0.43
t1170	−17.51144	−149.42014	Papenoo river mixing zone	RMW	25.1	125.00	2040	135.5	40.7	42.2	8.92	42.19	7.62	2.53	8.83	1.14	7.00	1.53	4.35	0.58	3.23	0.54
t1139	−17.76023	−149.38468	Lagoon water	B&L	31.4	78.57	2190	208.1	64.8	177.7	18.84	81.05	15.91	5.51	17.51	2.42	14.95	3.14	8.38	1.12	6.71	1.07
t1350	−17.76980	−149.48220	Beach water	B&L	32.5	–	–	143.8	48.1	51.0	9.50	41.09	7.83	2.44	8.41	1.12	6.83	1.58	4.56	0.61	3.36	0.54
t1153	−17.52481	−149.53697	Lagoon 0.5 m water depth	B&L	34	–	2550	133.5	17.1	33.4	4.44	22.24	4.22	1.58	5.48	0.89	6.02	1.48	4.57	0.58	3.87	0.64
t1144	−17.50734	−149.46183	Beach water	B&L	34.5	–	2890	219.2	126.4	150.1	25.57	102.77	12.48	4.26	15.13	2.01	12.05	2.62	7.71	0.91	5.47	0.88
t1145	−17.51808	−149.50800	Beach water	B&L	34.7	–	2530	440.1	293.0	673.1	83.40	354.70	66.89	18.53	59.91	7.94	42.69	8.00	21.52	2.62	15.23	2.50
t1154	−17.52481	−149.53697	Lagoon 1.5 m water depth	B&L	34.8	–	3110	152.9	13.9	29.3	3.86	18.27	3.69	1.53	5.71	0.87	6.32	1.67	5.33	0.72	4.64	0.87
t355	−17.63260	−149.62090	La source	SGD	35.7	–	–	75.7	7.6	10.1	1.78	7.68	1.60	0.35	1.76	0.25	1.82	0.51	1.48	0.20	1.13	0.18
t356	−17.63260	−149.62090	La source	SGD	27	–	–	40.8	4.1	4.7	0.83	3.81	0.71	0.19	0.79	0.14	0.98	0.24	0.71	0.12	0.55	0.10
t352	−17.63260	−149.62090	La source	SGD	22.4	–	–	61.6	8.3	6.1	1.81	8.19	1.38	0.40	1.83	0.24	1.91	0.42	1.49	0.23	1.21	0.22
t1130	−17.51469	−149.52847	Lagoon water	Seawater	36.1	–	2450	103.7	22.1	25.5	5.67	25.82	4.83	1.58	5.27	0.76	4.88	1.09	2.97	0.39	2.28	0.29
t324	−17.51710	−149.50860	coastal water	Seawater	36.1	–	–	104.2	20.5	28.4	3.96	18.85	3.68	1.18	4.91	0.68	4.30	0.98	3.12	0.47	2.70	0.45
t357	−17.63260	−149.62090	La source seawater	Seawater	36.2	–	–	90.8	20.6	25.0	4.31	19.98	3.60	1.06	3.78	0.52	3.41	0.78	2.12	0.27	1.41	0.24
t358	−17.63260	−149.62090	La source seawater	Seawater	36.2	–	–	107.7	23.0	27.5	5.04	22.58	4.51	1.34	5.06	0.67	4.20	0.96	2.84	0.37	1.98	0.29
t351	−17.63260	−149.62090	La source	contaminated	35.6	–	–	84.6	520.3	652.0	6.09	19.14	3.34	0.81	6.33	0.46	2.88	0.65	1.79	0.26	1.41	0.16
t354	−17.63260	−149.62090	La source	contaminated	30.6	–	–	81.9	192.4	323.4	6.50	22.34	3.82	0.91	5.00	0.50	3.02	0.73	1.86	0.23	1.63	0.25

\*Category indicates the classification of the samples used for this study according to their geographical location: RMW, River Mixed Waters; B&L, Beaches and lagoons; and SGD, Submarine Groundwater Discharge. See text for further details.



collection through 0.2  $\mu\text{m}$  25 mm Sartorius Minisart syringe filters with a CA membrane into acid cleaned PE bottles. The samples were acidified within 24 h of collection with trace metal grade  $\text{HNO}_3$  to a pH of  $\leq 2$ .

The open ocean seawater samples of this study were obtained during RV Sonne cruise SO-225 from three profiles above the Manihiki Plateau in December 2012 (**Figure 1**, **Tables 2, 3**) using a CTD rosette equipped with 24  $\times$  12 L standard Niskin bottles (Ocean Test Equipment Inc.). All samples were filtered directly from the Niskin bottles using AcroPak500 filter cartridges with 0.8/0.2  $\mu\text{m}$  pore size into acid-cleaned PE bottles and cubitainers, 125 ml for REE analysis and 10 L for Nd isotope compositions, respectively. All samples were acidified to pH 2 onboard using distilled 6 N HCl and were stored at 4°C. REE concentrations for profile 21-1 (except for 5,172 m) and sample 53-4-3088 m were previously published in Osborne et al. (2017).

## Measurement of YREE Concentrations

Yttrium and REE concentrations were measured at GEOMAR using a seaFAST online pre-concentration system (Elemental Scientific Inc., Nebraska, USA) directly connected to an Agilent 7500ce ICP-MS (Hathorne et al., 2012, 2015; Osborne et al., 2015). This method was part of the GEOTRACES intercalibration for REE concentrations (van de Flierdt et al., 2012). Tahitian samples were measured with a 4 mL loop as in Hathorne et al. (2012), while Manihikian samples were measured with an 8 mL sample loop. Calibration standards were prepared with a mixed YREE solution of a seawater-like composition in a natural seawater matrix, and the Manihikian samples were measured by time resolved analysis (Osborne et al., 2015). As the seaFAST column quantitatively removes the matrix (e.g., Hathorne et al., 2012) the same calibration standards were used for all samples regardless of their salinity. Total procedural blanks for the Tahitian samples, including filtering pure water in the field and storage in sample bottles, before being run through the preconcentration system just like samples, were  $<0.1$  ppt for all REE and  $<0.2$  ppt for Y. These were below the detection limits for most YREE and negligible except for the fresh water samples with very low conductivity. Although no procedural blanks were taken during the Manihiki campaign, comparable shipboard blanks from the GEOMAR lab obtained during other cruises using essentially the same methods were  $<0.1$  ppt for La and Ce and below the detection limit for the other REEs. Repeated analyses of GEOTRACES BATS reference seawater samples (van de Flierdt et al., 2012) were used to assess the accuracy and precision of the analyses (**Table 3**).

## Measurement of Radiogenic Nd Isotope Compositions

For details on the laboratory procedure see Behrens et al. (2018). Briefly, Nd was preconcentrated from 10 L of seawater using  $\text{C}_{18}$  SepPak® cartridges (modified after Shabani et al., 1992; Jeandel et al., 1998). Neodymium isotope ratios were measured on a Thermo Neptune Plus multicollector-inductively coupled plasma-mass spectrometer (MC-ICP-MS) at the ICBM, University of Oldenburg. The measured  $^{143}\text{Nd}/^{144}\text{Nd}$  ratios were corrected for instrumental mass fractionation to a  $^{146}\text{Nd}/^{144}\text{Nd}$

ratio of 0.7219 (O’Nions et al., 1977) using an exponential law. The mass bias-corrected  $^{143}\text{Nd}/^{144}\text{Nd}$  ratios were normalized to 0.512115, the accepted value for the JNdi-1 standard (Tanaka et al., 2000), which was measured at the beginning and end of a session and after every third sample together with an in-house Nd standard. External reproducibility, checked with multiple JNdi-1 analyses during each session, was typically better than  $\pm 0.3$   $\epsilon_{\text{Nd}}$  units ( $2\sigma$ ,  $n = 11$ –19 per session). For individual samples, the  $2\sigma$  propagated error derived from the internal error and external error (mean values of JNdi measurements of the respective session) is provided (**Table 2**). Standards and samples were run at the same concentrations. The accuracy of our measurements was checked using total procedural duplicates of seawater samples from two water depths of the GEOTRACES intercalibration station BATS (Bermuda Atlantic Time-Series Station) and one sample from the SAFe intercalibration (Sampling and Analysis of Iron) (Pahnke et al., 2012; van de Flierdt et al., 2012). Our measured average  $\epsilon_{\text{Nd}}$  values of seawater at BATS (15 and 2,000 m) and SAFe (3,000 m) are identical within analytical uncertainties to the measurements of the average  $\epsilon_{\text{Nd}}$  values reported by van de Flierdt et al. (2012) (see Behrens et al., 2018). Column chemistry blanks were  $<1.5$  pg Nd ( $n = 6$ ).

## RESULTS

All the results presented in this study are available in the database of PANGAEA (<https://doi.org/10.1594/PANGAEA.884775>).

### REE Compositions of Tahitian Waters

The Tahitian water samples show large differences in their absolute REE concentrations, with the largest range found for the freshwaters, ranging from 1.7 pmol Nd/kg (t141; a well water with very low conductivity) and 875 pmol Nd/kg (t197 river water), but at the same time exhibiting similarities in their PAAS normalized patterns, mostly resembling Tahitian basaltic rocks (**Figures 2A–C**). The REE concentrations and pattern indices (e.g., HREE/LREE, MREE enrichment, Ce and Eu anomalies), of the Tahitian water samples do not correlate with properties such as salinity, alkalinity or dissolved silicate (**Figure S2**). However, the classification of the samples according to salinity (**Table 1**) reveals systematic variations based on different REE pattern indices (**Figure S3**) as discussed in section “Basaltic influence on Tahitian coastal waters.”

Two seawater samples (t354 and t351) (**Table 1**) have clearly anomalous enrichments of La (520 and 192 pmol/kg) and Ce (652 and 323 pmol/kg) indicative of contamination by petroleum products (Olmez et al., 1991) and are not discussed further.

### Seawater Profiles From the Manihiki Plateau

#### Water Mass Identification

It is difficult to distinguish intermediate and deep water masses in the Pacific Ocean on the basis of temperature and salinity characteristics and thus information from additional tracers such as oxygen concentrations is required (**Figure 3**). The data for all three stations above the Manihiki Plateau show similar patterns, with southernmost station 53-4 being characterized

**TABLE 2 |** Hydrological characteristics and neodymium (Nd) isotopic compositions (IC) with external reproducibilities ( $2\sigma$ ) for open ocean seawater obtained at the Manihiki Plateau presented from north to south.

	Depth	Potential temperature ( $\theta$ )	Salinity	Potential density ( $\sigma_\theta$ )	Oxygen	Nd IC	Ext. reprod.
Stations	(m)	$^{\circ}\text{C}$		$\text{kg/m}^3$	ml/l	$\epsilon_{\text{Nd}}$	$2\sigma$
SO225-21-1	14	27.96	35.52	22.80	5.58	-1.4	0.4
3°3.0'S	54	27.94	35.52	22.80	5.55	-1.7	0.4
165° 3.5'W	153	21.58	35.52	24.73	3.54	-1.2	0.2
	202	15.31	35.15	26.02	2.58	-2.4	0.4
	450	8.77	34.64	26.87	1.95	-2.4	0.3
	649	6.38	34.54	27.14	1.54	-1.5	0.4
	997	4.42	34.53	27.37	2.30	-2.1	0.3
	1,493	3.01	34.57	27.54	2.66	-2.0	0.2
	2,009	2.09	34.62	27.66	3.04	-2.3	0.3
	3,005	1.41	34.66	27.74	3.80	-3.6	0.3
	3,992	1.08	34.67	27.78	4.34	-4.2	0.3
	5,172	0.82	34.68	27.80	5.16	-6.5	0.2
SO225-2-2	10	29.75	35.35	22.07	5.44	-1.3	0.4
9° 59.8'S	51	29.62	35.37	22.14	5.42	-1.8	0.3
166° 12.0'W	133	24.75	36.35	24.44	4.62	-1.5	0.6
	240	17.70	35.37	25.63	4.01	-2.2	0.2
	283	13.88	34.92	26.15	3.12	-5.1	0.3
	382	9.19	34.64	26.81	2.53	-3.5	0.2
	492	7.31	34.55	27.02	3.02	-2.9	0.2
	730	5.54	34.50	27.21	2.81	-4.0	0.3
	1,028	4.15	34.52	27.39	2.70	-3.8	0.3
	1,525	2.69	34.58	27.58	3.21	-4.4	0.2
	2,023	2.02	34.62	27.67	3.42	-4.2	0.2
	2,627	1.66	34.64	27.71	3.58	-4.5	0.2
SO225-53-4	11	29.05	35.72	22.58	5.40	-0.4	0.3
13° 30.6'S	50	28.10	36.07	23.17	5.66	-0.9	0.3
162° 7.6'W	99	25.85	36.24	24.02	5.10	-1.0	0.4
	168	23.54	36.27	24.74	4.59	-2.1	0.5
	278	15.55	35.09	25.92	4.05	-4.4	0.4
	396	9.82	34.59	26.66	2.81	-3.1	0.3
	506	7.86	34.52	26.92	3.02	-3.2	0.3
	703	5.64	34.47	27.18	3.22	-3.1	0.3
	1,001	4.27	34.49	27.35	3.17	-3.3	0.3
	1,499	2.76	34.57	27.56	3.28	-3.5	0.4
	2,006	1.97	34.62	27.67	3.50	-3.7	0.4
	3,088	1.43	34.66	27.74	3.72	-3.8	0.3

$\theta$ , Potential temperature;  $\sigma_\theta$ , Potential density.

by the highest  $[\text{O}_2]$  values (5.7 ml/l at  $\sim 50$  m water depth, representing SPEW) while northernmost station 21-1 close to the equator shows the lowest oxygen concentrations (1.4 ml/l at  $\sim 650$  m water depth, representing pure SEqPIW), reflecting the progressive northward dilution of Southern Ocean-derived, oxygen-rich waters toward the equator. All three stations exhibit a reduction of oxygen concentration with water depth with a  $[\text{O}_2]$  minimum between 26.4 and 27.4  $\sigma_\theta$  (corresponding to a water depth between 220/330 m (St. 21-1/St.2-2 and St. 53-4)

and  $\sim 1,100$  m), with the increased presence of PDW. A steady increase in  $[\text{O}_2]$  from  $\sim 1,100$  m depth to the bottom marks the presence of UCDW. The deepest samples of station 21-1, at 3,992 and 5,172 m water depth correspond to LCDW, which is even more enriched in oxygen than UCDW (Callahan, 1972), given that the latter contains a higher proportion of oxygen depleted PDW that dominates mid-depths (Kawabe and Fujio, 2010; Molina-Kescher et al., 2014). Another distinct feature observed in **Figure 3** is the presence of diluted AAIW at a

**TABLE 3 |** Rare Earth element data for open ocean seawater obtained at the Manihiki Plateau and GEOTRACES intercalibration measurements (BATS) for this study presented from north to south.

Stations	Depth	Y	La	Ce	Pr	Nd	Sm	Eu	Gd	Tb	Dy	Ho	Er	Tm	Yb	Lu	Eu/ Eu* <sub>PAAS</sub>	Ce/ Ce* <sub>PAAS</sub>	HREE/ LREE <sub>PAAS</sub>	MREE/ MREE* <sub>PAAS</sub>	Er/ Lu <sub>PAAS</sub>	Y/H <sub>PAAS</sub>
<b>SO225-21-1</b>																						
3°30'S	14	66	6.7	2.36	1.08	5.4	0.93	0.30	1.70	0.32	2.57	0.58	1.81	0.28	1.39	0.24	0.42	0.38	0.15	0.61	7.50	113.36
165° 3.5'W	54	65	6.3	1.87	1.14	5.1	1.15	0.30	1.56	0.29	2.15	0.59	1.78	0.25	1.49	0.25	0.35	0.32	0.16	0.55	7.22	110.62
	153 <sup>a</sup>	70	0.2	0.20	0.02	0.0	0.04	0.04	0.07	0.06	0.09	0.10	0.11	0.11	0.11	0.09	—	—	—	—	—	—
	202	71	7.8	1.69	1.10	4.6	0.72	0.24	1.52	0.24	2.01	0.56	2.12	0.26	1.73	0.27	0.88	1.33	0.18	0.76	1.23	706.88
	450	102	14.3	4.88	1.64	7.9	1.76	0.42	2.25	0.38	3.29	0.92	3.52	0.54	3.61	0.61	0.44	0.25	0.17	0.48	7.79	125.57
	649	113	16.3	5.01	1.79	7.8	1.48	0.44	2.47	0.43	3.33	1.02	3.76	0.61	3.79	0.74	0.32	0.40	0.20	0.41	5.78	110.81
	997	132	16.4	3.15	1.95	9.6	1.95	0.52	2.76	0.49	3.73	1.22	3.98	0.67	4.84	0.90	0.39	0.37	0.20	0.40	5.09	110.16
	1,493	162	20.7	2.06	2.45	11.6	2.28	0.56	3.96	0.59	4.71	1.56	5.40	0.92	5.94	1.19	0.36	0.22	0.23	0.41	4.41	108.20
	2,009	200	37.9	12.79	4.07	19.3	4.21	0.97	5.17	0.84	7.18	2.02	7.43	1.16	7.71	1.53	0.32	0.12	0.23	0.43	4.55	104.23
	3,005	198	33.6	1.80	4.27	20.2	3.94	1.00	5.94	0.91	7.32	2.02	7.48	1.28	8.33	1.57	0.32	0.40	0.17	0.37	4.86	99.21
	3,992	216	42.2	2.25	6.16	26.9	5.75	1.40	7.44	1.14	9.19	2.53	8.64	1.35	9.01	1.69	0.34	0.06	0.19	0.41	4.77	97.91
	5,172	181	37.7	2.79	5.56	24.8	5.06	1.06	6.04	0.98	7.59	2.02	7.04	1.14	7.71	1.29	0.33	0.06	0.16	0.41	5.12	85.30
<b>SO225-2-2</b>																						
9° 59.8'S	10 <sup>a</sup>	54	63.9	122.26	1.16	4.8	1.07	0.28	2.09	0.24	1.66	0.42	1.31	0.16	0.81	0.17	—	—	—	—	—	—
166° 12.0'W	51	56	6.9	4.03	0.93	4.4	1.05	0.26	1.17	0.20	1.75	0.40	1.31	0.15	1.00	0.14	0.34	0.67	0.11	0.46	9.19	140.27
	133	54	4.3	1.91	0.64	3.2	0.66	0.23	0.90	0.17	1.42	0.40	1.27	0.17	1.10	0.13	0.46	0.49	0.17	0.52	9.51	134.52
	240	61	5.3	1.31	0.75	3.6	0.83	0.19	1.06	0.17	1.55	0.46	1.41	0.18	1.11	0.21	0.31	0.28	0.16	0.50	6.71	133.00
	283 <sup>a</sup>	76	39.2	39.94	3.02	9.4	1.07	0.30	2.12	0.28	2.27	0.60	2.13	0.29	1.74	0.34	—	—	—	—	—	—
	382	93	13.2	4.59	1.30	7.1	1.18	0.29	1.96	0.29	2.87	0.80	3.00	0.45	3.06	0.60	0.38	1.37	0.05	0.17	6.28	127.01
	492	104	20.3	11.85	1.87	7.4	1.60	0.37	2.42	0.36	3.22	0.92	3.56	0.63	3.83	0.71	0.33	0.41	0.19	0.40	5.03	116.02
	730	118	16.3	4.82	1.71	8.1	1.56	0.45	2.46	0.43	3.35	1.04	3.90	0.64	4.36	0.82	0.31	0.74	0.17	0.34	5.00	112.99
	1,028	132	18.2	3.77	1.84	8.9	1.86	0.46	2.72	0.43	3.87	1.17	4.23	0.73	4.86	0.94	0.38	0.36	0.22	0.39	4.73	113.62
	1,525	157	23.7	6.44	2.46	10.9	2.31	0.52	3.80	0.52	4.68	1.47	5.42	0.86	6.31	1.19	0.33	0.25	0.23	0.40	4.48	112.80
	2,023	177	25.7	2.69	2.99	12.9	2.22	0.56	4.08	0.67	5.54	1.74	5.64	0.99	7.12	1.39	0.30	0.33	0.23	0.40	4.54	106.47
	2,627	189	27.6	1.43	3.06	14.4	2.76	0.79	4.22	0.70	5.94	1.78	6.38	1.04	7.08	1.38	0.33	0.13	0.23	0.40	4.05	101.26
<b>SO225-53-4</b>																						
13° 30.6'S	11	55	5.7	2.17	0.85	3.8	0.88	0.25	1.07	0.17	1.25	0.45	1.26	0.16	0.74	0.11	0.39	0.43	0.10	0.44	1.66	123.02
162° 7.6'W	50	59	5.2	1.59	0.82	4.5	0.80	0.27	1.43	0.19	1.66	0.49	1.41	0.19	1.05	0.18	0.44	0.32	0.13	0.55	7.91	120.43
	99	58	3.6	1.25	0.72	2.9	0.74	0.18	1.13	0.20	1.57	0.48	1.47	0.18	0.98	0.15	0.32	0.37	0.18	0.67	9.65	121.93
	168	57	3.8	1.36	0.67	3.2	0.77	0.20	0.94	0.14	1.40	0.37	1.32	0.17	0.85	0.13	0.35	0.38	0.15	0.56	10.38	153.51
	278	63	6.4	2.28	0.79	4.1	0.64	0.21	1.18	0.23	1.76	0.49	1.52	0.24	1.31	0.22	0.42	0.40	0.16	0.48	6.89	128.61
	396	84	9.8	1.36	1.18	5.9	1.23	0.33	1.87	0.26	2.26	0.75	2.59	0.44	2.46	0.44	0.37	0.16	0.20	0.44	5.93	112.98
	506	97	10.9	0.92	1.41	6.7	1.08	0.39	2.20	0.30	2.79	0.82	3.20	0.55	3.22	0.59	0.35	0.10	0.23	0.43	5.40	118.96
	703	115	13.2	0.95	1.55	7.1	1.40	0.38	2.20	0.36	3.35	1.08	3.65	0.64	4.25	0.72	0.36	0.08	0.26	0.43	5.09	106.53
	1,001	127	18.3	7.16	1.99	9.7	1.83	0.51	3.09	0.47	4.15	1.22	4.61	0.67	4.94	0.87	0.37	0.46	0.22	0.42	5.31	104.68
	1,499	154	22.1	4.32	2.48	11.2	2.44	0.53	3.75	0.56	4.43	1.40	5.18	0.91	5.67	1.14	0.29	0.23	0.22	0.40	4.54	110.36
	2,006	170	27.8	6.86	3.05	13.0	2.91	0.73	4.38	0.60	5.88	1.59	5.98	0.96	6.47	1.26	0.34	0.30	0.20	0.41	4.75	106.96
	3,088	187	34.1	9.43	4.39	19.4	3.50	0.92	5.12	0.81	6.16	1.82	6.50	1.05	7.44	1.39	0.35	0.32	0.17	0.36	4.66	102.46
<b>GEOTRACES BATS INTERCALIBRATION:</b>																						
<b>BATS (15 m)</b>		<b>Y</b>	<b>La</b>	<b>Ce</b>	<b>Pr</b>	<b>Nd</b>	<b>Sm</b>	<b>Eu</b>	<b>Gd</b>	<b>Tb</b>	<b>Dy</b>	<b>Ho</b>	<b>Er</b>	<b>Tm</b>	<b>Yb</b>	<b>Lu</b>						
Average		122.09	13.55	10.20	2.91	13.60	3.36	0.80	4.75	0.76	5.83	1.45	4.71	0.66	4.12	0.67						
2σ		4.59	0.47	0.48	0.24	0.83	0.46	0.14	0.34	0.08	0.49	0.17	0.23	0.06	0.27	0.07						
%2σ		3.76	3.45	4.70	8.24	6.13	13.56	16.94	7.06	10.46	8.45	11.61	4.97	9.85	6.56	10.10						
<b>BATS (2,000 m)</b>		<b>Y</b>	<b>La</b>	<b>Ce</b>	<b>Pr</b>	<b>Nd</b>	<b>Sm</b>	<b>Eu</b>	<b>Gd</b>	<b>Tb</b>	<b>Dy</b>	<b>Ho</b>	<b>Er</b>	<b>Tm</b>	<b>Yb</b>	<b>Lu</b>						
Average		127.05	21.99	3.89	3.78	16.41	3.61	0.79	4.51	0.75	5.47	1.42	4.72	0.73	4.67	0.81						
2σ		5.08	1.07	0.22	0.47	0.72	0.52	0.42	0.42	0.08	0.37	0.11	0.36	0.13	0.37	0.10						
%2σ		4.00	4.86	5.54	12.44	4.40	14.46	2.68	9.35	10.30	6.82	7.50	7.56	18.35	7.84	12.99						

<sup>a</sup> Probably contaminated data, therefore excluded from the plots and discussion of the main text.

HREE/LREE = [Tm]+[Yb]+[Lu]/[La]+[Pr]+[Nd], Ce/Ce\* = 3[Ce]/2[Nd]+[La].

Eu/Eu\*<sub>PAAS</sub> = 3[Eu]/2[Sm]+[Tb].MREE/MREE\*<sub>PAAS</sub> = 2[Gd + Tb + Dy]/[La + Pr + Nd + Tm + Yb + Lu] (after Martin et al., 2010.)

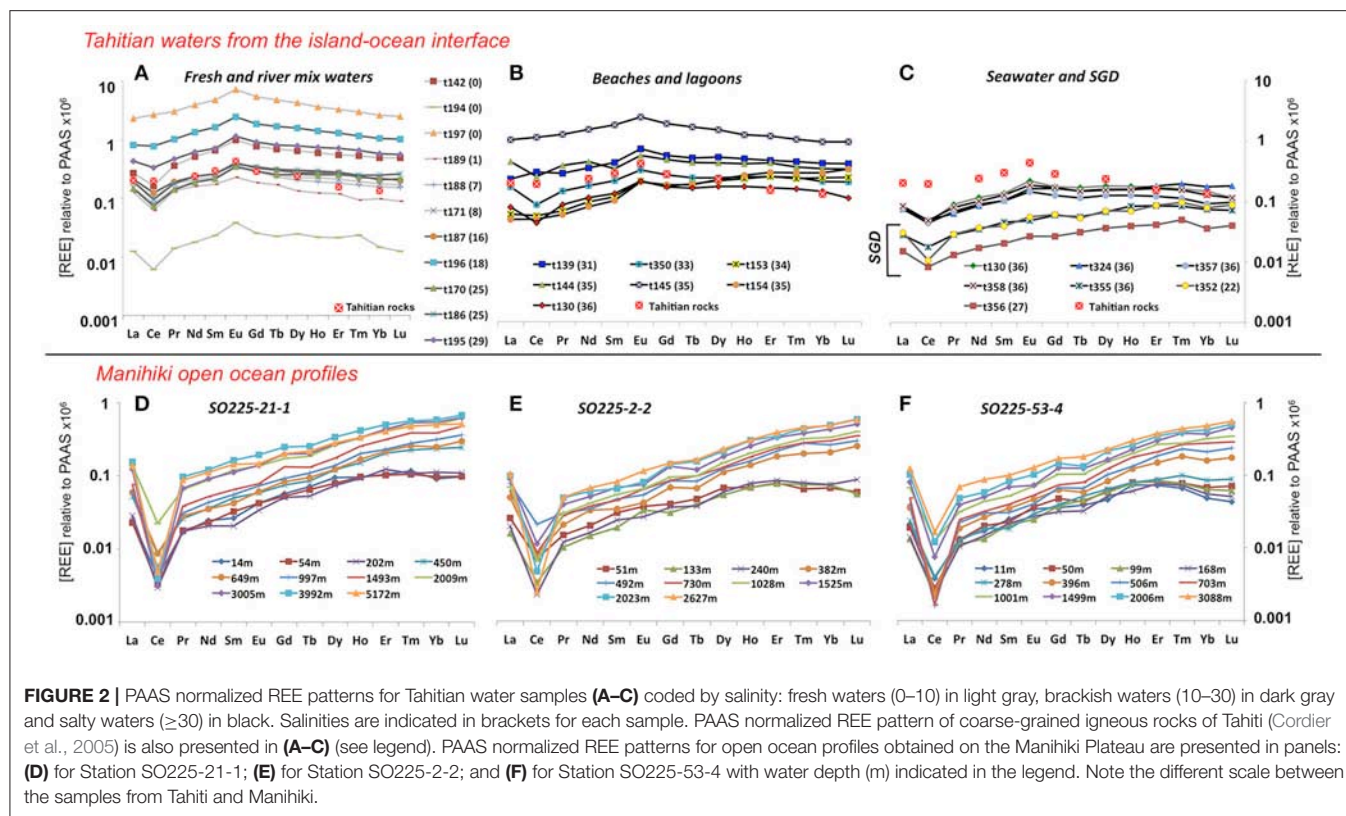


**FIGURE 2 |** PAAS normalized REE patterns for Tahitian water samples (A–C) coded by salinity: fresh waters (0–10) in light gray, brackish waters (10–30) in dark gray and salty waters ( $\geq 30$ ) in black. Salinities are indicated in brackets for each sample. PAAS normalized REE pattern of coarse-grained igneous rocks of Tahiti (Cordier et al., 2005) is also presented in (A–C) (see legend). PAAS normalized REE patterns for open ocean profiles obtained on the Manihiki Plateau are presented in panels: (D) for Station SO225-21-1; (E) for Station SO225-2-2; and (F) for Station SO225-53-4 with water depth (m) indicated in the legend. Note the different scale between the samples from Tahiti and Manihiki.

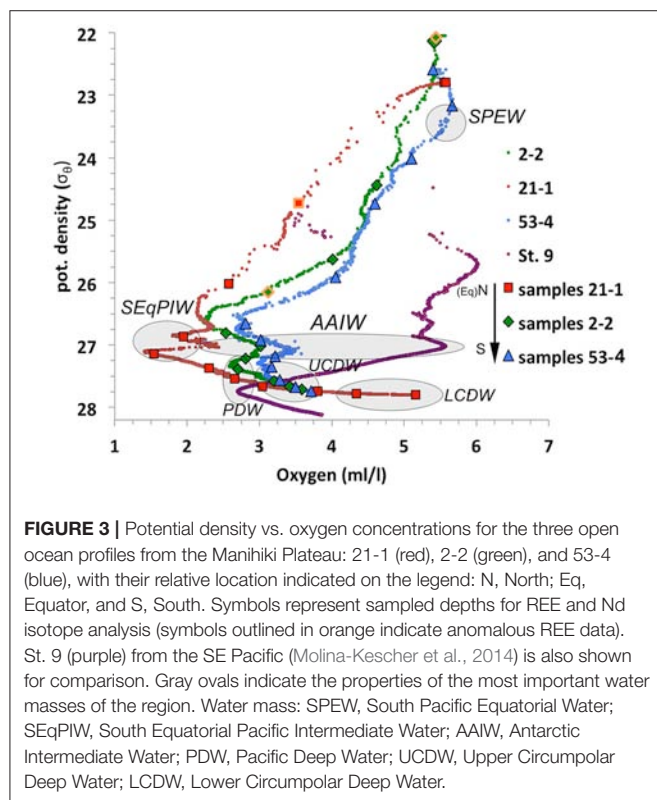


**FIGURE 3 |** Potential density vs. oxygen concentrations for the three open ocean profiles from the Manihiki Plateau: 21-1 (red), 2-2 (green), and 53-4 (blue), with their relative location indicated on the legend: N, North; Eq, Equator; S, South. Symbols represent sampled depths for REE and Nd isotope analysis (symbols outlined in orange indicate anomalous REE data). St. 9 (purple) from the SE Pacific (Molina-Kescher et al., 2014) is also shown for comparison. Gray ovals indicate the properties of the most important water masses of the region. Water mass: SPEW, South Pacific Equatorial Water; SEqPIW, South Equatorial Pacific Intermediate Water; AAIW, Antarctic Intermediate Water; PDW, Pacific Deep Water; UCDW, Upper Circumpolar Deep Water; LCDW, Lower Circumpolar Deep Water.

potential density of  $\sim 27$ , which can be distinguished by a small oxygen enrichment at all three stations that is most pronounced at the southernmost station 53-4 and weaker near the equator

(St. 21-1). This shows that AAIW in the study area is considerably diluted (maximum  $[O_2]_{AAIW} = 3.5$  ml/l for St. 53-4) compared to its source region in the Southeast Pacific ( $[O_2]_{AAIW} = 5.5$  ml/l for St. 9, Molina-Kescher et al., 2014) (Figure 3 and Figure S1). The presence and progressive northward disappearance of near surface SPEW can be also identified in Figure 3 by a reduction in oxygen concentrations at a potential density of  $\sim 23.2 \sigma_\theta$  from southernmost station 53-4 to the northernmost station 21-1.

### REE Concentrations

Both LREE (Nd) and HREE (Er) concentrations (Figures 4A,B) generally increase with depth as expected for open ocean waters (Nozaki, 2001). Equatorial station 21-1 has slightly higher Nd and Er concentrations in the uppermost 200 m water depth than stations 53-4 and 2-2 and the difference in concentration is more pronounced below 1,500 m depth. All three stations have their lowest Nd concentrations at  $\sim 100$  to  $\sim 300$  m water depth while HREE/LREE ratios (Figure 4C) reach a maximum (up to 8) at intermediate depths (400–1,500 m water depth) at all stations.

All samples of the three stations (except for the anomalous results of samples 2-2-10m, 2-2-283m, and 21-1-153m (Table 1), which will therefore not be further discussed) show typical seawater PAAS normalized patterns (Figures 2D–F) with negative Ce anomalies ranging between 0.03 and 0.34 (Figure 4E) and increasing PAAS normalized HREE enrichments with depth. The shallowest samples (above  $\sim 300$  m) of all three profiles show the highest MREE enrichments (Figure 4D) of the entire water column, with  $MREE/MREE^*_{PAAS}$  values  $[MREE/MREE^*_{PAAS} = [2 * (Gd + Tb + Dy)_{PAAS} / (La + Pr + Nd + Tm + Yb + Lu)$



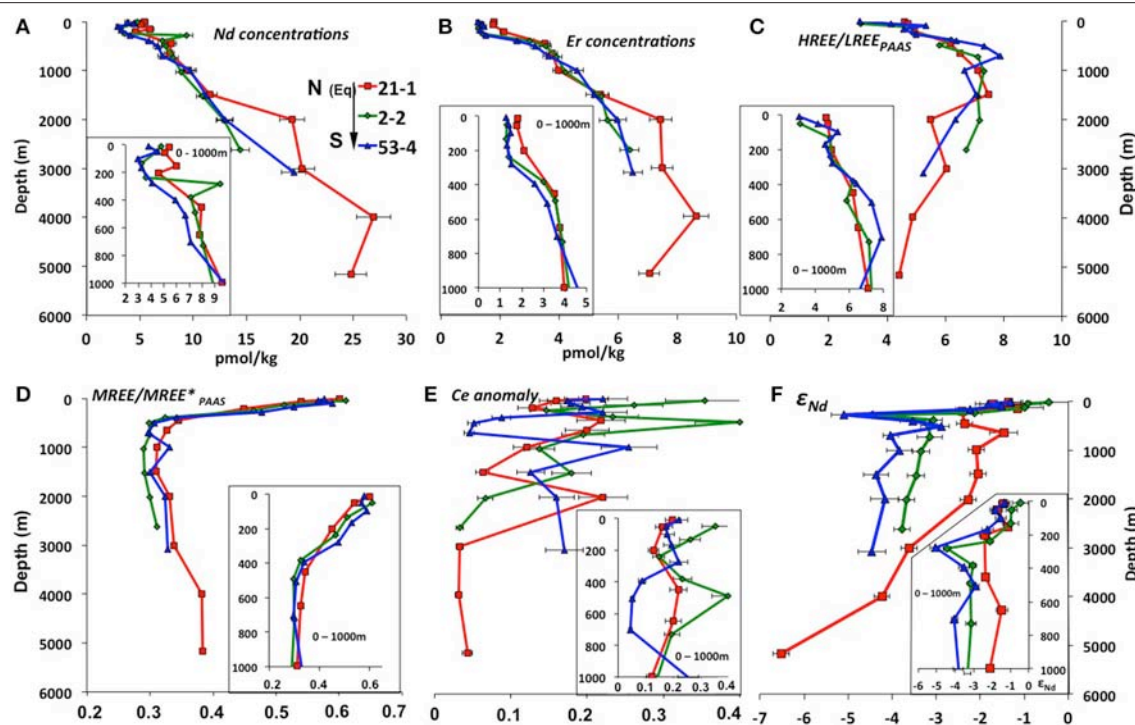


**FIGURE 4** | REE concentrations, Nd isotope compositions and other REE relationships plotted against water depth for open ocean stations 21-1 (red), 2-2 (green), and 53-4 (blue), with their relative location indicated on the legend: N, North; Eq, Equator, and S, South. Detail of the first 1,000 m water depth is shown in the bottom of each panel. **(A)** Nd concentrations (pmol/kg); **(B)** Er concentrations (pmol/kg); **(C)** HREE/LREE =  $[Tm] + [Yb] + [Lu] / [La] + [Pr] + [Nd]$ ; **(D)** PAAS normalized MREE enrichment  $[MREE/MREE^*]_{PAAS} = [2 * (Gd + Tb + Dy)_{PAAS} / (La + Pr + Nd + Tm + Yb + Lu)_{PAAS}]$ ; Martin et al. (2010)]; **(E)** PAAS normalized Ce anomalies  $(Ce/Ce^* = 2 * [Ce] / ([Pr] + [Nd]))$ ; **(F)** Nd isotope compositions. Note that samples 2-2-10m, 2-2-283m, and 21-1-153m are not presented here due to anomalous results (see section REE concentrations). The error bars are the combined 2sigma errors for the elements used (from BATS in Table 3) (in the  $Ce^*/Ce$  calculations: Ce, Pr and Nd).

$PAAS$ ]; Martin et al. (2010)] ranging from 0.5 to 0.6, whereas intermediate to deep waters show values around 0.3. Near surface samples are also characterized by a depletion of the heaviest REEs Tm, Yb and Lu, resulting in flat or even decreasing PAAS normalized patterns from Er to Lu (Figures 2D–F).

### Nd Isotope Compositions

The open ocean seawater  $\epsilon_{Nd}$  signatures at the Manihiki Plateau range from  $-0.4 \pm 0.4$  ( $2\sigma$ ) to  $-6.5 \pm 0.2$  ( $2\sigma$ ) (Figure 4F). The most radiogenic values at all three stations are consistently found (between  $-0.4$  and  $-1.8$ ) in the uppermost  $\sim 250$  m of the water column. At  $\sim 280$  m water depth, an excursion to less radiogenic values of  $-4.4 (\pm 0.2)$  and  $-5.1 (\pm 0.3)$  is observed at southern stations 2-2 and 53-4, respectively, indicating the influence of Antarctic derived Nd isotope compositions, perhaps corresponding to remains of SAMW. In the intermediate depth water column ( $\sim 650$  to  $\sim 2,000$  m), the three profiles show essentially constant  $\epsilon_{Nd}$  signatures that become progressively more radiogenic from S to N, consistent with the decreasing influence of unradiogenic (around  $-8$ , Molina-Kescher et al., 2014) Antarctic derived waters ( $\epsilon_{Nd}$  values ranging from:  $-4.2 (\pm 0.3)$  to  $-3.8 (\pm 0.3)$  for station 53-4;  $-3.7 (\pm 0.2)$  to  $-3.1 (\pm 0.3)$  for station 2-2; and  $-2.3 (\pm 0.2)$  to  $-1.5 (\pm 0.3)$  for station 21-1). The latter value (the most radiogenic apart from the

surface samples) corresponds to 649 m depth at equatorial station 21-1, which coincides with the lowest oxygen concentrations measured for all open ocean samples of this study and thus the core of SEqPIW. Stations 2-2 and 53-4 have similar  $\epsilon_{Nd}$  values of  $\sim -4$  between  $\sim 2,000$  m water depth and the bottom of the profiles at 2,627 m and 3,088 m depth, respectively. Equatorial station 21-1 reaches a depth of 5,172 m and displays a progressive decrease in  $\epsilon_{Nd}$  signatures toward the bottom with a minimum value of  $-6.5 (\pm 0.2)$  for LCDW. The Nd isotope compositions clearly reflect water mass mixing below 240 m as indicated by the high correlation coefficient ( $R^2 = 0.77$ ) between  $\epsilon_{Nd}$  signatures and oxygen concentrations (Figure S4).

## DISCUSSION

### Basaltic Influence on Tahitian Coastal Waters

Despite the warm and wet conditions favorable for the chemical weathering of the fresh basaltic minerals, the Tahitian waters have relatively low total dissolved solids due to extremely high precipitation rates (up to 8,000 mm/a), which dilutes the solute concentrations, and short groundwater residence times in the sediments ( $< 50$  a) (Hildenbrand et al., 2005) that limit the

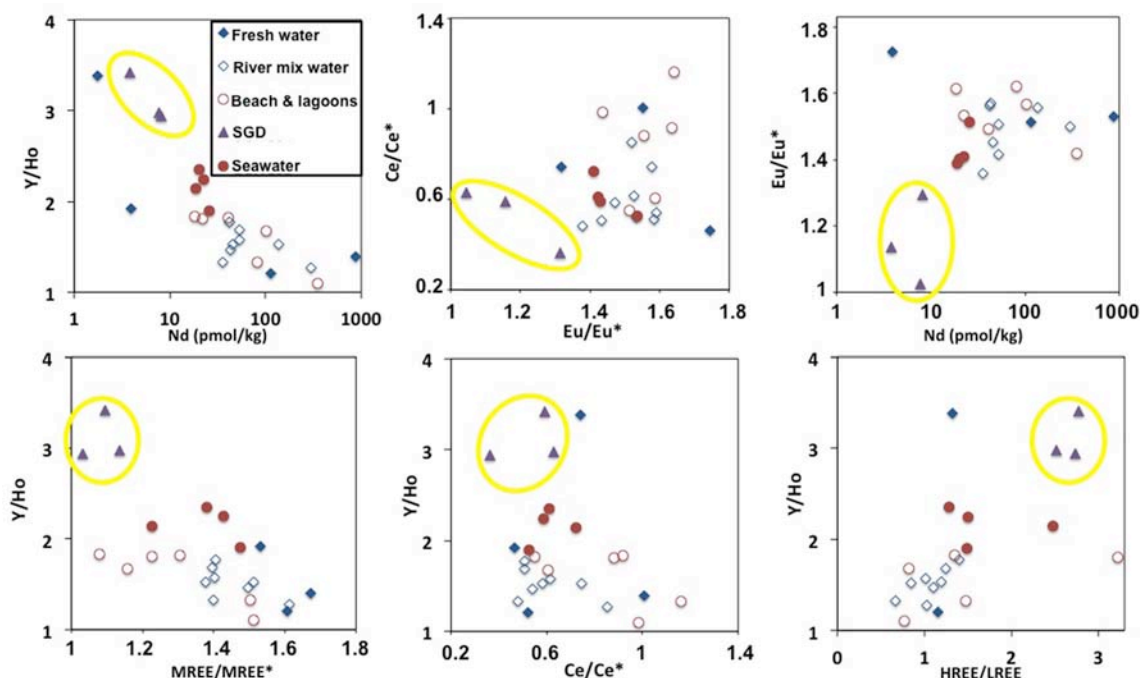


**FIGURE 5** | Selection of the most representative Tahitian “REE space plots” that combine different REE indices in order to find systematic variations of submarine groundwater discharge (SGD) samples (indicated by yellow circles) with respect to other environments (see legend). Definition of REE indices is provided in **Figure S3**.

exposure time of solids to the solutions. For comparison, relative to the size of the river catchment area, the discharge of Tahitian rivers from all parts of the island is similar to that of the biggest rivers on Earth (**Table S1**).

The large range of REE concentrations found for the Tahitian waters and the fact that there are no significant correlations between REE concentrations or pattern indices with salinity, alkalinity or dissolved silicate (section REE compositions of Tahitian waters, **Figure S2**) suggests a reversible absorption-desorption based exchange process, likely involving precipitation-dissolution of secondary minerals, where recirculating seawater via SGD (e.g., Duncan and Shaw, 2003) through the basaltic and coral reef sedimentary rocks plays an important role. This is supported by both well-developed negative Ce anomalies ( $\leq 0.5$ ) (seawater derived signal) and high Eu anomalies ( $\geq 1.5$ ) (basaltic weathering signal) found in many of the samples regardless of their origin (**Figures 2A–C**). A multitude of systematic variations in the REE patterns and concentrations (**Figure 5** and **Figure S3**) reveals the consistent offset of SGD influenced waters from the other seawater, freshwater and mixture samples. A clear example of this can be seen in the plot of Nd concentrations against Y/Ho where the SGD samples exhibit the most fractionated values (**Figure 5**). Y and Ho have very similar speciation in seawater so such a strong fractionation is likely to be the result of the preferential removal of Ho by secondary precipitates such as Fe–Mn oxides (Bau et al., 1997). Y/Ho fractionation during carbonate mineral precipitation is also well documented (e.g., Tanaka et al., 2008) and the high Y/Ho ratios of the SGD may also reflect secondary

precipitation within the reef carbonate rocks. Given the affinity of REEs for carbonate complexes in seawater (e.g., Cantrell and Byrne, 1987; Schijf et al., 2015) it should be expected that reef carbonate rocks surrounding the tropical basaltic islands play an important role in SGD recirculation process. This is the case for the Faaromai river mouth, which exhibits the highest Nd concentrations that decrease exponentially with increasing salinity ( $t_{197} < t_{196} < t_{195}$ ). This river is located on the northern coast of Tahiti where an edifice collapse caused two giant landslides (Hildenbrand et al., 2006), which most likely occurred around 870 ka, and coral reefs have not yet grown back. Extrapolation to seawater salinity of 36.2 using the exponential fit (**Figure 6**) gives a Nd concentration of 89 pmol/kg, which is the largest flux of REEs from the studied rivers. In contrast, the two other salinity gradients sampled at river mouths exhibit a more typical estuarine REE behavior with removal during initial mixing and subsequent release as salinity increases (e.g., Elderfield, 1988; Sholkovitz, 1995) producing concentrations around 40–50 pmol/kg in the saltiest samples.

The highly variable REE concentrations of freshwater and SGD observed on Tahiti make the selection of an endmember value for traditional flux calculations (e.g., Kim and Kim, 2011) beyond the feasibility of such spatially and temporally coarse sampling. What is remarkably consistent in the Tahitian data are the REE concentrations of the high salinity ( $\sim 36$ ) water samples (**Table 1**), from both lagoon and beyond the reef break “open ocean” settings (**Figure 1**). With an average Nd concentration of  $21.8 \pm 3.1$  pmol/kg (1 SD), Tahitian coastal waters have Nd concentrations at least 4 times that of South Pacific surface

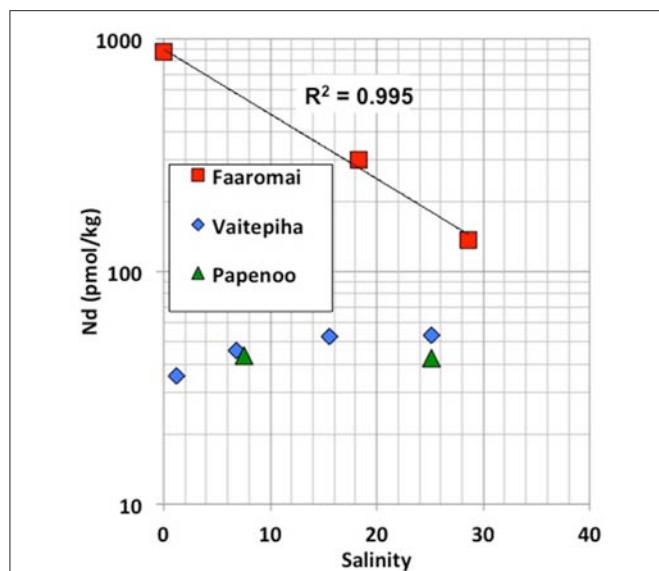


**FIGURE 6** | Salinity vs. Nd concentrations (in logarithmic scale) for the three rivers studied on Tahiti (see Legend).  $R^2$  coefficient shown for the Faaromai river.

waters ( $<5$  pmol/kg, Amakawa et al. (2013); Jeandel et al. (2013); this study). The MREE enrichment and Eu/Eu\* found in these Tahitian coastal seawaters, both  $1.4 \pm 0.1$  (1 SD), is clearly derived from the basaltic rocks present on the island (Figures 2C, 7), with a very similar REE pattern like those found on other central Pacific islands [see compilation by Grenier et al. (2013) in their Figure 12] and in groundwaters from the basaltic islands of Jeju (Korea) (Kim and Kim, 2011) and Hawai'i (Johannesson et al., 2017) (Figure 7), thus suggesting a typical REE signal for land-sourced waters supplied from Pacific volcanic islands. Estuarine REE patterns from Papua-New Guinea (Sepik and Fly rivers), although showing common characteristics (such as the Eu peak) to the basaltic island PAAS normalized distributions described above, also present some differences resembling the brackish Amazon estuarine water samples (Figure 7; Rousseau et al., 2015). This suggests that the presence of suspended particulate matter carried by relatively larger rivers (such as these found in Papua-New Guinea) exerts a considerable influence on the coastal seawater REE patterns which differ from those of small islands that lack high volumes of channeled water, like Tahiti, Jeju, or Hawaii. Johannesson et al. (2017) suggested the aridity of the Kona area (in the rain shadow of both Mauna Loa and Mauna Kea) may play a role in the lack of modification of SGD REEs upon mixing with seawater.

The similar PAAS normalized pattern observed between Tahiti, Jeju, and Hawaii (Figure 7) clearly indicates a common signature of basaltic rock REE sources in the Pacific Ocean.

### Imprint of Volcanic Islands on Surface and Subsurface Waters (0–300 m Water Depth, $<26 \sigma_\theta$ ) of the Open Central Pacific

Similar to other locations such as offshore Hawaii (Fröllje et al., 2016), the markedly radiogenic  $\epsilon_{Nd}$  signatures of shallow Pacific

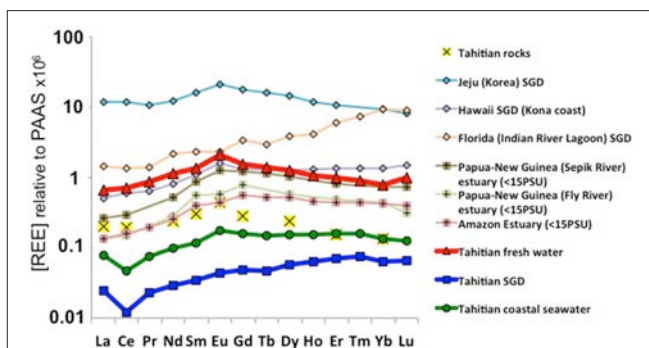


**FIGURE 7** | Averages of PAAS normalized water samples obtained on the land-ocean interphase from Tahiti (this study), Jeju Island (Korea) (Kim and Kim, 2011), Hawaii (Johannesson et al., 2017), Sepik and Fly river estuaries (Papua New Guinea) (Sholkovitz and Szymczak, 2000), Florida (Johannesson et al., 2011) and the Amazon estuary (Rousseau et al., 2015).

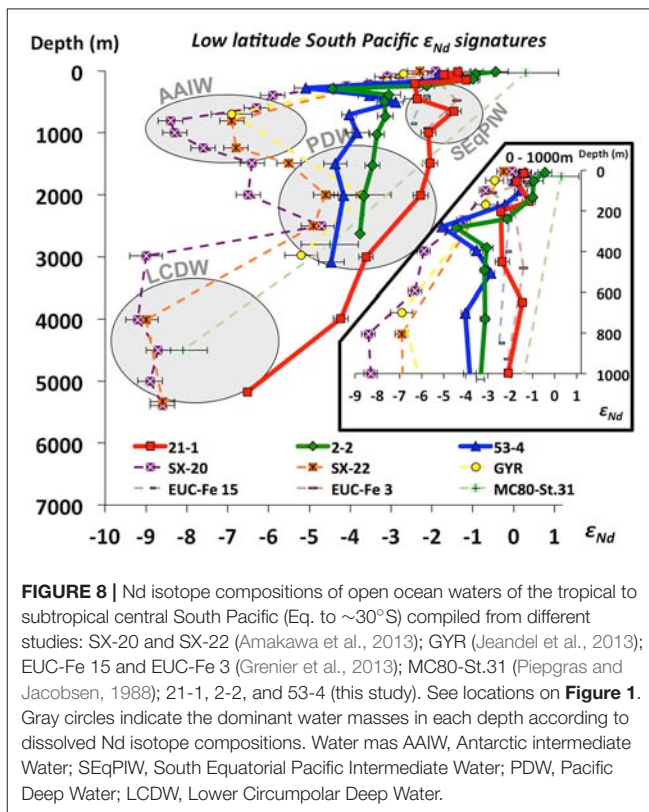


**FIGURE 8** | Nd isotope compositions of open ocean waters of the tropical to subtropical central South Pacific (Eq. to  $\sim 30^\circ$ S) compiled from different studies: SX-20 and SX-22 (Amakawa et al., 2013); GYR (Jeandel et al., 2013); EUC-Fe 15 and EUC-Fe 3 (Grenier et al., 2013); MC80-St.31 (Piepgras and Jacobsen, 1988); 21-1, 2-2, and 53-4 (this study). See locations on Figure 1. Gray circles indicate the dominant water masses in each depth according to dissolved Nd isotope compositions. Water mas AAIW, Antarctic intermediate Water; SEQPIW, South Equatorial Pacific Intermediate Water; PDW, Pacific Deep Water; LCDW, Lower Circumpolar Deep Water.

waters strongly suggest the influence of basaltic island weathering (Figure 8). This observation is consistent with previous studies (e.g., Sholkovitz et al., 1999; Lacan and Jeandel, 2001; Amakawa et al., 2004; Hongo et al., 2006; Allègre et al., 2010; Fröllje et al., 2016), which proposed island weathering as a prominent source of REE to the surface ocean, in particular taking into account the high solubility of basaltic rocks in weathering solutions and seawater (Pearce et al., 2013). However, about 2,000 km downstream from Tahiti, Manihiki surface waters have



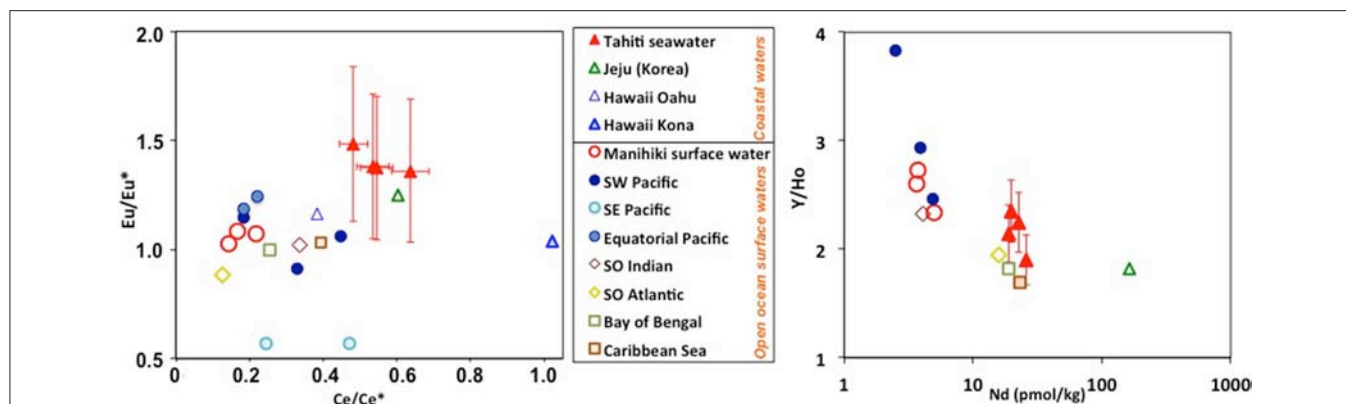


**FIGURE 9** | Comparison of different REE indices (see axes) between coastal waters from Pacific islands (Tahiti, Jeju, and Hawaii) and open ocean surface waters from the Pacific and other ocean basins. The error bars are the combined 2-sigma errors for the elements used (from BATS in **Table 3**) (in the  $\text{Eu}^*/\text{Eu}$  calculations: Sm, Eu, and Tb). Open ocean data corresponds to averages from the top 50 m water depth, except for the Atlantic Southern Ocean (top 100 m). Data from this study (Tahiti and Manihiki); (Kim and Kim, 2011) (Jeju, Korea); (Fröllje et al., 2016) (Oahu, Hawaii); (Johannesson et al., 2017) (Kona, Hawaii); (Zhang and Nozaki, 1996) (stations SA-5, SA-7, and SA-12, SW Pacific); (Grenier et al., 2013) (stations Fe1+Fe2+Fe3 and Fe13+Fe14+Fe15, Equatorial Pacific); (Nozaki and Alibo, 2003b) (stations PA-9-Bay of Bengal); (Nozaki and Alibo, 2003a) (station PA-4, Indian Southern Ocean); (Hathorne et al., 2015) (all stations, Atlantic Southern Ocean); and (Osborne et al., 2015) (all stations, Caribbean Sea).

evolved different REE patterns compared to Tahitian coastal waters (**Figure 9**). Despite transiting the South Pacific gyre, presumably one of the most particle poor regions of the oceans, REE concentrations decrease (e.g., Nd 4-fold), Ce anomalies strengthen, and Eu anomalies disappear. Interestingly, Y/Ho ratios remain elevated and perhaps even strengthen slightly between Tahiti and Manihiki, producing values similar to those found in surface waters of the SW Pacific (Zhang and Nozaki, 1996). Unfortunately, most studies, including recent works (e.g., Grenier et al., 2013; Jeandel et al., 2013; Fröllje et al., 2016; Johannesson et al., 2017), don't include Y data, therefore limiting the extent of this comparison. However, given the results here and the fact that Y/Ho fractionation most likely requires interaction with particles (e.g., Bau et al., 1997), future studies should include Y in their measurement routines. A volcanic island imprint on the open ocean surface waters cannot be unambiguously attributed but remains the most likely explanation for the radiogenic Nd isotope signatures observed. Hopefully, Nd isotope compositions of Tahitian waters will be obtained in the frame of future investigations but these will likely be very radiogenic, similar to the groundwater and surface water data from Oahu Island (Fröllje et al., 2016), clarifying the impact of basaltic island weathering on the tropical South Pacific Nd budget. To make a first order calculation of the potential Tahitian REE flux to seawater, we have chosen to assume that the consistently measured coastal seawater Nd concentrations of  $\sim 20$  pmol/kg are found only in the upper layers and close to the coastline. Future work should test this assumption with transects perpendicular to the shoreline sampling the entire water column and measurements of current velocities near the coast. With such conservative assumptions in mind, water transport in the South Equatorial Current south of  $9^\circ\text{S}$  (between  $150^\circ$  and  $160^\circ\text{W}$ ) around  $13.4 \times 10^6$  m<sup>3</sup>/s and a mean speed ( $\bar{u}$ ) of 4.9 cm/s (4234 m/d) near Tahiti (Wyrski and Kilonsky, 1984)

and a general 15 pmol/kg Nd enrichment around the entire 193 km of the Tahitian coast with respect to superficial open ocean values ( $<5$  pmol/kg, Amakawa et al. (2013); Jeandel et al. (2013); this study), requires a Nd flux of between 126 and 0.016 mol/d depending on the area used for the transport calculation (**Table 4**). The largest flux estimate is remarkably similar to the estimated SGD Nd flux of  $120 \pm 60$  mol/d from the similar sized Jeju island (Kim and Kim, 2011) but this is unlikely as it would require all waters transiting the Tahitian coastline to have open ocean Nd concentrations, a scenario which is unrealistic as waters moving along the coast would likely already have elevated Nd concentrations. The smaller estimates are similar in size to estimates of the SGD Nd flux from the Kona coast (Tahiti is approximately 1/10 the size of Hawai'i). In order to tentatively assess the effect of volcanic islands such as Tahiti in the global REE budget, we take our conservative estimates from an island of 1,045 km<sup>2</sup> and extrapolate that using the global "island volcanic rock surface area" of  $2.02 \times 10^6$  km<sup>2</sup> estimated by Allègre et al. (2010) to obtain estimates ranging from  $1.1 \times 10^4$  mol Nd year<sup>-1</sup> to  $8.87 \times 10^7$  mol Nd year<sup>-1</sup> (**Table 4**). A second way to estimate the flux is to ignore the large variability in freshwater and SGD Nd concentrations measured on Tahiti, and follow the approach of Allègre et al. (2010) for Sr, use the averaged rainfall minus evapotranspiration on the total cumulative surface area of volcanic islands globally with an average Tahitian freshwater Nd concentration (249 pmol/kg) to obtain a flux of  $3.17 \times 10^5$  mol Nd year<sup>-1</sup> (assuming 70% removal on mixing with seawater; e.g., Rousseau et al., 2015). These first order extrapolations produce a global Nd flux from volcanic island weathering that is probably at least two orders of magnitude lower than the global sediment pore water flux estimated to be  $>18 \times 10^6$  mol Nd year<sup>-1</sup> (Abbott et al., 2015). However, that estimate is also extrapolated from a single location where a reactive radiogenic phase (possibly basalt minerals) enhance fluxes (Abbott et al., 2016). If the basaltic



**TABLE 4 |** Tahitian Nd flux estimates and global extrapolation.

Scenario	Horizontal coastline $\times 10$ m	Vertical mixed layer 24 $\times 10$ m	Vertical mixed layer 24 $\times 100$ m
Velocity (cm s <sup>-1</sup> )	4.9	4.9	4.9
Area (km <sup>2</sup> )	1.93	2.40E-04	2.40E-03
Transport (m <sup>3</sup> s <sup>-1</sup> )	9.46E+04	1.18E+01	1.18E+02
Transport (m <sup>3</sup> s <sup>-1</sup> )	8.17E+09	1.02E+06	1.02E+07
Excess Nd (pmol/kg)	15	15	15
Excess Nd (pmol/m <sup>3</sup> )	15390	15390	15390
Nd flux (pmol d <sup>-1</sup> )	1.26E+14	1.56E+10	1.56E+11
Nd flux (mol d <sup>-1</sup> )	125.7	0.016	0.156
Tahiti area (km <sup>2</sup> )	1045	1045	1045
Island volcanic rock surface area <sup>a</sup>	2.02E+06	2.02E+06	2.02E+06
Tahiti relative to global volcanic islands	1.93E+03	1.93E+03	1.93E+03
Global flux (mol/day)	2.43E+05	3.02E+0.1	3.02E+0.2
Global flux (mol/year)	8.87E+07	1.0E+04	1.0E+05

Mixed layer depth from Schneider and Müller (1990).

<sup>a</sup>South equatorial current velocity near Tahiti (Wyrski and Kilonsky, 1984).

<sup>a</sup>Allègre et al. (2010).

island SGD fluxes from Jeju island are more representative, basaltic island weathering could easily fulfill the model budget requirements for the missing Nd source to the ocean (Tachikawa et al., 2003; Arsouze et al., 2009). Knowing which basaltic island fluxes are most representative will require many more studies from other basaltic islands but we have identified factors such as groundwater residence time, the presence of coral reefs or carbonate sediments and landslides spreading more of the volcanic material into contact with seawater, that should all be studied further. Although surface water REE distributions can be clearly altered by volcanic islands there may also potentially be an influence on intermediate depth water masses.

## Mixing of Southern Ocean Derived Water Masses Along the Southern Pacific

On AAIW's pathway from its source region in the SE Pacific sector of the Southern Ocean until it loses its geochemical identity in the volcanic WPWP region (Lacan and Jeandel, 2001; Grenier et al., 2013, 2014), AAIW characteristics are modified by mixing with other water masses, and by potential input/exchange from basaltic islands of the South Pacific. At the Manihiki Plateau, AAIW corresponds to a potential density of around 27  $\sigma_\theta$  between ~400 and ~1,300 m (see section "General Hydrography"), and is considerably diluted as observed in Figure 3 and Figure S1, displaying  $\epsilon_{Nd}$  signatures ranging between -3.1 and -4.0, similar to deeper PDW (Figure 4F). This indicates that the original Nd isotope composition of AAIW (-8 to -9  $\epsilon_{Nd}$ , Molina-Kescher et al., 2014) vanishes in this area, which is evident when compared to other stations south of our studied stations (Figure 8). Particularly remarkable is the comparison of stations 53-4 and SX-22 (Figure 8), which are located close to each other (see locations on Figure 1 and Figure S1) but present a marked offset of about 3 epsilon units

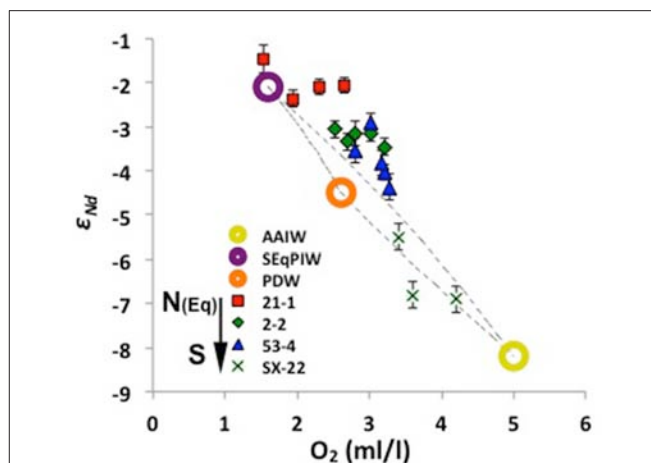
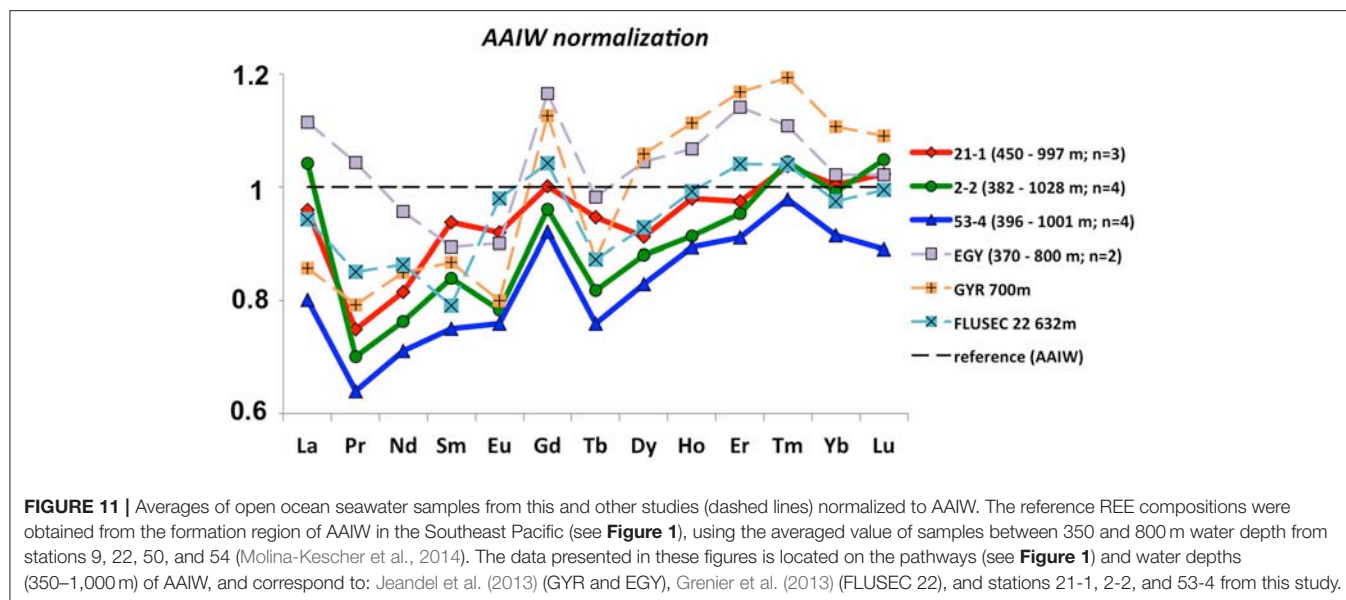


**FIGURE 10 |** Mixing arrays of oxygen concentrations vs. Nd isotope compositions between pure compositions of the most prominent intermediate to mid-depth water masses of the central S Pacific (circles, see legend). Presented are also samples above the Manihiki Plateau between ~400 and ~1,500 m water depth (red squares, green diamonds, and blue triangles), which show increasing influence of SEqPIW toward the north (see legend) whereas SX-22 samples (~800 to ~1,500 m water depth) (crosses) (Amakawa et al., 2013; Amakawa, personal communication) fall in the mixing array of PDW and AAIW. See exact locations on Figure 1 and Figure S1. The values of the endmembers are from: sample EUC-Fe3-928m (Grenier et al., 2013) for SEqPIW; sample MC80-St.31-2800m (Piepgras and Jacobsen, 1988) for PDW; and averaged value of samples between 350 and 800 m water depth from stations 9, 22, 50, and 54 (Molina-Kescher et al., 2014) for AAIW. Water mas: AAIW, Antarctic intermediate Water; SEqPIW, South Equatorial Pacific Intermediate Water; PDW, Pacific Deep Water.

in the depth range of AAIW. This change corresponds to the progressive mixing of AAIW and SEqPIW in this area (Figure 3 and Figure S1; Bostock et al., 2010), which is most evident in [O<sub>2</sub>] (Figure 10). Purer SEqPIW sampled at equatorial station 21-1 (649 m water depth) is even more radiogenic at  $\epsilon_{Nd}$  value of -1.5 (Figure 8), which is accompanied by an oxygen minimum of 1.5 ml/l, with both,  $\epsilon_{Nd}$  and [O<sub>2</sub>] changing toward more negative  $\epsilon_{Nd}$  and higher [O<sub>2</sub>] values above and below that depth. Plotting the Manihiki intermediate waters on the AAIW – SEqPIW mixing array (Figure 10) clearly reveals an offset toward more radiogenic signatures suggesting an additional Nd input/exchange along route which may derive from volcanic Society, Tuamotu and Tubuai Islands (including Tahiti). This observation supports the suggestions of Amakawa et al. (2013), who estimated a large Nd supply from these islands to AAIW of  $2.08 \pm 1.53 \times 10^5$  mol Nd year<sup>-1</sup>, within error of the estimate provided in section "Imprint of volcanic islands on surface and subsurface waters (0–300 m water depth, <26 $\sigma_\theta$ ) of the open central Pacific."

In order to determine changes in the REE composition of AAIW we normalized the available REE data along its pathway to averaged REE concentrations in the formation region and depth of this water mass. This is shown in Figure 11, which includes averaged data in the depth range (370–~1,000 m) of AAIW from the EGY and GYR stations (unfiltered samples) in the SE Pacific near the formation region of AAIW (Jeandel et al., 2013); stations 53-4 and 2-2 (this study) located downstream of the first



encounter of AAIW with volcanic islands; and FLUSEC 22 in the WPWP (Grenier et al., 2013). Station 21-1 (this study) is also shown in order to evaluate differences with respect to SEqPIW, which dominates the intermediate water at this location. In general, all samples have lower LREE concentrations compared with original AAIW, which is expected as the more readily scavenged LREEs are preferentially removed from the water column as the water masses age (e.g., Osborne et al., 2017). The fact that the source AAIW normalized REEs are  $<1$ , especially for the LREEs, clearly indicates the importance of removal by particles during transit through the gyre, despite relatively low productivity. Station GYR shows a LREE pattern more similar to Manihiki stations than the much more proximally located EGY station (**Figure 1**). However, the GYR station is located in ocean current downstream (only  $\sim 500$  km to the East) of another volcanic island, Easter Island (Rapa Nui) including three inactive volcanoes. Given the similarity between REE patterns of basaltic islands separated by such large distances in the Pacific (section “Basaltic influence on Tahitian coastal waters”), the similar REE signals of the GYR and Manihiki stations possibly originate from volcanic REE inputs into intermediate waters. Nevertheless, the interpretation of the GYR and EGY data needs to be considered with caution given that these samples were not filtered prior to analysis, which potentially explains the apparent HREE enrichment with respect to original AAIW observed at these stations. SEqPIW (station 21-1) reflects characteristics similar to neighboring stations 2-2 and 53-4, indicating similar geochemical characteristics of SEqPIW and AAIW in terms of REE concentrations.

## CONCLUSIONS

The large range of REE concentrations found for the Tahitian freshwaters analyzed suggests that a dynamic

absorption-desorption process, likely involving precipitation-dissolution of secondary minerals, controls the release of REEs to freshwaters and the lack of correlations between the variation of REE concentrations or pattern indices with salinity, alkalinity or dissolved silicate in the brackish Tahitian samples suggests a variable mixture between freshwaters and seawater caused by SGD. The PAAS normalized REE pattern of Tahitian coastal waters is characterized by a MREE enrichment with an Eu peak, which is almost identical to that observed in groundwater and coastal waters of other volcanic islands of the Pacific, such as Jeju (Korea) (Kim and Kim, 2011) and Hawaii (Fröllje et al., 2016; Johannesson et al., 2017). These patterns are also in accordance with the REE compositions of Tahitian rocks (Cordier et al., 2005) and central Pacific sediments and rocks (Grenier et al., 2013), providing strong evidence for the important role of weathered volcanic island basalts in the Pacific REE budget, although with the currently available data estimates of the volcanic island REE flux range over 4 orders of magnitude. However, these basaltic weathering REE characteristics (with the possible exception of elevated Y/Ho ratios) are lost in surface and subsurface water masses such as SPEW, which exhibit highly radiogenic Nd isotope compositions in the area of the Manihiki Plateau. At intermediate water depths, AAIW loses its characteristic unradiogenic signature ( $-6$  to  $-9$ ) in the area of the Manihiki plateau, where it mixes with oxygen depleted SEqPIW, which show more radiogenic signatures ( $\epsilon_{Nd} = -1.5$ ). An offset of the observed data from the mixing array of AAIW and SEqPIW to more radiogenic Nd isotope compositions documents an additional Nd input/exchange along AAIW's pathway, presumably originating from volcanic particles of the Society, Tuamotu and Tubuai Islands (including Tahiti), thus suggesting the Nd isotope composition of AAIW may be elevated by volcanic islands in this region of the Pacific Ocean.

## AUTHOR CONTRIBUTIONS

EH and MK collected the Tahiti samples; AO and MB conducted the shipboard sampling; EH, AO, and MB carried out the sample preparation and analyses; MF and KP supervised the project. EH and MM-K developed the theoretical framework. MM-K wrote the manuscript and designed the figures with subsequent contributions from all co-authors.

## ACKNOWLEDGMENTS

The RV Sonne Cruise SO225 was funded by the German Ministry of Education and Research (BMBF, Bundesministerium für Bildung und Forschung) as part of Manihiki II (03G0225B), a joint project of the GEOMAR Helmholtz Centre for Ocean Research Kiel and the Alfred Wegener Institute Helmholtz Centre for Polar and Marine Research (AWI). AO was funded by DFG grants FR1198/8-1 and OS499/2-1; MK and KP were funded by DFG grant PA2411/1-1. We thank Jan Hoffmann for collecting and measuring Tahitian samples of the 2009 campaign. We appreciate the editorial handling by Prof. Sunil Singh and the constructive comments of Dr. Hiroshi Amakawa and Dr. Vineet Goswami that improved the quality of the manuscript.

## SUPPLEMENTARY MATERIAL

The Supplementary Material for this article can be found online at: <https://www.frontiersin.org/articles/10.3389/fmars.2018.00050/full#supplementary-material>

**Figure S1 | (a)** Oxygen concentrations (ml/l) and salinity at 50 m water depth for the South Pacific. HSEA stands for High Surface Evaporation Area, characterized

by high salinities and high oxygen concentrations, which is the formation region of South Pacific Equatorial Water (SPEW), a subsurface water mass that flows west toward the Western Equatorial Pacific. **(b)** Oxygen concentrations (ml/l) and salinity at 1,000 m water depth of the South Pacific, corresponding to the domains of Antarctic Intermediate Water (AAIW), characterized by high oxygen and low salinity contents; South Equatorial Pacific Intermediate Water (SEQPIW), characterized by intermediate oxygen and high salinity contents; and North Equatorial Pacific Intermediate Water (NEQPIW), characterized by low oxygen and high salinity contents.

**Figure S2 |** Cross-plots of Nd concentration, Cerium anomaly ( $Ce/Ce^* = 2*[Ce]/([La] + [Pr])$ ), Europium anomaly ( $Eu/Eu^* = 3*[Eu]/2*[Sm] + [Tb]$ ), heavy vs. light REE enrichment ( $HREE/LREE = ([Tm] + [Yb] + [Lu])_{PAAS} / ([La] + [Pr] + [Nd])_{PAAS}$ ) and middle REE enrichment ( $MREE/MREE^*_{PAAS} = [2 * (Gd + Tb + Dy)]_{PAAS} / ([La + Pr + Nd + Tm + Yb + Lu]_{PAAS})$ ; Martin et al. (2010)) vs. salinity, dissolved silicon and alkalinity with  $R^2$  correlations. PAAS normalized REE data was used.

**Figure S3 |** "REE space plots" for Tahitian samples show all possible paired combinations of different REE indices in order to find systematic variations of samples from different environments (see legend). A selection of the most representative ones is provided in **Figure 6**. REE indices are as follows: heavy vs. light REE enrichment ( $HREE/LREE_{PAAS} = ([Tm] + [Yb] + [Lu])_{PAAS} / ([La] + [Pr] + [Nd])_{PAAS}$ ); middle REE enrichment ( $MREE/MREE^*_{PAAS} = [2 * (Gd + Tb + Dy)]_{PAAS} / ([La + Pr + Nd + Tm + Yb + Lu]_{PAAS})$ ; Martin et al. (2010)); Cerium anomaly ( $Ce/Ce^*_{PAAS} = 2*[Ce]/([La] + [Pr])$ ); Europium anomaly ( $Eu/Eu^*_{PAAS} = 3*[Eu]/2*[Sm] + [Tb]$ ); Erbium vs. lutetium ( $Er/Lu_{PAAS}$ ); Yttrium vs. holmium ( $Y/Ho_{PAAS}$ ) and neodymium (Nd) concentrations expressed in pmol/kg.

**Figure S4 |** Oxygen concentrations (ml/l) vs. Nd isotope compositions ( $\epsilon_{Nd}$ ) for the open ocean samples of this study (see legend). Data with yellow rim correspond to samples in the top 240 m of the water column, which were not used for the calculation of the  $R^2$  correlation presented in the figure. Nd isotope compositions below 240 m water depth present a clear correlation with oxygen concentrations, indicating a clear conservative behavior of Nd isotope compositions in terms of water mass mixing in the intermediate to deep water column.

**Table S1 |** Nine of the most voluminous rivers on Earth compared to the three largest rivers on Tahiti (Laffourge, 1993; Gupta, 2007).

## REFERENCES

- Abbott, A. N., Haley, B. A., and McManus, J. (2016). The impact of sedimentary coatings on the diagenetic Nd flux. *Earth Planet. Sci. Lett.* 449, 217–272. doi: 10.1016/j.epsl.2016.06.001
- Abbott, A. N., Haley, B. A., McManus, J., and Reimers, C. E. (2015). The sedimentary flux of dissolved rare earth elements to the ocean. *Geochim. Cosmochim. Acta*, 154, 186–200. doi: 10.1016/j.gca.2015.01.010
- Allègre, C. J., Louvat, P., Gaillardet, J., Meynadier, L., Rad, S., and Capmas, F. (2010). The fundamental role of island arc weathering in the oceanic Sr budget. *Earth Planet. Sci. Lett.* 292, 51–56. doi: 10.1016/j.epsl.2010.01.019
- Amakawa, H., Nozaki, Y., Alibo, D. S., Zhang, J., Fukukawa, K., and Nagai, H. (2004). Neodymium isotopic variations in Northwest Pacific waters. *Geochim. Cosmochim. Acta*, 68, 715–727. doi: 10.1016/S0016-7037(03)00501-5
- Amakawa, H., Tazoe, H., Obata, H., Gamo, T., Sano, Y., and Chuan-Chou, S. (2013). Neodymium isotopic composition and concentration in the Southwest Pacific Ocean. *Geochem. J.* 47, 409–422. doi: 10.2343/geochemj.2.0260
- Aries, S., Valladon, M., Plové, M., and Dupré, B. (2000). A routine method for oxide and hydroxide interference corrections in ICP-MS chemical analysis of environmental and geological samples. *Geostandards Newslett.* 24, 19–31. doi: 10.1111/j.1751-908X.2000.tb00583.x
- Arsouze, T., Dutay, J. C., Lacan, F., and Jeandel, C. (2009). Reconstructing the Nd oceanic cycle using a coupled dynamical–biogeochemical model. *Biogeosciences* 6, 2829–2846. doi: 10.5194/bg-6-2829-2009
- Basak, C., Pahnke, K., Frank, M., Lamy, F., and Gersonde, R. (2015). Neodymium isotopic characterization of Ross Sea Bottom Water and its advection through the southern South Pacific. *Earth Planet. Sci. Lett.* 419, 211–221. doi: 10.1016/j.epsl.2015.03.011
- Bau, M., and Dulski, P. (1996). Anthropogenic origin of positive gadolinium anomalies in river waters. *Earth Planet. Sci. Lett.* 143, 245–255. doi: 10.1016/0012-821X(96)00127-6
- Bau, M., Möller, P., and Dulski, P. (1997). Yttrium and lanthanides in eastern Mediterranean seawater and their fractionation during redox-cycling. *Mar. Chem.* 56, 123–131. doi: 10.1016/S0304-4203(96)00091-6
- Behrens, M. K., Pahnke, K., Schnetger, B., and Brumsack, H.-J. (2018). Sources and processes affecting the distribution of dissolved Nd isotopes and concentrations in the West Pacific. *Geochim. Cosmochim. Acta* 222, 508–534. doi: 10.1016/j.gca.2017.11.008
- Bertram, C. J., and Elderfield, H. (1993). The geochemical balance of the rare earth elements and Nd isotopes in the oceans. *Geochim. Cosmochim. Acta*, 57, 1957–1986. doi: 10.1016/0016-7037(93)90087-D
- Bostock, H. C., Opdyke, B. N., and Williams, M. J. M. (2010). Characterising the intermediate depth waters of the Pacific Ocean using  $^{13}C$  and other geochemical tracers. *Deep Sea Res. I* 57, 847–859. doi: 10.1016/j.dsr.2010.04.005
- Burnett, W. C., Bokuniewicz, H., Huettel, M., Moore, W. S., and Taniguchi, M. (2003). Groundwater and pore water inputs to the coastal zone. *Biogeochemistry* 66, 3–33. doi: 10.1023/B:BIOG.0000006066.21240.53
- Byrne, R. H., and Kim, K.-H. (1990). Rare earth element scavenging in seawater. *Geochim. Cosmochim. Acta* 54, 2645–2656.
- Byrne, R. H., and Sholkovitz, E. R. (1996). "Marine chemistry and geochemistry of the lanthanides," in *Handbook on the Physics and Chemistry of Rare Earths*, Vol. 23, eds. K. A. Gschneidner Jr and L. Eyring (North Holland: Elsevier), 498–593.
- Callahan, J. E. (1972). The structure and circulation of deep water in the Antarctic. *Deep Sea Res.* 19, 563–575.



- Cantrell, K. J., and Byrne, R. H. (1987). Rare earth element complexation by carbonate and oxalate ions. *Geochim. Cosmochim. Acta* 51, 597–605. doi: 10.1016/0016-7037(87)90072-X
- Chen, T.-Y., Rempfer, J., Frank, M., Stumpf, R., and Molina-Kescher, M. (2013). Upper ocean vertical supply: a neglected primary factor controlling the distribution of neodymium concentrations of open ocean surface waters? *J. Geophys. Res. Oceans* 118, 3887–3894. doi: 10.1002/jgrc.20288
- Cordier, C., Clément, J.-P., Caroff, M., Hémond, C., Blais, S., Cotton, J., et al. (2005). Petrogenesis of Coarse-grained Intrusives from Tahiti Nui and Raiatea (Society Islands, French Polynesia). *J. Petrol.* 46, 2281–2312. doi: 10.1093/petrology/egi055
- Du, J., Haley, B. A., and Mix, A. C. (2016). Neodymium isotopes in authigenic phases, bottom waters and detrital sediments in the Gulf of Alaska and their implications for paleo-circulation reconstruction. *Geochim. Cosmochim. Acta* 193, 14–35. doi: 10.1016/j.gca.2016.08.005
- Duncan, T., and Shaw, T. (2003). The mobility of rare earth elements and redox sensitive elements in the groundwater/seawater mixing zone of a shallow coastal aquifer. *Aquat. Geochem.* 9, 233–255. doi: 10.1023/B:AQUA.0000022956.20338.26
- Elderfield, H. (1988). The oceanic chemistry of the rare-earth elements. *Philos. Trans. Roy. Soc. Lond. A* 325, 105–126. doi: 10.1098/rsta.1988.0046
- Elderfield, H., and Greaves, M. J. (1982). The rare earth elements in seawater. *Nature* 296, 214–219
- Elderfield, H., and Sholkovitz, E. R. (1987). Rare earth elements in the pore waters of reducing nearshore sediments. *Earth Planet. Sci. Lett.* 82, 280–288
- Frank, M. (2002). Radiogenic isotopes: tracers of past ocean circulation and erosional input. *Rev. Geophys.* 40:1001, doi: 10.1029/2000RG000094
- Fröllje, H., Pahnke, K., Schnetger, B., Brumsack, H.-J., Dulai, H., and Fitzsimmons, J. N. (2016). Hawaiian imprint on dissolved Nd and Ra isotopes and rare earth elements in the central North Pacific: local survey and seasonal variability. *Geochim. Cosmochim. Acta* 189, 110–131. doi: 10.1016/j.gca.2016.06.001
- Goldstein, S. J., and Jacobsen, S. B. (1987). The Nd and Sr isotopic systematics of river-water dissolved material: implications for the sources and Nd and Sr in seawater. *Chem. Geol.* 66, 245–272.
- Goldstein, S. L., and Hemming, S. R. (2003). “Long-lived isotopic tracers in oceanography, paleoceanography and ice sheet dynamics,” in *The Oceans and Marine Geochemistry*, ed H. Elderfield (Oxford: Elsevier-Pergamon), 453–489.
- Grasse, P., Bosse, L., Hathorne, E. C., Böning, P., Pahnke, K., and Frank, M. (2017). Short-term variability of dissolved rare earth elements and neodymium isotopes in the entire water column of the Panama Basin. *Earth Planet. Sci. Lett.* 475, 242–253. doi: 10.1016/j.epsl.2017.07.022
- Grasse, P., Stichel, T., Stumpf, R., Stramma, L., and Frank, M. (2012). The distribution of neodymium isotopes and concentrations in the Eastern Equatorial Pacific: water mass advection versus particle exchange. *Earth Planet. Sci. Lett.* 353–354, 198–207. doi: 10.1016/j.epsl.2012.07.044
- Grenier, M., Jeandel, C., and Cravatte, S. (2014). From the subtropics to the equator in the Southwest Pacific: continental material fluxes quantified using neodymium data along modelled thermocline water pathways. *J. Geophys. Res. Oceans* 119, 3948–3966. doi: 10.1002/2013JC009670
- Grenier, M., Jeandel, C., Lacan, F., Vance, D., Venchiarutti, C., Cros, A., et al. (2013). From the subtropics to the central equatorial Pacific Ocean: neodymium isotopic composition and rare earth element concentration variations. *J. Geophys. Res. Oceans* 118, 592–618. doi: 10.1029/2012JC008239
- Gupta, A. (2007). *Large rivers: geomorphology and management*. John Wiley and Sons.
- Hannigan, R. E., and Sholkovitz, E. R. (2001). The development of middle rare earth element enrichments in freshwaters: weathering of phosphate minerals. *Chem. Geol.* 175, 495–508. doi: 10.1016/S0009-2541(00)00355-7
- Hartin, C. A. A., Fine, R., Sloyan, B. M., Talley, L. D., Chereskin, T. K., and Happell, J. (2011). Formation rates of Subantarctic mode water and Antarctic intermediate water within the South Pacific. *Deep Sea Res. I* 58, 524–534. doi: 10.1016/j.dsr.2011.02.010
- Hathorne, E. C., Haley, B., Stichel, T., Grasse, P., Zieringer, M., and Frank, M. (2012). Online preconcentration ICP-MS analysis of rare earth elements in seawater. *Geochem. Geophys. Geosy.* 13:Q01020. doi: 10.1029/2011GC003907
- Hathorne, E. C., Stichel, T., Brück, B., and Frank, M. (2015). Rare earth element distribution in the Atlantic sector of the Southern Ocean: the balance between particle scavenging and vertical supply. *Marine Chem.* 177, 157–171. doi: 10.1016/j.marchem.2015.03.011
- Hildenbrand, A., Gillot, P.-Y., and Bonneville, A. (2006). Offshore evidence for a huge landslide of the northern flank of Tahiti-Nui (French Polynesia). *Geochem. Geophys. Geosys.* 7:Q03006. doi: 10.1029/2005GC001003
- Hildenbrand, A., Marlin, C., Conroy, A., Gillot, P.-Y., Filly, A., and Massault, M. (2005). Isotopic approach of rainfall and groundwater circulation in the volcanic structure of Tahiti-Nui (French Polynesia). *J. Hydrol.* 302, 87–208. doi: 10.1016/j.jhydrol.2004.07.006
- Hongo, Y., Obata, H., Alibo, D. S., and Nozaki, Y. (2006). Spatial variations of rare earth elements in North Pacific surface water. *J. Oceanogr.* 62, 441–455. doi: 10.1007/s10872-006-0067-1
- Howe, J. N. W., Piotrowski, A. M., Noble, T. L., Mulitza, S., Chiessi, C. M., and Bayon, G. (2016). North Atlantic Deep Water Production during the Last Glacial Maximum. *Nat. Commun.* 7:11765. doi: 10.1038/ncomms11765
- Hu, D., Wu, L., Cai, W., Gupta, A. S., Ganachaud, A., Qiu, B., et al. (2015). Pacific western boundary currents and their roles in climate. *Nature* 522, 299–308. doi: 10.1038/nature14504
- Hu, R., Noble, T. L., Piotrowski, A. M., McCave, I. N., Bostock, H. C., and Neil, H. L. (2016). Neodymium isotopic evidence for linked changes in Southeast Atlantic and Southwest Pacific circulation over the last 200 kyr. *Earth Planet. Sci. Lett.* 455, 106–114. doi: 10.1016/j.epsl.2016.09.027
- Jacobsen, S. B., and Wasserburg, G. J. (1980). Sm-Nd isotopic composition of chondrites. *Earth Planet. Sci. Lett.* 50, 139–155.
- Jeandel, C., and Oelkers, E. H. (2015). The influence of terrigenous particulate material dissolution on ocean chemistry and global element cycles. *Chem. Geol.* 395, 50–66. doi: 10.1016/j.chemgeo.2014.12.001
- Jeandel, C., Delattre, H., Grenier, M., Pradoux, C., and Lacan, F. (2013). Rare earth element concentrations and Nd isotopes in the Southeast Pacific Ocean. *Geochem. Geophys. Geosyst.* 14, 328–341. doi: 10.1029/2012GC004309
- Jeandel, C., Thouvenot, D., and Fieue, M. (1998). Concentrations and isotopic compositions of neodymium in the eastern Indian Ocean and Indonesian straits. *Geochim. Cosmochim. Acta* 62, 2597–2607.
- Johannesson, K. H., and Burdige, D. J. (2007). Balancing the global oceanic neodymium budget: evaluating the role of groundwater. *Earth Planet. Sci. Lett.* 253, 129–142. doi: 10.1016/j.epsl.2006.10.021
- Johannesson, K. H., Chevis, D. A., Burdige, D. J., Cable, J. E., Martin, J. B., and Roy, M. (2011). Submarine groundwater discharge is an important net source of light and middle REEs to coastal waters of the Indian River Lagoon, Florida, USA. *Geochim. Cosmochim. Acta* 75, 825–843. doi: 10.1016/j.gca.2010.11.005
- Johannesson, K. H., Palmore, C. D., Fackrell, J., Prouty, N. G., Swarzenski, P. W., Chevis, D. A., et al. (2017). Rare earth element behavior during groundwater-seawater mixing along the Kona Coast of Hawaii. *Geochim. Cosmochim. Acta* 198, 229–258. doi: 10.1016/j.gca.2016.11.009
- Kawabe, M., and Fujio, S. (2010). Pacific Ocean circulation based on observation. *J. Oceanogr.* 66, 389–403. doi: 10.1007/s10872-010-0034-8
- Kim, I., and Kim, G. (2011). Large fluxes of rare earth elements through submarine groundwater discharge (SGD) from a volcanic island, Jeju, Korea. *Marine Chem.* 127, 12–19. doi: 10.1016/j.marchem.2011.07.006
- Kwon, E. Y., Kim, G., Primeau, F., Moore, W. S., Cho, H.-M., DeVries, T., et al. (2014). Global estimate of submarine groundwater discharge based on an observationally constrained radium isotope model. *Geophys. Res. Lett.* 41, 8438–8444. doi: 10.1002/2014GL061574
- Lacan, F., and Jeandel, C. (2001). Tracing Papua New Guinea imprint on the central Equatorial Pacific Ocean using neodymium isotopic compositions and Rare Earth Element patterns. *Earth Planet. Sci. Lett.* 186, 497–512. doi: 10.1016/S0012-821X(01)00263-1
- Lacan, F., and Jeandel, C. (2005). Neodymium isotopes as a new tool for quantifying exchange fluxes at the continent-ocean interface. *Earth Planet. Sci. Lett.* 232, 245–257. doi: 10.1016/j.epsl.2005.01.004
- Laffourge, A. (1993). “L’hydrologie,” in *Atlas de la Polynésie Française*, ed Orstom (Paris: Edition de l’ORSTOM), 250.
- Martin, E. E., Blair, S. W., Kamenov, G. D., Scher, H. D., Bourbon, E., Basak, C., et al. (2010). Extraction of Nd isotopes from bulk deep sea sediments for paleoceanographic studies on Cenozoic time scales. *Chem. Geol.* 269, 414–431. doi: 10.1016/j.chemgeo.2009.10.016
- Merschel, G., Bau, M., and Dantas, E. L. (2017). Contrasting impact of organic and inorganic nanoparticles and colloids on the behavior of particle-reactive



- elements in tropical estuaries: an experimental study. *Geochim. Cosmochim. Acta* 197, 1–13. doi: 10.1016/j.gca.2016.09.041
- Moffett, J. M. (1990). Microbially mediated cerium oxidation in sea water. *Nature* 345, 421–423. doi: 10.1038/345421a0
- Molina-Kescher, M., Frank, M., and Hathorne, E. (2014). South Pacific dissolved Nd isotope compositions and rare earth element distributions: water mass mixing versus biogeochemical cycling. *Geochim. Cosmochim. Acta* 127, 171–189. doi: 10.1016/j.gca.2013.11.038
- Molina-Kescher, M., Frank, M., Tapia, R., Ronge, T. A., Nürnberg, D., and Tiedemann, R. (2016). Reduced admixture of North Atlantic Deep Water to the deep central South Pacific during the last two glacial periods. *Paleoceanography* 31, 651–668. doi: 10.1002/2015PA002863
- Moore, W. S. (1996). Large groundwater inputs to coastal waters revealed by  $^{226}\text{Ra}$  enrichments. *Nature* 380, 612–614.
- Moore, W. S. (2003). Sources and fluxes of submarine groundwater discharge delineated by radium isotopes. *Biogeochemistry* 66, 75–93. doi: 10.1023/B:BIOG.0000006065.77764.a0
- Moore, W. S., Sarmiento, J. L., and Key, R. M. (2008). Submarine groundwater discharge revealed by  $^{228}\text{Ra}$  distribution in the upper Atlantic Ocean. *Nat. Geosci.* 1, 309–311. doi: 10.1038/ngeo183
- Nozaki, Y. (2001). “Rare earth elements and their isotopes in the ocean,” in *Encyclopedia of Ocean Sciences*, ed H. S. John (Oxford: Academic Press), 2354–2366.
- Nozaki, Y., and Alibo, D. S. (2003a). Dissolved rare earth elements in the Southern Ocean, southwest of Australia: unique patterns compared to the South Atlantic data. *Geochem. J.* 37, 47–62. doi: 10.2343/geochemj.37.47
- Nozaki, Y., and Alibo, D. S. (2003b). Importance of vertical geochemical processes in controlling the oceanic profiles of dissolved rare earth elements inferred from the study in the northeastern Indian Ocean. *Earth Planet. Sci. Lett.* 205, 155–172. doi: 10.1016/S0012-821X(02)01027-0
- Olmez, I., Sholkovitz, E. R., Hermann, D., and Eganhouse, R. P. (1991). Rare-earth elements in sediments off Southern California — a new anthropogenic indicator. *Environ. Sci. Technol.* 25, 310–316. doi: 10.1021/es00014a015
- O’Nions, K., Hamilton, P. J., and Evensen, N. M. (1977). Variations in  $^{143}\text{Nd}/^{144}\text{Nd}$  and  $^{87}\text{Sr}/^{86}\text{Sr}$  ratios in oceanic basalts. *Earth Planet. Sci. Lett.* 34, 13–22.
- Osborne, A. H., Haley, B. A., Hathorne, E. C., Plancherel, Y., and Frank, M. (2015). Rare earth element distribution in Caribbean seawater: continental inputs versus lateral transport of distinct REE compositions in subsurface water masses. *Marine Chem.* 177, 172–183. doi: 10.1016/j.marchem.2015.03.013
- Osborne, A. H., Haley, B., Hathorne, E. C., Flögel, S., and Frank, M. (2014). Neodymium isotopes and concentrations in Caribbean seawater: tracing water mass mixing and continental input in a semi-enclosed ocean basin. *Earth Planet. Sci. Lett.* 406, 174–186. doi: 10.1016/j.epsl.2014.09.011
- Osborne, A. H., Hathorne, E. C., Schijf, J., Plancherel, Y., Böning, P., and Frank, M. (2017). The potential of sedimentary foraminiferal rare earth element patterns to trace water masses in the past. *Geochem. Geophys. Geosystems* 18, 1550–1568. doi: 10.1002/2016GC006782
- Pahnke, K., Goldstein, S. L., and Hemming, S. R. (2008). Abrupt changes in Antarctic Inter-mediate Water circulation over the past 25,000 years. *Nat. Geosci.* 1, 870–874. doi: 10.1038/ngeo360
- Pahnke, K., van de Fliedert, T., Jones, K. M., Lambelet, M., Hemming, S. R., and Goldstein, S. L. (2012). GEOTRACES intercalibration of neodymium isotopes and rare earth element concentrations in seawater and suspended particles. Part 2: Systematic tests and baseline profiles. *Limnol. Oceanogr. Methods* 10, 252–269. doi: 10.4319/lom.2012.10.252
- Pearce, C. R., Jones, M. T., Oelkers, E. H., Pradoux, C., and Jeandel, C. (2013). The effect of particulate dissolution on the neodymium (Nd) isotope and rare earth element (REE) composition of seawater. *Earth Planet. Sci. Lett.* 369–370, 138–147. doi: 10.1016/j.epsl.2013.03.023
- Piepgas, D. J., and Wasserburg, G. J. (1982). Isotopic composition of neodymium in waters from the Drake Passage. *Science* 217, 207–214.
- Piepgas, D. J., and Wasserburg, G. J. (1987). Rare earth element transport in the western North Atlantic inferred from Nd isotopic observations. *Geochim. Cosmochim. Acta* 51, 1257–1271. doi: 10.1016/0016-7037(87)90217-1
- Piepgas, D. J., and Jacobsen, S. B. (1988). The isotopic composition of neodymium in the North Pacific. *Geochim. Cosmochim. Acta* 52, 1373–1381. doi: 10.1016/0016-7037(88)90208-6
- Qu, T., and Lindstrom, E. J. (2002). A climatological interpretation of the circulation in the Western South Pacific. *J. Phys. Oceanogr.* 32, 2492–2508. doi: 10.1175/1520-0485-32.9.2492
- Reid, J. L. (1997). On the total geostrophic circulation of the Pacific Ocean: flow patterns, tracers and transports. *Prog. Oceanogr.* 39, 263–352.
- Rempfer, J., Stocker, T. F., Joos, F., Dutay, J. C., and Siddall, M. (2011). Modelling Nd-isotopes with a coarse resolution ocean circulation model: sensitivities to model parameters and source/sink distributions. *Geochim. Cosmochim. Acta* 75, 5927–5950. doi: 10.1016/j.gca.2011.07.044
- Rousseau, T. C. C., Sonke, J. E., Chmieleff, J., van Beek, P., Souhaut, M., Boaventura, G., et al. (2015). Rapid neodymium release to marine waters from lithogenic sediments in the Amazon estuary. *Nat. Commun.* 6:7592. doi: 10.1038/ncomms8592
- Schijf, J., Christenson, E. A., and Byrne, R. H. (2015). YREE scavenging in seawater: a new look at an old model. *Mar. Chem.* 177, 460–471. doi: 10.1016/j.marchem.2015.06.010
- Schneider, N., and Müller, P. (1990). The meridional and seasonal structures of the mixed-layer depth and its diurnal amplitude observed during the Hawaii-to-Tahiti Shuttle experiment. *J. Phys. Oceanogr.* 20, 1395–1404.
- Schopka, H. H., and Derry, L. A. (2012). Chemical weathering fluxes from volcanic islands and the importance of groundwater: the Hawaiian example. *Earth Planet. Sci. Lett.* 339–340, 67–78. doi: 10.1016/j.epsl.2012.05.028
- Shabani, M. B., Akagi, T., and Masuda, A. (1992). Preconcentration of trace rare-earth elements in seawater by complexation with bis(2-ethylhexyl) hydrogen phosphate and 2-ethylhexyl dihydrogen phosphate adsorbed on a C18 cartridge and determination by inductively coupled plasma mass-spectrometry. *Anal. Chem.* 64, 737–743.
- Sholkovitz, E. R. (1995). The aquatic chemistry of rare earth elements in rivers and estuaries. *Aquat. Chem.* 1, 1–34. doi: 10.1007/BF01025229
- Sholkovitz, E. R., and Szymczak, R. (2000). The estuarine chemistry of rare earth elements: comparison of the Amazon, Fly, Sepik and the Gulf of Papua systems. *Earth Planet. Sci. Lett.* 179, 299–309. doi: 10.1016/S0012-821X(00)00112-6
- Sholkovitz, E. R., Elderfield, H., Szymczak, R., and Casey, K. (1999). Island weathering: river sources of rare earth elements to the Western Pacific Ocean. *Mar. Chem.* 68, 39–57.
- Siddall, M., Khattiwala, S., van de Fliedert, T., Jones, K., Goldstein, S. L., Hemming, S., et al. (2008). Towards explaining the Nd paradox using reversible scavenging in an ocean general circulation model. *Earth Planet. Sci. Lett.* 274, 448–461. doi: 10.1016/j.epsl.2008.07.044
- Singh, S. P., Singh, S. K., Goswami, V., Bhushan, R., and Rai, V. K. (2012). Spatial distribution of dissolved neodymium and  $\epsilon\text{Nd}$  in the Bay of Bengal: role of particulate matter and mixing of water masses. *Geochim. Cosmochim. Acta* 94, 38–56. doi: 10.1016/j.gca.2012.07.017
- Sloyan, B. M., and Rintoul, S. R. (2001). Circulation, renewal, and modification of Antarctic mode and intermediate water. *J. Phys. Oceanogr.* 31, 1005–1030. doi: 10.1175/1520-0485(2001)031<1005:CRMOA>2.0.CO;2
- Stichel, T., Hartman, A. E., Dugan, B., Goldstein, S. L., Scher, H., and Pahnke, K. (2015). Separating biogeochemical cycling of neodymium from water mass mixing in the Eastern North Atlantic. *Earth Planet. Sci. Lett.* 412, 245–260. doi: 10.1016/j.epsl.2014.12.008
- Tachikawa, K., Athias, V., and Jeandel, C. (2003). Neodymium budget in the modern ocean and paleo-oceanographic implications. *J. Geophys. Res.* 108:3254. doi: 10.1029/1999JC000285
- Tanaka, K., Takahashi, Y., and Shimizu, H. (2008). Local structure of Y and Ho in calcite and its relevance to Y fractionation from Ho in partitioning between calcite and aqueous solution. *Chem. Geol.* 248, 104–113. doi: 10.1016/j.chemgeo.2007.11.003
- Tanaka, T., Togashi, S., Kamioka, H., Amakawa, H., Kagami, H., Hamamoto, T., et al. (2000). JNdi-1: a neodymium isotopic reference in consistency with LaJolla neodymium. *Chem. Geol.* 168, 279–281. doi: 10.1016/S0009-2541(00)00198-4
- Tapia, R., Nürnberg, D., Ronge, T., and Tiedemann, R. (2015). Disparities in glacial advection of Southern Ocean Intermediate Water to the South Pacific Gyre. *Earth Planet. Sci. Lett.* 410, 152–164. doi: 10.1016/j.epsl.2014.11.031
- Taylor, S. R., and McLennan, S. M. (1985). *The Continental Crust: Its Composition and Evolution, An Examination of the Geochemical Record Preserved in Sedimentary Rocks*. Oxford: Blackwell.

- Tomczak, M., and Godfrey, J. S. (1994). *Regional Oceanography: An Introduction*. New York, NY: Pergamon Press.
- Tomczak, M., and Godfrey, J. S. (2003). "Hydrology of the Pacific Ocean," in *Regional Oceanography: An Introduction, 2nd Edn.* (New Delhi: Daya Publishing House), 137–156.
- Tomczak, M., and Hao, D. (1989). Water masses in the thermocline of the Coral Sea. *Deep Sea Res.* 36, 1503–1514.
- Tsuchiya, M., Lukas, R., Fine, R., Firing, E., and Lindstrom, E. (1989). Source waters of the Pacific Equatorial Undercurrent. *Prog. Oceanogr.* 23, 101–147.
- van de Flierdt, T., Pahnke, K., Amakawa, H., Andersson, P., Basak, C., Coles, B., et al. (2012). GEOTRACES intercalibration of neodymium isotopes and rare earth element concentrations in seawater and suspended particles. Part 1: reproducibility of results for the international intercomparison. *Limnol. Oceanogr. Methods* 10, 234–251. doi: 10.4319/lom.2012.10.234
- Wei, R., Abouchami, W., Zahn, R., and Masque, P. (2016). Deep circulation changes in the South Atlantic since the Last Glacial Maximum from Nd isotope and multi-proxy records. *Earth Planet. Sci. Lett.* 434, 18–29. doi: 10.1016/j.epsl.2015.11.001
- Wilson, D. J., Piotrowski, A. M., Galy, A., and Banakar, V. K. (2015). Interhemispheric controls on deep ocean circulation and carbon chemistry during the last two glacial cycles. *Paleoceanography* 30, 621–641. doi: 10.1002/2014PA002707
- Wyrtki, K., and Kilonsky, B. (1984). Mean water and currents structure during Hawaii-to-Tahiti shuttle experiment. *J. Phys. Oceanogr.* 14, 242–254. doi: 10.1175/1520-0485(1984)014<0242:MWACSD>2.0.CO;2
- Zhang, J., and Nozaki, Y. (1996). Rare earth elements and yttrium in seawater: ICP-MS determinations in the East Caroline, Coral Sea, and South Fiji basins of the western South Pacific Ocean. *Geochim. Cosmochim. Acta* 60, 4631–4644.

**Conflict of Interest Statement:** The authors declare that the research was conducted in the absence of any commercial or financial relationships that could be construed as a potential conflict of interest.

Copyright © 2018 Molina-Kescher, Hathorne, Osborne, Behrens, Kölling, Pahnke and Frank. This is an open-access article distributed under the terms of the Creative Commons Attribution License (CC BY). The use, distribution or reproduction in other forums is permitted, provided the original author(s) and the copyright owner are credited and that the original publication in this journal is cited, in accordance with accepted academic practice. No use, distribution or reproduction is permitted which does not comply with these terms.



# Rare Earth Element Distribution in the NE Atlantic: Evidence for Benthic Sources, Longevity of the Seawater Signal, and Biogeochemical Cycling

Kirsty C. Crocket<sup>1\*</sup>, Emily Hill<sup>1†</sup>, Richard E. Abell<sup>1</sup>, Clare Johnson<sup>1</sup>, Stefan F. Gary<sup>1</sup>, Tim Brand<sup>1</sup> and Ed C. Hathorne<sup>2</sup>

<sup>1</sup> Scottish Association for Marine Science, Scottish Marine Institute, Oban, United Kingdom, <sup>2</sup> GEOMAR Helmholtz Centre for Ocean Research, Kiel, Germany

## OPEN ACCESS

### Edited by:

Catherine Jeandel,  
UMR5566 Laboratoire d'Études en  
Géophysique et Océanographie  
Spatiales (LEGOS), France

### Reviewed by:

Melanie Grenier,  
UMR5566 Laboratoire d'Études en  
Géophysique et Océanographie  
Spatiales (LEGOS), France  
Alan M Shiller,  
University of Southern Mississippi,  
United States

### \*Correspondence:

Kirsty C. Crocket  
crocketki@gmail.com

### †Present Address:

Emily Hill,  
Department of Biology, Norwegian  
University of Science and Technology,  
Trondheim, Norway

### Specialty section:

This article was submitted to  
Marine Biogeochemistry,  
a section of the journal  
Frontiers in Marine Science

**Received:** 23 November 2017

**Accepted:** 10 April 2018

**Published:** 30 April 2018

### Citation:

Crocket KC, Hill E, Abell RE,  
Johnson C, Gary SF, Brand T and  
Hathorne EC (2018) Rare Earth  
Element Distribution in the NE Atlantic:  
Evidence for Benthic Sources,  
Longevity of the Seawater Signal, and  
Biogeochemical Cycling.  
Front. Mar. Sci. 5:147.  
doi: 10.3389/fmars.2018.00147

Seawater rare earth element (REE) concentrations are increasingly applied to reconstruct water mass histories by exploiting relative changes in the distinctive normalised patterns. However, the mechanisms by which water masses gain their patterns are yet to be fully explained. To examine this, we collected water samples along the Extended Ellett Line (EEL), an oceanographic transect between Iceland and Scotland, and measured dissolved REE by offline automated chromatography (SeaFAST) and ICP-MS. The proximity to two continental boundaries, the incipient spring bloom coincident with the timing of the cruise, and the importance of deep water circulation in this climatically sensitive gateway region make it an ideal location to investigate sources of REE to seawater and the effects of vertical cycling and lateral advection on their distribution. The deep waters have REE concentrations closest to typical North Atlantic seawater and are dominated by lateral advection. Comparison to published seawater REE concentrations of the same water masses in other locations provides a first measure of the temporal and spatial stability of the seawater REE signal. We demonstrate the REE pattern is replicated for Iceland-Scotland Overflow Water (ISOW) in the Iceland Basin from adjacent stations sampled 16 years previously. A recently published Labrador Sea Water (LSW) dissolved REE signal is reproduced in the Rockall Trough but shows greater light and mid REE alteration in the Iceland Basin, possibly due to the dominant effect of ISOW and/or continental inputs. An obvious concentration gradient from seafloor sediments to the overlying water column in the Rockall Trough, but not the Iceland Basin, highlights release of light and mid REE from resuspended sediments and pore waters, possibly a seasonal effect associated with the timing of the spring bloom in each basin. The EEL dissolved oxygen minimum at the permanent pycnocline corresponds to positive heavy REE enrichment, indicating maximum rates of organic matter remineralisation and associated REE release. We tentatively suggest a bacterial role to account for the observed heavy REE deviations. This study highlights the need for fully constrained REE sources and sinks, including the temporary nature of some sources, to achieve a balanced budget of seawater REE.

**Keywords:** rare earths, biogeochemical cycle, ocean circulation, Northeast Atlantic, water mass tracer, chemical tracer, Extended Ellett Line, Iceland-Scotland Overflow Water

## INTRODUCTION

The rare earth elements (REE) form a suite of 14 elements (i.e., the lanthanides) with chemical properties that vary systematically across the group. The interpretation of relative changes in REE concentrations makes them a powerful tool to investigate advection, cycling and inputs of trace metals in seawater. When normalised to the Post-Archaean Australian Shale (PAAS; Taylor and McLennan, 1985), the balance of supply/removal processes that fractionate seawater REE away from their lithogenic origins is highlighted (e.g., Elderfield and Greaves, 1982; Bertram and Elderfield, 1993). This fractionation is mainly attributed to the increasing strength of REE complexation to carbonate ions as mass number increases (Byrne and Kim, 1990), described by the lanthanide contraction effect (Zhang and Nozaki, 1996). While the heavy (H)REE are almost entirely bound by stable carbonate complexes, the light (L)REE are present with a greater proportion of free metal ions that makes them more susceptible to removal from solution through adsorption reactions (Cantrell and Byrne, 1987; Byrne and Kim, 1990; Sholkovitz et al., 1994). This results in the characteristic PAAS-normalised seawater REE pattern of HREE enrichment relative to LREE (e.g., Elderfield and Greaves, 1982; Bertram and Elderfield, 1993; Alibo and Nozaki, 1999). One exception to this is Ce, whose microbially mediated redox chemistry results in substantially lower relative concentrations to neighbouring REE (Moffett, 1990).

The relative changes in the distinctive pattern of dissolved seawater REE are increasingly applied to reconstruct water mass histories, e.g., provenance, continental inputs, intensity of biogeochemical cycling, and water mass isolation time (e.g., Zhang et al., 2008; Grenier et al., 2013, 2018; Garcia-Solsona et al., 2014; Haley et al., 2014; Molina-Kescher et al., 2014, 2018; Hathorne et al., 2015; Zheng et al., 2016; Grasse et al., 2017). Dominant processes controlling the distribution of open ocean REE are lateral advection by deep water masses (e.g., Hathorne et al., 2015; Zheng et al., 2016) and the effects of biogeochemical cycling (particle sorption/desorption, remineralisation) on vertical profiles of REE (e.g., Sholkovitz et al., 1994). Also important are the processes operating at the continent-ocean interface, that dictate sources and sinks of REE to seawater (e.g., Jeandel et al., 2011), and, gaining recognition, are the role of organics in altering the reactivity and therefore the fractionation of the REE (Schijf et al., 2015). Demonstrating and ultimately quantifying the impact of these mechanisms on seawater REE is essential for complete data interpretation. Resolving seawater REE behaviour will also contribute to constraining the marine Nd budget (i.e., the “Nd paradox”; Goldstein and Hemming, 2003), the isotope compositions of which are currently one of the most powerful chemical tracers of water masses in modern oceanography (e.g., Grenier et al., 2014; Lambelet et al., 2016) and palaeoceanographic reconstruction (e.g., Wilson et al., 2014).

Processes operating at continental margins and the seawater-sediment interface are amongst the least resolved. The emerging picture of REE cycling in the ocean is one of dominant removal (~70%) of riverine REE in estuaries (Goldstein and Jacobsen, 1988; Sholkovitz, 1993), ~20% (Nd) contribution

from aeolian deposition (Tachikawa et al., 1999), negligible REE from hydrothermal venting (German et al., 1990), and variable contributions from sediments. This latter point includes diagenetic release of REE from pore waters (Abbott et al., 2015b; Haley et al., 2017), partial dissolution of particulates (Grenier et al., 2013; Pearce et al., 2013), and release from river-borne particulates in estuarine environments (Rousseau et al., 2015). These seawater-sediment interactions are described by “boundary exchange” and can result in release or scavenging of REE (Lacan and Jeandel, 2005b; Jeandel et al., 2007, 2011; Jeandel and Oelkers, 2015; Jeandel, 2016). This incomplete understanding of the marine REE budget is reflected most acutely by the input deficit in the marine Nd budget of  $\leq 11,000$  tons per year (Arsouze et al., 2009), and serves to highlight the importance of refining our knowledge of these seawater-sediment processes.

Organic complexation of seawater REE likely plays a role in the distribution of REE through their affinity for negatively charged sites on organic molecules (Byrne and Kim, 1990). However, it remains a relatively unconstrained quantity at present (e.g., Haley et al., 2014), with some identification of organic uptake associated with surface ocean productivity (Stichel et al., 2015; Grasse et al., 2017) but no complete explanation of the process. Work on organic complexation has identified strong HREE binding to bacterial phosphate functional groups (Ngwenya et al., 2010; Takahashi et al., 2010), and strong organic ligand complexation (Schijf et al., 2015). Uptake of REE by biogenic silica has also been proposed (Akagi, 2013). Where present in sufficient density, these functional groups may serve to further fractionate seawater REE and could represent one mechanism by which the nutrient-like vertical profiles of dissolved REE are attained (Schijf et al., 2015). As rather tenuous support of this, the often cited lack of a biological function for the REE is starting to be countered by evidence for an active role of the REE in bacterial processes (Lim and Franklin, 2004; Martinez-Gomez et al., 2016, and references therein).

Here we present the seawater REE concentrations collected on an annual oceanographic transect, the Extended Ellett Line (EEL), which runs between Scotland and Iceland (~60°N, ~-20°E) and occupies a climatically sensitive gateway region in the NE Atlantic. The EEL is ideally positioned to record the influx of North Atlantic upper waters into the Greenland-Iceland-Norwegian (GIN) Seas, the overflow of deep water masses exiting the GIN Seas across the Iceland-Scotland Ridge at depth, and their recirculation within the Rockall Trough and Iceland Basin. Samples collected at five open ocean stations provide full water column REE profiles, and contribute to the growing resolution of REE distributions in water masses in the NE Atlantic, previously sampled in the neighbouring Norwegian Sea (Lacan and Jeandel, 2004b), Irminger Basin (Lacan and Jeandel, 2004a), Iceland Basin (Lacan and Jeandel, 2005a), and Labrador Sea (Filippova et al., 2017). The comparison to data collected recently and ~16 years prior allows the first evaluation of the temporal and spatial stability of the dissolved REE signature as chemical water mass tracers. Samples were also collected from three coastal stations at the Icelandic and Scottish extremes of the EEL (**Figure 1**). The proximity of these two continental margins and the complex bathymetry crossed by the EEL make it an ideal location to



investigate the impact of various REE sources on the seawater signatures of different water masses. In addition, the timing of the spring bloom, coincident with the EEL cruise, provides further insight into the effects of vertical biogeochemical cycling on REE distributions.

## MATERIALS AND METHODS

### Hydrography

The EEL spans the Rockall Trough, the Rockall-Hatton Plateau and the Iceland Basin (**Figure 1**). The collection of oceanographic data on at least an annual basis since 1975 in the Rockall Trough and extended to the Iceland Basin from 1996 onwards makes the EEL an exceptional resource (Holliday and Cunningham, 2013), with many publications detailing the circulation of water masses and their hydrographic and chemical properties. The overall circulation along the EEL is one of warm and salty Atlantic upper waters flowing in a north-easterly direction into the Nordic Seas, underlain by a permanent thermocline that separates the surface from the generally cyclonic circulation of dense, cold waters at depth (Holliday et al., 2015; **Figures 2, 3**). Here, we summarise the salient points.

The upper waters are dominated by the North Atlantic Current (NAC) that draws in subtropical Eastern North Atlantic Water (ENAW) and subpolar Western North Atlantic Water (WNAW). Upper waters in the Rockall Trough are warmer and saltier ( $>9.5^{\circ}\text{C}$ ,  $>35.4$  salinity) compared to the Iceland Basin ( $>7.0^{\circ}\text{C}$ ,  $>35.10$  salinity; **Figure 3**; Holliday et al., 2000; Johnson et al., 2013). These upper ocean waters have potential densities of  $27.20\text{--}27.50\text{ kg/m}^3$ , and are overlain by a shallow layer of seasonally affected surface waters ( $<27.20\text{ kg/m}^3$ ; Holliday et al., 2015), although in 2015 water with these densities was observed as a thin veneer over the surface of the Rockall Trough ( $<35\text{ m}$  deep) and did not extend into the Iceland Basin (**Figure 2**). Typically WNAW has higher concentrations of silica ( $\geq 7.3\text{ }\mu\text{mol/kg}$ ), phosphate ( $1.0\text{--}1.1\text{ }\mu\text{mol/kg}$ ) and nitrate ( $14.6\text{--}15.6\text{ }\mu\text{mol/kg}$ ), whereas the ranges in ENAW tend to be lower (silica:  $2.4\text{--}5.8\text{ }\mu\text{mol/kg}$ , phosphate:  $0.6\text{--}1.0\text{ }\mu\text{mol/kg}$ , nitrate  $10.0\text{--}12.2\text{ }\mu\text{mol/kg}$ ; Fogelqvist et al., 2003; McGrath et al., 2012; Johnson et al., 2013). The values recorded during EEL 2015 cruise for both upper water masses fall at the lower end or just below these ranges (**Table 1**), highlighting broader climate-induced changes in ocean circulation that influence nutrient concentrations (Johnson et al., 2013).

The permanent thermocline forms a coherent density layer ( $27.50\text{--}27.70\text{ kg/m}^3$ ) at  $\sim 900\text{--}1,400$  dbar in the Rockall Trough, but becomes broader and less well defined in the Iceland Basin where it rises to  $\sim 400$  dbar (**Figure 2**). The oxygen depletion zone (ODZ) and maximal nutrient concentrations are well defined in the Rockall Trough but more diffuse in the Iceland Basin. Minimum dissolved oxygen concentrations in the Rockall Trough during the 2015 EEL cruise were  $209\text{ }\mu\text{mol/kg}$ , with concomitant peaks in nutrients in silica ( $9.8\text{ }\mu\text{mol/kg}$ ), phosphate ( $1.17\text{ }\mu\text{mol/kg}$ ) and total nitrogen ( $18.2\text{ }\mu\text{mol/kg}$ ; **Table 1**).

Below the permanent pycnocline in both basins, circulation is dominated by Labrador Sea Water (LSW), present as a relatively

homogenous body of water ( $3\text{--}4^{\circ}\text{C}$ ,  $34.90\text{--}34.95$  salinity,  $27.70\text{--}27.85\text{ kg/m}^3$ ; Holliday et al., 2015). Long-term observations highlight the consistently fresher and colder properties of LSW in the Iceland Basin compared to its signature in the Rockall Trough (Holliday et al., 2015), reflecting greater mixing along its pathway to reach the northern Rockall Trough. Typical dissolved oxygen concentrations associated with LSW in the Rockall Trough are  $260\text{--}270\text{ }\mu\text{mol/kg}$ , and relatively high concentrations of silica ( $10.7\text{--}14.7\text{ }\mu\text{mol/kg}$ ), phosphate ( $1.0\text{--}1.2\text{ }\mu\text{mol/kg}$ ) and nitrate ( $11.7\text{--}19\text{ }\mu\text{mol/kg}$ ; Fogelqvist et al., 2003; McGrath et al., 2012; Johnson et al., 2013). During the 2015 EEL cruise, LSW identified in both the Rockall Trough and the Iceland Basin had dissolved oxygen and nutrient concentrations within these ranges (**Table 1**).

The deepest depths of the Iceland Basin are occupied by Iceland Scotland Overflow Water (ISOW;  $<3.0^{\circ}\text{C}$ ,  $>27.85\text{ kg/m}^3$ ) from the Nordic Seas that enters mostly via the Faroe Bank Channel and circulates along the western boundary of the Iceland Basin. Cyclonic recirculation results in a smaller flow of ISOW along the eastern side of the Basin (Kanzow and Zenk, 2014), likely mixed to varying extent with the overlying LSW (Holliday et al., 2015). ISOW is well ventilated ( $268\text{--}286\text{ }\mu\text{mol/kg}$ ), with elevated concentrations of silica ( $9\text{--}12.6\text{ }\mu\text{mol/kg}$ ) and nitrate ( $10\text{--}16\text{ }\mu\text{mol/kg}$ ; Fogelqvist et al., 2003; McGrath et al., 2012). During the 2015 EEL cruise, ISOW had nutrient concentrations within range of typical values, although silica was low ( $9.8\text{ }\mu\text{mol/kg}$ ) and total nitrogen was high ( $15.3\text{ }\mu\text{mol/kg}$ ; **Table 1**). **Table 1** also highlights comparison to published values of ISOW (Lacan and Jeandel, 2004b), collected in the Faroe Shetland Channel in 1999. Several differences to the properties of this ISOW (e.g., lower potential temperature and salinity, greater potential density and dissolved oxygen) can be ascribed to the effects of mixing and dilution as ISOW travels through the overflow channels and the shallower depths of the Iceland Basin, mixing with overlying NAC and LSW. This is discussed in more detail in section Circulation Effects on REE Distribution.

At the point the EEL crosses the Rockall Trough, water masses denser than LSW ( $>27.85\text{ kg/m}^3$ ) are not consistently observed. When present, Lower Deep Water (LDW;  $\sim 2.8^{\circ}\text{C}$ ,  $34.95$  salinity; Holliday et al., 2000) is a cold, dense water mass influenced by Antarctic Bottom Water (New and Smythe-Wright, 2001). In 2015, only the deep eastern side of the Rockall Trough carried water denser than LSW (not sampled in this study), which has typical characteristics of elevated silica ( $35.3\text{ }\mu\text{mol/kg}$ ) and nitrate ( $20.4\text{ }\mu\text{mol/kg}$ ; McGrath et al., 2013).

### Methods

Samples were collected from nine stations during the EEL on the RRS *Discovery* between 29 May and 17 June 2015 (**Figure 1**). Of the open ocean stations, five have full profiles (6 depths sampled) and station P has two samples. Seawater was collected from Niskin bottles on a CTD rosette and immediately filtered through  $0.4\text{ }\mu\text{m}$  polycarbonate Cyclopore filter membranes into LDPE bottles, followed by acidification, double bagging and refrigeration until analysis in the home laboratory. All equipment in contact with the sample seawater was rigorously acid cleaned

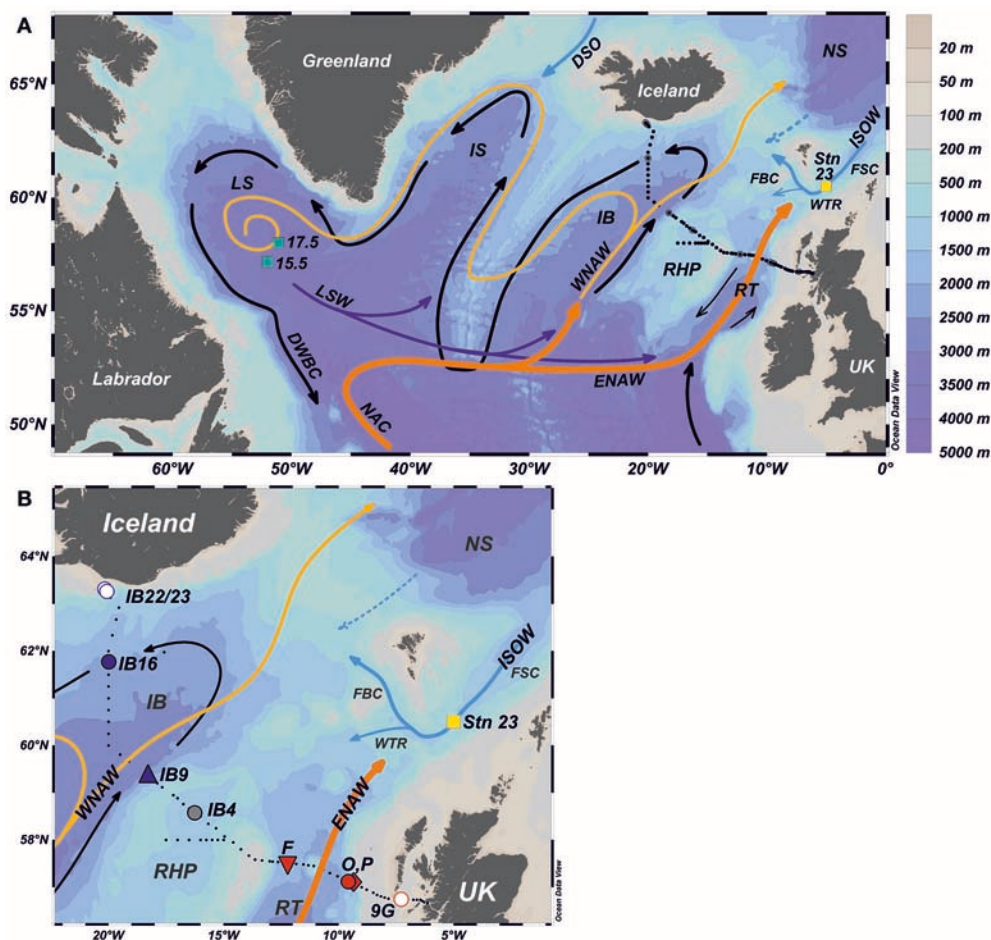


**FIGURE 1 | (A)** Location map with the 2015 Extended Ellett Line (EEL) stations in black dots. Deep, ocean currents are indicated by black arrows (below the pycnocline). The cold overflow currents are shown by blue arrows. Dotted lines represent intermittent currents. Orange and yellow lines reflect the warm surface waters. The locations of the Faroe-Shetland Channel (FSC), Faroe Bank Channel (FBC) and Wyville Thomson Ridge (WTR) are shown. For reference in the discussion, also shown are the locations of Station 23 in the FSC (yellow square; Lacan and Jeandel, 2004b) and Stations 15.5 and 17.5 in the Labrador Sea (green squares; Filippova et al., 2017). **(B)** Detailed view of the 2015 EEL stations, with those sampled in this study highlighted by large labelled symbols (blue, red, grey). *Water masses:* DWBC, Deep Western Boundary Current; LSW, Labrador Sea Water; ISOW, Iceland-Scotland Overflow Water; DSO, Denmark Strait Overflow; NA, North Atlantic Current; WNAW, Western North Atlantic Water; ENAW, Eastern North Atlantic Water. *Ocean basins:* LS, Labrador Sea; IB, Iceland Basin; IS, Irminger Sea; RHP, Rockall-Hatton Plateau; RT, Rockall Trough; NS, Norwegian Sea. The figure was created using ODV software, available at <https://odv.awi.de/> (Schlitzer, 2016). (For interpretation of the references to colour in this and other figures herein, the reader is referred to the electronic version of this article).

prior to use (Buck and Paytan, 2012; Cutter et al., 2014). Station 9G and surface samples from Station O were not filtered.

The REE concentrations were determined on 20 ml seawater by ICP-MS (ThermoScientific Xseries 2) following off-line preconcentration and removal of the salt matrix using a SeaFAST system (ESI, USA), adapted from the on-line method of Hathorne et al. (2012). External standardisation was applied using a 6 point calibration, the solutions of which were processed through the SeaFAST in the same manner as the samples. Calibration standards, reference seawater aliquots, and samples were indium doped to monitor and correct for instrumental drift. Oxide formation and interferences on the HREE were minimised during tuning, and monitored by measurement of mass 156 (CeO). They were found to be <1% of the 140 Ce intensity

for the majority of samples. The exceptions were two samples with a 156/140 ratio of ~3%. These have not been included in the dataset. Barium concentrations in the purified sample solutions were monitored for oxide interference on europium.  $^{137}\text{Ba}$  intensities were <20% of  $^{153}\text{Eu}$ , and would require >10% BaO formation to generate significant interferences on europium (i.e., >2%) and so are not considered to be significant. All data are presented in Table S1.

External reproducibility was determined by repeat measurement of the GEOTRACES intercalibration seawater from the Bermuda Atlantic Time Series (BATS 2,000 m) and NRC NASS-6 coastal water. Over the course of this study, values ranged from 6 to 16% (2RSD) for the BATS and 7–16% for the NASS-6 (Table 2). Comparison of the BATS 2,000 m

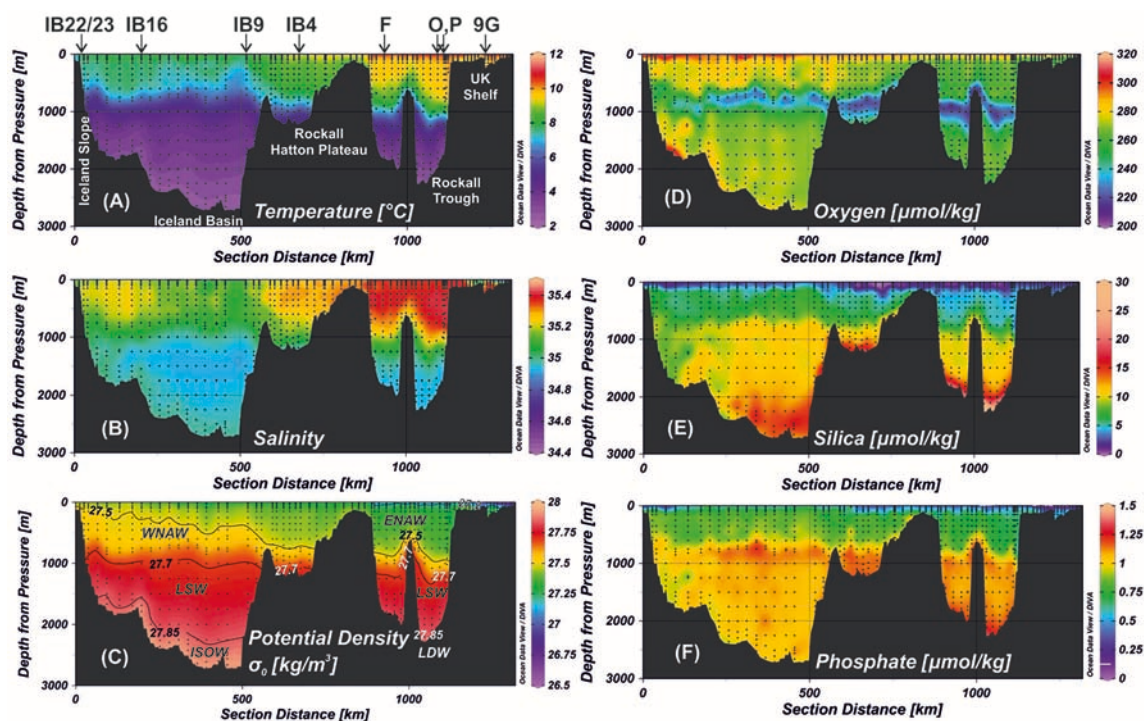


**FIGURE 2 |** Sections of: (A) temperature ( $^{\circ}\text{C}$ ), (B) salinity, (C) potential density  $\sigma_{\theta}$  ( $\text{kg/m}^3$ ), (D) dissolved oxygen ( $\mu\text{mol/kg}$ ), (E) silica ( $\mu\text{mol/kg}$ ), (F) phosphate ( $\mu\text{mol/kg}$ ). The potential density section has contours delineating the ranges identified by Holliday et al. (2015) as representative of different water masses, with acronyms identifying the dominant water mass (see Figure 1 caption for acronyms). The data are from 920 bottle samples (black dots) collected from 85 stations over  $\sim 1,300\text{ km}$  of cruise track during the 2015 EEL campaign. The figure was created using ODV software, available at <https://odv.awi.de/> (Schlitzer, 2016).

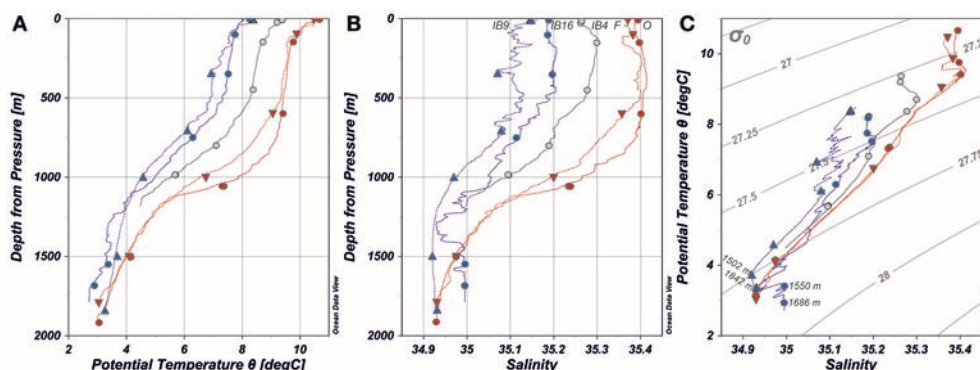


**FIGURE 3 |** (A) Depth (m) vs. potential temperature ( $^{\circ}\text{C}$ ), (B) depth (m) vs. salinity, (C) potential temperature ( $^{\circ}\text{C}$ ) vs. salinity with the isopycnals defined by the grey lines, for the open ocean stations in this study during the 2015 EEL. The bottle data are indicated by symbols that correspond to those on the location map (Figure 1), superimposed on the CTD data. Small discrepancies between CTD and bottle data arise due to CTD data collection on the downcast and bottle data collection on the up-cast. The depths of the deepest samples at IB16 are indicated in (C) with reference to section Circulation Effects on REE Distribution. The figure was created using ODV software, available at <https://odv.awi.de/> (Schlitzer, 2016).

concentrations to the consensus values (van de Flierdt et al., 2012) reveal deviations of  $<7\%$ , with the exceptions of Ce and Sm (both  $14\%$ ). We report the deviation to published values of NASS-6 (Wang et al., 2014) for information only as no certified values exist (Table 2). Duplicate samples (same Niskin vs. different Niskin/similar depth) have relative

differences similar to the external reproducibility, and on a few occasions were larger. Total procedural blanks run through the preconcentration system were  $<1\%$  of the average sample signal, with the exceptions of Ce and Sm that represented 17 and 10% respectively of the smallest sample signal.



**TABLE 1 |** Water mass properties of selected stations and depths along the EEL 2015 cruise, with comparison to end-member water masses in published work.

Water mass	Potential temp (°C)	Salinity	$\sigma_\theta$ (kg/m <sup>3</sup> )	Oxygen (μmol/kg)	Silica (μmol/kg)	Phosphate (μmol/kg)	Total N (μmol/kg)	MREE/MREE* (a)	HREE/LREE (b)	References
<b>EEL 2015 STATIONS</b>										
ENAW (O, 149 m)	9.79	35.40	27.31	270.7	1.88	0.60	10.42	1.01	3.73	
WNAW (IB16, 351 m)	7.56	35.20	27.50	279.4	6.58	0.89	14.00	0.99	3.51	
LSW (F, 1,000–1,499 m)	4.22	34.98	27.77	261.0	11.20	1.13	16.87	0.89	4.15	
LSW (IB9, 1,502 m)	3.84	34.92	27.76	269.3	11.76	1.08	17.09	0.87	3.93	
ISOW (IB16, 1,550 m)	3.53	35.00	27.85	279.1	9.75	1.01	15.32	1.01	3.62	
ISOW (IB16, 1,686 m)	3.10	35.00	27.89	280.4	10.17	1.03	15.67	1.06	3.34	
<b>PUBLISHED WORK</b>										
ISOW (Stn 23)	−0.35	34.89	28.03	440.66*				1.05	3.45	(1)
DLSW (Stns 15.5, 17.5)	3.49	34.92	27.77	264.42 <sup>§</sup>				0.89	3.86	(2)
BATS 2,000 m								0.92	4.11	(3)

The PAAS normalised REE concentrations are presented as (a) the MREE anomaly ( $MREE/MREE^* = (Gd+Tb+Dy)/[(La+Pr+Nd+Tm+Yb+Lu)/2]$ ) and (b) the HREE/LREE ratio ( $(Tm+Yb+Lu)/(La+Pr+Nd)$ ).

References: (1) (Lacan and Jeandel, 2004b); (2) (Filippova et al., 2017); (3) (van de Flierdt et al., 2012).

\*Conversion from 10.14 ml/l.

§Conversion from 6.09 ml/l.

**TABLE 2 |** Dissolved REE concentrations in reference samples measured during the course of this study: consensus values of the GEOTRACES intercalibration seawater from the Bermuda time series station (BATS) 2,000 m (van de Flierdt et al., 2012); published values of (Wang et al., 2014) for NASS-6 (National Research Council Canada) coastal seawater.

Element	La	Ce	Pr	Nd	Sm	Eu	Gd	Tb	Dy	Ho	Er	Tm	Yb	Lu	Y
<b>BATS 2,000 m (n = 19)</b>															
Mean concentration (pmol/kg)	23.76	4.41	4.31	18.48	3.93	0.93	5.07	0.82	6.00	1.54	5.23	0.76	5.07	0.84	153
2SD	2.05	0.55	0.31	1.14	0.62	0.13	0.55	0.09	0.58	0.14	0.50	0.08	0.52	0.09	14
2RSD (%)	9	12	7	6	16	14	11	10	10	9	10	10	10	10	9
Consensus values (pmol/kg)	23.61	5.12	4.03	17.33	3.45	0.91	4.84	0.79	5.780	1.52	5.04	0.75	4.76	0.81	
2SD of consensus values	2.79	2.27	0.35	1.22	0.354	0.10	0.53	0.08	0.38	0.09	0.25	0.05	0.25	0.04	
Deviation to consensus (%)	1	−14	7	7	14	2	5	4	3	1	4	2	6	4	
<b>NASS-6 (n = 12)</b>															
Mean concentration (pmol/kg)	72.15	28.71	10.76	45.50	8.05	1.59	9.74	1.39	9.81	2.39	8.01	1.12	7.74	1.26	229
2SD	7.69	4.56	0.75	3.70	0.80	0.15	0.84	0.13	0.84	0.21	0.66	0.1	0.6	0.1	23
2RSD (%)	11	16	7	8	10	10	9	10	9	9	8	12	7	8	10
Published values (pmol/kg)	75.20	31.25	11.72	45.90	8.79	1.76	8.30	1.46	9.77	2.34	7.81	1.07	7.42	1.17	264
2SD of published values	8.79	5.86	1.95	7.81	0.98	0.20	1.76	0.59	0.98	0.68	0.98	0.29	1.56	0.39	39
Deviation to published (%)	−4	−8	−8	−1	−8	−9	17	−5	0	2	3	5	4	7	−13

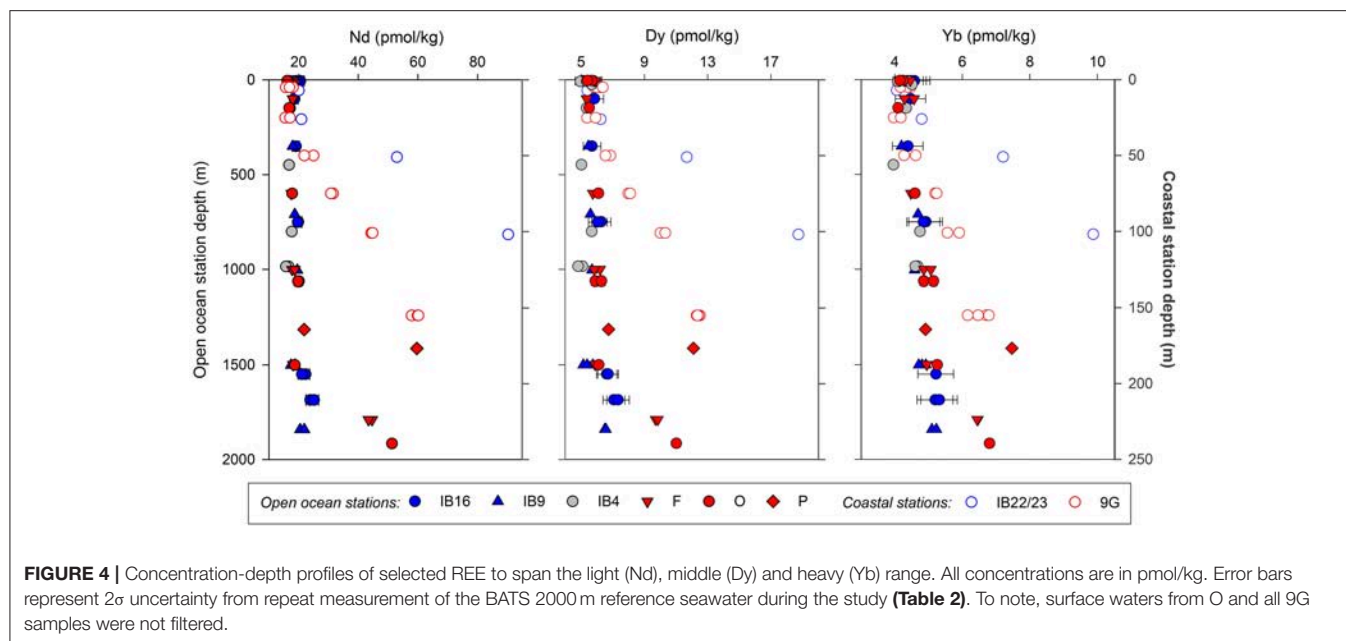
## RESULTS

The REE concentrations show relatively small increases with depth (Figure 4, Table S1) that are atypical of open ocean profiles (e.g., De Baar et al., 1985; Alibo and Nozaki, 1999; Hathorne et al., 2015). The absence of pronounced increases with depth most likely reflects the circulation of relatively young water masses, ISOW in the Iceland Basin, and LSW in both basins, and therefore the time limited accumulation of remineralised loads of dissolved REE. In addition, the relatively short water column depth (~2,000 m) of the sampled stations reduces the remineralisation time of particulates and therefore the release of REE into solution. At the stations in the Rockall Trough (F, O, P), excluding the deepest samples, a relatively

small spread in REE concentrations is observed (e.g., 16.2–21.8 pmol/kg Nd). The Iceland Basin stations (IB16, IB9) have a greater spread in REE concentrations with higher concentrations below ~1,500 m ( $\leq 25.1$  pmol/kg Nd) than in the surface waters. Station IB4 on the Rockall-Hatton Plateau has the reverse trend, with slightly lower concentrations at depth (~16 pmol/kg Nd) compared to the surface (~18 pmol/kg Nd). The variation in REE concentrations at each station is associated with clear changes in temperature, salinity, potential density, dissolved oxygen and nutrient concentrations (Table S2; see Discussion—Lateral advection).

The exceptions to this pattern are the samples in the deep Rockall Trough (F, O, P) with high REE concentrations (e.g., 43–60 pmol/kg Nd), where samples were collected close to the





sediment surface (<40 m above seafloor), and the coastal stations (IB22/23, 9G) with exceptionally high REE concentrations (e.g.,  $\leq 90$  pmol/kg). The coastal stations show a linear increase in REE concentration with depth that does not correspond to the variation in beam transmission intensity (Supplementary Figure 1). Furthermore, the deeper waters at 9G (unfiltered) have lower concentrations than comparable depths at IB22/23, which were filtered. Along this part of the UK shelf, open ocean North Atlantic water migrates onto the shelf at depth (Jones et al., 2018), supported by the high salinity ( $\geq 35.35$ ), temperature ( $\geq 9.6^\circ\text{C}$ ) and density anomaly ( $\geq 27.27$  kg/m<sup>3</sup>) at depths below  $\sim 75$  m. The low REE concentrations in these open North Atlantic waters result in lower REE concentrations at depth at 9G compared to IB22/23. The productive shelf waters at 9G, collected in May/June, mean a component of planktonic organisms is likely included in the sample. This is reflected by the trend towards average marine biogenic carbonate REE in **Figure 9C** (see discussion in section Source of Elevated REE Concentrations in the Deep Rockall Trough Samples).

In contrast to the coastal stations, the REE increase at depth in the Rockall Trough appears abruptly in the deepest samples at each station and is associated with collection from water with a high particulate load as determined from the beam transmission data (Supplementary Figure 1). To note, IB4 has the strongest decrease in beam transmission but no sample was collected from within this layer. These samples with high REE concentrations are discussed in section Source of Elevated REE Concentrations in the Deep Rockall Trough Samples.

Normalisation to REE concentrations of Post-Archaean Australian Shale (PAAS) is used to demonstrate the extent of fractionation of seawater REE from REE in the typical continental source materials. Patterns of normalised seawater REE typically reveal HREE (e.g., Tm, Yb, Lu) enrichment and LREE (e.g., La, Pr, Nd) depletion, due to preferential LREE removal from

solution onto particles relative to the greater stability of aqueous carbonate complexes of the HREE (Cantrell and Byrne, 1987; Byrne and Kim, 1990; Sholkovitz et al., 1994). We use the PAAS values in Taylor and McLennan (1985) to normalise the EEL data. This highlights: (i) reduced HREE enrichment in surface waters, (ii) enrichment of all REE in deeper water masses, and (iii) exceptional MREE (e.g., Gd, Tb, Dy) enrichment in sub-surface coastal waters (**Figure 5**). The lack of HREE enrichment in surface waters relative to thermocline waters is more pronounced in the Rockall Trough than the Iceland Basin, with the largest difference noted in the data of both the coastal stations (IB22/23, 9G). As noted above, all the REE show increases with depth (with the exception of IB4), although the greatest spread from surface to deep in LREE and MREE (excluding the large increases at depth at stations F, O, and P) is noted at station IB16. The coastal station data show the greatest increases in normalised REE profiles with depth (**Figure 5**). The Iceland Slope (IB22/23) data have a pronounced positive Eu anomaly in the deepest sample, reflecting the dominant mafic nature of Iceland's geology. Similar positive Eu anomalies were identified in seawater following sediment interaction experiments using Icelandic particulate material collected in rivers and estuaries (Pearce et al., 2013) and in seawater surrounding Tahiti (Molina-Kescher et al., 2018).

## DISCUSSION

### Circulation Effects on REE Distribution

Water masses along the EEL are to a certain extent related. However, the two most clearly differentiated by source region are LSW and ISOW, originating in the North Atlantic subpolar gyre and the Nordic Seas respectively. They are identified in the 2015 EEL data on the basis of their T/S, density anomalies and dissolved oxygen concentrations (**Figure 2**, Table S2). Here we evaluate the ability of the REE to fingerprint these water masses in

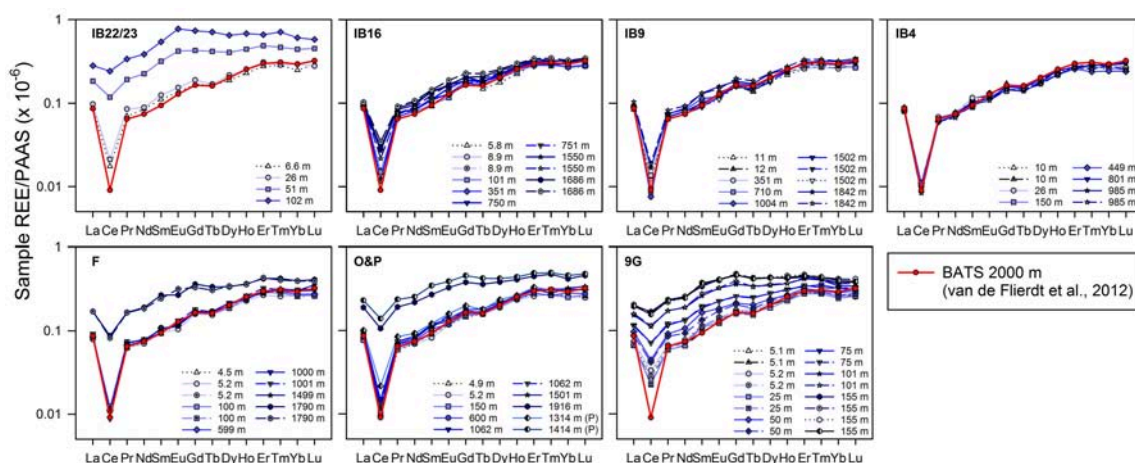


**FIGURE 5 |** REE concentrations normalised to the Post-Archaean Australian Shale (PAAS) values of Taylor and McLennan (1985) as presented in Freslon et al. (2014). The BATS 2000 m pattern (van de Flierdt et al., 2012) is shown for comparison in each panel (bold red line). To note, surface waters from O and all 9G samples were not filtered.

the NE Atlantic and the stability of their REE signature over time and distance by comparing to (1) a proximal record of ISOW REE collected 16 years prior to this study (Lacan and Jeandel, 2004b), and (2) a distal record of deep Labrador Sea Water (DLSW) REE collected in 2013 at the site of formation in the Labrador Sea (Filippova et al., 2017).

The HREE are reported in the literature as better tracers of water masses than LREE (e.g., Zheng et al., 2016) within ocean basins due to their longer residence times arising from their stronger aqueous complexation and thus reduced particle reactivity compared to the LREE (Cantrell and Byrne, 1987; Byrne and Kim, 1990). However, the limited distances and correspondingly short timescales for the movement of these young water masses (ISOW and LSW) in the NE Atlantic in this study limits the extent to which particle reactivity would influence the distribution of the REE (with the exception of Ce). We therefore assume the REE behave conservatively and mainly reflect the lateral advection of the water mass, with alteration of the REE signature chiefly attributable to mixing with other water masses and extraneous inputs. In this section, we focus on the preformed nature of REE at depth in the water column (below the permanent pycnocline).

### Temporal Record of ISOW

The ISOW data used for comparison to data in this study, expressed hereafter as pISOW, were collected from the Faroe-Shetland Channel (Stn 23 in Figure 1) in 1999 and represent a mean of REE concentrations in waters sampled at three depths (599, 800, 988 m; Lacan and Jeandel, 2004b). Based on potential density (Figures 2C, 3C), station IB16 “sees” ISOW at depths of  $\geq 1,500$  m, while along the eastern Iceland Basin the deepest sample at IB9 (1,842 m) is influenced by both ISOW and LSW (Figure 3C). Of the two, IB16 has the strongest, least dilute signal of ISOW because it lies immediately downstream of ISOW’s passage through the Faroe Bank Channel, with a path length

between Stn 23 and IB16 being relatively short at  $\sim 1,000$  km. At IB9, ISOW lies at greater depth and the potential density gradient with the overlying LSW is shallower indicating more diffuse recirculation and some mixing with LSW. This is observable in Figure 3C by the greater deviation of the deep waters towards LSW compared to IB16.

To test the similarity between ISOW collected in 1999 and in 2015, we first normalise REE concentrations at IB16 (1,550 m), i.e., the sample with the strongest ISOW signal (i.e.,  $\sigma_\theta$  27.85 kg/m<sup>3</sup>), by the pISOW REE concentrations. This is presented in Figures 6A,F (inverted light green triangles) with a combined  $2\sigma$  external error envelope of the IB16 (1,550 m) and pISOW samples. The same data are also normalised to DLSW in Figures 6G–L for comparison. Presenting the data in this way emphasises similarities between samples that are potentially related to the origin of the water mass. The data match between IB16 (1,550 m) and pISOW is surprisingly good, reflected by most of the pISOW-normalised REE in the IB16 sample having a value close to unity.

The similarity raises the question of how discriminatory the REE are at identifying ISOW along the EEL. For example, is the REE data match between IB16 and pISOW simply fortuitous? Normalisation of all intermediate and deep ( $> 700$  m) EEL station data by pISOW reveals clear differences between the Iceland Basin vs. the Rockall Trough and the Rockall-Hatton Plateau (Figures 6A–E). As a first broad appraisal, these differences are ascribed to the dominant presence of LSW in the Rockall Trough and both LSW and ISOW in the Iceland Basin.

A more detailed appraisal of the pISOW-normalised values within the Iceland Basin brings to attention sample depths that lie above (IB16 1,686 m) and below (IB9 1,502 m) the error envelope. The higher LREE and MREE concentrations observed in IB16 (1,686 m) suggest interaction with sediments (Pearce et al., 2013; Abbott et al., 2015b; Molina-Kescher et al., 2018), but this is not supported by the beam transmission data, which do not

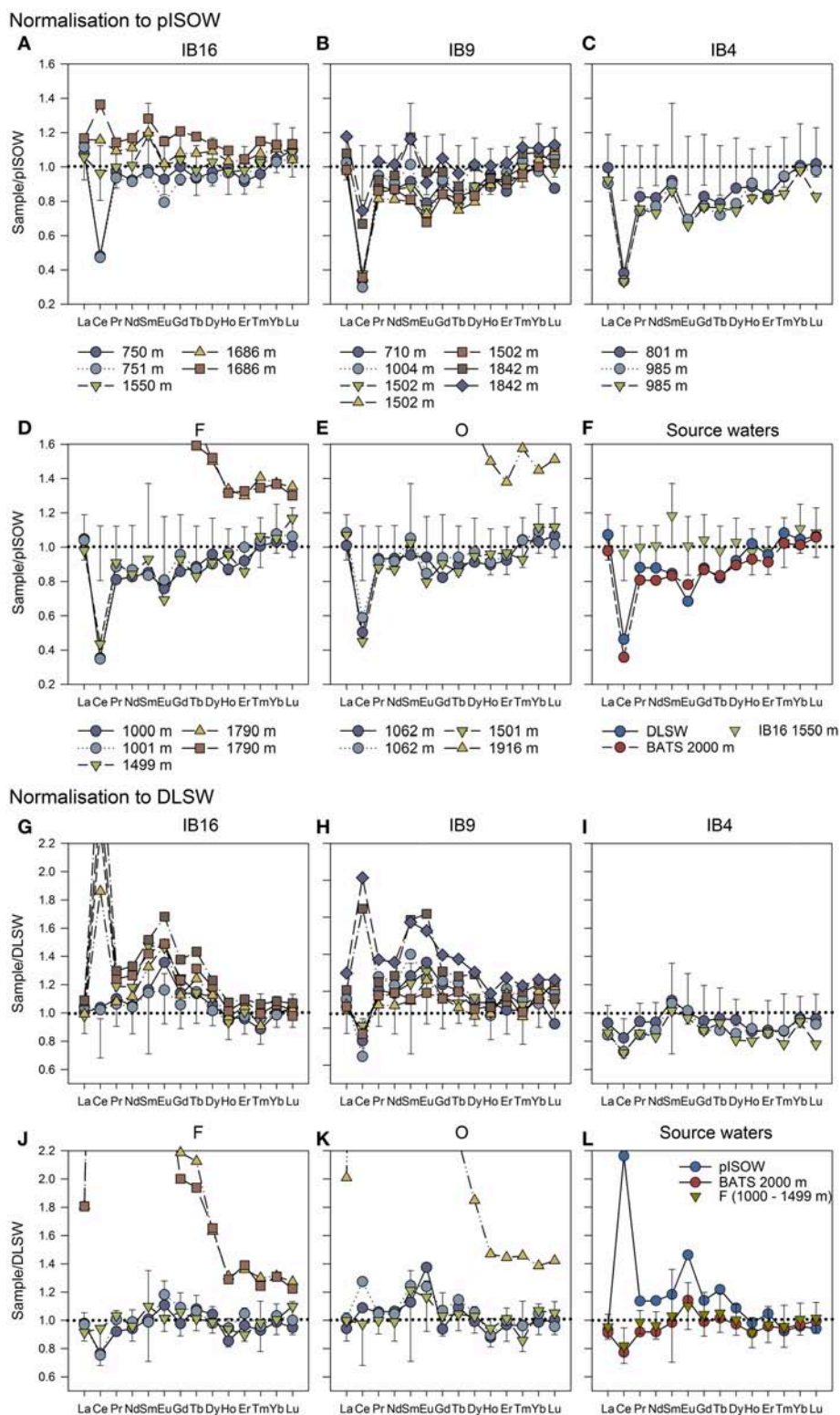


**FIGURE 6 |** Normalisation by pISOW of (A–E) the 5 open ocean stations along the EEL and (F) DLSW and BATS 2000 m. Normalisation by DLSW of (G–K) the 5 open ocean EEL stations and (L) pISOW and BATS 2000 m. The error bars shown in (A–F) represent the combined 2SD from normalisation of IB16 (1550 m, shown in F) by pISOW, and in (G–L) are based on the combined 2SD from normalisation of F (1000–1499 m) by DLSW. The REE concentrations are from the literature: BATS 2000 m (van de Flierdt et al., 2012), pISOW (Lacan and Jeandel, 2004b), and deep (D)LSW (Filippova et al., 2017).



indicate significant suspended sediment (discussed in section Source of Elevated REE Concentrations in the Deep Rockall Trough Samples). Rather the excess dissolved LREE and MREE point to sediment interaction prior to arriving at IB16, possibly during overflow through the Faroe Shetland and Faroe Bank Channels. The sample that lies below the error envelope (IB9 1,502 m) shows greater similarity to LSW. This is expected since waters at this depth at IB9 are largely dominated by LSW (sample  $\sigma_\theta$  of 27.76 kg/m<sup>3</sup>).

The shallower samples (e.g., IB16 750 m, IB9 1,004 m) in the Iceland Basin also fall within the pISOW error envelope, despite the unlikely presence of ISOW at these depths. Some of the LREE and MREE are on the lower edge of the error envelope or below it (Nd, Sm, Eu, Gd). However, the HREE show greater similarity to pISOW. These samples lie within the pycnocline, which is weaker in the Iceland Basin than elsewhere on the EEL (**Figure 2C**), and have properties that are intermediate between surface and deep currents (e.g., respectively  $\sigma_\theta$  of 27.61 and 27.70 kg/m<sup>3</sup>, 6.4 and 4.7°C, 35.11 and 34.97 salinity). As the northeasterly flowing, shallower WNAW ultimately contributes to the return flow of underlying ISOW, we would expect similarity in the HREE but a reduced match in LREE and MREE since the higher concentrations of these in ISOW are postulated to be acquired through sediment interaction during its return transit at depth through the Faroe-Shetland and Faroe Bank Channels. The Iceland Basin is also an area of water recirculation and mixing, and these depths at IB16 and IB9 may reflect the mixing of WNAW with both LSW entering the Iceland Basin from the south and ISOW as it emerges through the Faroe Bank Channel at relatively shallow depths (sill depth of 840 m).

The similarity of the pISOW-normalised REE at IB9 (1,842 m) is problematic in that it shows values close to unity although the potential density of the sample ( $\sigma_\theta$  27.80 kg/m<sup>3</sup>) does not fall in the range normally occupied by ISOW (i.e.,  $\geq 27.85$  kg/m<sup>3</sup>). This deepest IB9 sample also appears to lie within the potential temperature and salinity range of LSW (**Figures 2, 3**). We can use mixing proportions to identify the percentage contributions of each water mass in this sample, assuming two-component mixing. The LREE and MREE are the most discriminatory based on the pISOW-normalised deep DLSW of Filippova et al. (2017; **Figures 6E,L**; **Table 1**). The DLSW signature is based on a mean of REE concentrations at stations 15.5 (1,700 m) and 17.5 (2,000 m). Taking DLSW as unaltered LSW and IB16 (1,550 m) as representative of ISOW, an average contribution can be calculated of ~80% ISOW and ~20% DLSW in the LREE and MREE (Pr, Nd, Eu, Gd, Tb, Dy) in the deep IB9 sample. The calculation excludes La due to similarity in concentration between ISOW at IB16 and DLSW (see **Figure 6L**), and Ce because removal through oxidation makes it less reliable for this purpose. This ratio of ~80:20 ISOW:DLSW in the REE is at odds with the mixing ratio of ~20:80 ISOW:DLSW based on the more conservative properties of potential temperature and salinity. The disparity between the actual REE concentrations at IB9 (1,842 m) and the hypothetical concentrations based on a mixing ratio of ~20:80 ISOW:DLSW reveals the largest increases in Ce, Sm and Eu (25–28%), with lesser increases in the other LREE and MREE ( $\leq 11\%$ ), and HREE ( $\leq 4\%$ ). On the assumption that

two-component ISOW:DLSW mixing is an accurate reflection of the waters at IB9 (1,842 m), this pattern of excess LREE and MREE points to input of a sedimentary or pore water source to the overlying water column, discussed in more detail in section Source of Elevated REE Concentrations in the Deep Rockall Trough Samples. The beam transmission data (Supplementary Figure 1) also show evidence of suspended sediments over the bottom ~14 m. Another mechanism to increase the REE at IB9 (1,842 m), which is ~36 m above the sediment surface, is through particulate desorption of REE in the low beam transmission zone and upward mixing. The impact of external inputs on the distribution of seawater REE concentrations is discussed in more detail in section Source of Elevated REE Concentrations in the Deep Rockall Trough Samples.

### Distal Record of LSW

More generally the pISOW-normalised LREE of intermediate and deep EEL station samples lie below the 2 $\sigma$  error envelope (**Figures 6A–E**), except the deepest sample at each of IB16, IB9, F and O. The trend for the MREE is similar, with an additional prominent Eu depletion relative to pISOW. Based on comparison of characteristic water mass properties (**Table 1**), these intermediate to deep depths at all stations are dominated by LSW, and therefore the REE patterns would not be expected to show similarity to pISOW if they are indeed discriminatory of different water masses. This is further reinforced when the REE concentrations in DLSW collected at source (Filippova et al., 2017) are normalized by pISOW REE (stations 15.5 and 17.5 in **Figures 1A, 6F**). Both this DLSW and the LSW observed along the EEL have shared features relative to pISOW of ~15% lower LREE concentrations (with the exception of La, which is similar in pISOW, DSLW and BATS 2,000 m), fairly prominent depletions of 50% in Ce and 30% in Eu, and steadily rising MREE to HREE concentrations between Tb and Lu.

In **Figures 6G–K**, we normalise the deep EEL data to DLSW to provide a comparison to the other dominant deep water mass encountered in the Iceland Basin and the Rockall Trough. The error envelope in this case represents the combined external error of deep waters at station F (1,000–1,499 m) and DSLW (stations 15.5 and 17.5). There are clear differences between the two basins. Stations F and O have normalised values close to unity (with the exceptions of the deepest samples), indicating similarity to DLSW, and mostly fall within the error envelope (**Figures 6F,K**). Similarities to DLSW are also observed at IB4. At this station, the circulation pattern and origin of the deeper waters (>800 m) are not well constrained, with possible inflow across the Rockall-Hatton Plateau from either the NE Atlantic or from overflow across the Wyville Thomson Ridge (WTR; **Figure 1**). The data presented here strongly suggest an origin in the NE Atlantic and entry via the southern end of the Rockall-Hatton Plateau. If the waters on the Rockall-Hatton Plateau were sourced from ISOW, the LREE and MREE would be expected to have significantly higher concentrations than observed. The strong similarity between the average deep water at station F (1,000–1,499 m) and BATS 2,000 m (**Figure 6L**) suggests a common origin through mixing in the sub-polar gyre before



divergence to the Rockall Trough and the subtropical gyre respectively.

The clearest differences in DLSW relative to pISOW are the lower LREE and MREE concentrations, defined by the depletions in Ce and Eu, in DLSW (**Figures 6F,L**). We can explain these differences by examining the origin of the water masses and their pathways to the point of sampling. From the location of formation in the Labrador Sea, LSW circulates in the NE Atlantic and has less contact than ISOW with continental margins, therefore with the marine sediments and pore waters that carry elevated LREE and MREE in contrast to seawater REE (Abbott et al., 2015b), before arriving in the Rockall Trough. The pISOW on the other hand, travels through narrow channels such as the Faroe-Shetland and Faroe Bank Channels. This provides the opportunity to raise the LREE and MREE concentrations through contact with sedimentary sources (Zhang et al., 2008; Pearce et al., 2013; Abbott et al., 2015b), characterised by the higher Ce concentrations and also the distinctly higher Eu from the regional mafic geology (i.e., Faroe Islands, Iceland).

## Source of Elevated REE Concentrations in the Deep Rockall Trough Samples

The REE concentrations at depth in the coastal stations (IB22/23, 9G) and the Rockall Trough (stations F, O, P) are high (**Figures 4, 5**). These latter open ocean samples also diverge the most from pISOW and DLSW (**Figures 6D,E,J,K**), supporting an extraneous REE contribution. No such anomaly is observed in the Iceland Basin (IB9, IB16) or the Rockall Hatton Plateau (IB4, although no samples were collected from within the zone of low beam transmission). The discussion in the literature on sources of REE to the deep marine water column describes vertical scavenging by particulate REE capture in surface waters and release at depth (e.g., Tachikawa et al., 1999; Siddall et al., 2008). A benthic flux from pore waters to the overlying water column may also be important for the overall marine REE budget (Elderfield and Sholkovitz, 1987; Haley et al., 2004, 2017; Lacan and Jeandel, 2005b; Abbott et al., 2015a,b), where vertical scavenging alone cannot account for deep water REE concentrations (Elderfield and Greaves, 1982). Similar to the benthic flux are REE released into solution during sediment resuspension, through processes of fine particle dissolution, dissolution of labile phases adhered to the particles, and pore water release through disturbance of the sediment (Jeandel et al., 1998; Zhang and Nozaki, 1998; Lacan and Jeandel, 2005b; Arsouze et al., 2009; Pearce et al., 2013; Stichel et al., 2015; Grenier et al., 2018).

The abrupt nature of the concentration change in the deep Rockall Trough points to an upward flux rather than REE desorption from sinking particulates, which generally shows a steadier increase with depth (e.g., Hathorne et al., 2015). In addition the main deep water masses (LSW, ISOW) are young and the water column is not especially deep at the selected stations (<2,000 m), reducing the influence of dissolved REE (and nutrient) accumulation through remineralisation. While advective transport is the dominant process controlling REE concentrations in the intermediate and deep ocean (Elderfield, 1988; Lambelet et al., 2016; Zheng et al., 2016), the restricted

nature of the Rockall Trough and its proximal location to the UK shelf mean other processes are likely to dominate (Jeandel, 2016).

To highlight both the abrupt nature of the concentration change in the deep Rockall Trough and the influence of young water masses circulating in a relatively shallow water column (e.g., <2,300 m) in the northern Rockall Trough, the ratio of increases at depth relative to surface water Nd concentrations ( $[\text{Nd}]_{\text{depth}}/[\text{Nd}]_{\text{surface}}$ ) from stations along the EEL are compared to Southern Ocean data in Hathorne et al. (2015; **Figure 7**). This reveals a divergence in trends below ~1,000 m depth, with low relative increases with depth at the EEL stations and larger relative increases in the Southern Ocean. The exceptions are the deepest samples in the Rockall Trough that show a steep concentration gradient and an increase in Nd concentration relative to the surface waters that is similar to those observed in the Southern Ocean at ~4,500 m depth.

The most obvious reason for the elevated REE concentrations is sample collection from depths where beam transmission is reduced (Supplementary Figure 1), inferring the presence of a benthic nepheloid layer and high particulate concentrations. Based on beam attenuation data, this occurs as a layer ~50 m thick above the sediment surface along UK slope (stations O and P), decreasing to <14 m in mid-Rockall Trough (F), Rockall-Hatton Plateau (IB4) and Iceland Basin (IB9), before disappearing completely in the NW Iceland Basin (IB16).

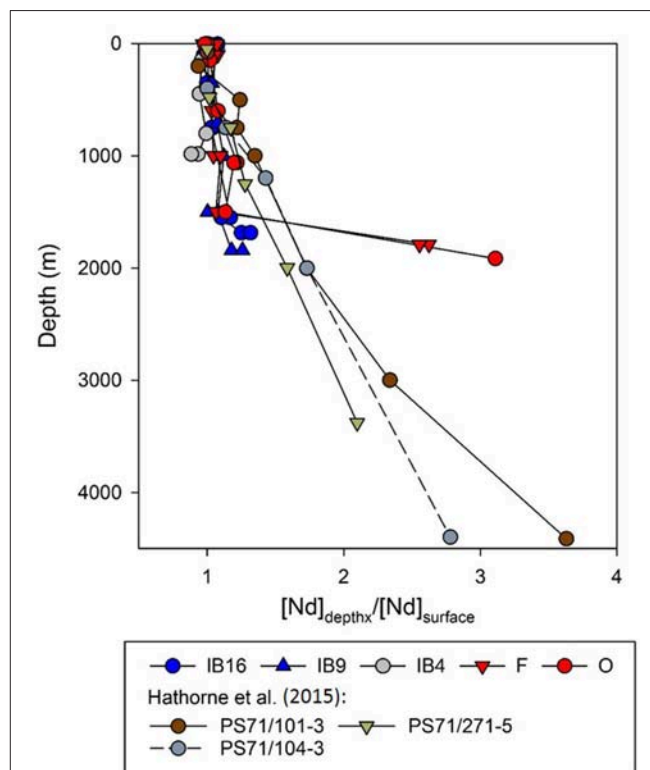


**FIGURE 7** | The water column increase of Nd concentrations at depth relative to the surface ocean ( $[\text{Nd}]_{\text{depth}}/[\text{Nd}]_{\text{surface}}$ ) for the 5 open ocean stations, with comparison to selected stations in the Southern Ocean in Hathorne et al. (2015).

Similarly elevated REE concentrations have been noted at depth in the Sagami Trough, Japan (Zhang and Nozaki, 1998), and on the Mauritanian slope (Stichel et al., 2015), and attributed to REE release from resuspended slope sediments. Resuspension of sediments by currents has been noted in the Rockall Trough, where currents are strong to moderate and flow parallel to bathymetric contours (Lonsdale and Hollister, 1979).

Zhang and Nozaki (1998) postulated that if the REE are chemical analogues to actinium, then the observed release (rather than scavenging) of actinium from slope sediments (Nozaki and Yang, 1987) may also operate for the REE. In this study, the decreased beam transmission close to the seafloor confirms sediment suspension, probably driven by current action that would encourage desorption from resuspended sediments and release of associated pore waters into the overlying water column. The typically higher LREE and MREE concentrations in pore waters, relative to seawater (Abbott et al., 2015b), would drive those deep waters adjacent to the seafloor to acquire REE profiles with higher LREE and MREE concentrations that deviate from typical seawater values. Release of REE from suspended particulates as the source of elevated LREE and MREE, rather than pore waters, is also possible. Here we investigate the potential of pore waters and sediment resuspension to act as a benthic source of dissolved REE to the overlying water column and evaluate the impact on seawater REE distribution.

### Potential Sources

We use the relative differences in PAAS-normalised REE concentrations (see caption to **Figure 8**) and their concentrations to constrain the potential sources (**Figure 8**). Each of the REE sources in **Figure 8** represents an average for clarity, and hides the range of MREE/MREE\* and HREE/LREE associated with specific phases. Both desorption from sediments and pore water release are potential candidates for the elevated REE concentrations observed in the deep water column samples. An indirect analogy is the observation of nutrient release during sediment resuspension experiments, which identified the requirement of both desorption processes and pore water release to account for the observed nutrient increases (Couceiro et al., 2013). The deepest samples with high REE concentrations show greatest similarity in the MREE/MREE\* to labile Fe phases and pore waters (**Figure 8B**). The relationship is less clear cut with the HREE/LREE ratio because the REE sources (labile Fe phases, sedimentary organic matter, Icelandic ash) are less well differentiated by this ratio (**Figure 8C**), although the data are clearly closer to the composition of these sources than typical seawater (represented by BATS 2,000 m and 15 m).

Both the MREE/MREE\* and HREE/LREE (**Figure 8**) show a prominent kink in the trend at ~20% height above seafloor (we present relative depth in this figure to make the coastal station data legible). This represents an artefact of the sampling depths and not the depth to which the benthic nepheloid layer influences the dissolved REE. The thickness of the decreased transmission layer ( $\leq 50$  m) is significantly less than ~20% height above seafloor (i.e., ~290–390 m at F, O, P). Station IB4 has the greatest decrease in beam transmission (80%) of all the stations, but no

apparent influence on the REE concentrations of the deepest sample (985 m) that is located above the decreased transmission layer (top of layer is at ~1,190 m). As a general observation, this suggests that the high REE concentrations observed in benthic nepheloid layers do not “leak” significant REE into the overlying water column. We observe no correlation between the thickness of the benthic nepheloid layer (or low beam transmission) and the REE concentrations of those samples collected within the layer. However, there is a correlation between the extent of beam attenuation and REE concentrations (Supplementary Figure 2). More detailed sampling is necessary to constrain the full extent of influence of the turbid layer on dissolved REE concentrations.

On the basis that the pattern of PAAS-normalised REE concentrations is indicative of the phase or source, the “excess” REE component in the deepest samples can be isolated through subtraction of the overlying water sample to reaffirm the origin of the elevated deep water concentrations (**Figure 9**). The Iceland Basin and Rockall-Hatton Plateau samples show no significant increase, with flat profiles and values close to zero, implying no extraneous inputs of REE at these depths and locations. The Rockall Trough and both coastal stations have positive MREE anomalies, including a prominent positive Eu anomaly for IB22/23 derived from the predominantly volcanic origin of the sediments. The “excess” component in the deep Rockall Trough and coastal samples has concentrations not dissimilar to seawater but the source of the excess REE is not discernible because the potential sources examined here have very similar PAAS normalised profiles (**Figure 9B**). Examination of the Y/Ho ratio (not shown) did not clarify the identification of the contributory phases. However, on the basis that pore waters are derived from a combination of Fe-rich phases, dissolution of volcanic ash, and diagenesis of organic matter, we attribute the excess REE to pore water inputs for the purposes of establishing mixing proportions.

### Mixing Proportions

Considering pore waters as the source of excess REE in the deepest water column samples, the REE composition (MREE/MREE\* and HREE/LREE) can be combined with concentration data to determine the proportional input of pore waters (**Figure 10**). Pore water concentrations can be highly variable, but are generally at least one order of magnitude greater than seawater REE concentrations (Elderfield and Sholkovitz, 1987). In the absence of pore water REE data specific to sediments in the NE Atlantic at the time of sampling, we use the pore water concentrations from Abbott et al. (2015b), which are from a similar shelf to open ocean setting (Oregon margin, eastern North Pacific). Mixing trends are calculated between pore waters from shelf and deep ocean sediment samples, and BATS 15 and 2,000 m seawater respectively, representative of seawater that is unaffected by pore water contributions in both coastal and open ocean water columns. The data are clearly differentiated between the coastal station and deep Rockall Trough samples with high concentrations, and the rest that have little apparent contribution of pore water REE (e.g.,  $\sim \leq 2\%$  HREE from pore waters; **Figure 10**). In this instance a pore water contribution of the order of ~10% for both LREE and MREE is required, relative to the BATS seawater, to account for the observed increase in

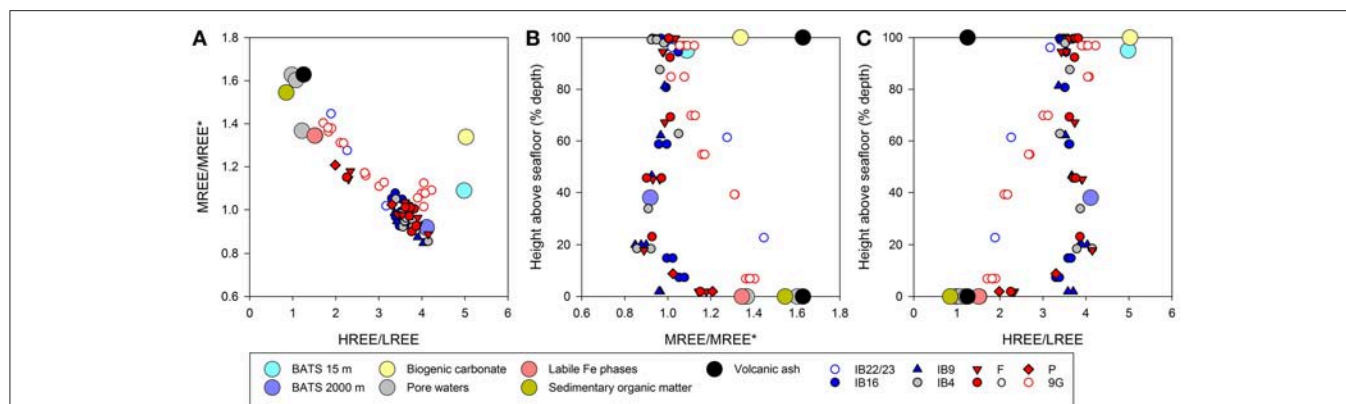


**FIGURE 8 | (A)** The PAAS normalised REE concentrations presented as the MREE anomaly ( $MREE/MREE^* = (Gd+Tb+Dy)/[(La+Pr+Nd+Tm+Yb+Lu)/2]$ ) vs. the HREE/LREE ratio ( $(Tm+Yb+Lu)/(La+Pr+Nd)$ ). Sample depth presented as height above seafloor as a % of the water column depth vs. **(B)**  $MREE/MREE^*$  and **(C)** HREE/LREE. The REE source data (large circles) are collated REE concentrations representing different potential sources of REE in the marine environment, both solid and aqueous phases: Bermuda Atlantic Time Series (BATS) reference seawater from 15 m and 2000 m water depths (van de Flierdt et al., 2012), biogenic carbonate from warm water corals in the North Atlantic (Sholkovitz and Shen, 1995), marine sedimentary pore waters collected in the Northeast Pacific along the Oregon margin, from cores in a depth transect (Abbott et al., 2015b), labile Fe phases (Bayon et al., 2004; Gutjahr et al., 2007; Du et al., 2016), sedimentary organic matter (Freslon et al., 2014), Icelandic ash (Tepe and Bau, 2014). Details of average values used in this study are in Table S3. The pore water data (Abbott et al., 2015b) represent the average REE concentrations in pore waters of the top 5 cm of sediment from cores HH200, HH500, HH1200, and HH3000, corresponding to water column depths of 202, 500, 1,216, and 3,060 m respectively. The depth-related differences in pore water  $MREE/MREE^*$  and HREE/LREE are more clearly seen in **Figure 10**. To note, surface waters from O and all 9G samples were not filtered.

the deep Rockall Trough (F, O, P) and up to 25% at the coastal stations (IB22/23, 9G), with the caveat that actual pore water REE concentrations from the sediments below the EEL may diverge from those of Abbott et al. (2015b). The higher contributions to coastal station water columns are discussed below.

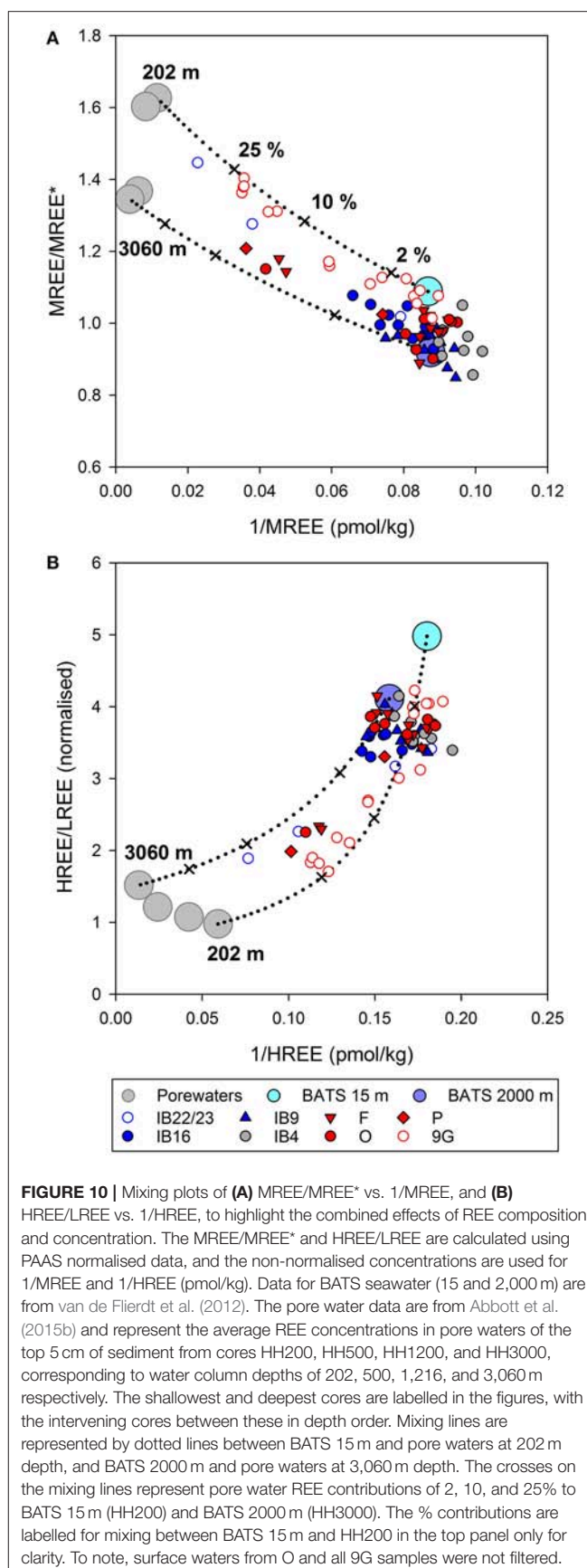
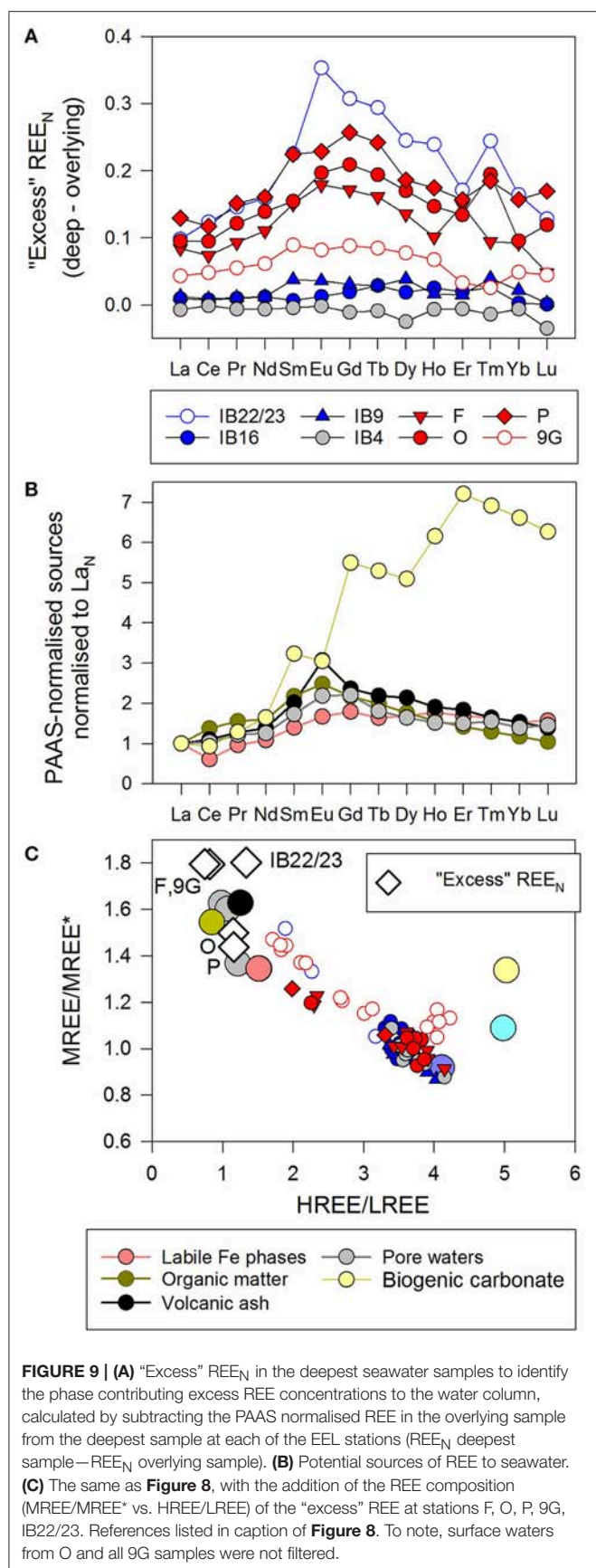
The four water column depths represented by the pore water data of Abbott et al. (2015b) are 202, 500, 1,216, 3,060 m, and they display a depth-related range of REE compositions most clearly seen in **Figure 10B**. The data from the deepest sites (F 1,825 m, O 1,953 m) form a trend defined by mixing between the deeper pore waters and BATS 2,000 m seawater, and not surface ocean water (BATS 15 m) and the shallowest pore water (202 m). This trend towards the deep data supports the observed variation in pore water composition reported by Abbott et al. (2015b) and suggests similar depth-related differences in pore water composition and concentration are also present in the NE Atlantic. The reasons for REE compositional gradients in pore waters are likely associated with sediment composition, reflecting the input of both different particle types and different amounts and reactivities of organic matter to the seafloor to drive diagenetic reactions, as well as current action and benthic activity that determines irrigation of the sediments and therefore contributes to the redox status of the pore waters.

When estimating the sedimentary REE contribution to the water column, the effect of the spring bloom on the seafloor needs to be considered. The samples in this study were collected in late May/early June during the spring bloom. This represents a period of increased transfer of organic matter to the seafloor and heightened benthic activity (e.g., Honjo and Manganini, 1993; Lochte et al., 1993; Pfannkuche, 1993; Rice et al., 1994; Hughes and Gage, 2004). This in itself could increase the rate of transfer

of REE from sediment sources to the overlying water column through bioturbation and bioirrigation. The start of the spring bloom in 2015, defined here as the time at which chlorophyll- $\alpha$  concentrations first exceed  $0.5 \text{ mg/m}^3$ , is identified as late April at stations F and O. This is based on satellite-reported chlorophyll- $\alpha$  concentrations (<http://hermes.acri.fr/>) over the period January to July 2015, and by using mean Chl- $\alpha$  at the pixel closest to the station plus the five surrounding pixels on each side ( $\pm 0.05$  latitude,  $\pm 0.075$  longitude). Particulate fluxes associated with the spring bloom are pulsed and rapid, with observed particle flux transit rates of the order of 4–6 weeks (Lochte et al., 1993). The sampling of stations F and O in June 2015 may therefore have allowed sufficient time for material to reach the seafloor from a bloom initiated in late April 2015. Therefore the REE concentrations in the deep Rockall Trough observed in this study may represent a temporary or seasonal shift.

A further consideration, as mentioned above, is the resuspension of sediments by currents, which occurs along the slopes of the Rockall Trough (Lonsdale and Hollister, 1979). Sediment resuspension experiments noted significant increases in nutrient release, especially silica, attributable to pore waters, desorption and potentially microbial activity on particle surfaces (Couceiro et al., 2013). These features are notable in the silica concentrations in the deep Rockall Trough, and to a lesser extent in phosphate (**Figure 11**). They are possibly linked to the silica biogeochemical cycle dominated by remineralisation of diatom frustules that are hypothesised to have high REE contents (Akagi, 2013). Taken together, diffusion, benthic activity and sediment resuspension may result in enhanced sedimentary REE fluxes to the water column. The seasonal aspect of the sedimentary source of REE to seawater, as a response to the spring bloom, cannot







be evaluated in this study and requires further sampling either side of the spring bloom, when the diffusive flux and sediment resuspension are likely to dominate.

The conspicuous differences between the water column profiles of REE concentrations at the two coastal stations and the five open ocean stations can be partly attributed to effects related to water depth, e.g., <200 m vs. ~1,900 m, with the caveat for station 9G samples that were not filtered. The drivers of diagenesis in the sediments are likely to be more intense on the shelf, for example the reactivity and quantity of organic matter input, the intensity of benthic activity, which shows an inverse relationship with water depth (Henderson et al., 1999), and sediment resuspension due to currents and benthic activity. To establish a quantitative evaluation of the benthic flux (i.e., the cumulative effects of diffusion, benthic activity, sediment resuspension), combined Nd isotope and REE concentration measurements are required under different seasonal conditions.

### Implications for Water Mass Identification

One last point to mention, based on inference from the REE concentrations, is alteration of other deep water characteristics when located in the benthic nepheloid layer (or decreased beam transmission) and/or during heightened benthic activity associated with the spring bloom. The REE concentrations in those samples that lie within nepheloid layers demonstrate the influence of pore water release and/or release from suspended particulates on elevated LREE and MREE concentrations in particular. What of the other measured characteristics, e.g., nutrient and dissolved oxygen concentrations, that may also be present in different concentrations in pore waters compared to seawater? The deep Rockall Trough REE data demonstrate up to ~10% contribution to the seawater REE load. This implies other chemical characteristics of waters in the nepheloid layer may also be shifted to higher or lower values, depending on their concentrations in pore waters, with no significant alteration in the defining properties of a water mass (i.e., temperature, salinity, potential density). All measured nutrients are present in higher concentrations in the very deepest parts of the eastern Rockall Trough, especially silica (Figures 2, 11). More detailed sampling of the lower water column and direct sampling and analysis of sediment pore waters is needed to identify the influence of these on deep water characteristics.

### Biogeochemical Cycling of REE

Haley et al. (2014) identified a “bio-reactive pool” of REE present in the surface ocean, characterized by noticeably lower HREE concentrations. They attributed this to the indirect effects of microbial cycling of iron, possibly as a consequence of the affinity of dissolved REE for organic molecules and ligands associated with iron reduction (Christenson and Schijf, 2011). The presence of a “bio-reactive pool” goes some way to accounting for the frequently observed absence of HREE enrichment that is typical of surface ocean REE profiles (e.g., as observed in the tropical South Atlantic; Zheng et al., 2016), when the expectation is the opposite; i.e., that LREE are preferentially removed from solution, compared to the HREE, due to their greater particle reactivity and also the relatively stronger solution complexation

of the HREE (Cantrell and Byrne, 1987; Byrne and Kim, 1990; Sholkovitz et al., 1994). In this section, we examine the data to determine how the pronounced decrease in dissolved oxygen across the EEL relates to vertical cycling of dissolved REE between the surface ocean and the permanent pycnocline, and if this can elucidate on the “bio-reactive pool” of REE identified by Haley et al. (2014).

### Oxygen Depletion Zone (ODZ)

The Northeast Atlantic has an exceptionally productive annual spring bloom that results in Fe limitation by the summer months (Nielsdottir et al., 2009). The impact of the spring bloom on the water column can be observed in the distribution of dissolved oxygen concentrations, with a minimum at the permanent pycnocline (Figures 2, 12). This ODZ is caused by particles rich in organic matter from the surface ocean that linger and decay during their downward transit to the seafloor. In the Rockall Trough, the ODZ is further enhanced by winter mixing that typically reaches depths of 600 m, and therefore not as deep as the ODZ (i.e., ~800–1,200 m in the Rockall Trough), although it may reach ~1,000 m in severe winters (Meincke, 1986). Lateral advection at these depths in the Rockall Trough is low (Holliday et al., 2000), implying a minimal inherited component of dissolved REE but also a longer residence time of the water that equates to greater potential to accumulate REE compared to elsewhere in the water column. This is not the case in the Iceland Basin, where the ODZ is shallower and more diffuse, and hence more susceptible to obliteration by annual winter mixing and by lateral advection. Also, at the time of sampling the spring bloom was not as well developed in the Iceland Basin, with productivity at least ~4 times lower than in the Rockall Trough (details below).

The combined effects in the Rockall Trough of remineralisation of organic matter from the annual spring bloom, restricted winter mixing depths ( $\leq \sim 600$  m), and minimal lateral advection, likely explain most of the marked depletion of oxygen and/or maximal apparent oxygen utilisation (AOU) values (Figure 12) and the local maxima of nutrient concentrations (Figure 11). These have possibly accumulated over several years until obliterated by mixing during the less frequent severe winters. These effects are not observed in the Iceland Basin because the ODZ is shallower and within the depth range of annual winter mixing. While the dissolved oxygen concentrations in the ODZ are not particularly low (minimum value of  $\sim 209 \mu\text{mol/kg}$ ), they are superimposed on a background of much younger, well ventilated deep waters (ISOW, LSW with  $> 260 \mu\text{mol/kg}$ ) and the well mixed upper water column. These features highlight the cycling of nutrients along the EEL, with removal from the surface ocean during the spring bloom and focused remineralisation of organic matter at the permanent pycnocline, possibly with limited annual return of the remineralised products to the surface ocean. The influence of these processes on dissolved REE in the Rockall Trough between the surface ocean and the permanent pycnocline is therefore dominated by biogeochemical cycling, rather than advection or extraneous inputs.

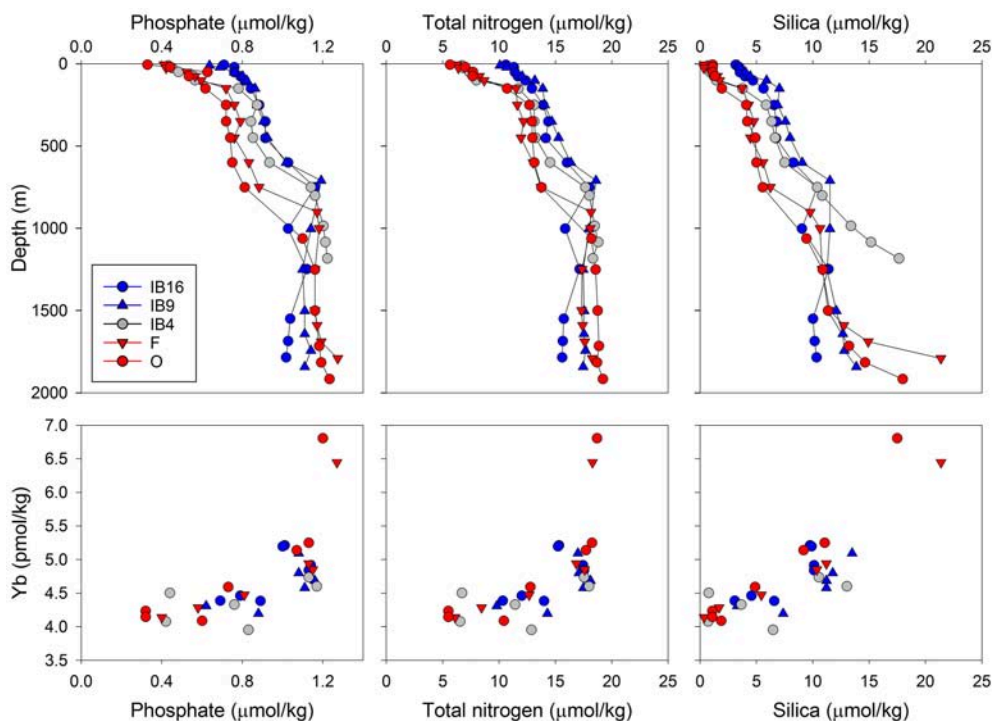


**FIGURE 11 |** Depth variation of the nutrient concentrations ( $\mu\text{mol/kg}$ ) at the 5 open ocean stations in this study. The lower panels show variation in Yb concentration ( $\text{pmol/kg}$ ) vs. each of the three nutrients (phosphate, total nitrogen, silica).

### Differences in REE Between the Surface Ocean and the Permanent Pycnocline—Concentrations and Normalised Distribution Patterns

At each of the five open ocean stations, we took the REE sample with the lowest oxygen concentration in the profile and subtracted the surface water REE to highlight inputs or accumulations of REE due to remineralisation at the permanent pycnocline. The PAAS-normalised REE concentrations in the surface and ODZ samples at stations F and O are shown in **Figure 13C**. To note, the surface samples at O were not filtered. The surface water REE are the very shallowest samples in the dataset, i.e., within 12 m of the surface. In the Rockall Trough, these correspond to the thin veneer ( $<35\text{ m}$ ) of seasonally affected waters ( $\geq 10.5^\circ\text{C}$ ,  $\sigma_\theta < 27.16\text{ kg/m}^3$ ), whereas in the Iceland Basin colder and denser waters outcropped at the surface ( $8.3^\circ\text{C}$ ,  $\sigma_\theta 27.34\text{--}27.38\text{ kg/m}^3$ ) at the time of sampling.

We restrict this comparison to stations F and O, because the Iceland Basin and Rockall-Hatton Plateau did not demonstrate any significant trends. The (ODZ-surface) REE signal of these stations show a depletion in Ce and fairly flat normalised profiles, with up to  $\sim 10\%$  higher REE concentrations at the ODZ than the surface ocean. The absence of a strong remineralisation signal is attributed to the shallower depth of the ODZ in the Iceland Basin and Rockall-Hatton Plateau and the greater frequency with which winter mixing obliterates the annual accumulation of remineralised products. The accumulation of REE, therefore, is less pronounced than in the Rockall Trough.

### Biogeochemical Cycling of HREE in the Rockall Trough

The key feature of the (ODZ-surface) data at stations F and O is the nuanced increase in the HREE concentrations at the ODZ relative to the surface ocean (**Figure 13B**). The depletion in surface ocean HREE and the gain in HREE at the permanent pycnocline requires a mechanism that specifically targets surface water HREE complexation and removal to the pycnocline. An increasing body of work has identified the external complexation of HREE by functional groups on bacterial cell walls (e.g., Takahashi et al., 2005, 2007, 2010; Ngwenya et al., 2009, 2010), the partitioning behaviour of which is illustrated in **Figure 13A**. The HREE enrichment observed on bacteria cell walls is due to the strong binding by multiple phosphate sites (Takahashi et al., 2010), which is not as marked in the other REE. The relative increase in partitioning with increasing atomic mass can be interpreted as an indicator of bacterial activity. In this case, the (ODZ-surface) data and the bacteria/water partition coefficients have striking similarities (**Figure 13**), and suggest biogeochemical cycling of HREE by bacteria in the water column.

It is noted that fish milt accomplishes a very similar effect by an almost identical mechanism to bacteria, with preferential HREE complexation to external phosphate functional groups confirmed in salmon milt (Takahashi et al., 2014). Fish milt is also likely to be present in the pelagic waters of the Rockall Trough (e.g., blue whiting are known to spawn in this region, Hátún et al., 2009). We cannot differentiate between these two possible agents

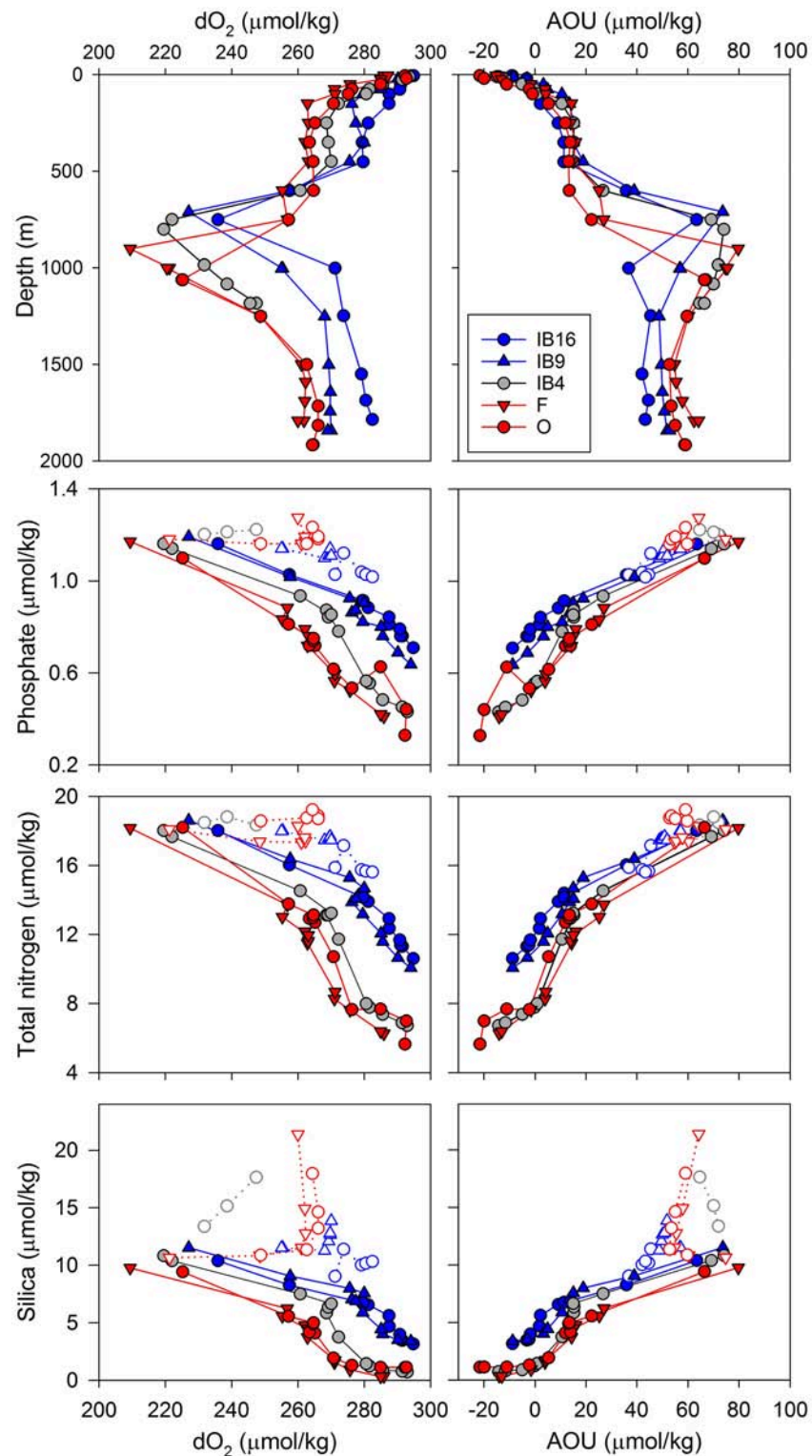


**FIGURE 12 |** Depth variation of dissolved oxygen concentrations ( $\mu\text{mol/kg}$ ) at the 5 open ocean stations in this study (**left column**). The apparent oxygen utilisation (AOU;  $\mu\text{mol/kg}$ ) is also shown for comparison (**right column**). Lower panels show nutrient concentrations (phosphate, total nitrogen, silica) vs. dissolved oxygen and AOU ( $\mu\text{mol/kg}$ ) at the same stations. The open symbols represent waters below the permanent pycnocline.

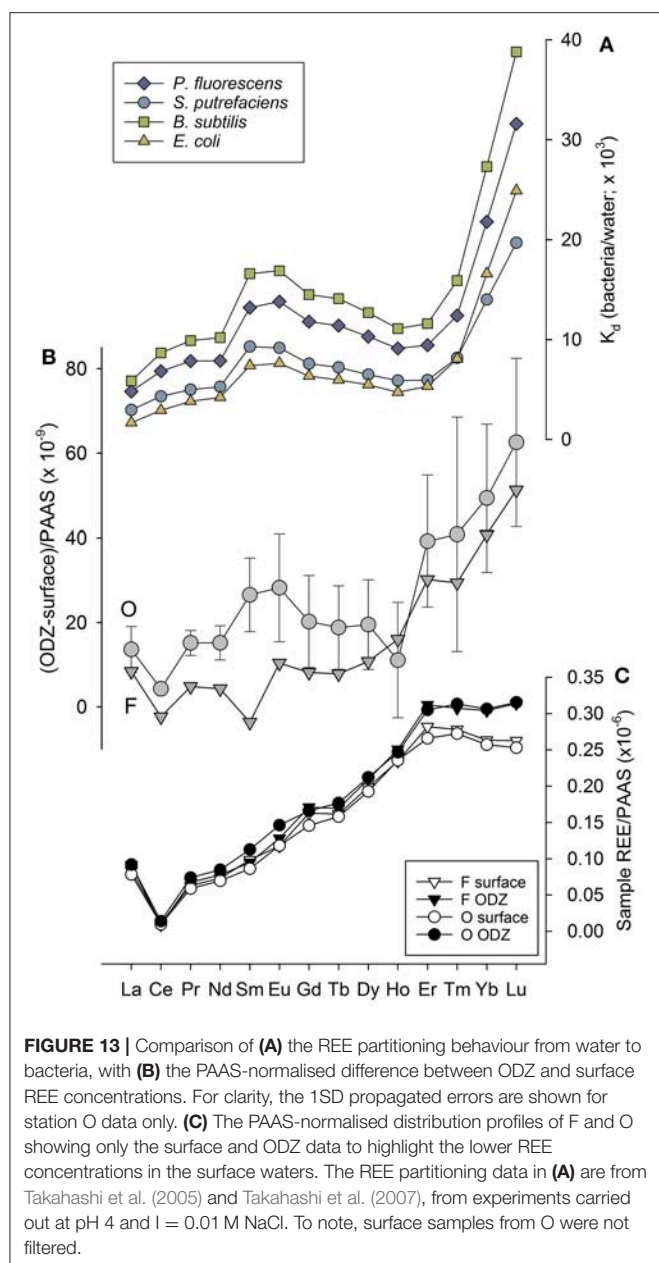


**FIGURE 13 |** Comparison of (A) the REE partitioning behaviour from water to bacteria, with (B) the PAAS-normalised difference between ODZ and surface REE concentrations. For clarity, the 1SD propagated errors are shown for station O data only. (C) The PAAS-normalised distribution profiles of F and O showing only the surface and ODZ data to highlight the lower REE concentrations in the surface waters. The REE partitioning data in (A) are from Takahashi et al. (2005) and Takahashi et al. (2007), from experiments carried out at pH 4 and  $I = 0.01$  M NaCl. To note, surface samples from O were not filtered.

of HREE depletion, but the end result is likely to be the same with either process, i.e., the preferential complexation and removal from solution of dissolved HREE. Fish milt, if not converted into fish spawn, is likely consumed, excreted and exported out of the surface waters. Overall, the greater body of evidence for the rapid increases in the bacterial population during the spring bloom (discussed below) and the similarities in ODZ HREE enrichment to seawater/bacteria REE partitioning behaviour suggest bacterial cycling may be a significant process.

In support of a bacterioplanktonic origin of the relative HREE enrichment at the ODZ, previous studies of the North Atlantic spring bloom have identified a significant and highly variable population of bacteria associated with the development of the

bloom (Ducklow et al., 1993), showing a five-fold increase after initiation of the bloom that constitutes 20–30% of the particulate organic carbon in the surface waters (<50 m). We tentatively propose that the (ODZ-surface) HREE signature observed in this study reflects external sorption of HREE on bacteria in the surface waters, removal of the bacteria to depth by sinking organic matter, and the release of the HREE at the ODZ due to decay of the bacteria. The presence of ODZ bacteria would result in further HREE sorption at these depths. However, in this case, the bacteria would need to be smaller than the filter membrane pore size ( $0.4 \mu\text{m}$ ) in order for the signal to be captured in the measured filtrate.

In summary, the (ODZ-surface) HREE signal is visible in the Rockall Trough by virtue of a combination of factors. The intensity of the spring bloom provides the organic matter that drives the increase in both the surface water and pycnocline bacterial populations. Satellite-reported chlorophyll-*a* concentrations (<http://hermes.acri.fr/>) in May 2015 demonstrate the difference in productivity between the two basins, with higher concentrations in the surface of the Rockall Trough ( $2.4$  and  $1.5 \text{ mg/m}^3$  at stations F and O) than on the Rockall-Hatton Plateau ( $1.0 \text{ mg/m}^3$  at IB4) or in the Iceland Basin ( $0.4$  and  $0.2 \text{ mg/m}^3$  at stations IB9 and IB16). The spring bloom also provides the source of respirable material for oxygen consumption at the pycnocline, resulting in a well-defined ODZ and nutrient maximum. Added to these features, the restricted winter mixing and minimal lateral advection at the depths of the ODZ in the Rockall Trough (described above) mean vertical cycling results in a “distillation” effect, preserving the signal of remineralisation of the REE in the waters of the pycnocline.

The importance of bacteria as a proportion of total biomass in the Rockall Trough during the spring bloom supports the potential extent of this process in productive surface waters. However, this needs further targeted investigation to conclusively demonstrate the role that bacterial activity plays in REE cycling, and if preferential bacterial HREE uptake/release can account for the proportionally greater increase in dissolved HREE accumulation with depth than the LREE, and ultimately the convex shape of that increase (Schijf et al., 2015).

As an addendum to this section about the biological effects on dissolved REE fractionation, we mention the growing evidence for REE involvement in bacterial processes (Martinez-Gomez et al., 2016, and references therein) and the recent observations of seawater LREE depletion associated with methanotrophy following the Deepwater Horizon incident (Shiller et al., 2017). The role of LREE (particularly La) in these biological processes is an active one, rather than the apparently more passive complexation of HREE by phosphate functional groups on bacterial cell or fish milt surfaces (e.g., Takahashi et al., 2010, 2014). Thus far, LREE depletions have been identified in bacteria associated with methanotrophy, and appear to be essential or superior to Ca in the catalysis of enzymes in methanotrophs (Pol et al., 2014). These and similar processes, while not significant in the surface ocean along the EEL, may potentially be relevant in the interpretation of REE variations in other locations



that experience more extreme oxygen depletion or where methanotrophs and similar bacteria are abundant (Pol et al., 2014).

## CONCLUSIONS

The two main deep water masses along the EEL, i.e., LSW and ISOW, are readily identifiable and differentiated through their LREE and MREE concentrations. The HREE are not discriminatory in this instance. The REE profile of ISOW at IB16 is remarkably similar to that of pISOW measured 16 years prior, although the physical properties of the water mass are slightly different. The REE profile of LSW across the EEL was identifiable, relative to ISOW, by its characteristically lower LREE and MREE concentrations, e.g., ~15% lower LREE, prominent depletion of Ce (50%) and Eu (30%). These discrepancies in LREE and MREE concentrations most likely reflect their different trajectories to arrive in the Iceland Basin and the Rockall Trough, with circulation of LSW in the North Atlantic relatively free of contact with continental margin sediments. By comparison ISOW experiences channelling through the Faroe-Shetland and Faroe-Bank Channels that brings it into contact with continental margin sediments and other terrigenous inputs.

The elevated REE concentrations observed in the deep Rockall Trough (but not the Iceland Basin) are attributed to desorption from resuspended sediments and pore water release to the overlying water column. This is based on the similarity in REE composition between the “excess” component identified in the deep samples and typical compositions of pore water REE. In addition, the base of the water column at these stations is characterised by decreased beam transmission, typically associated with suspended particulates in benthic nepheloid layers. The high REE concentrations are also possibly a temporary feature as a result of enhanced bioirrigation and bioturbation in response to the heightened flux of organic matter from the surface ocean during the NE Atlantic spring bloom, already underway by the time of the cruise. An estimated  $\sim \leq 10\%$  contribution from pore waters to the overlying water column is based on mixing between typical pore water and open ocean REE compositions (MREE/MREE\* vs. HREE/LREE). The presence of high dissolved REE concentrations in regions near the seafloor in association with high suspended contents raises the question of how reliably these water masses can be characterised and identified by these, or other, (geo)properties.

A role for the vertical bacterial cycling of HREE is tentatively proposed based on clear similarities between the (ODZ-surface) data and seawater/bacteria partitioning behaviour. The multiple phosphate binding sites on bacterial cell walls preferentially take

up dissolved HREE from the surface ocean and release the HREE into solution during focused remineralisation at the permanent pycnocline. This accounts for the HREE depletion in the highly productive surface waters of the Rockall Trough that, at the time of sampling, were experiencing the spring bloom, and also the relative increase in HREE at the permanent pycnocline. We recognise that the conditions in the Rockall Trough allow for a “distillation” effect to be preserved in the waters of the pycnocline, which may not be present elsewhere.

## AUTHOR CONTRIBUTIONS

All authors contributed to the design of the research and the preparation and revising of the manuscript. All authors approved the final version. EH collected and processed the samples as part of her final year bachelor research project.

## FUNDING

This work was supported by the Scottish Association for Marine Science (SAMS). NERC National Capability Funding for the Extended Ellett Line (R8-H12-85) supported the participation of EH, TB, and SG on the cruise. We acknowledge the MASTS Visiting Fellowship (VF41) received from the Marine Alliance for Science and Technology for Scotland (MASTS) that funded ECH's visit to SAMS and collaboration with KCC in summer 2014 to set up the techniques for the measurement of seawater REE. CJ and SG received funding from the European Union's Horizon 2020 research and innovation programme under grant agreement No 678760 (ATLAS). This output reflects only the authors' views and the European Union cannot be held responsible for any use that may be made of the information contained therein.

## ACKNOWLEDGMENTS

We thank Dr. Tina van de Flierdt, Imperial College London, for providing the GEOTRACES reference seawater BATS 2,000 m for use in this study, and Catherine Jeandel for her editorial handling of the manuscript. We also thank the reviewers for their helpful and insightful comments. Notably we appreciate the assiduity of Reviewer 1 whose comments and observations contributed to greatly clarifying and improving the manuscript.

## SUPPLEMENTARY MATERIAL

The Supplementary Material for this article can be found online at: <https://www.frontiersin.org/articles/10.3389/fmars.2018.00147/full#supplementary-material>

## REFERENCES

- Abbott, A. N., Haley, B. A., and McManus, J. (2015a). Bottoms up: sedimentary control of the deep North Pacific Ocean's  $\epsilon$ Nd signature. *Geology* 43:1035. doi: 10.1130/G37114.1
- Abbott, A. N., Haley, B. A., McManus, J., and Reimers, C. E. (2015b). The sedimentary flux of dissolved rare earth elements to the ocean. *Geochim. Cosmochim. Acta* 154, 186–200. doi: 10.1016/j.gca.2015.01.010
- Akagi, T. (2013). Rare earth element (REE)-silicic acid complexes in seawater to explain the incorporation of REEs in opal and the “leftover” REEs in surface water: new interpretation of dissolved REE distribution profiles. *Geochim. Cosmochim. Acta* 113, 174–192. doi: 10.1016/j.gca.2013.03.014

- Alibo, D. S., and Nozaki, Y. (1999). Rare earth elements in seawater: particle association, shale-normalization, and Ce oxidation. *Geochim. Cosmochim. Acta* 63, 363–372. doi: 10.1016/S0016-7037(98)00279-8
- Arsouze, T., Dutay, J. C., Lacan, F., and Jeandel, C. (2009). Reconstructing the Nd oceanic cycle using a coupled dynamical – biogeochemical model. *Biogeosciences* 6, 2829–2846. doi: 10.5194/bg-6-2829-2009
- Bayon, G., German, C. R., Burton, K. W., Nesbitt, R. W., and Rogers, N. (2004). Sedimentary Fe-Mn oxyhydroxides as paleoceanographic archives and the role of aeolian flux in regulating oceanic dissolved REE. *Earth Planet. Sci. Lett.* 224, 477–492. doi: 10.1016/j.epsl.2004.05.033
- Bertram, C. J., and Elderfield, H. (1993). The geochemical balance of the rare-earth elements and neodymium isotopes in the oceans. *Geochim. Cosmochim. Acta* 57, 1957–1986. doi: 10.1016/0016-7037(93)90087-d
- Buck, C. S., and Paytan, A. (2012). Evaluation of commonly used filter substrates for the measurement of aerosol trace element solubility. *Limnol. Oceanogr. Methods* 10, 790–806. doi: 10.4319/lom.2012.10.790
- Byrne, R. H., and Kim, K. H. (1990). Rare-earth element scavenging in seawater. *Geochim. Cosmochim. Acta* 54, 2645–2656. doi: 10.1016/0016-7037(90)90002-3
- Cantrell, K. J., and Byrne, R. H. (1987). Rare-earth element complexation by carbonate and oxalate ions. *Geochim. Cosmochim. Acta* 51, 597–605. doi: 10.1016/0016-7037(87)90072-x
- Christenson, E. A., and Schijf, J. (2011). Stability of YREE complexes with the trihydroxamate siderophore desferrioxamine B at seawater ionic strength. *Geochim. Cosmochim. Acta* 75, 7047–7062. doi: 10.1016/j.gca.2011.09.022
- Couceiro, F., Fones, G. R., Thompson, C. E. L., Statham, P. J., Sivy, D. B., Amos, C. L., et al. (2013). Impact of resuspension of cohesive sediments at the Oyster Grounds (North Sea) on nutrient exchange across the sediment-water interface. *Biogeochemistry* 113, 37–52. doi: 10.1007/s10533-012-9710-7
- Cutter, G., Andersson, P., Codispoti, L. A., Croot, P., Francois, R., and van der Loeff, M. (2014). “Sampling and Sample-handling Protocols for GEOTRACES Cruises (Version 2.0).” 2015. Available online at: <http://www.geotraces.org/images/stories/documents/intercalibration/Cookbook.pdf>
- De Baar, H. J. W., Bacon, M. P., Brewer, P. G., and Bruland, K. W. (1985). Rare-earth elements in the Pacific and Atlantic Oceans. *Geochim. Cosmochim. Acta* 49, 1943–1959. doi: 10.1016/0016-7037(85)90089-4
- Du, J., Haley, B. A., and Mix, A. C. (2016). Neodymium isotopes in authigenic phases, bottom waters and detrital sediments in the Gulf of Alaska and their implications for paleo-circulation reconstruction. *Geochim. Cosmochim. Acta* 193, 14–35. doi: 10.1016/j.gca.2016.08.005
- Ducklow, H. W., Kirchman, D. L., Quinby, H. L., Carlson, C. A., and Dam, H. G. (1993). Stocks and dynamics of bacterioplankton carbon during the spring bloom in the eastern North Atlantic Ocean. *Deep Sea Res. II Top. Stud. Oceanogr.* 40, 245–263. doi: 10.1016/0967-0645(93)90016-G
- Elderfield, H. (1988). The oceanic chemistry of the rare-earth elements. *Philos. Trans. R. Soc. Math. Phys. Eng. Sci.* 325, 105–126. doi: 10.1098/rsta.1988.0046
- Elderfield, H., and Greaves, M. J. (1982). The rare-earth elements in sea-water. *Nature* 296, 214–219. doi: 10.1038/296214a0
- Elderfield, H., and Sholkovitz, E. R. (1987). Rare-earth elements in the pore waters of reducing nearshore sediments. *Earth Planet. Sci. Lett.* 82, 280–288. doi: 10.1016/0012-821X(87)90202-0
- Filippova, A., Frank, M., Kienast, M., Rickli, J., Hathorne, E., Yashayaev, I. M., et al. (2017). Water mass circulation and weathering inputs in the Labrador Sea based on coupled Hf–Nd isotope compositions and rare earth element distributions. *Geochim. Cosmochim. Acta* 199, 164–184. doi: 10.1016/j.gca.2016.11.024
- Fogelqvist, E., Blindheim, J., Tanhua, T., Osterhus, S., Buch, E., and Rey, F. (2003). Greenland-Scotland overflow studied by hydro-chemical multivariate analysis. *Deep-Sea Res. I Oceanogr. Res. Papers* 50, 73–102. doi: 10.1016/S0967-0637(02)00131-0
- Freslon, N., Bayon, G., Toucanne, S., Bermell, S., Bollinger, C., Cheron, S., et al. (2014). Rare earth elements and neodymium isotopes in sedimentary organic matter. *Geochim. Cosmochim. Acta* 140, 177–198. doi: 10.1016/j.gca.2014.05.016
- Garcia-Solsona, E., Jeandel, C., Labatut, M., Lacan, F., Vance, D., Chavagnac, V., et al. (2014). Rare earth elements and Nd isotopes tracing water mass mixing and particle-seawater interactions in the SE Atlantic. *Geochim. Cosmochim. Acta* 125, 351–372. doi: 10.1016/j.gca.2013.10.009
- German, C. R., Klinkhammer, G. P., Edmond, J. M., Mitra, A., and Elderfield, H. (1990). Hydrothermal scavenging of rare-earth elements in the ocean. *Nature* 345, 516–518. doi: 10.1038/345516a0
- Goldstein, S. L., and Hemming, S. (2003). Long-lived isotopic tracers in oceanography. *Treatise Geochem.* 6, 453–489. doi: 10.1016/B0-08-043751-6/06179-X
- Goldstein, S. J., and Jacobsen, S. B. (1988). REE in the great-whale river estuary, Northwest Quebec. *Earth Planet. Sci. Lett.* 88, 241–252. doi: 10.1016/0012-821X(88)90081-7
- Grasse, P., Bosse, L., Hathorne, E. C., Böning, P., Pahnke, K., and Frank, M. (2017). Short-term variability of dissolved rare earth elements and neodymium isotopes in the entire water column of the Panama Basin. *Earth Planet. Sci. Lett.* 475(Suppl. C), 242–253. doi: 10.1016/j.epsl.2017.07.022
- Grenier, M., Garcia-Solsona, E., Lemaitre, N., Trull, T. W., Bouvier, V., and Jeandel, C. (2018). Differentiating lithogenic supplies, water mass transport and biological processes on and off the Kerguelen Plateau using rare earth element concentrations and neodymium isotopic compositions. *Front. Mar. Sci.* 5.
- Grenier, M., Jeandel, C., and Cravatte, S. (2014). From the subtropics to the equator in the Southwest Pacific: continental material fluxes quantified using neodymium data along modeled thermocline water pathways. *J. Geophys. Res. Oceans* 119, 3948–3966. doi: 10.1002/2013jc009670
- Grenier, M., Jeandel, C., Lacan, F., Vance, D., Venchiarutti, C., Cros, A., et al. (2013). From the subtropics to the central equatorial Pacific Ocean: neodymium isotopic composition and rare earth element concentration variations. *J. Geophys. Res. Oceans* 118, 592–618. doi: 10.1029/2012jc008239
- Gutjahr, M., Frank, M., Stirling, C. H., Klemm, V., van de Flierdt, T., and Halliday, A. N. (2007). Reliable extraction of a deepwater trace metal isotope signal from Fe–Mn oxyhydroxide coatings of marine sediments. *Chem. Geol.* 242, 351–370. doi: 10.1016/j.chemgeo.2007.03.021
- Haley, B. A., Frank, M., Hathorne, E., and Pisias, N. (2014). Biogeochemical implications from dissolved rare earth element and Nd isotope distributions in the Gulf of Alaska. *Geochim. Cosmochim. Acta* 126, 455–474. doi: 10.1016/j.gca.2013.11.012
- Haley, B. A., Klinkhammer, G. P., and McManus, J. (2004). Rare earth elements in pore waters of marine sediments. *Geochim. Cosmochim. Acta* 68, 1265–1279. doi: 10.1016/j.gca.2003.09.012
- Haley, B., Du, J., Abbott, A. N., and McManus, J. (2017). The impact of benthic processes on rare earth element and neodymium isotope distributions in the oceans. *Front. Marine Sci.* 4:426. doi: 10.3389/fmars.2017.00426
- Hathorne, E. C., Haley, B., Stichel, T., Grasse, P., Zieringer, M., and Frank, M. (2012). Online preconcentration ICP-MS analysis of rare earth elements in seawater. *Geochem. Geophys. Geosyst.* 13:Q01020. doi: 10.1029/2011gc003907
- Hathorne, E. C., Stichel, T., Brück, B., and Frank, M. (2015). Rare earth element distribution in the Atlantic sector of the Southern Ocean: the balance between particle scavenging and vertical supply. *Mar. Chem.* 177, 157–171. doi: 10.1016/j.marchem.2015.03.011
- Hátún, H., Payne, M. R., and Jacobsen, J. A. (2009). The North Atlantic subpolar gyre regulates the spawning distribution of blue whiting (*Micromesistius poutassou*). *Can. J. fish. Aquat. Sci.* 66, 759–770. doi: 10.1139/F09-037
- Henderson, G. M., Lindsay, F. N., and Slowey, N. C. (1999). Variation in bioturbation with water depth on marine slopes: a study on the Little Bahamas Bank. *Mar. Geol.* 160, 105–118. doi: 10.1016/S0025-3227(99)00018-3
- Holliday, N. P., and Cunningham, S. A. (2013). The extended ellett line: discoveries from 65 years of marine observations west of the UK. *Oceanography* 26, 156–163. doi: 10.5670/oceanog.2013.17
- Holliday, N. P., Cunningham, S. A., Johnson, C., Gary, S. F., Griffiths, C., Sherwin, T., et al. (2015). Multidecadal variability of potential temperature, salinity, and transport in the eastern subpolar North Atlantic. *J. Geophys. Res. Oceans* 120, 5945–5967. doi: 10.1002/2015JC010762
- Holliday, N. P., Pollard, R. T., Read, J. F., and Leach, H. (2000). Water mass properties and fluxes in the Rockall Trough, 1975–1998. *Deep-Sea Res. I Oceanogr. Res. Papers* 47, 1303–1332. doi: 10.1016/S0967-0637(99)00109-0
- Honjo, S., and Manganini, S. J. (1993). Annual biogenic particle fluxes to the interior of the North Atlantic Ocean; studied at 34°N 21°W and 48°N 21°W. *Deep Sea Res. II Top. Stud. Oceanogr.* 40, 587–607. doi: 10.1016/0967-0645(93)90034-K
- Hughes, D. J., and Gage, J. D. (2004). Benthic metazoan biomass, community structure and bioturbation at three contrasting deep-water sites on the

- northwest European continental margin. *Prog. Oceanogr.* 63, 29–55. doi: 10.1016/j.pocean.2004.09.002
- Jeandel, C. (2016). Overview of the mechanisms that could explain the 'Boundary Exchange' at the land-ocean contact. *Philos. Trans. R. Soc. A Math. Phys. Eng. Sci.* 374:20150287. doi: 10.1098/rsta.2015.0287
- Jeandel, C., Arsouze, T., Lacan, F., Techine, P., and Dutay, J. C. (2007). Isotopic Nd compositions and concentrations of the lithogenic inputs into the ocean: a compilation, with an emphasis on the margins. *Chem. Geol.* 239, 156–164. doi: 10.1016/j.chemgeo.2006.11.013
- Jeandel, C., and Oelkers, E. H. (2015). The influence of terrigenous particulate material dissolution on ocean chemistry and global element cycles. *Chem. Geol.* 395, 50–66. doi: 10.1016/j.chemgeo.2014.12.001
- Jeandel, C., Peucker-Ehrenbrink, B., Jones, M. T., Pearce, C. R., Oelkers, E. H., Arsouze, T., et al. (2011). Ocean margins: the missing term in oceanic element budgets? *Eos Trans. Am. Geophys. Union* 92, 217–218. doi: 10.1029/2011EO260001
- Jeandel, C., Thouron, D., and Fieux, M. (1998). Concentrations and isotopic compositions of neodymium in the eastern Indian Ocean and Indonesian straits. *Geochim. Cosmochim. Acta* 62, 2597–2607. doi: 10.1016/s0016-7037(98)00169-0
- Johnson, C., Inall, M., and Haekkinen, S. (2013). Declining nutrient concentrations in the northeast Atlantic as a result of a weakening Subpolar Gyre. *Deep Sea Res. I Oceanogr. Res. Papers* 82, 95–107. doi: 10.1016/j.dsr.2013.08.007
- Jones, S. M., Cottier, F. R., Inall, M., and Griffiths, C. (2018). Decadal variability on the Northwest European continental shelf. *Prog. Oceanogr.* 161, 131–151. doi: 10.1016/j.pocean.2018.01.012
- Kanzow, T., and Zenk, W. (2014). Structure and transport of the Iceland Scotland Overflow plume along the Reykjanes Ridge in the Iceland Basin. *Deep-Sea Res. I Oceanogr. Res. Papers* 86, 82–93. doi: 10.1016/j.dsr.2013.11.003
- Lacan, F., and Jeandel, C. (2004a). Denmark Strait water circulation traced by heterogeneity in neodymium isotopic compositions. *Deep Sea Res. I Oceanogr. Res. Papers* 51, 71–82. doi: 10.1016/j.dsr.2003.09.006
- Lacan, F., and Jeandel, C. (2004b). Neodymium isotopic composition and rare earth element concentrations in the deep and intermediate Nordic Seas: constraints on the Iceland Scotland Overflow Water signature. *Geochem. Geophys. Geosyst.* 5:Q11006. doi: 10.1029/2004GC000742
- Lacan, F., and Jeandel, C. (2005a). Acquisition of the neodymium isotopic composition of the North Atlantic Deep Water. *Geochemistry Geophysics Geosystems* 6:Q12008. doi: 10.1029/2005GC000956
- Lacan, F., and Jeandel, C. (2005b). Neodymium isotopes as a new tool for quantifying exchange fluxes at the continent-ocean interface. *Earth Planet. Sci. Lett.* 232, 245–257. doi: 10.1016/j.epsl.2005.01.004
- Lambele, M., van de Flierdt, T., Crockett, K., Rehkämper, M., Kreissig, K., Coles, B., Steinfeldt, R., et al. (2016). Neodymium isotopic composition and concentration in the western North Atlantic Ocean: results from the GEOTRACES GA02 section. *Geochim. Cosmochim. Acta* 177, 1–29. doi: 10.1016/j.gca.2015.12.019
- Lim, S., and Franklin, S. J. (2004). Lanthanide-binding peptides and the enzymes that Might Have Been. *Cell. Mol. Life Sci.* 61, 2184–2188. doi: 10.1007/s00018-004-4156-2
- Lochte, K., Ducklow, H. W., Fasham, M. J. R., and Stienen, C. (1993). Plankton succession and carbon cycling at 47°N 20°W during the JGOFS North Atlantic Bloom Experiment. *Deep Sea Res. II Top. Stud. Oceanogr.* 40, 91–114. doi: 10.1016/0967-0645(93)90008-B
- Lonsdale, P., and Hollister, C. D. (1979). A near-bottom traverse of Rockall Trough: hydrographic and geologic inferences. *Oceanol. Acta* 2, 91–105.
- Martinez-Gomez, N. C., Vu, H. N., and Skovran, E. (2016). Lanthanide chemistry: from coordination in chemical complexes shaping our technology to coordination in enzymes shaping bacterial metabolism. *Inorg. Chem.* 55, 10083–10089. doi: 10.1021/acs.inorgchem.6b00919
- McGrath, T., Kivimäe, C., McGovern, E., Cave, R. R., and Joyce, E. (2013). Winter measurements of oceanic biogeochemical parameters in the Rockall Trough (2009–2012). *Earth Syst. Sci. Data* 5, 375–383. doi: 10.5194/essd-5-375-2013
- McGrath, T., Nolan, G., and McGovern, E. (2012). Chemical characteristics of water masses in the Rockall Trough. *Deep Sea Res. I Oceanogr. Res. Papers* 61, 57–73. doi: 10.1016/j.dsr.2011.11.007
- Meincke, J. (1986). Convection in the oceanic waters west of Britain. *Proc. R. Soc. Edinb. Sec. B Biol. Sci.* 88, 127–139. doi: 10.1017/S0269727000004504
- Moffett, J. W. (1990). Microbially mediated cerium oxidation in sea-water. *Nature* 345, 421–423. doi: 10.1038/345421a0
- Molina-Kescher, M., Frank, M., and Hathorne, E. (2014). South Pacific dissolved Nd isotope compositions and rare earth element distributions: water mass mixing versus biogeochemical cycling. *Geochim. Cosmochim. Acta* 127, 171–189. doi: 10.1016/j.gca.2013.11.038
- Molina-Kescher, M., Hathorne, E. C., Osborne, A., Behrens, M. K., Kölling, M., Pahnke, K., et al. (2018). The influence of basaltic islands on the oceanic REE distribution: a case study from the Tropical South Pacific. *Front. Mar. Sci.* 5:50. doi: 10.3389/fmars.2018.00050
- New, A. L., and Smythe-Wright, D. (2001). Aspects of the circulation in the Rockall Trough. *Cont. Shelf Res.* 21, 777–810. doi: 10.1016/S0278-4343(00)00113-8
- Ngwenya, B. T., Magennis, M., Olive, V., Mosselmans, J. F. W., and Ellam, R. M. (2010). Discrete site surface complexation constants for lanthanide adsorption to bacteria as determined by experiments and linear free energy relationships. *Environ. Sci. Technol.* 44, 650–656. doi: 10.1021/es9014234
- Ngwenya, B. T., Mosselmans, J. F. W., Magennis, M., Atkinson, K. D., Tournay, J., Ellam, R. M., et al. (2009). Macroscopic and spectroscopic analysis of lanthanide adsorption to bacterial cells. *Geochim. Cosmochim. Acta* 73, 3134–3147. doi: 10.1016/j.gca.2009.03.018
- Nielsdottir, M. C., Moore, C. M., Sanders, R., Hinz, D. J., and Achterberg, E. P. (2009). Iron limitation of the postbloom phytoplankton communities in the Iceland Basin. *Global Biogeochem. Cycles* 23:GB3001. doi: 10.1029/2008gb003410
- Nozaki, Y., and Yang, H.-S. (1987). Th and Pa isotopes in the waters of the western margin of the Pacific near Japan: evidence for release of <sup>228</sup>Ra and <sup>227</sup>Ac from slope sediments. *J. Oceanogr. Soc. Japan* 43, 217–227. doi: 10.1007/bf02109817
- Pearce, C. R., Jones, M. T., Oelkers, E. H., Pradoux, C., and Jeandel, C. (2013). The effect of particulate dissolution on the neodymium (Nd) isotope and Rare Earth Element (REE) composition of seawater. *Earth Planet. Sci. Lett.* 369–370, 138–147. doi: 10.1016/j.epsl.2013.03.023
- Pfannkuche, O. (1993). Benthic response to the sedimentation of particulate organic matter at the BIOTRANS station, 47°N, 20°W. *Deep Sea Res. II Top. Stud. Oceanogr.* 40, 135–149. doi: 10.1016/0967-0645(93)90010-K
- Pol, A., Barends, T. R., Dietl, A., Khadem, A. F., Eygensteyn, J., Jetten, M. S., et al. (2014). Rare earth metals are essential for methanotrophic life in volcanic mudpots. *Environ. Microbiol.* 16, 255–265. doi: 10.1111/1462-2920.12249
- Rice, A. L., Thurston, M. H., and Bett, B. J. (1994). The IOSDL Deep Seas Program - Introduction and photographic evidence for the presence and absence for a seasonal input of phytodetritus at contrasting abyssal sites in the Northeastern Atlantic. *Deep-Sea Res. I Oceanogr. Res. Papers* 41, 1305–1320. doi: 10.1016/0967-0637(94)90099-x
- Rousseau, T. C., Sonke, J. E., Chmieleff, J., van Beek, P., Souhaut, M., Jeandel, C., et al. (2015). Rapid neodymium release to marine waters from lithogenic sediments in the Amazon estuary. *Nat. Commun.* 6:7592. doi: 10.1038/ncomms8592
- Schijf, J., Christenson, E. A., and Byrne, R. H. (2015). YREE scavenging in seawater: a new look at an old model. *Mar. Chem.* 177(Pt 3), 460–471. doi: 10.1016/j.marchem.2015.06.010
- Schlitzer, R. (2016). *Ocean Data View*.
- Shiller, A. M., Chan, E. W., Joung, D. J., Redmond, M. C., and Kessler, J. D. (2017). Light rare earth element depletion during Deepwater Horizon blowout methanotrophy. *Sci. Rep.* 7:10389. doi: 10.1038/s41598-017-11060-z
- Sholkovitz, E. R. (1993). The geochemistry of rare-earth elements in the Amazon River Estuary. *Geochim. Cosmochim. Acta* 57, 2181–2190. doi: 10.1016/0016-7037(93)90559-f
- Sholkovitz, E. R., Landing, W. M., and Lewis, B. L. (1994). Ocean particle chemistry - the fractionation of rare-earth elements between suspended particles and seawater. *Geochim. Cosmochim. Acta* 58, 1567–1579. doi: 10.1016/0016-7037(94)90559-2
- Sholkovitz, E., and Shen, G. T. (1995). The incorporation of rare earth elements in modern coral. *Geochim. Cosmochim. Acta* 59, 2749–2756. doi: 10.1016/0016-7037(95)00170-5
- Siddall, M., Khaliwala, S., van de Flierdt, T., Jones, K., Goldstein, S. L., Anderson, R. F., et al. (2008). Towards explaining the Nd paradox using reversible scavenging

- in an ocean general circulation model. *Earth Planet. Sci. Lett.* 274, 448–461. doi: 10.1016/j.epsl.2008.07.044
- Stichel, T., Hartman, A. E., Duggan, B., Goldstein, S. L., Scher, H., and Pahnke, K. (2015). Separating biogeochemical cycling of neodymium from water mass mixing in the Eastern North Atlantic. *Earth Planet. Sci. Lett.* 412, 245–260. doi: 10.1016/j.epsl.2014.12.008
- Tachikawa, K., Jeandel, C., and Roy-Barman, M. (1999). A new approach to the Nd residence time in the ocean: the role of atmospheric inputs. *Earth Planet. Sci. Lett.* 170, 433–446. doi: 10.1016/S0012-821X(99)00127-2
- Takahashi, Y., Aondo, K., Miyaji, A., Watanabe, Y., Fan, Q., Honma, T., et al. (2014). Recovery and separation of rare earth elements using salmon milt. *PLoS ONE* 9:e114848. doi: 10.1371/journal.pone.0114858
- Takahashi, Y., Chatellier, X., Hattori, K. H., Kato, K., and Fortin, D. (2005). Adsorption of rare earth elements onto bacterial cell walls and its implication for REE sorption onto natural microbial mats. *Chem. Geol.* 219, 53–67. doi: 10.1016/j.chemgeo.2005.02.009
- Takahashi, Y., Hirata, T., Shimizu, H., Ozaki, T., and Fortin, D. (2007). A rare earth element signature of bacteria in natural waters? *Chem. Geol.* 244, 569–583. doi: 10.1016/j.chemgeo.2007.07.005
- Takahashi, Y., Yamamoto, M., Yamamoto, Y., and Tanaka, K. (2010). EXAFS study on the cause of enrichment of heavy REEs on bacterial cell surfaces. *Geochim. Cosmochim. Acta* 74, 5443–5462. doi: 10.1016/j.gca.2010.07.001
- Taylor, S. R., and McLennan, S. M. (1985). *The Continental Crust: Its Composition and Evolution*. Oxford: Blackwell Scientific Publishers.
- Tepe, N., and Bau, M. (2014). Importance of nanoparticles and colloids from volcanic ash for riverine transport of trace elements to the ocean: evidence from glacial-fed rivers after the 2010 eruption of Eyjafjallajökull Volcano, Iceland. *Sci. Total Environ.* 488, 243–251. doi: 10.1016/j.scitotenv.2014.04.083
- van de Flierdt, T., Pahnke, K., Amakawa, H., Andersson, P., Basak, C., Coles, B., et al. (2012). GEOTRACES intercalibration of neodymium isotopes and rare earth element concentrations in seawater and suspended particles. Part 1: reproducibility of results for the international intercomparison. *Limnol. Oceanogr. Methods* 10, 234–251. doi: 10.4319/lom.2012.10.234
- Wang, B.-S., Lee, C.-P., and Ho, T.-Y. (2014). Trace metal determination in natural waters by automated solid phase extraction system and ICP-MS: the influence of low level Mg and Ca. *Talanta* 128, 337–344. doi: 10.1016/j.talanta.2014.04.077
- Wilson, D. J., Crocket, K. C., van de Flierdt, T., Robinson, L. F., and Adkins, J. F. (2014). Dynamic intermediate ocean circulation in the North Atlantic during Heinrich Stadial 1: a radiocarbon and neodymium isotope perspective. *Paleoceanography* 29, 1072–1093. doi: 10.1002/2014PA002674
- Zhang, J., and Nozaki, Y. (1996). Rare earth elements and yttrium in seawater: ICP-MS determinations in the East Caroline, Coral Sea, and South Fiji basins of the western South Pacific Ocean. *Geochim. Cosmochim. Acta* 60, 4631–4644. doi: 10.1016/S0016-7037(96)00276-1
- Zhang, J., and Nozaki, Y. (1998). Behavior of rare earth elements in seawater at the ocean margin: a study along the slopes of the Sagami and Nankai troughs near Japan. *Geochim. Cosmochim. Acta* 62, 1307–1317. doi: 10.1016/S0016-7037(98)00073-8
- Zhang, Y., Lacan, F., and Jeandel, C. (2008). Dissolved rare earth elements tracing lithogenic inputs over the Kerguelen Plateau (Southern Ocean). *Deep Sea Res. II Top. Stud. Oceanogr.* 55, 638–652. doi: 10.1016/j.dsr2.2007.12.029
- Zheng, X.-Y., Plancherel, Y., Saito, M. A., Scott, P., and Henderson, G. M. (2016). Rare earth elements (REEs) in the tropical South Atlantic and quantitative deconvolution of their non-conservative behaviour. *Geochim. Cosmochim. Acta* 177, 217–237. doi: 10.1016/j.gca.2016.01.018

**Conflict of Interest Statement:** The authors declare that the research was conducted in the absence of any commercial or financial relationships that could be construed as a potential conflict of interest.

The reviewer MG and handling Editor declared their shared affiliation.

Copyright © 2018 Crocket, Hill, Abell, Johnson, Gary, Brand and Hathorne. This is an open-access article distributed under the terms of the Creative Commons Attribution License (CC BY). The use, distribution or reproduction in other forums is permitted, provided the original author(s) and the copyright owner are credited and that the original publication in this journal is cited, in accordance with accepted academic practice. No use, distribution or reproduction is permitted which does not comply with these terms.





## OPEN ACCESS

### Edited by:

Sunil Kumar Singh,  
Physical Research Laboratory, India

### Reviewed by:

Ed Hathorne,  
Christian-Albrechts-Universität zu Kiel,  
Germany  
Maxime M. Grand,  
Moss Landing Marine Laboratories,  
United States  
Vineet Goswami,  
Colorado State University,  
United States

### \*Correspondence:

Melanie Grenier  
melanie.grenier@legos.obs-mip.fr;  
melaniegrenier14@yahoo.fr

### †Present Address:

Ester Garcia-Solsona,  
GRC Geociències Marines,  
Departament de Dinàmica de la Terra i  
de l'Oceà, Facultat de Ciències de la  
Terra, Universitat de Barcelona,  
Barcelona, Spain  
Nolwenn Lemaître,  
Department of Earth Sciences,  
Institute of Geochemistry and  
Petrology, ETH-Zürich, Zurich,  
Switzerland  
Vincent Bouvier,  
GET, Université de Toulouse, CNRS,  
CNRS, IRD, Toulouse, France

‡Francois Lacan  
orcid.org/0000-0001-6794-2279

### Specialty section:

This article was submitted to  
Marine Biogeochemistry,  
a section of the journal  
Frontiers in Marine Science

Received: 04 December 2017

Accepted: 24 October 2018

Published: 20 November 2018

# Differentiating Lithogenic Supplies, Water Mass Transport, and Biological Processes On and Off the Kerguelen Plateau Using Rare Earth Element Concentrations and Neodymium Isotopic Compositions

Melanie Grenier<sup>1,2\*</sup>, Ester Garcia-Solsona<sup>1,3†</sup>, Nolwenn Lemaître<sup>1,4†</sup>, Thomas W. Trull<sup>2,5</sup>, Vincent Bouvier<sup>1†</sup>, Philippe Nonnotte<sup>6</sup>, Pieter van Beek<sup>1</sup>, Marc Souhaut<sup>1</sup>, Francois Lacan<sup>1‡</sup> and Catherine Jeandel<sup>1</sup>

<sup>1</sup> LEGOS, Université de Toulouse, CNES, CNRS, IRD, Toulouse, France, <sup>2</sup> Antarctic Climate and Ecosystems CRC, University of Tasmania, Hobart, TAS, Australia, <sup>3</sup> Institut de Ciència i Tecnologia Ambientals, Universitat Autònoma de Barcelona, Bellaterra, Spain, <sup>4</sup> Laboratoire des sciences de l'environnement marin (LEMAR), Université de Bretagne Occidentale, Brest, France, <sup>5</sup> CSIRO Oceans and Atmosphere, Hobart, TAS, Australia, <sup>6</sup> Laboratoire Géosciences Océan, Université de Bretagne Occidentale, CNRS, IRD, UMR6539, IUEM, Technopole Brest Iroise, Plouzané, France

Distributions of dissolved rare earth element (REE) concentrations and neodymium isotopic compositions (expressed as  $\epsilon_{Nd}$ ) of seawater over and off the Kerguelen Plateau in the Southern Ocean are presented. The sampling took place during the austral spring bloom in October–November 2011 (KEOPS2 project, GEOTRACES process study) and aimed to further the investigations of the KEOPS1 austral summer study in terms of sources and transport of lithogenic material, and to investigate the impact of local biogeochemical cycles on the REE distributions. The REE signature of the coastal eastern Kerguelen Islands waters was characterized by negative europium anomalies ( $Eu/Eu^*$ ) and negative  $\epsilon_{Nd}$  in filtered samples. By contrast, the unfiltered sample showed a positive  $Eu/Eu^*$  and more radiogenic  $\epsilon_{Nd}$ . These distinct signatures could reflect either differential dissolution of the local flood basalt minerals or differential leaching of local trachyte veins. The dissolved Kerguelen coastal REE patterns differ from those observed close to Heard Island, these latter featuring a positive  $Eu/Eu^*$  and a less radiogenic  $\epsilon_{Nd}$  (Zhang et al., 2008). These differences enabled us to trace the transport of waters (tagged by the Kerguelen REE signature) 200 km downstream from the coastal area, north of the Polar Front. Northward transport of the central Plateau shallow waters, enriched by both local vertical supplies and lateral advection of inputs from Heard Island, was also evident. However, the transport of Kerguelen inputs southeastward across the Polar Front could not be discerned (possibly as a result of rapid dilution or scavenging of REE signatures), although evidence for such transport was found previously using Ra isotopes (Sanial et al., 2015). Comparison of the REE patterns at stations sampled prior, during and at the

demise of the bloom revealed diverse fractionations, including production of significant lanthanum and europium anomalies, which are tentatively ascribed to chemical reactions with various inorganic and biogenic phases, including surface coatings, barite crystals, and biogenic silica.

**Keywords:** Southern Ocean, Kerguelen Islands, rare earth elements, fractionation, anomalies, lithogenic, biologic, GEOTRACES

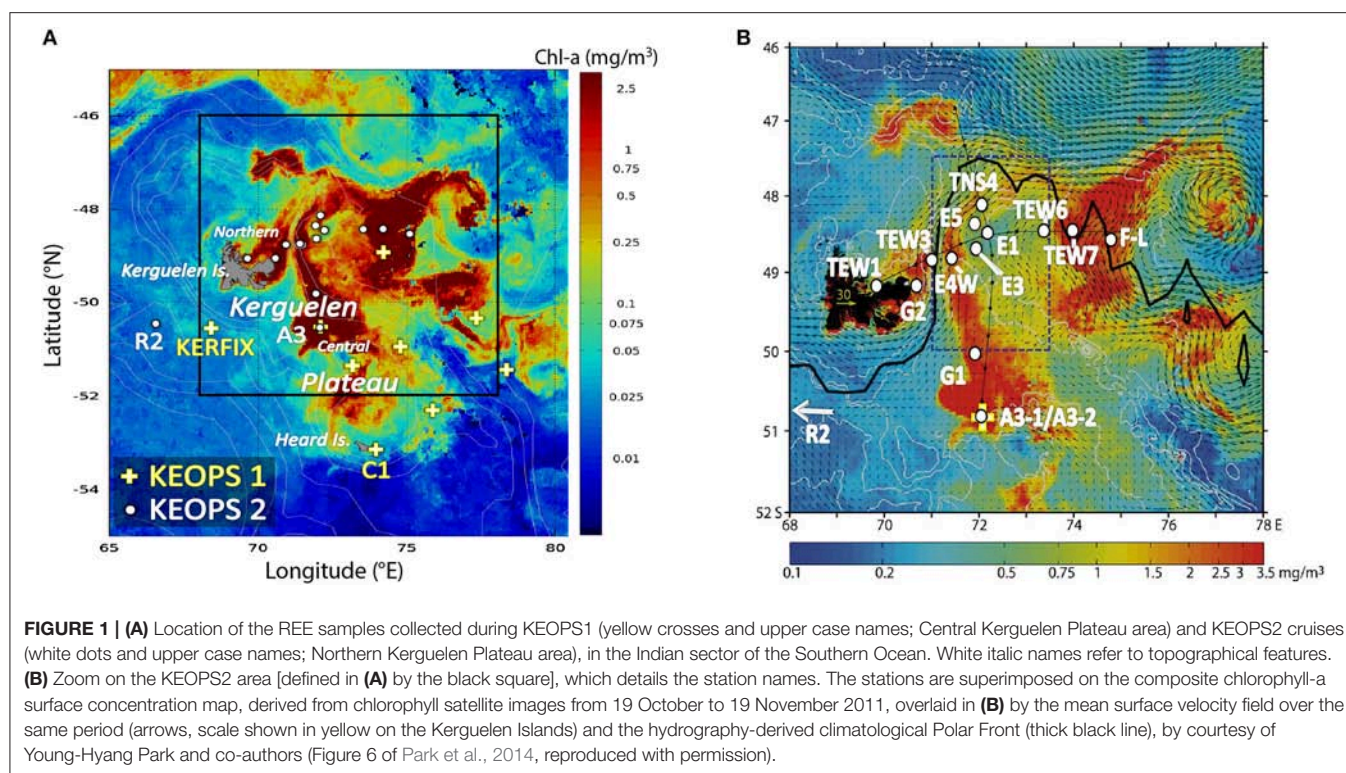
## INTRODUCTION

The Southern Ocean is recognized as the major high-nutrient, low-chlorophyll (HNLC) oceanic region, where phytoplankton growth is limited by a low availability of the micronutrient iron (Fe; Martin, 1990; de Baar et al., 1995; Boyd et al., 2007). Nevertheless, natural iron fertilization occurs in some locations of the Southern Ocean, as a consequence of the release of Fe from the shelf sediments (Tagliabue et al., 2009, 2014). Thus, patches of high phytoplankton biomass can be observed off the Antarctic continental shelf (Moore and Abbott, 2002; Arrigo et al., 2008) or around subantarctic islands (Blain et al., 2001; Korb et al., 2004; Pollard et al., 2007; Tarling et al., 2012; Measures et al., 2013). A recurrent annual phytoplankton bloom is notably observed in the Indian sector of the Southern Ocean, in the vicinity of the Kerguelen Plateau (Blain et al., 2001, 2007). This bloom—one of the largest of the Southern Ocean—extends more than 1,000 km downstream of the Kerguelen Islands, on either side of the Polar front (PF; **Figure 1**). The northern branch extends northeast of the island, off the Northern Kerguelen Plateau, while the larger southern part mostly extends over the Central Kerguelen Plateau (Mongin et al., 2008). The KEOPS1 and KEOPS2 (Kerguelen Ocean and Plateau compared Study, PI: S. Blain) projects aimed at understanding the physical, chemical and biological processes that are responsible for the phytoplankton bloom observed over and downstream of the Kerguelen Plateau. The KEOPS1 cruise was conducted in the Central Kerguelen Plateau area in austral summer 2005, during the decline of the bloom (Blain et al., 2007). The complementary KEOPS2 cruise was mostly conducted in the Northern Kerguelen Plateau area in spring 2011, during the onset of the bloom (Carlotti et al., 2015; **Figure 1**).

The major dissolved Fe sources to the upper ocean are considered to be the dissolution of atmospheric aerosols and of sedimentary particles deposited onto continental margins (Coale et al., 1996; Johnson et al., 1999; Elrod et al., 2004; Blain et al., 2008; Tagliabue et al., 2009; Jeandel et al., 2011; Labatut et al., 2014). Similarly to Fe, rare earth elements (REEs) are supplied to the oceans from the continents (Goldstein and Hemming, 2003), notably from the dissolution of sedimentary particles deposited onto shelves and upper slopes (Jeandel et al., 1998; Lacan and Jeandel, 2001, 2005; Grenier et al., 2013). As in many other areas (Arsouze et al., 2007; Jeandel et al., 2011; Radic et al., 2011), the sedimentary source was suggested to be the dominant source of Fe and REEs in seawater in the central part of the Kerguelen Plateau, refueling the stocks through vertical supplies from the plateau sediments (Blain et al., 2008; Zhou et al., 2014) or through lateral advection of supplies from the continental shelf

of Heard Island (van Beek et al., 2008; Zhang et al., 2008; Chever et al., 2010). KEOPS1 results revealed that marine Fe and REEs had the same main sedimentary origin in the Kerguelen area, underlining the relevance of the use of REEs to trace the local lithogenic sources and their transport along the circulation for the complementary KEOPS2 project.

REEs are a set of elements with similar atomic structure and chemical properties and hence behave coherently in natural systems (Elderfield and Greaves, 1982; Elderfield, 1988). They are mostly found in the 3+ oxidation state and are particle reactive, exhibiting increasing concentrations with depth (e.g., Elderfield, 1988). Despite their chemical coherence, several processes (e.g., adsorption, re-mineralisation, scavenging, oxidation, etc.) may cause slight fractionations within the group with respect to the average continental source, which are revealed by shale-normalized REE patterns. A typical open-ocean shale-normalized REE pattern displays a heavy REE (HREE; Tb-Lu) enrichment relative to the light REE (LREE; La-Gd) that has commonly been attributed to preferential LREE scavenging by marine particles (Elderfield, 1988; Byrne and Kim, 1990; McLennan, 1994). However, it was also recently attributed to dissolution of HREE-enriched diatom opal (Akagi et al., 2011). In addition, the shale-normalized REE pattern is typically depleted in dissolved cerium ( $\text{Ce}^{3+}$ ) relative to its neighboring REEs, due to the low solubility of the oxidized form of this element ( $\text{Ce}^{4+}$ ; Elderfield, 1988; Byrne and Kim, 1990; Moffett, 1990; Bertram and Elderfield, 1993; Sholkovitz et al., 1994; German et al., 1995; Tachikawa et al., 1999b). Variations from this typical pattern can provide information on the types of processes occurring during particulate-dissolved exchange. Close to a lithogenic source, the Ce anomaly will tend to be much smaller and the shale normalized  $\text{Nd}_n/\text{Yb}_n$  ratio much higher than in the open-ocean; however, the dissolved REE pattern may also reveal specific characteristics of the geological nature of the weathered lithogenic matter (Sholkovitz et al., 1999; Chavagnac et al., 2007, 2008; Zhang et al., 2008; Grenier et al., 2013). The dissolved REE pattern may be influenced by additional processes occurring *in situ* in the water column, i.e., exchanges between the dissolved phase and authigenic inorganic or biological particles such as calcium carbonate, opal, barite, organic matter, or Fe/Mn oxy-hydroxide coatings (Sholkovitz et al., 1994; Lerche and Nozaki, 1998; Alibo and Nozaki, 1999; Tachikawa et al., 1999b; Nozaki and Alibo, 2003; Haley et al., 2004, 2014; Hara et al., 2009; Akagi et al., 2011; Stichel et al., 2012; Garcia-Solsona et al., 2014; Molina-Kescher et al., 2014; Strady et al., 2015; Shiller et al., 2017).



Among the LREEs, neodymium (Nd) is studied to a greater extent because its radiogenic isotopic composition (IC), expressed as  $\epsilon_{\text{Nd}}^1$ , is a useful tool to trace oceanic processes given that it is not affected by biological or thermodynamic fractionation. As the  $\epsilon_{\text{Nd}}$  of the rocks varies according to their nature, and more specifically according to the age and samarium content of the rock, the  $\epsilon_{\text{Nd}}$  of the rocks outcropping around the ocean margins is heterogeneous and tags the seawater accordingly, mostly through particle dissolution (Jeandel et al., 2007). Furthermore, because Nd has an oceanic residence time long enough to be transported within the global thermohaline circulation without complete homogenization (Tachikawa et al., 1999a; Siddall et al., 2008; Arsouze et al., 2009),  $\epsilon_{\text{Nd}}$  variations of a water mass along its circulation are a powerful tracer of lithogenic supplies to the ocean and/or tracer of mixing with a water mass tagged by a distinct  $\epsilon_{\text{Nd}}$  signature (Piepgras et al., 1979; Frank, 2002; Goldstein and Hemming, 2003; Tachikawa et al., 2003, 2004; Lacan and Jeandel, 2004, 2005; Carter et al., 2012; Grenier et al., 2013, 2014; Jeandel et al., 2013; Garcia-Solsona et al., 2014; Osborne et al., 2014).

Recent publications of lithogenic tracer distributions measured in the framework of the KEOPS2 project have already brought complementary information to the KEOPS1 results. Notably, high contents of radium isotopes (including the short-lived nuclides) were observed in the eastern Kerguelen coastal waters and also further east both north and south of the

PF indicating recent input of waters that had interacted with the shallow sediments of the Kerguelen plateau, and suggesting rapid transport of these waters across the PF (Sanial et al., 2015). These results led to the conclusion that the PF does not act as a complete physical barrier for the south-eastward transport of lithogenic material of Kerguelen origin. These observations were corroborated by the dissolved Fe and particulate trace metal distributions (Qu  rou   et al., 2015; van der Merwe et al., 2015). These latter studies have also presumed a contribution from direct fluvial runoff and/or glacial melting from the Kerguelen and Heard Islands. Other works characterized different spatial and temporal systems of production, remineralization, and export associated with the Kerguelen phytoplankton bloom (e.g. Christaki et al., 2014; Jouandet et al., 2014; Lasbleiz et al., 2014; Jacquet et al., 2015; Laurenceau-Cornec et al., 2015; Planchon et al., 2015; Trull et al., 2015). Discerning the impacts that these different processes may have on local REE distributions is very useful given the expanding use of REEs to explore biogeochemical cycles.

The KEOPS2 work presented here seeks to complement the KEOPS1 observations of Zhang et al. (2008) regarding the REE distributions in the Kerguelen Plateau area during the productive season, focusing on the sources, transport and fate of the dissolved REEs in this naturally fertilized region. More precisely, this paper presents the dissolved REE concentrations and Nd IC of 13 supplementary stations collected upstream, over and downstream of the Northern Kerguelen Plateau, from coastal areas to deep offshore stations, north and south of the PF, in and outside of the phytoplankton bloom core. This diverse sampling aims to characterize the REE features in

<sup>1</sup> $\epsilon_{\text{Nd}} = [({}^{143}\text{Nd}/{}^{144}\text{Nd})_{\text{SAMPLE}}/({}^{143}\text{Nd}/{}^{144}\text{Nd})_{\text{CHUR}} - 1] \times 10^4$ , where  $({}^{143}\text{Nd}/{}^{144}\text{Nd})_{\text{CHUR}} = 0.512638$  (Wasserburg et al., 1981). CHUR, Chondritic Uniform Reservoir; present day average Earth value.



the different environments that compose the area in order to investigate the lithogenic supplies and authigenic processes—inorganically or biologically mediated—that shape the local REE distribution. This work contributes to the larger KEOPS objective to characterize the Kerguelen Plateau, a key area of the Southern Ocean in terms of ecosystems and the carbon dioxide biological pump.

## HYDROLOGICAL FEATURES OF THE STATIONS

### Location of the Stations in the Regional Physical and Biological Context

Station locations are represented in **Figure 1** on the composite chlorophyll-*a* surface concentration map, derived from chlorophyll-*a* satellite images from 19 October to 19 November 2011, overlaid in **Figure 1B** by the mean surface velocity field over the same period, by courtesy of Young-Hyang Park and co-authors (Figure 6 of Park et al., 2014). The largescale view (**Figure 1A**) shows the location of stations sampled for the REE analysis—hereafter “REE stations”—during the two KEOPS cruises. The KEOPS1 sampling (Zhang et al., 2008) mostly documented the central part of the plateau, extending as far south as the Heard Island coastal station, whereas the KEOPS2 cruise (austral spring 2011) mostly documented the northern part of the plateau, and offshore waters east of the Kerguelen Islands. West of the Kerguelen Islands, KERFIX and R2 were chosen as reference stations for Antarctic Circumpolar Current waters prior to contact with the Kerguelen Plateau for KEOPS1 and KEOPS2, respectively. Over the Central Plateau, at the location displaying the highest chlorophyll-*a* content, station A3 was sampled twice during KEOPS1 and reoccupied and sampled twice again during KEOPS2, around the beginning and the end of each cruise. This repeated sampling of the same site at four different times of the bloom season provides a time series perspective.

Zooming in on the area delimited by the black square in **Figure 1A** allows us to focus on the location characteristics of the KEOPS2 stations (**Figure 1B**). Kerguelen coastal waters were sampled at two stations, TEW1 and G2, which were the only stations located north of the Polar Front (PF; thick black line, from Park et al., 2014). Four stations were located in the PF vicinity: R2, west of the Kerguelen Plateau; TEW3, northeast of the coastal stations, over the plateau, surrounded by chlorophyll-*a*-rich waters on its western side and a tongue of low surface chlorophyll concentration on its eastern side; TEW7 and F-L, in the eastern part of the cyclonic meander structure of the PF, marked by high surface chlorophyll concentrations.

All the other stations were located south of the PF. Two stations were sampled over the plateau: A3 (visited twice: A3-1 and A3-2), and G1, north of A3 and located in the same high surface chlorophyll-*a* concentration patch that extends northward (**Figure 1**). The other stations were sampled in the PF cyclonic meander area. Turning clockwise from the west, E4-W, TNS4, and TEW6 were located within the strong flow of the recirculation, marked by a decreasing gradient of surface

chlorophyll concentrations from high to moderate (from  $\sim 3.5$  to  $\sim 1 \text{ mg m}^{-3}$ ). Going from E5 to E3 to E1, the chlorophyll-*a* concentration decreased from moderate to low, similarly to the flow strength, E1 being located in the vicinity of the recirculation center. The complex topography and circulation scheme characterizing the Kerguelen Plateau region have been suggested to play an important role in the mosaic structure of the phytoplankton bloom observed in **Figure 1** (Lasbleiz et al., 2014; Park et al., 2014; d'Ovidio et al., 2015; Sanial et al., 2015). They also largely explain the variety of water masses observed locally, as described below.

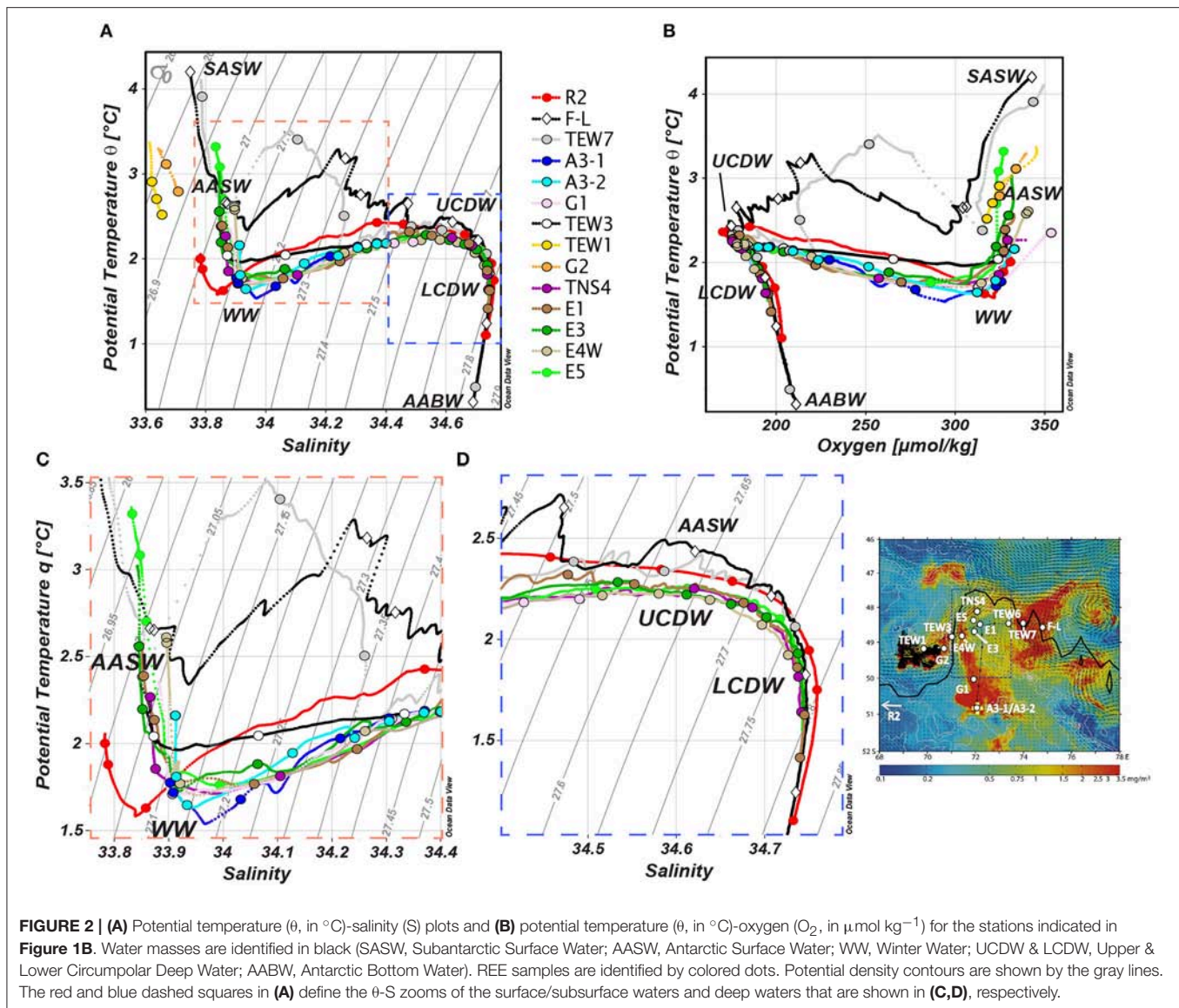
### Water Mass Characteristics

The water masses observed at the stations sampled during KEOPS2 were characterized with potential temperature-salinity  $\theta$ - $S$  and theta-oxygen  $\theta$ - $O_2$  diagrams (**Figure 2**), from surface to bottom.

The coastal stations TEW1 and G2 were very shallow stations ( $< 100 \text{ m}$ ) that exhibited homogeneous waters, relatively warm and distinctly fresher than the offshore stations ( $\theta = [2.5\text{--}3.5]^\circ\text{C}$ ;  $S = [33.6\text{--}33.7]$ ; **Figure 2A**). This feature likely reflects freshwater supplies from the Kerguelen Islands (van der Merwe et al., 2015). However, they have the same range of oxygen concentrations than all the other surface waters ( $O_2 = [320\text{--}350] \mu\text{mol kg}^{-1}$ ; **Figure 2B**). These coastal waters were clearly distinct from the surface mixed layer waters of station TEW3, which exhibited saltier, colder, and thus denser waters, these hydrological characteristics being in the ranges typical of the Antarctic Surface Water (AASW) that flows south of the PF ( $S \sim 33.85$ ;  $\theta = [2.0\text{--}2.5]^\circ\text{C}$ ; **Figure 2C**). Thus, TEW3 is likely located in the vicinity of the southern side of the PF (Park et al., 2014). Among the other stations located in the vicinity of the PF, the reference station R2 exhibits fresher AASW than TEW3 ( $S \sim 33.8$ ). Stations F-L and TEW7 exhibit surface waters as fresh as R2 but warmer than all the other surface waters of the REE stations ( $\theta = [3.0\text{--}4.0]^\circ\text{C}$ ; **Figure 2A**), revealing some influence of Subantarctic Surface Water (SASW), flowing in the Polar Frontal Zone (PFZ), between the Polar Front (PF) and the Subantarctic Front (SAF; Park et al., 2014). The surface waters of the stations located south of the PF were mainly AASW. The “purest” AASW hydrological characteristics were observed at the southernmost station (i.e., station A3;  $S \sim 33.9$ ;  $\theta \sim 2.0^\circ\text{C}$ ). Northward, closer to the PF in the recirculation area, the influence of the warmer and fresher SASW was observed (**Figure 2C**).

Below the surface waters lies the Winter Water (WW), likely advected into the study area from the southeast of the Kerguelen Islands (Park et al., 2014) and characterized by a temperature minimum centered at approximately 180 m depth (potential density  $\sigma_\theta \sim 27.15 \text{ kg m}^{-3}$ ; **Figure 2C**). All the stations located south of the PF show similar WW features ( $S \sim 33.95$ ;  $\theta \sim 1.7^\circ\text{C}$ ;  $O_2 = [260\text{--}325] \mu\text{mol kg}^{-1}$ ). By contrast, the stations sampled in the vicinity of the PF show distinct patterns around this density: the WW found at station R2 was significantly fresher and colder in its core ( $S \sim 33.85$ ;  $\theta \sim 1.6^\circ\text{C}$ ;  $z = 180 \text{ m}$ ) than the one found at the stations south of the PF. However, it warms more quickly with depth ( $\theta \sim 2.0^\circ\text{C}$  at 250 m). The WW at station TEW3





was slightly fresher and warmer ( $S \sim 33.90$ ;  $\theta \sim 2.0^{\circ}\text{C}$ ;  $\text{O}_2 \sim 300 \mu\text{mol kg}^{-1}$ ) than the one found at the stations south of the PF. The most distinguishable features around this density are however observed at stations TEW7 and F-L, which exhibit much warmer, saltier and less oxygenated subsurface waters ( $\theta = [2.5\text{--}3.5]^{\circ}\text{C}$ ;  $S \sim 34.10$ ;  $\text{O}_2 = [225\text{--}260] \mu\text{mol kg}^{-1}$ ). Following Park et al. (2014), these waters were likely associated with intrusion of PFZ subsurface waters occurring during recent frontal exchange with the SAF. The warmer and saltier contents found at R2 and TEW3 may also be, although to a lesser extent, imprints of some PFZ water influence.

These PFZ exchanges seem to be able to impact the profiles of the stations of this PF area until depths  $>1,000$  m, as suggested by the “noisy” warmer  $\theta$ - $S$  profile of stations TEW7 and F-L at the depth range of the Upper Circumpolar Deep Water (UCDW; **Figure 2D**; Park et al., 2014). The UCDW is characterized by typical oxygen concentration minima and local temperature

maxima between 500 and 1,000 m depth ( $\theta \sim 2.3^{\circ}\text{C}$ ;  $\text{O}_2 \sim [170\text{--}180] \mu\text{mol kg}^{-1}$ ). The deeper salinity maximum ( $S \sim 34.75$ ) centered on 1,800 m characterizes the core of the Lower Circumpolar Deep Water and was, as for the UCDW, sampled at all the stations located off the plateau. Finally, the fresher, colder and more oxygenated Antarctic Bottom Water (AABW;  $S \sim 34.7$ ;  $\theta \sim 0.8^{\circ}\text{C}$ ;  $\text{O}_2 \sim 210 \mu\text{mol kg}^{-1}$ ) was sampled only at the bottom of the two deepest stations TEW7 and F-L.

## ANALYTICAL METHODS

Each station was sampled at several depths covering the whole water column. All sample handling, processing and measurements were performed in accordance with general GEOTRACES protocols (<http://www.geotraces.org/>, <http://www.geotraces.org/images/stories/documents/intercalibration/>

Cookbook\_v1\_2010.pdf). Water samples were collected using 12 L Niskin bottles equipped with Teflon-coated springs and mounted on a rosette frame with a CTD sensor. The samples were filtered on-board through SARTOBran 150 0.45/0.2  $\mu\text{m}$  pore size filters, these latter being pre-cleaned with 10 L of Milli-Q water (except one coastal sample that remained unfiltered and had afterwards to be digested to dissolve or eliminate matter prior to be loaded on the first chromatographic columns). The filters were preconditioned with 500 mL of the seawater sample before the beginning of the filtrate collection. About 10 L of filtrate were recovered in an acid-cleaned cubitainer for Nd IC analysis, then an aliquot of 500 mL was collected in an acid-cleaned 500 mL Nalgene low-density polyethylene bottle for dissolved REE concentrations. All water samples were acidified to pH = 2 with twice-distilled HCl and stored at room temperature.

## Rare Earth Element Concentrations

All sample treatments were performed in a clean lab. Similarly to KEOPS1 REE analyses (Zhang et al., 2008), the REE purification and preconcentration of KEOPS2 samples were performed following the method published by Tachikawa et al. (1999b) and Lacan and Jeandel (2001). Briefly, the acidified seawater samples were spiked with  $^{150}\text{Nd}$  and  $^{172}\text{Yb}$ . Then 2.5 mg of Fe (dissolved and purified  $\text{FeCl}_3$ ) were added, and samples were vigorously shaken. After isotopic equilibration for at least 24 h, the pH was increased to 7–8 by addition of Suprapur  $\text{NH}_4\text{OH}$ , yielding REE– $\text{Fe}(\text{OH})_3$  co-precipitation. The precipitate was then extracted by centrifugation and rinsed 5 times with deionized water in order to remove salts. After dissolving the precipitate in 1 mL of 6 M HCl, an anion exchange column (AG 1X8; 2 mL) was used to extract the REE from the remaining matrix (mostly Fe). REE concentrations were then measured on a high resolution (sector field) Inductively Coupled Plasma Mass Spectrometer (ICP-MS; Thermo Scientific Element XR<sup>TM</sup>) by the external standard method, while Nd and Yb were additionally determined by isotopic dilution. Comparison of these two methods allowed us to determine the analytical recovery, equal to 83% for Nd and to 79% for Yb on average. Linear interpolation and extrapolation relative to mass was then used to estimate the recoveries for the other REEs. A desolvating nebulizer (Aridus II) was coupled to the Element XR in order to minimize oxide formation and, thus, oxide interferences ( $\text{CeO} < 0.05\%$ ; Chung et al., 2009; Pahnke et al., 2012). Notably, this substantially reduced interferences of barium oxides ( $\text{BaO}$ ) on  $^{151}\text{Eu}$ ,  $^{152}\text{Sm}$ , and  $^{153}\text{Eu}$  ( $\text{BaO}$  interferences equal to 0–1% of the Eu signal; see Grenier et al., 2013), which are otherwise too high to be accurately corrected, leading to potential miss-estimations of Eu and Sm concentrations. Note that REE measurements of KEOPS1 samples were done without the use of a desolvating system and might have resulted in less accurate corrections of  $\text{BaO}$  interferences (Zhang et al., 2008); nevertheless, several arguments make us believe that the comparison of some KEOPS1 REE characteristics with the KEOPS2 dataset, including Eu, is legitimate and valuable, as discussed further. The accuracy of our analyses was assessed using the certified river water reference material SLRS-5. Our measurements were characterized by a bias

on Nd between 0.5 and 3% and a precision on Nd concentration of 4%, both with a 95% confidence interval ( $2\sigma$ ), based on replicates (A3-2 354 m and E4-W 1,382 m; **Table 1**). The average total procedural blank ( $n = 15$ ) was equal or lower than 0.3% of the analyzed  $\text{REE}^{3+}$  signal (averaged on 109 measurements) except for Ho (0.8%) and for  $\text{Ce}^{4+}$  (4.5%). The whole analytical procedure was validated through our successful participation in the GEOTRACES intercalibration exercise (van de Flierdt et al., 2012; Behrens et al., 2016).

## Neodymium Isotopic Compositions

Pre-concentration for Nd IC was performed either on board or in the land-based laboratory (LEGOS, Toulouse, France). To do that, Suprapur ammonium hydroxide was added to each 10 L sample to obtain a pH of  $3.8 \pm 0.2$ , necessary to quantitatively pre-concentrate all the REEs by slowly (max flow rate of  $20 \text{ mL min}^{-1}$ ) passing the water sample through SEP-PAK C18 cartridges (2 per sample), previously impregnated with 300 mg of complexing agent HDEHP.H2.MEHP (Shabani et al., 1992). The pre-concentrated REE on C18 cartridges were later eluted in the LEGOS laboratory. For that, 5 mL of 0.01 M HCl (flow rate of  $20 \text{ mL min}^{-1}$ ) were first passed through the cartridge to eliminate the remaining major salts and barium. Then, 35 mL of 6M HCl were used to elute the REE (and some remaining traces of other elements). The eluted sample was evaporated and treated with 0.1 mL of 16 M  $\text{HNO}_3$  to eliminate organic matter via further evaporation. Subsequently, two chemical extractions were performed: (i) a chromatographic extraction using cationic resin (Dowex AG 50WX8, 200–400 mesh; 1.4 mL) to separate the REEs from the remaining ions (traces of Fe, Ca, Sr, Ba, Mg) and (ii) a final separation of Nd from the other REE using a second cation exchange column with  $\alpha$ -hydroxyisobutyric acid ( $\alpha$ -HIBA) as the eluent (Choppin and Silva, 1956). This  $\alpha$ -HIBA separation method was beforehand validated by comparison with the Ln Spec separation method (Pin and Zalduegui, 1997). All measurements were made using Thermo Ionization Mass Spectrometers (TIMS) equipped with multicollectors (THERMO MAT 261 in Toulouse and THERMO Triton in Brest) and were mass bias corrected using  $^{146}\text{Nd}/^{144}\text{Nd}$  ratio of 0.7219. External precision and accuracy of both mass spectrometers were determined using La Jolla international Nd reference material. Thirteen analyses of La Jolla standard were performed to monitor instrumental drift and gave  $0.511853 \pm 0.000010$ , within the uncertainty of the generally accepted reference value of  $0.511860 \pm 0.000020$ . Blank contributions to the Nd isotopic measurement were of 6 pg on average, i.e., lower than 1% of the total signal. As for the REEs, the performance of our seawater Nd isotopic analyses was certified through the GEOTRACES intercalibration exercise (van de Flierdt et al., 2012).

## RESULTS

Results are given in **Table 1** and are displayed in **Figures 3–5**. For the sake of simplicity, we have shown the concentration vertical profiles of only some REEs: the lightest (La), the most particle-reactive REE in seawater (Ce), the two ones used for the isotope dilution (Nd and Yb –Yb being also representative of

**TABLE 1 |** Dissolved REE concentrations (in pmol kg<sup>-1</sup>) and  $\epsilon_{Nd}$  measured in our samples, with their associated standard errors (2 $\sigma$ ): ICP-MS method uncertainty—i.e., internal reproducibility of each element intensity for 2 runs of 5 passes—associated with each sample measurement after post-processing, i.e., including oxide rate and spike calibration uncertainties).

P	S	O <sub>2</sub>	σ <sub>0</sub>	La	2σ	Ce	2σ	Pr	2σ	Nd	2σ	Sm	2σ	Eu	2σ	Gd	2σ	Tb	2σ	Dy	2σ	Ho	2σ	Er	2σ	Tm	2σ	Yb	2σ	Lu	2σ	ε <sub>Nd</sub> <sup>a</sup>	2σ	Water mass
Kerguelen Beach (October 18, 2011; 70.20°E, 49.35°S, Golfe Du Morbihan)																																		
–	–	–	–	70.49	5.42	88.96	5.34	####	0.58	42.77	2.10	7.31	0.42	1.19	0.08	8.31	0.54	1.32	0.08	9.06	0.54	2.26	0.12	7.56	0.53	1.11	0.06	7.10	0.35	1.19	0.1	–1.4	0.2	–
A3-1 (October 21, 2011; 72.031°E, 50.645°S, Depth: 530 m)																																		
60	33.903	318	27.11	25.78	1.66	10.00	0.61	3.55	0.24	15.38	0.81	2.73	0.18	0.72	0.05	4.05	0.27	0.67	0.05	4.97	0.32	1.42	0.09	5.11	0.33	0.77	0.05	5.04	0.27	0.91	0.1	–7.2	1.1	AASW
152	33.910	314	27.12	30.52	1.84	13.74	0.77	4.00	0.26	16.95	0.87	2.98	0.18	0.74	0.05	4.15	0.25	0.70	0.05	5.03	0.31	1.44	0.08	5.01	0.33	0.77	0.05	4.99	0.26	0.89	0.1	–8.0	0.5	AASW
210	34.035	269	27.22	26.91	1.58	6.26	0.33	3.21	0.19	14.15	0.70	2.55	0.17	0.66	0.04	3.87	0.24	0.66	0.04	4.83	0.29	1.44	0.09	4.95	0.30	0.78	0.04	5.07	0.25	0.90	0.1	–	–	WW
305	34.217	224	27.34	29.45	1.93	7.46	0.45	3.34	0.23	14.89	0.88	2.68	0.19	0.70	0.05	3.89	0.26	0.69	0.05	4.91	0.36	1.46	0.09	5.09	0.35	0.78	0.05	5.25	0.31	1.00	0.1	–7.8	1.4	WW/UCDW
407	34.307	204	27.41	29.27	1.36	7.14	0.39	3.35	0.12	15.12	0.47	2.70	0.14	0.70	0.03	4.04	0.16	0.68	0.02	5.04	0.24	1.50	0.05	5.39	0.25	0.79	0.03	5.50	0.17	1.10	0	–	–	UCDW
508	34.373	191	27.45	28.02	1.24	7.86	0.24	3.43	0.13	15.11	0.45	2.65	0.14	0.70	0.03	4.20	0.21	0.62	0.02	5.46	0.22	1.46	0.06	5.67	0.25	0.84	0.03	5.58	0.16	1.04	0.1	–6.5	2.5	UCDW
TNS-4 (October 23, 2011; 72.065°E, 48.166°S, DEPTH: 1,800 m)																																		
41	33.866	330	27.04	24.62	1.30	8.05	0.50	3.42	0.17	14.59	0.66	2.58	0.14	0.68	0.04	4.01	0.24	0.64	0.04	4.94	0.26	1.46	0.08	4.88	0.26	0.78	0.04	4.94	0.22	0.85	0	–8.0	0.3	AASW
122	33.878	323	27.08	–	–	–	–	–	–	–	–	–	–	–	–	–	–	–	–	–	–	–	–	–	–	–	–	–	–	–	–	–5.4	0.6	AASW/WW
203	34.109	256	27.27	24.75	0.82	5.64	0.24	2.99	0.15	13.80	0.42	2.42	0.10	0.66	0.03	3.87	0.24	0.63	0.03	4.93	0.24	1.44	0.08	5.17	0.19	0.76	0.03	5.16	0.14	0.98	0	–	–	WW
406	34.406	191	27.48	26.53	0.88	4.43	0.21	3.06	0.16	14.08	0.45	2.49	0.11	0.68	0.03	3.98	0.23	0.67	0.03	5.12	0.28	1.47	0.08	5.48	0.21	0.80	0.04	5.54	0.17	1.05	0	–	–	UCDW
761	34.622	176	27.65	28.46	1.09	3.65	0.24	3.23	0.19	14.98	0.53	2.66	0.15	0.74	0.04	4.33	0.23	0.70	0.03	5.55	0.34	1.60	0.07	5.77	0.32	0.85	0.05	5.93	0.21	1.11	0	–	–	UCDW
1014	34.692	182	27.71	29.15	2.02	5.36	0.35	3.67	0.21	16.38	0.70	2.89	0.22	0.79	0.05	4.62	0.29	0.70	0.06	6.21	0.37	1.54	0.09	6.22	0.36	0.88	0.04	6.14	0.26	1.17	0.1	–	–	UCDW
1521	34.739	192	27.78	30.48	0.89	4.75	0.11	4.46	0.13	18.25	0.44	3.28	0.13	0.92	0.03	4.71	0.22	0.78	0.03	6.19	0.16	1.69	0.05	6.17	0.24	0.96	0.05	6.53	0.16	1.20	0	–9.6	0.5	UCDW
1805	34.741	194	27.79	30.29	1.11	4.63	0.13	4.78	0.18	19.25	0.60	3.48	0.14	0.98	0.04	4.92	0.22	0.85	0.04	6.34	0.31	1.74	0.06	6.36	0.28	0.98	0.04	6.68	0.25	1.21	0	–9.2	0.5	UCDW
R-2 (October 26, 2011; 66.693°E, 50.389°S, depth: 2,450 m)																																		
41	33.783	331	27.00	18.90	0.64	3.00	0.12	2.38	0.10	10.96	0.30	1.95	0.07	0.53	0.02	3.21	0.20	0.53	0.03	4.07	0.19	1.23	0.04	4.37	0.17	0.85	0.03	4.25	0.11	0.77	0	–	–	AASW
102	33.789	327	27.01	21.63	0.95	3.59	0.19	2.72	0.15	12.34	0.44	2.18	0.11	0.59	0.04	3.60	0.21	0.60	0.03	4.52	0.22	1.35	0.06	4.83	0.25	0.71	0.04	4.72	0.17	0.85	0	–7.9	0.1	AASW
203	33.858	316	27.08	24.53	1.05	5.57	0.28	2.95	0.14	13.43	0.40	2.40	0.12	0.65	0.03	3.73	0.20	0.64	0.03	4.63	0.24	1.39	0.06	4.92	0.22	0.74	0.03	4.84	0.14	0.88	0	–	–	WW
508	34.371	185	27.43	24.98	1.48	4.71	0.33	3.02	0.17	13.33	0.64	2.41	0.14	0.63	0.04	3.83	0.23	0.62	0.04	4.86	0.32	1.43	0.08	5.13	0.36	0.74	0.04	5.35	0.26	1.01	0.1	–	–	UCDW
609	34.458	174	27.50	25.53	1.46	2.82	0.15	2.89	0.20	12.94	0.45	2.38	0.15	0.64	0.05	3.84	0.32	0.63	0.04	5.05	0.38	1.43	0.10	5.40	0.38	0.82	0.05	5.61	0.19	1.06	0	–	–	UCDW
812	34.583	170	27.61	22.72	1.36	3.25	0.20	3.12	0.17	13.64	0.58	2.48	0.13	0.68	0.03	4.11	0.26	0.64	0.03	5.53	0.26	1.54	0.07	5.56	0.29	0.90	0.04	5.90	0.24	1.07	0.1	–	–	UCDW
1011	34.663	175	27.68	26.54	1.66	3.92	0.31	3.33	0.23	14.98	0.82	2.74	0.23	0.74	0.05	4.37	0.32	0.71	0.06	5.66	0.41	1.63	0.11	5.96	0.44	0.91	0.06	6.12	0.33	1.12	0.1	–	–	UCDW
1520	34.750	192	27.78	27.13	0.85	3.90	0.12	4.21	0.11	17.41	0.49	3.22	0.12	0.90	0.04	4.65	0.10	0.78	0.02	6.10	0.25	1.67	0.06	6.10	0.21	0.91	0.03	6.44	0.20	1.16	0	–8.8	0.4	UCDW
1831	34.759	199	27.80	34.21	2.08	3.86	0.29	4.24	0.33	19.16	1.04	3.53	0.24	0.92	0.07	5.33	0.38	0.86	0.06	6.36	0.51	1.81	0.14	6.36	0.42	0.97	0.07	6.58	0.35	1.23	0.1	–10.5	0.5	UCDW
2473	34.732	203	27.82	34.01	1.31	4.61	0.17	5.44	0.20	21.70	0.86	4.00	0.37	1.01	0.07	5.65	0.32	0.91	0.04	6.80	0.29	1.90	0.09	6.62	0.33	1.03	0.04	6.98	0.27	1.32	0.1	–9.6	0.6	AASW
E-1 (October 30, 2011; 72.178°E, 48.498°S, depth: 2,058 m)																																		
61	33.855	328	27.02	22.91	1.25	4.96	0.21	2.82	0.15	12.97	0.42	2.36	0.12	0.61	0.04	3.71	0.21	0.61	0.04	4.60	0.23	1.38	0.06	4.96	0.23	0.73	0.03	4.85	0.15	0.88	0	–8.8	0.3	AASW
102	33.875	327	27.06	23.26	1.35	5.28	0.25	2.87	0.16	13.26	0.52	2.34	0.13	0.63	0.03	3.73	0.20	0.63	0.05	4.63	0.24	1.41	0.08	4.97	0.26	0.74	0.04	4.86	0.19	0.89	0	–8.0	0.2	AASW
192	34.082	269	27.24	24.54	1.28	4.08	0.21	2.87	0.17	13.33	0.84	2.39	0.15	0.65	0.03	3.71	0.24	0.65	0.05	4.79	0.28	1.45	0.08	5.04	0.27	0.77	0.04	5.10	0.24	0.96	0.1	–	–	WW
303	34.247	222	27.37	25.91	1.20	4.42	0.16	2.69	0.13	13.23	0.38	2.35	0.11	0.65	0.03	3.87	0.17	0.67	0.02	5.07	0.20	1.37	0.06	5.53	0.23	0.74	0.03	5.45	0.15	1.08	0	–	–	WW/UCDW
505	34.476	179	27.53	27.05	1.17	3.59	0.12	2.89	0.11	13.51	0.43	2.48	0.11	0.68	0.03	3.92	0.24	0.68	0.03	5.26	0.24	1.43	0.05	5.86	0.29	0.73	0.04	5.67	0.18	1.17	0	–	–	UCDW
637	34.554	176	27.59	28.40	1.46	3.41	0.15	2.91	0.16	14.33	0.47	2.56	0.13	0.72	0.04	4.16	0.23	0.71	0.03	5.35	0.27	1.52	0.07	5.88	0.32	0.81	0.04	5.95	0.19	1.20	0	–	–	UCDW
1010	34.676	180	27.70	29.79	1.25	3.84	0.12	3.41	0.13	15.76	0.45	2.82	0.12	0.78	0.03	4.51	0.22	0.78	0.03	5.88	0.23	1.53	0.06	6.18	0.26	0.86	0.04	6.11	0.17	1.21	0	–	–	UCDW
1498	34.781	191	27.77	31.95	1.64	4.31	0.14	4.12	0.14	18.25	0.54	3.33	0.16	0.87	0.05	5.32	0.24	0.74	0.04	6.59	0.24	1.75	0.05	6.46	0.27	0.96	0.03	6.52	0.19	1.23	0	–	–	UCDW
1803	34.745	195	27.80	36.08	1.58	3.85	0.21	4.01	0.22	19.61	0.60	3.70	0.19	0.96	0.06	5.32	0.31	0.94	0.03	6.47	0.36	1.87	0.07	6.58	0.34	0.90	0.07	6.72						

TABLE 1 | Continued

P	S	O <sub>2</sub>	ε <sub>o</sub>	La	2σ <sub>o</sub>	Ce	2σ <sub>c</sub>	Pr	2σ <sub>p</sub>	Nd	2σ <sub>n</sub>	Sm	2σ <sub>s</sub>	Eu	2σ <sub>e</sub>	Gd	2σ <sub>g</sub>	Tb	2σ <sub>t</sub>	Dy	2σ <sub>d</sub>	Ho	2σ <sub>h</sub>	Er	2σ <sub>e</sub>	Tm	2σ <sub>t</sub>	Lu	2σ <sub>l</sub>	ε <sub>Nd</sub> <sup>a</sup>	2σ <sub>ε</sub>	Water mass		
TEW-6 (November 2, 2011; 73.4° E, 48.466° S; depth: 2,410 m)																																		
2423	34.708	204	27.83	37.53	1.50	5.90	0.19	6.17	0.21	24.57	0.83	4.55	0.20	1.21	0.05	6.04	0.25	0.98	0.04	7.32	0.31	1.94	0.06	6.86	0.29	1.03	0.04	7.18	0.24	1.26	0.05	-9.4	0.3	AABW
TEW-7 (November 2, 2011; 73.999° E, 48.467° S; depth: 2,510 m)																																		
41	33.788	330	26.85	18.99	0.51	7.47	0.15	2.88	0.07	12.06	0.23	2.16	0.05	0.57	0.02	3.28	0.12	0.54	0.01	4.44	0.12	1.24	0.03	4.62	0.13	0.71	0.04	4.44	0.09	0.80	0.02			SW
101	33.852	312	27.00	22.37	0.48	8.66	0.19	3.23	0.07	13.47	0.27	2.38	0.07	0.62	0.02	3.57	0.11	0.57	0.01	4.68	0.17	1.30	0.03	4.77	0.11	0.70	0.02	4.73	0.10	0.85	0.02			WW
202	34.105	252	27.13	18.35	0.57	3.20	0.09	2.61	0.07	10.57	0.28	1.92	0.07	0.55	0.02	2.93	0.11	0.50	0.02	4.05	0.12	1.15	0.04	4.36	0.14	0.88	0.02	4.39	0.12	0.79	0.02			CW
404	34.260	213	27.34	19.25	0.45	2.88	0.08	2.66	0.07	11.51	0.28	2.10	0.06	0.59	0.01	3.27	0.09	1.25	0.04	4.83	0.14	1.25	0.04	4.83	0.14	0.72	0.02	4.99	0.11	0.91	0.02			CW
606	34.484	179	27.53	23.09	0.54	3.63	0.10	3.09	0.09	13.15	0.30	2.35	0.06	0.66	0.02	3.65	0.10	0.59	0.02	4.96	0.11	1.37	0.04	5.23	0.13	0.79	0.02	5.48	0.12	1.02	0.02			UCDW
809	34.586	176	27.61	24.24	0.66	3.83	0.10	3.39	0.09	14.09	0.34	2.57	0.10	0.72	0.02	3.86	0.14	0.65	0.02	5.22	0.17	1.48	0.05	5.55	0.18	0.85	0.03	5.71	0.16	1.07	0.03			UCDW
1519	34.734	189	27.76	28.74	0.88	4.59	0.06	4.41	0.11	17.31	0.35	3.11	0.12	0.88	0.03	4.48	0.14	0.74	0.02	6.12	0.12	1.60	0.04	5.97	0.12	0.92	0.03	6.35	0.11	1.18	0.02			UCDW
2523	34.698	208	27.83	39.70	1.63	5.86	0.24	6.73	0.25	25.92	1.04	4.61	0.24	1.27	0.07	6.07	0.27	1.01	0.04	7.61	0.33	2.01	0.09	7.28	0.32	1.08	0.05	7.69	0.32	1.40	0.07			AABW
E-3 (November 4, 2011; 71.967° E, 48.701° S; depth: 1,910 m)																																		
50	33.846	330	27.00	23.44	1.37	4.68	0.25	2.87	0.19	13.11	0.68	2.45	0.17	0.63	0.04	3.66	0.24	0.64	0.04	4.73	0.30	1.42	0.08	4.83	0.28	0.76	0.04	4.83	0.25	0.87	0.05			AASW
106	33.853	322	27.04	22.00	0.45	5.48	0.12	2.92	0.07	12.88	0.24	2.29	0.09	0.64	0.03	3.60	0.14	0.59	0.02	4.80	0.17	1.33	0.03	4.85	0.11	0.73	0.02	4.84	0.08	0.90	0.02	-7.6	0.2	AASW
227	34.068	263	27.23	21.53	1.20	3.59	0.12	2.85	0.09	12.72	0.34	2.29	0.12	0.62	0.03	3.73	0.21	0.59	0.02	4.80	0.18	1.37	0.06	5.11	0.25	0.78	0.02	5.10	0.13	0.96	0.04			WW
404	34.344	202	27.43	25.49	1.03	3.51	0.14	2.89	0.16	13.33	0.49	2.43	0.12	0.68	0.03	3.82	0.26	0.88	0.04	4.88	0.27	1.49	0.07	5.19	0.21	0.80	0.04	5.41	0.20	1.00	0.04			UCDW
606	34.535	175	27.58	24.64	1.44	3.49	0.14	3.22	0.13	14.13	0.51	2.48	0.12	0.70	0.04	4.17	0.21	0.82	0.04	5.36	0.23	1.56	0.07	5.38	0.28	0.86	0.03	5.73	0.20	1.03	0.06			UCDW
810	34.614	177	27.64	28.21	1.38	3.43	0.17	3.33	0.20	15.10	0.66	2.78	0.16	0.74	0.04	4.34	0.28	0.74	0.05	5.47	0.31	1.62	0.09	5.54	0.28	0.90	0.04	5.92	0.26	1.11	0.05			UCDW
1013	34.664	179	27.69	29.81	1.24	3.66	0.12	3.18	0.12	15.63	0.45	2.88	0.13	0.79	0.03	4.47	0.22	0.78	0.03	5.73	0.26	1.64	0.06	6.24	0.28	0.81	0.03	6.14	0.17	1.25	0.04			UCDW
1215	34.703	183	27.73	29.06	2.19	3.86	0.24	3.59	0.23	16.33	0.75	3.05	0.21	0.79	0.06	4.71	0.37	0.77	0.05	5.99	0.45	1.69	0.11	6.13	0.44	0.83	0.05	6.23	0.30	1.19	0.08			UCDW
1519	34.738	190	27.77	32.64	1.66	3.90	0.19	3.75	0.18	17.85	0.50	3.32	0.15	0.88	0.05	4.92	0.19	0.87	0.03	6.08	0.21	1.77	0.08	6.23	0.27	0.91	0.04	6.45	0.16	1.24	0.05			UCDW/LCDW
1909	34.742	194	27.79	34.32	1.99	4.00	0.27	4.35	0.21	19.85	0.77	3.62	0.26	0.92	0.05	5.38	0.44	0.87	0.05	6.46	0.43	1.83	0.14	6.55	0.38	0.99	0.05	6.75	0.25	1.35	0.07			LCOW
F-L (November 7, 2011; 74.807° E, 48.821° S; depth: 2,739 m)																																		
30	33.749	342	26.77	20.94	0.45	6.88	0.13	2.90	0.06	12.58	0.22	2.27	0.05	0.57	0.02	3.47	0.09	0.57	0.01	4.48	0.13	1.26	0.02	4.63	0.11	0.88	0.02	4.38	0.08	0.80	0.02	-6.8	0.1	SW
106	33.866	300	27.01	—	—	—	—	—	—	—	—	—	—	—	—	—	—	—	—	—	—	—	—	—	—	—	—	—	—	—	-7.2	0.3	WW	
107	33.873	304	27.02	20.96	0.47	6.97	0.17	3.12	0.07	12.93	0.28	2.28	0.09	0.62	0.02	3.44	0.13	0.55	0.02	4.58	0.16	1.27	0.03	4.63	0.13	0.89	0.02	4.65	0.10	0.85	0.02	-6.5	0.4	WW
304	34.265	213	27.28	19.72	0.48	4.00	0.08	2.80	0.06	12.19	0.25	2.25	0.05	0.63	0.01	3.42	0.08	0.56	0.01	4.42	0.10	1.23	0.02	4.63	0.11	0.69	0.01	4.67	0.12	0.86	0.02			CW
405	34.317	201	27.36	20.56	0.55	3.05	0.06	2.79	0.09	11.89	0.29	2.16	0.07	0.61	0.02	3.33	0.11	0.55	0.02	4.49	0.12	1.25	0.04	4.83	0.15	0.71	0.02	4.94	0.12	0.91	0.02			CW
608	34.473	178	27.49	21.39	0.62	3.49	0.11	3.01	0.10	12.82	0.37	2.33	0.08	0.66	0.02	3.62	0.12	0.80	0.02	4.85	0.16	1.37	0.05	5.18	0.16	0.79	0.02	5.45	0.16	1.02	0.03			CW/LCDW
909	34.621	175	27.63	24.58	0.72	4.38	0.12	3.46	0.10	14.34	0.41	2.60	0.08	0.74	0.03	3.89	0.13	0.86	0.04	5.22	0.20	1.49	0.04	5.49	0.19	0.82	0.03	5.83	0.15	1.08	0.03			UCDW
1215	34.707	184	27.72	25.84	0.41	4.45	0.09	3.83	0.11	15.80	0.41	2.96	0.10	0.80	0.02	4.26	0.14	0.72	0.02	5.69	0.16	1.60	0.03	5.67	0.20	0.87	0.02	6.00	0.16	1.09	0.02			UCDW
1773	34.746	194	27.79	30.52	0.87	4.63	0.12	4.63	0.16	18.95	0.55	3.35	0.12	0.95	0.03	4.84	0.17	0.81	0.03	6.33	0.19	1.65	0.04	6.25	0.18	0.85	0.04	6.68	0.17	1.20	0.04	-9.9	0.3	LCOW
2229	34.735	200	27.82	34.99	0.55	4.96	0.10	5.88	0.12	22.31	0.46	3.99	0.14	1.13	0.03	5.45	0.14	0.91	0.02	7.02	0.18	1.88	0.06	6.58	0.22	1.04	0.03	7.12	0.13	1.29	0.03			LCOW/AABW
2742	34.690	211	27.84	41.19	1.88	6.48	0.26	7.29	0.28	27.05	1.20	4.89	0.24	1.33	0.06	6.30	0.35	1.05	0.04	7.77	0.42	2.00	0.09	7.09	0.35	1.08	0.04	7.62	0.30	1.45	0.06	-9.0	0.2	AABW
G-1 (November 8, 2011; 71.9° E, 48.9° S; depth: 580 m)																																		
29	33.881	354	27.05	22.79	0.92	7.10	0.30	3.27	0.14	13.81	0.57	2.45	0.10	0.66	0.03	3.61	0.15	0.59	0.03	4.72	0.19	1.32	0.05	4.91	0.20	0.73	0.03	4.77	0.18	0.84	0.03			AASW
151	33.908	318	27.12	22.80	0.68	5.02	0.21	3.07	0.12	13.43	0.30	2.43	0.11	0.66	0.03	3.83	0.19	0.62	0.03	4.91	0.20	1.41	0.06	5.14	0.17	0.78	0.03	5.12	0.11	0.94	0.03			WW
305	34.314	208	27.41	25.01	1.85	5.74	0.26	3.16	0.24	14.04	0.47	2.53	0.18	0.67	0.05	3.96	0.25	0.83	0.05	5.09	0.34	1.41	0.07	5.44	0.29	0.81	0.05	5.48	0.17	1.02	0.05			UCDW
459	34.434	189	27.50	24.43	0.68	4.85	0.11	3.45	0.11	14.02	0.39	2.51	0.09	0.70	0.02	3.78	0.11	0.62	0.02	4.99	0.17	1.44	0.04	5.23	0.16	0.81	0.02	5.52	0.15	1.01	0.03			UCDW
576	34.490	182	27.55	25.64	1.38	5.93	0.30	3.39	0.19	14.50	0.51	2.59	0.16	0.72	0.04	4.06	0.24	0.87	0.03	5.25	0.27	1.53	0.06	5.63	0.25	0.89	0.04	5.79	0.20	1.07	0.05.			



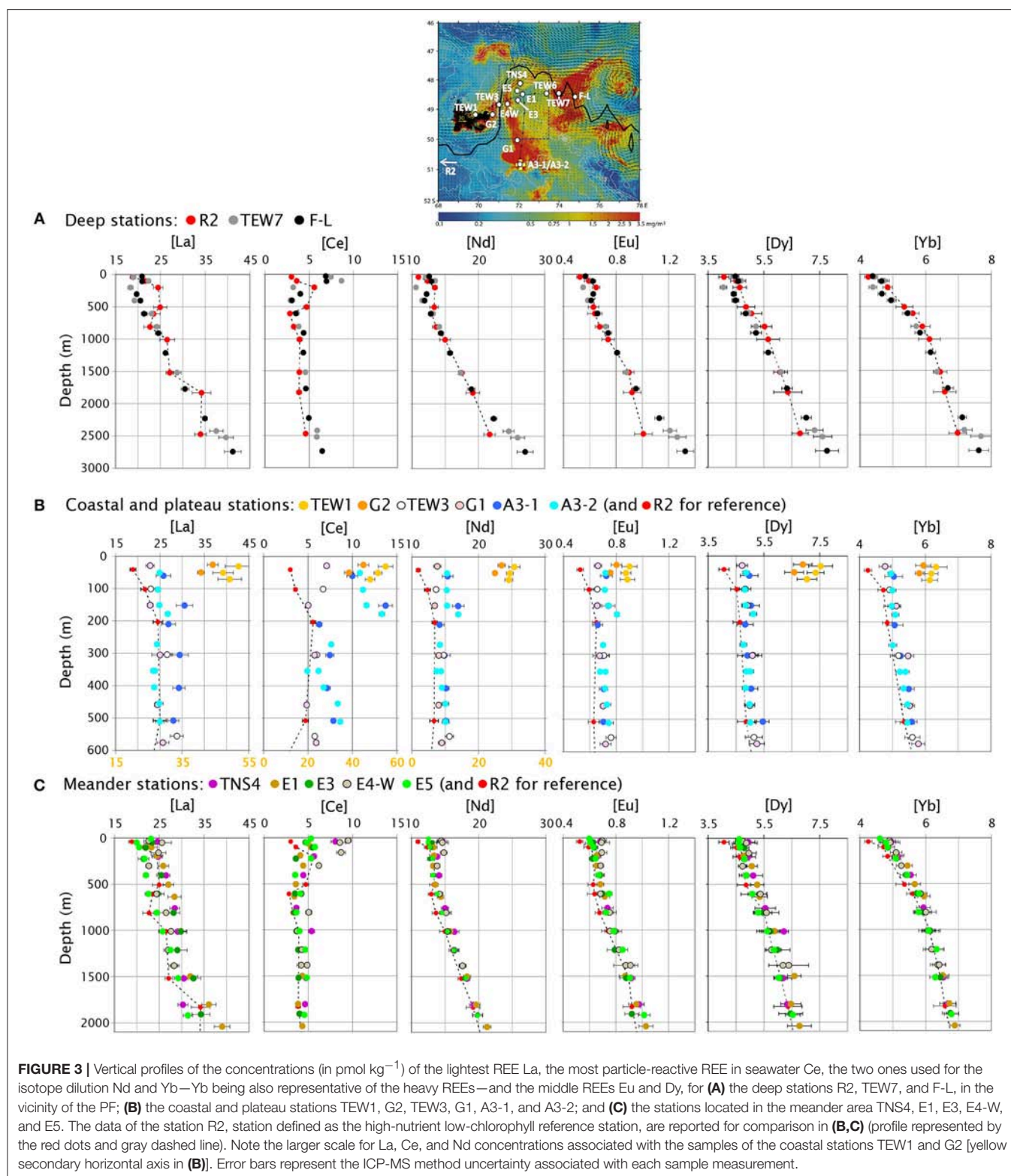
TABLE 1 | Continued

TABLE 1   Continued																																		
P	S	O <sub>2</sub>	σ <sub>θ</sub>	La	Ce	Pr	Nd	Sm	Eu	Gd	Tb	2σ <sub>Tb</sub>	2σ <sub>Dy</sub>	2σ <sub>Ho</sub>	2σ <sub>Er</sub>	2σ <sub>Tm</sub>	2σ <sub>Yb</sub>	2σ <sub>Lu</sub>	ε <sub>Nd</sub> <sup>a</sup>	2σ	Water mass													
1011	34.641	178	27.67	27.61	1.06	3.74	0.23	2.63	0.16	4.44	0.33	0.74	0.03	5.66	0.31	1.57	0.06	6.06	0.28	0.90	0.04	6.07	0.16	1.16	0.04	UCDW								
1214	34.700	183	27.73	26.98	0.95	4.27	0.14	3.94	0.13	16.34	0.54	3.00	0.15	0.82	0.03	4.38	0.16	0.74	0.03	5.77	0.22	1.63	0.06	5.88	0.23	0.89	0.03	6.18	0.19	1.12	0.04	UCDW		
1382	34.726	–	27.76	28.29	1.17	4.20	0.48	4.04	0.19	17.60	0.54	3.28	0.34	0.88	0.09	4.88	0.46	0.89	0.15	6.39	0.71	1.54	0.10	6.43	0.43	0.96	0.08	6.37	0.22	1.12	0.10	–9.5	0.3	UCDW/LCDW
1382	34.726	–	27.76	28.31	0.78	4.86	0.15	4.29	0.12	17.58	0.49	3.21	0.12	0.91	0.03	4.69	0.18	0.79	0.03	6.19	0.22	1.64	0.05	6.06	0.22	0.91	0.04	6.41	0.20	1.14	0.04	–9.7	0.8	UCDW/LCDW
A3-2 (November 15, 2011; 72.056°E, 50.624°S; depth: 526 m)																																		
51	33.912	333	27.09	24.92	0.54	10.85	0.23	3.60	0.08	15.29	0.28	2.67	0.07	0.72	0.02	3.87	0.09	0.60	0.01	4.86	0.12	1.33	0.03	4.97	0.14	0.74	0.02	4.95	0.09	0.91	0.02			AASW
103	33.913	332	27.09	24.55	0.60	11.19	0.26	3.62	0.09	15.25	0.35	2.67	0.07	0.71	0.02	3.82	0.10	0.61	0.02	4.81	0.12	1.35	0.03	4.97	0.13	0.75	0.02	5.00	0.11	0.91	0.02			AASW
151	33.915	322	27.12	24.87	0.60	11.59	0.30	3.72	0.10	15.29	0.36	2.67	0.07	0.74	0.02	3.77	0.11	0.61	0.02	4.84	0.13	1.34	0.04	4.98	0.15	0.74	0.02	4.98	0.12	0.90	0.02	–6.7	0.6	WW
178	33.942	308	27.15	26.73	0.60	13.32	0.33	4.14	0.11	16.97	0.38	2.99	0.07	0.81	0.02	4.15	0.11	0.65	0.02	5.12	0.13	1.37	0.03	5.13	0.15	0.74	0.02	5.09	0.11	0.92	0.02			WW
272	34.134	260	27.28	24.33	0.55	7.61	0.20	3.44	0.09	14.22	0.38	2.50	0.07	0.70	0.02	3.62	0.10	0.60	0.02	4.76	0.12	1.32	0.03	4.92	0.12	0.74	0.02	5.01	0.12	0.90	0.02			WW/UCDW
354	34.248	223	27.37	23.87	0.57	6.18	0.15	3.42	0.09	14.38	0.35	2.59	0.07	0.72	0.02	3.84	0.09	0.62	0.02	5.01	0.12	1.38	0.03	5.24	0.14	0.77	0.02	5.39	0.12	0.97	0.02			UCDW
354	34.248	223	27.37	23.45	0.53	4.93	0.13	3.24	0.08	13.72	0.35	2.42	0.06	0.68	0.02	3.67	0.10	0.59	0.01	4.87	0.10	1.32	0.03	5.09	0.13	0.76	0.02	5.22	0.12	0.94	0.02			UCDW
405	34.310	209	27.41	23.88	0.57	6.76	0.14	3.56	0.08	14.51	0.32	2.53	0.08	0.71	0.02	3.68	0.09	0.61	0.01	4.85	0.12	1.38	0.03	5.09	0.13	0.78	0.02	5.34	0.11	0.99	0.02			UCDW
455	34.373	195	27.45	24.84	0.89	8.35	0.27	3.82	0.14	15.04	0.50	2.67	0.11	0.73	0.03	3.75	0.14	0.62	0.02	4.99	0.18	1.40	0.04	5.19	0.16	0.80	0.03	5.45	0.17	1.03	0.04			UCDW
511	34.401	190	27.48	24.95	0.98	8.63	0.28	3.72	0.13	15.06	0.54	2.63	0.11	0.74	0.04	3.78	0.17	0.62	0.02	5.01	0.20	1.38	0.05	5.24	0.20	0.78	0.04	5.45	0.22	1.00	0.04	–7.4	0.2	UCDW
E-5 (November 18-19, 2011; 71.9°E, 48.412°S; depth: 1,920m)																																		
10	33.832	327	26.92	23.16	0.46	5.31	0.10	2.85	0.05	12.51	0.23	2.22	0.06	0.60	0.02	3.50	0.10	0.56	0.01	4.61	0.13	1.30	0.03	4.74	0.10	0.70	0.02	4.61	0.08	0.84	0.02			AASW
51	33.847	324	26.96	20.00	0.47	4.81	0.12	2.81	0.08	12.47	0.25	2.22	0.05	0.61	0.02	3.50	0.09	0.56	0.02	4.60	0.12	1.31	0.03	4.85	0.14	0.72	0.02	4.79	0.10	0.87	0.02	–7.2	0.2	AASW
101	33.859	323	27.00	20.54	0.42	5.75	0.15	3.00	0.07	12.71	0.30	2.28	0.05	0.63	0.02	3.43	0.10	0.56	0.01	4.64	0.10	1.28	0.03	4.84	0.11	0.72	0.01	4.83	0.10	0.87	0.02			AASW/WW
225	33.994	285	27.18	21.77	0.49	5.32	0.14	3.10	0.08	13.16	0.32	2.34	0.06	0.65	0.02	3.57	0.09	0.59	0.02	4.80	0.11	1.34	0.03	5.02	0.13	0.75	0.02	5.09	0.12	0.93	0.02			WW
404	34.367	198	27.45	22.03	0.60	3.53	0.08	3.18	0.08	13.17	0.32	2.35	0.07	0.67	0.02	3.58	0.11	0.58	0.02	4.87	0.17	1.36	0.03	5.18	0.15	0.78	0.02	5.44	0.13	1.02	0.02			UCDW
606	34.509	181	27.56	22.61	0.76	4.08	0.12	3.53	0.09	13.82	0.33	2.51	0.09	0.75	0.02	3.74	0.12	0.65	0.02	5.09	0.15	1.43	0.03	5.38	0.22	0.83	0.03	5.80	0.17	1.11	0.03			UCDW
809	34.612	176	27.64	24.46	0.66	3.67	0.09	3.51	0.10	14.54	0.39	2.59	0.09	0.73	0.02	3.93	0.14	0.64	0.02	5.29	0.17	1.49	0.05	5.45	0.15	0.85	0.03	5.78	0.16	1.07	0.03			UCDW
1012	34.674	179	27.69	25.76	0.79	3.99	0.11	3.84	0.12	15.32	0.52	2.76	0.12	0.78	0.03	4.16	0.19	0.68	0.02	5.62	0.20	1.57	0.05	5.75	0.20	0.90	0.03	6.09	0.19	1.12	0.04			UCDW
1214	34.717	185	27.74	27.54	1.10	4.66	0.16	4.16	0.16	16.40	0.60	2.97	0.14	0.85	0.04	4.36	0.20	0.74	0.03	5.86	0.26	1.60	0.06	6.00	0.27	0.93	0.03	6.34	0.22	1.19	0.05			UCDW/LCDW
1518	34.739	191	27.77	29.24	0.88	4.83	0.08	4.58	0.17	18.12	0.38	3.24	0.12	0.91	0.03	4.62	0.15	0.79	0.02	6.03	0.11	1.61	0.03	6.10	0.17	0.89	0.02	6.29	0.17	1.16	0.04	–9.8	0.2	LCDW
1921	34.742	195	27.80	31.41	1.04	4.55	0.16	4.94	0.17	19.83	0.71	3.61	0.16	1.01	0.05	5.11	0.24	0.85	0.04	6.54	0.27	1.80	0.06	6.43	0.24	0.99	0.04	6.78	0.22	1.22	0.05	–9.7	0.5	LCDW
Surf <sup>a</sup>	–	–	–	–	–	4.79	0.10	2.89	0.05	12.48	0.25	2.30	0.09	0.60	0.02	3.60	0.13	0.54	0.03	4.54	0.16	1.31	0.06	4.75	0.12	0.70	0.03	4.60	0.09	0.84	0.02			LCDW
(Surf - E-5 10m)/100 (%)						–3%	0%	–1%	0%	0%	0%	0%	0%	0%	0%	0%	0%	0%	0%	0%	0%	0%	0%	0%	0%	0%	0%	0%	0%	0%	0%	0%	0%	

Only the Kerguelen beach water sample (collected close to TEW-1 station) is unfiltered and, thus, refers to the total fraction (dissolved + particulate). Pressure (P, in dB), salinity (S), dissolved dioxygen concentrations (O<sub>2</sub>, in μmol kg<sup>–1</sup>), potential density (σ<sub>θ</sub>, in kg m<sup>–3</sup>) and water masses associated with our samples are also reported here.

<sup>a</sup>Bold and italic values of ε<sub>Nd</sub> refer to high standard errors (>0.5).

\*Surface water from the boat pump, for comparison with Niskin surface sample below.



the heavy REEs) and two middle REEs (Eu and Dy; **Figure 3**). The REE fractionation patterns are shown by normalizing their concentrations to the average post-Archean upper continental crust (Post Archean Australian Shale, referred as the acronym

“PAAS” hereafter; McLennan, 1989) to highlight changes from the crustal input (Elderfield, 1988). Such normalization allows us to eliminate the effect of Oddo-Harkins’ Rule (whereby even atomic-numbered elements are more abundant than odd

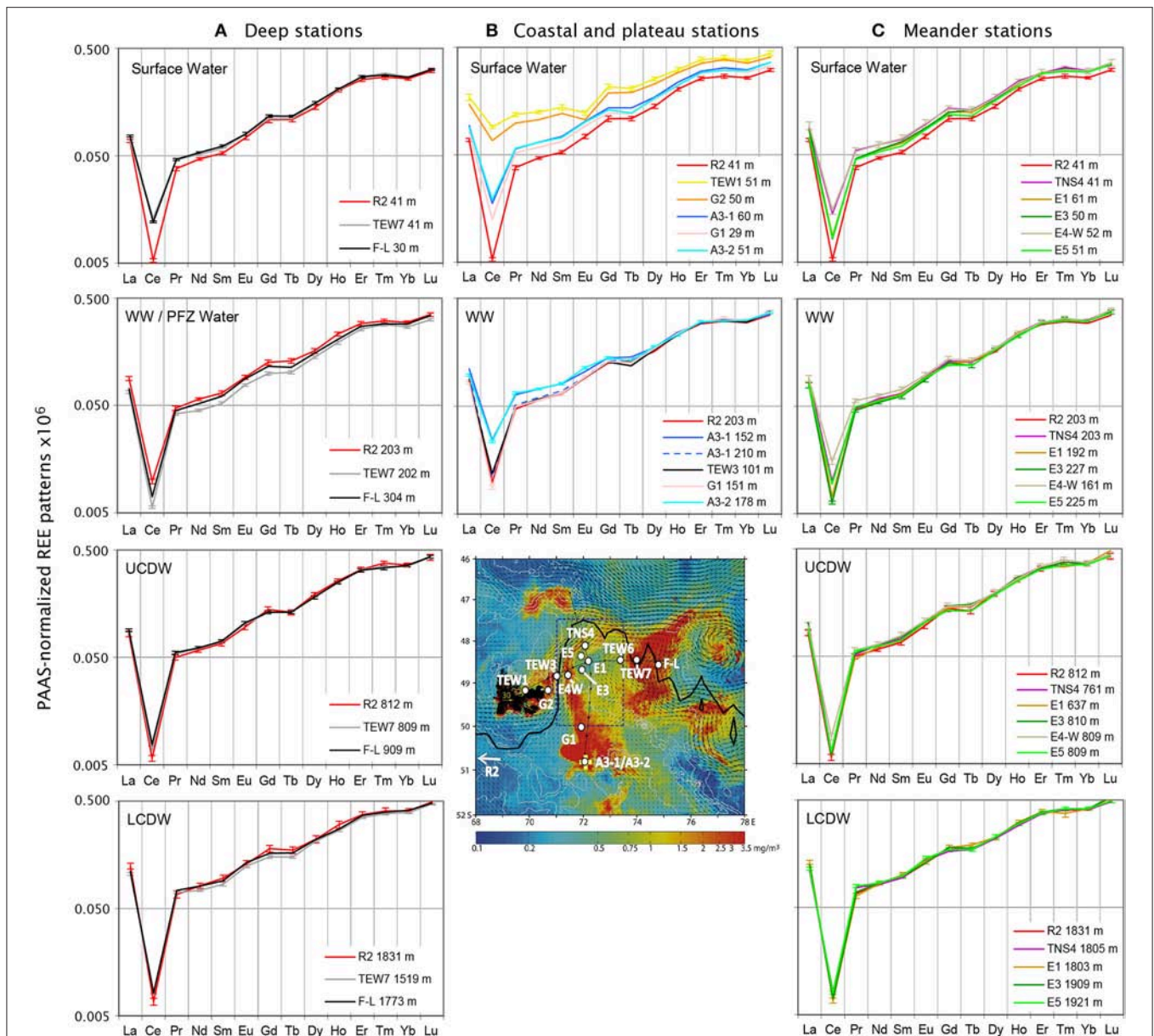


**FIGURE 4 |** PAAS-normalized REE patterns (PAAS, Post-Archean Australian Shale; McLennan, 1989; logarithmic scale) of the surface waters, the Winter Water (WW)/Polar Frontal Zone (PFZ) Water, the upper and the lower Circumpolar Deep Water (UCDW and LCDW), from top to bottom, for, as in **Figure 3**, **(A)** the deep stations R2, TEW7, and F-L, in the vicinity of the PF; **(B)** the coastal and plateau stations TEW1, G2, TEW3, G1, A3-1, and A3-2; and **(C)** the stations located in the meander area TNS4, E1, E3, E4-W, and E5. As in **Figure 3**, the patterns of the station R2 are reported for comparison in **(B,C)** (red pattern). For the sake of clarity, associated error bars are shown for some patterns only. They represent the ICP-MS method uncertainty associated with each sample measurement.

atomic-numbered elements; Schmidt et al., 1963), making any fractionation of an individual REE more discernible (**Figure 4**). Finally, some of these fractionations—for La, Ce, Eu, and Yb—are converted into anomalies that are calculated as follows:

$$\frac{La}{La^*} = \frac{[La]_n}{3[Pr]_n - 2[Nd]_n} \quad (1)$$

$$\frac{Ce}{Ce^*} = \frac{[Ce]_n}{2[Pr]_n - [Nd]_n} \quad (2)$$

$$\frac{Eu}{Eu^*} = \frac{4[Eu]_n}{3[Sm]_n + [Dy]_n} \quad (3)$$

$$\frac{Yb}{Yb^*} = \frac{[Yb]_n}{2[Er]_n - [Dy]_n} \quad (4)$$

where  $[X]_n$  refers to the concentration of the element X normalized to the concentration of this same element X in the PAAS standard [Equations (1) and (2) from Bolhar et al. (2004); Equations (3) and (4), respectively derived from the Gd

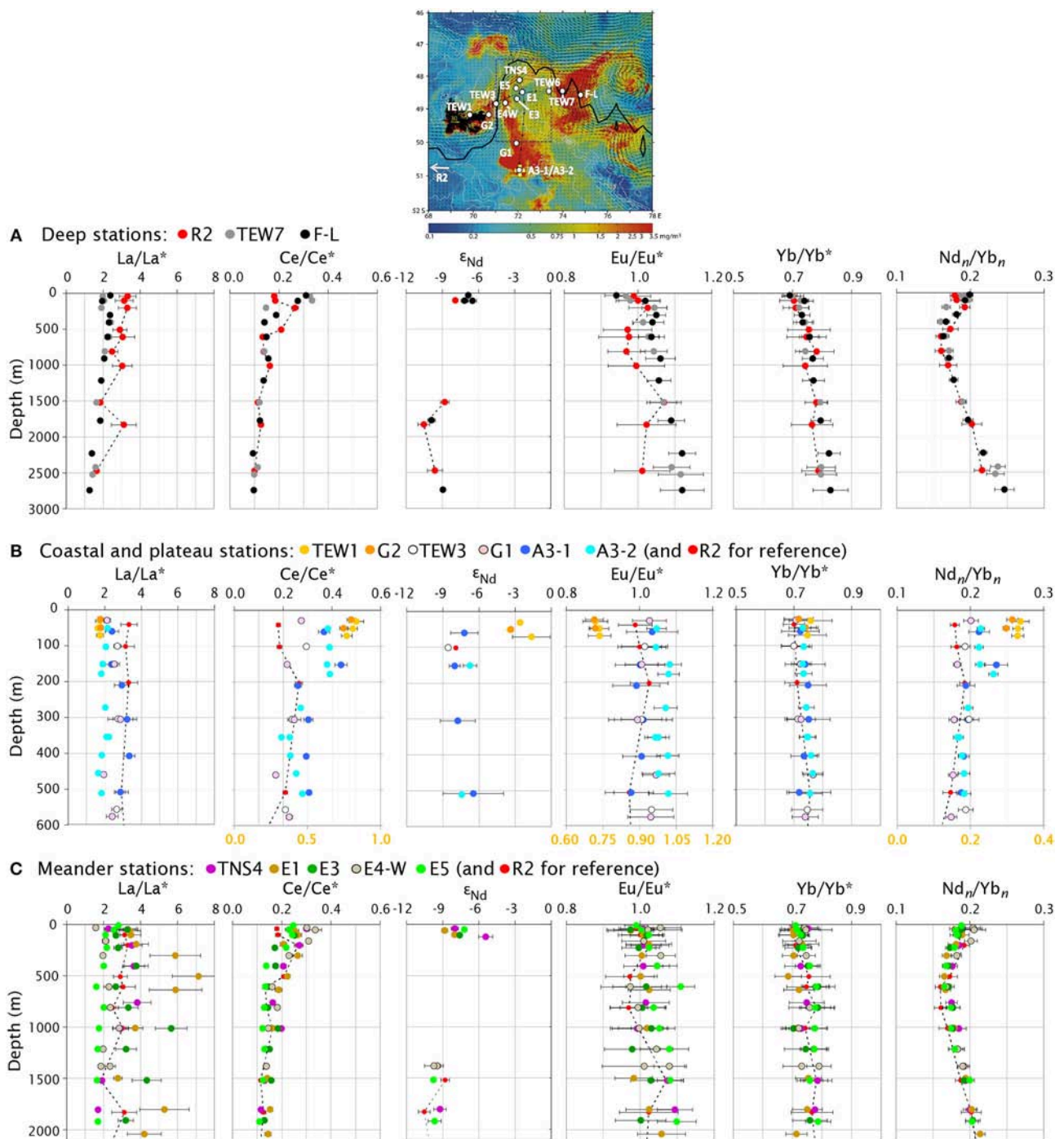


**FIGURE 5 |** Vertical profiles of the anomalies of La ( $\text{La}/\text{La}^*$ ), Ce ( $\text{Ce}/\text{Ce}^*$ ), Eu ( $\text{Eu}/\text{Eu}^*$ ), and Yb ( $\text{Yb}/\text{Yb}^*$ ), calculated following Garcia-Solsona et al. [2014; Equations (1–4) in the text], and of  $\text{Nd}_N/\text{Yb}_N$ , from the PAAS-normalized REE patterns shown in **Figure 4**. The vertical profiles of the dissolved Nd isotopic composition, expressed as  $\epsilon_{\text{Nd}}$ , are also shown. These six parameters complement the vertical profiles of the concentrations shown in **Figure 3**. As in **Figures 3, 4**: **(A)** deep stations R2, TEW7, and F-L, in the vicinity of the PF; **(B)** coastal and plateau stations TEW1, G2, TEW3, G1, A3-1, and A3-2; and **(C)** stations located in the meander area TNS4, E1, E3, E4-W, and E5. Also, as in **Figures 3** and **4**, the data of station R2 are reported for comparison in **(B,C)** (profile represented by the red dots and gray dashed line). Note the larger scale of  $\text{Ce}/\text{Ce}^*$ , of  $\text{Eu}/\text{Eu}^*$ , and of  $\text{Nd}_N/\text{Yb}_N$  associated with the coastal sample parameters of stations TEW1 and G2 [yellow secondary horizontal axis in **(B)**]. Error bars are given for each parameter, representing the TIMS method uncertainty ( $2\sigma$ ) for  $\epsilon_{\text{Nd}}$  and the uncertainty propagation from the anomaly Equations (1–4) for the other profiles (see the **Supplementary Material** for details).



anomaly expression of Bau et al. (1996), and from the Lu anomaly expression of Garcia-Solsona et al. (2014)]. The propagation of uncertainty is determined from these equations for each anomaly and detailed in the **Supplementary Material**. We refer to positive anomalies when they are  $>1$ , negative when lower than 1. Anomalies are defined as weak if close to 1, strong if much below or much above 1.

Along with these anomalies, two complementary parameters are also shown: (i) the  $\text{Nd}_n/\text{Yb}_n$  vertical profiles, which give information about the slope of the normalized pattern, and thus, information about the relative importance between potential recent lithogenic supplies and authigenic processes; (ii) the vertical profiles of Nd isotopic composition  $\epsilon_{\text{Nd}}$ , which give information about the potential occurrence of elemental inputs or water mass mixing.

All the results are similarly displayed, divided into three groups of stations: (i) the deep stations R2, TEW7, and F-L, in the vicinity of the PF; (ii) the coastal and plateau stations TEW1, G2, TEW3, G1, A3-1, and A3-2; and (iii) the stations located in the PF cyclonic meander area TNS4, E1, E3, E4-W, and E5 (subplots a, b, and c of **Figures 3, 5**, respectively). Because station R2 was considered as the high-nutrient low-chlorophyll reference station, R2 data were also reported in the subplots of the shallow (coastal and plateau) stations and meander stations for comparison (**Figures 3–5**).

On a broad geographical scale, our results are consistent with the dissolved REE concentrations and  $\epsilon_{\text{Nd}}$  data from the literature that are measured upstream in the Southern Ocean, in the southeast Atlantic Ocean, and especially with those measured between the Polar Front and the southern Antarctic Circumpolar Front (see **Table 2** for comparison with German et al., 1995; Stichel et al., 2012; Garcia-Solsona et al., 2014; Hathorne et al., 2015). Our results are also in agreement with those found by Zhang et al. (2008) in the same area, during KEOPS1 (**Table 2**). The main difference between the REE dataset reported upstream and in the Kerguelen area is observed for the Ce concentrations, which reach much higher values in the coastal environment of KEOPS1 and KEOPS2 areas compared to the open ocean environment of the upstream stations. These locally high Ce concentrations will be discussed in the following section.

## Deep Stations, On the Edges of the PF

Above 500 m depth, we observe three distinct features when considering the deep stations located on the edges of the PF. The first one is the convex shape of the R2 concentration profiles between 100 and 500 m depth, especially pronounced for the light and middle REEs (LREE—La to Nd—and MREE—Sm to Dy, respectively), which is not observed in stations TEW7 and F-L. These subsurface R2 samples are also characterized by a weaker Ce anomaly (higher Ce/Ce\* value) and a weaker  $\text{Nd}_n/\text{Yb}_n$  slope (higher  $\text{Nd}_n/\text{Yb}_n$  value; **Figure 5A**). All these characteristics suggest that recent lithogenic supplies are influencing the area of station R2, which challenges its definition as a “reference station.” The second distinct feature in the upper layer of the deep stations is the high LREE concentrations observed in the first 100 m at TEW7 and F-L, which are higher than in the underlying subsurface waters, especially pronounced in Ce

(**Figure 3A**). These high Ce concentrations are associated with weak Ce anomalies ( $\sim 0.3$ ), weak  $\text{Nd}_n/\text{Yb}_n$  slopes and slightly negative Eu anomalies, especially for the surface water sampled at station F-L (Surface Water subplot of **Figure 4A, 5A**). The  $\epsilon_{\text{Nd}}$  of the F-L surface water is also relatively high, compared to that measured at R2 (F-L:  $\epsilon_{\text{Nd}} = -6.8 \pm 0.1$ ; R2:  $\epsilon_{\text{Nd}} = -7.9 \pm 0.1$ ). Similar to the WW at station R2, these SASW also seem to be tagged by recent lithogenic inputs. The origin of these supplies will be discussed in the next section. The third distinct feature is the very low concentrations found between 200 and 500 m at F-L and TEW7 compared to all the other stations. These low concentrations, the lowest of our study, may reflect the different origin of the waters flowing at these depths. As discussed in the hydrological section, these waters are significantly warmer than the waters flowing at the same depth range at the other stations and are therefore thought to come from the SAF area. Their REE contents are in the same range as those found in the SAF area of the southeastern Atlantic Ocean (German et al., 1995: Nd = [9.5–11.0] pmol kg<sup>-1</sup>; Hathorne et al., 2015: Nd = [9.6–10.9] pmol kg<sup>-1</sup>; Stichel et al., 2012: Nd = [10.3–11.8] pmol kg<sup>-1</sup>; Garcia-Solsona et al., 2014: Nd = [9.5–11.0] pmol kg<sup>-1</sup>; this study: Nd = [10.6–12.2] pmol kg<sup>-1</sup>).

Below 500 m, the deep stations exhibit increasing REE concentrations with depth, commonly observed in deep open-ocean profiles (e.g., Elderfield, 1988; Sholkovitz et al., 1994; German et al., 1995; **Figure 3A**). East of Kerguelen, as the depth increases, stations TEW7 and F-L exhibit a positive Eu anomaly that progressively increases and a smooth accentuation of Ce anomaly, together with a smooth decrease in La anomaly and a  $\text{Nd}_n/\text{Yb}_n$  slope becoming weaker with depth (**Figures 4A, 5A**). Anomalies of La and Eu show jerkier variations at station R2, although weakly constrained due to higher standard deviations (i.e., error bars), especially for Eu and below 500 m depth, and thus, only significant in the surface layer compared to those at 1,500 m.  $\epsilon_{\text{Nd}}$  values measured for some R2 and F-L samples between 1,500 m and the bottom are in similar ranges, between  $-8.8$  and  $-10.5$ .

## Coastal and Plateau Stations

Compared to other stations, coastal stations are highly concentrated in REE, especially in LREE (note the extended scales in **Figures 3B, 5B** for coastal stations), which leads to a much flatter PAAS-normalized pattern (Surface Water subplot of **Figure 4B**). These patterns typically highlight recent substantial lithogenic supplies. Surprisingly, they are characterized by a prominent negative Eu anomaly (discussed below). They are also associated with the most radiogenic dissolved  $\epsilon_{\text{Nd}}$  values of the study ( $-2.6 \pm 0.2$ ;  $-3.4 \pm 0.2$ ; **Figure 5B**).

Over the plateau, concentrations are higher than at the reference station R2, even between 200 and 500 m depth where R2 exhibits—although to a lesser degree—concentrations abnormally high for a so-called HNLC station. Station A3 exhibits significantly higher Ce concentrations in the upper 200 m than below, with a maximum at 200 m, a feature also noticeable but much less marked for Nd, Eu, and La, even less in Yb and Lu (**Figure 3B**). Ce concentrations are significantly higher at station A3 than at G1 or TEW3 ( $\sim 2$ – $9$  pmol kg<sup>-1</sup> higher),

**TABLE 2** | Comparison of our data with those from the literature.

	La	Ce	Nd (pmol kg <sup>-1</sup> )	Eu	Yb	ε <sub>Nd</sub>
German et al., 1995 (station 47)	[10.8–50.8]	[3.0–14.6]	[7.7–37.3]	[0.4–1.7]	[2.2–8.3]	–
Zhang et al., 2008 (excluding their coastal station)	[14.8–42.6]	[2.9–27.5]	[10.3–27.6]	[0.4–1.2]	[4.5–7.6]	[(-11.1)–(-6.3)]
Stichel et al., 2012 (station 113: 150–2400 m)	–	–	[15.0–24.5]	–	–	[(-8.7)–(-8.0)]
Hathorne et al., 2015 (station 113: 381–1001 m)	[28.0–33.6]	[3.4–3.9]	[16.6–21.2]	[0.8–0.9]	[6.5–7.0]	–
Garcia-Solsona et al., 2014 (station S4)	[17.2–40.2]	[2.4–3.6]	[11.3–23.9]	[0.6–1.1]	[5.2–7.9]	[(-9.5)–(-7.0)]
This study (excluding our coastal stations)	[18.4–41.2]	[2.8–13.7]	[10.6–27.1]	[0.5–1.3]	[4.3–7.7]	[(-10.5)–(-5.4)]

German et al. (1995), Stichel et al. (2012), Hathorne et al. (2015), and Garcia-Solsona et al. (2014) measured dissolved REEs in seawater collected upstream in the Southern Ocean, in the southeast Atlantic Ocean. The stations from Stichel et al. (2012), Hathorne et al. (2015), and Garcia-Solsona et al. (2014) reported here were sampled between the Polar Front and the southern Antarctic Circumpolar Front; the station reported in German et al. (1995) was sampled further north, south of the Southern Tropical Front. Data from Zhang et al. (2008) come from the KEOPS1 cruise and document the area just south of the one studied here. Except Ce concentrations that reach high values in the coastal environment of KEOPS1 (Zhang et al., 2008) and KEOPS2 (this study), we observe consistent ranges of REE data among the different studies.

and La concentrations are significantly higher during the first visit to station A3 (A3-1, ~2–5 pmol kg<sup>-1</sup> higher) than at G1, TEW3, and A3-2; otherwise, all plateau stations exhibit similar REE vertical profiles. The weak Ce anomaly associated with the weak Nd<sub>n</sub>/Yb<sub>n</sub> slope (i.e., high Nd<sub>n</sub>/Yb<sub>n</sub> ratio) in the first 200 m depth of station A3 suggests relatively strong and recent inputs of lithogenic material (**Figures 4B, 5B**). Two features make the second visit to station A3 (A3-2) distinguishable from the first visit (A3-1): station A3-1 exhibits higher positive La anomalies than A3-2 and almost no Eu anomaly over the whole profile, while A3-2 shows significant positive Eu anomalies. However, considering the anomaly uncertainties, these features are more significant for the La anomalies than for the Eu ones (**Figure 5B**). The ε<sub>Nd</sub> values measured for station A3-1 and A3-2 are in the same range as the surface samples of the deep stations and are also similar to those found during KEOPS1 at this same station A3, varying between –6 and –8 (**Figure 8B**).

## Meander Stations

In the meander region, above 500 m depth, vertical profiles behave differently depending on which REE is considered. HREE (Ho to Lu) concentrations mostly increase with increasing depth. LREE except Ce, and MREE exhibit quite constant concentrations (**Figure 3C**). Ce is roughly twice more concentrated in the first 200 m than in the underlying waters, especially at stations E4-W and TNS4, which are located in the strongest streamline of the meander recirculation (see **Figure 1B**). This feature, associated with relatively low Ce anomalies and weak Nd<sub>n</sub>/Yb<sub>n</sub> slopes, is similar to the upper part characteristics of some other stations (TEW7, F-L, TEW1, G2, and A3; **Figures 3, 5**). Eu anomalies are low and variable from one station to the other, from slightly negative at E1 and E3 to slightly positive at E4-W, in the surface waters. Finally, ε<sub>Nd</sub> values are in a relatively narrow range [–9; –7], similarly to the surface waters sampled at R2 and at A3, and slightly less radiogenic than F-L surface waters. However, WW sampled at

TNS4 is characterized by a more radiogenic value (ε<sub>Nd</sub> = –5.4 ± 0.6).

Between 500 m depth and the bottom, vertical profiles of REE concentrations show general trends similar to those of the deep stations: a progressive increase with depth, less pronounced in Ce (**Figure 3C**, compared to **Figure 3A**). The REE concentrations are equivalent to or slightly higher than those observed at the reference station R2. Concerning the REE fractionations, the deep waters at station E5 exhibit the most pronounced Ce anomalies, even slightly more pronounced than in deep waters of R2, together with constant low La anomalies and positive Eu anomalies, slightly increasing with depth (**Figure 5C**). These characteristics resemble those observed in the deep waters at stations TEW7 and F-L. In contrast, the deep waters at stations E1 and E3—located in the vicinity of the meander center—exhibit jerky profiles of pronounced La anomalies (the highest of the study, albeit with relatively high error bars) and no clear Eu anomalies, similar to the characteristics of station R2. The ε<sub>Nd</sub> values, determined only for the LCDW, are constant (ranging from –10 to –9) and similar to those measured at the deep stations R2 and F-L.

## DISCUSSION

The results described above highlight that the distribution of dissolved REEs and ε<sub>Nd</sub> in the Kerguelen Plateau area are influenced by the following factors:

- 1) Recent lithogenic supplies, deduced from concentration increases (especially LREEs) and from weakening of Ce anomaly and of Nd<sub>n</sub>/Yb<sub>n</sub> slope, which impact most of the waters sampled between the surface and 500 m depth;
- 2) Two kinds of fractionation processes observed below 500 m depth: (i) constant low La anomalies and positive Eu anomalies, and (ii) high jerky La anomalies and no Eu anomalies. We hypothesize that these features—although less

significant for Eu than for La due to weaker overall variations relatively to the associated uncertainties—are related to authigenic processes operating within the water column.

The signatures of the lithogenic supplies are spatially and vertically nuanced. Surface lithogenic inputs are unequivocally observed at the coastal stations TEW1 and G2, at all stations sampled above the Central Kerguelen Plateau (e.g., A3, G1), at the deep stations TEW7 and F-L and at the meander stations E4-W and TNS4. The lithogenic signal imprint is much less obvious in the surface waters of the recirculation center (stations E1, E3, and E5), although higher than in the surface waters of R2, almost not impacted. By contrast, this latter station exhibits a clear imprint of lithogenic supplies at 200 m. Such subsurface input is also observed at the plateau stations, especially A3, and at the meander stations E4-W and TNS4. Between 200 and 500 m depth, lithogenic supplies are still observed—although to a lesser degree—at every station except at TEW-7, F-L, E3, and E5. Finally, below 500 m depth, only a minor remnant lithogenic signature could be suggested in the UCDW for stations E4-W and TNS4, compared to the other deep stations.

Such lithogenic signatures raise two questions: (i) Where do these supplies come from? (ii) Do they all exhibit similar REE characteristics? The relative REE fractionations could help to investigate further. The parameters showing the strongest variations when comparing the coastal samples—likely the most impacted by source effects—to the other sites are the Ce and Eu anomalies and the  $Nd_n/Yb_n$  ratio (Figure 5). While the intensity of the Ce anomaly and of the slope  $Nd_n/Yb_n$  are good indicators of the *freshness* of the lithogenic supplies, the direction and intensity of the Eu anomaly could help revealing the *nature* of the lithogenic supplies. These three parameters are displayed in Figure 6 and discussed below. For comparison, we also report these parameters for the KEOPS1 station C1, from Zhang et al. (2008), which characterizes Heard Island coastal waters (see yellow dots circled in red in Figure 6). Zhang et al. (2008) did not use a desolvating system for their REE analyses; therefore, they had to apply a more important correction of oxy-hydroxide interferences on their measurements, mainly impacting Eu (CeO ~ 3–4%; BaO interferences ranging from 20 to 40% of the Eu signal). However, the similarity of the Eu anomaly range between their study and ours ([0.97–1.15] and [0.98–1.13] pmol kg<sup>-1</sup>, respectively) for the off-plateau stations and the consistency of the variations observed in their dataset (notably between their 2 stations A3, both characterized by higher Eu anomalies than at the other stations of their study) make us believe that the comparison of our Eu data with theirs is legitimate.

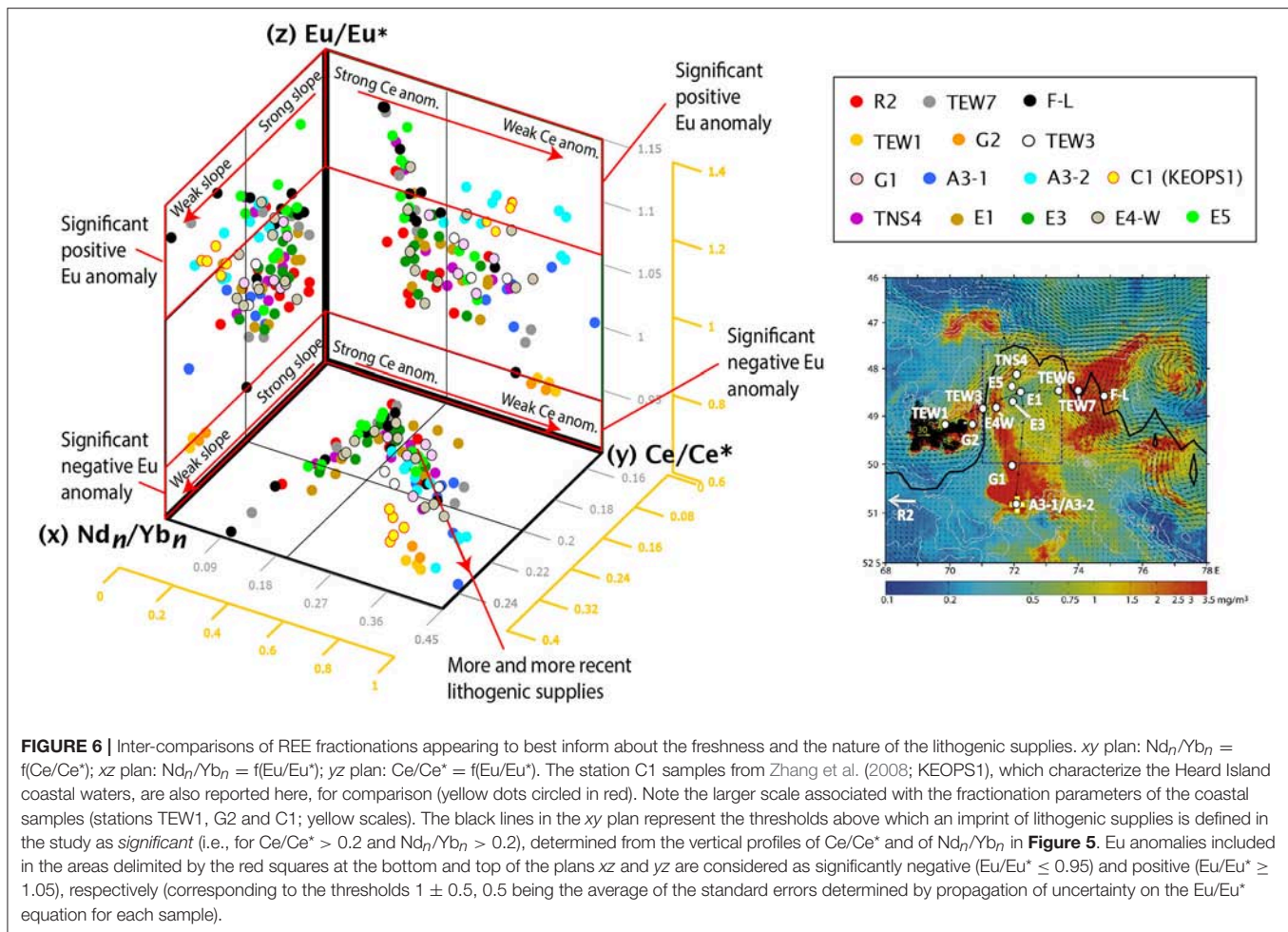
## Characterization of the Lithogenic Sources

We consider the imprint of lithogenic supplies as *significant* if  $Ce/Ce^* > 0.2$  and  $Nd_n/Yb_n > 0.2$  (see Figure 6). Following the general statements of the dissolved oceanic REE behavior (Elderfield, 1988; Byrne and Kim, 1990; Moffett, 1990), the freshest lithogenic supplies are tagged by the weakest Ce anomaly and  $Nd_n/Yb_n$  slope (see the red arrow in the *xy* plane, in Figure 6). As expected, they are observed on coastal samples near the Kerguelen and Heard Islands, which likely suggests a

recent release of lithogenic material into the dissolved phase. More surprisingly, these coastal samples exhibit distinct Eu anomaly signatures: while Kerguelen Islands samples exhibit a prominent negative Eu anomaly, Heard Island samples are, as previously noted by Zhang et al. (2008), characterized by a significant positive one (*z*-planes in Figure 6; see TEW1 and G2 dots for Kerguelen samples and C1 dots for Heard samples). This latter pattern could reflect REE release from Heard margin basaltic sediments, characterized by a positive Eu anomaly (dotted light gray pattern in Figure 7B; Weis et al., 2002; Doucet et al., 2005; Arevalo and Jr, 2008). Such basaltic imprint was also suggested to explain the positive Eu anomaly observed in seawater in several areas of the equatorial and tropical Pacific, in the vicinity of basaltic islands (Grenier et al., 2013; Fröllje et al., 2016; Molina-Kescher et al., 2018). However, the Kerguelen samples are characterized by a REE pattern displaying a negative Eu anomaly. To our knowledge, such significant negative Eu anomalies were observed only once before, by Elderfield and Greaves (1982), in the surface and deep waters of the Eastern Equatorial Atlantic, and in deep Mediterranean outflow water. These authors attributed this negative Eu anomaly to be the result of leaching of aeolian loess particles of Saharan origin.

Using the online geological database EarthChem (www.earthchem.org/), we compared the PAAS-normalized REE patterns and  $\epsilon_{Nd}$  of the Kerguelen coastal samples to those of the sediments and rocks of the Kerguelen Plateau area (Figures 7A,B). We also reported the REE patterns and  $\epsilon_{Nd}$  of two beach water samples collected from a zodiac during the KEOPS2 cruise. One was collected in the *Golfe du Morbihan*, W-SW of station G2, and was filtered, like the other samples reported in this work. The other one was collected in the *Baie des Baleiniers*, near TEW1 (S-SE of it) and was not filtered, in order to get the total “particulate + dissolved” signal. The filtered beach water sample exhibits a REE pattern very similar to those observed at TEW1 and G2—although logically slightly more concentrated and flatter—with a similar prominent negative Eu anomaly (brown pattern in Figures 7A,B; G2 pattern shown in Figure 4B). By contrast, the unfiltered beach water sample shows a much more concentrated PAAS-normalized REE pattern, increasing from La to Eu and decreasing from Eu to Lu (orange continuous pattern in Figure 7B). This pattern is very similar in shape to the average PAAS-normalized pattern for the Kerguelen flood basalt (light gray pattern in Figure 7B; Doucet et al., 2005; Xu et al., 2007). This could suggest that the unfiltered beach water is tagged by a release of basaltic REEs, consistent with the signature of some particulate trace metal ratios measured at the Kerguelen coastal stations (van der Merwe et al., 2015). But how to explain the negative Eu anomaly in the dissolved phase if it results from basaltic release, while most of the studies reporting dissolved REE patterns in the vicinity of basaltic islands observed a positive Eu anomaly (e.g., Zhang et al., 2008; Grenier et al., 2013; Fröllje et al., 2016; Molina-Kescher et al., 2018)? To our knowledge, such negative Eu anomaly in the *dissolved* fraction during exchanges between basaltic sediments and seawater was only observed in laboratory experiments (Pearce et al., 2013). While performing particulate dissolution experiments on marine





sediments taken from a core top collected at C1 during the KEOPS1 cruise, Pearce et al. (2013) observed the formation of a negative dissolved Eu anomaly within the first 14 days of their experiment, presumably caused by the stronger incorporation of Eu during the initial precipitation of the over-saturated rhabdophane, a secondary REE-phosphate mineral (dashed dark red patterns in **Figure 7A**). However, this negative Eu anomaly was eroded within 1 month and eventually turned to be positive (Figure 5 of Pearce et al., 2013; dotted dark red patterns in **Figure 7A**). Thus, according to these experimental results, if the lithogenic inputs impacting the Kerguelen Islands waters are pure basaltic release, they would have to be very fresh to explain the concomitant opposed Eu anomalies observed in the dissolved and total REE patterns of our coastal samples. Nevertheless, the rock/water ratio of the *in vitro* experiments performed by Pearce et al. (2013) was most likely higher than in the environment of the coastal samples studied here and potentially led to formation of minerals that may not occur in natural settings. These setting differences may explain why the REE pattern and  $\varepsilon_{Nd}$  of the Heard Island coastal C1 sample measured by Zhang et al. (2008) differ significantly from those acquired by Pearce et al. (2013) at the end of their experiment (**Figure 7A**).

As such, the basaltic origin of the lithogenic signature is more strongly presumed in the total phase than in the dissolved phase of the coastal Kerguelen samples and is likely mainly derived from the particulate fraction. In order to remove this particulate basaltic imprint, we normalized the unfiltered beach water to the average Kerguelen flood basalts, assuming that the remaining signal would reveal information about the dissolved fraction included in this total phase. This basalt-normalization leads to a pattern enriched in LREE and marked by a significant negative Eu anomaly, indeed reminding the characteristic of the dissolved Kerguelen coastal samples (orange dashed pattern in **Figure 7B**). The only geological formations that look like to these patterns are trachytes and rhyolites (discontinuous pattern with gray squares and continuous thick dark gray pattern in **Figure 7B**, respectively; Ingle et al., 2002; Gagnevin et al., 2003). Fedele et al. (2015) showed that the negative Eu anomaly of trachytes comes from the dominant glassy matrix, the minerals (dominated by alkali feldspars and plagioclases) being rather characterized by a positive Eu anomaly. Numerous veins of trachytes and rhyolites are present in the Kerguelen flood basalts (Bitschene et al., 1992; Damien Guillaume, LMV, Saint-Etienne, and Léandre Ponthus, GET, Toulouse, personal communication).



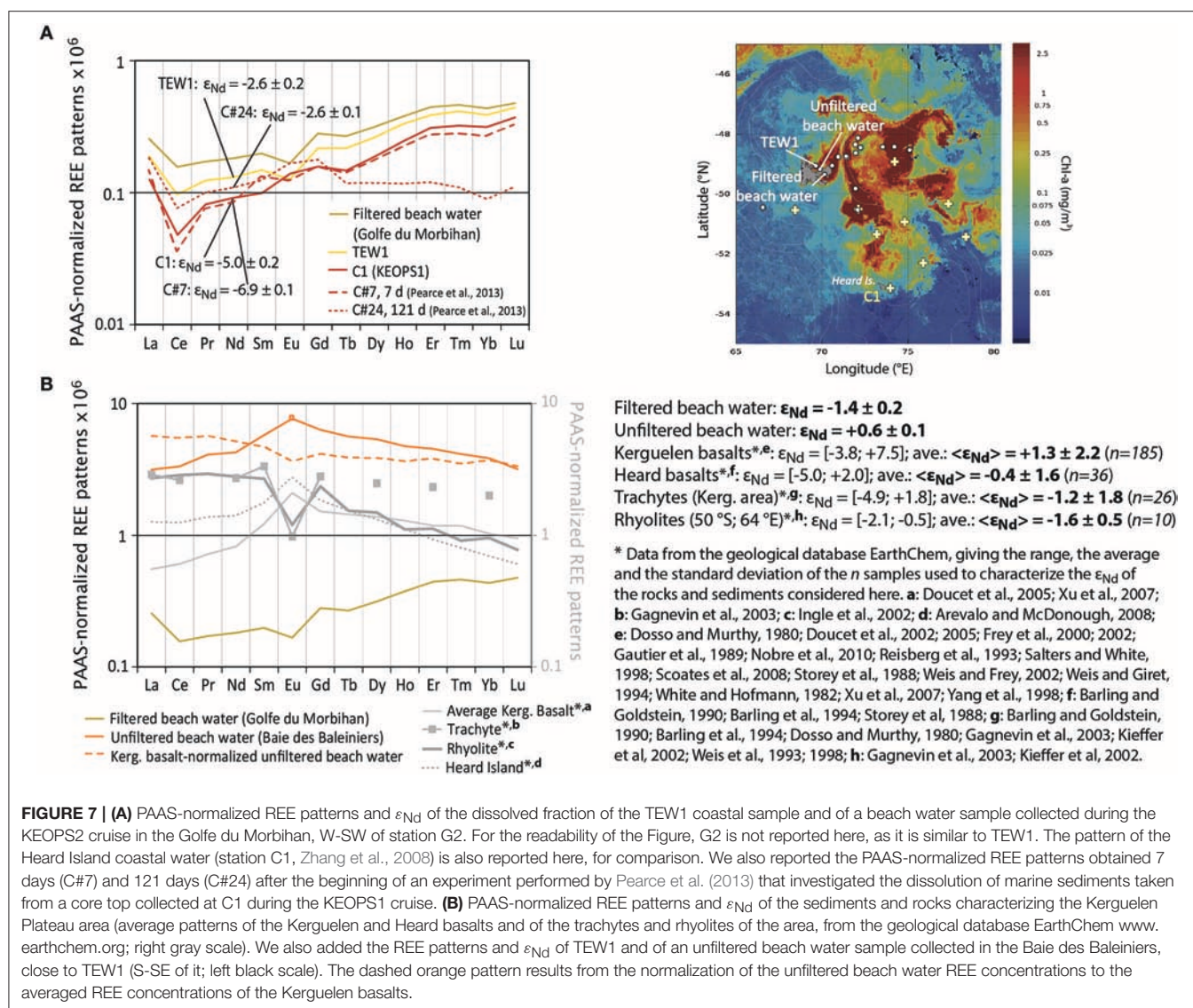


**FIGURE 7 | (A)** PAAS-normalized REE patterns and  $\epsilon_{Nd}$  of the dissolved fraction of the TEW1 coastal sample and of a beach water sample collected during the KEOPS2 cruise in the Golfe du Morbihan, W-SW of station G2. For the readability of the Figure, G2 is not reported here, as it is similar to TEW1. The pattern of the Heard Island coastal water (station C1, Zhang et al., 2008) is also reported here, for comparison. We also reported the PAAS-normalized REE patterns obtained 7 days (C#7) and 121 days (C#24) after the beginning of an experiment performed by Pearce et al. (2013) that investigated the dissolution of marine sediments taken from a core top collected at C1 during the KEOPS1 cruise. **(B)** PAAS-normalized REE patterns and  $\epsilon_{Nd}$  of the sediments and rocks characterizing the Kerguelen Plateau area (average patterns of the Kerguelen and Heard basalts and of the trachytes and rhyolites of the area, from the geological database EarthChem www.earthchem.org; right gray scale). We also added the REE patterns and  $\epsilon_{Nd}$  of TEW1 and of an unfiltered beach water sample collected in the Baie des Baleiniers, close to TEW1 (S-SE of it; left black scale). The dashed orange pattern results from the normalization of the unfiltered beach water REE concentrations to the averaged REE concentrations of the Kerguelen basalts.

Interestingly, Mungall and Martin (1994) observed a significant leaching of trachyte lava without devitrification at ambient groundwater conditions in Azores area. This differential leaching between trachytes and basalts could explain why the dissolved seawater off the Kerguelen coast exhibits an imprint of trachytic glass leaching, while the total seawater (dissolved + particulate) exhibits a dominant basalt signature, with a positive Eu anomaly and decreasing PAAS-normalized concentrations from Eu to Lu.

This hypothesis is strengthened by the  $\epsilon_{Nd}$  results. The unfiltered beach water has a radiogenic  $\epsilon_{Nd}$  value of  $+0.6 \pm 0.1$ . As the  $\epsilon_{Nd}$  of surface offshore seawater varies between  $-7$  and  $-8$ , this beach water must have been strongly enriched by a more radiogenic source. Lithogenic particles have presumably been dissolved during the etching process of this unfiltered sample. Among trachytes, rhyolites and basalts, the sole candidate characterized by  $\epsilon_{Nd}$  values higher than  $+0.6$  are the basalts

( $\langle \epsilon_{Nd} \rangle = +1.3 \pm 2.2$ ; **Figure 7B**; Dosso and Murthy, 1980; White and Hofmann, 1982; Storey et al., 1988; Gautier et al., 1989; Barling and Goldstein, 1990; Reisberg et al., 1993; Weis et al., 1993, 1998; Barling et al., 1994; Weis and Giret, 1994; Salters and White, 1998; Yang et al., 1998; Frey et al., 2000, 2002; Doucet et al., 2002, 2005; Kieffer et al., 2002; Weis and Frey, 2002; Xu et al., 2007; Scoates et al., 2008; Nobre Silva et al., 2010). The filtered beach water has a less radiogenic value, consistent with a higher contribution of the less radiogenic trachytes or rhyolites (see values in **Figure 7B**). Finally, the Kerguelen coastal waters are the freshest waters of the study, suggesting a supply of meteoric water runoff or groundwater that could erode the local lithogenic material (**Figure 2A**). The ongoing measurements of  $\epsilon_{Nd}$  and REE concentrations of the particulate phases of the coastal samples will help us to determine which of these hypotheses—signature of basalts only or of both trachytes and basalts—is the most plausible.

By contrast, the REE patterns of the Heard Island coastal samples do not reveal such evidence of trachyte imprint in their lithogenic signature (Zhang et al., 2008; **Figure 7A**). Compared to the Kerguelen coastal area, the marine influence seems to be more pronounced in the Heard Island area, as supported by the lower REE concentrations, especially LREE, added to the less radiogenic  $\epsilon_{Nd}$ . This suggests a more efficient water mass renewal in the coastal area of Heard Island, consistent with the proximity of this area to the Fawn Trough, a favored zonal passage for the circumpolar flow (Park et al., 2008). Alternatively, the REE patterns of Heard Island coastal water samples could also reflect hydrothermal input. Indeed, hydrothermal activity—which was recently discovered between Heard and McDonald Islands (Holmes et al., 2017), a shoal area of maximum depth of 300 m—is known to (i) preferentially scavenge the LREEs from the surrounding waters, thus becoming a sink rather than a source of REEs dissolved in seawater; and (ii) result in a rapidly weakening Eu enrichment in the surrounding waters (Klinkhammer et al., 1983; Olivarez and Owen, 1991).

## Transport of the REE Lithogenic Signature as Tracer of Water Mass Pathways

Although less pronounced than at coastal stations, lithogenic signatures were also observed offshore, both above and off the Plateau, in various depth ranges. This presumes a transport of lithogenic supplies, laterally or vertically, away from the sources.

The slight negative Eu anomaly observed north of the PF, in the surface samples of the easternmost stations F-L and, at a lower degree, TEW7, hints at the signature of the Kerguelen coastal dissolved samples (**Figures 5A, 6**). This suggests that surface waters freshly enriched in lithogenic supplies were transported relatively quickly from the north-eastern Kerguelen coast to the location of these offshore stations, along a path confined to north of the PF. This is in agreement with (i) the PF location and the circulation of the surface/subsurface waters (Figure 1; Figure 15 of Park et al., 2014; d'Ovidio et al., 2015), (ii) the water mass characteristics displayed in **Figure 2A**, and (iii) the trajectories of the drifters launched during KEOPS2 (Sanial et al., 2015). This interpretation is also supported by the KEOPS2 radium data (Sanial et al., 2015) and particulate trace metal data (van der Merwe et al., 2015).

Based on the distance from the eastern Kerguelen coast, we could expect stronger surface lithogenic imprints at stations located in the meander area, south of the PF, than at the further stations TEW7 or F-L. Yet, the lithogenic imprints observed in the core of the meander, at E1, E3, and E5, are negligible. They are at best as pronounced as at TEW7 and F-L at stations further away from the core of the meander, where surface currents were stronger, but by contrast, they do not show any visible Eu anomaly (E4-W and TNS4; **Figures 5A, 6**). Sanial et al. (2015) reported significant short-lived Ra isotope activities in this region located downstream of Kerguelen Islands, south of the PF, indicative of recent continental supplies. Using Ra isotopes as a chronometer, these authors estimate a transit time for the surface waters between the shelf and stations E4-W or TNS4 of the order of 1–2 months. Considering the transit times and

pathways of the surface waters, they presumed that these recent supplies were coming from the Kerguelen shelves—rather than from Heard Island or from the Central Kerguelen Plateau—and were sporadically transported through the PF. It is therefore highly plausible that the initial negative Eu anomaly of the Kerguelen supplies was quickly eroded within this time interval, either by authigenic process, or by dilution with water tagged by a different REE pattern. Since F-L and E4-W show similar biological characteristics, any biogenic scavenging could be ruled out (Cavagna et al., 2015; Jacquet et al., 2015; Laurenceau-Cornec et al., 2015; Planchon et al., 2015). In addition, F-L surface waters were advected slower than E4-W ones from the Kerguelen coast (in  $\sim 2$  months for F-L; Sanial et al., 2015), while they preserve their Eu anomaly. As such, the erosion of the negative Eu anomaly more likely results from dilution with water tagged by a null to positive Eu anomaly, presumably coming from the south, than from a local authigenic process. This hypothesis is consistent with the back-trajectories of water parcels as calculated from altimetry (d'Ovidio et al., 2015).

Central Plateau stations exhibit strong lithogenic signatures characterized by null to positive Eu anomalies (**Figures 5B, 6**). The difference of Eu anomaly between A3-1 (first visit) and A3-2 (second visit) will be discussed in the following subsection. As suggested by other lithogenic tracers, vertical supplies from the Central Kerguelen Plateau sediments likely contribute dominantly to the signatures observed from the bottom to 200 m depth (Bowie et al., 2015; Sanial et al., 2015; van der Merwe et al., 2015). However, lithogenic imprints are more pronounced in the first 200 m of our stations A3 than in the underlying waters, suggesting that lateral supplies are added to the vertical ones, especially in the upper layer. The signature of these upper supplies shares no similarities with those characterized in the eastern Kerguelen coastal samples, and circulation investigations rather suggest a southern source, most likely from the Heard Island area (Charrassin et al., 2004; Park et al., 2008; Figures 6, 15 from Park et al., 2014; Figure 9 from Sanial et al., 2015). This advective supply of southern origin was already suggested from the KEOPS1 results, first by the dissolved radium-228 distribution observed on the Central Kerguelen Plateau, and confirmed by the REE distribution at station A3 (van Beek et al., 2008; Zhang et al., 2008). This southern advection is also supported by the particulate trace metal distribution (van der Merwe et al., 2015). Overall, our REE results support the hypotheses for regional circulation drawn by Park et al. (2014, their Figure 15): a surface/subsurface southern source—of water and of lithogenic material—that is transported toward the Central Plateau (A3), with its lithogenic signature fading along its northward pathway, as shown by the weaker imprint at G1. As it reaches the meander area, just south of the PF and East of Kerguelen Islands, this southern flow mixes with the western flow, itself tagged by Kerguelen continental material, explaining the enhanced lithogenic signature in the REE data at E4-W and TNS4 compared to G1 or TEW3 (**Figures 3B,C, 5B,C, 6**). The residual signal observed between 500 and 1,000 m at stations E4-W and TNS4 (meander area) can be explained by supply of sediments from the Kerguelen plateau and their partial lateral advection. The core of the meander area (stations E1, E3,

and E5) seems to be more affected by a local recirculation, being therefore likely more isolated from the area of lithogenic material transit, as previously explained.

The sporadic “permeability” of the PF (i.e., transport across it) is not only confirmed by data of the off-core meander stations but also by the subsurface data obtained at station R2. Samples collected at 200 m depth and, to a lesser degree, at 500 m depth, exhibit a clear lithogenic imprint that contrasts with shallower and deeper samples (local maxima of LREE and MREE concentrations, of  $Ce/Ce^*$  and of  $Nd_Y/Yb_Y$ ; **Figures 3A, 5A**). Local maxima were not only observed in REEs but also in other lithogenic tracers (Lasbleiz et al., 2014; Qu  rou   et al., 2015; Sanial et al., 2015; van der Merwe et al., 2015). The closest upstream source is Leclaire Rise (or Skiff Bank; Kieffer et al., 2002; Weis and Frey, 2002), a seamount located west of Kerguelen Islands, just northwest of station R2, which rises up to 200 m depth below the sea level and is on the northern border of the PF circulation, following Park et al. (2014; their Figure 15). Therefore, and as suggested by the KEOPS2 tracer studies cited above, lithogenic supplies seem to be transferred through the PF, from its northern border to its southern one, to be detected at station R2.

## Relationship Between REE Distribution and Authigenic Processes

Zhang et al. (2008) found a pronounced positive Eu anomaly at their twice-visited station A3 that was attributed to basaltic signature from Heard Island sediments. Station A3 was also sampled twice during the KEOPS2 study but negligible or much weaker positive Eu anomalies were observed, this time. Although the 1st/2nd and 3rd/4th samplings at station A3 occurred 6 years apart, similar profiles of  $\epsilon_{Nd}$  and weak Ce anomalies were observed at this station during four different visits, suggesting a relatively constant flux of lithogenic supplies likely coming from the same source (**Figure 8**). In addition, the circulation patterns show similar southern origin of the A3 waters during KEOPS1 and KEOPS2 (Park et al., 2008, 2014). These observations led us to suggest that the lithogenic fraction observed at this station was similar during the four visits and thus that concentration and fractionation differences observed between these four profiles were rather related to authigenic processes occurring during the different stages of the phytoplankton bloom. The section below is dedicated to the identification of these processes. Note that some features, notably the Eu anomaly variations, remain to be confirmed due to their overall weak variations relatively to their associated uncertainties—although still significant. In addition, the time series proposed below is built on the results of two cruises conducted 6 years apart. Therefore, the preliminary interpretations discussed in the following have to be cautiously considered and mainly aim at giving food for thought for future investigations.

We defined the stations A3-1, A3-2, A3-3, and A3-4, following the seasonal chronology rather than the date of sampling (spring first—KEOPS2, then summer—KEOPS1). Similar circulation scheme and chl-*a* distribution—positioning A3 in the core of the chl-*a* maximum—argue in favor of a seasonal (spring vs.

summer) rather than interannual (2005 vs. 2011) interpretation. This seasonal approach was followed in several other studies (e.g., Bowie et al., 2015; Jacquet et al., 2015). A3-1 was sampled just before the development of the spring bloom; A3-2 was sampled during the maturing phase of a fast growing and large diatom bloom (Lasbleiz et al., 2014; Carlotti et al., 2015; Trull et al., 2015), in an autotrophic mixed layer production system, with photosynthesis exceeding respiration (Christaki et al., 2014). A3-3 and A3-4 correspond to the visits at station A3 at the beginning and at the end of the austral summer cruise KEOPS1 during the bloom decline, in a heterotrophic system (Lef  vre et al., 2008).

During the development of the bloom (from A3-1 to A3-2, KEOPS2), MREE slightly decreased, except Eu, leading to the formation of a small positive Eu anomaly; both La concentrations and the positive La anomaly substantially decreased, especially below 200 m depth (**Figure 8**). In summer, most of the REE, notably the LREE and MREE, were significantly less concentrated than in spring, especially in the first 200 m, except Eu, which was instead equivalently or slightly more concentrated (**Figure 8**; Zhang et al., 2008). Therefore, the upper layer REE pattern slope was more pronounced in summer and the weak positive Eu anomaly observed during the bloom development was much more marked over the whole water column as the bloom was declining. Also, the positive La anomaly was, in summer, similar to A3-1 pre-bloom values (**Figure 8**). These characteristics significantly differ from the REE pattern features observed by Haley et al. (2014) in the upper Gulf of Alaska, defined by these authors as “bio-reactive” REE patterns and suggested to be mediated by microbial processes. Our hypothesis is that the REE distribution variations observed at these different stages of the Kerguelen Plateau bloom are mainly related to interactions between these elements and marine particulate phases (carbonated and/or oxidized surface coatings, diatoms and barite), as discussed in the following subsections.

## Positive Eu Anomaly

We speculate that the positive Eu anomaly results from the combination of two processes: a net removal of the REEs (especially LREEs and MREEs) onto particles, increasing as the bloom ages, and a constant REE supply from the basaltic sediments. LREE and MREE are preferentially scavenged onto surface coatings such as ferro-manganese oxy-hydroxides and carbonate phases in the upper water column and preferentially released at depth, compared to the HREE (Sholkovitz et al., 1994). Such coatings might have developed onto organic matter and tests before their export, contributing to the LREE and MREE depletion of the upper layer observed in the summer period (A3-3 and A3-4; **Figure 8A**). This hypothesis is consistent with the decrease of dissolved inorganic carbon observed in the upper layer between spring and summer (**Figure 8B**; Jouandet et al., 2008; Lo Monaco et al., 2014). However, based on the MREE-enriched patterns of the acetic acid leaching of suspended and sinking particles (Sholkovitz et al., 1994; Lerche and Nozaki, 1998), Eu concentrations should decrease as the other LREEs and MREEs in the upper layer between spring and summer at A3, instead of being preserved as observed. A compensative source of dissolved REEs such as the Heard Island sediments,



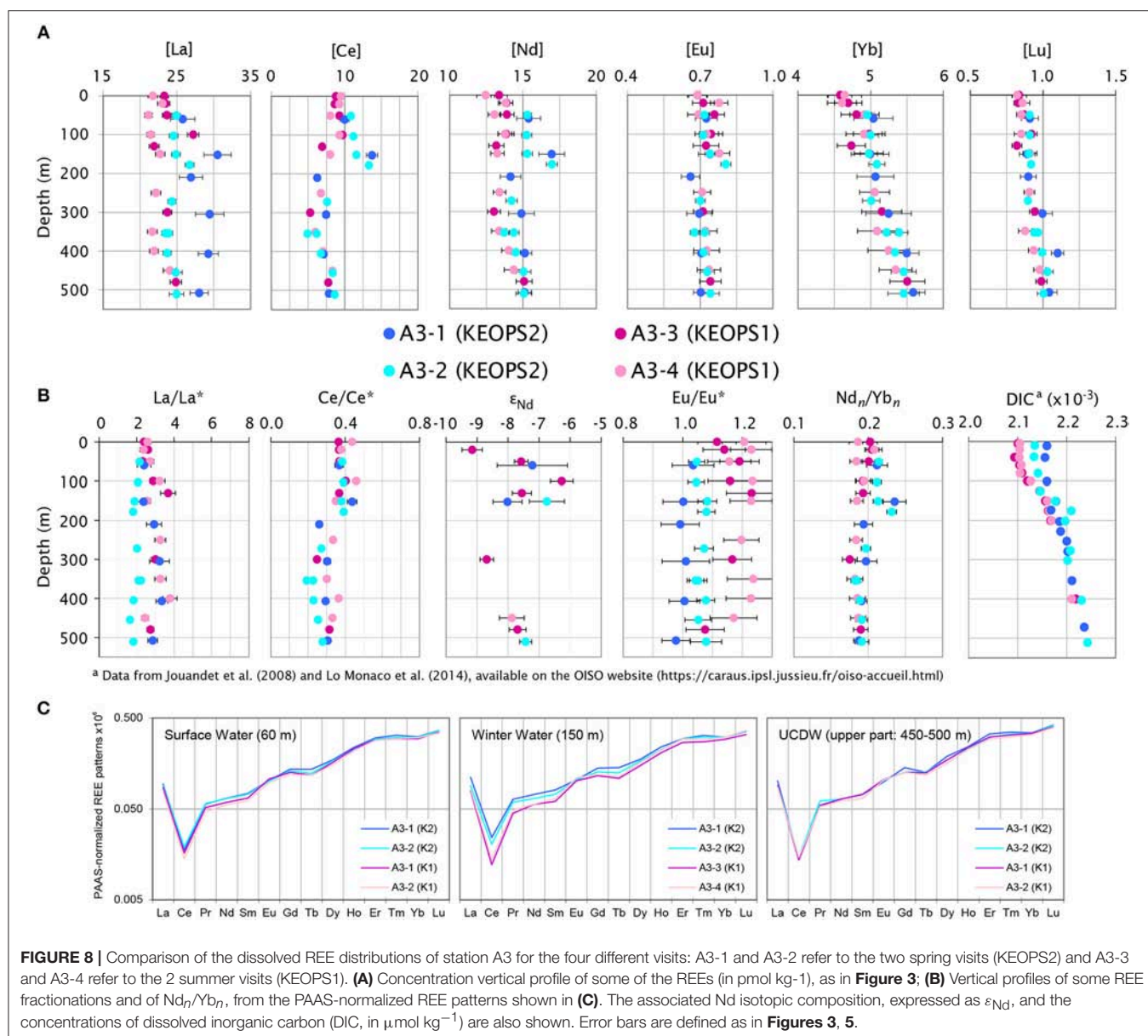


**FIGURE 8 |** Comparison of the dissolved REE distributions of station A3 for the four different visits: A3-1 and A3-2 refer to the two spring visits (KEOPS2) and A3-3 and A3-4 refer to the 2 summer visits (KEOPS1). **(A)** Concentration vertical profile of some of the REEs (in pmol kg<sup>-1</sup>), as in **Figure 3**; **(B)** Vertical profiles of some REE fractionations and of Nd<sub>n</sub>/Yb<sub>n</sub>, from the PAAS-normalized REE patterns shown in **(C)**. The associated Nd isotopic composition, expressed as  $\epsilon_{Nd}$ , and the concentrations of dissolved inorganic carbon (DIC, in  $\mu\text{mol kg}^{-1}$ ) are also shown. Error bars are defined as in **Figures 3, 5**.

enriched in Eu (light gray pattern in **Figure 7B**; Zhang et al., 2008), would allow the Eu stock to be maintained throughout the bloom development and balance its removal through the LREE and MREE scavenging onto coatings.

Interestingly, there seems to be a relationship between some REE fractionations and the export efficiency at the investigated stations that would be consistent with the two processes described above. A positive Eu anomaly seems to progressively be formed with depth for stations characterized by low export efficiency (e.g., station F-L; **Figures 4, 5**; Laurenceau-Cornec et al., 2015). This might result from the progressive dissolution of Eu-enriched secondary minerals included in the basaltic lithogenic particles (such as rhabdophanes) that settle to the seafloor. In case of increasing export, we could expect an erosion of this Eu lithogenic signature in seawater through

the preferential removal of Eu onto the sinking particles. This may explain the absence of Eu anomaly observed at stations characterized by a high export, such as R2 and E1 (**Figure 5**; Laurenceau-Cornec et al., 2015). Nevertheless, further investigations are necessary to verify the link between the REE fractionation processes and the export efficiency relative to the ocean dynamics of the area.

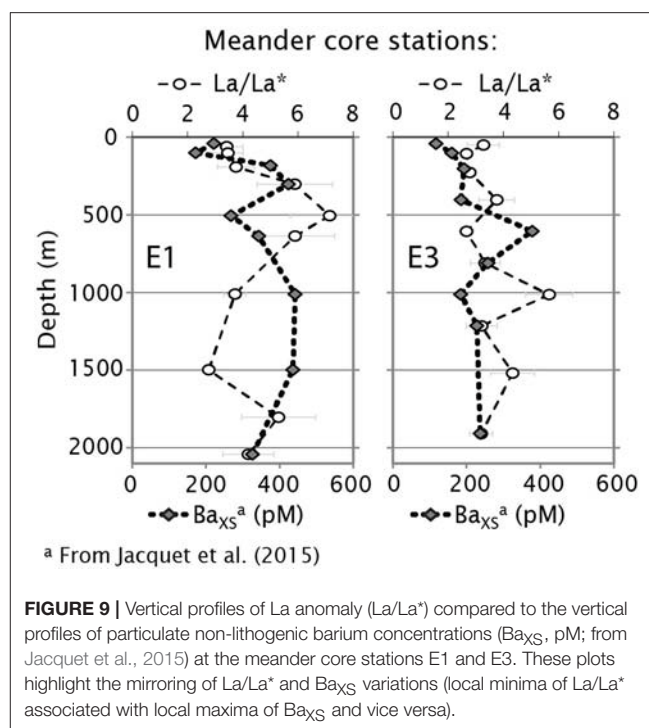
### La Behavior

The KEOPS2 dissolved samples display ubiquitous positive La anomalies. This feature is commonly observed in the ocean and presumably results from the empty 4f electron shell of La that increases its relative stability in solution (de Baar et al., 1985; Byrne and Kim, 1990; Byrne et al., 1996). Nevertheless, both La concentration and La anomaly variations throughout the



four visits to A3 are surprisingly different from the other LREE variations. The sharp decrease of La concentrations between A3-1 and A3-2 over the whole water column is not observed for the other REEs, which explains the associated decrease of La anomalies. Thus, unless a real difference of kinetics exists for a preferential adsorption and desorption of La onto and from carbonated and/or oxidized surface coatings, these latter patterns might not be the sole driver to explain the marine La distribution and fractionation in the Kerguelen area. Barite ( $\text{BaSO}_4$ ), which is known to incorporate more La than the other LREEs when precipitating in the water column (Guichard et al., 1979; Hein et al., 2007), could also contribute to the observed differential behavior of La. An enhancement of barite formation over the water column during the KEOPS2 bloom stage could contribute to the observed diminution of the La concentrations and anomalies. It is currently believed that barite crystals mainly precipitate within supersaturated micro-environments, mostly constituted by aggregates of organic material (Dehairs et al., 1980; Bishop, 1988; Stroobants et al., 1991; Ganeshram et al., 2003; van Beek et al., 2007). During remineralization of these aggregates through heterotrophic bacterial activity, suspended barite crystals are released (Ganeshram et al., 2003). Jacquet et al. (2008, 2015) characterized the distribution of biogenic barite during KEOPS1 and KEOPS2 by measuring the amount of particulate barium in excess (denoted by  $\text{Ba}_{\text{XS}}$ ), which is the total Ba corrected for the Ba associated with the lithogenic fraction (Dehairs et al., 1980, 1990). The decrease of La concentrations between A3-1 and A3-2 is not accompanied by an increase in the particulate  $\text{Ba}_{\text{XS}}$  concentrations, which suggests that there is no significant increase in the synthesis of suspended barite between the two visits. However, barite may also be included in the dense fast-sinking particles, a pool that was not investigated by Jacquet et al. (2008, 2015), since their sampling techniques (Niskin bottles and *in situ* pumps) allowed them to only characterize the suspended fraction of barite. We know that the sinking particles were not the dominant fraction at A3-2, but were still present (Laurenceau-Cornec et al., 2015). The differential behavior of La between A3-1 and A3-2 might thus be related to a slight enhancement of barite crystallization within large aggregates, a pool of particles that was not studied at A3-2.

In summer, the slowing down of productivity and aggregate formation might have led to a slowing down of barite formation and La incorporation, explaining why La concentrations only slightly decreased, compared to spring. However, La anomalies increased again, compared to A3-2. This indicates a process that allowed the dissolved stock of La to be better maintained in the water column than the Pr and Nd stocks. Therefore, another factor contributing to the REE fractionation may be involved, in addition to surface coatings, to explain the differential behavior of La compared to Pr and Nd. We again presume an impact from the barite cycle, and more precisely, some La release from the suspended barites, which were more abundant at that time (Jacquet et al., 2008, 2015). Once released from the aggregates into the undersaturated waters of the Southern Ocean (Monnin et al., 1999), suspended barites are more susceptible to be redissolved and therefore to release their La. The hypothesis linking La distribution and barite cycle has already been recently



suggested, upstream in the Southern Ocean (Garcia-Solsona et al., 2014).

The role of barite production or dissolution on dissolved La depletion or enrichment compared to the other LREE is also suggested at other KEOPS stations. A mirror effect between  $\text{Ba}_{\text{XS}}$  and  $\text{La}/\text{La}^*$  vertical profiles is notably observed over the whole water column at the meander stations E1 and E3 (Figure 9). Jacquet et al. (2015) suggested from these  $\text{Ba}_{\text{XS}}$  profiles that remineralization processes were not ongoing anymore at these stations and were resulting from a previous bloom. Thus, the high La concentrations and anomalies might represent a post-remineralization state, where barite has been released following disaggregation and then dissolved.

## HREE Behavior

The HREE vertical profiles at the deep and meander stations show a slope break at around 600 m, with a slower increase of their concentrations below this depth. This vertical structure looks strikingly similar to the vertical profiles of silicic acid; a clear relationship appears from the comparison of the evolution of Yb concentrations with the dissolved silicon ones ( $\text{H}_4\text{SiO}_4$  or  $\text{DSi}$ ; Figure 10). In addition, the  $\text{Nd}_n/\text{Yb}_n$  profiles of the deep and meander stations exhibit a pronounced re-increase with depth below their inversion of slope, compared to the rate we usually observe in the ocean (e.g., Jeandel et al., 2013; Haley et al., 2014; Molina-Kescher et al., 2014; Figures 5A,C). We propose here that HREE uptake-remineralization processes are more linked to the Si cycle than the MREE and LREE are, in agreement with Akagi and co-authors' hypotheses (Akagi et al., 2011; Akagi, 2013) and with REE profiles sampled in other areas of the Southern Ocean (Garcia-Solsona et al., 2014; Molina-Kescher et al., 2014).

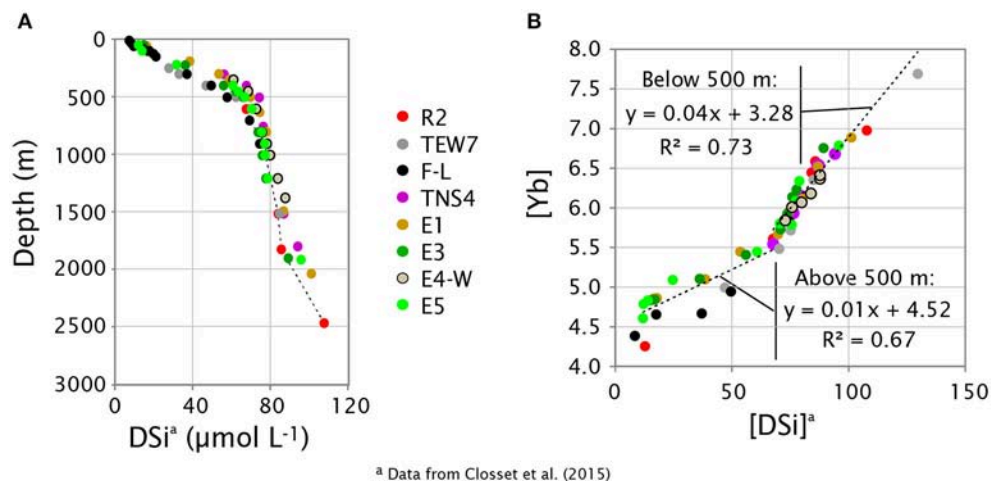
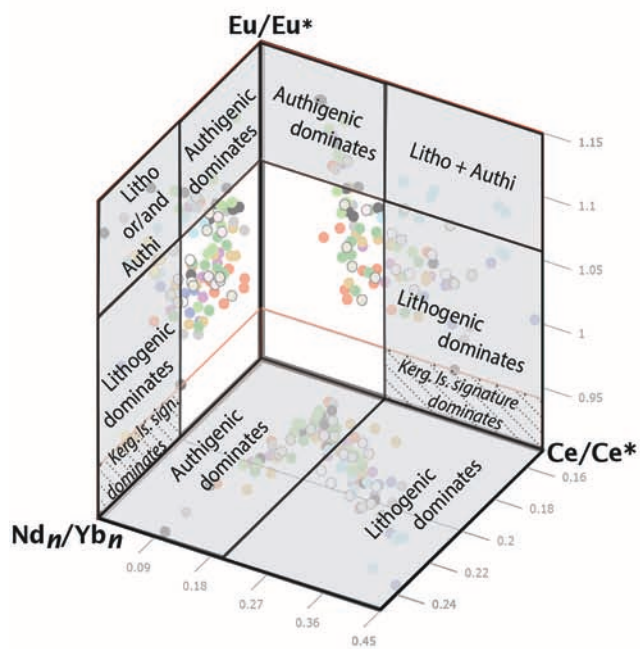


**FIGURE 10 | (A)** Vertical profiles of the  $\text{H}_4\text{SiO}_4$  concentrations ( $\text{DSi}$ , in  $\mu\text{mol L}^{-1}$ ; from Closset et al., 2014) of the deep and meander stations; **(B)** Relationships between Yb concentrations (in  $\text{pmol kg}^{-1}$ ) and  $\text{DSi}$  concentrations (in  $\mu\text{mol L}^{-1}$ ) of these same stations, excluding the samples tagged by lithogenic signatures. Two linear regressions are given to characterize the distribution above and below 500 m depth, which corresponds to the slope break depth of the  $[\text{DSi}]$  vertical profile shown in **(A)**.

### REE distribution on and downstream the Kerguelen Plateau:

#### A lithogenic vs. authigenic dominance



#### B lithogenic sources and transport

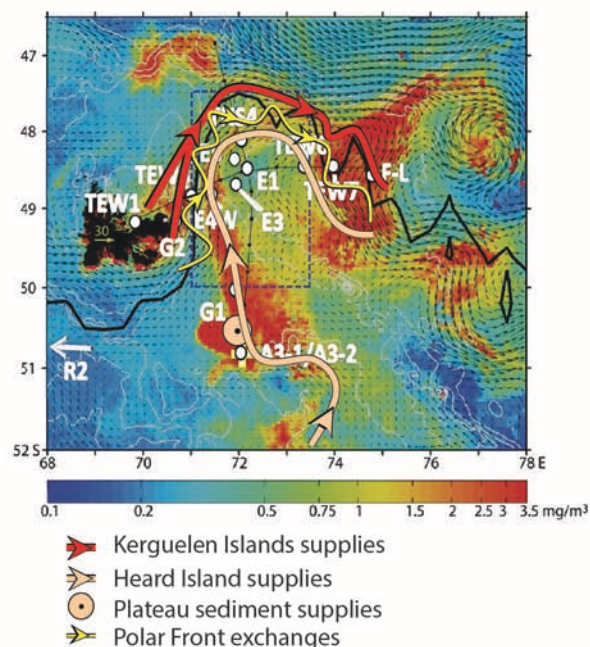


**FIGURE 11 |** Synthesis of the main processes that control the REE distribution in the Kerguelen Plateau area: **(A)** schematic summary of Figure 6 identifying the dominance of lithogenic vs. authigenic processes in REE fractionations; **(B)** schematic representation of the different sources of lithogenic material -Kerguelen Islands, Heard Island, Central Plateau sediments- and their transports via the different oceanic pathways identified in Park et al. (2014), north of, south of, and across the Polar Front.

The slower dissolution rates of biogenic silica compared to the remineralization/dissolution rates of the LREE and MREE carrier phases could thus explain the pronounced slope inversion.

## CONCLUSIONS

The shallow and coastal environments of the Kerguelen Plateau strongly modify the dissolved rare earth element (REE) distributions and neodymium isotopic compositions (expressed as  $\epsilon_{Nd}$ ) of the upstream offshore waters. Consequently, the KEOPS2 sampling covers a large range of REE concentrations, depending on whether they were sampled upstream, on, or downstream the Kerguelen Plateau. The concentration and fractionation variations of the dissolved REE result from significant lithogenic supplies and authigenic processes (Figure 11A).

Eastern Kerguelen coastal samples clearly reveal a local source of lithogenic material, most likely coming from some weathering and/or dissolution of the shallow sediments. Moreover, the comparison of REE patterns of filtered and unfiltered samples reveals distinct features, with negative europium anomalies ( $Eu/Eu^*$ ) and  $\epsilon_{Nd}$  in the filtered samples but a positive  $Eu/Eu^*$  and more radiogenic  $\epsilon_{Nd}$  in the unfiltered one. These discrepancies presumably reflect differential dissolution and/or weathering processes of the local flood basalts and/or trachyte veins from which the margin sediments mainly result. Interestingly, these REE coastal signatures contrast with those observed close to Heard Island, although also attributed to the interaction of seawater with the margin sediments (Zhang et al., 2008). Thus, the nature or the supply processes of lithogenic material from the Kerguelen Islands likely differ from those from Heard Island. Coastal environments are not the sole areas enriching seawater with dissolved lithogenic supplies in the vicinity of the Kerguelen Plateau: contributions are also presumably coming from seamounts like the Leclaire Rise, upstream from the Kerguelen Islands (this study; Qu  rou   et al., 2015; Sanial et al., 2015), and Gallieni Spur (Grenier et al., 2015), downstream. The Central Kerguelen Plateau also plays a key role in terms of lithogenic supplies, likely providing a vertical enrichment from the sediments to the overlying water.

The REE and  $\epsilon_{Nd}$  distributions allow us to identify two main routes for the transport of these supplies (Figure 11B). The atypical signature of the dissolved Kerguelen coastal samples traces an eastward transport of the enriched waters north of the Polar Front (red route on Figure 11B). This signature rapidly vanishes, likely through mixing, and precludes us to identify the Kerguelen contribution among the lithogenic signatures observed across and south of the Polar Front, although indicated by other tracers (e.g., radium isotopes; Sanial et al., 2015). The sediment/particulate signature of Heard Island is presumably advected north-westward, toward the Central Kerguelen Plateau where it mixes with the signature of the vertical supplies from the sediments. These signatures are likely advected up to the meander area where they can mix with Kerguelen supplies sporadically crossing the front (light pink and yellow routes on Figure 11B, respectively).

Variations in REE concentrations and fractionations are also partly driven by authigenic processes, both inorganically and biologically mediated. More particularly, the REE behavior seems to be closely related to biogeochemical cycles resulting directly and indirectly from the recurrent diatom-dominated bloom observed in austral spring/summer above and downstream the Plateau. The more pronounced decrease of the concentrations of light REEs with the bloom aging seems to mainly reflect their preferential scavenging by surface coatings, such as carbonate phases and/or (ferro)manganese oxides. A more important involvement of La in the barite cycle could explain an additional differentiation compared to the other light REEs. Fractionation of the heavy REEs seems to be more closely related to the opal cycle. A difference of reversible scavenging kinetics between the surface coatings and opal could explain the evolution changes of the  $Nd_n/Yb_n$  ratio with depth, decreasing in the upper layer and increasing below.

This study highlights the role of the lithogenic and authigenic particles on the dissolved REE distributions in the Kerguelen Plateau area. It raises the importance of a future complementary work to compare dissolved and particulate REE fractions in order to better describe and understand the main active processes that govern the oceanic cycle of the REEs.

## AUTHOR CONTRIBUTIONS

EG-S did most of the sample collection, helped by PvB and MS. PvB was the onboard scientific representative of the seawater sampling for the REE analyses. EG-S carried out the onboard chemical treatments of the samples and part of the on land neodymium isotopic composition (Nd IC) chemical analyses. VB and MG carried out part of the on land Nd IC chemical analyses. NL and MG did the on land chemical analyses of the rare earth element (REE) concentrations. MG and CJ conducted the REE concentration measurements on the Inductively Coupled Plasma Mass Spectrometer. MG, NL, and CJ were in charge of the Nd IC measurements of samples on the Thermo Ionization Mass Spectrometers (TIMS) in Toulouse. CJ and PN conducted the Nd IC measurement of samples on the TIMS in Brest. MG drafted the manuscript and figures. MG, EG-S, CJ, NL, TT, PvB, FL, and MS contributed to the data representation and interpretation. MG, CJ, EG-S, NL, PvB, FL, and TT revised the form and content revisions of the manuscript. CJ and TT supervised the postdoctoral position of MG during which the chemical analyses were done. CJ supervised the postdoctoral position of MG during which the manuscript was drafted.

## FUNDING

KEOPS2 project was funded by the French Research program of INSU-CNRS LEFE-CYBER (Les enveloppes fluides et l'environnement—Cycles biog  ochimiques, environnement et ressources), ANR (Agence Nationale de la Recherche, SIMI-6 program, ANR-10-BLAN-0614), CNES (Center National d'Etudes Spatiales), and IPEV (Institut Polaire Paul-  mile Victor). MG was mostly supported by a conjoint LEGOS and



ACE CRC postdoctoral appointment and a CAMPUS FRANCE grant (FASIC award #30418QG; campusfrance.org), and also by a European Union's Horizon 2020 research and innovation programme (Marie Skłodowska-Curie action, grant agreement # 657853) while finishing the redaction.

## ACKNOWLEDGMENTS

We thank the captain B. Lassiette, officers and crew of RV *Marion Dufresne*, Pierre Sangiardi (Institut Paul-Émile Victor) and the Institut National des Sciences de l'Univers for voyage logistics and their support of the science, and Bernard Quéguiner (Institut Méditerranéen d'Océanologie) and Stéphane Blain (Université Pierre et Marie Curie, LOMIC) for the KEOPS2 expedition leadership. We are grateful to Anne Royer, Lionel Scouarnec, and Fabien Perault (DT-INSU) for their technical support. We thank Bruno Lansard for help during sampling at sea. Thanks to ACE-CRC people Emmanuel Laurenceau-Cornec, Andy Bowie, and

Pier van der Merwe for fruitful discussions concerning biological export and trace metal distribution interpretations, and Zanna Chase and Taryn Noble (University of Tasmania) for feedbacks and comments about our REE distribution interpretations. MG and CJ also acknowledge Sebastien Fabre (Université Paul Sabatier, IRAP) for insights into aqueous model perspectives using the PHREEQC program. We thank Catherine Pradoux for her technical support in the clean laboratory. We also acknowledge Jerome Chmieleff and Frederic Candaudap (Center National de la Recherche Scientifique, GET) for their technical support on the ICP-MS. The manuscript was significantly improved by the comments provided by three reviewers.

## SUPPLEMENTARY MATERIAL

The Supplementary Material for this article can be found online at: <https://www.frontiersin.org/articles/10.3389/fmars.2018.00426/full#supplementary-material>

## REFERENCES

- Akagi, T. (2013). Rare earth element (REE)-silicic acid complexes in seawater to explain the incorporation of REEs in opal and the "leftover" REEs in surface water: new interpretation of dissolved REE distribution profiles. *Geochim. Cosmochim. Acta* 113, 174–192. doi: 10.1016/j.gca.2013.03.014
- Akagi, T., Fu, F.-F., Hongo, Y., and Takahashi, K. (2011). Composition of rare earth elements in settling particles collected in the highly productive North Pacific Ocean and Bering Sea: implications for siliceous-matter dissolution kinetics and formation of two REE-enriched phases. *Geochim. Cosmochim. Acta* 75, 4857–4876. doi: 10.1016/j.gca.2011.06.001
- Alibo, D. S., and Nozaki, Y. (1999). Rare earth elements in seawater: particle association, shale-normalization, and Ce oxidation. *Geochim. Cosmochim. Acta* 63, 363–372. doi: 10.1016/S0016-7037(98)00279-8
- Arevalo, R., Jr, and McDonough, W. (2008). Tungsten geochemistry and implications for understanding the Earth's interior. *Earth Planet. Sci. Lett.* 272, 656–665. doi: 10.1016/j.epsl.2008.05.031
- Arrigo, K. R., van Dijken, G. L., and Bushinsky, S. (2008). Primary production in the Southern Ocean, 1997–2006. *J. Geophys. Res.* 113:C08004. doi: 10.1029/2007JC004551
- Arsouze, T., Dutay, J.-C., Lacan, T., and Jeandel, C. (2007). Modeling the neodymium isotopic composition with an ocean global circulation model. *Chem. Geol.* 239, 165–177. doi: 10.1016/j.chemgeo.2006.12.006
- Arsouze, T., Dutay, J. C., Lacan, F., and Jeandel, C. (2009). Reconstructing the Nd oceanic cycle using a coupled dynamical-biogeochemical model. *Biogeosci. Discuss.* 6, 5549–5588. doi: 10.5194/bgd-6-5549-2009
- Barling, J., and Goldstein, S. L. (1990). Extreme isotopic variations in Heard Island lavas and the nature of mantle reservoirs. *Nature* 348, 59–62. doi: 10.1038/348059a0
- Barling, J., Goldstein, S. L., and Nicholis, I. A. (1994). Geochemistry of Heard Island (Southern Indian Ocean): characterization of an enriched mantle component and implications for enrichment of Sub-Indian Ocean Mantle. *J. Petrol.* 35, 1017–1053. doi: 10.1093/petrology/35.4.1017
- Bau, M., Koschinsky, A., Dulski, P., and Hein, J. R. (1996). Comparison of the partitioning behaviours of yttrium, rare earth elements, and titanium between hydrogenetic marine ferromanganese crusts and seawater. *Geochim. Cosmochim. Acta* 60, 1709–1725.
- Behrens, M. K., Muratli, J., Pradoux, C., Wu, Y., Böning, P., Brumsack, H.-J., et al. (2016). Rapid and precise analysis of rare earth elements in small volumes of seawater – Method and intercomparison. *Mar. Chem.* 186, 110–120. doi: 10.1016/j.marchem.2016.08.006
- Bertram, C. J., and Elderfield, H. (1993). The geochemical balance of the rare earth elements and neodymium isotopes in the oceans. *Geochim. Cosmochim. Acta* 57, 1957–1986. doi: 10.1016/0016-7037(93)90087-D
- Bishop, J. K. B. (1988). The barite-opal-organic carbon association in oceanic particulate matter. *Nature* 332, 341–343. doi: 10.1038/332341a0
- Bitschene, P. R., Mehl, K. W., and Schmincke, H.-U. (1992). "Composition and origin of marine ash layers and epiclastic rocks from the Kerguelen Plateau, southern Indian Ocean (Legs 119 and 120)," in *Proc. ODP, Sci. Results*, eds S. W. Wise Jr, R. Schlich, et al. (College Station, TX: Ocean Drilling Program), 135–149.
- Blain, S., Quéguiner, B., Armand, L., Belviso, S., Bombled, B., Bopp, L., et al. (2007). Effect of natural iron fertilization on carbon sequestration in the Southern Ocean. *Nature* 446, 1070–1074. doi: 10.1038/nature05700
- Blain, S., Sarthou, G., and Laan, P. (2008). Distribution of dissolved iron during the natural iron-fertilization experiment KEOPS (Kerguelen Plateau, Southern Ocean). *Deep Sea Res. II*, 55, 594–605. doi: 10.1016/j.dsr2.2007.12.028
- Blain, S., Tréguer, P., Belviso, S., Bucciarelli, E., Denis, M., Desabre, S., et al. (2001). A biogeochemical study of the island mass effect in the context of the iron hypothesis: Kerguelen Islands, Southern Ocean. *Deep Sea Res. Part I*, 48, 163–187. doi: 10.1016/S0967-0637(00)00047-9
- Bolhar, R., Kamber, B. S., Moorbath, S., Fedo, C. M., and Whitehouse, M. J. (2004). Characterisation of early Archaean chemical sediments by trace element signatures. *Earth Planet. Sci. Lett.* 222, 43–60. doi: 10.1016/j.epsl.2004.02.016
- Bowie, A. R., van der Merwe, P., Quéroué, F., Trull, T., Fourquez, M., Planchon, F., et al. (2015). Iron budgets for three distinct biogeochemical sites around the Kerguelen archipelago (Southern Ocean) during the natural fertilisation study, KEOPS-2. *Biogeosciences* 12, 4421–4445. doi: 10.5194/bg-12-4421-2015
- Boyd, P. W., Jickells, T., Law, C. S., Blain, S., Boyle, E. A., Buesseler, K. O., et al. (2007). Mesoscale iron enrichment experiments 1993–2005: synthesis and future directions. *Science* 315, 612–617. doi: 10.1126/science.1131669
- Byrne, R. H., and Kim, K. H. (1990). Rare earth element scavenging in seawater. *Geochim. Cosmochim. Acta* 54, 2645–2656. doi: 10.1016/0016-7037(90)90002-3
- Byrne, R. H., Liu, X., and Schijf, J. (1996). The influence of phosphate coprecipitation on rare earth distributions in natural waters. *Geochim. Cosmochim. Acta* 60, 3341–3346. doi: 10.1016/0016-7037(96)00197-4
- Carlotti, F., Jouandet, M.-P., Nowaczyk, A., Harmelin-Vivien, M., Lefèvre, D., Guillou, G., et al. (2015). Mesozooplankton structure and functioning during the onset of the Kerguelen phytoplankton bloom during the Keops2 survey. *Biogeosciences* 12, 2381–2427. doi: 10.5194/bg-12-4543-2015
- Carter, P., Vance, D., Hillenbrand, C. D., Smith, J. A., and Shoosmith, D. R. (2012). The neodymium isotopic composition of waters masses in the eastern



- Pacific sector of the Southern Ocean. *Geochim. Cosmochim. Acta* 79, 41–59. doi: 10.1016/j.gca.2011.11.034
- Cavagna, A. J., Fripiat, F., Elskens, M., Mangion, P., Chirurgien, L., Closset, I., et al. (2015). Production regime and associated N cycling in the vicinity of Kerguelen Island, Southern Ocean. *Biogeosciences* 12, 6515–6528. doi: 10.5194/bg-12-6515-2015
- Charrassin, J. B., Park, Y.-H., LeMaho, Y., and Bost, C.-A. (2004). Fine resolution 3D temperature fields off Kerguelen from instrumented penguins. *Deep-Sea Res. I* 51, 2091–2103. doi: 10.1016/j.dsr.2004.07.019
- Chavagnac, V., Lair, M., Milton, J. A., Lloyd, A., Croudace, I. W., Palmer, M. R., et al. (2008). Tracing dust input to the Mid-Atlantic Ridge between 14°45'N and 36°14'N: geochemical and Sr isotope study. *Mar. Geol.* 247, 208–225. doi: 10.1016/j.margeo.2007.09.003
- Chavagnac, V., Wanick, J. J., Atkin, D., Milton, J. A., Leipe, T., Green, D. R. H., et al. (2007). Source of lithogenic derived element fluxes to the deep subtropical North East Atlantic Ocean. *Geophys. Res. Lett.* 34:L21604. doi: 10.1029/2007GL030985
- Chever, F., Sarthou, G., Bucciarelli, E., Blain, S., and Bowie, A. R. (2010). An iron budget during the natural iron fertilisation experiment KEOPS (Kerguelen Islands, Southern Ocean). *Biogeosciences* 7, 455–468. doi: 10.5194/bg-7-455-2010
- Choppin, G. R., and Silva, R. J. (1956). Separation of the lanthanides by ion exchange with alpha-hydroxy isobutyric acid. *J. Inorg. Nucl. Chem.* 3, 153–154. doi: 10.1016/0022-1902(56)80076-6
- Christaki, U., Lefèvre, D., Georges, C., Colombet, J., Catala, P., Courties, C., et al. (2014). Microbial food web dynamics during spring phytoplankton blooms in the naturally iron-fertilized Kerguelen area (Southern Ocean). *Biogeosciences* 11, 6739–6753. doi: 10.5194/bg-11-6739-2014
- Chung, C.-H., Brenner, I., and You, C.-F. (2009). Comparison of microconcentric and membrane-desolvation sample introduction systems for determination of low rare earth element concentrations in surface and subsurface waters using sector field inductively coupled plasma mass spectrometry. *Spectrochim. Acta B* 64, 849–856. doi: 10.1016/j.sab.2009.06.013
- Closset, I., Lasbleiz, M., Leblanc, K., Quéguiner, B., Cavagna, A.-J., Elskens, M., et al. (2014). Seasonal evolution of net and regenerated silica production around a natural Fe-fertilized area in the Southern Ocean estimated with Si isotopic approaches. *Biogeosciences* 11, 5827–5846. doi: 10.5194/bg-11-5827-2014
- Coale, K. H., Fitzwater, S. E., Gordon, R. M., Johnson, K. S., and Barber, R. T. (1996). Control of community growth and export production by upwelled iron in the equatorial Pacific Ocean. *Nature* 379, 621–624.
- de Baar, H. J. W., Bacon, M. P., Brewer, P. G., and Bruland, K. W. (1985). Rare earth elements in the Pacific and Atlantic oceans. *Geochim. Cosmochim. Acta* 49, 1943–1959. doi: 10.1016/0016-7037(85)90089-4
- de Baar, H. J. W., de Jong, J. T. M., Bakker, D. C. E., Löscher, B. M., Veth, C., Bathmann, U., et al. (1995). Importance of iron for plankton blooms and carbon dioxide drawdown in the Southern Ocean. *Nature* 373, 412–415.
- Dehairs, F., Chesselet, R., and Jedwab, J. (1980). Discrete suspended particles of barite and the barium cycle in the open ocean. *Earth Planet. Sci. Lett.* 49, 528–550. doi: 10.1016/0012-821X(80)90094-1
- Dehairs, F., Goeyens, L., Stroobants, N., Bernard, P., Goyet, C., Poisson, A., et al. (1990). On the suspended barite and the oxygen minimum in the Southern Ocean. *Glob. Biogeochem. Cycles* 4, 85–102.
- Dosso, L., and Murthy, V. R. (1980). A Nd isotopic study of the Kerguelen Islands: inferences on enriched oceanic mantle sources. *Earth Planet. Sci. Lett.* 48, 268–276. doi: 10.1016/0012-821X(80)90190-9
- Doucet, S., Scoates, J. S., Weis, D., and Giret, A. (2005). Constraining the components of the Kerguelen mantle plume: a Hf–Pb–Sr–Nd isotopic study of picrites and high-MgO basalts from the Kerguelen Archipelago. *Geochem. Geophys. Geosyst.* 6:Q04007. doi: 10.1029/2004GC000806
- Doucet, S., Weis, D., Scoates, J. S., Nicolaysen, K., Frey, F. A., and Giret, A. (2002). The depleted mantle component in the Kerguelen Archipelago basalts: petrogenesis of tholeiitic-transitional basalts from the Loranget Peninsula. *J. Petrol.* 43, 1341–1366. doi: 10.1093/petrology/43.7.1341
- d'Ovidio, F., Della Penna, A., Trull, T. W., Nencioli, F., Pujol, M. I., Rio, M. H., et al. (2015). The biogeochemical structuring role of horizontal stirring: lagrangian perspectives on iron delivery downstream of the Kerguelen Plateau. *Biogeosciences* 12, 5567–5581. doi: 10.5194/bg-12-5567-2015
- Elderfield, H. (1988). The oceanic chemistry of the rare earth elements. *Philos. Trans. R. Soc. Lond. A* 325, 105–126. doi: 10.1098/rsta.1988.0046
- Elderfield, H., and Greaves, M. J. (1982). The rare earth elements in seawater. *Nature* 296, 214–219. doi: 10.1038/296214a0
- Elrod, V. A., Berelson, W. M., Coale, K. H., and Johnson, K. S. (2004). The flux of iron from continental shelf sediments: a missing source for global budgets. *Geophys. Res. Lett.* 31:L12307. doi: 10.1029/2004GL020216
- Fedele, L., Lustrino, M., Meluso, L., Morra, V., Zanetti, A., and Vannucci, R. (2015). Trace-element partitioning between plagioclase, alkali feldspar, Timagnetite, biotite, apatite and evolved potassic liquids from Campi Flegrei (Southern Italy). *Am. Mineral.* 100, 233–249. doi: 10.2138/am-2015-4995
- Frank, M. (2002). Radiogenic isotopes: tracers of past ocean circulation and weathering inputs. *Rev. Geophys.* 40, 1–1–1–38. doi: 10.1029/2000RG000094
- Frey, F. A., Nicolaysen, K., Kubit, B. K., Weis, D., and Giret, A. (2002). Flood basalt from Mont Tourmente in the Central Kerguelen Archipelago: the change from transitional to alkalic basalt at ~25 Ma. *J. Petrol.* 43, 1367–1387. doi: 10.1093/petrology/43.7.1367
- Frey, F. A., Weis, D., Yang, H. J., Nicolaysen, K., Leyrit, H., and Giret, A. (2000). Temporal geochemical trends in Kerguelen Archipelago basalts: evidence for decreasing magma supply from the Kerguelen Plume. *Chem. Geol.* 164, 61–80. doi: 10.1016/S0009-2541(99)00144-8
- Fröllje, H., Pahnke, K., Schnetger, B., Brumsack, H.-J., Dulai, H., and Fitzsimmons, J. N. (2016). Hawaiian imprint on dissolved Nd and Ra isotopes and rare earth elements in the central North Pacific: local survey and seasonal variability. *Geochim. Cosmochim. Acta* 189, 110–131. doi: 10.1016/j.gca.2016.06.001
- Gagnevin, D., Ethien, R., Bonin, B., Moine, B., Féraud, G., Gerbe, M. C., et al. (2003). Open-system processes in the genesis of silica-oversaturated alkaline rocks of the Rallierdu-Baty Peninsula, Kerguelen Archipelago (Indian Ocean). *J. Volcanol. Geotherm. Res.* 123, 267–300. doi: 10.1016/S0377-0273(02)00509-7
- Ganeshram, R. S., Francois, R., Commeau, J., and Brown-Leger, L. (2003). An experimental investigation of barite formation in seawater. *Geochim. Cosmochim. Acta* 67, 2599–2605. doi: 10.1016/S0016-7037(03)00164-9
- Garcia-Solsona, E., Jeandel, C., Labatut, M., Lacan, F., Vance, D., Chavagnac, V., et al. (2014). Rare earth elements and Nd isotopes tracing water mass mixing and particle-seawater interactions in the SE Atlantic. *Geochim. Cosmochim. Acta* 125, 351–372. doi: 10.1016/j.gca.2013.10.009
- Gautier, I., Weis, D., Mennessier, J.-P., Vidal, P., Giret, A., and Loubet, M. (1989). Petrology and geochemistry of Kerguelen basalts: evolution of an hotspot from a ridge to an intraplate position. *Earth Planet. Sci. Lett.* 100, 59–76.
- German, C. R., Masuzawa, T., Greaves, M. J., Elderfield, H., and Edmond, J. M. (1995). Dissolved rare earth elements in the Southern Ocean: cerium oxidation and the influence of hydrography. *Geochim. Cosmochim. Acta* 59, 1551–1558. doi: 10.1016/0016-7037(95)00061-4
- Goldstein, S. L., and Hemming, S. R. (2003). *Long-lived Isotopic Tracers in Oceanography, Paleoclimatology, and Ice-sheet Dynamics*. Palisades, NY: Columbia University.
- Grenier, M., Della Penna, A., and Trull, T. W. (2015). Autonomous profiling float observations of the high-biomass plume downstream of the Kerguelen Plateau in the Southern Ocean. *Biogeosciences* 12, 2707–2735. doi: 10.5194/bg-12-2707-2015
- Grenier, M., Jeandel, C., and Cravatte, S. (2014). From the subtropics to the equator in the Southwest Pacific: continental material fluxes quantified using neodymium data along modeled thermocline water pathways. *J. Geophys. Res. Oceans* 119, 3948–3966. doi: 10.1002/2013JC009670
- Grenier, M., Jeandel, C., Lacan, F., Vance, D., Venchiarutti, C., Cros, A., et al. (2013). From the subtropics to the central equatorial Pacific Ocean: neodymium isotopic composition and rare earth element concentration variations. *J. Geophys. Res. Oceans* 118, 592–618. doi: 10.1029/2012JC008239
- Guichard, F., Church, T. M., Treuil, M., and Jaffrezic, H. (1979). Rare earths in barites: distribution and effects on aqueous partitioning. *Geochim. Cosmochim. Acta* 43, 983–997. doi: 10.1016/0016-7037(79)90088-7
- Haley, B. A., Frank, M., Hathorne, E., and Pisias, N. (2014). Biogeochemical implications from dissolved rare earth element and Nd isotope distributions in the Gulf of Alaska. *Geochim. Cosmochim. Acta* 126, 455–474. doi: 10.1016/j.gca.2013.11.012
- Haley, B. A., Klinkhammer, G. P., and McManus, J. (2004). Rare earth elements in pore waters of marine sediments. *Geochim. Cosmochim. Acta* 68, 1265–1279. doi: 10.1016/j.gca.2003.09.012

- Hara, Y., Obata, H., Doi, T., Hongo, Y., Gamo, T., Takeda, S., et al. (2009). Rare earth elements in seawater during an iron-induced phytoplankton bloom of the western sub-arctic Pacific (SEEDS-II). *Deep-Sea Res. II Top. Stud. Oceanogr.* 56, 2839–2851. doi: 10.1016/j.dsr2.2009.06.009
- Hathorne, E. C., Stichel, T., Brück, B., and Frank, M. (2015). Rare earth element distribution in the Atlantic sector of the Southern Ocean: the balance between particle scavenging and vertical supply. *Mar. Chem.* 177, 157–171. doi: 10.1016/j.marchem.2015.03.011
- Hein, J. R., Zierenberg, R. A., Maynard, J. B., and Hannington, M. D. (2007). Multifarious barite-forming environments along a rifted continental margin, Southern California Borderland. *Deep-Sea Res. II* 54, 1327–1349. doi: 10.1016/j.dsr2.2007.04.011
- Holmes, T. M., Chase, Z., Van Der Merwe, P., Townsend, A. T., and Bowie, A. R. (2017). Detection, dispersal and biogeochemical contribution of hydrothermal iron in the ocean. *Mar. Freshw. Res.* 68, 1–21. doi: 10.1071/MF16335
- Ingle, S., Weis, D., and Frey, F. A. (2002). Indian continental crust recovered from Elan Bank, Kerguelen Plateau (ODP Leg 183, Site 1137). *J. Petrol.* 43, 1241–1257. doi: 10.1093/petrology/43.7.1241
- Jacquet, S. H. M., Dehairs, F., Lefèvre, D., Cavnaga, A. J., Planchon, F., Christaki, U., et al. (2015). Early spring mesopelagic carbon remineralization and transfer efficiency in the naturally iron-fertilized Kerguelen area. *Biogeosciences* 12, 1713–1731. doi: 10.5194/bg-12-1713-2015
- Jacquet, S. H. M., Dehairs, F., Savoye, N., Obernosterer, I., Christaki, U., Monnin, C., et al. (2008). Mesopelagic organic carbon remineralization in the Kerguelen Plateau region tracked by biogenic particulate Ba. *Deep-Sea Res. Part II*, 868–879. doi: 10.1016/j.dsr2.2007.12.038
- Jeandel, C., Arsouze, T., Lacan, F., Téchiné, P., and Dutay, J.-C. (2007). Isotopic Nd compositions and concentrations of the lithogenic inputs into the ocean: a compilation, with an emphasis on the margins. *Chem. Geol.* 239, 156–164. doi: 10.1016/j.chemgeo.2006.11.013
- Jeandel, C., Delattre, H., Grenier, M., Pradoux, C., and Lacan, F. (2013). Rare earth element concentrations and Nd isotopes in the South East Pacific Ocean. *Geochim. Geophys. Geosyst.* 14, 328–341. doi: 10.1029/2012GC004309
- Jeandel, C., Peucker-Ehrenbrink, B., Jones, M. T., Pearce, C. R., Oelkers, E. H., Godderis, Y., et al. (2011). Ocean margins: the missing term for oceanic element budgets? *Eos Trans. AGU* 92, 217–219. doi: 10.1029/2011EO260001
- Jeandel, C., Thouron, D., and Fieux, M. (1998). Concentrations and isotopic compositions of Nd in the Eastern Indian Ocean and Indonesian Straits. *Geochim. Cosmochim. Acta* 62, 2597–2607. doi: 10.1016/S0016-7037(98)00169-0
- Johnson, K. S., Chavez, F. P., and Friederich, G. E. (1999). Continental shelf sediments as a primary source of iron to coastal phytoplankton. *Nature* 398, 697–700.
- Jouandet, M.-P., Jackson, G. A., Carlotti, F., Picheral, M., Stemann, L., and Blain, S. (2014). Rapid formation of large aggregates during the spring bloom of Kerguelen Island: observations and model comparisons. *Biogeosciences* 11, 4393–4406. doi: 10.5194/bg-11-4393-2014
- Jouandet, M. P., Blain, S., Metzl, N., Brunet, C., Trull, T., and Obernosterer, I. (2008). A seasonal carbon budget for a naturally iron-fertilized bloom over the Kerguelen Plateau in the Southern Ocean. *Deep-Sea Research II* 55, 265–279. doi: 10.1016/j.dsr2.2007.12.037
- Kieffer, B., Arndt, N. T., and Weis, D. (2002). A bimodal alkaline shield volcano on Skiff Bank; its place in the evolution of the Kerguelen Plateau. *J. Petrol.* 43, 1259–1286. doi: 10.1093/petrology/43.7.1259
- Klinkhammer, G., Elderfield, H., and Hudson, A. (1983). Rare earth elements in seawater near hydrothermal vents. *Nature* 305, 185–188. doi: 10.1038/305185a0
- Korb, R. E., Whitehouse, M. J., and Ward, P. (2004). SeaWiFS in the southern ocean: spatial and temporal variability in phytoplankton biomass around South Georgia. *Deep Sea Res. Part II* 51, 99–116. doi: 10.1016/j.dsr2.2003.04.002
- Labatut, M., Lacan, F., Pradoux, C., Chmieleff, J., Radic, A., Murray, J. W., et al. (2014). Iron sources and dissolved particulate interactions in the seawater of the Western Equatorial Pacific, iron isotope perspectives. *Global Biogeochem. Cycles* 28, 1044–1065. doi: 10.1002/2014GB004928
- Lacan, F., and Jeandel, C. (2001). Tracing Papua New Guinea imprint on the central Equatorial Pacific Ocean using neodymium isotopic compositions and rare earth element patterns. *Earth Planet. Sci. Lett.* 186, 497–512. doi: 10.1016/S0012-821X(01)00263-1
- Lacan, F., and Jeandel, C. (2004). Subpolar mode water formation traced by neodymium isotopic composition. *Geophys. Res. Lett.* 31:L14306. doi: 10.1029/2004GL019747
- Lacan, F., and Jeandel, C. (2005). Neodymium isotopes as a new tool for quantifying exchange fluxes at the continent–ocean interface. *Earth Planet. Sci. Lett.* 232, 245–257. doi: 10.1016/j.epsl.2005.01.004
- Lasbleiz, M., Leblanc, K., Blain, S., Ras, J., Cornet-Barthaux, V., Hélias Nunige, S., et al. (2014). Pigments, elemental composition (C, N, P, and Si), and stoichiometry of particulate matter in the naturally iron fertilized region of Kerguelen in the Southern Ocean. *Biogeosciences* 11, 5931–5955. doi: 10.5194/bg-11-5931-2014
- Laurenceau-Cornec, E. C., Trull, T. W., Davies, D. M., Bray, S. G., Doran, J., Planchon, F., et al. (2015). The relative importance of phytoplankton aggregates and zooplankton fecal pellets to carbon export: insights from free-drifting sediment trap deployments in naturally iron-fertilised waters near the Kerguelen Plateau. *Biogeosciences* 12, 1007–1027. doi: 10.5194/bg-12-1007-2015
- Lefèvre, D., Guigue, C., and Obernosterer, I. (2008). The metabolic balance at two contrasting sites in the Southern Ocean: the iron-fertilized Kerguelen area and HNLC waters. *Deep-Sea Res. Part II* 55, 766–776. doi: 10.1016/j.dsr2.2007.12.006
- Lerche, D., and Nozaki, Y. (1998). Rare earth elements of sinking particulate matter in the Japan Trench. *Earth Planet. Sci. Lett.* 159, 71–86. doi: 10.1016/S0012-821X(98)00066-1
- Lo Monaco, C., Metzl, N., D'Ovidio, F., Lloret, J., and Ridame, C. (2014). Rapid establishment of the CO<sub>2</sub> sink associated with Kerguelen's bloom observed during the KEOPS2/OISO20 cruise. *Biogeosci. Discuss.* 11, 17543–17578. doi: 10.5194/bgd-11-17543-2014
- Martin, J. H. (1990). Glacial-interglacial CO<sub>2</sub> change: the iron hypothesis. *Paleoceanography* 5, 1–13.
- McLennan, S. M. (1989). "Rare earth elements in sedimentary rocks: influence of provenance and sedimentary processes. Geochemistry and Mineralogy of Rare Earth Elements," in *Reviews in Mineralogy*, Vol. 21, eds B. R. Lipin and G. H. Mckay (Washington, DC: Mineralogical Society of America), 170–200.
- McLennan, S. M. (1994). Rare earth element geochemistry and the tetrad effect. *Geochim. Cosmochim. Acta* 58, 2025–2033. doi: 10.1016/0016-7037(94)90282-8
- Measures, C. I., Brown, M. T., Selph, K. E., Apprill, A., Zhou, M., Hatta, M., et al. (2013). The influence of shelf processes in delivering dissolved iron to the HNLC waters of the Drake Passage, Antarctica. *Deep-Sea Res. Part II* 90, 77–88. doi: 10.1016/j.dsr2.2012.11.004
- Moffett, J. W. (1990). Microbially mediated cerium oxidation in seawater. *Nature* 345, 421–423. doi: 10.1038/345421a0
- Molina-Kescher, M., Frank, M., and Hathorne, E. (2014). South Pacific dissolved Nd isotope compositions and rare earth element distributions: water mass mixing versus biogeochemical cycling. *Geochim. Cosmochim. Acta* 127, 171–189. doi: 10.1016/j.gca.2013.11.038
- Molina-Kescher, M., Hathorne, E. C., Osborne, A. H., Behrens, M. K., Kölling, M., Pahnke, K., et al. (2018). The influence of Basaltic Islands on the Oceanic REE distribution: a case study from the Tropical South Pacific. *Front. Mar. Sci.* 5:50. doi: 10.3389/fmars.2018.00050
- Mongin, M., Molina, E., and Trull, T. W. (2008). Seasonality and scale of the Kerguelen plateau phytoplankton bloom: a remote sensing and modeling analysis of the influence of natural iron fertilization in the Southern Ocean. *Deep Sea Res. II* 55, 880–892. doi: 10.1016/j.dsr2.2007.12.039
- Monnin, C., Jeandel, C., Cattalio, T., and Dehairs, F. (1999). The marine barite saturation state of the world's oceans. *Mar. Chem.* 65, 253–261.
- Moore, J. K., and Abbott, M. R. (2002). Surface chlorophyll concentrations in relation to the Antarctic Polar Front: seasonal and spatial patterns from satellite observations. *J. Mar. Syst.* 37, 69–86. doi: 10.1016/S0924-7963(02)00196-3
- Mungall, J. E., and Martin, R. F. (1994). Severe leaching of trachytic glass without devitrification, Terceira, Azores. *Geochim. Cosmochim. Acta* 58, 75–83. doi: 10.1016/0016-7037(94)90447-2
- Nobre Silva, I. G., Weis, D., and Scoates, J. S. (2010). Effects of acid leaching on the Sr-Nd-Hf isotopic compositions of ocean island basalts. *Geochim. Geophys. Geosyst.* 11:Q09011. doi: 10.1029/2010GC003176

- Nozaki, Y., and Alibo, D. S. (2003). Importance of vertical geochemical processes in controlling the oceanic profiles of dissolved rare earth elements in the northeastern Indian Ocean. *Earth Planet. Sci. Lett.* 205, 155–172. doi: 10.1016/S0012-821X(02)01027-0
- Olivarez, A. M., and Owen, R. M. (1991). The europium anomaly of seawater: implications for fluvial versus hydrothermal REE inputs to the oceans. *Chem. Geol.* 92, 317–328.
- Osborne, A. H., Haley, B. A., Hathorne, E. C., Flögel, S., and Frank, M. (2014). Neodymium isotopes and concentrations in Caribbean seawater: tracing water mass mixing and continental input in a semi-enclosed ocean basin. *Earth Planet. Sci. Lett.* 406, 174–186. doi: 10.1016/j.epsl.2014.09.011
- Pahnke, K., van de Flierdt, T., Jones, K., Hemming, S. R., and Goldstein, S. L. (2012). GEOTRACES intercalibration of neodymium isotopes and rare earth element concentrations in seawater and particles—Part 2: systematic tests and baseline profiles. *Limnol Oceanogr. Methods* 10, 252–269. doi: 10.4319/lom.2012.10.252
- Park, Y.-H., Durand, I., Kestenare, E., Rougier, G., Zhou, M., d'Ovidio, F., et al. (2014). Polar Front around the Kerguelen Islands: an up-to-date determination and associated circulation of surface/subsurface waters. *J. Geophys. Res.* 119, 6575–6592. doi: 10.1002/2014JC010061
- Park, Y.-H., Roquet, F., Durand, I., and Fuda, J. L. (2008). Large-scale circulation over and around the Northern Kerguelen Plateau. *Deep Sea Res. Part II* 55, 566–581. doi: 10.1016/j.dsr2.2007.12.030
- Pearce, C. R., Jones, M. T., Oelkers, E. H., Jeandel, C., and Pradoux, C. (2013). The importance of particulate dissolution for the marine neodymium (Nd) isotope and Rare Earth Element (REE) budgets. *Earth Planet. Sci. Lett.* 369–370, 138–147. doi: 10.1016/j.epsl.2013.03.023
- Piegras, D. J., Wasserburg, G. J., and Dasch, E. J. (1979). The isotopic composition of Nd in different ocean masses. *Earth Planet. Sci. Lett.* 45, 223–236. doi: 10.1016/0012-821X(79)90125-0
- Pin, C., and Zalduendi, J. F. S. (1997). Sequential separation of light rare-earth elements, thorium and uranium by miniaturized extraction chromatography: application to isotopic analyses of silicate rocks. *Anal. Chim. Acta* 339, 79–89. doi: 10.1016/S0003-2670(96)00499-0
- Planchon, F., Ballas, D., Cavagna, A.-J., Bowie, A. R., Davies, D., Trull, T., et al. (2015). Carbon export in the naturally iron-fertilized Kerguelen area of the Southern Ocean based on the 234Th approach. *Biogeosciences* 12, 3831–3848. doi: 10.5194/bg-12-3831-2015
- Pollard, R., Sanders, R., Lucas, M., and Statham, P. (2007). The crozet natural iron bloom and export experiment (CROZEX). *Deep Sea Res. II* 54, 1905–1914. doi: 10.1016/j.dsr2.2007.07.023
- Quéroué, F., Sarthou, G., Planquette, H. F., Bucciarelli, E., Chever, F., van der Merwe, P., et al. (2015). High variability of dissolved iron concentrations in the vicinity of Kerguelen Islands (Southern Ocean). *Biogeosciences* 12, 3869–3883. doi: 10.5194/bg-12-3869-2015
- Radic, A., Lacan, F., and Murray, J. W. (2011). Isotopic composition of dissolved iron in the equatorial Pacific Ocean: new constraints for the oceanic iron cycle. *Earth Planet. Sci. Lett.* 306, 1–10. doi: 10.1016/j.epsl.2011.03.015
- Reisberg, L., Zindler, A., Marcantonio, F., White, W., Wyman, D., and Weaver, B. (1993). Os isotope systematics in ocean island basalts. *Earth Planet. Sci. Lett.* 120, 149–167. doi: 10.1016/0012-821X(93)90236-3
- Salters, V., and White, W. (1998). Hf isotope constraints on mantle evolution. *Chem. Geol.* 145, 447–460. doi: 10.1016/S0009-2541(97)00154-X
- Sanial, V., van Beek, P., Lansard, B., Souhaut, M., Kestenare, E., d'Ovidio, F., et al. (2015). Use of Ra isotopes to deduce rapid transfer of sediment-derived inputs off Kerguelen. *Biogeosciences* 12, 1415–1430. doi: 10.5194/bg-12-1415-2015
- Schmidt, R. A., Smith, R. H., Lasch, J. E., Mosen, A. W., Olehy, D. A., and Vasiljevshis, J. (1963). Abundances of fourteen rare-earth elements, scandium, and yttrium in meteoritic and terrigenous matter. *Geochim. Cosmochim. Acta* 27, 577–622. doi: 10.1016/0016-7037(63)90014-0
- Scoates, J. S., Weis, D., Franssens, M., Mattioli, N., Annel, H., Frey, F. A., et al. (2008). The Val Gabbro plutonic suite: a sub-volcanic intrusion emplaced at the end of flood basalt volcanism on the Kerguelen Archipelago. *J. Petrol.* 49, 79–105. doi: 10.1093/petrology/egm071
- Shabani, M. B., Akagi, T., and Masuda, A. (1992). Preconcentration of trace rare earth elements in seawater by complexation with (2-ethylhexyl) hydrogen phosphate and 2-ethylhexyl dihydrogen phosphate adsorbed on a C18 cartridge and determination by inductively coupled plasma mass spectrometry. *Anal. Chem.* 64, 737–743.
- Shiller, A. M., Chan, E. W., Joung, D. J., Redmond, M. C., and Kessler, J. D. (2017). Light rare earth element depletion during Deepwater Horizon blowout methanotrophy. *Sci. Rep.* 7:10389. doi: 10.1038/s41598-017-11060-z
- Sholkovitz, E. R., Elderfield, H., Szymczak, R., and Casey, K. (1999). Island weathering: river sources of rare earth elements to the Western Pacific Ocean. *Mar. Chem.* 68, 39–57. doi: 10.1016/S0304-4203(99)00064-X
- Sholkovitz, E. R., Landing, W. M., and Lewis, B. L. (1994). Ocean particle chemistry: the fractionation of rare earth elements between suspended particles and seawater. *Geochim. Cosmochim. Acta* 58, 1567–1580. doi: 10.1016/0016-7037(94)90559-2
- Siddall, M., Khattiwala, S., van de Flierdt, T., Jones, K., Goldstein, S. L., Hemming, S., et al. (2008). Towards explaining the Nd paradox using reversible scavenging in an ocean general circulation model. *Earth Planet. Sci. Lett.* 274, 448–461. doi: 10.1016/j.epsl.2008.07.044
- Stichel, T., Frank, M., Rickli, J., and Haley, B. A. (2012). The hafnium and neodymium isotope composition of seawater in the Atlantic sector of the Southern Ocean. *Earth Planet. Sci. Lett.* 317–318, 282–294. doi: 10.1016/j.epsl.2011.11.025
- Storey, M., Saunders, A. D., Tarney, J., Leat, P., Thirlwall, M. F., Thompson, R. N., et al. (1988). Geochemical evidence for plume–mantle interactions beneath Kerguelen and Heard Islands, Indian Ocean. *Nature* 336, 371–374. doi: 10.1038/336371a0
- Strady, E., Kim, I., Radakovitch, O., and Kim, G., (2015). Rare earth element distributions and fractionation in plankton from the northwestern Mediterranean Sea. *Chemosphere* 119, 72–82. doi: 10.1016/j.chemosphere.2014.05.049
- Stroobants, N., Dehairs, F., Goeyens, L., Vanderheijden, N., and van Grieken, R. (1991). Barite formation in the Southern Ocean water column. *Mar. Chem.* 35, 411–421. doi: 10.1016/S0304-4203(09)90033-0
- Tachikawa, K., Athias, V., and Jeandel, C. (2003). Neodymium budget in the modern ocean and paleo-oceanographic implications. *J. Geophys. Res.* 108:3254. doi: 10.1029/1999JC000285
- Tachikawa, K., Jeandel, C., and Roy-Barman, M. (1999a). A new approach to the Nd residence time in the ocean: role of atmospheric input. *Earth Planet. Sci. Lett.* 170, 433–446.
- Tachikawa, K., Jeandel, C., Vangriesheim, A., and Dupré, B. (1999b). Distribution of rare earth elements and neodymium isotopes in suspended particles of the Tropical Atlantic Ocean (EUMELI site). *Deep-Sea Res. I* 46, 733–756.
- Tachikawa, K., Roy-Barman, M., Michard, A., Thouvenot, D., Yeghicheyan, D., and Jeandel, C. (2004). Neodymium isotopes in the Mediterranean Sea: comparison between seawater and sediment signals. *Geochim. Cosmochim. Acta* 68, 3095–3106. doi: 10.1016/j.gca.2004.01.024
- Tagliabue, A., Bopp, L., and Aumont, O. (2009). Evaluating the importance of atmospheric and sedimentary iron sources to Southern Ocean iron biogeochemistry. *Geophys. Res. Lett.* 36:L13601. doi: 10.1029/2009gl038914
- Tagliabue, A., Sallée, J.-B., Bowie, A. R., Lévy, M., Swart, S., and Boyd, P. W. (2014). Surface-water iron supplies in the Southern Ocean sustained by deep winter mixing. *Nat. Geosci.* 7, 314–320. doi: 10.1038/ngeo2101
- Tarling, G. A., Stowasser, G., Ward, P., Poulton, A. J., Zhou, M., Venables, H. J., et al. (2012). Seasonal trophic structure of the Scotia Sea pelagic ecosystem considered through biomass spectra and stable isotope analysis. *Deep-Sea Res. Pt. II* 59–60, 222–236. doi: 10.1016/j.dsr2.2011.07.002
- Trull, T. W., Davies, D. M., Dehairs, F., Cavagna, A.-J., Lasbleiz, M., Laurenceau-Cornec, E. C., et al. (2015). Chemometric perspectives on plankton community responses to natural iron fertilisation over and downstream of the Kerguelen Plateau in the Southern Ocean. *Biogeosciences* 12, 1029–1056. doi: 10.5194/bg-12-1029-2015
- van Beek, P., Bourquin, M., Reyss, J.-L., Souhaut, M., Charette, M. A., and Jeandel, C. (2008). Radium isotopes to investigate the water mass pathways on the Kerguelen Plateau (Southern Ocean). *Deep Sea Res. Pt. II* 55, 622–637. doi: 10.1016/j.dsr2.2007.12.025
- van Beek, P., Francois, R., Conte, M., Reyss, J.-L., Souhaut, M., and Charette, M. (2007). 228Ra/226Ra and 226Ra/Ba ratios to track barite formation and transport in the water column. *Geochim. Cosmochim. Acta* 71, 71–86. doi: 10.1016/j.gca.2006.07.041

- van de Flierdt, T., Pahnke, K., Andersson, P., Basak, C., Coles, B., Colin, C., et al. (2012). GEOTRACES intercalibration of neodymium isotopes and rare earth element concentrations in seawater and suspended particles. Part 1: reproducibility of results for the international intercomparison. *Limnol. Oceanogr. Methods* 10, 234–251. doi: 10.4319/lom.2012.10.234
- van der Merwe, P., Bowie, A. R., Quéroué, F., Armand, L., Blain, S., Chever, F., et al. (2015). Sourcing the iron in the naturally fertilised bloom around the Kerguelen Plateau: particulate trace metal dynamics. *Biogeosciences* 12, 739–755. doi: 10.5194/bg-12-739-2015
- Wasserburg, G. J., Jacobsen, S. B., De Paolo, D. L., McCulloch, M. T., and Wen, T. (1981). Precise determination of Sm/Nd ratios, Sm and Nd isotopic abundances in standard solutions. *Geochim. Cosmochim. Acta* 45, 2311–2323.
- Weis, D., and Frey, F. A. (2002). Submarine basalts of the Northern Kerguelen Plateau: interaction between the Kerguelen plume and the Southeast Indian Ridge revealed at ODP Site 1140. *J. Petrol.* 43, 1287–1309. doi: 10.1093/ptrology/43.7.1287
- Weis, D., Frey, F. A., Giret, A., and Cantagrel, J. M. (1998). Geochemical characteristics of the youngest volcano (Mount Ross) in the Kerguelen Archipelago: inferences for magma flux and composition of the Kerguelen Plume. *J. Petrol.* 39, 973–994. doi: 10.1093/ptrology/39.5.973
- Weis, D., Frey, F. A., Leyrit, H., and Gautier, I. (1993). Kerguelen Archipelago revisited: geochemical and isotopic study of the SE Province lavas. *Earth Planet. Sci. Lett.* 118, 101–119.
- Weis, D., Frey, F. A., Schlich, R., Schaming, M., Montigny, R., Damasceno, D., et al. (2002). Trace of the Kerguelen mantle plume: evidence from seamounts between the Kerguelen Archipelago and Heard Island, Indian Ocean. *Geochim. Geophys. Geosyst.* 3, 1–27. doi: 10.1029/2001GC000251
- Weis, D., and Giret, A. (1994). Kerguelen plutonic complexes: Sr, Nd, Pb isotopic study and inferences about their sources, age and geodynamic setting. *Geol. Geochim. Geophys.* 166, 47–59.
- White, W. M., and Hofmann, A. W. (1982). Sr and Nd isotope geochemistry of oceanic basalts and mantle evolution. *Nature* 296, 821–825. doi: 10.1038/296821a0
- Xu, G., Frey, F. A., Weis, D., Scoates, J. S., and Giret, A. (2007). Flood basalts from Mt. Capitole in the central Kerguelen Archipelago: Insights into the growth of the archipelago and source components contributing to plume-related volcanism. *Geochim. Geophys. Geosyst.* 8:Q06007. doi: 10.1029/2007gc001608
- Yang, H.-Y., Frey, F. A., Weis, D., Giret, A., Pyle, D., and Michon, G. (1998). Petrogenesis of the flood basalts forming the Northern Kerguelen Archipelago: implications for the Kerguelen Plume. *J. Petrol.* 39, 711–748. doi: 10.1093/ptrology/39.4.711
- Zhang, Y., Lacan, F., and Jeandel, C. (2008). Dissolved rare earth elements tracing lithogenic inputs over the Kerguelen Plateau (Southern Ocean). *Deep Sea Res. Pt. II* 55, 638–652. doi: 10.1016/j.dsr2.2007.12.029
- Zhou, M., Zhu, Y., d'Ovidio, F., Park, Y.-H., Durand, I., Kestenare, E., et al. and Blain, S. (2014). Surface currents and upwelling in Kerguelen Plateau regions. *Biogeosci. Discuss.* 11, 6845–6876. doi: 10.5194/bgd-11-6845-2014

**Conflict of Interest Statement:** The authors declare that the research was conducted in the absence of any commercial or financial relationships that could be construed as a potential conflict of interest.

**Citation:** Grenier M, Garcia-Solsona E, Lemaitre N, Trull TW, Bouvier V, Nonnotte P, van Beek P, Souhaut M, Lacan F and Jeandel C (2018) Differentiating Lithogenic Supplies, Water Mass Transport, and Biological Processes On and Off the Kerguelen Plateau Using Rare Earth Element Concentrations and Neodymium Isotopic Compositions. *Front. Mar. Sci.* 5:426. doi: 10.3389/fmars.2018.00426

Copyright © 2018 Grenier, Garcia-Solsona, Lemaitre, Trull, Bouvier, Nonnotte, van Beek, Souhaut, Lacan and Jeandel. This is an open-access article distributed under the terms of the Creative Commons Attribution License (CC BY). The use, distribution or reproduction in other forums is permitted, provided the original author(s) and the copyright owner(s) are credited and that the original publication in this journal is cited, in accordance with accepted academic practice. No use, distribution or reproduction is permitted which does not comply with these terms.



# Advantages of publishing in Frontiers



## OPEN ACCESS

Articles are free to read  
for greatest visibility  
and readership



## FAST PUBLICATION

Around 90 days  
from submission  
to decision



## HIGH QUALITY PEER-REVIEW

Rigorous, collaborative,  
and constructive  
peer-review



## TRANSPARENT PEER-REVIEW

Editors and reviewers  
acknowledged by name  
on published articles

## Frontiers

Avenue du Tribunal-Fédéral 34  
1005 Lausanne | Switzerland

**Visit us:** [www.frontiersin.org](http://www.frontiersin.org)

**Contact us:** [info@frontiersin.org](mailto:info@frontiersin.org) | +41 21 510 17 00



## REPRODUCIBILITY OF RESEARCH

Support open data  
and methods to enhance  
research reproducibility



## DIGITAL PUBLISHING

Articles designed  
for optimal readership  
across devices



## FOLLOW US

[@frontiersin](https://twitter.com/frontiersin)



## IMPACT METRICS

Advanced article metrics  
track visibility across  
digital media



## EXTENSIVE PROMOTION

Marketing  
and promotion  
of impactful research



## LOOP RESEARCH NETWORK

Our network  
increases your  
article's readership